On the Failure of Total Ankle Replacement:
A Retrieval Analysis

Ashley Alexander Stratton-Powell

Submitted in accordance with the requirements for the degree of
Doctor of Philosophy

The University of Leeds
School of Mechanical Engineering

February 2018

The candidate confirms that the work submitted is his own and that appropriate credit has been given where reference has been made to the work of others.

This copy has been supplied on the understanding that it is copyright material and that no quotation from the thesis may be published without proper acknowledgement.

Dedicated to Zena Stratton

Himinninn er að hrynja,
en stjörnurnar fara þér vel.

Acknowledgements

First and foremost, thank you to Dr Claire Brockett, my primary supervisor. Claire's empathy, perspicacity and humility made seemingly impenetrable dilemmas appear insignificant. I admire the dedication she has to each of her students and feel fortunate to have been one of them.

I would also like to thank my entire supervisory team: Professor Anthony Redmond, Dr Sophie Williams and Professor Joanne Tipper. Their advice was invaluable and their commitment to academic freedom was fundamental to my development and success.

I will cherish the time I spent with my fellow PhD students who infused humour, art and thoughtful debate into our perpetual study breaks. A special thanks to Dr Robert Cooper in particular, he was an unreasonably generous sidekick; parting is such sweet sorrow.

I would like to express my deepest gratitude to the research participants and clinical care teams whose engagement with this project was fundamental to its completion. I am also thankful to the Engineering and Physical Sciences Research Council (EPSRC) for funding the research and supporting me financially.

Finally, thank you to Hilary and Dave Stratton-Powell, my beloved parents, whose unfaltering support and optimism kept me grounded, focused and cheerful in the face of adversity.

Abstract

Total ankle replacement (TAR) has been under development for 40 years but is not considered as successful as other lower limb total joint replacements (TJR). The failure rate of TAR is more than double that of total hip replacement at 10 years, yet the failure mechanisms remain largely unknown. The research in this thesis aimed to identify the wear modes and possible origins of failure for a cohort of failed TARs using a retrieval analysis approach.

Explants, medical imaging and periprosthetic tissue samples were retrieved for 44 participants following revision TAR surgery. Five TAR brands were retrieved, all of which were uncemented, three-component, mobile-bearing designs. Each resource was investigated using established and novel retrieval analysis methods including, but not limited to: photogrammetry, microscopy, non-contacting 3D surface profilometry, computed tomography and wear particle isolation.

Ballooning osteolysis was highly prevalent. Component alignment was within alignment variations considered acceptable in the published literature, yet high rates of edge-loading (70.5%) and impingement (57%) were evident. Fixation and bearing surface wear affected 98% of tibial components. The volumetric wear rate for eight bearing inserts was 2.5 times higher than the greatest wear rate reported by in-vitro simulation studies. Hydroxyapatite wear particles were micron-sized with a high aspect ratio (AR = 3.7). Flake-like micron-sized cobalt chromium alloy and large titanium wear particles (>10 μm) were also isolated and characterised. The total wear particle population for TAR was generally larger and more elongated than the wear particle characteristics identified for other TJRs.

Edge-loading, bearing insert subluxation and impingement contributed to wear modes 2, 3 and 4, which indicate device dysfunction and should be minimised by design. Mobile-bearing constraint, cortical window surgical approach and the rapid accrual of wear particles may be important contributors to the failure of TAR.

Table of Contents

List of Tables

List of Figures

Abbreviations

AOR	Antero-posterior offset ratio
CAD	Computer aided design
CoCr	Cobalt chromium alloy
CoP	Ceramic-on-polyethylene
CPTi	Commercially pure titanium
CT	Computed tomography
DMS	Damage mode score
ECD	Equivalent circle diameter
EDX	Energy dispersive X-ray analysis
FDA	Food and Drugs Administration
HA	Hydroxyapatite
KOH	Potassium hydroxide
MC-SWD	Metal and Ceramic Silicon Wafer Display
MoP	Metal-on-polyethylene
MOR	Medio-lateral offset ratio
NaOH	Sodium hydroxide
NJR	National Joint Registry
OA	Osteoarthritis
SDS	Sodium dodecyl sulphate
SEM	Scanning electron microscopy
SPT	Sodium polytungstate
SWD	Silicon Wafer Display
TAR	Total ankle replacement
THR	Total hip replacement
TiN	Titanium nitride
TKR	Total knee replacement
UHMWPE	Ultra high molecular weight polyethylene

Chapter 1
Introduction

1.1   **Introduction**

Ankle osteoarthritis (OA) is a debilitating chronic syndrome and develops after traumatic ankle injuries for the majority of cases. Ankle OA causes approximately 29,000 referrals to foot and ankle specialists in the UK annually, of which 3,000 are treated surgically.

Total ankle replacement (TAR) is a motion-restoring procedure used to treat deterioration of the ankle joint. This surgical option offers the potential to recover natural ankle biomechanics but is expensive and complex. The simpler, less expensive and more popular treatment is ankle arthrodesis (or fusion) but is motion-restricting. Despite the potential benefits of a motion-restoring therapy, currently both TAR and arthrodesis are considered to have equivalent clinical outcomes.

Over the 40 year development of TAR, many attempts have been made to produce a reliable design that can endure 10 years in-vivo with failure rates comparable to that of total hip replacement (THR). In the UK, the failure rate of TAR at five years is higher than that of THR at 10 years.

The early development of osteolysis is a commonly reported indication for revision TAR surgery, yet, the pathogenesis of osteolysis in TAR remains to be elucidated. Device malalignment, inadequate fixation, and excessive wear debris production have been suggested to be important contributors to the development of osteolysis, but the scientific investigation of such phenomenon is still in its infancy.

Post-marketing surveillance and retrieval analyses include: (1) medical imaging review, (2) explant analysis, and; (3) histological investigation and are an essential aspect of any medical device performance review. Integrating the results from these three resources for TAR may offer an insight into the type, extent and location of wear generated by TAR and its potential effect on the surrounding biological environment.

Retrieval analysis has not been extensively used for TAR, in fact, only four studies using this approach have been published. The research in this thesis focuses on the function and failure of TAR from an engineering perspective, using a retrieval analysis approach.

1.2   Rationale, Aims and Objectives

The function and failure of total ankle replacement has not been analysed in the context of the established wear modes of total joint replacement (McKellop, 2007). Mode 1 wear is the articulation between the primary bearing surfaces as intended by the manufacturer. Wear modes 2 (non-bearing on bearing contact), 3 (third body abrasion), and 4 (non-bearing on non-bearing contact) represent device dysfunction and should be avoided by design. There are seemingly two possible outcomes for TAR during failure:

1) The TAR device functioned as intended with mode 1 wear but failed due to excessive primary bearing wear or a reason unrelated to the device itself. For example, problems with wound care, infection or nerve tissue damage.

2) The TAR device did not function as intended having undergone wear modes 2, 3 and/or 4. The evidence of which may be present on the device surfaces, in the surrounding tissue or identified by medical imaging.

Medical imaging review, explant analysis and histological investigation may aid the identification of wear modes and offer a more specific understanding of the origin of TAR failure.

The research in this thesis aimed to:

- Determine possible wear modes and origins of failure for a cohort of failed TARs using a retrieval analysis approach.

The objectives of the research in this thesis were:

I.   Characterise TAR device orientation and the geometry of the surrounding bony anatomy (including pathology) from medical imaging for a cohort of failed TARs.

II.   Characterise the type, extent and severity of damage/wear modes present on the components of failed TARs.

III.   Isolate wear particles from periprosthetic tissue surrounding failed TARs and characterise their composition, size and morphology.

1.3   Thesis Overview
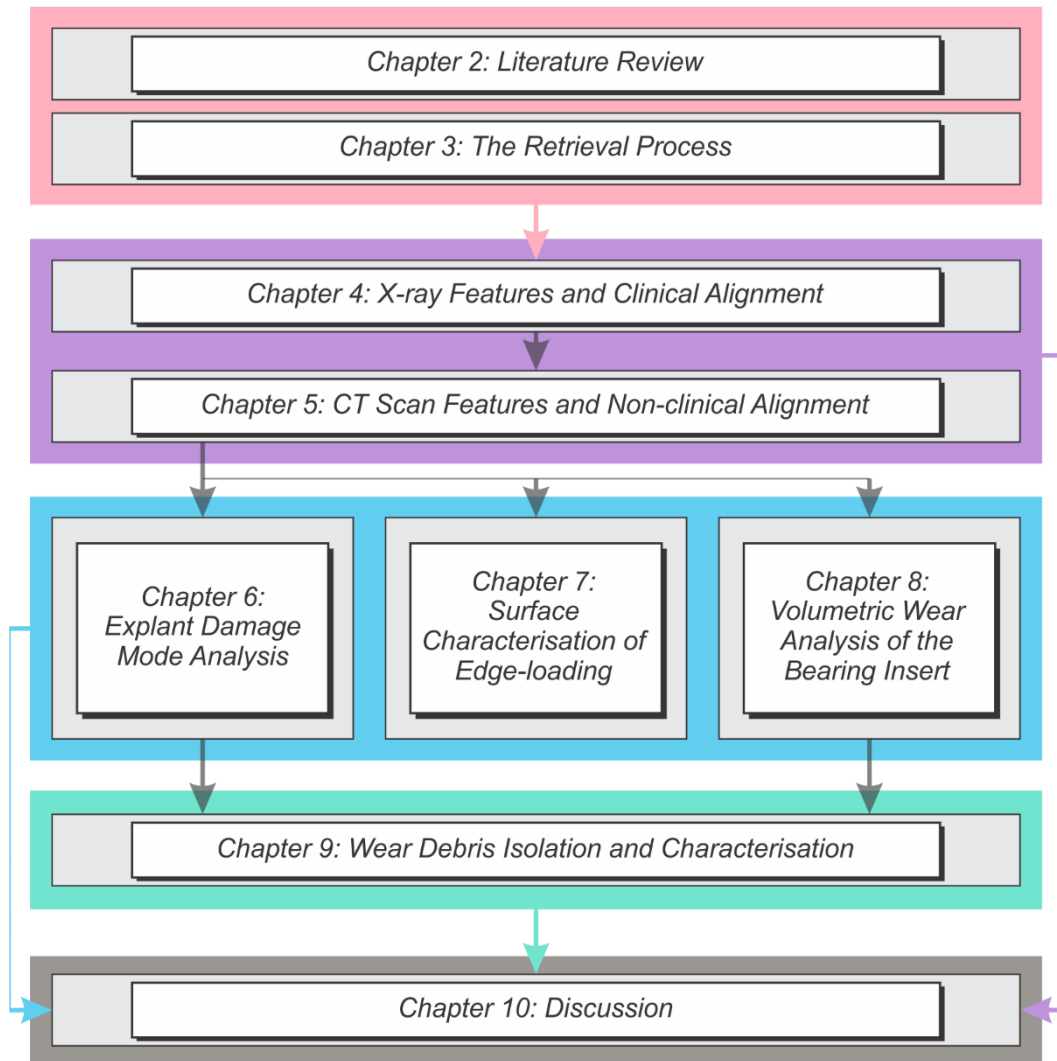
Figure 1.1. Thesis overview. Three resources were retrieved and analysed: medical imaging (purple), explants (blue) and tissue samples (green). In Chapter 2, the previously published literature relevant to the design principles, performance and failure mechanisms of TAR is highlighted. In Chapter 3, the retrieval programme and processes are detailed. Demographics of the research participants are outlined and the retrieved TAR brands are described. In Chapter 4, metallic component alignment determined using standard clinical measurements from X-ray imaging is assessed. In Chapter 5, the process of segmenting TAR components and the surrounding anatomy is detailed. Non-clinical measurements of component alignment and osteolysis volume are reported. In Chapter 6, a damage mode analysis for each TAR component is described. Photogrammetry and microscopy was used to determine the type, extent and location of damage modes. In Chapter 7, the prevalence of edge-loading and its effect on the superior surface of the bearing insert was quantified using non-contacting 3D surface profilometry. In Chapter 8, the volumetric wear loss for eight 5 mm AES (2nd Gen) bearing inserts is reported. Three methods for determining volume were used including: gravimetric analysis, pycnometry and computed tomography. In Chapter 9, a novel modified wear particle isolation method and its development is described. This method was successfully used to extract wear particles of differing composition from periprosthetic tissue surrounding TAR. In Chapter 10, the wear modes and possible origins of TAR failure are discussed.

Chapter 2
Literature Review

2.1 Clinical Need

Osteoarthritis (OA) is a debilitating chronic syndrome with symptoms including joint dysfunction and pain (Reginster, 2002, Buckwalter et al., 2004). Once developed, OA increases in severity throughout the person's lifetime and has thus become a substantial burden for healthcare systems worldwide (Reginster, 2002, Buckwalter et al., 2004). In the UK, ankle OA leads to approximately 29,000 referrals to foot and ankle specialists annually, 3,000 of which are treated surgically (Goldberg et al., 2012).

Primary OA is typically idiopathic, associated with aging and occurs predominantly in hip and knee joints (Egloff et al., 2012). In the ankle, the origin of OA is different to hips and knees for majority of OA cases (~70%) and is typically a product of prior traumatic ankle injury, also known as post-traumatic OA (Saltzman et al., 2005). Prior ankle trauma, such as pilon fracture and ankle sprain, facilitate the development of joint incongruency and instability which are suggested to contribute to the formation of OA (Anderson et al., 2011, Egloff et al., 2012). Kinematic and kinetic changes in the ankle are caused by the disease (Valderrabano et al., 2007a, Valderrabano et al., 2007b, Philippe et al., 2008, Ingrosso et al., 2009). These pathological changes result in a restricted range of movement (Valderrabano et al., 2007b) and exacerbated disease severity (Tochigi et al., 2005, McKinley et al., 2006). The mental and physical disability suffered by patients with ankle OA is equally as severe as patients who suffer hip OA (Glazebrook et al., 2008).

If OA is diagnosed early enough, conservative therapies such as glucosamine sulphate and viscosupplementation may be used (Bloch et al., 2015). Although, the quality of evidence supporting such treatments is variable (Migliore et al., 2011, Chang et al., 2013). Alternatively, minimally-invasive procedures such as osteotomies and ligament lengthening can be used effectively to re-establish congruency and stability (Pagenstert et al., 2007, Barg and Saltzman, 2014). If the early opportunity is missed however, realignment interventions may not be suitable for end-stage OA patients (Pagenstert et al., 2007). Arthrodesis and total ankle replacement are the penultimate options before amputation is considered.

2.2 Ankle Arthrodesis

Ankle arthrodesis (or fusion) is a motion-restricting intervention that relies on internal (e.g. screws, dowel bone grafts) or external (e.g. metal plates, cast immobilisation) compression across the joint to eliminate articulation (Charnley, 1951) (Figure 2.1).

Figure 2.1. Screw fixation ankle arthrodesis. Adopted from Cottino et al. (2012).

In 2010, ankle arthrodesis was performed over six times more frequently than total ankle replacement in the US (Raikin et al., 2013). Functional improvements are perceived by the patient (Flavin et al., 2013, Singer et al., 2013) which has contributed to the popularity of ankle fusion. However, reoperation rates remain relatively high, one group reporting 19% at 11 years follow-up for 440 patients (Chalayon et al., 2015).

Functional improvement after fusion surgery is not comparable to a healthy person (Flavin et al., 2013, Singer et al., 2013), which is unsurprising given fusion by definition is motion-restricting. In comparison, the motion-preserving alternative total ankle replacement, has the prospect of enabling pain relief without functional limitation; a 'forgotten joint' (Behrend et al., 2012).

2.3 Total Ankle Replacement

Total ankle replacement (TAR) aims to restore motion, improve gait biomechanics relative to arthrodesis and provide analgesia (Valderrabano et al., 2007b, Saltzman et al., 2009, Brodsky et al., 2011, Hintermann et al., 2012). Unlike ankle arthrodesis, which fixes the ankle joint articulation, the TAR procedure exchanges the articulating cartilage lining of the distal tibia and talar trochlea with a TAR device (Figure 2.2).
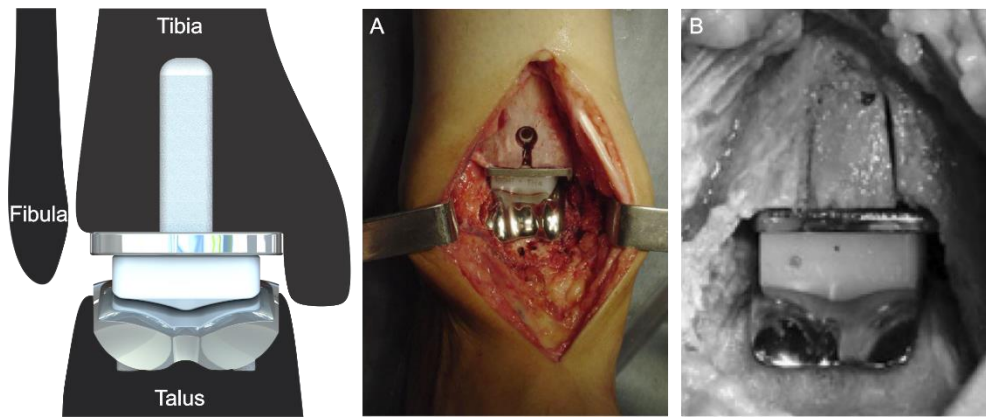
Figure 2.2. Anterior surgical approach with an implanted (A) Salto TAR adopted from Rodrigues-Pinto et al. (2013), and; (B) Buechel Pappas TAR adopted from Buechel (2008).

Despite 40 years of development, it is unknown which treatment, TAR or arthrodesis, is safer and/or more efficacious. The first randomised controlled trial comparing clinical outcomes between TAR and arthrodesis is currently underway in the UK (Goldberg et al., 2016). This trial is using a commercially available mobile-bearing device in the TAR trial arm, however more than 57 TAR devices have been developed for clinical use (Roukis and Prissel, 2013). Consensus is yet to be reached on many design aspects of TAR design, which is evident by the varied approaches taken throughout the technology's history and development.

2.3.1   Design Principles

In an attempt to replicate the success of the total hip replacement, the first of an influx of 1st generation TARs was developed in the 1970's (Lord and Marotte, 1979, Jamal et al., 2014). This device featured a long metallic stem which was implanted into the tibia and articulated with a cup cemented to the calcaneus, after the talus had been removed. The earliest TARs resembled 'reverse' THRs and were shortly discontinued due to unsatisfactory results (Gougoulias and Maffulli, 2013). Since these early failures, and throughout the chronology of TAR development, several design principles have been considered for TAR design, including: device constraint, device geometry, surgical approach, implant fixation and wear properties.

2.3.1.1   Mobile or Fixed Bearing Design?

Design constraint differs between mobile and fixed-bearing TAR designs. Both design types typically feature three components, however fixed-bearing designs require two of the components to be locked together to create one primary articulation. For mobile-bearing designs, the three components are independent of each other, resulting in two primary articulations. Fixed-bearing devices offer greater stability within the joint and a

highly conforming articulation which theoretically leads to improved wear characteristics. Whereas mobile-bearing designs sacrifice stability for less constrained motion.

The first mobile bearing TAR design was used in 1978 and featured a floating polyethylene bearing the device was called the Low Contact Stress (LCS) TAR (Buechel et al., 1988). LCS TAR featured a congruent talar bearing designed to decrease contact stresses by increasing contact area, a feature that would later be included in the 3rd generation Buechel-Pappas (BP) TAR (Endotec, USA). The BP TAR was a recognisable design emulated by other device manufacturers (Buechel et al., 2004). The BP, Mobility (DePuy, UK) and Ankle Evolutive System (AES) (Transystem, FR) TARs all shared common design features: three-component, semi-constrained, cementless fixation and a singular tibial stem. These were almost indistinguishable to the untrained eye and followed a similar design rationale. European enthusiasm for the BP-type design was high (Roukis and Prissel, 2013) but the success rate was poor. In one study, 31% of patients with the Mobility TAR suffered reoperation after a mean time of 14 months (Summers and Bedi, 2013). The BP, AES and Mobility TARs were all withdrawn from the commercial market by their respective manufacturers (Figure 2.3).
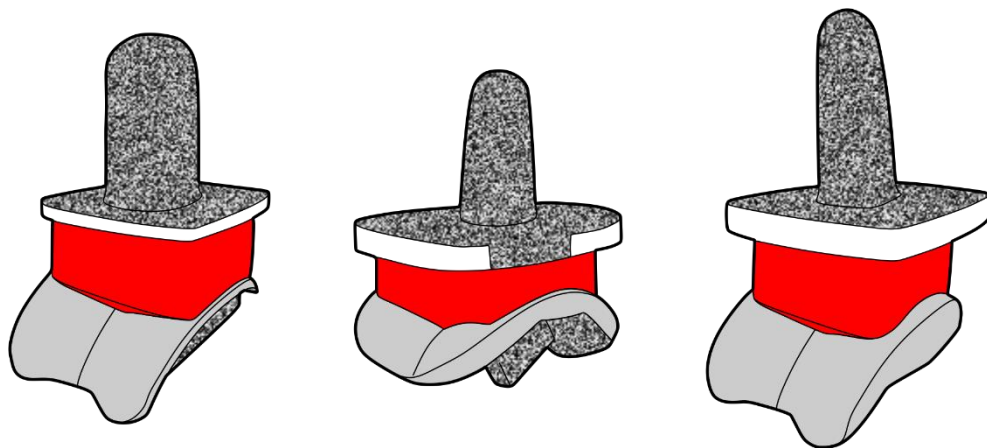
Figure 2.3. Buechel Pappas (BP)-type TAR examples. Each TAR has three components and is mobile bearing, semi-constrained, has a stemmed tibial component and is implanted using the anterior approach. Buechel Pappas (BP) TAR (left), Mobility TAR (centre), and; Ankle Evolutive System (AES) TAR (right). Red denotes the bearing insert.

Other mobile-bearing TAR designs were also popular, such as the Scandinavian Total Ankle Replacement (STAR; Small Bone Innovations, USA) (Anderson et al., 2004). The STAR was the first mobile-bearing device to acquire US Food and Drugs Administration (FDA) approval and featured cylindrical bars for the tibial fixation instead of a central stem. This was emulated by the Bologna-Oxford (BOX) TAR (MATOrtho Ltd, UK) and Salto TAR (Tornier, FR) which also featured cylindrical bars for tibial fixation (Figure 2.4).
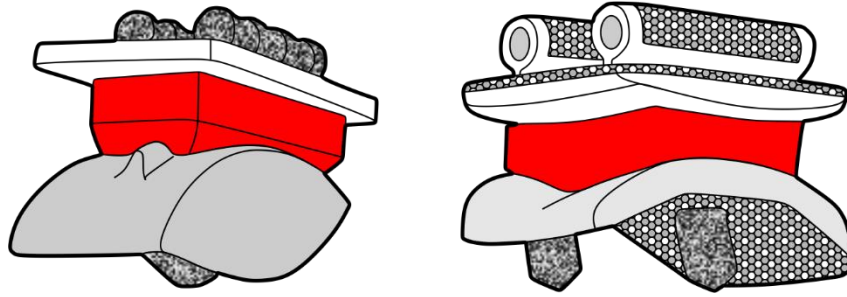
Figure 2.4. Mobile-bearing TAR examples. Scandinavian TAR (STAR) (left) and Bologna-Oxford (BOX) TAR (right). Red denotes the bearing insert.

Since 1982, mobile-bearing TARs have been considered more risky than fixed bearing devices in the US which is reflected in their classification system (Food and Drugs Administration, 1982). Mobile bearing devices are class III devices whereas fixed bearing TARs are class II. Fixed-bearing designs require a less rigorous pathway to market and as a result, there are less mobile-bearing TARs available in the US (Roukis and Prissel, 2013). The Agility TAR (DePuy, USA), a two component constrained device, initially suffered high rates of failure possibly caused by high stresses being transferred to the implant-bone interface (Alvine, 2002). To mitigate this, later iterations included a larger talar component to disperse forces (Alvine, 2002). Implant failure was 15.8% in 234 devices after a mean 6.6 year follow-up (Gougoulias et al., 2010). The Inbone Total Ankle System (Wright Medical, UK) is an alternative fixed bearing device that features a modular stem and an innovative surgical approach; the approach being from the plantar axial surface of the foot as opposed to being at the joint level in the coronal or sagittal plane. This device only accounted for 8.1% of the TARs implanted in 2016 in the UK (National Joint Registry, 2017). Enthusiasm for fixed-bearing TAR devices has increased in the past few years. The fixed-bearing Infinity TAR accounted for 30.1% of TARs implanted in 2016 in the UK, which was double the number implanted from 2015 (National Joint Registry, 2017) (Figure 2.5).
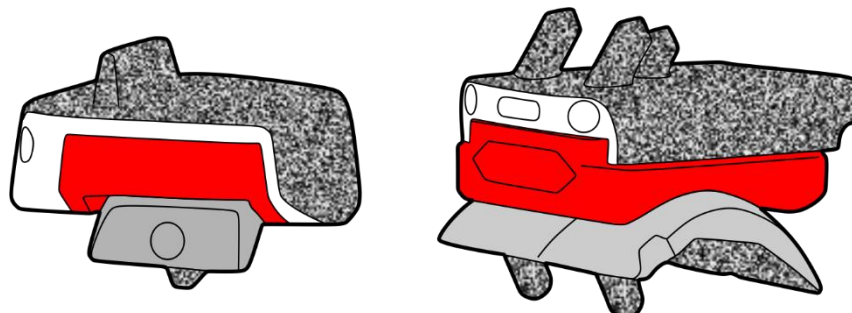
Figure 2.5. Fixed-bearing TAR examples. Agility TAR (Left) and Infinity TAR (Right). Red denotes the bearing component which for these designs is attached to the tibial component.

2.3.1.2 'Anatomical' or Non-anatomical Design?

The geometry of TAR devices have been marketed as 'anatomical' or 'non-anatomical'. Anatomical devices attempt to replicate the natural ankle anatomy whereas non-anatomical designs tend to be symmetrical in the coronal plane and feature talar components with a constant radii.

The ankle joint was once considered to be a one-degree of freedom joint featuring a fixed axis of rotation (Close and Inman, 1952, Close, 1956, Inman, 1976). Cadaveric measurements suggested the trochlear surface was best represented as a frustum of a cone. The apex of the cone lay medially with the major axis of the cone being a line connecting the tips of the lateral and medial malleolus (Close and Inman, 1952, Inman, 1976). This description of ankle joint anatomy had been refuted by many studies (Barnett and Napier, 1952, Hicks, 1953, Sammarco, 1977, Siegler et al., 1988, Lundberg et al., 1989) but despite this, several total ankle replacement designs integrated the idea of a truncated cone with its apex directed medially into its geometry (Hintermann et al., 2004).

The most recent refutation of the research completed by Close and Inman (1952) was by Siegler et al. (2014) who scanned 26 healthy ankles using computed tomography. From these scans, the talus was segmented, 3D renderings created and geometric measurements calculated. The medial talar facet was found to feature a significantly larger radii (~ 4 mm) than the lateral talar facet (Figure 2.6). Therefore, the apex of the cone was directed laterally, the inverse of what was previously suggested by the seminal works of Close and Inman (1952).
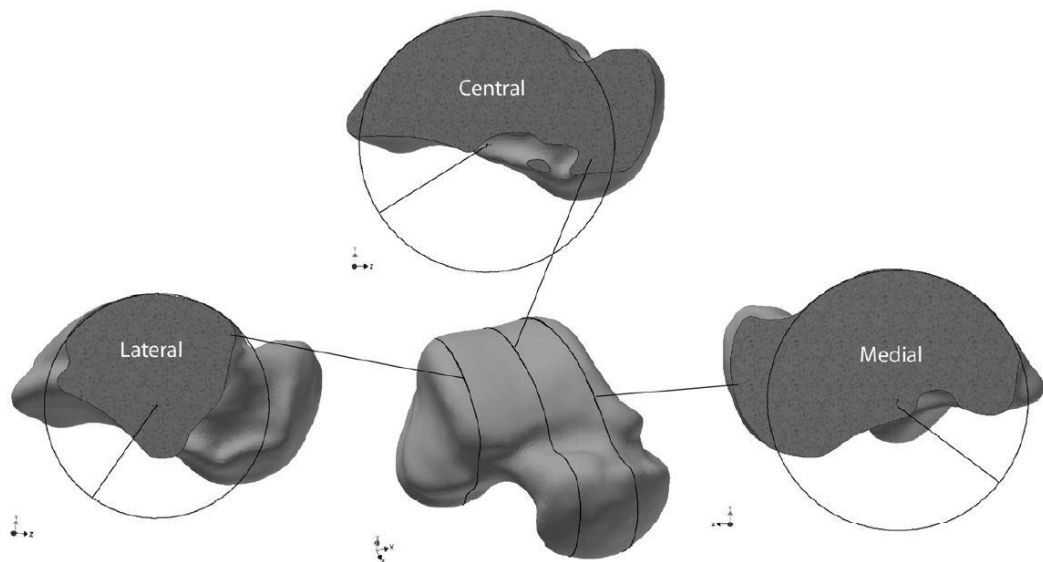
Figure 2.6. Geometry of the talus determined using computed tomography renderings. Note the lateral aspect has a smaller radii than the medial aspect. Adopted from Siegler et al. (2014).

Since the publication of the research by Siegler et al. (2014), the Cadence TAR (Integra Lifesciences, USA), another total ankle replacement design featuring the assumptions used by Close and Inman (1952) was been released into the market (Figure 2.7). 'Anatomical' TAR designs currently do not accurately represent the geometry of the talus currently accepted in the scientific literature.
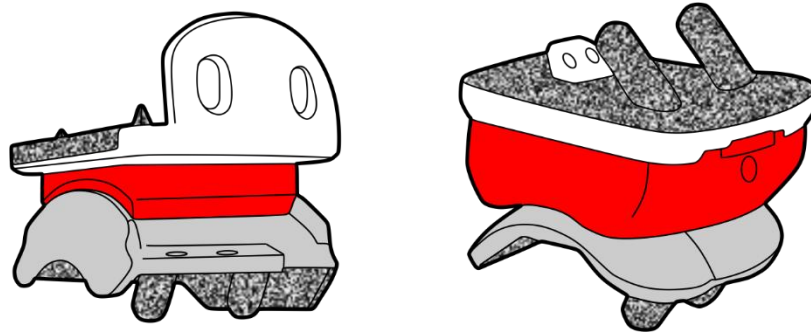
Figure 2.7. Hintegra TAR (Left) was the predicate to the Cadence TAR (right). Both design types are marketed as 'anatomical', yet neither device feature a greater radii for the medial aspect of the talar component rather than the lateral aspect.

2.3.1.3 Surgical Approach

The anterior approach has been used since the conception of ankle arthroplasty (Gougoulias and Maffulli, 2013). In 2016, the anterior surgical approach was used in at least 89% of all primary TARs performed in the UK (National Joint Registry, 2017). This approach offers a good field of view for surgery and is thought to preserve proprioception at the ankle (Conti et al., 2008). However, scar tissue formation, maturation and contraction has been suggested to limit plantarflexion range of movement following this approach (Ajis et al., 2013).

A lateral approach has been introduced in one of the more recently developed TAR devices, the Trabecular Metal TAR (Demetracopoulos et al., 2013). The lateral approach for this device requires a fibula osteotomy which, on the one hand, was integrated to improve force dissipation; the curved cuts made to the tibia and talus theoretically dissipate forces to the trabecular bone perpendicularly. On the other hand, the fibula needs to be replaced at the end of the procedure that not only obscures the surgeon's view when reviewing component size and ligament tensions. But also, substantial time is added to the patients' recovery (Demetracopoulos et al., 2013). Other approaches are available such as a posterior approach (Bibbo, 2013) and a device that is delivered, in part, through the sole of the foot (Ellis and DeOrio, 2010). The published literature is yet to favour any one approach, however currently, the anterior approach is the most commonly used.

2.3.1.4   Fixation Methods

Primary fixation is the immediate intraoperative steps used to achieve fixation, for example: bone cement, fixation screws or a press-fitted implant. Bone cement is a successful method of fixation in total hip and knee replacement (National Joint Registry, 2017), however, high failure rates were suspected to be related to cement use within the first decade of TAR development and has been widely disbanded since (Gougoulias and Maffulli, 2013). Bone cement is still used within the US because the FDA stipulate its use. Although, off-label uncemented use of these implants has been reported (Roukis and Prissel, 2014). Screw fixation is integrated in the Hintegra TAR design, although similar outcomes were reported independent of screw use (Preyssas et al., 2012, Yoon et al., 2014). BP-type devices require a cortical window to be cut in order to insert the stemmed tibial component using an anterior approach. However, this technique may damage the surrounding bone crucial for implant support. Other fixation geometries may reduce the quantity of bone resection (Goetz et al., 2016, Bischoff et al., 2017) (Figure 2.8).
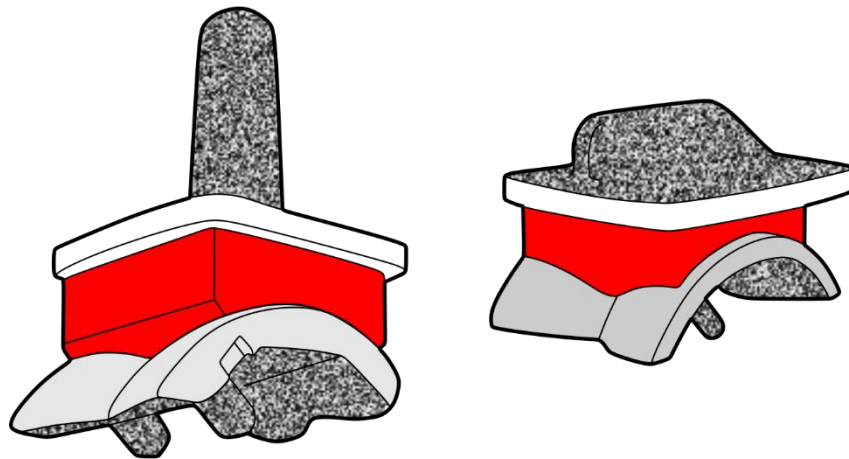
Figure 2.8. Examples of mobile-bearing TARs with different tibial fixation methods.The Zenith TAR (left) has a stemmed tibial component whereas the CCI TAR (right) features a fin.

Secondary fixation is the process of attachment between the bone and implant following the surgical procedure and is also known as osteointegration. The process is facilitated by the compression of the implant on the bone, hence why a press-fit between the implant and bone is often desirable. In a process similar to fracture healing, osteointegration occurs within 12 weeks but could longer depending on patient physiology (Zweymuller et al., 1988). Two distinct methods of osteointegration are available, plain porous or rough coatings such as plasma-sprayed titanium and/or bioactive coatings such as hydroxyapatite. The BP TAR used porous coated components without a bioactive component and reported no specific issues (Buechel and Pappas, 2003, Ali et al., 2007). Hydroxyapatite was used without a porous coating in the early

generations of the AES TAR. Delamination of this surface was a commonly cited cause of failure (Wood and Deakin, 2003, Koivu et al., 2012, Dalat et al., 2013). A similar complication was described for the TNK TAR which featured hydroxyapatite applied directly to a ceramic surface; 50% of the devices in this study failed within 33.8 months (Nagashima et al., 2004). The latest generation of the AES introduced a dual-layer combination of porous titanium coated with hydroxyapatite as featured in several other designs (e.g. Zenith, Akile). This change was not sufficient to drastically improve clinical outcomes (Besse et al., 2009). Trabecular metal is a porous structure made of tantalum which extends away from the implant in order to maximise volumetric osteointegration. The Trabecular Metal TAR (Zimmer-Biomet, UK) has integrated the use of this material with the aim of improving bone ongrowth by better resembling the elastic modulus of cancellous bone.

2.3.1.5   Biomaterial Selection and Wear

The biomaterials used for TAR have been adopted from total hip and knee replacements, namely cobalt chromium alloy, titanium alloy and ultra-high molecular weight polyethylene (UHMWPE). The wear of such materials has been tested in vitro by simulators designed to mimic the in vivo kinematics and kinetics of the ankle (Affatato et al., 2007, Bell and Fisher, 2007, Bischoff et al., 2015, Reinders et al., 2015, Smyth et al., 2017). The wear rates reported ranged 2.1 mm^3 per million cycles (Mc) for the Trabecular Metal TAR (Bischoff et al., 2015) and 25.8 mm^3/Mc for the Zenith TAR (Smyth et al., 2017). These values were considered similar to the wear rates reported for total knee replacement using similar biomaterials. However, when interpreting the results of in vitro simulation studies, critical methodological factors such as which kinematics and lubricants were used need to be considered. For example, wear rates for the Zenith TAR varied between 1.2 ± 0.6 mm^3/Mc and 25.8 mm^3/Mc dependent on kinematics (Smyth et al., 2017). Wear was significantly reduced for unidirectional flexion/extension conditions compared to those integrating flexion/extension with additional rotation and displacement motions. Cross shear wear conditions are generally accepted to generate greater volumes of wear for total joint replacements (McEwen et al., 2005, Smyth et al., 2017). The differences between fixed-bearing and mobile-bearing designs may be important for the production of wear, but this remains untested for TAR.

Wear resistant coatings such as titanium nitride and diamond-like carbon; and, variants of UHMWPE (e.g. highly crosslinked, vitamin E infused) have been introduced to the latest generation of TAR designs. The implication is a reduction of primary bearing wear may improve the longevity of TAR. While in theory this may be true, the use of such biomaterials has not transformed survivorship statistics for TAR. The Akile TAR was recently commercialised and features a diamond-like carbon coating yet the survivorship

was 79% at five years with a high prevalence of osteolysis (Lucas y Hernandez et al., 2014). Biomaterial selection is an important feature of TAR design but may not be the predominant factor causing failure.

2.3.2 Implantation Rates

The brand and type of TAR devices implanted differ between countries. Most notably, surgeons in the US generally implant fixed-bearing cemented TARs, whereas surgeons in the countries of Europe tend to implant mobile-bearing uncemented devices (Roukis and Prissel, 2013). Four general global trends of TAR implantation have been identified from worldwide registry data (Prissel and Roukis, 2016): Abandonment, minimal use, initial embracement with diminished use and initial embracement with sustained growth. Abandonment was defined as zero implantations in two consecutive years (Figure 2.9). Minimal use was defined as a TAR being implanted until the analysis end date (i.e. 2013) but having not been implanted more than 50 times in any given year. Initial embracement with diminished use was defined as a device reaching more than 50 implantations in any given year at its peak but then falling below 50 implantations in subsequent years. Initial embracement with sustained growth was defined as a TAR with more than 50 implantations at its peak and sustained growth since (Figure 2.9). Notably, these definitions use the limit of '50' implantations. Fifty implantations is unlikely to be a sufficient sample size for comparable survivorship/failure statistics between TAR designs. The high turnover of devices possibly shows the lack of confidence the orthopaedic community has for most TAR designs.
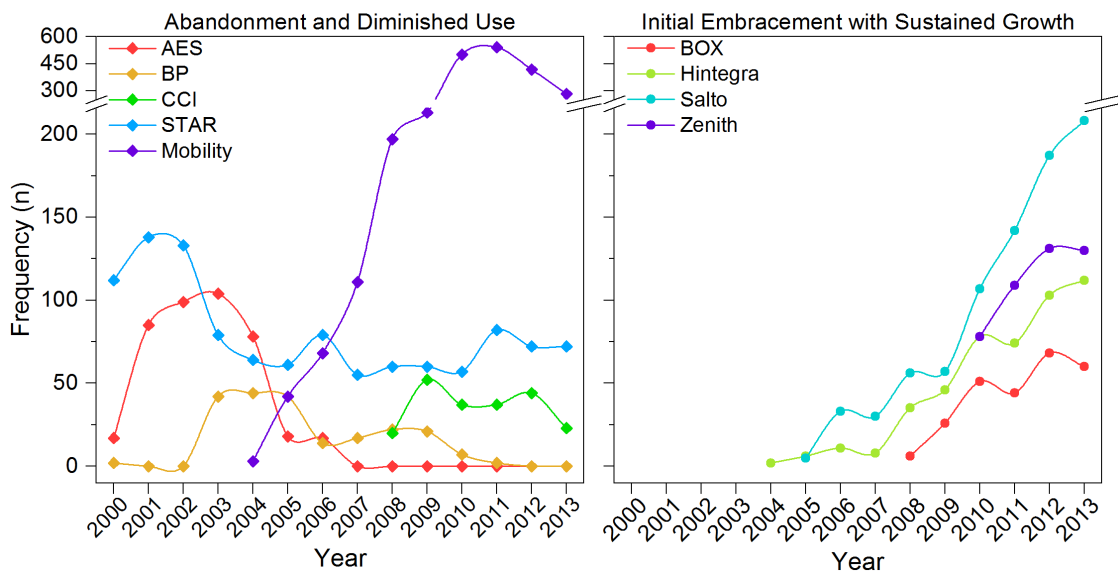
Figure 2.9. Rate of implantation for TARs which have undergone abandonment and diminished use (left) and initial embracement with sustained growth (right).

Since 2010, the UK has developed the most comprehensive TAR joint registry (Goldberg et al., 2009b). The implantation rates of five TARs have increased recently (Figure 2.10).

The Zenith, BOX, STAR and Salto TARs are mobile-bearing uncemented designs which are not dissimilar in design principles to previous TARs implanted in the UK. For example, the Zenith is a BP-style device, similar to the disused Mobility, BP and AES in both geometry and surgical approach. The BOX has similar features to the STAR except for its curved tibial component bearing surface which was seemingly designed to disperse stresses more effectively under greater ranges of motion (Giannini et al., 2011). Interestingly, the Infinity TAR has recently undergone sustained growth in the UK despite being a fixed-bearing device (Figure 2.10). This may signify a change in culture from mobile-bearing designs to fixed-bearing designs for foot and ankle specialists in the UK.
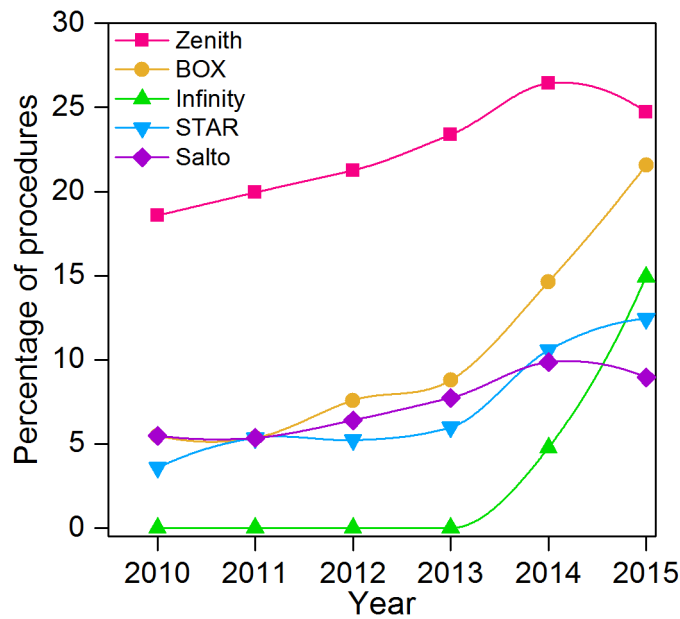
Figure 2.10. Commonly implanted TAR devices in the UK. Adapted from the National Joint Registry (2017)

The popular devices currently being implanted are not unique by design and often feature improvements to surgical approach and instrumentation rather than substantial changes to device geometry. Improving TAR performance will likely require fundamental design changes in combination with improvements in surgical technique. Understanding which TAR designs perform poorly and why, is crucial to prevent unnecessary harm.

2.3.3 Failure Rates

The term 'failure' has been used interchangeably with revision surgery (Jehan and Hill, 2012). Failure however, denotes the criteria by which a patient requires or desires revision surgery. The inverse of failure is success; a notion used to calculate implant survivorship and patient satisfaction. Revision TAR surgery is defined as the removal of one or more components, not including meniscus exchange, throughout the implants lifetime (Henricson et al., 2011a). This is the commonly cited endpoint for survivorship analyses of TAR cohorts.

According to the UK National Joint Registry, the cumulative percentage probability of revision surgery for TAR is 6.83 (95% CI 5.47-8.52) at 5 years (National Joint Registry, 2017). The estimated survivorship of 93.2% at 5 years is below the benchmark for survivorship set for THR at 10 years, which is 95% (Kandala et al., 2015). Despite the high revision rate relative to other joint replacements, the UK NJR failure rates are lower than other national joint registries (Figure 2.11) and the published literature more generally for TARs (Zaidi et al., 2013). However, The British Orthopaedic Foot and Ankle Society believe the UK NJR data is likely to be an underestimation due to under-reporting (National Joint Registry, 2017).
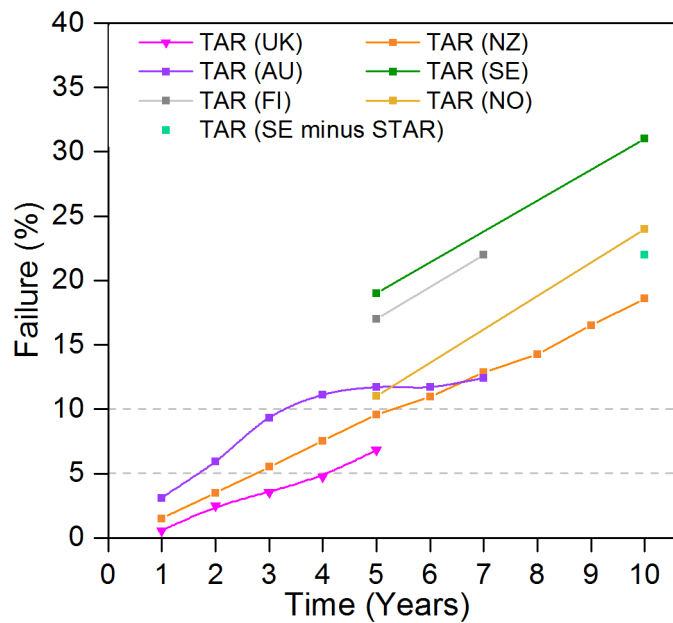
Figure 2.11. Failure rates of TAR reported in global national joint registries.

There are three levels of survivorship data for TAR: 1) Registry data, 2) Independent research groups, and; 3) Surgeon designer studies. With each level, starting from registry data and ending the surgeon designer studies, the generalisability decreases whereas the survivorship increases. Zaidi et al (2013) reported the mean annual failure rate to decrease from 3.2% for registry data, to 1.7% for independent research groups, to 1.1% for surgeon designer studies. Therefore, for expert surgeons familiar with a device and surgical approach, a failure rate of 11% at 10 years could be expected. Whereas, the registry data suggested a 10 year failure rate of 27% (95% CI 18 to 36). An analysis of 34 studies with cohorts of more than 100 TARs also shows a failure rate less than 5% at five years and 10% at ten years is yet to be reliably achieved regardless of TAR design or surgeon ability (Figure 2.12). One study reported a 5% failure rate at six years for the STAR brand, however their five year data was not available (Wood et al., 2009).
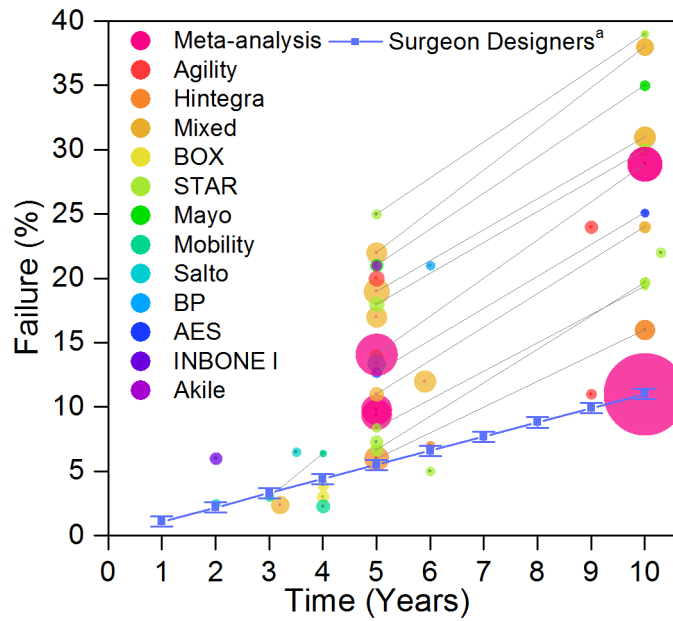
Figure 2.12. Failure rates reported in studies with a sample size of ≥100 TARs. 'Mixed' represents studies with mixed TAR design populations. Blue line[a] represents the failure rates for surgeon designers reported in a systematic review published by Zaidi et al. (2013). Grey lines indicates data linked by the same study. Circle size is proportional to the sample size of the study. The following studies were included: Kitaoka et al. (1994), Kofoed and Lundberg-Jensen (1999), Alvine (2002), Wood and Deakin (2003), Knecht et al. (2004), Spirt et al. (2004), Weber et al. (2004), Stengel et al. (2005), Fevang et al. (2007), Henricson et al. (2007), Hosman et al. (2007), Leardini et al. (2008), Wood et al. (2008), Hobson et al. (2009), Wood et al. (2009), Besse et al. (2010), Gougoulias et al. (2010), Skytta et al. (2010), Barg et al. (2011a), Giannini et al. (2011), Henricson et al. (2011b), Rippstein et al. (2011), Schenk et al. (2011), Zhao et al. (2011), Pinar et al. (2012), Barg et al. (2013b), Rodrigues-Pinto et al. (2013), Lewis et al. (2014), Lucas y Hernandez et al. (2014), Henricson and Carlsson (2015), Lewis et al. (2015), Kerkhoff et al. (2016b), Koivu et al. (2017).

Acceptable long-term survivorship rates are possible. For example, Buechel et al. (2004), the surgeon designers for the BP TAR, reported a 20 year survivorship of 74.2% for 40 TARs in 38 patients. However, TAR has been developed over 40 years and substantial improvements in survivorship have not occurred. A recent analysis of survivorship across the three generations of total ankle replacement showed only small differences between the generations up to 10 years follow-up (Roukis and Bartel, 2016) (Figure 2.13).
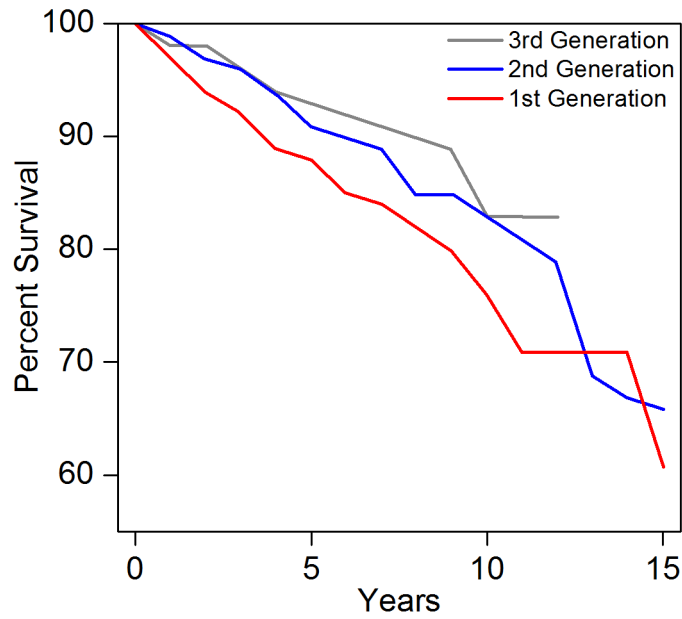
Figure 2.13. Survivorship for TAR designs considered to be 1st Generation (earliest), 2nd Generation and 3rd Generation (latest). Adopted from Prissel and Roukis (2016).

Design changes between TAR generations appear not to have had a substantial effect on survivorship. Despite this, reductions in low to medium risk complications are important to the development of the technology and may not be represented in the survivorship data. For example, the AES TAR was disused in 2008 and withdrawn from market in 2012, yet the survivorship data was comparable to that of other devices during the same time period (Skytta et al., 2010) (Figure 2.14). The reason given for recall was high rates of osteolysis, an indication for failure but a complication sometimes manageable without component removal (Prissel and Roukis, 2014, Roukis and Prissel, 2014). The complications contributing to TAR failure need to be analysed and understood before drastic improvements in survivorship are likely to be made.
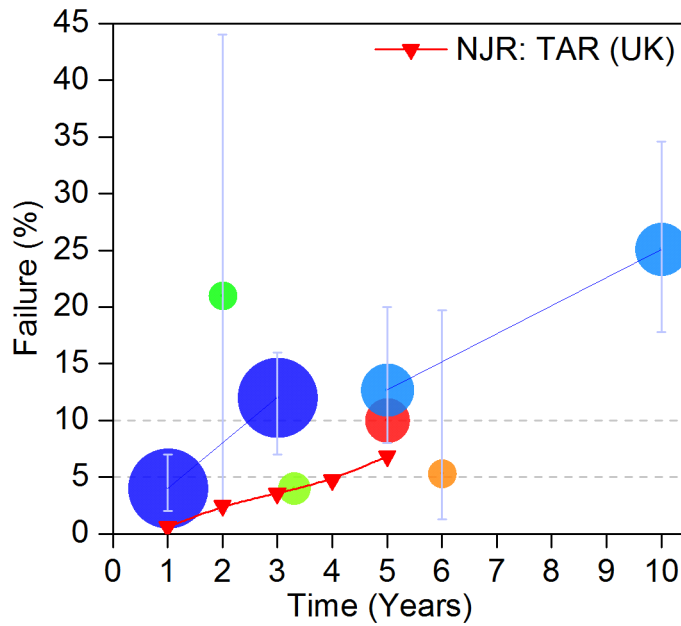
Figure 2.14. Failure rates reported for the Ankle Evolutive System (AES) TAR. Red line represents the national joint registry data for the UK (National Joint Registry, 2017). Circle size is proportional to the sample size of the study. The following studies were included: Besse et al. (2009), Henricson et al. (2010), Morgan et al. (2010), Skytta et al. (2010), Kokkonen et al. (2011), Koivu et al. (2017).

2.3.4 Clinical Indications for Failure

Implant revision was the standard end-point criterion by which TARs have been judged for success (Gougoulias et al., 2010). However, implant survivorship is not sufficient, in isolation, to describe the condition of the implant or patient for which revision surgery was indicated. Additional criteria have been implemented to classify and report joint failure and/or success (Saltzman et al., 2009, Datir et al., 2013). For example, Table 2.1 details the criteria used to define overall success in a multi-centre clinical trial (Saltzman et al., 2009). The first three criteria were primarily for safety and the fourth was for efficacy. Failure was assumed if these requirements were not met, although the trial allowed for categorised failures to be overturned (Saltzman et al., 2009). While relatively encompassing, patient satisfaction was omitted and implant function/performance bears minimal weighting, both of which may be crucial to indicating failure. Some patients may refuse revision surgery even after clinical failure (Koivu et al., 2009) and cases like these are omitted from revision surgery statistics.

Table 2.1. Criteria for TAR success used for a multi-centre clinical trial (Saltzman et al., 2009)
1. No radiographic evidence of component migration or loosening (Safety criterion). 2. No device failures, revisions, or removals (Safety criterion). 3. No significant infection, delayed wound healing, postoperative fractures or bony changes, any of which that required surgical intervention (Safety criterion). 4. 40-point increase in Buechel Pappas ankle score (Efficacy criterion).

The criteria for TAR success (and inversely, failure) (Table 2.1) offer an absolute and binary outcome for each individual ankle, a metric useful for generalisable survivorship statistics, however, less informative when considering the chronology or causes of such outcomes.

There are many complications that facilitate TAR failure; some of which are associated with the: device, surgical procedure, patient selection, pre-existing diagnosis or anatomical variation (Figure 2.15). Glazebrook et al. (2009) attempted to stratify the most common TAR complications by severity. The complications were extracted from 20 studies with cohorts of at least 25 implants with a minimum mean follow-up of 24 months between the years 1997 and 2007. Three complications including deep infection, aseptic loosening and implant failure were identified as 'high-grade' and led to failure 50% of the time. Whereas, technical error, component subsidence and post-op bone fracture were classified as 'medium-grade' complications, leading to failure less than 50% of the time. Gadd et al. (2014) applied the classification system to their foot and ankle centre TAR outcomes. Both the 'high-grade' and 'medium-grade' complications identified by Gadd et al. (2014) all led to failure over 50% of the time and were therefore more severe and inconsistent with the original classification (Glazebrook et al., 2009).
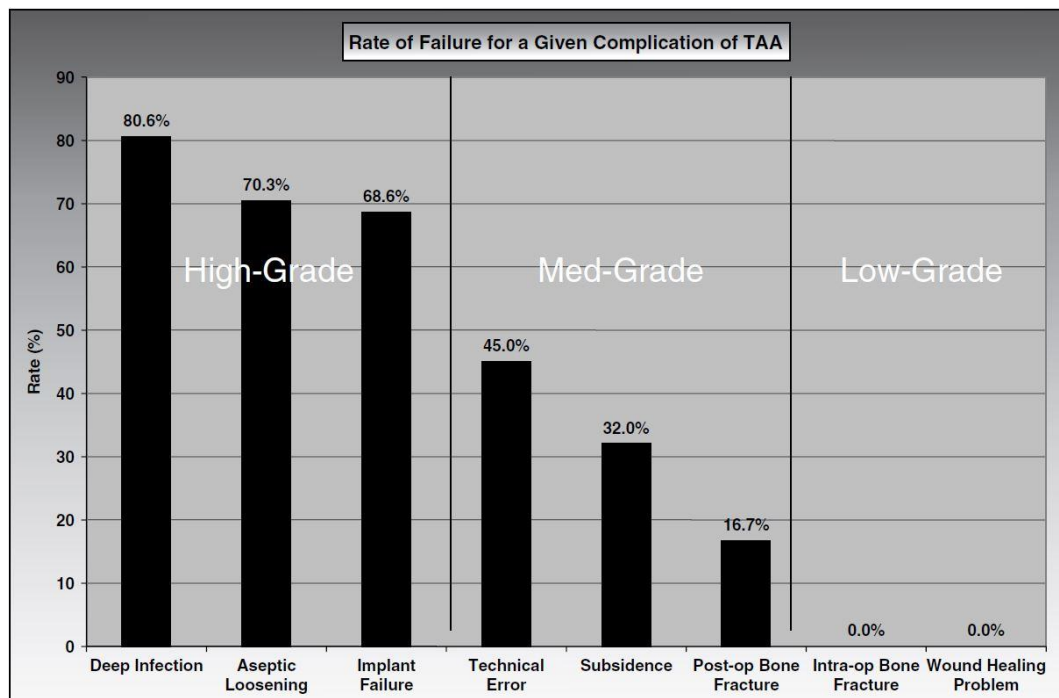
Figure 2.15. Rate of failure for a given complication of TAR. Adopted from Glazebrook et al. (2009).

The lexicon by which complications are classified matters. The complication category 'loosening/osteolysis' was reported in 63% of 117 TAR studies with 115 different terms describing the same complication (Mercer et al., 2016). Understanding and reporting the

reasons for TAR failure with clarity, is essential for the patient and surgeon to comprehend the inherent risks associated with prospective treatment options.

2.3.5 Incidence of Osteolysis

Osteolysis is a pathological reduction of bone density, often proximate to joint replacement components and is typically characterised by an area devoid of bone trabeculae, identified by radiolucency in radiography (Figure 2.16). If persistent and progressive, osteolysis can lead to the gradual component migration, collapsed bones and further mechanical problems (Besse, 2015). Osteolysis is both a clinical indication and cause of TAR failure (National Joint Registry, 2017). Treatment options for severe osteolysis include bone grafts, yet the clinical outcomes following this are poor resulting in further surgery (Koivu et al., 2017).
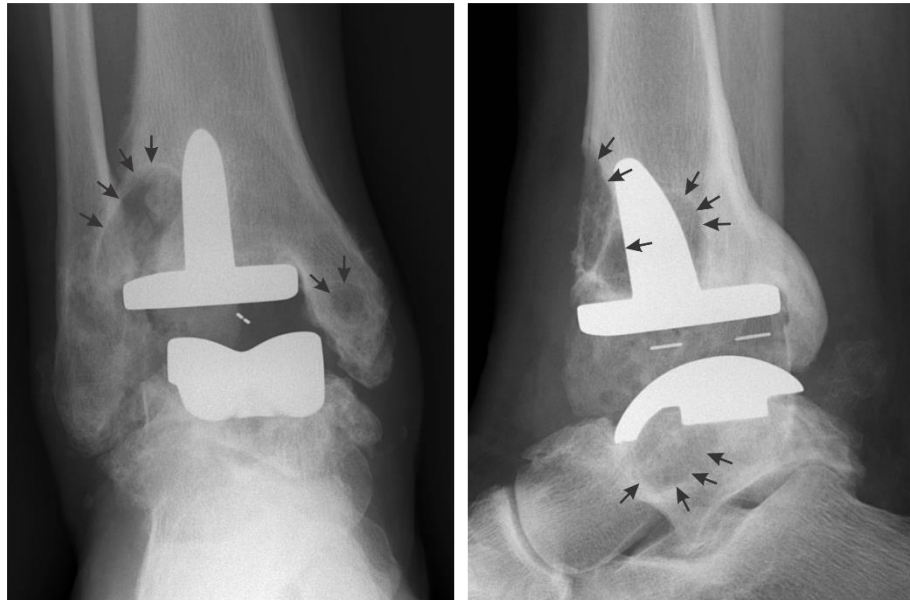
Figure 2.16. Example of osteolysis surrounding TAR. Arrows identify the areas of osteolysis.

The incidence of osteolysis for TAR is considered high across the breadth of available TAR designs (Besse, 2015). For example, Bonnin et al. (2011) showed 19% of the Salto TARs assessed to have osteolytic cysts >5 mm in size. For 100 STAR devices and 100 BP TARs, 7% showed osteolytic cavities at 3 years follow-up (Wood et al., 2009). At 5 years follow-up, 26% of patients (n = 90) implanted with the BP (n = 15) or CCI (n = 75) TARs had osteolytic lesions greater than 10 mm in size (Nieuwe Weme et al., 2015). The Akile TAR was recently introduced to the market yet showed small osteolytic lesions in 67% of the cohort (n = 127) at a mean follow-up of 88 months (Lucas y Hernandez et al., 2014).

The early development of osteolysis is a specific concern for TAR. In a multi-centre multi-surgeon study, 173 TARs (82 Salto, 41 Hintegra, 19 AES, 15 Coppelia, 11 STAR, 4

Ramses and 1 Akile) were retrospectively analysed for osteolytic lesions and radiolucency. Osteolytic lesions were identified in 33% of TARs and 72% showed radiolucency. Lesions over 8 mm were identified in 20% of the entire cohort. The mean follow-up for this study was 34 months and the AES TARs showed the highest incidence of osteolysis (52%).

The AES TAR was withdrawn from the UK market by the manufacturer in 2012 because of a high incidence of osteolysis. The problem was first flagged in the published literature in 2009 in a prospective study including 50 AES TARs (Besse et al., 2009). At 45 months follow-up, severe osteolysis (>10 mm) identified in the tibia and talus was 29% and 22%, respectively. Similar results were reported in the published literature that followed, Koivu et al. (2009) reported severe lesions in 21% of AES TARs at 31 months. Morgan et al. (2010) reported significant lesions in 24% of AES TARS at 58 months. Rodriguez et al. (2010) and Kokkonen et al. (2011) both used CT scans to identify osteolysis at a rate of 100% at 39 months follow-up and 79% at 28 months follow-up, respectively. The incidence of osteolysis for the AES TAR was high, but this TAR should not be considered an outlier given the equally high rates of osteolysis reported for other TAR brands (Besse, 2015).

2.4 Mechanisms of Total Ankle Replacement Failure

Many factors contribute to the long term success of total joint replacement, these include but are not limited to: patient selection, surgeon expertise, diagnosis, surgical approach, implant design, bone anatomy and physiology. Each of these factors are, however, subject to error, misjudgement or variance, some of which may lead to failure. A comprehensive review of the failure mechanisms affecting TAR is detailed in the following sections.

2.4.1 Patient Selection and Clinical Factors

The indications for TAR have expanded over time and differ between countries, surgeons and devices (Murnaghan et al., 2005, Pugely et al., 2013). A breadth of patient demographics have had successful short term clinical outcomes, including patients with poliomyelitis (Morgan et al., 2012) or diabetic neuropathies (Lee et al., 2008). Obese populations have been used with caution (Lagaay and Schuberth, 2010, Sproule et al., 2013). Sproule et al. (2013) identified the first six failure cases within their cohort to be obese (>30 Body Mass Index, BMI) and some surgeons contraindicate patients with a BMI over 35 (Ajis et al., 2013). Lagaay and Schuberth (2010) suggested that patients aged over 60 years old and with a BMI less than 30 were statistically more likely to be

satisfied with their outcome. Criswell et al. (2012) also recommended that TAR recipients should be older than 60 years old. A consensus has not been reached on what the indications for TAR should be.

The low volumes of TARs performed per surgeon (Goldberg et al., 2009b) and the potential for a learning curve (Mroczek, 2003, Wood and Deakin, 2003, Murnaghan et al., 2005, San Giovanni et al., 2006, Henricson and Ågren, 2007, Hurowitz et al., 2007, Barg et al., 2010c, Lee et al., 2010, Criswell et al., 2012, Barg et al., 2013b, Clement et al., 2013, Rodrigues-Pinto et al., 2013, Schimmel et al., 2014) may affect patient outcome. Although, not all surgeons experience reduced patient outcomes during their initial operations (van der Heide et al., 2009, Bleazey et al., 2013, Lee et al., 2013, Summers and Bedi, 2013). Experience with other orthopaedic endoprostheses such as hip and knee replacements may aid surgeon learning, though the evidence for this is only anecdotal (Lee et al., 2013).

Postoperative rehabilitation may also be crucial to outcomes (Claridge and Sagherian, 2009). Postoperative changes in gait from highly variable reductions in leg strength (Valderrabano et al., 2007a) and altered proprioception (Conti et al., 2008) may affect patient perceived outcomes and implant function. More research is required to determine which post-operative rehabilitation programs are successful and require emulation in hospitals more broadly.

Many of the aforementioned factors are subjective, anecdotal or have no established causal relationship with poor clinical outcomes. Without well-designed controlled clinical trials testing each factor in isolation, guidelines for such factors will remain subjective and in the hands of the surgeon.

2.4.2 Pre-operative Ankle Alignment

Four broad measures of pre-operative ankle alignment have been defined: 1) Lateral distal tibial angle (LDTA), 2) anterior distal tibial angle (ADTA), 3) tibio-talar angle and, 4) center of rotational angulation (CORA) (Bonasia et al., 2010) (Figure 2.17). These measures can be affected at three levels which adds to the complexity of normalising patients for TAR. These levels are: 1) the tibial diaphysis or metaphysis, 2) the ankle joint and, 3) the hindfoot (Bonasia et al., 2010).
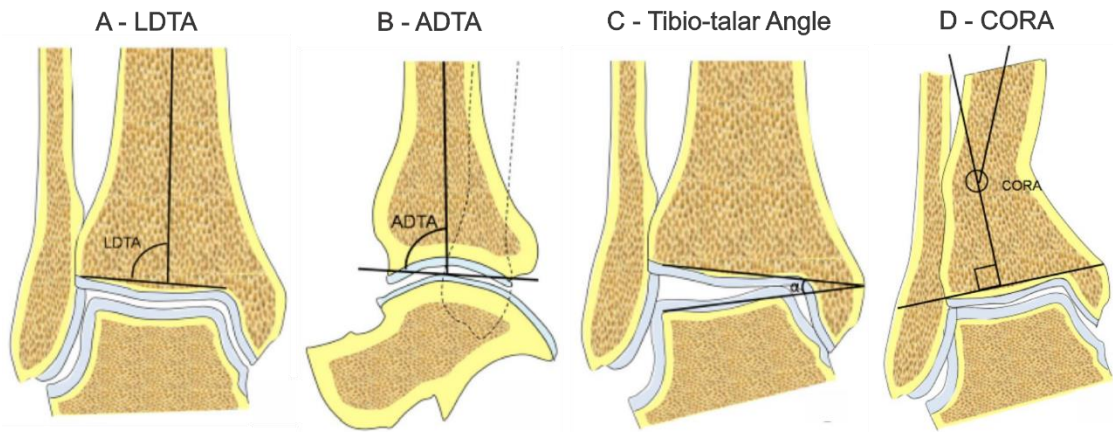
Figure 2.17. Preoperative alignment measures. LDTA, lateral distal tibial angle (A). ADTA, anterior distal tibial angle (B). Tibio-talar angle (C), and; CORA, centre of rotation of angulation (D). Adopted from Bonasia et al. (2010).

Distal tibial deformities may cause increased contact pressures within the ankle joint (Tarr et al., 1985, Smith and Wood, 2007). Deformities greater than 10° in any direction have been contraindicated for TAR, particularly in the coronal plane (Doets et al., 2008), yet other surgeons have reported success in patient cohorts with deformities of this magnitude (Daniels et al., 2008). Correcting natural deformities to an anatomical norm dictated by the device manufacturer reduces the contact pressures endured within the device (Coetzee, 2010), but an inherent conflict exists between matching the device to the patient or fitting the patient to the device. High incidences of osteolysis may suggest the latter is more prevalent but this is yet to be understood.

2.4.3 Device Fixation

The primary fixation of TAR devices has been suggested to be insufficient for several TAR designs, leading to abrasion and delamination of the fixation surface (Besse et al., 2009, Cottrino et al., 2016, Singh et al., 2016). Consequentially, the production of wear particles produced at the implant bone interface (e.g. titanium, hydroxyapatite) has been suggested to feed into a sequalae of adverse biological reactions intensifying the early development of osteolysis (Koivu et al., 2009, Dalat et al., 2013, Besse, 2015). Defective material properties and insufficient fixation coating adhesive strength were suggested to be the cause of failure in devices under investigation (Dalat et al., 2013, Besse, 2015, Cottrino et al., 2016). However, this hypothesis is heavily reliant on histological data (Koivu et al., 2009, Koivu et al., 2012, Dalat et al., 2013) and the presence of fixation surface debris embedded in explanted bearing inserts (Cottrino et al., 2016). The location or frequency of coating abrasion/delamination has yet to be evidenced in the published literature.

Once implanted, the longevity of the implant can be divided into four stages: 1) Early stable phase, this is the implant becoming fixed surgically; 2) Late stable phase which

forms the rest of the implants life after the early stable phase; 3) Late unstable phase which is the failure of the implant. Finally the 4th stage is an early unstable phase which is characterised as early failure due to surgical error (Karachalios et al., 2014) (Figure 2.18). Early failure due to surgical error is currently uncommon in total hip and knee replacement, but surgical errors such as implant malpositioning remain causes of early failure for TAR (Goldberg et al., 2009a). The following section details failures specific to device alignment.
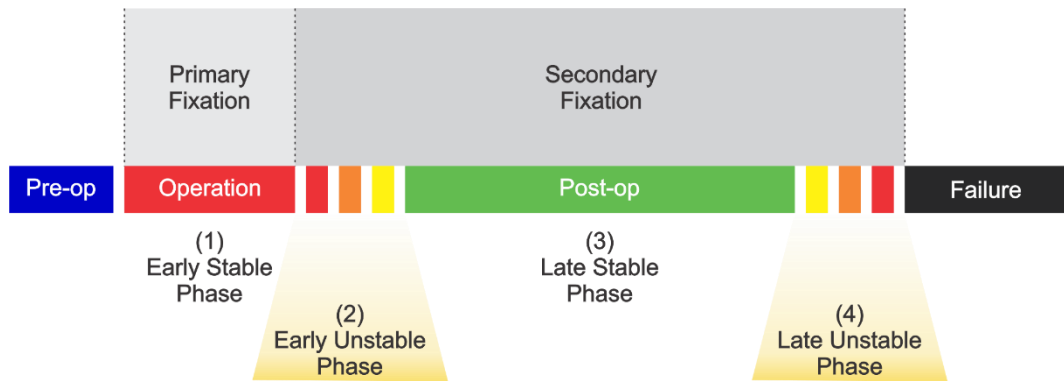
Figure 2.18. The life cycle of total joint replacements.

2.4.4   Post-operative Device Alignment and Positioning

Ankle failure secondary to technical errors such as implant malpositioning and malalignment is a common clinical problem (Glazebrook et al., 2009, National Joint Registry, 2017). In a cohort of 101 failed ankles, 17 were caused by implant malpositioning and malalignment (Henricson and Ågren, 2007). In another study, all failures (10% of the cohort) were due to malpositioning (Dhawan et al., 2012). The poor perioperative visibility of bone surfaces contributes to the potential for implant malpositioning; a consequence of which is a loss of joint congruency that results in: a reduction of contact area and concentration of high stresses (Assal et al., 2003); edge loading (Haskell and Mann, 2004a); excessive polyethylene wear and a risk of meniscal dislocation or cracking (Assal et al., 2003). One of the complexities of determining malpositioning is being able to define it, in all three planes. A more detailed discussion of how device alignment is defined is included in Section 2.5.1.1.

2.4.5   Component Migration/Subsidence

Component migration occurs in both components (Pyevich et al., 1998, Knecht et al., 2004, Datir et al., 2013) and sometimes in close to 50% of the patient cohort (Kopp et al., 2006). Component migration or subsidence has been defined as a change in component position by at least 5° or 5 mm in one or more planes (Pyevich et al., 1998, Knecht et al., 2004, Saltzman et al., 2009). For the effective monitoring of component

subsidence, radiostereometric analyses are recommended (Christensen et al., 2016). At a minimum, medical imaging captured during the primary procedure or directly post-operatively is required to assess initial TAR positioning.

2.4.6 Stress Distribution (Stress Shielding)

Bone thrives off mechanical stimuli. After prosthesis implantation, new loading patterns activate bone remodelling which, under ideal conditions, creates a rigid bone-implant interface as reflected by Wolff's Law (Wolff et al., 1986). While excessive bone compression is likely to impair bone growth (Elliott and Goswami, 2012), the inverse, insufficient mechanical stimuli, is more commonly associated with joint replacement failure. Stress shielding is the phenomenon where insufficient stress applied to bone causes osteolysis.

Radiolucencies secondary to stress shielding were reported to be relatively small and benign (Wood et al., 2000, Bonnin et al., 2011). Wood et al. (2000), Mann et al. (2011) and Rodrigues (2013) suggested that the STAR prosthesis could be susceptible to stress shielding if the bone was not contiguous with the implant between the dual tibial fixation cylinders. Talar component design may also inadvertently facilitate stress shielding. Oppermann et al. (2013) demonstrated the difficulty of achieving complete bone coverage using the STAR design in a cadaver study (Figure 2.19). The talar component may be more susceptible to stress shielding because the metal flanges that flank the talus in most TAR designs obstruct intraoperative bone-interface alignment.
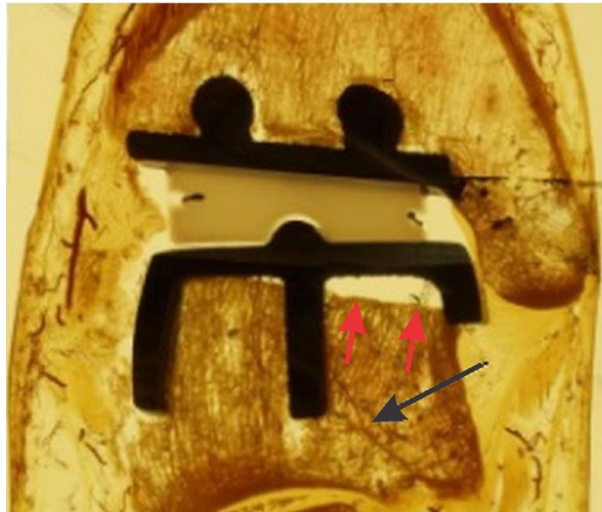
Figure 2.19. Bone-implant interface gap left after implantation of the Scandinavian TAR (Red arrows). Black arrow shows vasculature near talar component stem at risk of severance. Adapted from Oppermann et al. (2013).

2.4.7 Micromotion

Large shear strains between orthopaedic implants and interfacial bone produces a mechanical environment that favours fibrocartilage cell differentiation (Claes and Heigele, 1999, Michelson et al., 2000, Lacroix and Prendergast, 2002). The quality of bone at the TAR fixation surface, in theory, will be inversely proportional to the magnitude of micromotion. Ankle replacements are susceptible to micromotion, especially when exposed to high multidirectional forces and an inadequate primary fixation (Greisberg et al., 2004). Continued interfacial motion may lead to membrane formation which has a radiolucent presentation on radiography (Pegg et al., 2014). In a cadaver study, McInnes et al. (2014) showed micromotion for the Agility TAR and STAR to be considerably greater than the generally accepted 150 μm limit. Sopher et al. (2017) used a finite element model to determine the effect of malpositioning on micromotion for the BOX, Mobility and Salto TARs. A gap at the implant-bone interface was the condition which resulted in the greatest micromotion. Leaving a gap peri-operatively was recommended to be avoided, even at the expense of other forms of malpositioning (Sopher et al., 2017).

2.4.8 Wear Particle Induced Osteolysis

Historically, periprosthetic osteolysis was predominantly linked with an adverse cellular response to wear particles. Wear particles activate proinflammatory cytokine release which ultimately results in the up-regulation of osteoclastogenesis (Ingham and Fisher, 2000). However, merely the presence of UHMWPE wear particles within tissue samples is not sufficient to indicate this type of biological reaction. The quantity, size and morphology of these particles affect the aggressiveness of the reaction, as does the concentration of particles accumulated over time (Hallab and Jacobs, 2009). The early onset of osteolysis in total ankle replacement and the supposed lack of UHMWPE wear upon visual analysis has led authors to suggest UHMWPE wear is not the driving factor (Koivu et al., 2009, Koivu et al., 2012, Besse, 2015). A more detailed discussion of this failure mechanism is discussed in Section 2.5.3.

2.4.9 Fluid Pressure

Fluid volume and pressure are escalated within the dysfunctional physiology of the replaced joint (Schmalzried et al., 1997), which has been shown to be greater in failing hip replacements than clinically stable hips (Robertsson et al., 1997). Supraphysiological intracapsular pressures have been hypothesised to induce a pro-resorptive osteolytic response in periprosthetic tissue, independent of the presence bone-implant interfacial membrane (Nam et al., 2013). This cascade of events may be exacerbated further by the transportation of wear debris and necrotic tissue within the same flow of fluid (Linder, 1994).

The current designs of total ankle prostheses leave the subchondral bone in the talar neck and the medial and lateral sides of the tibia exposed to synovial fluid which may be an inlet for debris perfusion (Rodriguez et al., 2010). Fluid pressure has only been hypothesised to have an osteolytic potential within the ankle joint (Koivu et al., 2012, Yoon et al., 2014), no research has been conducted to date.

2.4.10 Ligamentous Support

Peri-implant ligaments were suggested to have a greater effect on the Agility TAR's implant motion than the contours of the implant itself (Saltzman et al., 2004). Because of this, individual ligaments can be re-tensioned to create desirable TAR biomechanics as per the manufacturer's guidelines (Merian et al., 2011). These techniques are completed during the primary procedure and may require revision post-operatively. Strain-gauge distraction methods have attempted to directly quantify optimised ligament tension for a reproducible surgical technique, however inconsistent results shrouded the usability of this technique (McIff et al., 2004). Insufficient ligamentous support (Kopp et al., 2006) and/or excessive ligament strain (Pyevich et al., 1998) has been correlated clinically with early implant failure. Ligamentous support is essential for maintaining ankle alignment, congruency and implant function.

2.4.11 Bone Quality

Poor bone quality has been suggested to facilitate aseptic loosening by the reduced ability of the bone to remodel and osteointegrate within the fixation surface (Barg et al., 2010b, Barg et al., 2011b). In one study, 65% (N=93) of the patient cohort undergoing TAR suffered from osteopenia; 12% of which were severe cases (Doets, 2009). Coping with poor bone quality is a surgical challenge which has been treated by improving the primary fixation (Bianchi et al., 2012). Cement fixation with poly methyl methacrylate (PMMA) has been used for patients with thin cortices (Bianchi et al., 2012). This seems counterintuitive however, because PMMA cementation was disbanded due to excessive bone loss at revision. Other solutions include the use of synthetic bone stock (Bibbo, 2013), use of screw fixation for the talar component (Bai et al., 2010), an implant design with a large contact area to dissipate stresses (Barg and Hintermann, 2010) and, prophylactic malleolar screws to prevent malleolar fractures; a common ailment in TAR patients with low bone stock (Barg and Hintermann, 2010). Although, the use of TAR for patients with low bone stock remains controversial (Martin et al., 2007, Noelle et al., 2013).

2.4.12 Postoperative Bone Formation

Proliferative bone and heterotopic ossifications are commonly identified in the medical imaging follow-up of TAR (Jung et al., 2016) and can affect the function of the device or anatomical gutters below the device (Schuberth et al., 2016). Of 80 patients, 25% were shown to develop heterotopic ossifications after an average of 31.9 months (Lee et al., 2011). Bony growth within the joint space may be a continuation of the initial inflammatory joint disease affecting the patient or form as part of the bone healing process following the bone cuts made during the primary surgery (Hintermann et al., 2017). If the TAR components do not sufficiently overhang the cortices, space is left available for bone to form (King et al., 2013). Bone formation within the joint space can cause stiffness and pain (Hintermann et al., 2017), however the symptoms may not be sufficient to warrant surgical intervention (Richardson et al., 2012).

2.4.13 Necrotic Tissue

Tissue necrosis is a product of numerous surgical factors such as ischemia associated with reduced or injured vasculature (Koivu et al., 2012), micromotion of a poorly integrated implant (Konttinen et al., 2005) and heat damage caused by the polymerisation of bone cement (Willert et al., 1974, Calderale et al., 1983). However, necrosis surrounding the implant tends to heal, allowing the growth of the interfacial membrane between the implant and bone; causing no further complications (Willert et al., 1974, Konttinen et al., 2005). Koivu et al. (2012) however, noted substantial quantities of necrotic bone embedded in the periprosthetic tissues in 10 patients with the AES ankle replacement. Immunohistopathology analyses showed that despite an aggressive infiltration of macrophages within the periprosthetic tissue, large quantities of necrotic bone was present. The authors suggested that the phagocytic macrophages were overwhelmed, but the origin of the necrotic tissue in this study remained unknown. The morcellation of heterotopic ossifications during surgical interventions for TAR impingement have been identified as another source for residual necrotic tissue fragments (San Giovanni et al., 2006). These relatively common bony spurs grow asymptomatically and require arthroscopic removal if they restrict motion (Schuberth et al., 2016).

2.4.14 Blood Vessel Damage

The access for blood vessels to the talus is limited by widespread cartilage coverage (Dörenberg, 1983, Oppermann et al., 2013) and is uniquely sensitive to trauma or surgical insult (Tennant et al., 2014). Three arteries supply the talus, the: posterior tibial artery, dorsalis pedis artery and the peroneal artery; all of which have previously been transected as a product of surgical error during total ankle replacement (Saltzman et al.,

2003, Kopp et al., 2006, Claridge and Sagherian, 2009, Summers and Bedi, 2013). While arterial transection is a problematic complication, it is uncommon. The intraoperative saw cuts, on the other hand, puts the intraosseous vascular network at risk, some trauma at least is unavoidable (Oppermann et al., 2013, Tennant et al., 2014). Vascular damage is a precursor to reduced periprosthetic vascularity (Koivu et al., 2012) and potentially osteonecrosis; an ailment current imaging modalities are unable to assess in the talus. Current surgical approaches and devices seem likely to cause vascular trauma despite best efforts, therefore a combination of less intrusive fixation designs, improved instrumentation and intraoperative care may mitigate this risk.

2.4.15 Nerve Manipulation

Nerve manipulation is essential for several different TAR surgical approaches (Buechel and Pappas, 2003, Anderson et al., 2004, Besse et al., 2011, Brigido et al., 2014). Nerve damage due to soft tissue retraction and accessory operations (e.g. osteotomies) are not uncommon (Kofoed and Danborg, 1995, Saltzman et al., 2003, Haskell and Mann, 2004b, Pinar et al., 2012, Barg et al., 2013a, Jung et al., 2013, Schimmel et al., 2014, Sung et al., 2014). The transection of neural tissue is a substantial complication (Pinar et al., 2012, Summers and Bedi, 2013). In most cases however, the patient has reduced lower-limb sensation but without functional deficit (Kofoed and Danborg, 1995, Hintermann et al., 2004, Valderrabano et al., 2004, Summers and Bedi, 2013). Neuropathies can stimulate osteolysis (Jeffcoate, 2004) but whether this is clinically relevant to the TAR is yet to be discerned.

2.5   Failure Analysis of Total Ankle Replacement

Engineering failure may be defined as the implant not functioning as intended by the manufacturers and is not mutually inclusive with clinical failure. Independent of surgical factors, the device may lose congruency or not follow the intended kinematic profile. Biomaterials may change over time and/or cause an adverse biological reaction surrounding the device. A comprehensive failure analysis may contribute to the understanding of TAR failure from an engineering perspective.

Failure analyses require an integration of analyses to account for the many factors discussed in Section 2.4 which determine how joint replacements function and fail. Holistic approaches for failure analysis usually include the following resources:

- Medical imaging review
- Retrieval analysis
- Histological investigation.

Only a handful of studies have included all three aspects and have focused on the following replaced joints: knee (Ranawat et al., 1986, Cadambi et al., 1994, Engh et al., 1994, Goldvasser et al., 2013), hip (Ellison et al., 2012), shoulder (Kepler et al., 2010) and spine (Austen et al., 2012). No study to date has used this approach to examine TAR failure.

2.5.1 Medical Imaging Review

Most orthopaedic devices undergo a level of post-implantation clinical follow-up. In cases where a TAR device has been flagged for recall, an annual follow-up by X-ray may be recommended by regulatory bodies such as the UK's Medicines and Healthcare products Regulatory Agency (MHRA).

Catastrophic TAR failures, such as fractured components, can be identified immediately using medical imaging (Bestic et al., 2008, Mulcahy and Chew, 2015). However, risk factors such as component malalignment or subtle indicators of failure such as radiolucency require closer scrutiny of the available medical imaging.

2.5.1.1 Implant Position and Alignment

The generalised norms for TAR alignment and positioning are not particularly evidence-based, the 'ibisne in medio tutissimus' ethos is commonly applied; down the middle is safest.

During the primary surgery, TAR components are positioned and aligned as close as practicable to the surgical guidelines offered by the manufacturer. However, variation in TAR position is inevitable and can be detrimental to the patient. For example, rotational variation of the tibial component >4° was associated with higher pain scores (Pyevich et al., 1998). Likewise, translational variation of the tibial component was shown to result in a length change of one or more periprosthetic ligaments, potentially leading to excessive strain and pain for the patient (Saltzman et al., 2004).

Therefore, the definition of 'implant position' used throughout the research in this thesis is the location and orientation of each component at the time-point of the relevant medical imaging. Several factors affect why the component is orientated how it is, for example component migration or variance in surgical alignment, however a retrieval analysis cannot identify these phenomena. Perioperative measures of alignment using standardised protocols and a comprehensive radiostereometric analysis follow-up (i.e. the use of high density markers surrounding the joint to register component migration) would be required to assess component position change over time, neither of which are routinely undertaken in clinical practice.

Characterising component position variation, regardless of cause, is important to understand how the device functioned in vivo and gives context to the damage modes identified by retrieval analysis.

The Surgical Datum: Tibial Axis

The longitudinal axis of the tibia, defined as the centre line between the tibial cortices in the coronal and sagittal planes (Komistek et al., 2000), is the datum most TARs are designed to align with (Figure 2.20). The tibial axis is the central geometric axis not the biomechanical (loading) axis. Basic centric measurements simplify the surgical approach but may not replicate the axial loading regime most TARs aim to withstand. The clinical relevance of this distinction is yet to be established.
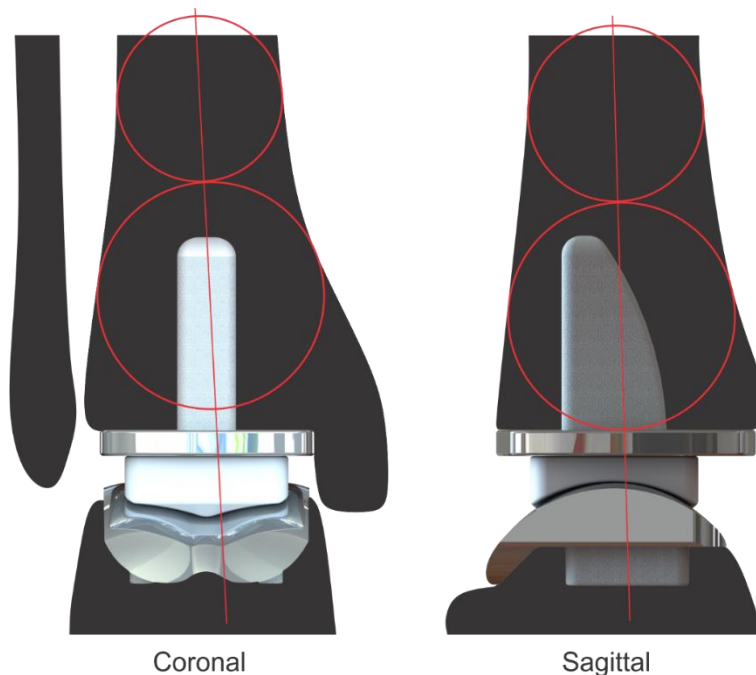
Figure 2.20. Tibial axis in the coronal plane (left) and sagittal plane (right).

Mobile bearing TARs are designed to function as an aligned stack of components. The UHMWPE bearing insert is assumed to align with the talar component due to their conforming curvatures at the talar articulation and lack of constraint at the tibial component bearing surface (Barg et al., 2010a). Aligning the talar component so that the bearing insert is central to the tibial component maximises the articulation area afforded to the tibial bearing articulation.

Relative to the tibial axis, both rotational and translational variation occur in each plane (i.e. coronal and sagittal) individually or concomitantly, in both or one of the tibial and talar components.

Rotational Variation

The rotational (or angular) position of the tibial component is defined by the angle between a line drawn along the top of the tibial base plate and the tibial axis (Doets et al., 2006, Choi et al., 2013) (Figure 2.21). Pyevich et al. (1998) showed higher pain scores in patients with tibial component rotation greater than 4°. Alignment angles greater than 5° from the tibial axis in either plane is generally considered excessive, regardless of implant design (Hintermann et al., 2004, Rippstein et al., 2011, Braito et al., 2015a, Kerkhoff et al., 2016c, Kim et al., 2016). Although, acceptable tolerances can vary between surgeons for the same device, for example Braito et al. (2015a) implanted the Hintegra TAR with ± 5° rotational variance, whereas Usuelli et al. (2016a) considered ± 2° was an acceptable tolerance for the same device.
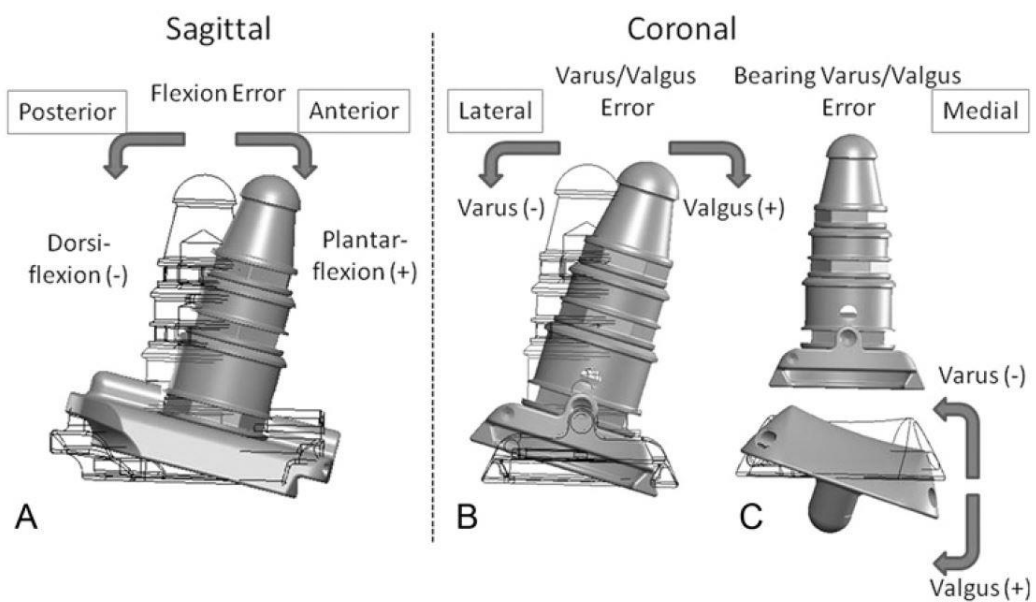
Figure 2.21. Definitions of rotational variation. A, flexion-extension. B, varus-valgus. C, varus-valgus alignment between components. Adopted from Berlet et al. (2014).

Excessive rotational variance has been shown to affect fixed-bearing and mobile-bearing designs differently (Espinosa et al., 2010). In a finite element analysis study comparing the fixed-bearing Agility TAR and the mobile-bearing Mobility TAR, the effect of malpositioning on contact stresses was analysed. The conditions used were up to ± 10° inversion/eversion (referred to as 'version') and 5° axial rotational deviation from the manufacturer's guidelines. Version of the Agility components resulted in increased contact pressures, which were mirrored for symmetrical malpositioning errors in the same plane due to the implant's symmetrical design. Rotational error in the transverse plane did not affect pressure distributions for the Mobility TAR, although the effect of these errors on soft tissue strain was not discussed and could be crucial for implant failure (Fukuda et al., 2010). Substantial increases in peak and mean contact pressures occurred in both implants after a version variation >5°. The Mobility TAR was more

sensitive to version errors; version variation >2° shifted pressure distributions towards the edge of the meniscus closest to the origin of the version. Contact pressures increased above 10 MPa in response to these version errors, reflective of the decrease in contact area. The tibia and talus were rigid entities in this study, which eliminated the effect of the surrounding ligaments. Fukuda et al. (2010) demonstrated the passive realignment of components under load using a cadaveric in vitro approach, therefore, the contact pressures indicated by Espinosa et al. (2010) may be overestimated.
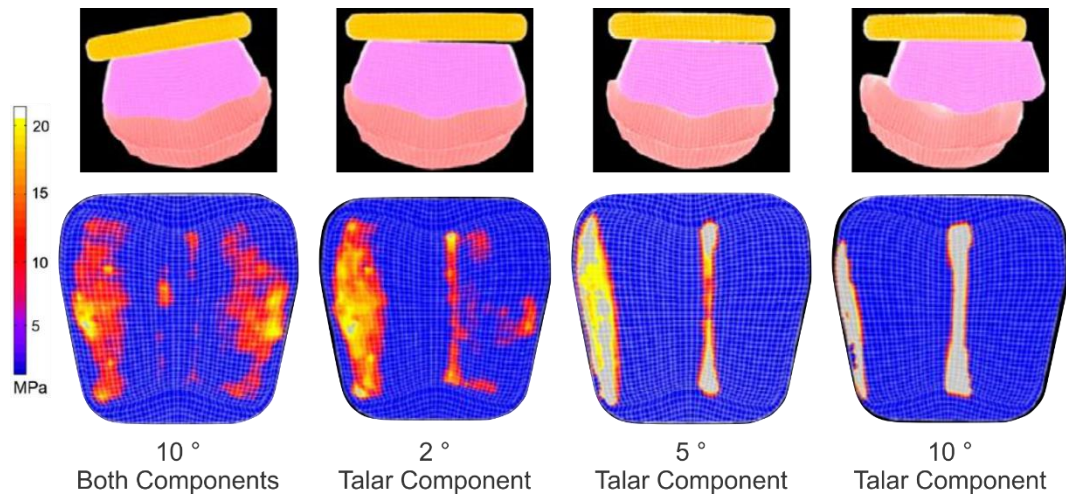
Figure 2.22. Pressure distributions for the Mobility TAR in different alignment conditions shown by finite element analysis. Adapted from Espinosa et al. (2010).

Practically, the angular orientation of the talar component can be difficult to measure in either the sagittal or coronal planes due to the often indistinguishable silhouette created by rotated metallic components in X-ray imaging. Component rotation may also obscure the visualisation of the bone-implant interface (Rippstein et al., 2011).

Translational Variation

Anteroposterior offset of the talar component relative to the tibial axis is the most commonly measured translational position measurement (Tochigi et al., 2005, Barg et al., 2011a, Braito et al., 2015a). A relative measure of translational variation was developed by Barg et al. (2010a) named the antero-posterior offset ratio (AOR). This was defined as the perpendicular distance of the centre of the talar component relative to the tibial axis. The distance was reported as a ratio of the total length of the tibial base plate in the sagittal plane. For example, an AOR of 0.1 equates to an anterior (positive) offset of 10% of the length of the tibial base plate.
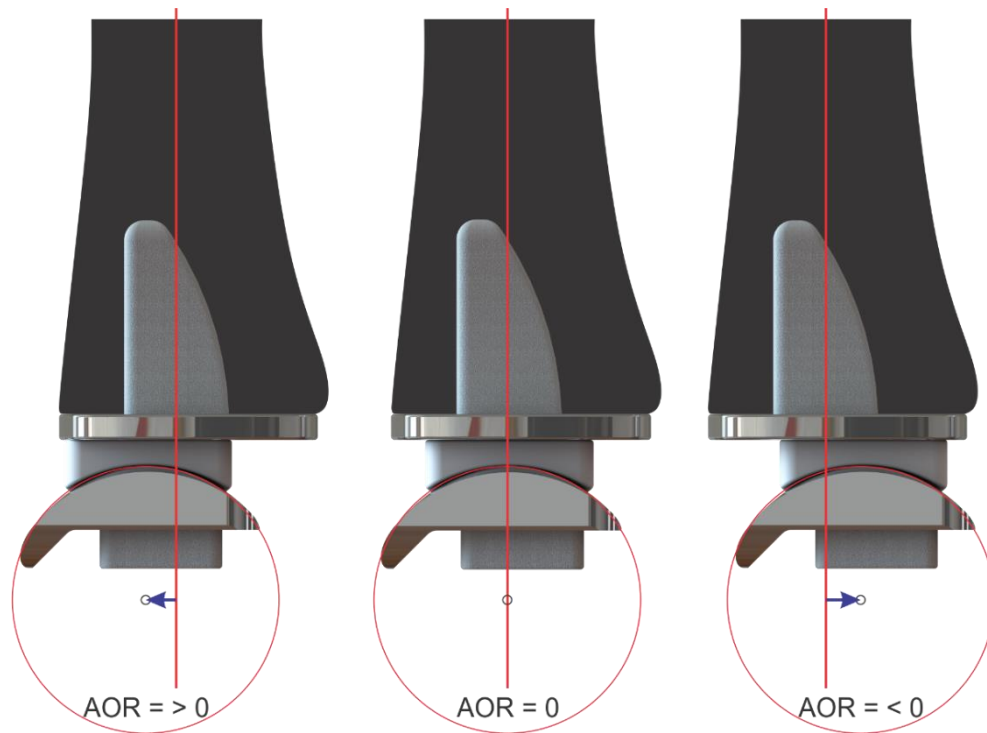
Figure 2.23. Antero-posterior offset ratio (AOR). The arrows denote talar component offset from the tibial axis in the anterior (left) and posterior (right) directions.

Acceptable tolerances for the AOR have not been proposed but the metric has been associated with clinical outcomes such as perceived pain. Barg et al. (2010a) measured anteroposterior offset in 368 Hintegra TARs and 34.5% of the ankles had an anteroposterior offset of 0. The mean anterior offset was 0.06 (range, 0.01 to 0.16; ± 0.04 SD) and the mean posterior offset was 0.07 (range, − 0.21 to − 0.01; ± 0.04 SD). In a follow-up study comprising of 317 ankles of the original cohort, an AOR of 0 was associated with reduced pain, reduced AOFAS hind foot score and increased range of movement (Barg et al., 2011a). Braito et al. (2015a) measured a mean AOR of 0.1 (± 0.1 SD) for 84 ankles with implanted Hintegra TARs. This suggests the components were placed anterior relative to the tibial axis in the majority of cases. No significant differences for clinical outcomes were identified between positive (>0), neutral (0) and negative (< 0) AOR ankles. In a cadaver study, placement of the bearing insert anteriorly by 3 and 6 mm led to reduced ankle flexion and extension. The limiting factor on range of movement was thought to be either ligamentous strain or bearing lift off caused by axial forces being focussed on the posterior of the bearing insert (Tochigi et al., 2005).

Translational variance of the talar component in the coronal plane has been identified as a potential cause of edge-loading. Edge-loading has been defined as the overlap of the tibial component edge across the edge of the talar component. Rippstein et al. (2011) used coronal plane weight-bearing X-ray images to measure the distance between the tibial and talar component for a cohort patients with mobile-bearing Mobility TARs. Of 228 ankles, 7% had a difference of ≥2 mm between the components which was

categorised as excessive. Koivu et al. (2009) identified nine (7%) of 130 TARs with the AES TAR to have an excessive metallic component offset indicative of edge-loading. Although, excessive translational offset was defined as ≥3 mm (Koivu et al., 2009), rather than ≥2 mm (Rippstein et al., 2011). Haskell and Mann (2004a) defined progressive edge-loading as a ≥4° difference in alpha angle between the metallic components. This was a different definition of edge-loading to Rippstein et al. (2011) and Koivu et al. (2009), and represented varus/valgus alignment rather than translational offset. Each of these alignment methods use coronal plane X-ray images and require the components to be perpendicular to the observer to be measured. If either of the tibial or talar components are rotated relative to the coronal plane, measurements may be impaired. Methodologies have been developed to calculate bearing insert rotation using the radiopaque marker, however, this method was specific to the STAR device and required a repeatable clinical medical imaging procedure which is uncharacteristic of standard clinical practice (Lundeen et al., 2016).
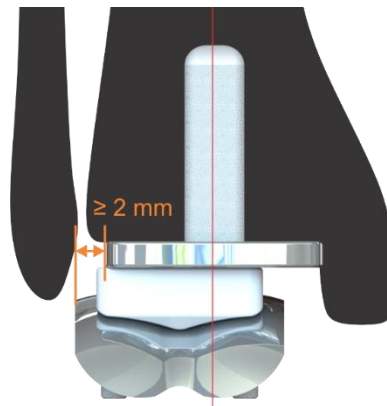
Figure 2.24. Edge-loading as defined by Rippstein et al. (2011). An offset between the tibial and talar components by at least 2 mm in the coronal plane.

2.5.1.2 Characterisation of Osteolysis

Conventional radiography is well known within the orthopaedic community to have a sensitivity of approximately 50% for identifying osteolysis compared to computed tomography (Claus et al., 2003, Walde et al., 2005). Similar sensitivity levels have been reported for identifying osteolysis surrounding TAR (Kohonen et al., 2013, Yoon et al., 2014). Accurately characterising the size and location of osteolysis serves several functions:

a) An indicator for the risk of further complications (e.g. talar component collapse, component loosening, subsidence, peri-prosthetic fracture).
b) Informs planning for revision surgery.
c) Allows accurate monitoring and reporting of device efficacy and safety.

d) The magnitude of the complication can be adequately understood by the surgeon and described to the patient.

Several methods have been developed to characterise the size and location of osteolysis in TAR.

Size

Early definitions of osteolysis described an ellipsoidal hypodense area of bone, greater than two millimetres in width and predominantly located on the lateral edge of the fixed bearing Agility total ankle replacement (Pyevich et al., 1998). Pyevich et al. (1998) named this 'ballooning' osteolysis but was later redefined by Knecht et al. (2004) as 'mechanical' osteolysis because the origin appeared to be caused by micromotion and friction at the bone implant interface. This focal presentation of mechanical osteolysis was non-progressive after approximately 12 months, evidenced by the presence of circumferential sclerotic lines after a relevant follow-up (Knecht et al., 2004). Ellipsoidal lesions, similar to those on the lateral border of the Agility TAR, but originate at the base of the tibial fixation stem or inferior to the fixation surface of the talar component have also been identified (Kohonen et al., 2013). Contrary to the mechanical osteolysis defined by Knecht et al. (2004), these lesions are: large (>5 mm), progressive, void of trabecular bone and have an unknown aetiology. These early progressive lesions have been referred to as osteolytic cysts (Bonnin et al., 2011), although the term 'ballooning' osteolysis has also been reused to describe such lesions (Besse et al., 2009).

A five category sizing criteria has broadly been accepted for use in the published literature (Table 2.2) and osteolytic cyst size is commonly reported to be category B or greater (i.e. >5 mm) (Besse et al., 2009, Rodriguez et al., 2010). In the 37 patients at 44.5 months follow-up, 54% showed osteolytic cysts around the tibial component >6 mm in size. Forty-three percent of the patients showed cysts >6 mm around the talar component. No association between severe osteolysis and pain was evident in this study (Besse et al., 2009). Osteolytic areas greater than 10 mm in size (maximum diameter) has been classified as 'severe' (Viste et al., 2015), and is used as a criterion for reoperation (bone grafting), but not necessarily revision surgery (Gross et al., 2016).

Table 2.2. Osteolysis size categories developed by Besse et al. (2009).

Category	Criteria
Normal	No radiolucency
Lucent	< 2mm Radiolucency
Cyst A	3 mm - 5 mm
Cyst B	5 mm - 10 mm
Cyst C	10 mm - 20 mm
Cyst D	20 mm - 30 mm
Cyst E	>30 mm

Notes: The 30 mm tibial stem was measured as a scale reference

Axial CT scans are suggested to be the most efficacious for determining osteolysis size and location when compared to conventional X-ray imaging (Viste et al., 2015). Computed tomography allows for areal measurements to be made and a more informative and accurate characterisation to be undertaken. Basic parameters, such as Feret's diameter (Hanna et al., 2007) and the area of the closest matching ellipse (Yoon et al., 2014) are used but assume uniform cyst shape and are only representative values, not true volumetric measures. Osteolytic lesions are likely to be asymmetrical and interconnected which further complicates accurate characterisation.

Osteolysis volume has been calculated by Jensen et al. (2014) for the STAR using 3D multiplanar reconstructed fluoroscopic imaging. In total, 100 cysts were measured, the average size was 1.55 cm^3 with a range between 0.02 and 8.19 cm^3. Gross et al. (2016) reported volumes of 25.7 cm^3 for tibia and 14.9cm^3 for the talus. Both of these studies estimated the volume of the osteolysis using ellipsoid calculations (volume = 4/3 π * x * y * z). These studies assessing osteolysis volume are the most accurate assessments of osteolysis size currently available for TAR, however still rely on the assumption that the osteolysis is of uniform ellipsoidal geometry.

Location

The spatial identification, size and frequency of osteolysis has previously been limited by the poor sensitivity of X-ray radiography to changes in relative bone density caused by the superimposition of all tissue layers (Yoon et al., 2014). The low sensitivity of X-ray imaging also means the interconnectivity of the lesions often cannot be identified (Alidousti et al., 2014). Nonetheless, osteolysis mapping grids have been developed for several TAR designs, including the AES TAR (Besse et al., 2009, Koivu et al., 2009, Rodriguez et al., 2010, Kohonen et al., 2013), Mobility TAR (Rippstein et al., 2011, Muir et al., 2013), Hintegra TAR (Yoon et al., 2014), Agility TAR (Pyevich et al., 1998), and; the Salto TAR (Bonnin et al., 2011).

Besse et al. (2009) developed a ten zone grid and classification method for the AES TAR (Figure 2.25). The base of the tibial stem was highlighted as the most common location for osteolysis, which had equal coverage in all four zones above the tibial component (zones 1, 2, 6, 7). Talar osteolysis originated predominantly at the anterior anchorage point of the talar component (zone 9). Equal distribution of osteolysis across the superior tibial surface and surrounding the anterior talar anchorage was consistent across other studies investigating the AES TAR (Koivu et al., 2009, Rodriguez et al., 2010, Dalat et al., 2013, Kohonen et al., 2013). A different trend was identified for a similar BP-type TAR device, the Mobility. The osteolytic cysts appeared to be predominantly located in the medial malleolus (Rippstein et al., 2011, Muir et al., 2013).
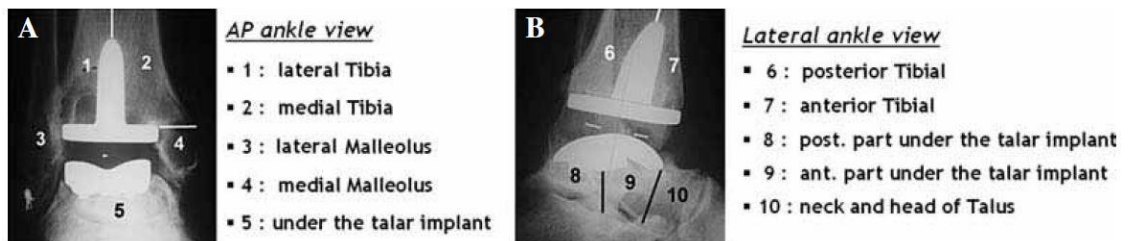
Figure 2.25. Zonal frequency mapping for osteolysis and radiolucency identified in coronal and lateral X-ray images. Adopted from Besse et al. (2009).

Clarity of visualising and measuring osteolysis has improved with the use of CT, however two-dimensional mapping techniques remain popular.

2.5.2 Retrieval Analysis

Explanted TAR components (or explants) and periprosthetic tissue samples are usually extracted and disposed of after the revision surgery procedure. However these materials offer a unique opportunity to investigate the environment within the joint space in which the TAR functioned. 'Retrieval analysis' is the process of examining these resources and allows for specific damage modes and wear mechanisms to be recognised.

The distinction between 'damage' and 'wear' is important to consider when analysing total joint replacement failure. Damage is defined as the visible and microscopic change in surface texture or geometry which includes both abrasion and creep, whereas 'wear' is a process that specifically causes damage *and* the liberation of material (McKellop, 2007). McKellop (2007) described four distinct wear modes by which a total joint replacement may function post-implantation. Mode 1 reflects the expected 'normal' wear of a device with two bearing surfaces interacting under load. In mode 2, a non-bearing surface wears against a bearing surface. Mode 3 includes third body abrasive wear particles within a 'normal' mode 1 articulation. Mode 4 represents two non-bearing surfaces interacting under load. Mode 1 wear is inevitable in standard conditions and

should be minimised, whereas modes 2, 3 and 4 are considered device malfunction and should be avoided by design and surgical approach.
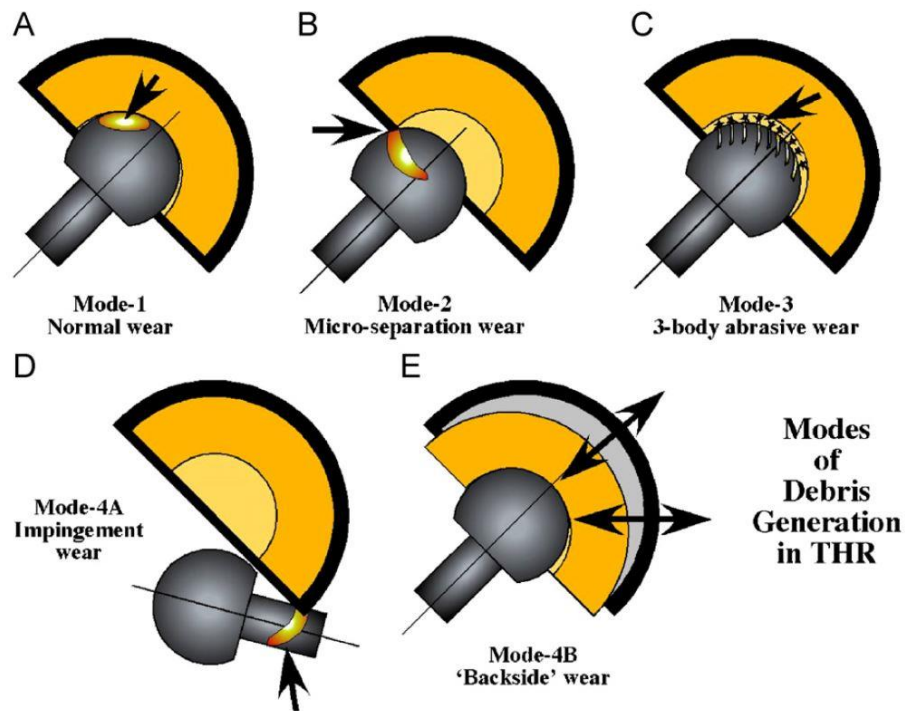
Figure 2.26. Illustration of four wear modes present for total hip replacement. Adopted from McKellop (2007).

Understanding the type of wear mechanisms associated with TAR allows their replication in the laboratory, providing knowledge on how to reduce them. Simulator studies attempting to emulate TAR function have suggested wear rates to be similar to TKR (Smyth et al., 2017), however, the evidence-base describing what type and quantity of wear is produced in vivo is limited. Current simulation methods for TAR have only investigated mode 1 wear, bearing-on-bearing articulation (McKellop, 2007), despite other wear modes being indicated in TAR failure (Besse et al., 2009).

This section reviews the evidence produced by TAR retrieval studies and the analysis methods suitable for use to characterise TAR damage/wear.

2.5.2.1   Damage Mode Identification

An extensive tribological vocabulary has been developed from the need to describe specific damage modes. Attempts to standardise damage modes have been relatively successful, given that the seven most commonly used terms for describing damage were identified in 1978 (Rostoker et al., 1978) (Table 2.3). Hood et al. (1983) developed the seven damage descriptors into a semi-quantitative scoring system which has been adopted in the retrieval analysis literature since (McKellop, 2007) (Table 2.4).

Table 2.3. Explant damage modes as described by Rostoker et al. (1978) and Hood et al. (1983).

Rostoker et al., (1978)	Hood et al., (1983)	Description
Wear Polishing	Burnishing	Progressive erasure of machining marks caused by high pressure articulation. Highly polished surface.
Scratches and Gouges	Scratches	Indented lines usually parallel with the direction of articulation. Gouges are deep trenches. Should not be confused with iatrogenic damage.
Folds	Surface Deformation	Permanent deformation of the articulating surface, presumably by cold flow and/or creep.
Pits, Indentations, and Craters	Pitting	Depressions visible to the eye in the articulating surface. Irregularly shaped, approx. 2-3mm across and 1-2mm deep.
Abrasion or Shredding	Abrasion	Tufts of material present after an area was torn from the substrate.
Cracks	Delamination	Subsurface failure typically surrounding an area of avulsed substrate caused by fatigue.
Embedded Bone Cement	Embedded Bone Cement	Different colour or texture between cement and polyethylene. May be extruding from surface or polished even with it.

The method developed by Hood et al. (1983) used stereomicroscopy (x10 magnification) to analyse knee replacement components and classify the location and extent of surface damage on a percentage scale. This was converted to a value between zero and three. The output was a damage score that was correlated with other clinical outcomes such as implantation time and patient demographic information.

Table 2.4. The Hood et al. (1983) damage assessment scale.

Damage Feature	%Area (AS)	Score
Burnishing Scratches	0	0
Surface Deformation	<10%	1
Pitting	10%-50%	2
Abrasion	50%-100%	3
Delamination		
Embedded Bone Cement		

Notes: Each implant zone is given a score for each damage feature.

Wasielewski et al. (1994) adjusted the scale developed by Hood et al. (1983) to distinguish between extent (or area) and severity by assigning a zero to three damage feature score to each of these factors separately. The overall damage score was a product of these two values (Table 2.5). The location of each damage mode was also noted. The area score (or damage extent) for both of these scales becomes saturated at 50% of the given area. This was a pragmatic method for the observer particularly if there were many explants in the sample. However, it was hypothesised that greater precision could be obtained if higher extent values were accounted for (Brandt et al., 2012).

Table 2.5. The Wasielewski et al. (1994) damage assessment scale.

Damage Feature	%Area (AS)	Score	Severity (SS)	Score
Burnishing	0	0	No Damage	0
Scratches	<10%	1	Mild Damage; just visible	1
Surface Deformation	10%-50%	2	Moderate Damage	2
Pitting	50%-100%	3	Severe Damage	3
Abrasion				
Delamination				
Embedded Bone Cement				

Notes: AS, Area Score; SS, Severity Score; Each implant zone is given an area and severity score for each damage feature. The damage feature score is obtained by multiplying AS by SS.

Brandt et al. (2012) extended the percentage values for the damage area score by five deciles for each zone in an attempt to improve damage score precision (Table 2.6). Both the Hood-Wasielewski scale and the method developed by Brandt et al. (2012) yielded similar correlations for knee replacement menisci implanted for less than 24 months. The majority of damage apparently occurred within the first 24 months which, as suspected, saturated the extent score in Hood-Wasielewski scale (Brandt et al., 2012). The Brandt et al. (2012) modified method could identify detectable changes above the 50% Hood-Wasielewski threshold after this early 'bedding in' wear period.

Table 2.6. The Brandt et al. (2012) damage assessment scale.

Damage Feature	%Area (AS)	Score	Severity (SS)	Score
Burnishing	0	0	No Damage	0
Scratches	10%-20%	1	Mild Damage; just visible	0.33
Surface Deformation	20%-30%	2	Moderate Damage	0.66
Pitting	30%-40%	3	Severe Damage	1
Abrasion	40%-50%	4		
Delamination	50%-60%	5		
Embedded Bone Cement	60%-70%	6		
	70%-80%	7		
	80%-90%	8		
	90%-100%	9		

Notes: AS, Area Score; SS, Severity Score; Each implant zone is given an area and severity score for each damage feature. The damage feature score is obtained by multiplying AS by SS.

The damage score (*DS*) for each of these scales can be expressed mathematically:

Equation 2.1.

$$DS = \sum_{i=1}^{n} DFS_i$$

where damage feature score (*DFS$_i$*) is the *AS$_i$* x *SS$_i$*, damage feature score for the ith feature; *AS$_i$* and *SS$_i$* are the area score and severity score for the ith damage feature, respectively; n is the total number of damage features.

The first published damage mode analysis of TAR was reported in US Food and Drug Administration (FDA) documentation for the post-market assessment of the mobile-bearing STAR (Small Bones Innovations Inc., 2007). Burnishing was the most common

damage mode followed by scratching, pitting and abrasion. Three of the 35 devices had material fracture. Nine bearing inserts presented with significant loss of material on the edges of the component, suggested to be caused by contact with bone. Finally, nine devices had significant damage to the keel-trough, which is a design feature specific to the STAR but the type of damage was not described. This analysis was limited to the bearing insert component and damage to the metallic components was not reported.

Affatato et al. (2009) conducted a damage mode analysis to compare in vitro tested mobile-bearing BOX TARs against three BOX explants. Damage was similar between the in vitro samples and the explants, showing burnishing on the bearing surfaces of the bearing insert. Pitting was only evident on the explants which may be explained by the difference in tribological conditions and wear mechanisms. For example, wear of the fixation surface and the production of third-body wear typically only occurs in vivo and not in vitro.

Vaupel et al. (2009) retrieved ten Agility TARs for analysis by optical microscopy and scanning electron microscopy. Six damage modes were evident: Abrasion, burnishing, pitting, scratching/grooving, dishing and embedding. The Agility TAR features a talar component with less surface area than the articulating polyethylene component in a fixed-bearing design. The high contact pressures associated with the small contact area led to gross deformation of the polyethylene which was dubbed the 'talar footprint'. Embedded titanium in the polyethylene side of the tibial component was confirmed using energy dispersive X-ray spectroscopy, which suggested the fixation surface had undergone wear, possibly caused by micromotion between the implant and cement.

Cottrino et al. (2016) analysed six retrieved mobile-bearing AES explants. This study characterised embedded debris on the surface of the bearing insert and its possible origins. Cobalt chromium alloy and titanium wear particles were identified and both particle types were thought to have originated from the metallic components. Scratching of both the bearing insert surface and the tibial component bearing surface was evident and was suggested to be the product of 3rd body wear. The bearing inserts had worn evenly and proportionally with implantation time, however this was determined visually, not quantitatively.

Notably, the above TAR retrieval analyses used the lexicon of Hood et al. (1983) but did not report damage mode scores. Semi-quantitative scales are limited by their subjectivity and low specificity (Harman et al., 2011, Childs et al., 2016). Damage modes such as scratching and embedded debris were more difficult to identify even after damage mode identification training had been undertaken (Harman et al., 2011). High damage scores does not necessarily reflect high wear rates and in fact, the opposite may be true (McKellop, 2007). Also, these damage mode scales may underestimate the severity of

damage if the damage was severe but localised to a small area, for example, a fractured and displaced section of the bearing (Cornwall et al., 1995). Third body wear appears to be a prevalent wear mode for TAR, however only a few retrieval analyses have been conducted featuring TAR devices.

2.5.2.2   Quantitative Damage Mode Analyses

Semi-quantitative damage mode analysis methods are limited by their subjective nature. Quantitative analysis methods may improve damage mode identification and allow for objective comparisons between analyses conducted by different research groups.

2.5.2.3   Photogrammetry

Photography is the gold standard for reporting the presence of damage modes and is used commonly in published retrieval analysis. Photogrammetry is the standardisation of the photography process, removing errors such a parallax and scaling images to allow accurate measurements to be made. Single camera (two-dimensional) digital photogrammetry based on scaled photographs, was shown to be an accurate, repeatable and inexpensive method for quantifying the area of wear on an implant's surface (Grochowsky et al., 2006, Cottrell et al., 2007, Harman et al., 2007). However, this method remains subjective given the observer is required to outline the area of wear and if three-dimensional measurements were desired (i.e. the measurement of surface height), a 3D coordinate measuring machine would be required. Photogrammetry quantifies the extent of damage and cannot distinguish damage mode characteristics numerically. The superimposition of more than one damage mode further complicates the identification of individual damage modes both visually and quantitatively. Understanding the quantitative characteristics of damage modes may indicate damage severity and also the variance within damage modes that are visually similar but characteristically different.

2.5.2.4   Surface Characterisation Methods

Photography typically captures two dimensions in the plane normal to the camera lens. However, changes in surface height (third dimension) is a surface characteristic that is valuable for determining damage modes and their origins. For example, the presence of scratches is identifiable using photographs, however the depth of the scratch may not be calculable and may indicate the type of wear particle or surface that caused the damage.

When characterising a surface, the analysis equipment identifies the 'surface heights'. Surface heights are the measured points on a surface that lie at a given height. The distribution of surface heights can be represented by a histogram and cumulative frequency curve, which is also known in the field of metrology as an Abbott-Firestone

curve (Blateyron, 2013) (Figure 2.27). From these surface heights, the surface can be characterised and compared. The method by which surface heights are obtained can be contacting (i.e. physically measuring the surface) or non-contacting (i.e. measurement without contact). Examples of different measurement methods and the associated surface parameters are discussed below.
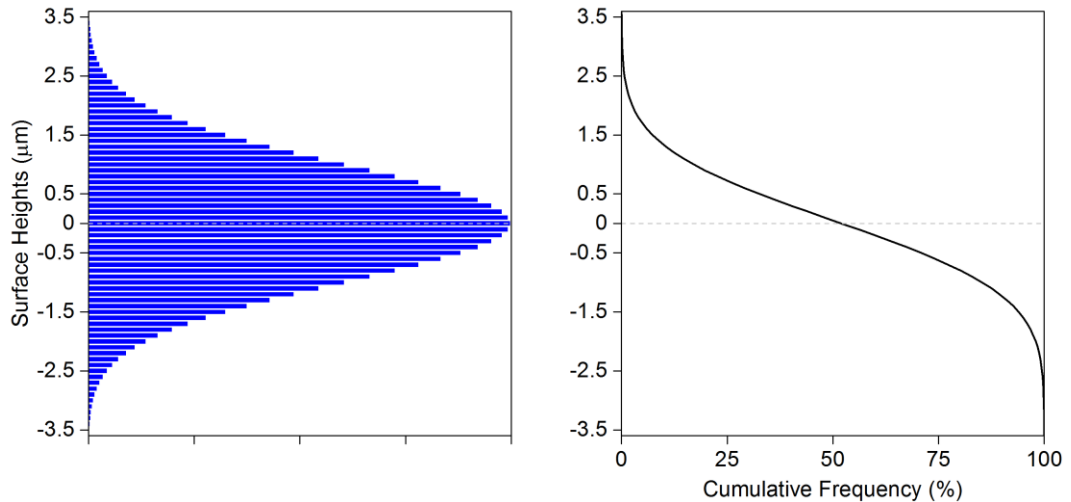
Figure 2.27. Surface height distribution (left) and the representative Abbott-firestone curve (right).

Profilometry (contacting)

Contacting profilometry is commonly used for obtaining two-dimensional measurements of surface finish typically for use in manufacturing quality assurance. This method uses a stylus that physically measures the surface roughness by tracing along a surface and measuring the surface heights. This method has been used to quantify scratch roughness for in vitro tested TARs (Bell and Fisher, 2007, Smyth et al., 2017), however not yet implemented for retrieved TARs.

When measuring highly polished surfaces using contacting profilometry, the resolution of the measurement is limited by the radius of the stylus tip. The conical shape of the stylus tip cannot record peaks or dales accurately without rounding the pinnacle of each surface height slightly (Figure 2.28). Contacting profilometry also risks damaging the measurement surface. Despite only millinewton forces travelling through the stylus, these forces are concentrated at the, sometimes nanoscale, tip diameter which may generate high enough contact stresses to damage soft surfaces. For example, if the preservation of thin organometallic films (i.e. tribofilms) was desired, a phenomenon associated with metal-on-metal hip replacements (Yan et al., 2010), contacting profilometry may not provide an accurate measure of surface heights in this case.
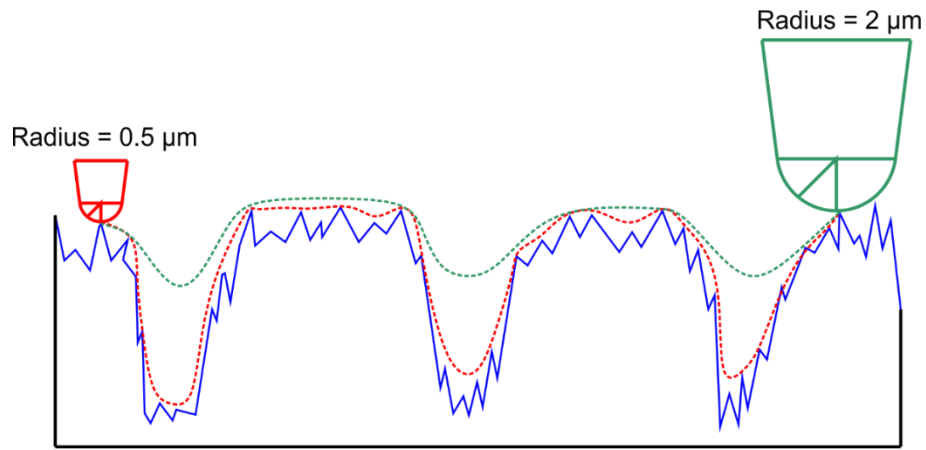
Figure 2.28. Mechanical filter effect caused by the path taken by two styli of different sizes. The larger stylus cannot measure the narrower valleys.

Coordinate Measuring Machine (contacting)

Methods using a coordinate measuring machine (CMM) have been developed to determine wear volume loss in joint replacements (Muratoglu et al., 2003). The CMM measures implant form and size by identifying surface heights within a three-dimensional point space. This technique can produce three-dimensional images of an implant's surface and can be used to calculate wear volume loss (Affatato et al., 2009).

Affatato et al. (2009) analysed three BOX TAR bearing insert retrievals using a CMM methodology to compare damage modes with in vitro tested devices. With over 4000 surface heights measured at a resolution of 0.4 mm x 0.4 mm, linear penetration of the superior bearing insert surface was 0.025 to 0.091 mm compared to a computer-aided design (CAD) model of the same component. Computer models of components represent the 'ideal' component and may not adequately reflect the variance in surface geometry created by manufacturing processes. Therefore, surface measurements are often limited by how representative the unworn or 'ideal' comparator is to the general population of manufactured components.

Coordinate measuring equipment is expensive, requires a specialist user and the process can be time-consuming. Depth/height gauges have been used as a simple alternative to the CMM to measure explant height and component thickness (Wright et al., 1992, Bartel et al., 1995). In addition to using the CMM, Affatato et al. (2009) used digital callipers to determine the change of TAR bearing insert width in the medio-lateral direction. Similarly to the CMM, a CAD model was used as a width comparator.

Optical Interferometry (non-contacting)

Non-contacting methods have been developed and used with explants to determine similar characteristics to contacting methods but the measurements tend to be quicker and captured at higher resolutions. Optical interference techniques function by

calculating either the phase shift between two independent beams of light, split and compared relative to each other; or, by measuring the coherence of the interference fringes of the two beams of light, instead of the phase shift. The latter method is called vertical scanning interferometry (VSI) and is typically used for measuring rougher surfaces, such as those present on retrieved orthopaedic implants.

Optical interferometry can achieve nanometre vertical and lateral resolution and the non-contacting nature of this measurement method reduces the risk of damage to the explant. However, the reliance of this technique on the return of light makes capturing an image challenging, particularly if the material absorbs (e.g. polyethylene) or disperses light effectively (e.g. highly curved metallic components). Slopes greater than ~ 15°, such as the edges of wear scars, may not be adequately captured using this technique. Applications which feature steep slopes, such as the talar component bearing surface of TAR may not be suitable for this type of analysis.

Quantitative Light Microscopy (non-contacting)

Quantitative light microscopes, such as the InfiniteFocus microscope (IFM; Alicona Imaging GmbH, HR), produces both true colour photographic images and high resolution topographical characteristics, simultaneously. This is achieved by compiling a stack of in-focus images at a pre-defined z-axis resolution. Surface height values are assigned to the relevant in-focus feature on each photograph. The total image stack height is the maximum measured height. The scratch characteristics of six AES TAR implants were determined using quantitative microscopy (Cottrino et al., 2016). The scratch height and width was 11 μm and 100 μm, respectively. The damage was assumed by the authors to be caused by third-body abrasive wear and that the particle was approximately 100 μm in size. Although, where on the component the measurements had been captured was not clearly detailed. Liza et al. (2011) used quantitative light microscopy to identify and quantify pitting on a total knee replacement inserts. Pit diameters of up to 60 μm were measured. Pits and gouging cannot easily be measured using contact profilometry because the stylus may snag on the relatively deep voids and steep gradients characteristic of this damage mode (Burnell et al., 2011).

Surface Characterisation Parameters

Cross-sectional profiles produced using two-dimensional profilometry parameters lose valuable information which may determine the nature of the feature e.g. is the profile a pit or a scratch? (Figure 2.29). Three-dimensional parameters reveal topographic features and their functional implications.
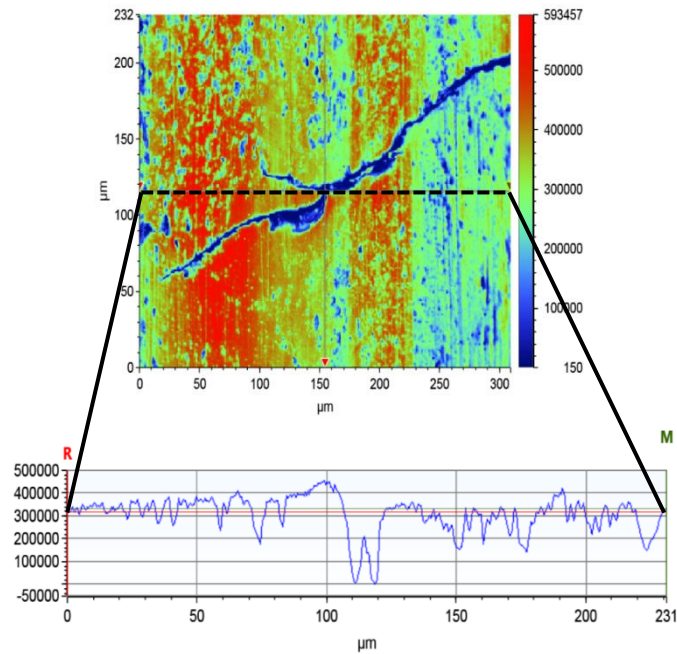
Figure 2.29. Pit, scratch or crack? A two-dimensional profile that requires the three-dimension context to describe what it represents.

Surface Height Parameters

The arithmetic mean of the heights (Sa) parameter is the arithmetic mean of the absolute height values within the measurement area. While surface roughness is commonly reported, the same roughness value can represent surfaces with substantially different surface profiles (Figure 2.30). For example, a surface with a positively skewed distribution of surface heights may have the same average roughness as a surface with a negatively skewed distribution. This is relevant to orthopaedic device design because the surface with a negative skew may be capable of retaining more synovial fluid for lubricant. A breadth of surface characterisation parameters are detailed in British Standard ISO 25178-2 (2012) however, the clinical relevance of identifying such parameters for explant surfaces, other than roughness, is yet to be developed.
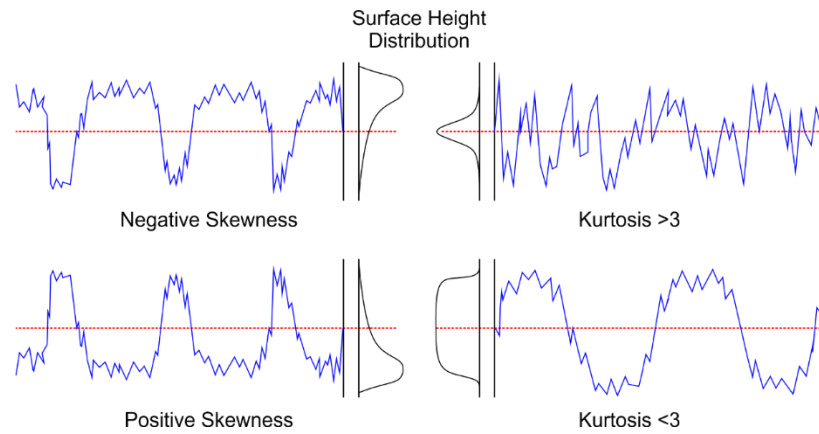
Figure 2.30. Four hypothetical surface profiles (blue lines) with the same mean surface height (red line) but with different surface texture characteristics e.g. skewness or kurtosis.

2.5.2.5   Wear Volume Analysis

Wear products are commonly detrimental to the surrounding biological environment, therefore minimising wear is a high priority for medical device designers. The distinction between damage and wear is the loss of material (McKellop, 2007). Damage such as plastic deformation may result in material redistribution, not wear. Whereas if material is lost, then the volume of the component changes. Identifying the wear rates of TAR is important to understand the risk of wear being a factor in the failure of this technology.

In vitro simulation tests use wear volume analysis methods to determine wear rates and the same component is used as its own comparator pre- and post-testing (Affatato et al., 2007, Bell and Fisher, 2007, Bischoff et al., 2015, Reinders et al., 2015, Smyth et al., 2017). For explants, it is not practical to measure component volume prior to implantation because such analyses may introduce unnecessary risks for the patient by jeopardising the components sterilisation or quality. Alternatively, the same patient may not return to the same surgeon for revision surgery, and therefore the post-implantation measurement may not be captured.

Computer models of the original component have been used to compare to explants and idealised shapes (e.g. sphere) have been used to estimate wear of components with ball and socket-type articulations (Bowden et al., 2005, Day et al., 2012). An identical component as manufactured may also be used as a comparator however, the manufacturing tolerance needs to be considered a possible limitation for accuracy. Teeter et al. (2011b) averaged the volume of six simulator samples prior to in vitro wear testing to determine the variance caused by manufacturing tolerances. An average geometry was created and used as a comparator, the overall variance for the bearing surface geometry was 15 ± 59 µm. The following methods can be used to determine wear volume loss of explants:

Gravimetric Analysis

Volume can be inferred from gravimetric measurements, such as weighing a component using a balance. The weight (or mass multiplied by gravity; *mg*) of a component is directly proportional to its volume (*V*) if the density (ρ) of the component is constant.

Equation 2.2.
$$V = \frac{mg}{\rho}$$

Gravimetric measurements are the most commonly used method for determining component volume in orthopaedic research because material characteristics are often known prior to testing, therefore the material density can be assumed to be the same before and after testing. This is a simple method that requires equipment (e.g. a high-precision balance) most retrieval laboratories have access to.

Fluid Displacement

Using Archimedes' principle, volumetric material loss has been measured by fluid displacement in THR acetabular cups (Rentfrow et al., 1996, Jasty et al., 1997, Yamamoto et al., 2003). Fluid is introduced between the ball and socket and the difference in fluid volume is compared between worn and unworn articulations. The ball and socket type articulation retains fluid well and suits this method of wear volume calculation. For flat or shallow articulations, such as in TAR, this method may not be suitable. Additionally, this method only measures one specific surface and cannot calculate the total volume loss including wear of the backside of the acetabular component.

Pycnometry

Pycnometry measures the entire volume of a component without assuming density unlike gravimetric analysis. This method does not require the weight of the component to calculate volume. Gas pycnometry measures the pressure change resulting from the displacement of gas by introducing a test component of unknown volume (V_x) to a chamber of known volume (V_s). A gas with known characteristics (i.e. helium) fills the chamber and the pressure is measured (P_s). A reference chamber of known volume (V_r) is pressurised (P_r), usually at a pressure greater than P_s and then a valve is released allowing the gas to flow between V_r to V_s and the total system pressure equilibrates. The change in pressure is directly proportional to the volume of the test component as shown by Equation 2.3.

Equation 2.3.
$$PV = nRT$$

Where, P is the gas pressure, V is the volume of gas, n is the amount of gas molecules, R is the universal gas constant and T is the gas temperature.
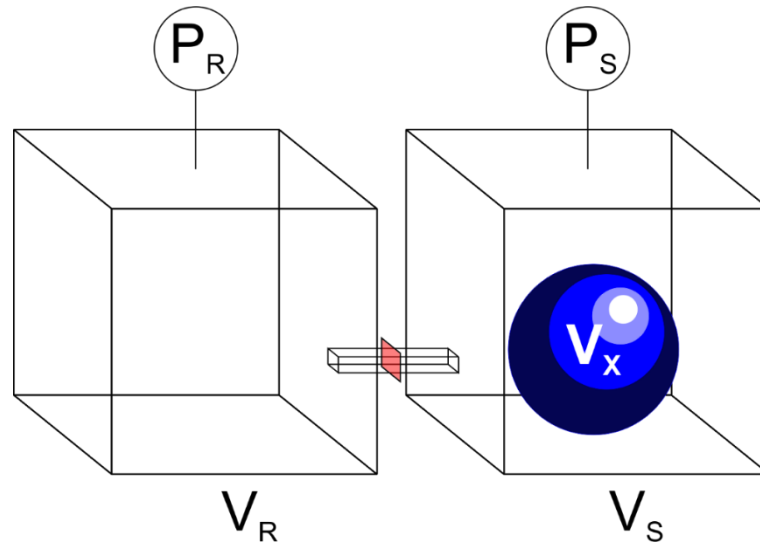
Figure 2.31. Schematic of pycnometry. The object of unknown volume (V_x) is placed in a chamber of known volume (V_s). A reference chamber (V_r) of equal volume to V_s is hyper-pressurised (P_r) relative to the pressure in V_s (P_s). A valve is released between the chambers (red rhomboid) and the pressure change measured is proportional to the volume of V_x.

As long as the number of gas molecules and the temperature remains the same throughout the test, Equation 2.3 applies. These two variables are typically controlled by maintaining the same gas of known characteristics throughout tests (e.g. helium) and using temperature-controlled equipment.

This method has not been used for explant analyses before which may be because THR and TKR components are too large for the measurement chambers of the equipment or the equipment is not available in the relevant laboratories. Balances for gravimetric analyses are more commonly available and inexpensive.

Computed Tomography

Computed tomography (CT) is an X-ray-based technology typically used clinically to determine defects in bone, such as osteolysis. Using similar technology, non-clinical high resolution CT, also known as micro-CT, can be used to calculate polymeric component volume loss (Bowden et al., 2005). Volume change has been calculated for THR acetabular cups (Bowden et al., 2005), total shoulder replacement glenoid components (Day et al., 2012) and TKR inserts (Teeter et al., 2011a). Micro-CT has been used to capture cross-sectional images of TAR bearing inserts to identify the presence of embedded debris (Cottrino et al., 2016), however, CT has not been used to measure volume change in TAR.

Computed tomography is a highly accurate volumetric measurement method used for UHMWPE components (Bowden et al., 2005, Teeter et al., 2010). Teeter et al. (2011a) compared unworn TKR insert volumes using gravimetric analysis and CT scan reconstructions. The mean difference between the two measurement methods was 0.04% with no significant statistical difference. The location of wear and volume change can be determined using CT methodologies contrary to gravimetric analyses which only measures non-specific volume loss. Substantial expertise in ionizing radiation is required for undertaking CT scan studies and the equipment is expensive to purchase and maintain.

2.5.3 Wear Particle Isolation and Characterisation

Aseptic loosening is the loosening of a joint replacement component without an indication of infection and is often the result of a combination of biological and mechanical events leading to the destruction of the bone-implant interface. The biological theory for aseptic loosening identifies wear debris as the most important contributor to osteolysis (Willert and Semlitsch, 1977), a phenomenon that has declined with the advent of advanced biomaterials (e.g. highly crosslinked and anti-oxidant polymers) (Veruva et al., 2015). The accumulation of wear particles usually develops as a function of implantation time and frustrate the cellular equilibrium between osteogenesis and osteoclastogenesis, resulting in osteolysis. Because of this, wear-particle induced osteolysis is predominantly a late complication (i.e. >10 years in vivo) for THR and TKR (Ulrich et al., 2008, Gallo et al., 2013). However, aseptic loosening remains an early to mid-term problem for TAR (Lucas y Hernandez et al., 2014) resulting in a mean TAR survivorship of 77% at 10 years (Gougoulias et al., 2010). The wear modes and mechanisms associated with TAR are yet to be fully understood and may be identified by the wear debris produced.

Particle isolation protocols combined with high resolution imaging modalities, such as those recommended in the British Standard ISO 17853 (2011) (e.g. electron microscopy), are required to precisely identify biologically active particles, especially in the nano- to submicron size range (ISO Standard, 2011). These techniques have been developed since the early 1990's (Campbell et al., 1994) and aim to remove all adherent molecules from the desired particles in preparation for high resolution imaging. The most appropriate method for particle isolation depends on the user's application and resources.

2.5.3.1 Wear Products of Total Ankle Replacement

Only one study has isolated wear debris from within the ankle joint (Kobayashi et al., 2004). Fifteen synovial fluid aspirates were obtained from patients with well-functioning TARs; four ankles were the fixed-bearing Agility TAR and 11 were mobile-bearing STAR

devices. Aspiration of the joint fluid was performed after 23.0 ± 6.5 months. The isolation technique used was a refinement of the method by Campbell et al. (1994) utilising density gradient ultracentrifugation. Particle shape descriptors including mean aspect ratio and roundness values were significantly lower than that of knee replacement controls. The particle shape discrepancy was attributed to differences in the biomechanical environment. The equivalent circle diameter (particle size) was similar between the ankle and knee replacement group and there were no differences in particle characteristics between the patients with the Agility TAR and those with the STAR. The statistical power of the study was low considering the overall sample size (n=15) and only four ankles composed the Agility TAR group. Importantly, in relation to this thesis, Kobayashi et al. (2004) used ankles that were not indicated for revision surgery; failed ankles may present with wear particle populations with different characteristics. Additionally, the wear particle isolation was conducted on synovial fluid aspirates and not periprosthetic tissues which may also contain different particle populations.

Several studies have investigated the presence of wear debris within the periprosthetic tissue surrounding failing TARs (Valderrabano et al., 2004, Johl et al., 2006, Harris et al., 2009, Koivu et al., 2009, Kokkonen et al., 2011, Koivu et al., 2012, Dalat et al., 2013, Yoon et al., 2014, van Wijngaarden et al., 2015, Cottrino et al., 2016, Gross et al., 2016, Singh et al., 2016, Schipper et al., 2017). All of the studies except one (Johl et al., 2006) showed evidence of UHMWPE wear debris using polarised light microscopy as the analytical method. Light microscopy can resolve the larger particles in the wear debris distribution (i.e. >0.2 μm). van Wijngaarden et al. (2015) used the median size of the largest three birefringent particles as a method of quantification. The largest polyethylene particles were 36.0um (range: 3 to 83 μm) across all of the 22 samples, which are relatively small compared to the millimetre sized particles isolated from other joints (Tipper et al., 2000). van Wijngaarden et al. (2015) also used a semi-quantitative scale to determine particle quantity in relation to cell types. The particle grading had no statistical relationship to cyst location or implantation-time. Considering biologically relevant particle sizes exist in the submicron size range, the exclusive use of light microscopy for particle characterisation is not sufficient at determining wear particle size distributions, given repeatable and extensively-validated particle isolation methods exist (British Standard ISO 17853, 2011).

Non-UHMWPE wear particles have also been identified in periprosthetic tissues surrounding TAR. Histological analysis of the AES TAR found histiocytes containing small sharp particles that were easier to see using polarised light but the elemental composition was not determined (Koivu et al., 2009). In a follow-up study, Koivu et al. (2012) suggested the cause of osteolysis to be necrotic bone fragments for the same cohort. Dalat et al. (2013) identified pale particles in the cell cytoplasm that had a flaky

morphology and was non-birefringent under polarised light. Both studies agreed on the hypothesis that insufficient primary fixation led to the delamination of the dual-layer coating and a foreign body reaction to titanium and calcium phosphate particles. Hydroxyapatite coating from four different TAR devices (STAR, Hintegra, Salto and Taric) was suggested to contribute to osteolysis in TAR after histological analyses identified large quantities of calcium deposits lacking bony architecture. High concentrations of calcium (>0.5 g/g) were associated with a 297-fold increased risk of ballooning osteolysis (Singh et al., 2016) and wear of the hydroxyapatite coating was suggested to be the cause. Metals, calcium phosphate (or hydroxyapatite) and UHMWPE particles have been identified in periprosthetic tissue surrounding TARs, all of which appear to contribute to the total wear particle burden and risk of osteolysis.

2.5.3.2   UHMWPE Wear Particle Isolation

A variety of UHMWPE wear particle isolation methods have been developed and consolidated into a similar format over the past two decades (Figure 2.32). The two most commonly used protocols for UHMWPE isolation from tissues are by Campbell et al. (1994) and Tipper et al. (2000), both of which have been refined and validated (Kobayashi et al., 1997, Richards et al., 2008). A major difference between the two protocols is the way particles are separated from tissue debris. Campbell et al. (1994) used ultracentrifugation with a sucrose gradient to separate tissue from UHMWPE particles, whereas Tipper et al. (2000) used repeated chloroform:methanol sequences with centrifugation and ethanol precipitation to achieve the same aim. A consequence of using ultracentrifugation however, was that only 3 ml of sample could be processed at once. The protocol developed by Tipper et al. (2000) could be used with high sample volumes meaning all of the particulate debris could be isolated in one process.
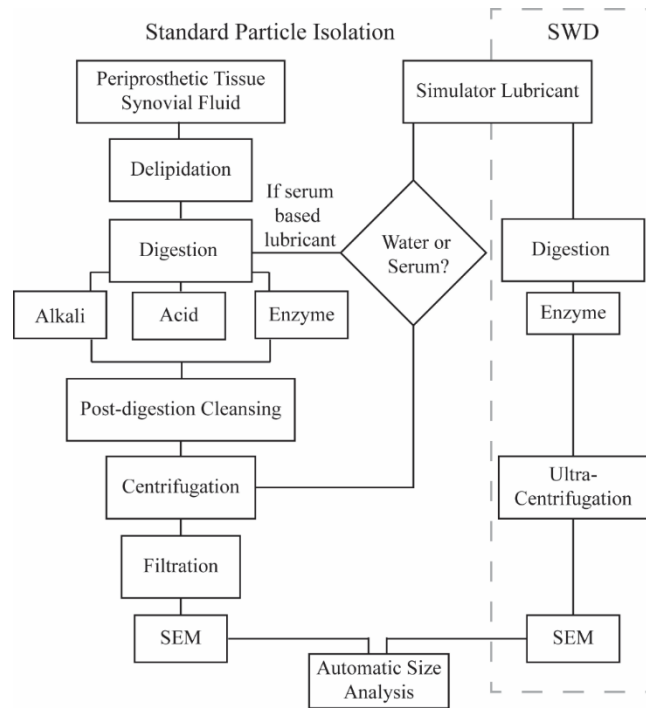
Figure 2.32. Decision pathway for the isolation and characterisation of UHMWPE wear debris. SWD, silicon wafer display. SEM, scanning electron microscopy.

Sample delipidisation is essential to recover purified particles. Lipids cause particle agglomeration and obscure the visualisation of particles if present during the characterisation of particles. Incubation of tissue samples in chloroform:methanol at room temperature for between 12 and 72 hours is common practice for sample delipidisation (Campbell et al., 1994, Tipper et al., 2000). Campbell et al. (1994) delipidised tissue prior to digestion, although conducting this step after digestion has been suggested to provide a more complete lipid removal (Tipper et al., 2000).

Three main digestion methods have been described: Base, acid and enzyme. Base digestion typically includes incubating tissue samples in potassium hydroxide (KOH) or sodium hydroxide (NaOH) at concentrations between 4 M and 12 M at 55 to 65°C for one to seven days (Campbell et al., 1994, Shanbhag et al., 1994, Tipper et al., 2000). Although Baxter et al. (2009) suggested 5 M KOH was sufficient to digest periprosthetic tissue. The composition of periprosthetic tissue differs between donors and anatomical location and some tissue samples require more aggressive concentrations. Tipper et al. (2000) found 12 M KOH to be most effective concentration for digesting formalin-fixed tissues from all locations. Nitric acid and hydrochloric acid have been used to similar effect for tissue digestion (Margevicius et al., 1994, Niedzwiecki et al., 2001, Scott et al., 2001, Šlouf et al., 2004). While both base and acid digestion are effective, the reagents used for these methods damage and dissolve metallic/ceramic particles (Catelas et al., 2001, Lal et al., 2016).

The most recent method developed to isolate UHMWPE particles used enzymatic digestion (Billi et al., 2012a). Billi et al. (2012a) introduced the Silicon Wafer Display

(SWD) technique for polyethylene isolation. The SWD protocol used proteinase K for digestion followed by a three-step purification using ultracentrifugation. Ultimately, the cleansed UHMWPE wear particles were floated onto a featureless silicon wafer coated with marine mussel glue. The SWD protocol had an 88% particle recovery rate which was 43% more than the control which used a method featuring NaOH digestion. This technique was developed using simulator lubricants, therefore its applicability to tissue samples is unknown and is yet to be validated by an external research group.

2.5.3.3   High Density Wear Particle Isolation

Low density wear particles like UHMWPE float in water, whereas high density wear particles, such as metals and ceramics, sink. The methods of isolation between high and low density materials differ on this principle. High speed centrifugation is required to separate high density wear particles from a digested tissue solution, however this process is complicated by the presence of proteins, lipids and contaminants which will also pellet when centrifuged. Therefore, particle isolation methods were required to separate wear particles by density and protect the target particles from damage and degradation during the process (Catelas et al., 2001). Catelas et al. (2001) demonstrated changes in metallic particle shape and size after using KOH and NaOH digestion protocols. Enzymatic protocols have since been used to isolate metal particles.

Schmiedberg et al. (1994) were the first to combine the enzymes, papain and proteinase K for tissue digestion which has been widely adopted since (Doorn et al., 1998, Catelas et al., 2001, Brown et al., 2007a). Bulky protein structures such as human tissue require papain to unfold the secondary, tertiary and quaternary protein structures. Proteinase K then cleaves the carboxylic ends of different amino acids, essentially dicing the protein into smaller molecules. The four most widely recognised metal particle isolation protocols were developed for metal-on-metal articulations and are laborious, time-consuming and demanding on resources (Schmiedberg et al., 1994, Doorn et al., 1998, Catelas et al., 2001, Brown et al., 2007a). For example, Brown et al. (2007a) used four different enzymes (papain, proteinase K, yeast lytic enzyme and zymolyase) and a broad range of other reagents to achieve complete isolation. This protocol consisted of 12 enzyme digestion steps, 12 washes and five boiling steps among many other steps.

In an attempt to minimise the total number of process steps, Billi et al. (2012b) introduced a SWD method for metal and ceramic called the MC-SWD, the MC being 'metal' and 'ceramic' abbreviated. The MC-SWD used a two-step protocol, 1) particle isolation and 2) particle purification. Proteinase K was used for digestion and purification was achieved using a complex ultracentrifugation gradient. The silicon wafer coated in mussel glue was placed at the bottom of the centrifugation tube, instead of at the top like in the SWD for UHMWPE particles. The metal particles were then centrifuged onto its surface. The

recovery rate was 92% for the MC-SWD, although gold beads were used as the test material, which was not a clinically-relevant comparator to the irregular-shaped protein-coated wear debris produced in vivo. In addition to this, the MC-SWD was particularly complicated with a host of expensive and dangerous (e.g. sodium azide) reagents.

Lal et al. (2016) developed a wear particle isolation technique with the aim to recover extremely low wear volumes characteristic of ceramic-on-ceramic bearing couples. Using similar principles to Billi et al. (2012b), an ultracentrifugation density gradient was adopted. Sodium polytungstate was used for the density gradient medium because it is highly soluble in water, nontoxic and acts as a protein denaturant (Lal et al., 2016). Caesium trifluoroacetate, which is toxic, was used in the custom density gradient by Billi et al. (2012b) and may add an unnecessary danger to researchers. The method developed by Lal et al. (2016) allows for the recovery of wear particles for subsequent biocompatibility testing. This is unique to this method however results validating this claim are yet to be published.

Neither protocol, Billi et al. (2012b) nor Lal et al. (2016), have been used to isolate particles from tissue. Both techniques rely solely on proteinase K for digestion which has been shown to be effective for serum lubricant from joint simulators (Niedzwiecki et al., 2001) but not yet for tissue.

2.5.3.4 Wear Particle Characterisation

Particle size and morphology affect its biological reactiveness (Lee et al., 1992). Therefore, it is important to determine particle characteristics once isolated. Historically, this was achieved by visual identification using polarised light microscopy. Polyethylene wear particles were typically observed by their birefringent 'glow' (Savio et al., 1994, Schmalzried and Callaghan, 1999). However, light microscopy has a limited resolution and agglomerates cannot not be separated from larger particles, therefore greater precision was sought using high-resolution scanning electron microscopy (SEM).

Particle Size

Particle size is typically measured by the Ferret's diameter which is the maximum length between two parallel lines constraining the particle. However, other methods such as equivalent circle diameter have also been used (Kobayashi et al., 2004).

Conventional UHMWPE has a size distribution ranging from nanometre granules (Scott et al., 2001, Richards et al., 2008) to millimetre fibrils (Tipper et al., 2000). Galvin et al. (2007) used magnifications of up to 200,000 times and identified particles as small as 10 nm from in vitro tests and similar particle types have since been isolated from tissue (Richards et al., 2008). UHMWPE Particles larger than 10 µm account for a substantial proportion of the wear volume but have a low biological reactivity (Tipper et al., 2000).

Highly cross-linked varieties of UHMWPE tend to wear less but produce smaller wear particles, therefore for the same volume, there are more wear particles in the biologically reactive size range, between 0.1 to 1µm (Endo et al., 2002). Both conventional and highly cross-linked varieties of UHMWPE are used for TAR.

Metal particles from articulating metal-on-metal surfaces tend to be in the nanometre size range (Brown et al., 2007a). Whereas, wear particles from the fixation side, tend to be larger in size due to the mechanism of wear which is likely to be fretting rather than abrasive wear (Brown et al., 2007b).

Particle Morphology

Particle morphology requires a more elaborate analysis compared to the size distribution (Billi et al., 2009). Multiple parameters are required to accurately describe the shape and texture of a particle. Kobayashi et al. (2004) used aspect ratio and circularity to determine particle shape, however, the ASTM Standard F561 (2013) specifies a multitude of morphological descriptors suitable for use. Two particles with the same value for any one metric may have a completely different shape (Billi et al., 2009), therefore combining parameters to describe individual particle morphologies is best practice to define particle distributions.

2.6   Summary

Despite 40 years of development and more than 57 commercially available devices, the failure rate for TAR are more than double that of THR at 10 years. Many mechanisms of TAR failure have been suggested to affect implant survivorship or cause osteolysis, such as fixation surface failure and inflammatory reaction to necrotic tissue, but the empirical evidence for such hypotheses is weak.

Post-marketing surveillance of total joint replacements (TJR) include medical imaging review, retrieval analysis and histological investigation. Integrating analyses for each of these three resources can offer an extensive understanding of how TJRs function in vivo, particularly the identification of wear modes indicative of device dysfunction.

The research in this thesis aimed to determine possible wear modes and origins of failure for a cohort of failed TARs using a retrieval analysis approach. The following chapter describes the retrieval process, the demographic information for the participants who consented for the study, which resources were retrieved and the design details for each of the retrieved TAR brands.

Chapter 3
The Retrieval Process and Device Details

3.1 Introduction

This chapter details the retrieval process including ethics approval, explant and tissue decontamination, medical imaging storage and total ankle replacement (TAR) brand details. The aim of the retrieval process was to collect a sufficient sample of TAR explants, medical imaging and periprosthetic tissue samples for inclusion in a comprehensive integrated retrieval analysis.

3.2 Ethics Approval

Ethical approval for this research was obtained by an application to the UK Health Research Authority for the collection, storage and research of explanted total joint replacement devices, demographic data, periprosthetic tissue and medical imaging (reference: Wear Analysis of Explanted Orthopaedic Prostheses 09/H1307/60). Dr Sophie Williams is the chief investigator for the retrieval programme. Dr Susan Partridge and Dr Dawn Groves managed the retrieval process throughout the duration of the research completed in this thesis.

3.3 Retrieval Processes

Once TAR failure was indicated and revision surgery scheduled, the participant was consented for the retrieval programme by the direct clinical care team. Medical imaging (including standard X-ray images and computed tomography scans), the explanted device, periprosthetic tissue samples and demographic data were securely packaged and transported according to UN Packaging Instruction P650 and UN3373 (Biological substances category B) shipping regulations. All retrieved resources were delivered to the retrieval laboratory at the School of Mechanical Engineering, University of Leeds. Hard copies of the consent forms were stored securely by the chief investigator. The explant and tissue samples were logged and listed for the decontamination process by the retrieval programme managers. Clinical data and medical images were received anonymised, identified by a unique code and stored electronically. Clinical data included:

device type, left or right ankle, sex, initial diagnosis, indicator for revision, time in vivo, and age.

3.3.1 Explant Decontamination and Storage

Explants and periprosthetic tissue samples required decontamination prior to long term storage. Formaldehyde (10% v/v) was selected as the decontaminant because of its efficacy at chemically bonding proteins and arresting biological activity. The explants were submerged in formaldehyde (10% v/v) for at least seven days and cleaned twice with water and a soft-bristled plastic toothbrush to minimise damage caused to the explant surfaces.

3.3.2 Periprosthetic Tissue Sample Storage

Tissue samples were stored in formaldehyde (10% v/v) for at least seven days followed by long-term storage in ethanol (70% v/v) at room temperature. Ethanol was used to store tissue for the long term as it is safer to handle than formaldehyde and effective at preventing biological activity which may degrade the tissue over time.

3.3.3 Medical Imaging Storage

Medical imaging of the ankle comprised of standard X-ray imaging (jpeg. format) and computed tomography (CT) scans (DICOM format). These files were received anonymised and subsequently stored on a secure university server.

3.4 Participant Demographics and Device Details

Research participant demographic data describes the population from which the devices had been retrieved. For the purpose of this project, demographic data was useful to identify trends between demographic variables (e.g. implantation time) and retrieval analysis outputs (e.g. damage mode score and wear volume loss). All personal data relating to the research participants was received anonymised. A unique code was assigned to each resource to blind the researcher to personal data.

Participant information may be missing because the primary surgery was not completed at the same hospital site as the revision surgery or because subjective data such as the cause of failure was reported by the clinical team inconsistently. Device specific details reported by the manufacturer such as type of UHMWPE and method of sterilisation was difficult to acquire once the brand is removed from the commercial market. Missing data was reported for each study cohort throughout the research in this thesis.

3.4.1 Participant Demographics

Forty-four participants consented to donate their TAR to the retrieval programme and were included in the research for this thesis. Each of the TARs were retrieved from one of two hospital sites (Musgrave Park Hospital, Belfast, UK and Chapel Allerton Hospital, Leeds, UK), however 41 devices were implanted and retrieved by the same orthopaedic surgeon. In total, 28 TARs were retrieved with X-ray imaging, 22 TARs had CT scans and 15 TARs had periprosthetic tissue samples (Table 3.2). Three TARs were retrieved with two tissue samples and one TAR had three tissue samples.

For two participants, all demographic data was missing and were therefore missing from the general demographic statistics. Missing individual demographic metrics were reported as 'missing' within the demographic summary statistics (Table 3.1).

Table 3.1. Summary of demographic and device details for all retrieved TARs

Factor		n	Factor	Mean (range)
Total		44	Time In vivo (Mo)	89.3 (4-168)
			Missing[a] (n)	7
Device Type	AES (2nd Gen)	27		
	AES (1st Gen)	6	Age (years)	60 (47-72)
	Rebalance	2	Missing[a] (n)	8
	Hintegra	3		
	Mobility	2		
	BP	2		
Side	Right	21		
	Left	21		
	Missing[a]	2		
Sex	Male	38		
	Female	4		
	Missing[a]	2		
Diagnosis	OA	24		
	PTOA	13		
	Haemochromatosis[b]	1		
	Missing[a]	6		
Indicator for Revision	Osteolysis	30		
	Pain	4		
	Pain and Osteolysis	5		
	Infection	1		
	Missing[a]	4		
Bearing Insert Thickness	5 mm	16		
	7 mm	18		
	9 mm	10		

Notes: AES, Ankle Evolutive System (Transysteme, Fr); Rebalance (Zimmer Biomet, UK); Hintegra (Integra, Fr); Mobility (Depuy Synthes, UK); [a] Data not available; Age was true at the time of primary surgery; OA, osteoarthritis; PTOA, post-traumatic osteoarthritis; [b] OA secondary to haemochromatosis; n, frequency; Mo, Months. HA, hydroxyapatite. Ti, titanium. 1st Gen denoted the single HA coated version of the AES TAR. 2nd Gen denoted the dual coated Ti-HA coated version of the AES TAR.

Table 3.2. Individual demographic details for each retrieved TAR.

	Device	Side	Sex	Diagnosis	Revision reason	Time In vivo	Age	Poly Size	E	X	CT	T
1	AES (1st)	Left	M	OA	Osteolysis	145	55	5mm	✓	✓	✓	✓
2	AES (1st)	Left	M	PTOA	Osteolysis	114	58	5mm	✓	✓	✓	
3	AES (1st)	Left	F	PTOA	P+O	126	55	5mm	✓	✓	✓	
4	AES (1st)	Right	F	PTOA	Osteolysis	131	59	5mm	✓	✓	✓	
5	AES (1st)	Right	M	OA	Osteolysis	76	59	7mm	✓	✓	✓	
6	AES (1st)	Right	M	PTOA	P+O	104	66	9mm	✓	✓		
7	AES (2nd)	Left	M	PTOA	Osteolysis	91	69	5mm	✓	✓	✓	✓
8	AES (2nd)	Right	M	OA	Osteolysis	114	54	7mm	✓	✓	✓	✓
9	AES (2nd)	Left	M	OA	Osteolysis	101	70	5mm	✓	✓	✓	✓
10	AES (2nd)	Right	M	OA	Osteolysis	87	68	7mm	✓	✓	✓	✓
11	AES (2nd)	Left	M	OA	Osteolysis	4	66	7mm	✓	✓	✓	✓
12	AES (2nd)	Right	M	-	Osteolysis	-	-	9mm	✓	✓	✓	✓
13	AES (2nd)	Right	M	OA	Osteolysis	68	53	9mm	✓	✓	✓	
14	AES (2nd)	Left	M	PTOA	Osteolysis	93	60	9mm	✓	✓	✓	
15	AES (2nd)	Left	M	PTOA	Pain	81	56	7mm	✓	✓	✓	
16	AES (2nd)	Right	M	PTOA	P+O	94	67	7mm	✓	✓	✓	
17	AES (2nd)	Right	M	OA	Osteolysis	92	65	9mm	✓	✓	✓	
18	AES (2nd)	Left	F	PTOA	Osteolysis	98	47	9mm	✓	✓	✓	
19	AES (2nd)	Right	M	OA Haem.	Osteolysis	87	52	7mm	✓	✓	✓	
20	AES (2nd)	Right	M	OA	Osteolysis	83	70	5mm	✓	✓	✓	
21	AES (2nd)	Right	M	OA	Osteolysis	87	72	9mm	✓	✓	✓	
22	AES (2nd)	Right	M	OA	Osteolysis	128	56	7mm	✓	✓	✓	
23	AES (2nd)	Left	M	PTOA	Osteolysis	-	-	5mm	✓	✓		
24	AES (2nd)	Right	M	OA	Osteolysis	70	53	7mm	✓	✓		
25	AES (2nd)	Left	M	OA	Osteolysis	78	55	5mm	✓	✓		
26	AES (2nd)	Right	M	OA	Osteolysis	109	71	5mm	✓	✓		✓
27	AES (2nd)	Left	M	OA	Osteolysis	120	-	7mm	✓			✓
28	AES (2nd)	Right	M	PTOA	-	97	49	7mm	✓			✓
29	AES (2nd)	Right	M	OA	Osteolysis	-	-	9mm	✓			✓
30	AES (2nd)	Left	M	PTOA	Osteolysis	70	60	5mm	✓			✓
31	AES (2nd)	Left	M	OA	Osteolysis	84	66	9mm	✓			✓
32	AES (2nd)	Left	M	-	Osteolysis	-	-	5mm	✓			
33	AES (2nd)	Right	M	OA	Osteolysis	64	67	9mm	✓			
34	AES (2nd)	-	-	-	-	-	-	5mm	✓			
35	AES (2nd)	-	-	-	-	-	-	7mm	✓			
36	BP	Right	M	OA	P+O	139	57	7mm	✓	✓		
37	BP	Left	M	-	-	168	66	7mm	✓			✓
38	Hintegra	Left	F	OA	Pain	46	55	7mm	✓			
39	Hintegra	Left	M	OA	Pain	36	64	5mm	✓			
40	Hintegra	Left	M	OA	Pain	46	63	5mm	✓			
41	Mobility	Left	M	OA	P+O	68	54	7mm	✓			
42	Mobility	Right	M	OA	Osteolysis	84	53	7mm	✓			
43	Rebalance	Right	M	PTOA	Infection	22	63	7mm	✓	✓	✓	
44	Rebalance	Left	M	-	Osteolysis	-	-	5mm	✓			✓

Notes: OA, Osteoathritis; PTOA, Post-traumatic Osteoarthritis; OA Haem.; Osteoarthritis secondary to Heamochromatosis; P+O, Pain and Osteolysis; Time in vivo denotes months. Age denotes years. E, Explant Retrieved. X, X-ray Retrieved. CT, Computed tomography retrieved. T, Tissue retrieved.

3.4.2 Retrieved TAR Design Features

All retrieved TARs were three component uncemented mobile-bearing devices implanted using an anterior surgical approach (Table 3.3). This surgical approach for these device designs required a central incision down the anterior of the shank/foot where the majority of the procedure was conducted. A range of different biomaterial combinations were

featured, notably for the fixation surface (Table 3.4). The following TAR device types were retrieved throughout the duration of this project:

Table 3.3. Design principles for the retrieved TARs.

Brand	Generation	Mobile/Fixed	Approach	Stem?	Anatomical?
BP		Mobile	Anterior	Yes	No
AES	1st Gen	Mobile	Anterior	Yes	No
	2nd Gen	Mobile	Anterior	Yes	No
Hintegra		Mobile	Anterior	No	Yes
Mobility		Mobile	Anterior	Yes	No
Rebalance		Mobile	Anterior	Yes	No

Notes: Mobile/fixed, Mobile or fixed bearing. Approach denotes surgical approach. Stem is whether the device features a tibial stem or not.

Table 3.4. Biomaterial combinations for the retrieved TARs.

Brand	Generation	Substrate	Bearing Insert	Fixation
BP		CoCrMo	UHMWPE	CoCrMo Beads
		Ti Alloy (TiN)	UHMWPE	TiN Beads
AES	1st Gen	CoCrMo	UHMWPE	HA
	2nd Gen	CoCrMo	UHMWPE	Ti-HA
Hintegra		CoCrMo	UHMWPE	Ti-HA
Mobility		CoCrMo	HXL UHMWPE	Ti
Rebalance		CoCrMo	Vit. E UHMWPE	Ti-HA

Notes: CoCrMo, Cobalt-chromium-molybdenum. Ti, Titanium. TiN, Titanium nitride. UHMWPE, Ultra-high molecular weight polyethylene. HA, Hydroxyapatite. HXL, highly cross-linked. Vit. E, Vitamin E.

Buechel-Pappas (BP) TAR (Endotec, US)

The Buechel-Pappas (BP) TAR consists of metallic tibial or talar components made of cobalt-chromium-molybdenum (CoCrMo) alloy or titanium nitride coated titanium alloy (Figure 3.1). The fixation surfaces are coated with sintered beads with similar composition to their substrate materials. The bearing surfaces are highly polished. Compared to previous iterations of the BP design, a deeper talar component sulcus was introduced to increase constraint with the separate UHMWPE bearing insert. The bearing insert features a flat superior surface to allow unconstrained articulation with the tibial component. The smaller size of the bearing insert relative to the tibial component allows multidirectional motion between the two components. The bi-concave geometry of the inferior surface of the bearing insert was introduced to allow talar component inversion and eversion motions (Buechel and Pappas, 2003).
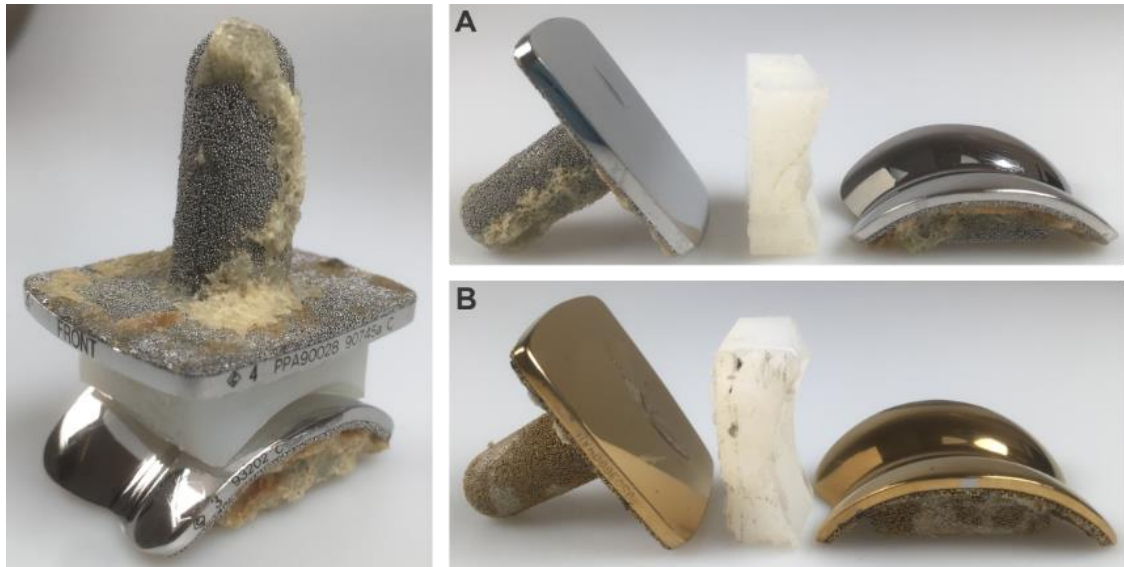
Figure 3.1. Buechel Pappas TAR in cobalt chromium alloy (A) and titanium nitride coated titanium alloy (B).

Ankle Evolutive System (AES) TAR (Transystem, FR)

The Ankle Evolutive System (AES) is considered a Buechel-Pappas (BP)-type device and features three components in a mobile-bearing configuration with a stemmed tibial component. Unlike the BP TAR which featured a tibial stem with a circular cross section, the AES tibial stem is triangular and thought to increase rotational stability (Henricson et al., 2010).

Two AES designs were used throughout its commercial lifetime. The first generation (1st Gen) of AES was introduced in 1989. The tibial stem was removable and fixed to the tibial component by a Morse taper joint. The fixation surfaces were composed of a single layer of hydroxyapatite (HA) applied directly to the cobalt chromium alloy substrate (Figure 3.2).

Figure 3.2. The first generation of the Ankle Evolutive System (AES) TAR.

After 2005, the tibial stem was manufactured fixed to the tibial component and the fixation surface was dual-coated with commercially pure titanium and hydroxyapatite (HA),

layered with the HA on top in order to interact directly with bone (Figure 3.3). The talar component featured two raised bars on the fixation surface similar to the BP TAR.

Figure 3.3. The second generation of the Ankle Evolutive System (AES) TAR.

Hintegra TAR (Integra, FR)

The Hintegra TAR is a three-component mobile-bearing TAR but is not a BP-style device (Figure 3.4). There are several distinct differences between the Hintegra and BP TARs including the lack of a tibial stem, a conical 'anatomically' shaped talar component and the capability for screw fixation. The tibial fixation surface was initially designed for a combination of screw fixation and bone ongrowth with a dual Ti-HA coating on pyramidal peaks. The screws were shown not to offer a clinical advantage and were later recommended as optional (Barg et al., 2012).

Figure 3.4. Hintegra TAR

The conically shaped talar component features a lateral radius greater than the medial radius (Figure 3.5). Designed to mimic what was known of the ankle geometry at the time (Close and Inman, 1952, Close, 1956), the medial radius of the talar trochlear has been found to be the inverse of previous knowledge and is, in the natural joint, larger than the lateral radius (Siegler et al., 2014). This device restricts inversion and eversion motions at the talar component by its conical design and lack of a biconcave geometry, unlike the BP-style devices. The talar component also features lateral and medial rims to constrain the bearing insert above the talar component.
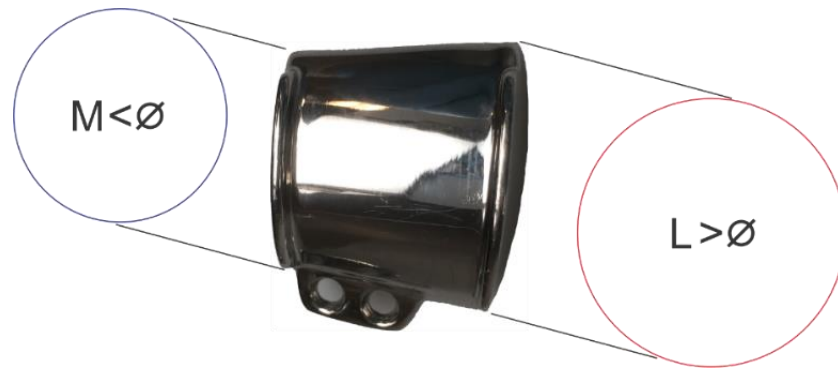
Figure 3.5. Asymmetrical coronal plane geometry of the talar component for the Hintegra TAR. The medial (M) aspect of the component has a smaller radii than the lateral (L) aspect which is inverse to the natural geometry of the talus.

Mobility TAR (DePuy International, UK)

The Mobility TAR was not intended to be a revolutionary design (Rippstein et al., 2011) and followed many of the design principles introduced by the BP TAR (Figure 3.6). The tibial stem was designed comparatively shorter to reduce bone resection at the primary surgery so to improve the bone stock at revision surgery. Improvements to the instrumentation were also fundamental to this design which were claimed to simplify the alignment of the tibial and talar component relative to each other in both the sagittal and coronal plane (Rippstein et al., 2011). The fixation surface was porous-coated titanium and the bearing insert was composed of highly cross-linked UHMWPE to improve wear resistance. Pegs were implemented on the talar component to enhance fixation.

Figure 3.6. Mobility TAR.

Rebalance TAR (Zimmer-Biomet, UK)

The Rebalance TAR is a BP-style device and is currently under a controlled-release clinical investigation which commenced in May 2011 (Harris et al., 2014) (Figure 3.7). Only limited details have been released about this TAR. The fixation surface coating is HA and is marketed by the name 'Bone master'. The UHMWPE is a vitamin E infused variant. The initial reports for this implant show seven ankles revised from a cohort of 220 at a follow-up of approximately 2 years (Harris et al., 2014).

Figure 3.7. Rebalance TAR.

3.5 Discussion

Forty four participants consented to having their medical imaging, explants and tissue samples retrieved at revision TAR surgery. The entire cohort was initially diagnosed with osteoarthritis (primary, secondary or post-traumatic), 98% were revised for osteolysis and/or pain, and; 91% were male. Males (59.1%) generally receive TAR more frequently than females in the UK (National Joint Registry, 2017) however the frequency of males represented in this cohort is high. The male sex has previously been associated with the early development of osteolysis in TAR (Koivu et al., 2017), however a limitation of retrieval analyses is that only information about the failed, and not well-functioning, devices is collected. The proportion of males to females undergoing primary TAR at the hospital sites was unknown. The implantation time was less than 10 years on average (89.3 months) and the mean age at primary surgery was 60 years (median, 59 years). The median age for TAR recipients in the UK is 68 years (IQR, 61-74 years) (National Joint Registry, 2017), therefore the participants for this retrieval analysis were younger than the general population of TAR recipients.

The resources retrieved included 44 explants, 28 weight bearing X-rays, 22 CT scans and 20 periprosthetic tissue samples (from 15 ankles). These sample sizes were each deemed suitable for statistical analysis and were comparably large for TAR retrieval analysis cohorts (Affatato et al., 2009, Vaupel et al., 2009, Cottrino et al., 2016).

Five TAR brands were retrieved in total, four of which featured the same design principles. These four brands (AES, Mobility, BP and Rebalance) were all mobile-bearing, non-anatomical designs implanted using the anterior surgical approach, each of which featured tibial components with a stem. These design principles are archetypal of the BP TAR, the first TAR to be designed in this way (Pappas et al., 1976, Buechel et al., 1988, Buechel and Pappas, 2003, Buechel et al., 2004), and as such, TARs using this combination of principles are commonly referred to as BP-type TARs. The Hintegra TAR brand was also retrieved but differs to the BP-type TARs by featuring a talar

component designed to replicate the natural anatomy and is asymmetrical in the coronal plane. Also the Hintegra TAR does not use a stem for tibial component fixation and features guides for constraining the bearing insert on each side of the talar component. The AES, Mobility and BP TARs have been withdrawn from global market whereas the Hintegra and Rebalance TARs remain commercially available.

3.6 Summary

The aim of the retrieval process was to collect a sufficient sample of TAR explants, medical imaging and periprosthetic tissue samples for inclusion in a comprehensive integrated retrieval analysis. Forty four participants consented to the retrieval programme. The resources retrieved included: 44 explants, 28 weight bearing X-rays, 22 CT scans and 20 periprosthetic tissue samples (from 15 ankles). The cohort featured five TAR brands, the majority of which were mobile bearing, semi-constrained BP-type TARs. The cohort represented a higher percentage of young male participants relative to the implantation statistics of TAR for the UK. Osteolysis and/or pain was the predominant indication for failure. The sample sizes for each resource and the cohort demographics were deemed sufficient for a comprehensive retrieval analysis.

The following research chapters use each individual resource (e.g. X-ray images, CT scans, explants and tissue samples) to investigate the function, wear and failure of TAR.

Chapter 4
X-ray Features and Clinical Alignment

4.1   Introduction

X-ray imaging is used for clinical follow-up after total ankle replacement (TAR) to monitor device function, identify complications and validate indications for revision surgery. Indicators of device dysfunction such as edge-loading (Morgan et al., 2010, Rippstein et al., 2011) and component fracture (Mulcahy and Chew, 2015) are commonly identified using standard medical imaging protocols. Pathological changes such as osteolysis (Besse et al., 2009, Viste et al., 2015) and heterotopic ossification (Lee et al., 2011, Schuberth et al., 2016) are also potentially indicative of device failure and can be identified using similar imaging modes. In the context of retrieval analysis, indicators of failure may be reflected in the damage present on the explanted device.

Weight-bearing X-ray imaging is commonly available to foot and ankle specialists and can be used for simple anatomical and device alignment metrics which can be used to infer device function. These quantitative measures of device orientation may indicate, sometimes subtle, factors relevant to the cause of TAR failure such as component malpositioning (Goldberg et al., 2009a). The foot is typically imaged from two planes, the coronal and sagittal planes, and measurements are taken from the resultant images. Guidelines for component positioning are dependent on TAR design and 'ideal' positioning tolerances are rarely documented by the manufacturer. The tolerances reported by individual surgeons likely reflect their expectations and can vary between surgeons for the same TAR brand (Braito et al., 2015a, Usuelli et al., 2016b). Generally, the tolerance given for rotational variation (e.g. alpha and beta angle) is approximately ± 5° from the reference line, which is usually the tibial axis (Hintermann et al., 2004, Rippstein et al., 2011, Braito et al., 2015a, Kerkhoff et al., 2016a, Kerkhoff et al., 2016b, Kerkhoff et al., 2016c, Kim et al., 2016). For translational measurements, such as the antero-posterior offset ratio (AOR), tolerances have not been suggested, however millimetre variances have been shown to affect clinical outcomes (Pyevich et al., 1998, Barg et al., 2011a). The device orientation at the time of revision surgery is likely to be a result of various factors including component migration, component positioning variance or anatomical failure (e.g. collapse of the talus).

Analysis of the 28 retrieved TARs with weight-bearing X-ray imaging may indicate which factors have contributed to failure. Also, reporting established quantitative alignment

metrics may allow for comparisons to be made to previously published literature and other variables identified throughout the research conducted for this thesis.

The aim of this chapter was to:

- Identify features and alignment variations indicative of TAR dysfunction and/or failure using weight-bearing X-ray images from a cohort of failed TAR devices.

In order to achieve this aim, the following objectives were explored:

- Inspect the medical imaging in a cohort of failed TARs to identify features that may be indicative of TAR device dysfunction and/or failure.
- Define the orientation and alignment of TAR components on standard weight bearing X-ray imaging using established methods.
- Determine whether component position captured at failure had changed relative to imaging captured earlier in the implants' lifetime.

4.2 Methods

4.2.1 Medical Imaging Details

Weightbearing coronal and sagittal ankle X-ray imaging was captured during follow-up appointments and prior to revision surgery by the clinical care team. The earliest and latest available coronal and sagittal X-ray images for each ankle were retrieved by the clinical team and de-identified prior to being delivered to the University of Leeds for analysis. The demographic details are summarised in Table 4.1. Individual donor demographics are reported in section 3.4.1.

The mean time from implantation to the earliest X-ray imaging was 34.1 months (± 24.7 SD; range: 0 to 98). The earliest medical imaging for three ankles could not be retrieved due to the primary procedure being completed in private practice. The mean time between pre-revision X-ray imaging (latest imaging) and revision surgery was 10.7 months (± 8.1 SD; range: 2 to 38). The mean time between the earliest and latest X-ray imaging was 55.4 months (± 18.6 SD; range: 13 to 80). All X-ray imaging was exported in de-identified jpeg format from the picture archiving and communication system (PACS) at the relevant hospital.

Table 4.1. Demographic details for the participants with retrieved standard X-ray imaging.

Factor		n	Factor	Mean (range)
Total		28	Time In vivo (Mo)	93.2 (4-145)
			Missing[a] (n)	2
Device Type	AES (2nd generation)	20		
	AES (1st generation)	6	Age (years)	61 (47-72)
	Rebalance	1	Missing[a] (n)	2
	BP	1		
Side	Right	17		
	Left	11		
Sex	Male	25		
	Female	3		
Diagnosis	OA	15		
	PTOA	11		
	Haemochromatosis[b]	1		
Indicator for Revision	Osteolysis	22		
	Pain	1		
	Pain and Osteolysis	4		
	Infection	1		

Notes: AES, Ankle Evolutive System (Transysteme, Fr); Rebalance (Zimmer Biomet, UK); BP, Buechel Pappas (Endotec, US); [a] Data not available; Age was true at the time of primary surgery; OA, osteoarthritis; PTOA, post-traumatic osteoarthritis; [b] OA secondary to haemochromatosis; n, frequency; Mo, Months.

4.2.2 X-ray Features

ImageJ is a public domain, image processing software developed at the National Institutes of Health, US (Schindelin et al., 2012). This software allows for images to be viewed and measurements captured from 2D and 3D image files. This software is used throughout the research in this thesis.

Initial inspection of the medical imaging was undertaken to identify macro-indicators of device malfunction. This included whether the components had fractured and how the anatomy surrounding the device appeared. Abnormal features such as edge-loading, component migration, varus/valgus alignment and osteolysis were noted and counted for the cohort. Coronal plane edge-loading has been defined as a translational mismatch between the tibial and talar components in the axial plane of either ≥2 mm (Rippstein et al., 2011) or ≥3 mm (Koivu et al., 2009) (Figure 2.24). In addition to inconsistency of magnitude, the measure of coronal plane edge-loading requires a scale. The length of the tibial stem is typically used as the scale because it is of known length. For the majority of retrieved images, the complete length of the stem was obscured by tibial component rotation and therefore edge-loading measures could not be obtained reliably. Coronal plane component rotation sometimes also obscured the measure of varus/valgus

alignment between the two metallic components which interfered with the reliable capture of this measure.

4.2.3 Clinical Measures of TAR Alignment

The following clinical measurements were acquired using the manual draw tools in ImageJ (Schindelin et al., 2012). Each of the measurements were normalised about the tibial axis, therefore the tibial axis was given the value zero in terms of angle and offset.

a. Tibial Axis (Coronal and Sagittal X-ray)

The tibial axis is the theoretical line that bisects the external edge of the tibial cortex in both the coronal and sagittal plane. Both planes were measured independently of each other.

Two circles were drawn in series from the distal tibia proximally. ImageJ software was used to calculate the centre of the circles numerically and the tibial axis was then defined as the vector intersecting the two circle centres (Figure 4.1).
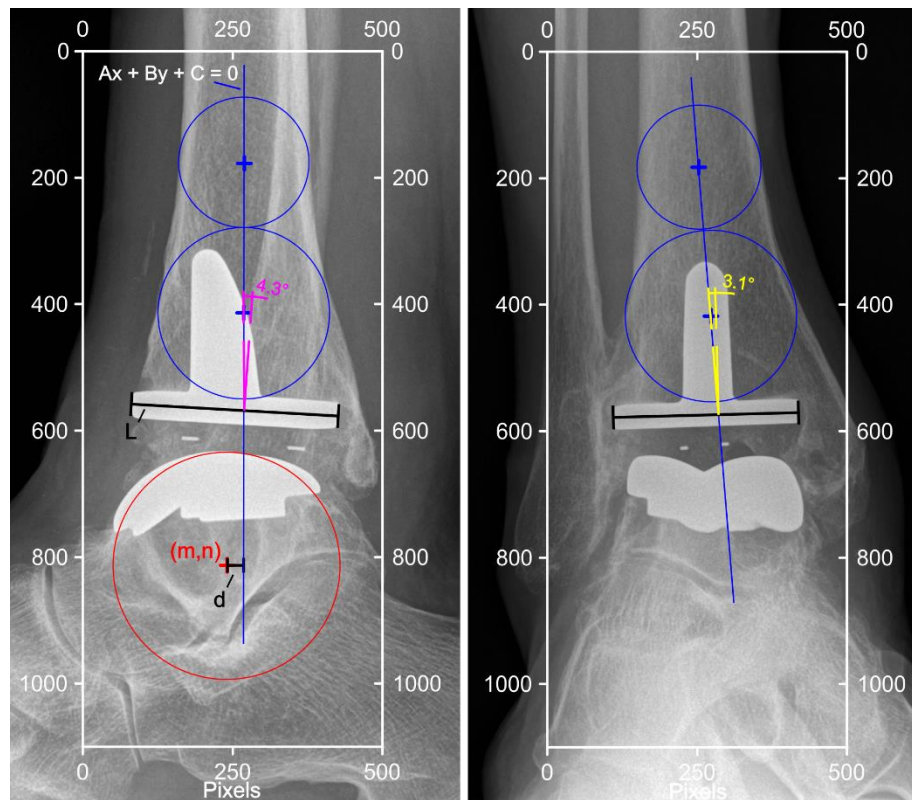
Figure 4.1. Total ankle replacement alignment metrics for conventional X-ray imaging. Blue markings identify the tibial axis in both the sagittal and coronal planes. The equation of the tibial axis is also shown in blue. Black markings show the length (L) (sagittal) and width (coronal) of the tibial component. The angle between the tibial axis (blue line) and the tibial component length (black line) describes the beta (magenta; sagittal) and alpha (yellow; coronal) angles. Red markings identify the talar component centre (m,n coordinates) in the sagittal plane. The perpendicular line between the centre of the red markings and the tibial axis (d) represents the talar component antero-posterior offset relative to the tibial axis.

b. Alpha Angle (Coronal X-ray)

The alpha angle is the angle between the tibial axis and the tibial plate in the coronal plane. The variance of alpha angle for all of the included devices was measured about 90° and therefore the alpha angle reported and compared was the positive or negative deviation angle from 90°.

A line was drawn along the fixation surface of the tibial component base plate. The angle between this line and the tibial axis was calculated using the angle measuring function in ImageJ.

c. Beta Angle (Sagittal X-ray)

The beta angle is the angle between the tibial axis and the tibial plate in the sagittal plane. The variance of beta angle for all of the included devices was measured about 90° and therefore the beta angle reported and compared was the positive or negative deviation angle from 90°.

A line was drawn along the fixation surface of the tibial component base plate. The angle between this line and the tibial axis was calculated using the angle measuring function in ImageJ.

d. Antero-posterior Offset Ratio (Sagittal X-ray)

The antero-posterior offset ratio (AOR) is a relative measure of talar component offset from the tibial axis in the sagittal plane (Barg et al., 2010a). The length of the tibial component base plate was the reference length for which the offset ratio was calculated relative to. Positive ratios signified anterior offsets.

Barg et al. (2010a) measured the AOR by drawing the tibial axis line between two circles on the tibia. The centre of the talar component was calculated by drawing and overlaying a third circle so that the radius was similar to that of the talar component. Finally, a perpendicular line was drawn between the tibial axis and the centre of the third circle, which was the length of the offset relative to the length of the tibial component.

The AOR can be calculated mathematically by quantifying the shortest distance (d) between the centre of the talar component circle (m,n) and the vector connecting the centre of the first two circles creating the tibial axis (line Ax + By + C = 0). The AOR is a ratio of d and L, where L is the anteroposterior length of the tibial component base plate. This was achieved using the following equation, where d denotes the required distance:

Equation 4.1.
$$d = \frac{|Am + Bn + C|}{\sqrt{A^2 + B^2}}$$

Equation 4.2.
$$AOR = \frac{d}{L}$$

Because AOR is a relative measure, the image pixels can be used as units which can be converted into the ratio of length between *d* and *L* (i.e. AOR).

4.2.4 Statistics

Descriptive statistics (mean, standard deviation) were calculated for the alpha angle, beta angle and AOR. Both the earliest and latest standard X-ray values were compared using paired t-tests as an indicator of the stability of the metrics measured. The alpha value was $p = 0.05$. Pearson's correlation coefficient (r) was used to identify the association between beta angle and AOR as a measure of how well aligned the metallic components are positioned relative to each other in the sagittal plane.

4.3 Results

4.3.1 X-ray Features

The medical imaging retrieved for this project was not captured using a standardised research protocol and as a result, the imaging was not normalised between ankles to any one component or surface. The TAR components were often rotated relative to each other and relative to the X-ray detector, making measurements of alignment challenging (Figure 4.2). Despite this, imaging features indicative of device dysfunction were identified qualitatively and three quantitative measures of orientation could be determined.
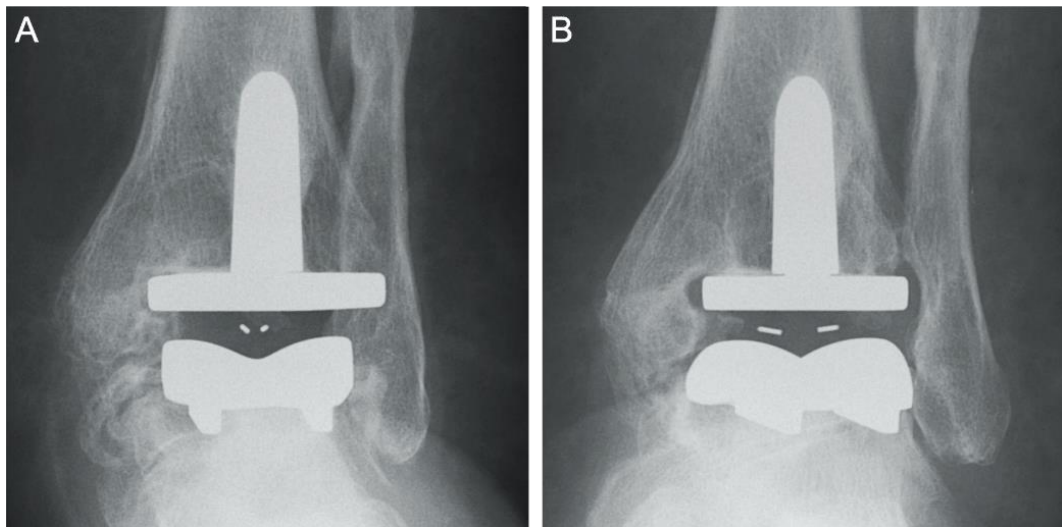
Figure 4.2. The same ankle, captured on the same day from two different angles. It is challenging to determine the rotational orientation of the tibial component in the transverse plane relative to the talar component. Without two images, the rotational mismatch between the components could be overlooked.

4.3.1.1 Edge-loading

A mismatch in translational alignment between the tibial and talar components indicated edge-loading of the bearing insert. For several cases, the bearing insert, identified by its radiopaque marker, appeared substantially medially, laterally or posteriorly offset relative to the centre of the tibial component (Figure 4.3). By extension, the bearing insert was offset from the tibial axis in the same direction. This phenomenon can be measured by the AOR, in the antero-posterior direction. In the medio-lateral direction however, a similar metric cannot be measured because, if rotated, the centre of the talar component or bearing insert is sometimes obscured which limits the measurement of offset in the coronal plane.
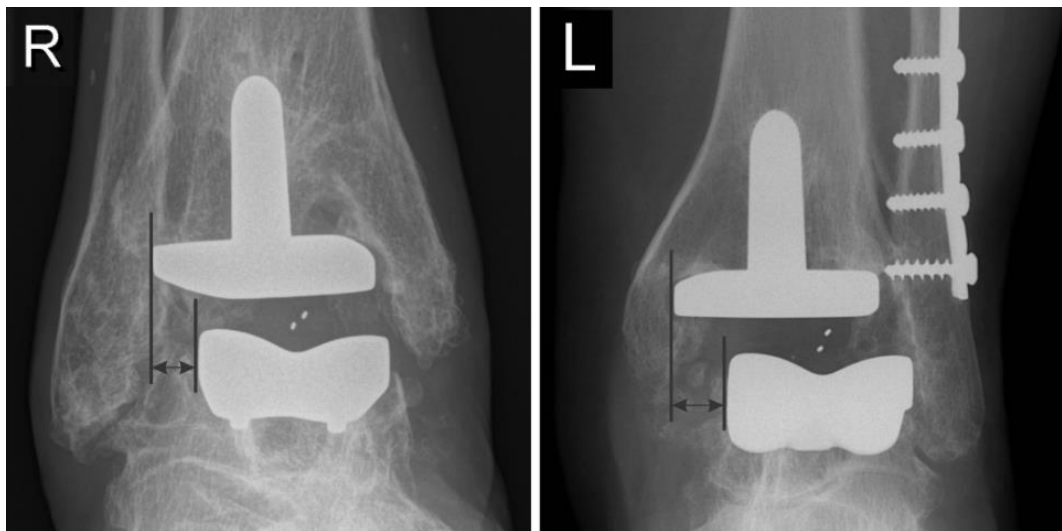
Figure 4.3. Two examples of TAR potentially in edge-loaded conditions. Black lines highlight the offset between the tibial and talar components.

4.3.1.2 Component Migration

For at least 11 ankles (39%) the height of the bone surrounding the device was above the level of the bearing surface (Figure 4.4). This suggests the talar component had either subsided into the talus or that bone had grown beyond the fixation surface, towards the bearing surface.
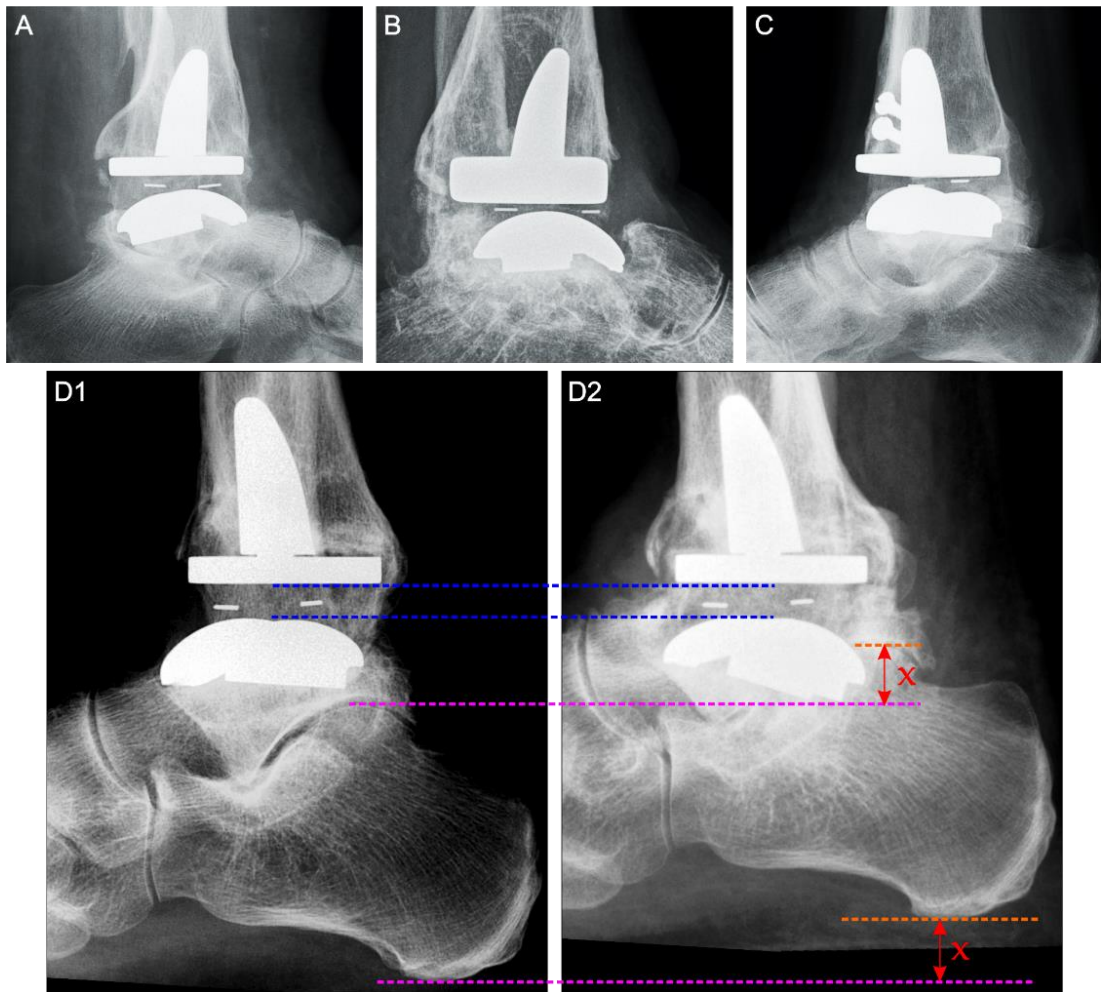
Figure 4.4. Examples of talar component migration into the talus (A-C). Two X-ray images were compared at an early (D1) and late (D2) time-point from the same ankle. The bearing insert maintained its location and thickness (blue lines). Anatomical markers below the device (red and magenta dashed lines) were translated proximally representing a loss of limb length of up to 10 mm (X).

4.3.1.3   Varus/valgus Alignment

The talar component was often tilted in a varus or valgus position, and for two components the talar component had tilted enough to seemingly cause contact with the bearing surface of the tibial component (Figure 4.5). For a BP TAR, a radiopaque marker had been liberated from the bearing insert and was embedded within the surrounding tissue (Figure 4.5D).
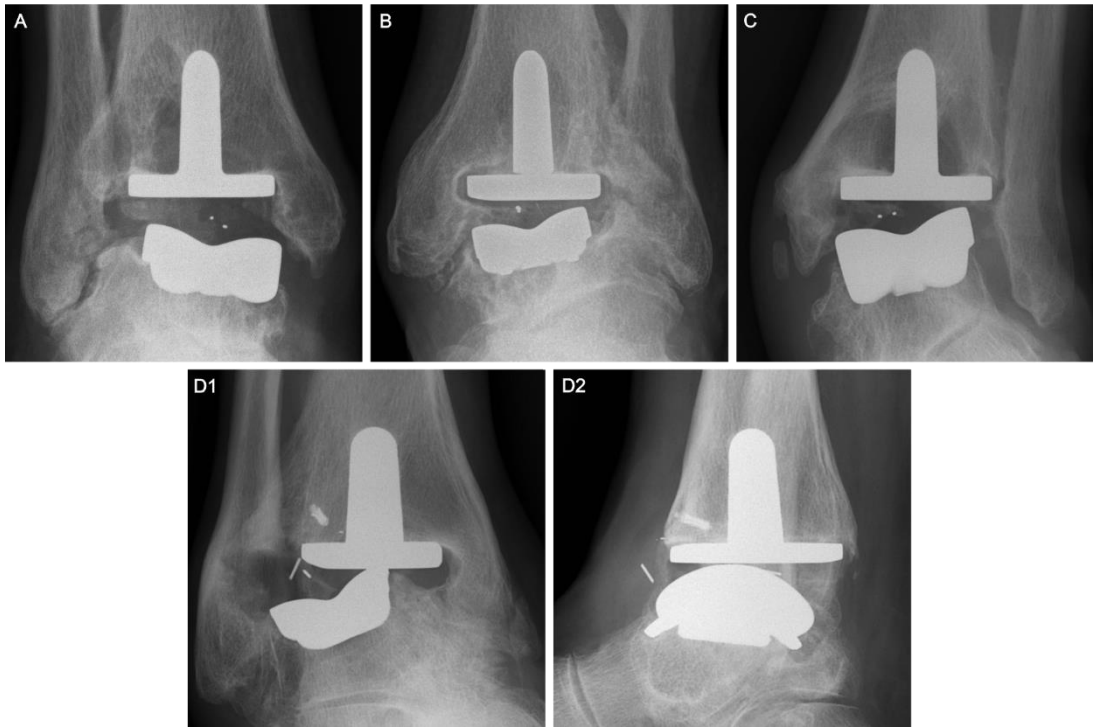
Figure 4.5. Examples of varus/valgus component malalignment (A-C). A Buechel-Pappas (BP) TAR with a severe varus tilt (D1). The radiopaque marker has been completely removed from the bearing insert (D2).

4.3.1.4 Osteolysis

Areas of massive osteolysis were identified in both the tibia and talus across the cohort. Osteolysis appeared spheroidal in geometry and was predominantly located unilaterally or bilaterally about the tibial stem (Figure 4.6). The location of osteolysis in the talus was challenging to identify because the talar component geometry shielded the area under the component for most ankles. Large areas of radiolucency were frequently identified in the X-ray images but were not counted because diagnosis of osteolysis may require the expertise and clinical experience of a radiologist.
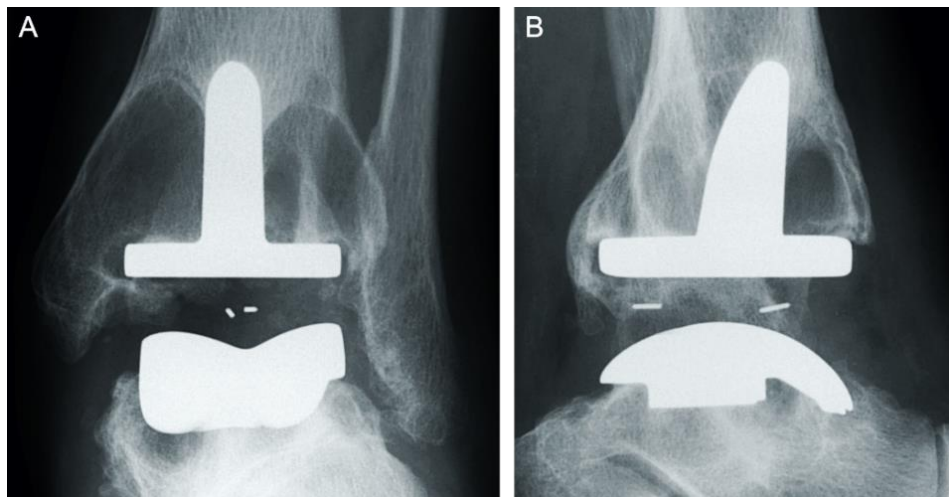
Figure 4.6. Massive osteolysis surrounding an AES (2nd Gen) TAR.

4.3.2 Clinical Measures of TAR Alignment

The mean alpha and beta angles when revision surgery was indicated were 0.9° (± 2.7° SD; range: - 5.2 to 8.1; negative is lateral) and 2.9° (± 4.6° SD; range: - 1.9 to 22.1; negative is posterior), respectively. Three TARs featured an alpha angle greater than ± 5° and five TARs featured a beta angle greater than ± 5°.

The mean AOR was 0.02 (± 0.15 SD; range: - 0.22 to 0.42; negative is posterior). Ten devices had an anterior offset whereas for 12 devices, the offset was posterior. None of the TARs were considered neutral (i.e. 0 ± 0.01).

Mean alpha angle (p = 0.06), beta angle (p = 0.35) and AOR (p = 0.23) were not significantly different between the earliest and latest X-ray imaging.

Beta angle and AOR were moderately correlated (r = 0.71). The TAR with the greatest beta angle (22.1°) also featured the greatest AOR (0.42) (Figure 4.7). For this device, both of the tibial and talar components appeared to have migrated substantially into their respective bones. The earliest X-ray imaging revealed a beta angle (10.6°) and AOR (0.27) approximately half of that of the latest medical imaging. The time between the medical imaging was 37 months.
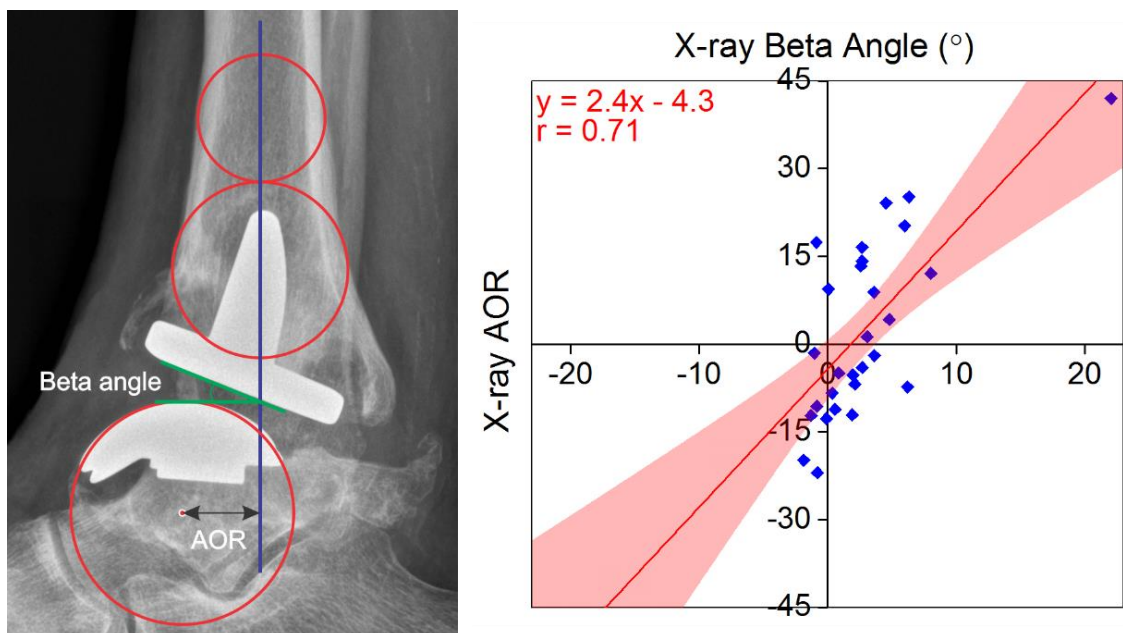
Figure 4.7. Association between beta angle and antero-posterior offset ratio (AOR) determined using Pearson's correlation coefficient (r). Red shaded area denotes 95% confidence intervals.

4.4 Discussion

4.4.1 X-ray Features

The standard X-ray images retrieved for the research in this thesis were captured without a consistent research protocol which led to some of the metallic components being rotated relative to the imaging plane. Despite this, important features indicative of TAR dysfunction and failure could be observed for several components in each case. Examples of TAR dysfunction included, tibial and talar component offset which indicated bearing insert edge-loading (Morgan et al., 2010). Talar component subsidence which was identified by the talar component lying below the talar cortices. Varus/valgus alignment of the talar component relative to the tibial component was observed and in one case, the bearing insert had dislocated causing severe varus rotation of the talar component. Osteolysis was prevalent, large and particularly noticeable above the tibial component. Silhouettes of the rotated metallic components made quantifying these features challenging, as previously acknowledged (Braito et al., 2015b). Consequently, only three quantitative measures (alpha angle, beta angle and AOR) were recorded using standard X-ray images and further investigation of the indicators of failure was undertaken using CT imaging, in the following chapter (Chapter 5).

4.4.2 Clinical Measures of TAR Alignment

The quantitative measures of TAR alignment were broadly within the 'acceptable' tolerances established in the published literature. Alpha and beta angles were used to measure the rotational variance of the tibial component and the acceptable limits for both are typically ± 5° (Hintermann et al., 2004, Rippstein et al., 2011, Braito et al., 2015a, Kerkhoff et al., 2016a, Kerkhoff et al., 2016b, Kerkhoff et al., 2016c, Kim et al., 2016). Of the 28 TARs with standard X-ray imaging, 89% and 82% were within ± 5° of the tibial axis for alpha and beta angles, respectively. The ± 5° tolerance is a guideline rather than a limit. The guideline is reflective of what is generally achievable between clinical teams in the orthopaedic community and is anecdotal rather than being substantiated with evidence-based clinically relevant outcomes. However, increased pain scores have been identified for patients with a tibial component rotation of greater than 4° (Pyevich et al., 1998). Pyevich et al. (1998) studied the fixed bearing Agility TAR, the results of which may not be applicable to mobile-bearing designs given the stress distributions between the device types differ significantly in malalignment (Espinosa et al., 2010).

The antero-posterior offset ratio (AOR) was introduced by Barg et al. (2010a). The AOR describes the translational relationship between the talar component and the tibial axis. Mean AOR for the cohort in the current study was 0.02 (± 0.15 SD) which is similar to

the values reported by Barg et al. (2010a) which were 0.0 (± 0.06 SD) for 368 Hintegra TARs and deemed acceptable. In a follow-up study using the same cohort, Barg et al. (2011a) split the patients into three groups: 1) AOR = 0; 2) AOR = >0; and, 3) AOR = < 0. Patients with a talar component in exact alignment with the tibial axis (AOR = 0) had higher postoperative pain relief and greater range of movement. This represented 41.1% of their cohort. No ankles in the current study had an AOR of 0 ± 0.01 and the variance of AOR measurements was double that of the results reported by Barg et al. (2010a). It is not yet understood what the acceptable variance limits are for an AOR greater than or less than zero. Braito et al. (2015a) reported a mean AOR of 0.1 (± 0.1 SD) for a cohort of Hintegra TARs, which was not deemed excessive. While the revision rate for their cohort was 15.5% after a short implantation time of 3.1 ± 1.3 years, more evidence about how sensitive clinical outcomes are to AOR is required before associations between AOR and failure can be inferred.

Component positioning did not change significantly between measurements taken from the earliest and latest standard X-ray imaging. This analysis was used to determine whether at the point of failure, macro changes such as talar collapse had occurred. There was a trend toward a systematic difference in alpha angle over time but this did not reach statistical significance. This may have represented small changes in component position or alternatively, variation in the repeatability of the imaging mode (Braito et al., 2015b). Component migration may occur throughout the in vivo lifetime of the TAR due to the development of osteolysis and component subsidence, however, the type of analysis used in this study was unlikely able to detect sub-millimetre positional changes. Radiostereometric analyses and standardised acquisition protocols would be required to accurately determine change in component position (Carlsson et al., 2005). The TAR with the greatest beta angle also featured the greatest AOR. For this TAR, both beta angle and AOR had approximately doubled between the two X-ray imaging time points. This device represents a macro change in component location, likely due to the collapse of the tibial bone due to osteolysis and a translational displacement of the talar component, simultaneously. It is not clear which component migrated first, however. For the majority of TARs, component alignment had not changed significantly.

The beta angle was moderately correlated (r = 0.71) to the AOR for this cohort. The steeper the angle of the tibial plate, the further the talar component was in the direction of the tibial bearing surface. In theory, this relationship is logical. For the flat superior bearing insert surface to maintain congruence with the flat tibial component, the bearing insert is able to rotate about the talar component. Once the bearing insert resides on one side of the talar component, the talus, which is constrained by ligaments only, is pushed in the direction the tibial bearing surface is facing. An extreme example of this relationship is shown in Figure 4.7, which showed the collapse of the anterior distal tibia

due to osteolysis and the displacement of the talar component. Barg et al. (2011a) investigated this relationship for non-failed Hintegra TARs but the variables beta angle and AOR were not associated. The moderate correlation identified for the cohort in the current study may reflect more tibial and talar component subsidence in opposing directions due to the presence of massive osteolysis. Less subsidence may be expected for well-functioning (or non-failed) TARs but controlled in-vitro studies would be required to determine this accurately.

4.4.3 Limitations

The selected measurements were chosen to minimise observer bias and the requirement for radiographic expertise. The measures were geometrical in nature and relied predominantly on identifying the device orientation as opposed to anatomical markers. Many other metrics could have been implemented but may require diagnostic expertise by a radiologist to determine (Datir et al., 2013). Manually drawing the tibial axis, which is the standard method used in the published literature, was avoided by the mathematical measurement protocol developed for this study although the alignment circles still required drawing which was subject to some operator variance. The retrospective nature of retrieval analyses meant the X-ray imaging was captured without a standardised research protocol. The ankle was often rotated relative to the X-ray detector making measures such like varus/valgus angle unable to be captured. The individual components were commonly rotated relative to each other, limiting the ability in some cases to acquire measures such as coronal plane edge-loading offsets. Despite obtaining measures of alignment between two time points, component migration could not be determined precisely. Not only may migration have occurred prior to the first imaging time point but millimetre changes in component alignment could have been due to a lack of imaging acquisition consistency. The sample size of 28 TARs is relatively low for statistical generalisations however, the cohort is homogenous in the fact all of the TARs were considered failed and imaging was obtained with a view to revise the device. The failure rate of TAR is approximately 10 to 20% at 10 years (Zaidi et al., 2013), therefore 28 failed TARs reflects a relatively large cohort of between approximately 280 to 560 TARs at 10 years follow-up.

4.5 Summary

The research described in this chapter aimed to identify features and alignment variance indicative of TAR dysfunction and/or failure using weight-bearing X-ray images. The recurring features indicative of device dysfunction included: Edge-loading, collapse of

the talus, varus/valgus malalignment between components, radiopaque marker extrusion, and massive osteolysis.

The quantitative measures of device alignment yielded results that were generally within the variances considered acceptable in the published literature. There were no significant differences overall for the alignment measures between the earliest and latest X-ray imaging. In selected cases however, component subsidence was substantial between time points, particularly at the extremes of the alignment measures.

X-ray imaging was particularly challenging to obtain detailed device orientation information from. The next chapter uses computed tomography to further analyse the anatomical features and device orientation indicated as dysfunctional in this chapter.

Chapter 5
CT Scan Features and Non-clinical Alignment

5.1   Introduction

In the previous chapter, weight-bearing X-ray imaging was analysed for 28 of the retrieved total ankle replacements (TARs). Edge-loading, collapse of the talus, varus/valgus malalignment between components, radiopaque maker extrusion, and massive osteolysis were recurring indicators of TAR dysfunction. Also, TAR alignment was quantified according to established measures and was considered within the variances considered acceptable by other authors.

Two dimensional X-ray imaging has several limitations including the obscuration of features and edges due to the indistinguishable silhouette created by rotated metallic components (Braito et al., 2015b). Also, the superimposition of anatomical features by the images taken from only two planes reduces the sensitivity of the modality to approximately 50% when identifying osteolysis, for example (Kohonen et al., 2013, Yoon et al., 2014). Given this, many authors recommend using computed tomography (CT) for TAR once device failure is suspected (Kokkonen et al., 2011, Kohonen et al., 2013, Viste et al., 2015). Computed tomography offers greater clarity for the identification of osteolysis, for which axial areal measurements have been suggested to be the most effective (Viste et al., 2015). Also, detailed views of the bearing insert can be captured allowing fractured components to be observed (Mulcahy and Chew, 2015). The increased use of CT imaging to determine indicators of failure in TAR creates an opportunity for this resource to feed into post-marketing surveillance studies, such as retrieval analysis.

The aims of this chapter were to:

- Investigate novel radiographic features and those identified from the weight-bearing X-ray imaging (Chapter 4) using re-orientated computed tomography scans.
- Characterise TAR device orientation and the geometry of the surrounding bony anatomy (including pathology), for a cohort of failed TAR devices.

In order to achieve these aims, the following objectives were explored:

- Develop a method to repeatably rotate, segment and compare CT scans between participants.

- Validate the developed method against established alignment measures used for weight-bearing X-ray imaging (Chapter 4).
- Inspect the re-orientated CT scans for features that may be indicative of TAR device dysfunction and/or failure.
- Use the re-orientated CT scans to define metrics of TAR component orientation which were previously unobtainable using X-ray imaging.
- Measure the volume and location of osteolysis, and compare to the established CT measurement method for areal osteolysis size.

5.2 CT Scan Details

Non-weight bearing pre-revision CT scans were retrieved in DICOM format for 22 participants. The scans were captured on average 8.9 months (± 5.3 SD; range: 1 to 21) prior to revision surgery and were associated with the participant demographics outlined in Table 5.1. Individual donor demographics are reported in section 3.4.1.

Table 5.1. Demographic details for the participants with retrieved computed tomography scans.

Factor		n	Factor	Mean (range)
Total		22	Time In-vivo (Mo)	91.5 (4-145)
			Missing[a] (n)	1
Device Type	AES (2nd generation)	16		
	AES (1st generation)	5	Age (years)	61 (47-72)
	Rebalance	1	Missing[a] (n)	1
Side	Right	13		
	Left	9		
Sex	Male	19		
	Female	3		
Diagnosis	OA	11		
	PTOA	9		
	Haemochromatosis[b]	1		
Indicator for Revision	Osteolysis	18		
	Pain	1		
	Pain and Osteolysis	2		
	Infection	1		

Notes: AES, Ankle Evolutive System (Transysteme, Fr); Rebalance (Zimmer Biomet, UK); [a] Data not available; Age was true at the time of primary surgery; OA, osteoarthritis; PTOA, post-traumatic osteoarthritis; [b] OA secondary to haemochromatosis; n, frequency; Mo, Months.

Each ankle was scanned in a clinical setting without a standardised research protocol. For this reason, the CT scans in this cohort lacked acquisition parameter consistency (e.g. resolution, scan orientation). The X and Y axes represent the grayscale values in

each individual image (or slice) and were the same value which determined slice resolution. The mean XY resolution was 0.35 mm (± 0.07 SD). Each CT scan is a composite of individual images, also known as an image stack (Z axis). The Z axis resolution was greater than the XY axes with a mean of 0.92 mm (± 0.11 SD). Anisotropic resolution is characteristic of clinical CT imaging because capturing less slices reduces exposure to ionising radiation and reduces patient discomfort by minimising the total scan time.

5.3   Method Development

CT scan slice orientation is fixed within the scanner, therefore to achieve repeatable scans and subsequent measurements, significant effort by the radiographer is required to align the ankle consistently, which may not be achieved. Slice orientation for a given anatomical landmark may vary between ankles and cross-sectional measurements of the same feature in two separate ankles may not be comparable. For example, an osteolytic lesion measured using CT slices captured at an angle of 10° may yield elliptical measurements compared to circular measurements from CT slices captured perpendicular to the lesion (Figure 5.1). By normalising clinical CT scans to a known surface, comparable measurements can be confidently obtained.

Zero Degrees   10 Degrees
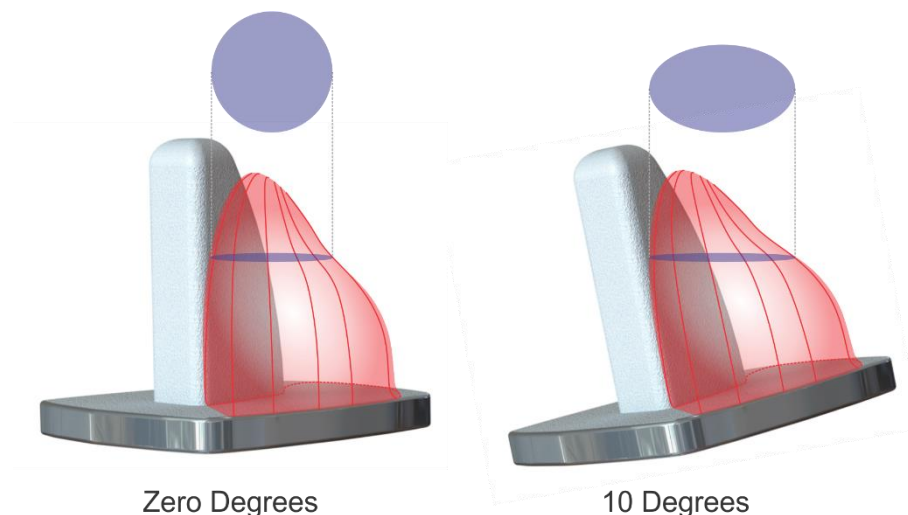
Figure 5.1. The effect of computed tomography scan orientation on the segmented geometries. Note the hypothetical geometry change between the segmented areas (purple) for osteolysis (red) between two ankles rotated at different angles.

Three dimensional segmentation allows complex features to be highlighted and measured for orientation and volume. However, manual selection methods may introduce selection bias which may plausibly alter the measured results. This method development section details how the clinical CT scans were re-orientated and

segmented. To ensure these methods were reliable and repeatable, inter- and intra-rater analyses were undertaken and detailed below.

5.3.1 CT Scan Reorientation and Reliability Analysis

5.3.1.1 Methods

CT Scan Reorientation

The tibial component fixation surface was used as a common surface to directly compare component locations between different participants. ScanIP (Simpleware, UK) was used to manually rotate each CT scan in all three planes (X,Y,Z). The X and Y dimensions were considered orientated correctly if the fixation surface of the tibial component appeared perpendicular to the observer when scrolling through the slices in the Z dimension. Each scan was cropped close to the foot in all three planes to reduce the image size and computational costs (e.g. data requirements, computing speed). An example of a re-orientated CT scan is shown in Figure 5.2.
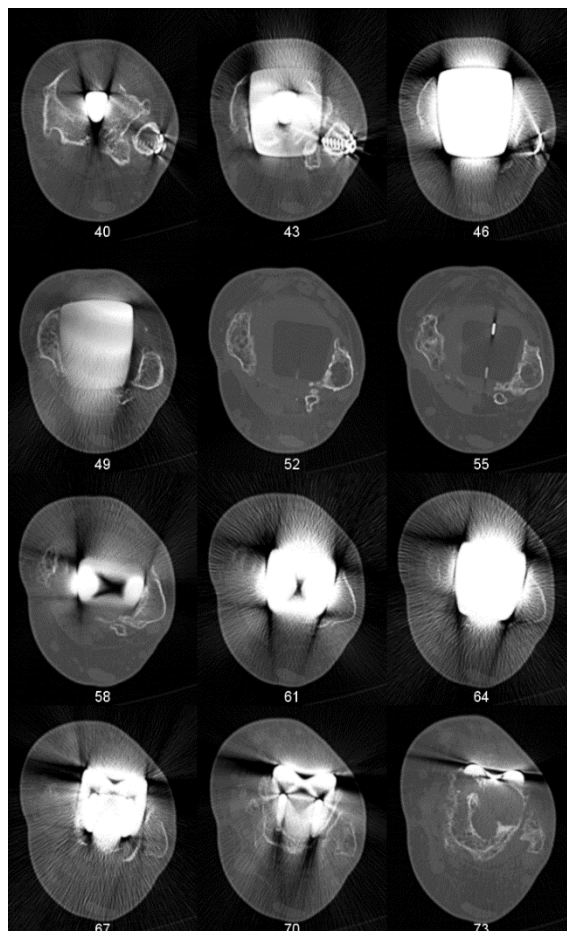
Figure 5.2. Montage of sequential computed tomography scan slices after scan reorientation. The tibial component fixation surface is perpendicular to the tibial axis (axial plane; slice 43). Edge-loading is shown by a mismatch of alignment with the tibial component (slices 49-52). Rotation of the talar component relative to the tibial component is evident (slice 64). Tibial and Talar osteolysis is also visible (Slices 40 and 73). Metal artefact is shown throughout the image stack but is not inhibitive of identifying key component outlines and features.

Reliability Analysis: CT Scan Reorientation

The original CT scans were reorientated so that the tibial component fixation surface was perpendicular to the axial plane. The subjective assessment of axial alignment was assessed by three observers who each rotated ten CT scans to axial alignment. The change in rotation in degrees was noted for each plane (X,Y,Z) and the mean difference compared between observers. The same ten CT scans were rotated by the same observer on three different days and the mean difference compared between measurements.

Statistics

Descriptive statistics for the rotation values for the entire cohort of CT scans was reported. Intraclass correlation coefficient (ICC) estimates and their 95% confidence intervals (CI) were determined using SPSS statistical package version 22 (IBM, Chicago, US). For inter-rater analyses, the ICC estimates were based on a mean-rating (k = 3), consistency, two-way random effects model. For intra-rater analyses, the ICC estimates were based on a mean-rating (k = 3), absolute, two-way mixed effects model. ICC estimates less than 0.5 indicated poor reliability, estimates between 0.5 and 0.75 indicated moderate reliability, estimates between 0.75 and 0.9 indicated good reliability and values above 0.9 were considered indicative of excellent reliability (Koo and Li, 2016). Systematic differences in intra- and inter-rater reliability were assessed using repeated measures ANOVAs. If the assumption of sphericity was violated, as indicated by Maulchy's test, then the Greenhouse-Geisser adjustment was used. The alpha value was 0.05 for all statistical comparisons.

5.3.1.2 Results

Rotation for All CT Scans

In the sagittal (X) plane, the CT scans were rotated by 0.9° (± 5.0 SD; range 0 to 10). In the coronal (Y) plane, the CT scans were rotated by 1.4° (± 3.9 SD; range 0 to 8). In the axial (Z) plane, the CT scans were rotated by 8.4° (± 19.8 SD; range 1 to 36).

Inter-rater Analysis

The ICC reliability between observers was: 0.989 (95% CI 0.968 to 0.997) in the X plane, 0.972 (95% CI 0.917 to 0.992) in the Y plane, and 0.999 (95% CI 0.996 to 0.999) in the Z plane, all of which indicated excellent reliability.

CT scan reorientation angles were not significantly different in the X (p = 0.75), Y (p = 0.14) or Z (p = 0.051) planes between three observers. While the Z plane values were not statistically different, the alpha value was close to the minimum confidence level (p = 0.05). The Z plane (axial plane) was manipulated to reorientate the tibial plate so that

the anterior of the component was consistently facing the same direction. On average, the Z plane required more manipulation compared to the X and Y planes which may have contributed to the inter-rater variance.

Intra-rater Analysis

The ICC reliability for three tests by the same observer was: 0.998 (95% CI 0.996 to 0.999) in the X plane, 0.979 (95% CI 0.940 to 0.994) in the Y plane, and 0.997 (95% CI 0.990 to 0.999) in the Z plane, all of which indicated excellent reliability.

No significant differences were measured in the X ($p = 0.067$), Y ($p = 0.389$) or Z ($p = 0.345$) planes after three measurements from the same observer.

5.3.1.3 Discussion

The original CT scans were reoriented to ensure all CT scan measurements were comparable between ankles. The aim was to orientate the tibial fixation surface perpendicular to the observer when viewing the CT scan in the axial plane. Typically, small amounts of rotation were required in each plane and the reliability of CT scan rotation between observers, and for three tests by the same observer, were considered excellent. The relatively low resolution of CT imaging may be a cause for the strong reliability. With each degree of rotation, substantial changes to the device geometry occurred. Because of this, only two or three slices showed the entirety of the tibial component fixation surface which appears to have caused the observers to select similar degrees of rotation in each plane. CT scan reorientation is a reliable method of normalising images between ankles prior to measurement or segmentation.

5.3.2 CT Scan Segmentation

5.3.2.1 Methods

3D Segmentation

Segmentation is the process by which regions of interest within an image are selected using software and measured (Figure 5.3). Specialised software can be used to segment features in three dimensions from image stacks or three dimensional point spaces. ScanIP (Simpleware, UK) was used to segment the TAR device, bones and osteolysis from reoriented CT Scans (Figure 5.4).
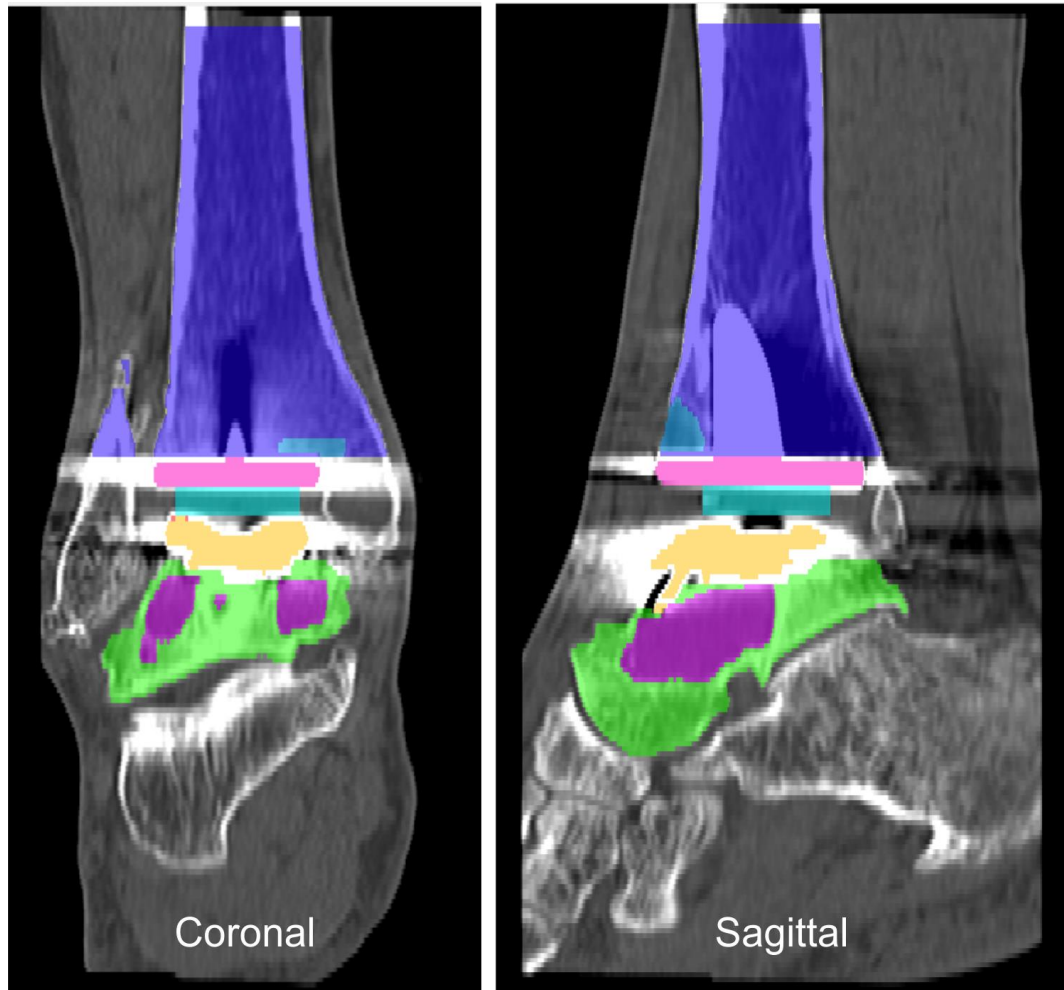
Figure 5.3. Segmented computed tomography scan. Each segmented element is highlighted in a different colour. Tibia (blue), Talus (green), Tibial component (pink), Bearing insert (light blue), talar component (yellow), talar osteolysis (purple).
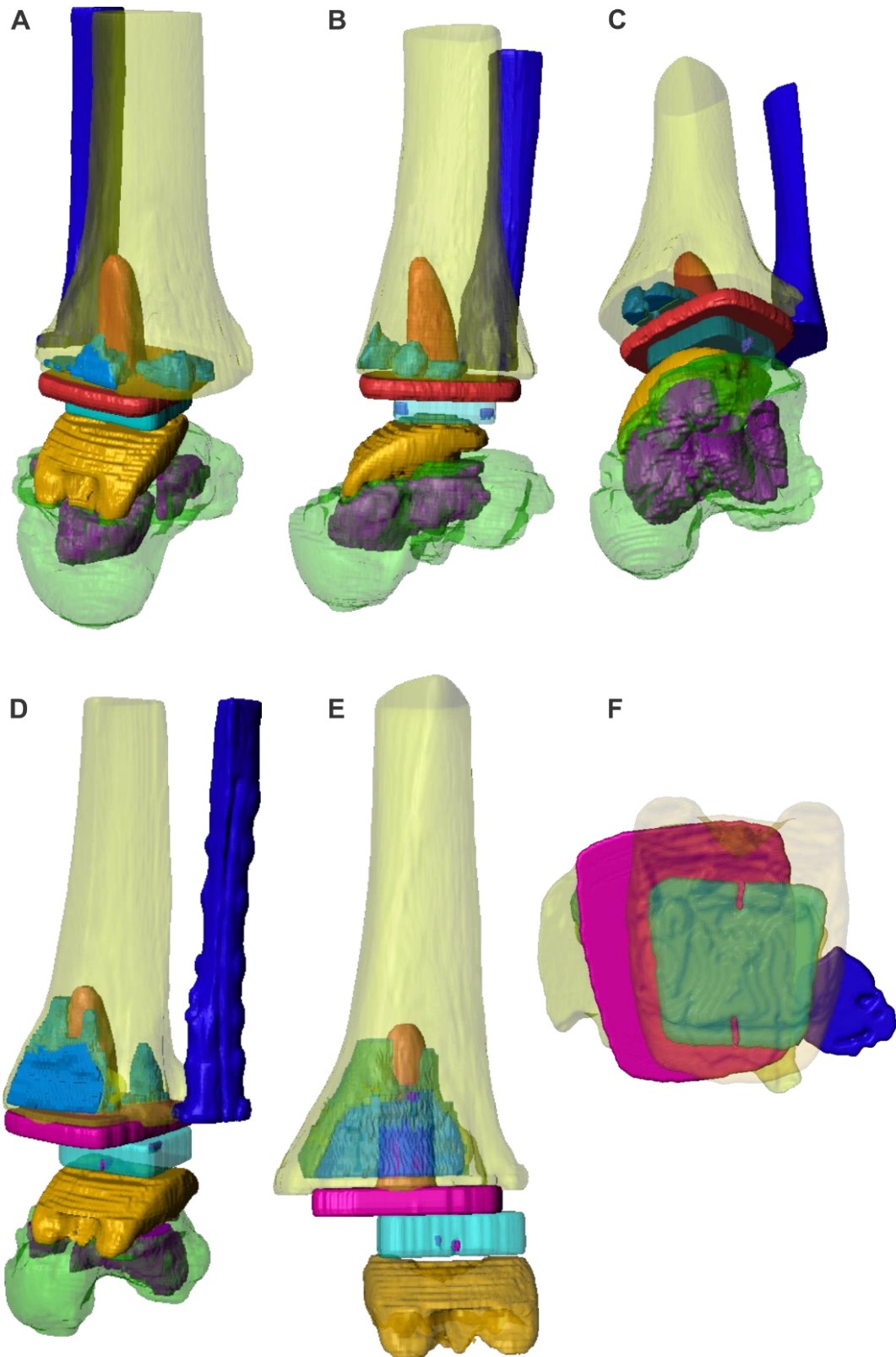
Figure 5.4. Three dimensional representation of segmented computed tomography scan regions of interest. The magnitude of osteolysis is visible (purple); and, rotational and translational offset of the components is evident (bottom right). Two examples are shown, ankle 1 (A-C) and ankle 2 (D-F).

These TAR and ankle features were identified and segmented using the following definitions and processes:

a) Tibia

Bone is predominantly composed of calcium phosphate which has a density of approximately 3.0 g/cm^3. Therefore, relative to soft tissues which are predominantly composed of water (density: 1.0 g/cm^3), bone appears bright in X-ray imaging. The histoarchitecture of the tibia features trabecular bone surrounded by cortical bone, both of which were identifiable and comparable to CT images commonly presented in the published literature. The tibia was segmented from the first slice proximal to the base plate, to the full height of the tibia within the scan. The entire shape of the tibia was segmented up to the outside edge of the cortices.

b) Metal Components (Tibial and Talar)

Metals attenuate X-rays and are the brightest object in an X-ray image. The tibial and talar components were simple to identify given their well-defined geometry and relative brightness. Despite the prevalence of metal artefact, the edges of the components were visible and could be selected by scrolling through the image stack. The most challenging devices to segment were those in CT scans with particularly low axial (XY) resolution, however in this study the majority of images featured sufficiently high resolution. The metallic components were segmented to their edges and care was taken to omit artefact, which presented as irregular dispersions of bright pixels.

c) Bearing Insert (and Radiopaque Markers)

The bearing insert material was UHMWPE and was the least dense material in the joint space of the CT imaging (density: 0.93 g/cm^3). Therefore, the outline of the bearing insert itself was relatively clear to identify (Figure 5.5). Within the bearing insert, the radiopaque markers were clearly demarcated and used as another indicator of component location. Both the outline of the bearing insert and the radiopaque tag were segmented. In one ankle, the outline of the bearing insert was not clear, possibly due to the low resolution of the scan, but the radiopaque tag was visible. Only the outline of the insert could be segmented and not the full depth of the component. The insert conformed to the metallic talar component, the artefact from which obscured the shape of the inferior surface of the bearing insert.
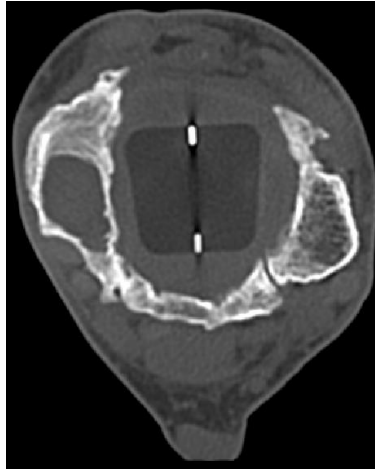
Figure 5.5. Bearing insert appearance in computed tomography imaging. Radiopaque markers are visible (brightest areas) within the bearing insert. The bone of the medial malleolus, posterior malleolus and fibula surround the bearing insert. Osteolysis is evident in the medial malleolus (left side).

d) Talus

The talus was of similar brightness to the tibia. The entire bone was segmented up to the outside edge of the cortices. The irregularity of shape in all dimensions made this feature particularly challenging to segment. Constant scrolling through the slices was required to ensure the talus was being segmented and not the surrounding bones in the foot, such as the calcaneus and cuneiform bones.

Segmenting the talus at the same level as the talar component could not be achieved as metal artefact obscured the bony geometry. However, the extremities of the talus such as the talar head, the talar-calcaneal posterior facet and, the posterior and lateral processes, were segmented.

e) Osteolysis (Tibial and Talar)

Osteolysis was defined as the absence of bone within a well-demarcated area of sclerotic bone (Figure 5.6). Osteolysis was segmented by selecting areas absent of bone within the tibia or talus. The first CT slice proximal to the device with the clearest appearance of osteolysis was used as the initial slice. Metal artefact obscured the area surrounding the tibial component stem in several CT scans, therefore osteolysis was segmented as close to the stem as possible. Metal artefact also obscured the fibular and medial malleolus as these were in line with the artefact-producing tibial base plate and talar component. These locations were omitted from segmentation but the frequency of osteolysis present was noted. Where the tibial cortex had been compromised, the line of the cortex was followed in form to estimate the volume of the osteolysis.
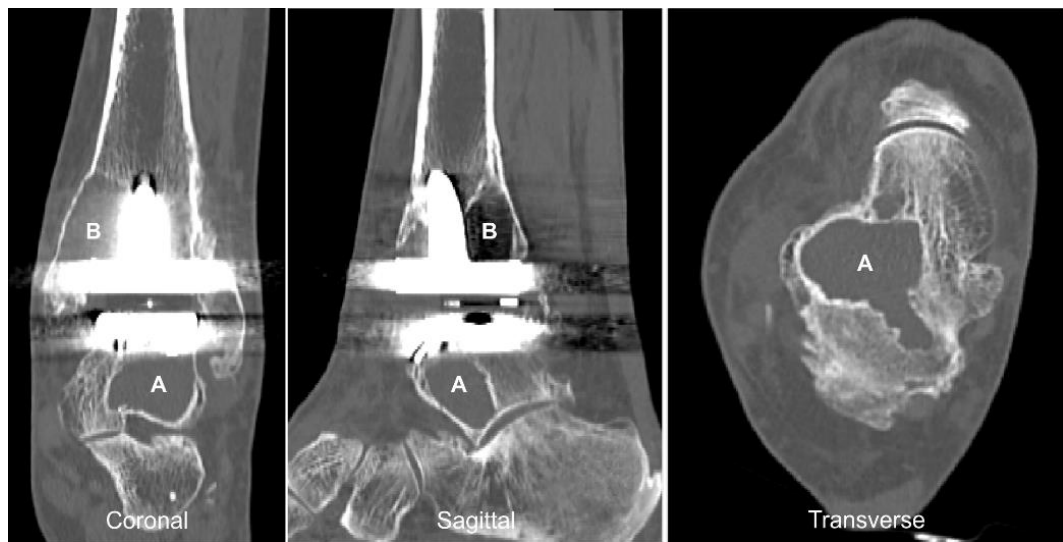
Figure 5.6. Orthogonal views of talar osteolysis. A, talar osteolysis. B, Tibial osteolysis.

Artefacts affected the clarity of the CT image by producing noise in the vicinity of the metallic components. While metal artefact can be reduced using metal suppression protocols, these techniques are not commonly used for clinical CT scans of TAR. Automated segmentation could not be used for this reason and therefore manual segmentation (i.e. using a computational paint tool to select regions of interest by hand) was used.

Segmented regions of interest (also known as masks) were binarised and exported for measurement using ImageJ. ImageJ was selected for the analysis because of its versatile 3D image manipulation tools and broad selection of measurement metrics.

Reliability Analysis: CT Scan Segmentation

Segmentation of TAR components was achieved predominantly using manual selection due to the high levels of metal artefact. There were three uses of segmentation analysed for repeatability:

    a) Tibial component location

Identifying the centre of the tibial component was essential for determining the relative location of itself to the tibial axis and to other components. Segmenting the outline of the tibial component could theoretically be achieved using one CT slice, however in practice, a few slices were required to ensure the entire shape was captured during segmentation.

    b) Talar component location

Similar to the tibial component, the centre coordinates of the talar component were required to determine its relative location. Unlike the tibial component, multiple slices were required to be segmented to determine the full size of this component due to its

irregular shape and orientation. This was a more complex and time-consuming component to segment.

c) Osteolysis volume.

Quantity of osteolysis was the only volumetric measure calculated using segmentation. Shapes on multiple CT slices needed to be segmented to create an accurate representation of the volume of osteolysis. This metric required careful manual selection and was the most time-consuming feature to segment.

Ten randomly selected CT scans were segmented by three observers for the above three metrics. For the same ten CT scans, one observer measured all three metrics three times on three different days. The mean difference in component location and osteolysis volume were compared for both inter- and intra-rater analyses.

Statistics

The statistical tests used to analyse the inter- and intra-rater reliability of segmentation were the same as those detailed in section 5.3.1. In brief, intraclass correlation coefficient (ICC) estimates and their 95% confidence intervals were determined. For inter-rater analyses, the ICC estimates were based on a mean-rating (k = 3), consistency, two-way random effects model. For intra-rater analyses, the ICC estimates were based on a mean-rating (k = 3), absolute, two-way mixed effects model. Systematic differences between observers or between the three tests of the same observer were calculated using repeated measures ANOVAs. The alpha value was 0.05 for all statistical comparisons.

5.3.2.2   Results

Tibial Component Location (2D Segmentation)

The ICC reliability between observers was: 0.999 (95% CI 0.999 to 0.999) in the X plane and 0.999 (95% CI 0.999 to 0.999) in the Y plane, all of which indicated excellent reliability. The tibial component centre coordinates were not significantly different in the X (p = 0.177) or Y (p = 0.155) planes between three observers (Figure 5.7).

The ICC reliability for three tests by the same observer was: 0.999 (95% CI 0.999 to 0.999) in the X plane and 0.999 (95% CI 0.999 to 0.999) in the Y plane, all of which indicated excellent reliability. No significant differences were measured in the X (p = 0.630) or Y (p = 0.630) planes after three measurements from the same observer.
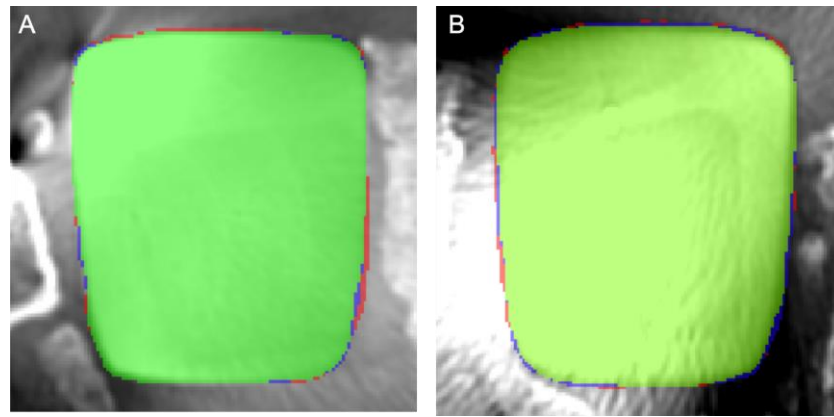
Figure 5.7. Examples of 2D tibial component segmentation. Observer 1 (green), observer 2 (blue) and observer 3 (red) are overlaid.

Talar Component Location (3D Segmentation)

The ICC reliability between observers was: 0.999 (95% CI 0.999 to 0.999) in the X plane and 0.999 (95% CI 0.999 to 0.999) in the Y plane, all of which indicated excellent reliability. The talar component centre was not significantly different in the X ($p = 0.226$) or Y ($p = 0.148$) planes between three observers (Figure 5.8).

The ICC reliability for three tests by the same observer was: 0.999 (95% CI 0.999 to 0.999) in the X plane and 0.999 (95% CI 0.999 to 0.999) in the Y plane, all of which indicated excellent reliability. No significant differences were measured in the X ($p = 0.422$) or Y ($p = 0.726$) planes after three measurements from the same observer.
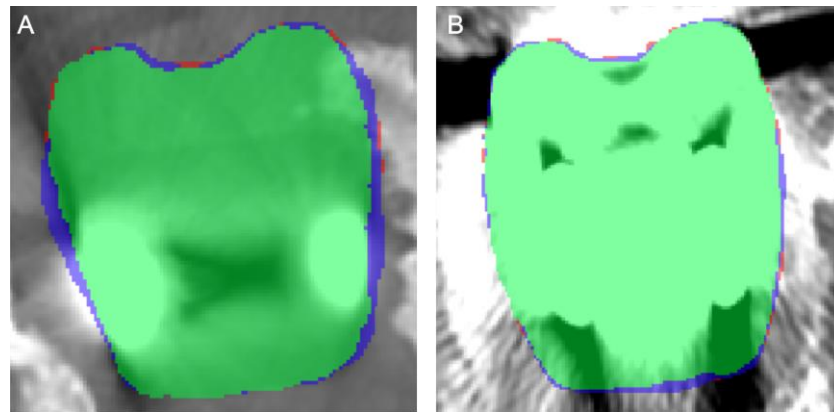
Figure 5.8. Examples of 3D talar component segmentation viewed form the axial plane. Observer 1 (green), observer 2 (blue) and observer 3 (red) are overlaid.

Osteolysis Volume (3D Volume Segmentation)

The ICC reliability between observers was: 0.998 (95% CI 0.996 to 0.999) for osteolysis volume, which indicated excellent reliability. Segmented osteolysis volume was not significantly different ($p = 0.169$) between three observers (Figure 5.9).

The ICC reliability for three tests by the same observer was: 0.999 (95% CI 0.999 to 0.999) for osteolysis volume, which indicated excellent reliability. No significant

differences were measured for osteolysis volume (p = 0.428) after three measurements from the same observer.
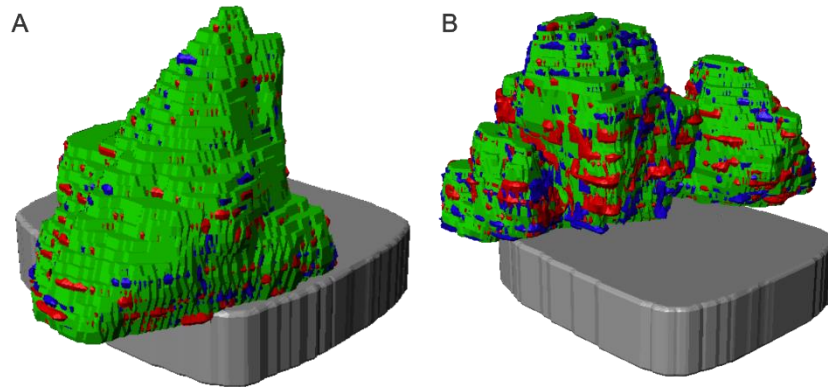
Figure 5.9. Examples of the segmentation of osteolysis volume. Observer 1 (green), observer 2 (blue) and observer 3 (red) are overlaid.

5.3.2.3   Discussion

The segmentation of CT scan features was broadly successful. Metal artefacts inhibited the segmentation of osteolysis close to the tibial stem and malleolar osteolysis. While this may underestimate the extent of osteolysis slightly, the shape and size of this feature was thought to have been segmented effectively. The talus was challenging and time consuming to segment due to its irregular shape and high quantities of metal artefact produced by the talar component. Therefore, neither bone nor osteolysis within the talar component space (i.e. between the fixation surface bars) could be segmented.

Three aspects of segmentation were investigated for reliability by inter- and intra-rater analyses. The first inter- and intra-rater study focussed on the two dimensional segmentation of the tibial component and whether the centre coordinates identified were similar or not. The second study considered the same coordinate analysis, but for an object where the centre coordinates could only be identified once the three dimensional (3D) shape had been segmented. The third study used the same principles as the second study, segmenting a 3D shape, however the measure was volume rather than the coordinates of the component centre. ICC estimates indicated excellent reliability for both inter- and intra-reliability metrics. There were no significant systematic statistical differences between observers for each of these three studies. Likewise, there were no significant systematic statistical differences for the same observer over three trials, for the three studies. Manual segmentation was deemed therefore to be an acceptable method of determining component location in 3D space and osteolysis volume. The relatively low resolution of clinical CT scans increased the likelihood of different observers selecting well-defined features repeatably.

5.4   Segmented CT Scan Measurement Validation

Weight-bearing two dimensional X-ray imaging is the current standard method for determining TAR alignment. In Chapter 4, measures of TAR alignment were captured using weight-bearing X-rays which defined device alignment in terms relatable to the previous literature.

Computed tomography is almost always captured in non-weight bearing conditions. Therefore, a comparison between the two imaging types was required to determine whether they produced statistically different outputs for the same metric. Antero-posterior offset ratio (AOR) was selected for comparison as it was the only common metric capable of being measured between the two imaging modalities.

5.4.1   Methods

The AOR values captured from X-ray imaging as detailed in section 4.3.2 were used for the same 22 participants who also had CT scans retrieved (Table 5.1).

Two methods were explored to determine AOR from segmented CT scans. The first method used coordinates from pre-determined slices (e.g. 30th and 60th slices) to mathematically calculate the AOR. This was the simplest method. The second method used a two dimensional image representation of the segmented CT scans to recreate the manual selection of AOR from X-ray images. This method was time consuming but was thought to accurately mimic the X-ray method of measuring AOR. The methods are described as follows:

a) Numerical Method (30/60 Slice)

A numerical method was tested that calculated the AOR from the centre of segmented components at fixed heights within the CT image stack. The tibial axis was defined as the line connecting the axial (X,Y) centre point of the segmented tibia at the 30th and 60th slices (Z-axis) above the tibial component fixation surface (Figure 5.10). The talar component position was defined by the centre coordinate in all three planes (x,y,z) for the segmented geometry. Talar component offset was determined relative to the tibial axis. All coordinate points were obtained from the image stacks produced using ImageJ.

Despite its simplicity, the main limitation of the numerical method was the location of the measurement points. These points were not precisely at the same location as the X-ray imaging comparator. For example, the centre of the talar component determined using this method was higher in the z-axis than the centre of a circle overlaid on the talar component, which is how the talar component is measured using the standard X-ray

method. Therefore, a second method to recreate the measure of AOR in standard X-ray images from the segmented CT scans was tested and compared.

b) Pseudo X-ray Images

This method aimed to re-create an X-ray type image from segmented CT scans. Binarised images for each component segmented from the TAR CT scans were superimposed on each other in different colours using ImageJ (Schindelin et al., 2012). The brightness of each individual component was proportional to the number of overlapping slices, the output of which was similar to a true X-ray image. The AOR was measured using the same method used for standard X-ray imaging. Creating pseudo X-ray images was time expensive but was the closest emulation of standard X-ray imaging.
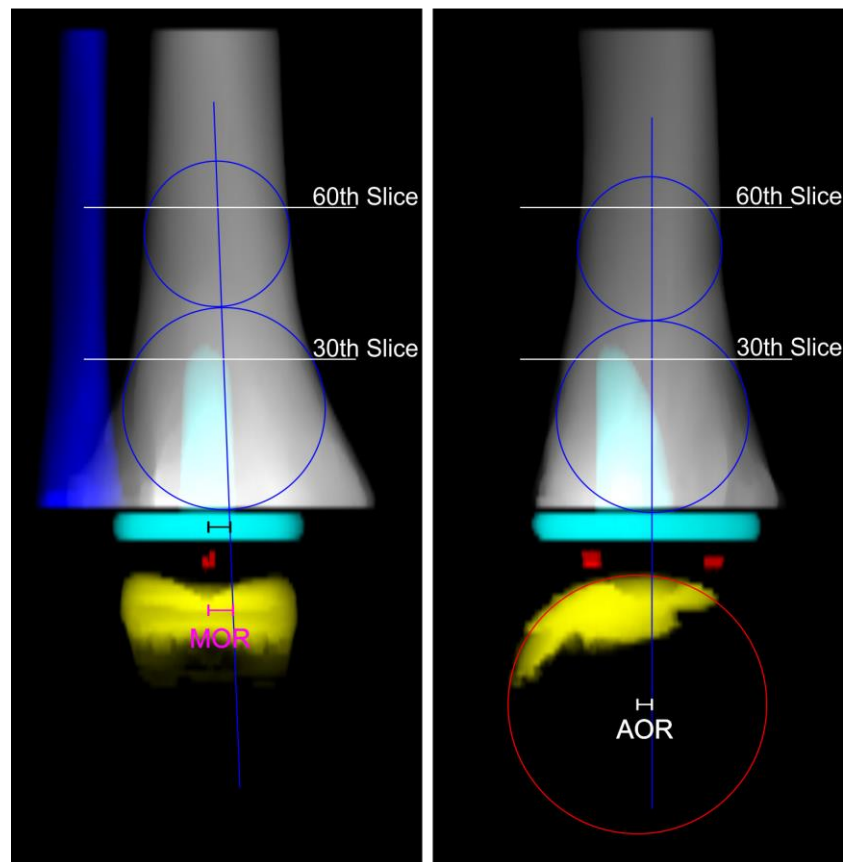
Figure 5.10. Total ankle replacement alignment metrics for segmented computed tomography (CT). Two methods of identifying the tibial axis were used: 1) Pseudo X-ray images were composed from the segmented CT scans by superimposing the slices on top of each other. Manual measurements were taken from the pseudo X-ray images. Blue markings identify the tibial axis in both the sagittal and coronal planes. Red markings identify the talar component centre in the sagittal plane. The perpendicular line between the centre of the talar component and the tibial axis in the coronal plane represents the medio-lateral offset distance. The perpendicular line between the centre of the red markings and the tibial axis represents the talar component antero-posterior offset relative to the tibial axis (sagittal plane). 2) Alignment metrics were also measured numerically by defining the tibial axis by the centre of the 30th and 60th slice. The centre of the talar component was determined by calculating the centre coordinates of the segmented talar component shape. The talar component offset was determined relative to the numerical calculation of the tibial axis.

5.4.1.1 Statistics

Two methods for measuring the AOR using segmented CT scans (30/60 slice and pseudo-Xray methods) were compared to the standard X-ray measure of AOR using a paired t-test. The alpha value was p = 0.05. Associations between the metrics were also determined using Pearson's correlation coefficient (r).

5.4.2 Results

The AOR measured for the numerical CT method was 0.04 ± 0.13 (range: - 0.21 to 0.26). Ten devices featured an anterior AOR whereas 12 talar components were posterior. Using the numerical AOR method, AOR was significantly different to the weight bearing X-ray AOR measured in Chapter 4 (see section 4.3.2) (p = 0.001). However, this method showed a strong correlation between the values (r = 0.93) (Figure 5.11).

The AOR measured by pseudo X-ray CT was 0.03 ± 0.12 (range: - 0.21 to 0.23). In millimetres, the mean antero-posterior offset was anteriorly by 2.02 mm (range: - 7.59 to 11.99 mm, negative is posterior). Ten devices featured an anterior AOR whereas 12 talar components were posterior. Using the pseudo X-ray AOR method, AOR was not significantly different to the weight bearing X-ray AOR measured in Chapter 4 (see section 4.3.2) (p = 0.051) and also showed a strong correlation between the values (r = 0.91).
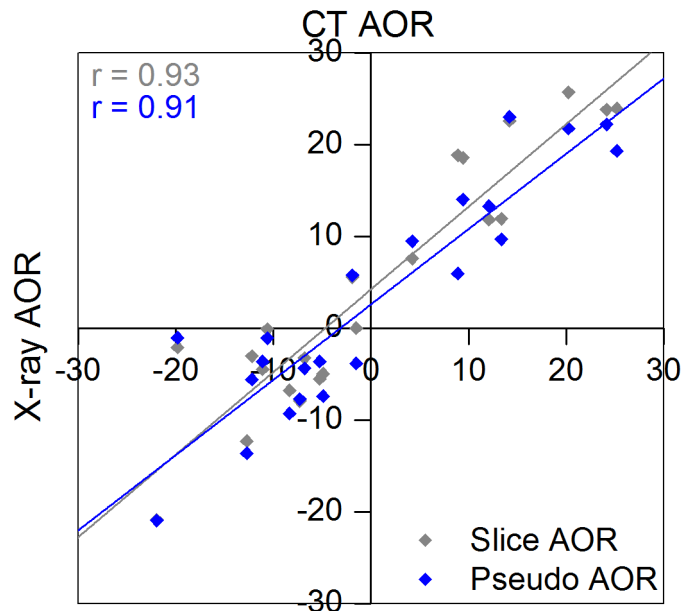
Figure 5.11. Antero-posterior offset ratio (AOR) values for two segmented CT scan methods associated with AOR values calculated from weight-bearing X-ray images. Associations were identified using Pearson's correlation coefficient (r). AOR values were multiplied by 100 to represent percentage values.

5.4.3 Discussion

The measurement of AOR for weight-bearing X-ray images was not significantly different to AOR values measured using pseudo X-ray images produced from segmented CT scans. This result was accepted cautiously given the alpha value for this comparison ($p = 0.051$) was close to the statistical confidence level ($p < 0.05$). While the result may be reflective of a difference in talar component position between weight bearing and non-weight bearing imaging, other confounding factors may have affected the outcome. For example, standard X-ray imaging was assumed to accurately represent the location of the talar component but in the absence of a controlled research protocol for acquiring the images, the orientation of the metallic components was challenging to identify, which has been corroborated in the published literature (Braito et al., 2015b). Additionally, segmenting the curved surface of the talar component was challenging due to metal artefact and may have created small differences in the measurement of AOR.

In an attempt to simplify the AOR measurement from CT scans, a mathematical method, termed the 'numerical method', was also used to calculate AOR. This method required minimal segmentation, less CT scan processing and could offer a measure of AOR in the absence of standard X-ray imaging. The measurement of AOR using the numerical method did however, yield significantly different results to the standard X-ray image measurements. This difference likely originated from the fact the numerical method measured the tibial axis and talar component centre at different levels on the z-axis within the image compared to manual measuring methods typically used in clinical practice. The relative location between the tibial axis and the talar components had not changed, but the lines defining the location of these components had, resulting in statistical differences in the magnitudes of the values. This explanation was supported by the strong correlation between these measures ($r = 0.93$) despite the systematic offset. The absolute values calculated using the numerical method may not accurately describe the AOR, however this method may be useful for understanding the relative variation of AOR within a cohort.

Segmented CT scans can be used to calculate AOR values which is similar to those measured from weight-bearing X-ray images for the cohort investigated in this current study.

5.5 CT Scan Features and Non-clinical Alignment

In the previous sections, re-orientated segmented CT scans have been shown to be effective at identifying the location and volume of TAR components and anatomical features. Also, a basic measure of TAR alignment (e.g. AOR) was shown to yield similar

values between weight-bearing X-ray images and non-weight bearing CT scans. The following sections investigate which features indicative of TAR dysfunction were evident within the re-orientated CT scans and which non-clinical measurements (i.e. measurements novel to re-orientated CT scans) could be captured from the segmented anatomy and TAR components.

5.5.1 Methods

5.5.1.1 CT Scan Features

Using a similar method to section 4.2.3 for identifying features on X-ray imaging, an initial inspection of the CT imaging was undertaken to identify macro-indicators of device dysfunction. Abnormal features such as edge-loading and impingement were noted and counted for the cohort.

5.5.1.2 Non-clinical Measurements

In addition to the measurement of AOR, which was determined for the method validation using the two methods detailed in section 5.4.1, the following non-clinical measurements were obtained from segmented CT scans:

a) Tibial Component Location

Typically, the desired location for the tibial component is in alignment with the tibial axis. The base plate of this component should also be large enough to ensure the tibial cortex is under-hanging sufficiently to support the device.

Tibial component translation in the axial plane was measured relative to the tibial axis. The perpendicular distance of the centre of the tibial component from the tibial axis was calculated using Equation 4.2 (see section 4.2.3). Both antero-posterior and medio-lateral distances were calculated in absolute terms (mm) using the scaled CT scan resolution. Tibial components >2 mm from the tibial axis in either direction were considered 'offset'.

Tibial cortex under-hang was identified by taking the outline of the tibial cortex on the closest clear CT slice to the tibial component base plate. Each tibial cortex outline was overlaid on a standardised template for a TAR base plate. The tibial cortex image was rescaled proportionally to the size of the template base plate so all ankles were comparable. The area of the base plate template outside of the tibial cortex was measured and defined as the area of tibial cortex under-hang. Under-hang was caluculated as a percentage of the tibial component template area. The tibial base plate was split into nine zones and the frequency of tibial cortex under-hang was identified visually and counted.

b) Bearing Insert Location.

For mobile-bearing TARs (all of this cohort), the bearing insert is a free-floating component within the TAR and its position is dependent on the position of the tibial and talar components. The bearing insert is usually assumed to be located directly above the talar component because of its highly conforming design (Barg et al., 2010a). The actual centre of the bearing inserts were identified in this study by two methods:

    I.   The centre point between the two radiopaque markers.

    II.   The centre of the minimum bounding box surrounding the outside of the segmented bearing insert area.

The first method was used for the majority of bearing inserts because in cases where the UHMWPE bearing insert had been fractured or destroyed, the outline of the component was considered an unreliable indicator of the component's centre.

The location of the bearing insert was determined by calculating the difference in millimetres between the tibial component and bearing insert. Bearing inserts >2 mm from the centre of the tibial component in either direction were considered offset.

The radiopaque markers represent a linear feature within the bearing insert which, when connected using imaging software, reveal the rotation of the bearing insert relative to the tibial component. The rotation of the bearing insert was measured using the angle tool in ImageJ. The bearing insert minimum bounding box was used to calculate rotation in the ankles without visible radiopaque markers.
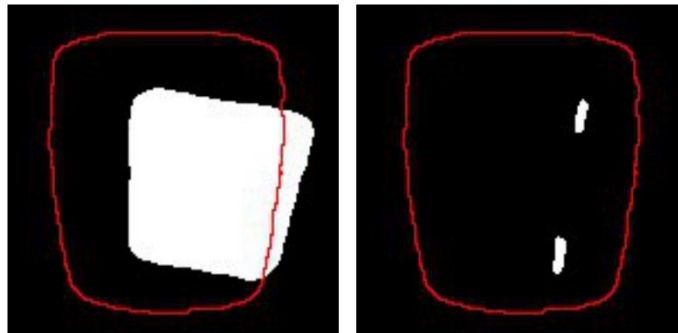
Figure 5.12. Example of binarised bearing insert outline (left) and radiopaque marker outline (right) for the same ankle. Red line indicates the segmented tibial component outline.

c) Talar Component Location

The antero-posterior translation of the talar component is measured by the clinical measurement, the anterio-posterior offset ratio (AOR). This measure was described in section 4.2.3.

The medio-lateral translation of the talar component relative to the tibial axis has not been previously obtained from conventional X-ray imaging because the talar component

is often rotated and its orientation a challenge to establish. Segmented CT scans were used to determine talar component orientation and therefore calculate the medio-lateral offset ratio (MOR). This measure is calculated using Equation 4.2 and used the medio-lateral perpendicular distance of the talar component to the coronal plane tibial axis vector. The MOR was reported in both absolute (mm) and relative units, the relative measure being the ratio of perpendicular distance to the width of tibial component. Reporting both absolute and relative units for the same measure gives a better understanding of the magnitude of offset reported. Also, standard X-ray imaging often cannot yield absolute measures because they are not commonly calibrated, unlike CT scans.

Talar component rotation was determined by measuring the angular difference between a minimum bounding box surrounding the talar component and the tibial component. Identifying the minimum bounding box instead of a standard bounding box was important because rotation affected the centre coordinates of the component as did translation (Figure 5.13). The talar component location and rotation were compared with the same metrics for the bearing insert to determine their relative relationship.

Standard Bounding Box   Minimum Bounding Box
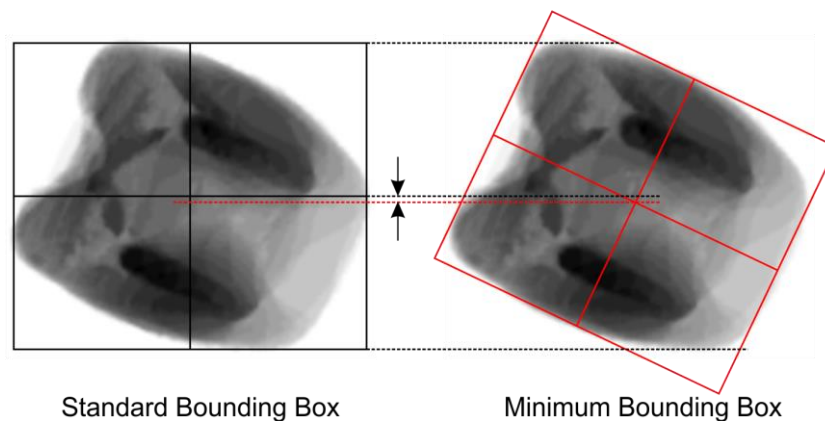
Figure 5.13. Difference in centre coordinates between two identical components using measurements from standard (black) and minimum (red) bounding box parameters.

d) Osteolysis Volume

The frequency and volume of osteolysis was determined for the tibia and talus. If osteolysis was present, volume was determined by summing the number of voxels in the mask. The voxels were scaled to the resolution of the CT scan and the volume converted to cm^3. Each binarised osteolysis mask was flattened in the axial, coronal and sagittal planes alongside an outline of the tibial or talar components. The location of osteolysis was overlaid on a template of a tibial or talar component in each plane. Each image was resized to fit the template to give a proportional osteolysis size that was comparable across ankles. The tibial base plate was split into nine zones and the talar component six zones. The frequency of osteolysis in each zone was identified visually and counted.

Viste et al. (2015) stated axial osteolysis area to be the most useful measure of osteolysis using CT scans and calculated this using a diametral measurement (Figure 5.14). The largest axial osteolysis area was measured for the tibia and talus of each ankle. The axial area was compared with volume to determine whether two dimensional clinical measures are sufficient to determine osteolysis severity.
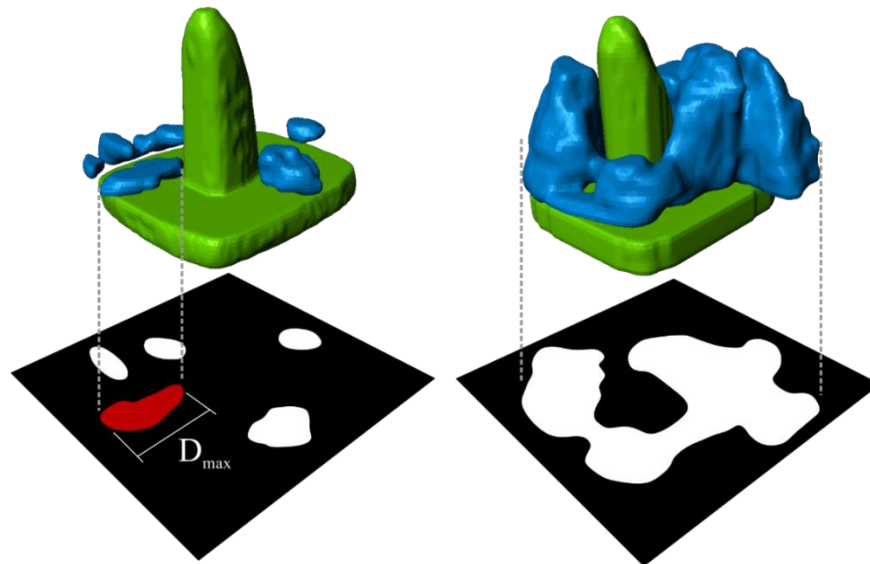
Figure 5.14. Osteolysis size measured by two and three dimensional measurements. The maximum diameter (Dmax) is used for two dimensional measurements. Segmented computed tomography scans can be used to measure osteolysis volume.

5.5.1.3   Statistics

Features

The frequency of features indicative of device dysfunction such as: edge-loading, impingement, component subsidence, and; radiopaque marker extrusion, were reported.

Tibial component location

The location of the tibial component relative to the tibial axis was reported in absolute terms (millimetres). Descriptive statistics were also produced for the location and percentage bone under-hang relative to the tibial component fixation surface.

Bearing insert location

Absolute bearing insert location and rotation relative to the tibial component were reported. The association and statistical difference between the bearing insert rotation and talar component rotation were determined using Pearson's correlation coefficient (r) and a paired t-test.

Talar component location

Descriptive statistics for the medio-lateral offset of the talar component relative to the tibial axis in both absolute (millimetres) and relative terms were calculated. The relative measure of medio-lateral offset was referred to as the medio-lateral offset ratio (MOR) and was the offset distance relative to the width of the tibial component.

Osteolysis Volume

Descriptive statistics for osteolysis volume (mean, standard deviation and range), maximum axial area and the location of osteolysis were reported. Associations between maximum osteolysis area and volume for both the tibia and talus were performed using Pearson's correlation coefficient (r). Correlations using the same statistic were also determined for maximum osteolysis height (z-axis; number of slices) and volume for both the tibia and talus.

5.5.2   Results

5.5.2.1   CT Scan Features

Unlike standard X-ray imaging, CT scans create a three-dimensional image representative of the ankle that can be observed from the axial plane. In this plane, edge-loading was evident in 77% of the TAR devices and was caused by either direct translational offset of the bearing insert or by translational offset in combination with rotation (Figure 5.15).
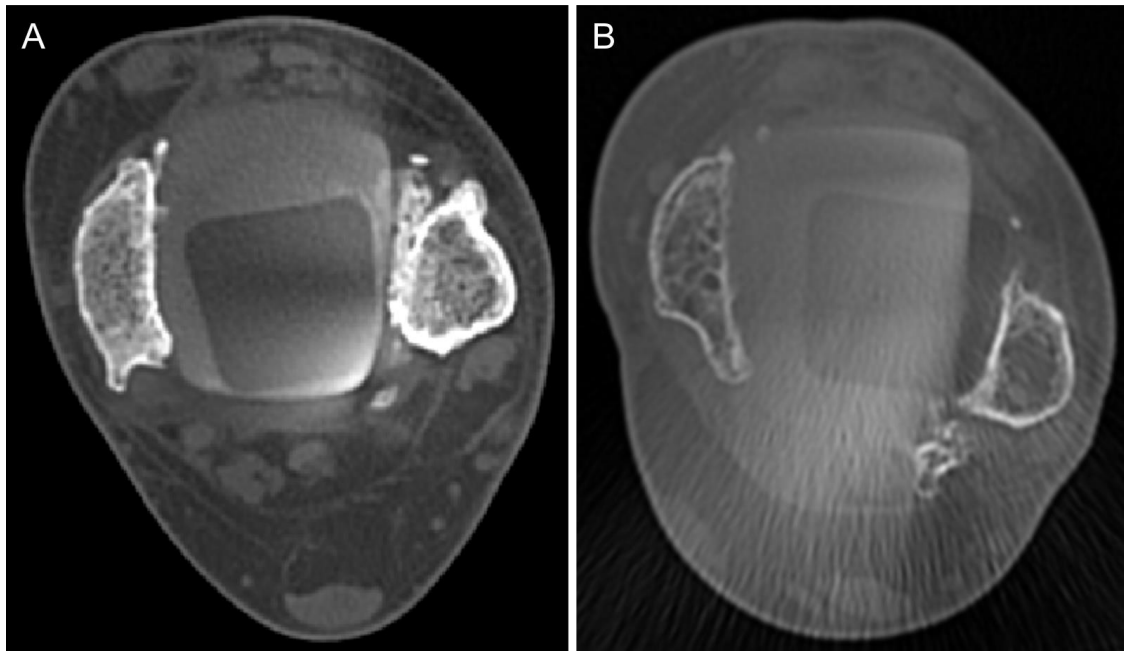
Figure 5.15. Examples of bearing inserts offset relative to the tibial component which was indicative of edge-loading.

Impingement between the bearing insert and the surrounding bone was identified for 55% of the cohort. This phenomena was identified by either, a change in the geometry of the bearing insert, indicative of gross material loss or, if the surrounding bone appeared to have adapted its geometry to conform with the shape of the bearing insert (Figure 5.16).
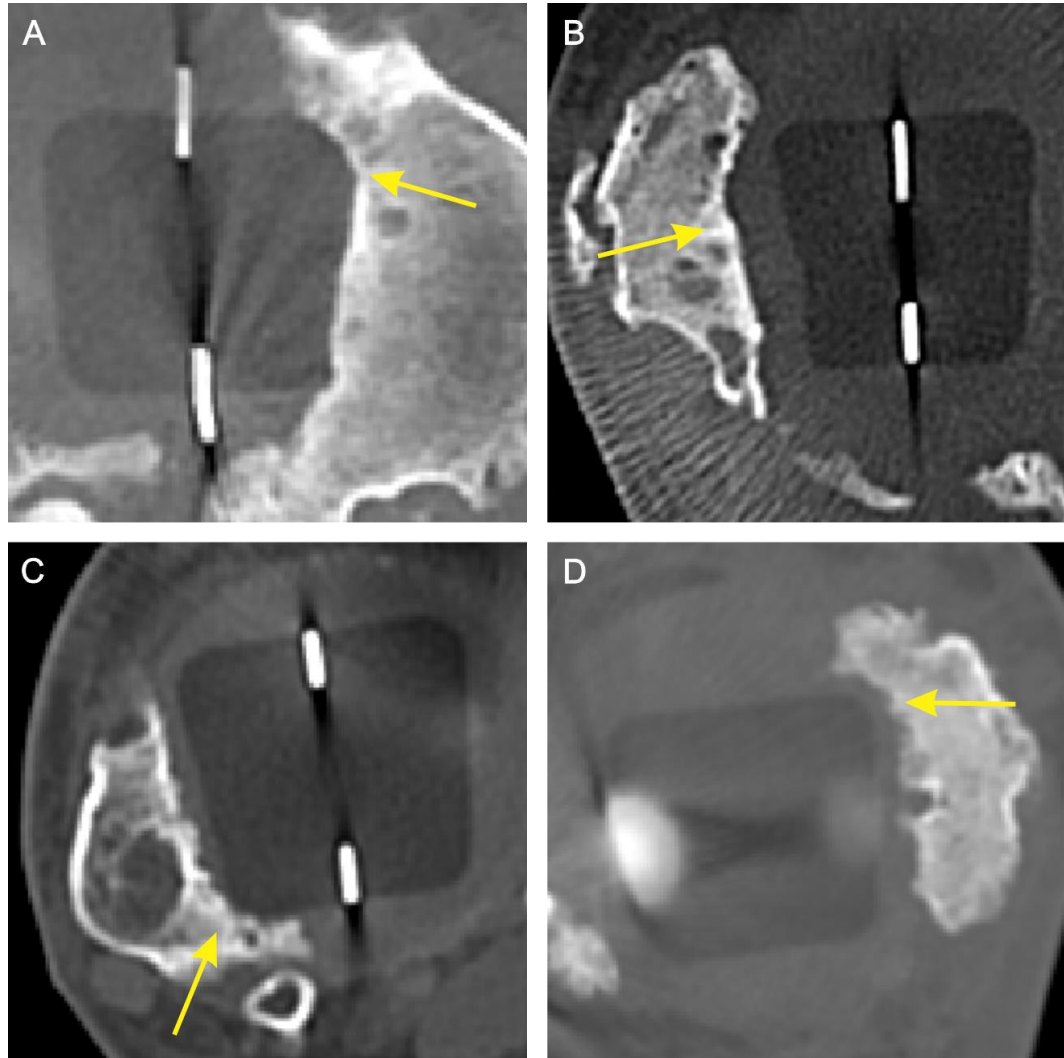
Figure 5.16. Impingement of the bearing insert with evidence of bone conforming to the shape of the component.

Edge-loading and impingement were not mutually inclusive. While 46% of TARs featured both edge-loading and impingement, 32% featured solely edge-loading and 9% exhibited only impingement. In the cases where only impingement was indicated, bone appeared to have grown within the joint space and interfaced with the bearing insert (Figure 5.17).
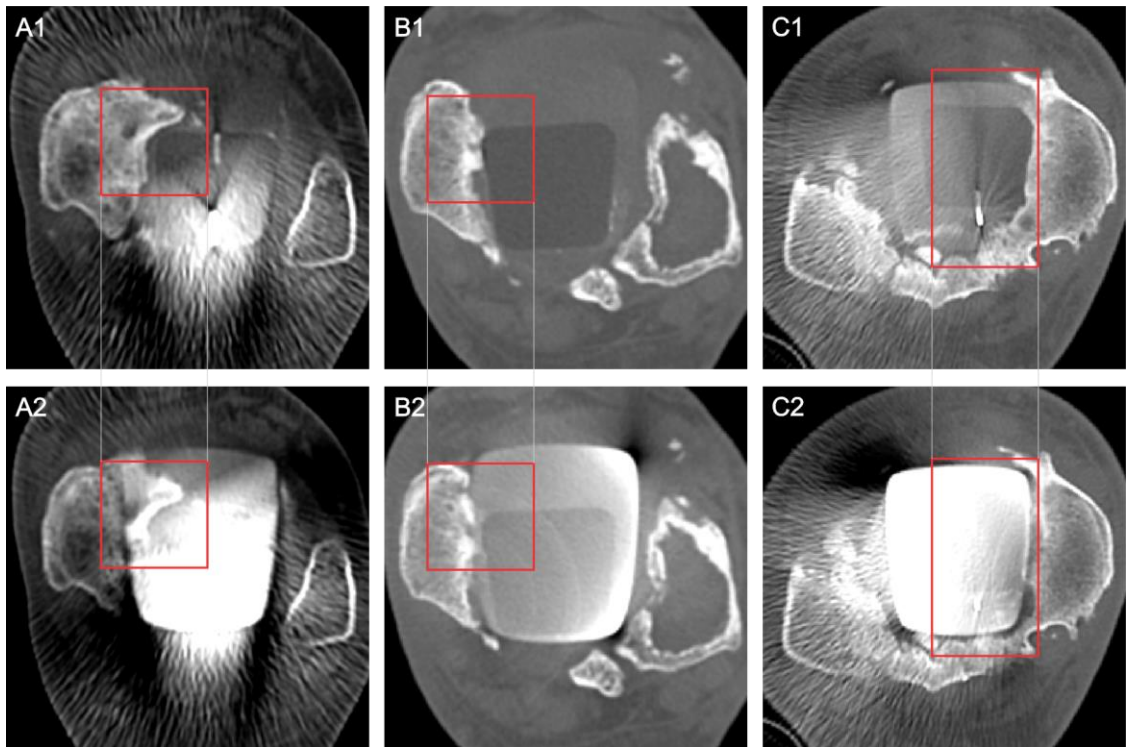
Figure 5.17. Examples of bone growth within the joint space between the tibial and talar components (A-C). The top row of images shows evidence of the bone in-growth. The bottom row of images shows the relative location of the tibial component. Red lines indicate the same location in each paired example (i.e. A1 and A2).

Talar component migration or subsidence was challenging to infer due to the metal artefact surrounding the talar component. Three talar components were deemed to have subsided because either; bone was present on all sides of the talar component at the level of the bearing surface or, the fixation bars of the talar component were resting on the calcaneus (Figure 5.18).
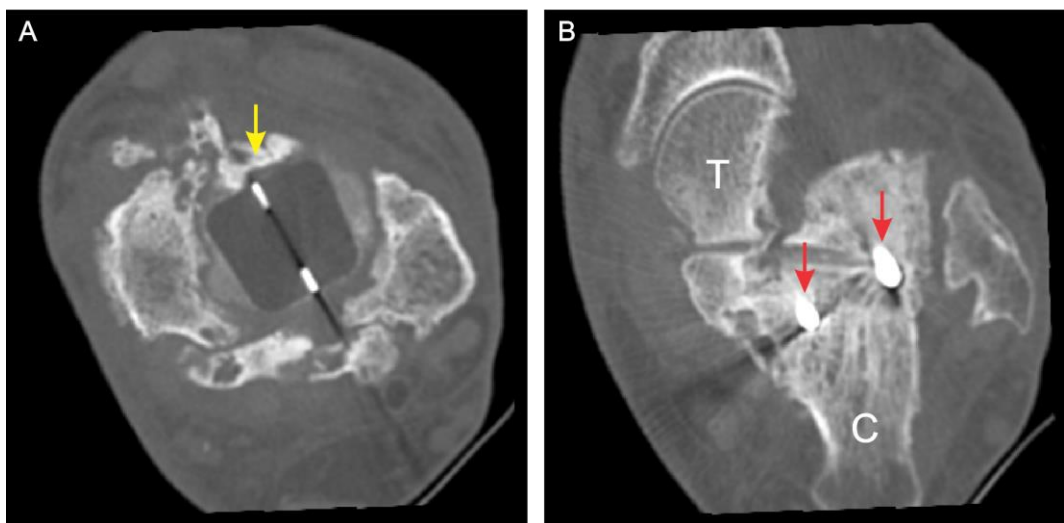
Figure 5.18. Talar component migration shown in the axial plane. A, talar bone was evident at the anterior of the bearing insert (yellow arrow). B, Talar component fixation bars (red arrows) were in contact with the calcaneus (C). T, talus.

None of the measurement metrics for standard X-ray imaging or segmented CT scans were found to adequately quantify valgus or varus alignment of the talar component. Given the re-orientated CT scans had been levelled to the tibial component base plate, the varus/valgus alignment of the talar component was determined by identifying which side of the bearing insert was closer to the tibial component (Figure 5.19). Six talar components were resting in a valgus position, eight components were in a varus position and eight components were considered symmetrical and therefore neutral.
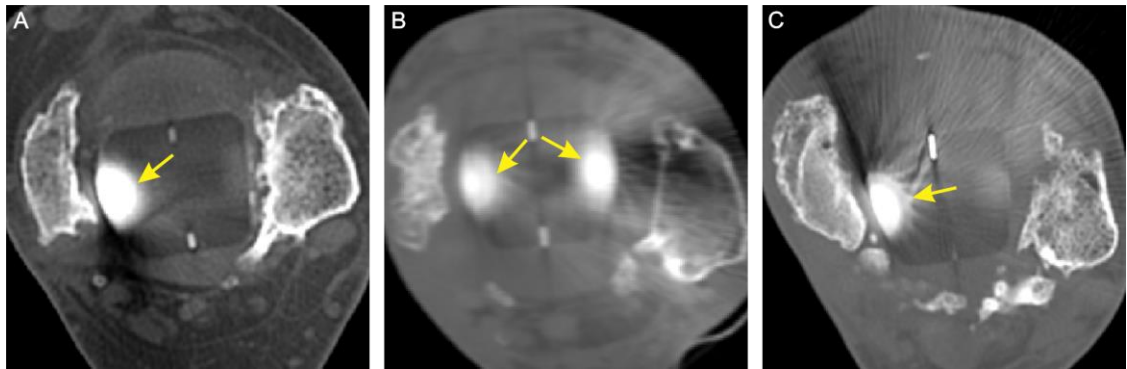
Figure 5.19. Varus/valgus alignment of the talar component viewed in the axial plane. Asymmetrical talar component height indicated varus/valgus alignment (A and C). Symmetrical talar component height indicated neutral alignment (B).

Radiopaque markers for three TARs were not congruent with the anterior and posterior sides of the bearing insert (Figure 5.20). These devices were considered to have undergone radiopaque marker extrusion. In addition to these three TARs, one ankle was absent of radiopaque markers.
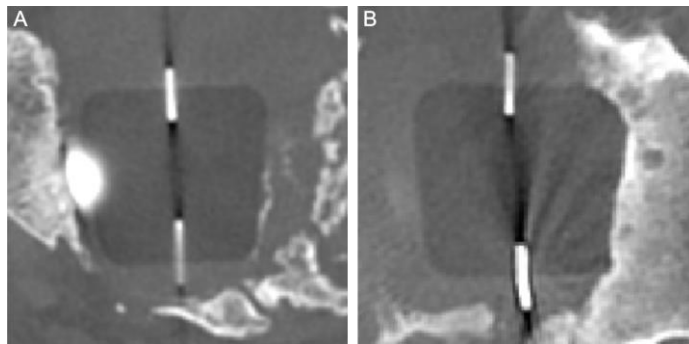
Figure 5.20. Radiopaque marker extrusion. Note the radiopaque markers are not congruent with the bearing insert component and are therefore considered extruded.

5.5.2.2   Non-clinical Measurements

Tibial Component

Mean tibial component translation, relative to the tibial axis, was posterior by - 0.4 mm (± 2.0 mm SD; range: - 3.5 to 2.9 mm; negative is posterior) in the AP plane and medially by 1.8 mm (± 2.7 mm SD; range: - 4.0 to 7.6 mm; negative is lateral) in the ML plane. Of

the 22 CT scans, four devices had an anterior offset, five devices had posterior offset and 13 devices were considered neutral (± 2 mm). Two devices had a lateral offset, seven devices had medial offset and 13 devices were considered neutral (± 2 mm). Four devices were translated greater than 2 mm from the tibial axis in both AP and ML planes.

Tibial cortex under-hang on the tibial component was measureable in 19 of the 22 CT scans. All of the included ankles showed evidence of under-hang, the mean magnitude of which was 3.8% (± 2.8% SD; range: 0.5 to 9.4%) of the tibial component area. In the three ankles with unquantifiable tibial under-hang, too much of the tibial cortex was missing (i.e. resorbed or fractured) to accurately identify where the bone once was. The most common site for tibial bone under-hang was the antero-lateral corner and the postero-lateral corner of the tibial component. Tibial bone for two devices crossed the centre of the tibial base-plate. This bone was trabecular in appearance and the cortices had possibly fractured or eroded due to osteolysis. The tibial cortex crossed the tibial component more frequently towards the anterior than the posterior side.
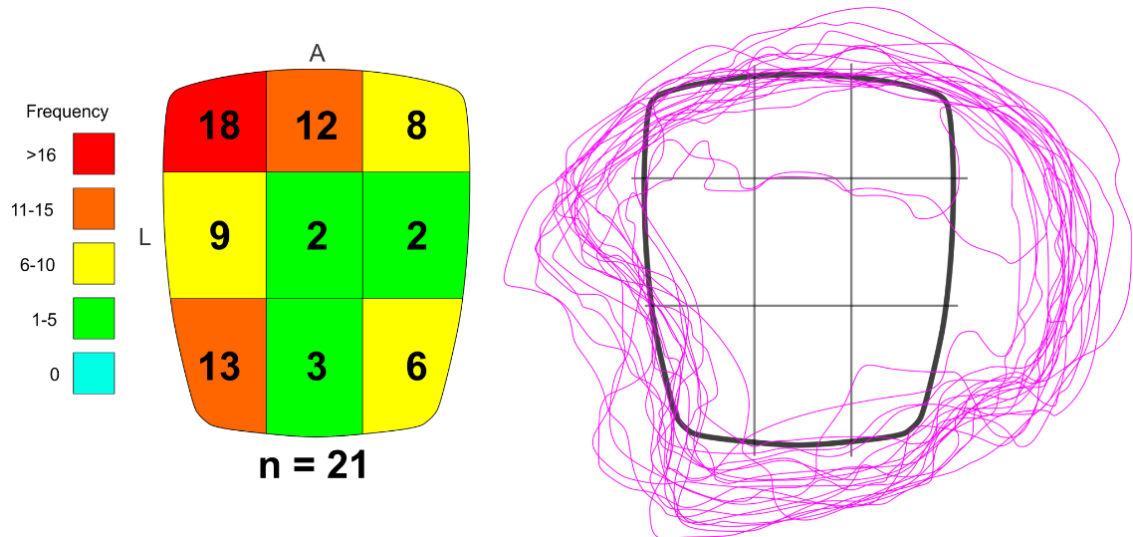
Figure 5.21. Frequency and location of tibial bone under- and over-hang relative to the tibial component. All bone outlines were normalised to the same side. A, anterior. L, lateral.

Bearing Insert

Mean axial plane bearing insert translation, relative to the tibial component, was posterior by - 1.9 mm (± 3.7 mm SD; range: - 8.1 to 5.4 mm; negative is posterior) in the AP plane and medially 0.6 mm (± 3.3 mm SD; range: - 7.0 to 6.5 mm; negative is lateral) in the ML plane. Of the 22 CT scans, four devices had an anterior offset, 13 devices had posterior offset and five devices were considered neutral. Three devices had a lateral offset, eight devices had medial offset and 11 devices were considered neutral. Eight of the inserts were translated greater than 2 mm from the centre of the tibial component in both AP

and ML planes. For one device, the radiopaque markers were absent and the outline of the insert was used to measure its location.

The bearing insert was rotated, on average, medially by 4.4° (± 9.0° SD; range: - 8.8 to 29.4°; negative is lateral) (Figure 5.22). Five bearing inserts were rotated lateral, 13 were rotated medially and four were considered neutral (i.e. within 2° of zero). Bearing insert rotation was not significantly different to talar component rotation (p = 0.33) and highly correlated (r = 0.98).
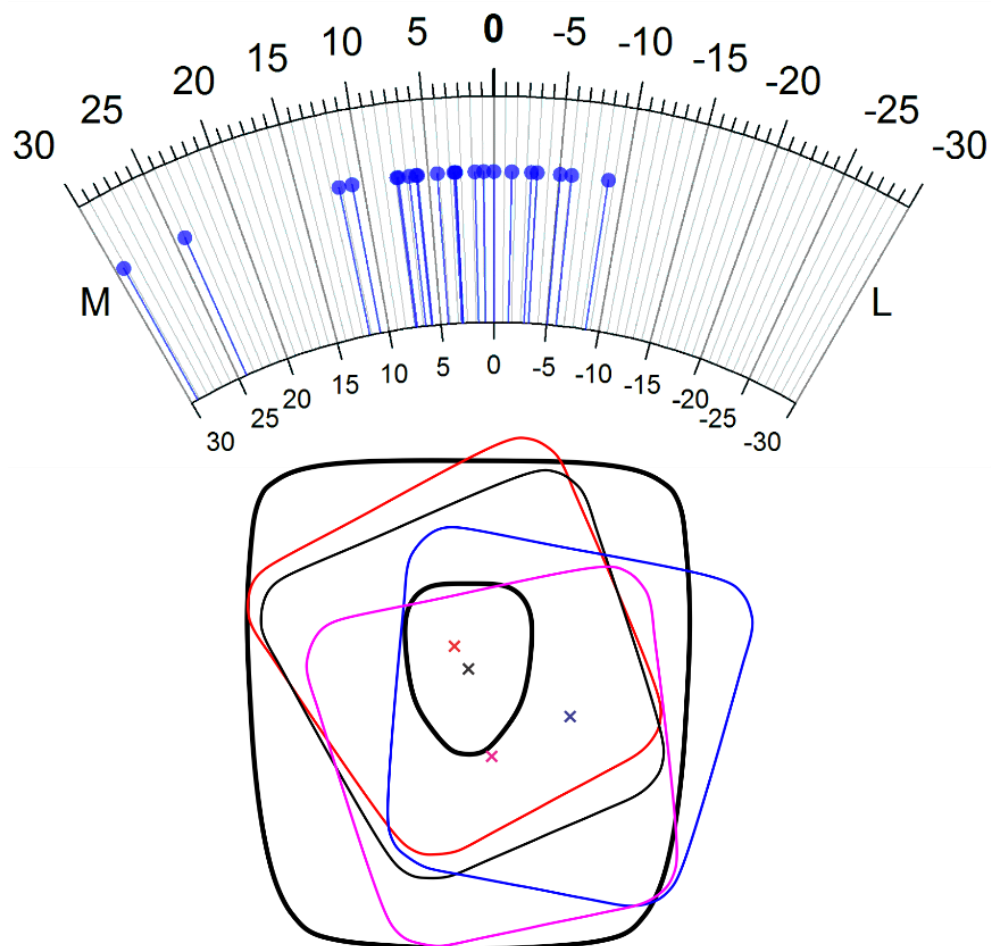
Figure 5.22. Rotation (°) of the bearing insert relative to the tibial component. M, medial. L, lateral.

Talar Component

The AOR measured by CT was reported in the method development (see section 5.4.2). The mean MOR, calculated from segmented CT scans using the numerical method (see section 5.4.1), was - 0.03 (± 0.13 SD). In millimetres, the mean medio-lateral offset was - 1.18 mm (range: -10.17 to 4.93 mm, negative is lateral). Eight devices had a lateral offset, eight devices had medial offset and six devices were considered neutral. Only two talar components were located within 2 mm of the tibial axis in both the AP and ML planes (Figure 5.23).
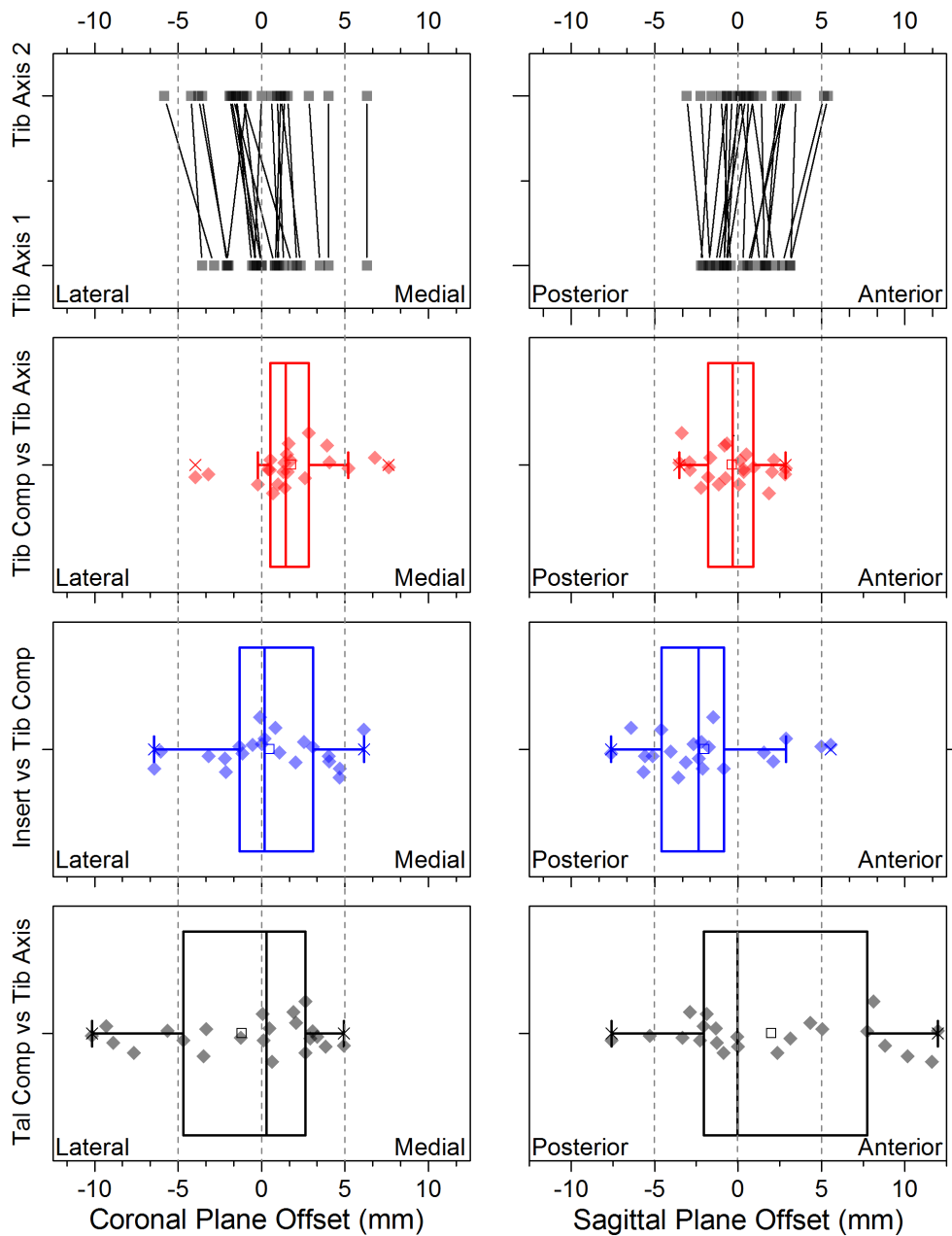
Figure 5.23. Location of total ankle replacement components relative to either the tibial component or tibial axis (Labelled).Tib Axis 1 and 2 were the two measurements used to calculate the tibial axis, which is represented by the lines connecting the two points. Each line represents one ankle. Tib Comp, tibial component. Tib Axis, tibial axis. Insert, Bearing insert. Tal Comp, talar component.

Osteolysis

Of the 22 participants with CT imaging, 21 presented with severe (>1 cm^3) tibial or talar osteolysis (Figure 5.24). Mean tibial osteolysis volume was 9.8 cm^3 ($\pm$ 7.5 cm^3 SD; range: 0 to 26.9 cm^3) and mean talar osteolysis volume was 4.3 cm^3 ($\pm$ 4.2 cm^3 SD; range: 0 to 15.9 cm^3). The greatest combined volume of osteolysis was 33.1 cm^3 and the mean was 14.1 cm^3 ($\pm$ 9.3 cm^3 SD). Only one ankle had no quantifiable indication of osteolysis, this ankle was implanted with a Rebalance TAR which endured for 22 months until being revised for infection.
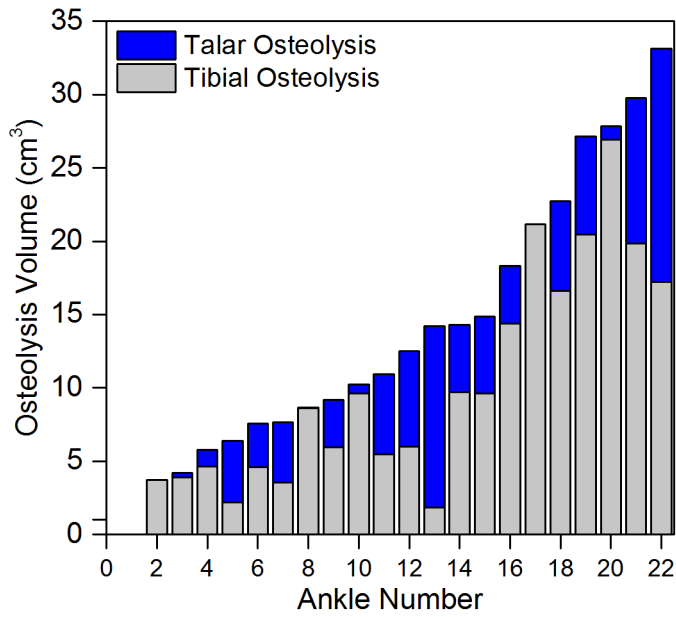
Figure 5.24. Volume of osteolysis for the tibial and talar side of each total ankle replacement device. Only one device had zero osteolysis and was the only device revised for infection.

The median frequency of osteolysis was 2 lesions for both the tibia (range: 0 to 6) and talus (range: 0 to 5). When combined, the median number of osteolytic lesions for the tibia and talus was 3.5 (range: 0 to 11).

A recurring phenomenon was degradation of the cortices as a result of the osteolysis (Figure 5.25). Breaches of the cortex were identified in 86% of the TARs. Eighteen of the breaches were identified in the tibia, two TARs featured tibial and talar breaches and one TAR featured a talar breach only.
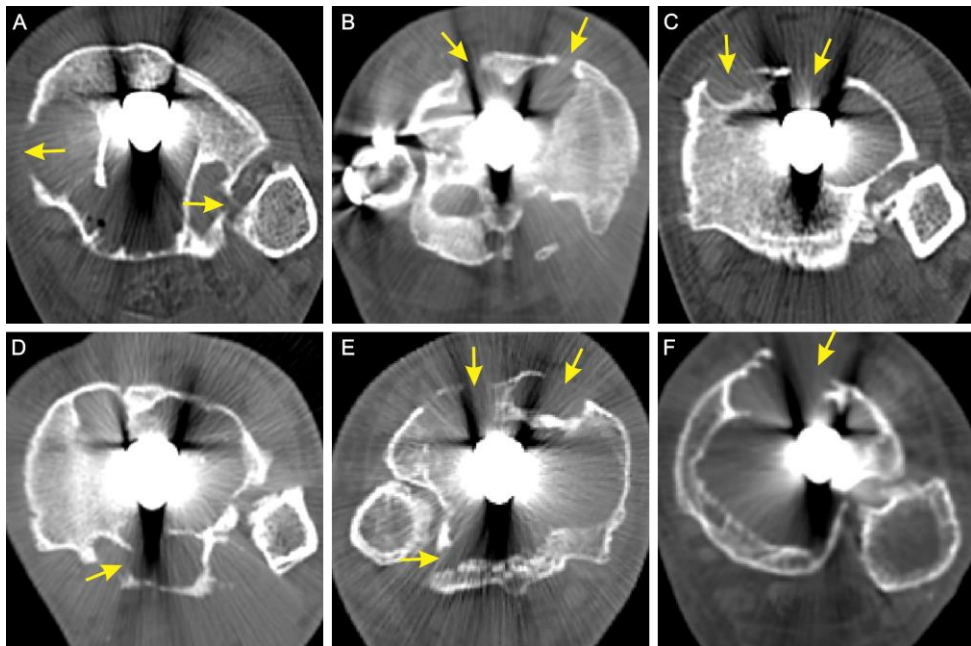
Figure 5.25. Examples of osteolysis where the tibial cortex was breached (yellow arrows).

Osteolysis was located evenly across the tibial component when viewed in the axial plane (Figure 5.26). The only zone absent of osteolysis was above the tibial component stem. Osteolysis within the medial malleolus and lateral malleolus (fibula) was obscured by metal artefact and could not be measured for volume, however the frequency of presence/absence was determined. Eleven TARs featured osteolysis in the medial malleolus and nine TARs featured osteolysis in the lateral malleolus, seven of which, featured osteolysis in both locations.
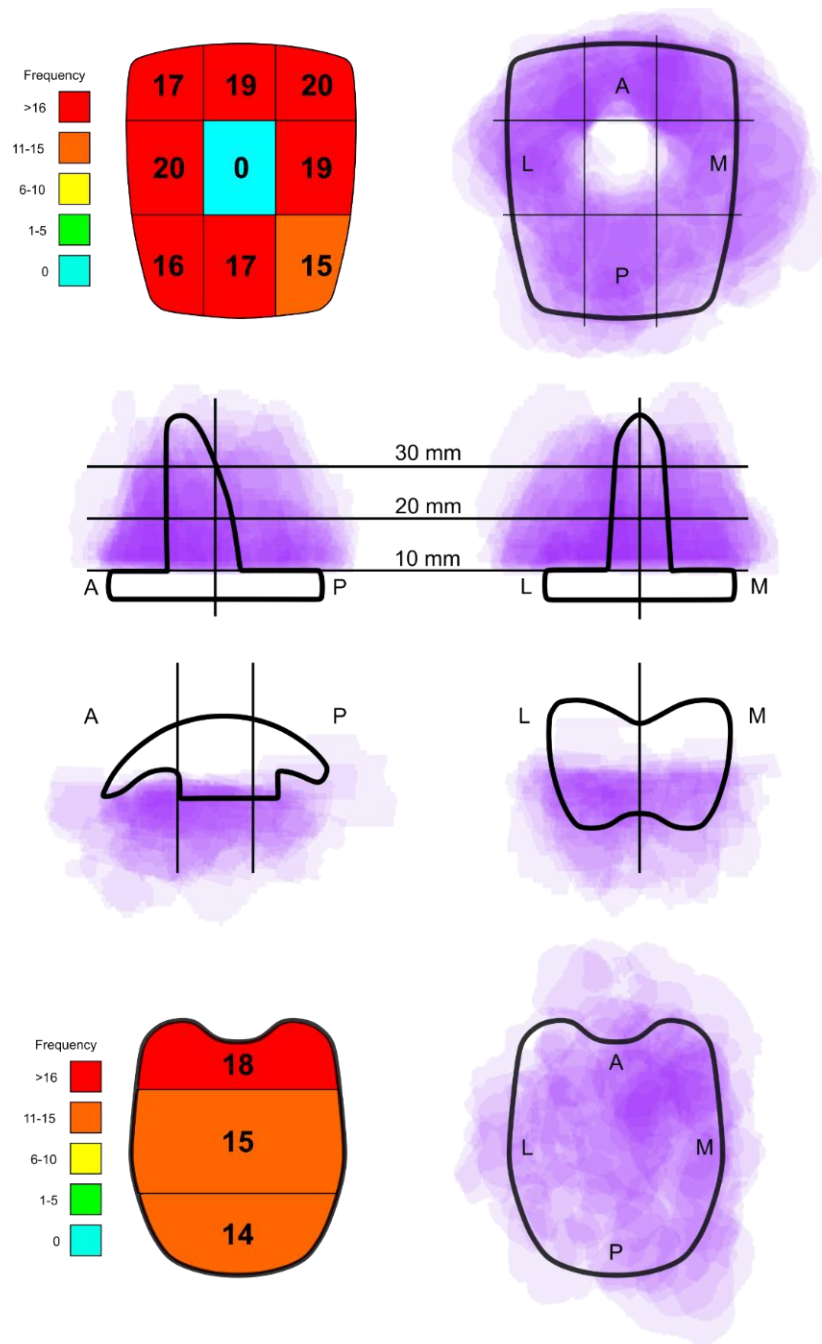
Figure 5.26. Location and frequency of osteolysis for failed total ankle replacements. The maximum area of osteolysis for each ankle was overlaid on a template in each plane, for both tibial (top) and talar (bottom) components. The middle zone of the tibial component represents the area above the tibial stem and no osteolysis was identified. A, anterior. P, posterior. L, lateral. M, medial.

The standard method of measuring osteolysis size in CT scans is by measuring the maximum area in the axial plane (Figure 5.27). The mean maximum axial area of osteolysis was 1647 mm^2 (± 886; range: 0 to 3046 mm) in the tibia and 922 mm^2 (± 732; range: 0 to 2579 mm) in the talus.
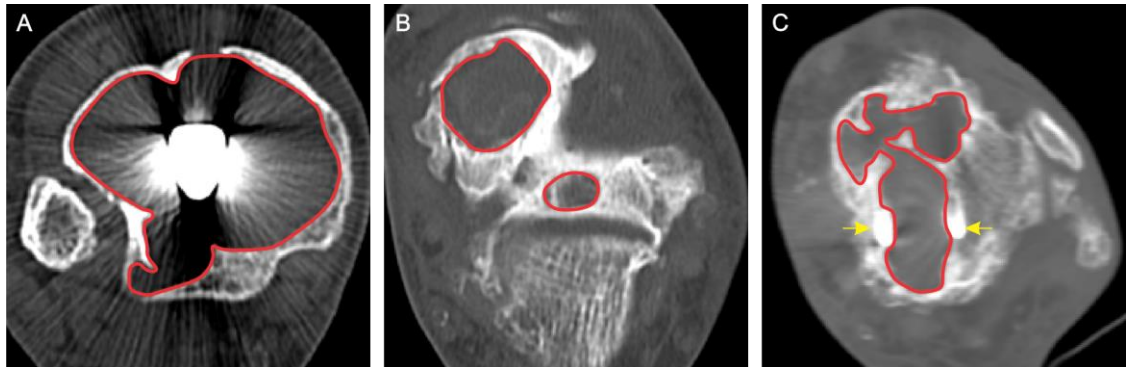
Figure 5.27. Examples of osteolysis from the axial plane. A, tibial osteolysis. B, talar osteolysis. C, osteolysis directly beneath the talar component; fixation bars are visible (yellow arrows).

There was a moderate correlation between tibial osteolysis maximum axial area and tibial osteolysis volume (r = 0.70). A strong correlation existed between talar osteolysis maximum axial area and talar osteolysis volume (r = 0.84). The axial height (z-distance) of osteolysis was equivalently correlated to axial area for both the tibial osteolysis volume (r = 0.67) and talar osteolysis volume (r = 0.86).
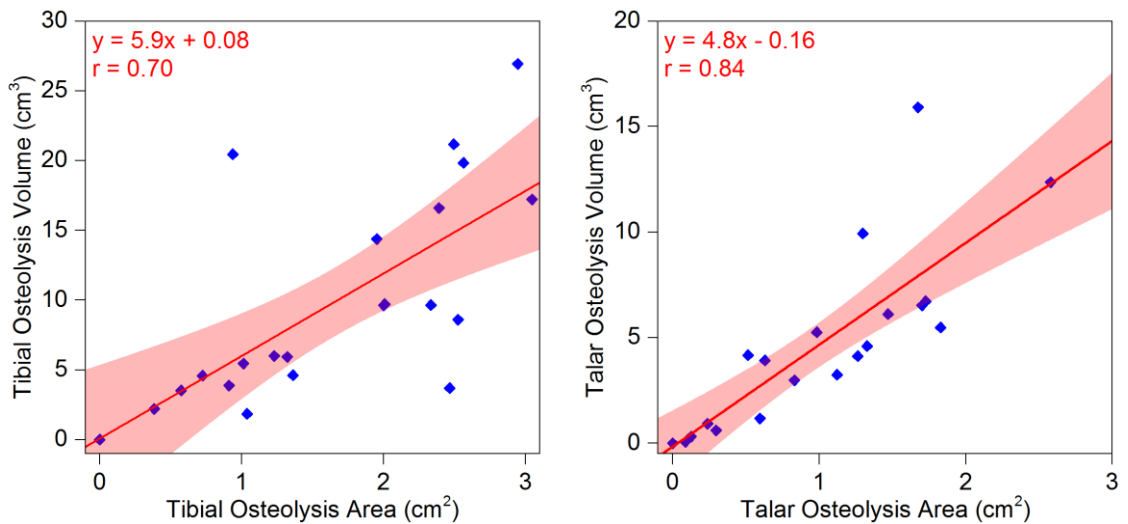
Figure 5.28. Association of maximum area of osteolysis to osteolysis volume. r, Pearson's correlation coefficient. Shaded red denotes 95% confidence intervals. Results for both tibial osteolysis (left) and talar osteolysis (right) are shown.

5.5.3 Discussion

5.5.3.1   CT Scan Features

Several indicators of failure were identified from the standard X-ray imaging which warranted further inspection using CT imaging, these included: edge-loading, collapse of the talus, varus/valgus malalignment between components, radiopaque marker extrusion and substantial osteolytic cysts.

Edge-loading was highly prevalent, featuring in 77% of TARs. Using the axial plane view, the offset of the bearing insert relative to the tibial component was considered edge-loading if the component edges overlapped. The magnitude of bearing insert offset is discussed in the non-clinical measurement section below, but an important aspect of TAR edge-loading to note is that the posterior corners of the bearing insert may overlap the tibial component edge without appearing abnormal from the coronal plane view. This is a limitation of the current methods used to determine the frequency of edge-loading using standard X-ray imaging (Koivu et al., 2009, Morgan et al., 2010, Rippstein et al., 2011).

The enhanced contrast offered by CT imaging compared to standard X-ray imaging, allowed for the integrity of the bearing insert to be inspected. Impingement between the bearing insert and surrounding bone was identified for 55% of the cohort. This phenomenon was unable to be determined using standard X-ray imaging. Impingement presented as either gross material loss from the bearing insert shown by a change in component geometry and/or the bone surrounding the component conformed to the geometry of the bearing insert. Impingement and edge loading were not mutually inclusive. It seems logical for an edge-loaded bearing insert to be at risk of impingement, given for edge-loading to occur, by definition, the component must have escaped, to some extent, the bounds of the tibial component. However, for 9% of the TARs, bone had appeared to have grown within the joint space and caused impingement independent of edge-loading. Postoperative bone growth within the joint space is a frequently identified complication for TAR (Lee et al., 2011) but remains asymptomatic unless it is impinged, be that on the device or in the anatomical gutters below the joint space (Schuberth et al., 2016).

Collapse of the talus and talar component orientation relative to the talus was easier to observe using standard X-ray imaging than CT imaging. Metal artefact obscured the region surrounding the metal component which often included the cortices of the talus. However, when scanning through reoriented CT scan slices in the axial plane view, the talar component often became visible asymmetrically. The tibial components had been re-orientated to be aligned with the axial plane in the CT scans included for the current study, therefore, when the medial or lateral edge of the talar component appeared closer

to the tibial component, this indicated either that the foot was in inversion or eversion slightly in the CT scanner or the talar component was in varus/valgus talar component alignment. The number of valgus/valgus TARs was 64% of the cohort. However, measuring talar component malalignment may best be achieved using weight-bearing X-ray imaging.

For one TAR, standard X-ray imaging showed a radiopaque marker suspended in the joint space having been liberated from the bearing insert. Using CT imaging, three bearing inserts featured radiopaque marker extrusion. This phenomenon had been identified previously in a case study by Dahabreh et al. (2006). They suggested varus/valgus component malalignment may cause the redistribution of stresses resulting in radiopaque marker extrusion. This phenomenon is investigated further in the explant analysis (Chapter 6).

5.5.3.2 Non-clinical Segmented CT Scan Measurements

Segmented CT scans yielded novel metrics for TAR component orientation and position that were previously unobtainable, particularly using standard X-ray imaging. These novel metrics include the relative and absolute location, and rotation, of each TAR component, in addition to the axial location of hard tissue anatomy and the volume of osteolysis. The location of each component and extent of osteolysis is discussed in the following sections.

Tibial Component

The majority of tibial components were within 2 mm of the tibial axis, with four devices being greater than 2 mm from the tibial axis in both coronal and sagittal planes. Of the retrieved TARs with CT imaging, 95% (n = 21 of 22) were AES TARs. Surgical guidelines published for the AES TAR by the surgeon designers recommended the tibial component to be implanted parallel with the tibia with the stem 2.5 cm from the anterior side (Asencio and Leonardi, 2005). Practically however, the tibial component was typically placed in alignment with the tibial axis, which was reflected by the results of this study. Asencio and Leonardi (2005) also recommended that the tibial plate should be large enough to be covered entirely by the distal tibial bone. Tibial cortex under-hang occurred for all TARs, yet this was predominantly located at the antero-lateral and postero-lateral corners of the component. The medial malleolus prevented tibial cortex under-hang on the medial edge of the component. If the recommendation by Asencio and Leonardi (2005) were to be interpreted rigidly, then the distal tibial cortex would have under-hung the tibial component equally for each zone on the anterior, lateral and posterior edges. The posterior side featured less under-hang than the anterior side, therefore some of the

components may be considered undersized. Given the variation in tibial anatomy between patients, under-hang around the entire component is practically unachievable.

Bearing Insert

Only two bearing inserts were within 2 mm of the centre of the tibial component in both antero-posterior and medio-lateral planes and eight bearing inserts (36%) were translated greater than 2 mm from the centre of the tibial component in both planes. Edge-loading was more likely when translation was combined with rotation. Bearing inserts were rotated medially by 4.4°, on average. Importantly, the most rotated bearing insert (29.4°) was also the least translated component yet still featured edge-loading. This showed both translation and rotation, independent of each other, and combined, were clinically relevant risk factors for edge-loading. Rippstein et al. (2011) defined edge-loading as a mismatch in translational location between the tibial and talar components in the coronal plane by ≥2 mm, although, different magnitudes of offset have been selected by different authors for the same definition (Koivu et al., 2009). The ≥2 mm limit may not adequately identify edge-loading for all TAR designs and it does not account for axial rotation, which is challenging to identify in standard X-ray imaging. For the AES TAR, the centre of the tibial component was used as the reference point for the alignment of all the TAR components. A specially designed retractor, which interlocked with the centre of the tibial component, was used in the primary surgery to prepare the talar surface and align the talar component (Asencio and Leonardi, 2005). This ensured central alignment between the tibial and talar components and by extension, the bearing insert. Aligning the bearing insert with the centre of the tibial component is not only meant to align it with the tibial axis, but also theoretically, the location of maximum range of motion. The high prevalence of offset between the bearing insert relative to the tibial component identified in this current study may indicate that either edge-loading is prevalent in this cohort or that when the ankle is in non-weight bearing conditions, the bearing insert is capable of moving beyond the edge of the tibial component. Analysis of the explanted bearing insert may further elucidate the prevalence and effect of edge-loading in this cohort (see Chapter 7).

Rotation of the bearing insert was strongly correlated with the rotation of the talar component ($r = 0.98$). Bearing insert location had previously been assumed to be identifiable by the location of the talar component, particularly for mobile-bearing TAR designs where the bearing insert is geometrically constrained by the talar component (Barg et al., 2010a). The constrained relationship between these two components is maintained regardless of the extent of axial talar component rotation. This may have particular relevance for in-vivo fluoroscopy studies where the bearing insert cannot be identified accurately, but the talar component is clearly identifiable (Iwamoto et al., 2014).

Talar Component

In the method validation (see section 5.4.1), the numerical method for calculating AOR was shown to lack accuracy but was highly precise. Therefore, this method was deemed suitable to identify the relative variation between ankles in the medio-lateral plane but not to determine the absolute value of offset. This metric was named the medio-lateral offset ratio (MOR). The MOR represented the offset of the talar component relative to the tibial axis with the distance being calculated as a ratio of the width of the tibial component. The average MOR was - 0.03 which equates to a 3% (or 1.2 mm) offset in the lateral direction. The variance was high with a range of 15.1 mm and the maximum offset in the lateral direction was double (10.2 mm) that of the medial direction (4.9 mm). The greater lateral MOR may represent an anatomical limitation provided by the medial malleolus. Bearing inserts may impinge on the medial malleolus before MORs of equivalent magnitude to those in the lateral direction are recorded. The high variance of MOR may be reflected in the high frequency of edge-loading identified for this cohort. This is the first study to define and measure MOR using CT scans.

Osteolysis

Of the 22 ankles with CT imaging assessed for osteolysis, 21 ankles were revised for osteolysis and the remaining ankle was revised for infection, this ankle did not feature osteolysis. All of the ankles revised for osteolysis presented with marked tibial and/or talar osteolysis. Nineteen (91%) of the 21 participants were male which was representative of the entire cohort of 42 complete TAR retrievals, of which 95% were from male participants and 83% were revised for osteolysis. Koivu et al. (2017) found the male sex to be a predictor for the early development of osteolysis for the AES TAR. The work described in this current study only assessed failed devices and it is unknown how many female patients were implanted with TARs by the same surgeons, therefore identifying the male sex as a risk factor could not be determined in the current study.

The greatest combined volume of osteolysis was 33.1 cm^3 and the mean was 14.1 cm^3 (± 9.3 cm^3 SD). In relatable terms, the maximum volume is equivalent to that of a squash ball (33.5 cm^3). This is the first study to calculate volume from CT scans using segmentation. Estimates of osteolysis volume for TAR have been determined using ellipsoid calculations (Jensen et al., 2014, Gross et al., 2016). Jensen et al. (2014) assessed 100 osteolytic cysts surrounding 42 STAR devices using a 3D fluoroscopic multiplanar slice reconstruction technique. The average cyst volume was 1.6 cm^3 with a range between 0.02 and 8.2 cm^3. Gross et al. (2016) investigated osteolytic cysts for 29 ankles implanted with one of three TARs: Inbone, Salto-talaris and STAR. The mean tibial cyst volumes were 25.7 cm^3 and 14.9 cm^3 for the talus. No range was reported. The average total cyst volume reported by Jensen et al. (2014) was 8.8 times less than

the mean volume reported in the current study. Whereas, the values reported by Gross et al. (2016) were 2.6 times and 3.5 times larger than the mean tibial and talar volumes reported in the current study, respectively. The smaller osteolysis volume reported by Jensen et al. (2014) may be explained by the short implantation time of 36 months, on average. However, the median follow-up for Gross et al. (2016) was 65.9 months, which was shorter than the 87 month median implantation time for the TARs included in the current study. Therefore, a large variance in osteolysis volume appears to occur between TAR devices and in many cases, the size of the cysts were severe. Compared to total hip replacement (THR) designs featuring non-highly crosslinked UHMWPE, similar to the TAR devices included in the current study, the mean volume of osteolysis in the hip was 1.5 cm^3 with a range of 0.07 to 5.2 cm^3 at 12.2 years follow-up (Broomfield et al., 2017). These values were similar to those reported by Jensen et al. (2014) for TAR, except the mean implantation time was four times longer. Similar to TAR, a broad variance of osteolytic cyst sizes have been reported for THR. Leung et al. (2007) reported mean cyst volumes of 7.5 cm^3 (range: 2.3 to 24.0 cm^3) surrounding THR acetabular cups at 6.1 years follow-up. Shon et al. (2009) reported a mean pelvic osteolytic cyst volume of 2.3 cm^3 and a range between 0.02 and 61.7 cm^3 at 82.1 months follow-up. The average osteolytic cyst sizes appear to be greater for TAR than THR accounting for similar or longer implantation times and non-crosslinked UHMWPE material properties.

Volumetric measurements of osteolysis were strongly associated with the axial areal measurements of osteolysis size commonly used in the literature (Viste et al., 2015). Talar osteolysis volume had a stronger correlation ($r = 0.84$) compared to tibial osteolysis volume ($r = 0.70$). The difference may suggest more consistency in osteolytic geometry for the talus compared to the tibia. These results suggest maximum areal measurements of osteolysis are a good to excellent representation of the osteolysis volume for TAR. Similar relationships have been determined for other total joint replacements. For example, Shon et al. (2009) compared osteolysis volume measured using CT and 2D X-ray measures for 118 THR patients with cementless acetabular cups. The maximum area of pelvic osteolysis had a moderate correlation to osteolytic volume ($r = 0.74$).

For TAR, severe osteolytic lesions are typically defined as >1 cm^2 (Besse et al., 2009, Viste et al., 2015). Using the linear regression equation from Figure 5.28 for tibial osteolysis, severe osteolytic lesions (>1 cm^2) equate approximately to a volume of 6.0 cm^3. Yoon et al. (2014) and Viste et al. (2015) reported maximum osteolysis areas of 5.22 cm^2 for a cohort of Hintegra TARs, and 7.08 cm^2 for a cohort of AES TARs, which can be predicted to be approximately 30.9 cm^3 and 41.96 cm^3 in volume, respectively. Monitoring osteolysis in 17 patients with the fixed-bearing Agility TAR, Hanna et al. (2007) reported a mean osteolysis area of 1.96 cm^2 which equates to a volume of approximately 11.7 cm^3. These values were of a similar magnitude to the maximum and

mean volumes measured in the current study and previous volumetric estimations (Jensen et al., 2014, Gross et al., 2016). The majority AES TAR cohort in the current study does not appear to be an outlier regarding osteolysis size when compared to other TAR designs or types.

Only one zone, above the tibial component stem, was absent from osteolysis for all TARs. All of the other zones above the tibial component featured osteolysis at a similar frequency. The anterior anchor of the talar component featured slightly more osteolysis than the centre or posterior, but only marginally. Besse et al. (2009) published a ten zone grid and classification method for the AES TAR. Similar to the results in the current study, Besse et al. (2009) found equal coverage of osteolysis across the tibial component and higher rates of osteolysis at the anterior anchor of the talar component. Similar trends were recognised for the AES TAR by other authors (Koivu et al., 2009, Rodriguez et al., 2010, Dalat et al., 2013, Kohonen et al., 2013). A different trend was identified for the Mobility TAR, another BP-type device; the osteolytic cysts appeared to be predominantly located in the medial malleolus (Rippstein et al., 2011, Muir et al., 2013). Approximately half of the cohort featured osteolytic lesions in the medial and/lateral malleoli, yet metal artefact made calculating the volume of osteolysis in this region unachievable. The large size of osteolysis in this cohort and its widespread coverage made identifying its origin a challenge. Capturing CT images early after implantation (< 2-3 years) may offer more information for where osteolysis originates.

5.5.3.3   Limitations

The retrospective nature of the current study meant the retrieved CT scans lacked acquisition parameter consistency (e.g. orientation, resolution). CT scans were re-aligned to a common surface (i.e. tibial component fixation surface) to ensure the measurements captured were comparable between ankles. The reliability of CT scan reorientation was demonstrated using inter- and intra-rater analyses. CT scan resolutions were comparatively low compared to X-ray imaging and were anisotropic. In the axial plane, the resolution was approximately three times higher (0.35 ± 0.07 mm) than for slice thickness (z-axis; 0.92 ± 0.11 mm). All measurements were captured in the axial plane to maximise measurement resolution.

The CT scans were non-weight-bearing which may have affected how relatable the measurements were to the equivalent weight-bearing position and the function of TARs. However, a validation study was undertaken to determine how similar the alignment measures were between the imaging modalities and they were found to be non-significantly different and highly correlated ($r = 0.93$). This validation study was limited to a comparison of AOR and other aspects of device alignment may have differed between the weight-bearing and non-weight-bearing imaging modalities, such as bearing insert

rotation, though this could not be measured using the methods in this current study. The high prevalence of edge-loading identified in this cohort may cause undue constraint within the device regardless of being weight-bearing or not. Also, comparing the CT scan measures to X-ray imaging is not necessarily the most effective validation. X-ray imaging is prone to producing inconsistent measures of alignment (Braito et al., 2015b) but X-ray imaging is the current clinical standard for such measurements and is therefore the best comparator available. Computed tomography may have been the more accurate method but an in-vitro cadaver study would be required to accurately validate this.

Metal artefact complicated the segmentation process. Osteolysis around the tibial stem, close to the tibial base plate and within the talar component were not capable of being segmented due to metal artefact which likely underestimated the volumetric measures of these features. Manual segmentation was required for the majority of features, the process for which was laborious and may have introduced observer bias. However, the reliability of manual segmentation was tested in this chapter and shown to be acceptable. Similar to the number of X-ray images, the sample size was relatively small (n = 22) for statistical analyses and were interpreted with caution.

5.6   Summary

Re-orientated CT scans highlighted the prevalence of edge-loading (77%) and impingement (55%) in this cohort. Varus/valgus talar component tilt was also prevalent (64%) but remained challenging to quantify. Radiopaque marker extrusion was evident in four TARs and may be linked to talar component subsidence.

Tibial components were broadly in alignment with the tibial axis in both planes. Under-hang of the tibia on the tibial component was predominantly antero-lateral and postero-lateral. Half of the bearing inserts (50%) were considered aligned (≤ 2 mm) with the tibial component in the coronal plane. However, translation and rotation of the bearing insert, independent of each other, and combined, were clinically relevant risk factors for edge-loading.

This was the first study to measure the medio-lateral offset ratio (MOR) using CT. This metric may be linked to the high incidence of edge-loading. The proximity of the device to the medial malleolus may increase the likelihood of impingement on this side.

Only two talar components were considered aligned with the tibial axis in both planes. Talar component position (a product of surgical positioning and subsidence) and differences in the anatomy of the talus between patients may be important considerations for future TAR designs.

Osteolysis was considered severe for all TARs revised for that indication. The volume measurements reported in the current study were similar to other published TAR studies but larger than lesions reported for THR. The volume of tibial osteolysis was more than twice that in the talus. Clinical areal measurements of osteolysis were considered an acceptable representation of osteolysis volume.

In the following three chapters, how the device is affected by edge-loading, impingement, varus/valgus talar tilt and radiopaque marker extrusion will be investigated further using established and novel explant analysis methods.

Chapter 6
Explant Damage Mode Analysis

6.1   **Introduction**

The development of osteolysis remains a short to mid-term (< 10 years) problem for total ankle replacement (TAR) (Lucas y Hernandez et al., 2014). The majority of participants included in the research for this thesis were revised for osteolysis and pain (98%) after < 10 years. The osteolysis was characterised and considered severe in all cases (Chapter 5). A commonly cited stimulus of osteolysis in total hip and knee replacements (THR, TKR) is the accrual of biologically reactive wear particles (Ingham and Fisher, 2000). However, the early development of osteolysis in TAR suggests that either wear debris is being generated rapidly in the initial years of implantation or that other failure mechanisms are prevalent (Knecht et al., 2004, Besse et al., 2009). Edge-loading, impingement, varus/valgus talar tilt and radiopaque marker extrusion were identified in the medical imaging (Chapters 4 and 5) and warrant further investigation using retrieval analysis methods.

Explant analysis studies aim to characterise the type, extent, location and quantity of damage and/or wear on total joint replacement components. To the author's knowledge, only four retrieval studies have been published over the 40 year development of TAR (Small Bones Innovations Inc., 2007, Affatato et al., 2009, Vaupel et al., 2009, Cottrino et al., 2016). These studies are detailed in section 2.5.2.1 but in brief, several damage modes were common across retrieval studies of TAR. Burnishing, scratching, pitting, abrasion and embedded debris were frequently associated with the bearing inserts (Small Bones Innovations Inc., 2007, Affatato et al., 2009, Vaupel et al., 2009, Cottrino et al., 2016). Deformation of the bearing insert was also identified at locations of high contact stress (Affatato et al., 2009, Vaupel et al., 2009). The origin of the embedded debris was suggested to be predominantly wear of the fixation surface (Vaupel et al., 2009, Cottrino et al., 2016), although wear on the metallic bearing surfaces was also identified (Cottrino et al., 2016). Histological analyses have also identified third body wear particles indicative of wear at the fixation surface and suggest this to be particularly problematic for TAR (Koivu et al., 2009, Koivu et al., 2012, van Wijngaarden et al., 2015). However, despite the evidence for third body wear originating from the fixation surface, the damage modes at this surface are yet to be reported. Likewise, damage modes evident at the other TAR surfaces have been analysed (Cottrino et al., 2016) but not

comprehensively documented for a large cohort. Vaupel et al. (2009) attempted to integrate the explant analysis with results from medical imaging but with only 10 devices, no statistical relationships could be determined. Of the four retrieval studies, three of the studies included ≤ 10 explants (Affatato et al., 2009, Vaupel et al., 2009, Cottrino et al., 2016). The relatively large cohort of failed TARs included in this thesis represents an opportunity to investigate the relationship between the damage modes produced by TAR and the results of the medical imaging identified in Chapters 4 and 5.

The visual identification of damage is integral to retrieval analyses (British Standard ISO 12891-2, 2014) but is limited by its subjective nature (Harman et al., 2011). The development of simple repeatable quantitative methods is desirable so that independent research groups can compare results with confidence.

The aim of this chapter was to:

- Identify the type, extent and possible causes of damage/wear modes present on the components of failed TARs.

In order to achieve this aim, the following objectives were explored:

- Inspect a cohort of failed TAR explanted devices for established and /or novel damage modes.
- Develop non-destructive quantitative and semi-quantitative methods to measure the extent and magnitude of the surface damage and wear of TAR.
- Identify the relationships, if any, between the results of the medical imaging measurements and the damage/wear modes associated with the explants.

6.2 Explant Details

Explanted TARs each with tibial, talar and bearing insert components from five brands were retrieved and analysed using macro-photography and microscopy. The demographic details are summarised in Table 6.1. Individual explant details are reported in section 3.4.1.

Table 6.1. Summary of demographic and device details for the TARs included for photogrammetry.

Factor		n	Factor	Mean (range)
Total		42	Time In-vivo (Mo)	89.3 (4-168)
			Missing[a] (n)	5
Device Type	AES (2nd generation)	27		
	AES (1st generation)	6	Age (years)	60 (47-72)
	Hintegra	3	Missing[a] (n)	4
	Rebalance	2		
	Mobility	2		
	BP	2		
Side	Right	21		
	Left	21		
Sex	Male	38		
	Female	4		
Diagnosis	OA	24		
	PTOA	13		
	Haemochromatosis[b]	1		
	Missing[a]	4		
Indicator for Revision	Osteolysis	30		
	Pain	4		
	Pain and Osteolysis	5		
	Infection	1		
	Missing[a]	1		

Notes: AES, Ankle Evolutive System (Transysteme, Fr); Rebalance (Zimmer Biomet, UK); Hintegra (Integra, Fr); Mobility (Depuy Synthes, UK); [a] Data not available; Age was true at the time of primary surgery; OA, osteoarthritis; PTOA, post-traumatic osteoarthritis; [b] OA secondary to haemochromatosis; n, frequency; Mo, Months.

6.3 General Methods

Stage I investigation detailed in the ISO Standard for retrieval analysis (British Standard ISO 12891-2, 2014) suggests macroscopic observation should be the first step in the analysis of retrievals. Macro photography is effective at recording the damage modes visible to the naked eye. Photography is low cost, readily available in most laboratories and images can be captured rapidly with minimal post-processing (Grochowsky et al., 2006, Cottrell et al., 2007, Harman et al., 2007).

Photogrammetry is the use of images captured by photography to acquire measurements between objects, although as a science/art/technology, it is used more broadly in other academic fields such as meteorology and geology (Butterfield et al., 1970, Dolan et al., 1978). Using calibrated photographs to measure surface features is beneficial for explant analyses because the extent of damage modes, such as scratching, can be quantified and compared statistically.

Scaling features in an image is a basic principle of photogrammetry and was achieved for the tibial component fixation and bearing surfaces in this project. A standardised photographic method is required to ensure all measurements are comparable.

6.3.1 Component Holders

Several of the analyses within this chapter required individual components to be constrained in specific orientations for measurement. This was to ensure the techniques were consistent and reliable between components. Also, so that reference surfaces could be controlled and utilised where required.

Three stainless steel component holders with either silicon or polymer grips were designed and manufactured to support the three separate TAR components in a reproducible orientation. The design specification for these holders included the following aspects:

- Constrain components repeatably in an orientation that allows perpendicular measurements.
- Large enough to constrain the full range of component sizes. This was 45 mm by 45 mm.
- Allow the measurement of both sides of each component.
- Non-damaging and chemically inert to the components and measuring equipment. The clasps were not to interact with the bearing surfaces as these were considered the more important surfaces to conserve, although every effort was made to eliminate user damage.
- Suitable for sterilisation or cleaning (e.g. autoclave)
- Endure several years of use (i.e. more than 100 measurements).
- Be operable by one user.

All three component jigs constrained the components at their edges to allow unobstructed bearing and fixation surface measurements. These jigs were also able to be inverted to allow measurement of both superior and inferior surfaces, if required. Each of the jigs fit to custom made base-plates which allowed the jig to be repeatably positioned on the measurement equipment following jig removal and component exchange (Figure 6.1).
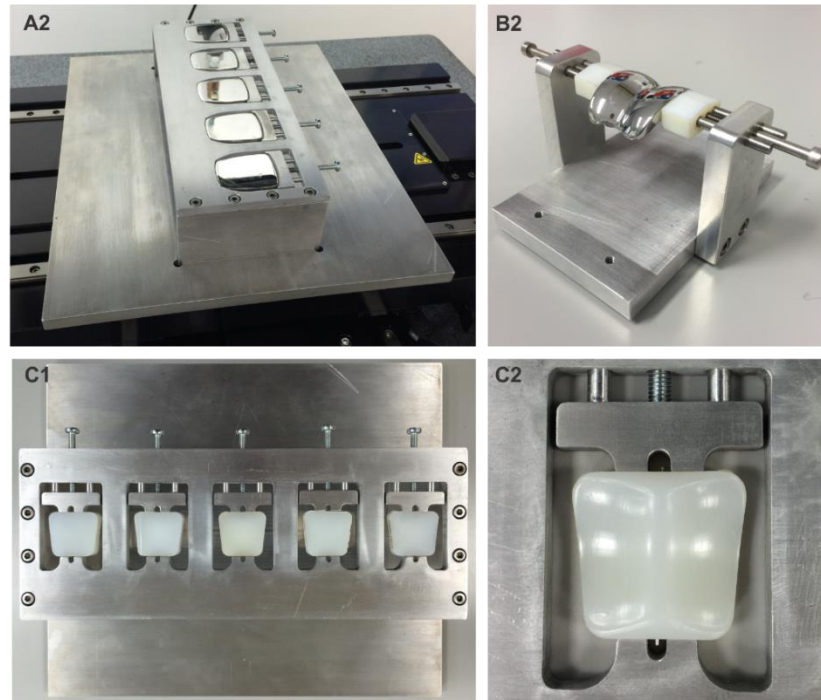
Figure 6.1. Manufactured component holders. A, Tibial component holder used to measure the tibial component bearing and fixation surfaces. B, Talar component holder used to photograph the bearing and fixation surfaces. C, Bearing insert holder used to analyse the bearing surfaces.

6.3.2 Sample Randomisation

Study cohorts composed of individual TAR devices (each with a unique identifying number) were assigned a randomly generated number in Microsoft Excel (Microsoft, US). The random numbers were then ordered smallest to largest, resulting in the associated component codes being randomised. This process of randomisation was conducted prior to the commencement of each study throughout thesis.

6.3.3 Photogrammetry Protocol

A Canon 700D SLR Camera with a 100 mm macro lens (Canon Ltd, UK) was used for all photogrammetry measurements (Figure 6.2). A vertical photography camera stand was used to hold the camera in a position perpendicular to the surface of interest. The base plate of the jig was secured to the camera stand and provided a secure plinth for the repeatable placement of the jig between measurements. The jig was slotted into the base plate, with the component constrained in position directly under the camera lens. The distance between the component and camera lens was 26 cm. A ring light was aligned halfway between the jig and camera, however its height was variable and moved to minimise the amount of light artefact on reflective surfaces. The camera and its settings were controlled through a computer to minimise vibrations and consequential image artefacts. A scale bar (10 mm) created using CorelDraw X8 version 18 (Corel

Corporation, CA) and printed in 1:1 scale was affixed to the component jig at the same distance from the lens as the surface of interest. The scale bar was used to calibrate the images in the post-processing software so that the regions of interest could be quantified.
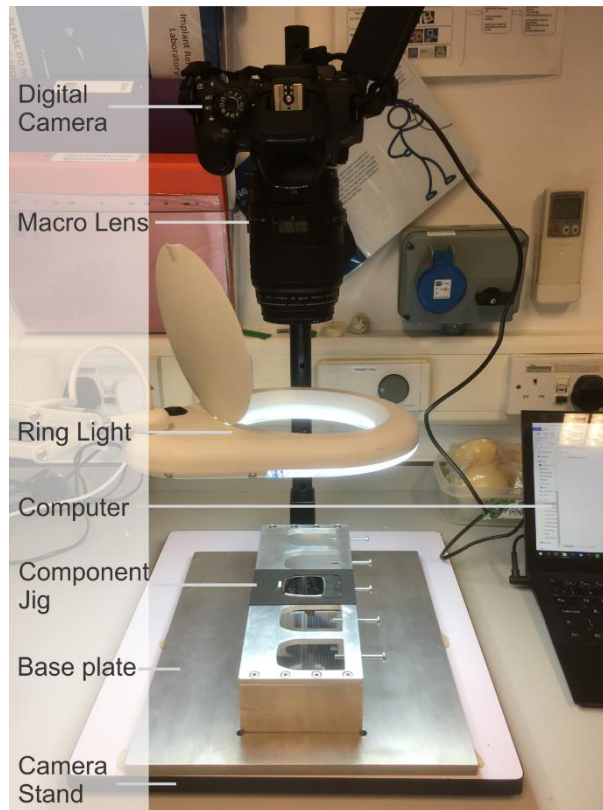
Figure 6.2. Setup for standardised photography. The camera was perpendicular to the component surface. A ring light was positioned in between the camera and component. The removable component holder was constrained by the baseplate to ensure repeatable photography.

The 'optimal' image quality was that which revealed the most amount of surface damage and minimised light artefact, both of which were identified visually. The subjective identification of damage is a limitation of commonly used damage mode analyses (Hood et al., 1983), however in-house experience and previously published pictographic atlases provided examples of established damage modes (Harman et al., 2011).

Two camera functions (exposure and depth of field) were varied to achieve the 'optimal' image for each surface type, which differed in surface composition and roughness. Exposure time is the length of time the camera sensor is exposed to light. The longer the exposure time, the brighter the image. Depth of field is determined by angle of view, object distance and the f-ratio. The standardised photography setup had a fixed angle of view and object distance, created by the camera stand and jig. The f-ratio is the ratio of camera focal length and the effective aperture, a parameter that is easily changed within the settings of the camera. Higher f-ratios lead to a greater depth of field. The following settings were used for each component surface:

a) Tibial Component Fixation Surface

Fixation surfaces are rough and composed of dull materials (e.g. hydroxyapatite and bone). High depth of field settings were used (f-ratio: 32) to ensure the voids in the fixation surface would be captured. The dull surface with deep voids was better illuminated using an exposure time of 0.6 seconds, which was relatively high compared to the polished tibial bearing surface.

b) Tibial Component Bearing Surface

Bearing surfaces are manufactured with a highly polished surface finish and therefore, when photographed, reflected the majority of the light, requiring a reduced exposure time of 0.008 seconds. The bearing surface was positioned perpendicular to the camera lens resulting in the camera being reflected in the surface. This artefact could be mitigated by selecting a lower f-ratio value of four (Figure 6.3).

No Ring Light   Ring Light - High F-ratio   Ring Light - Low F-ratio
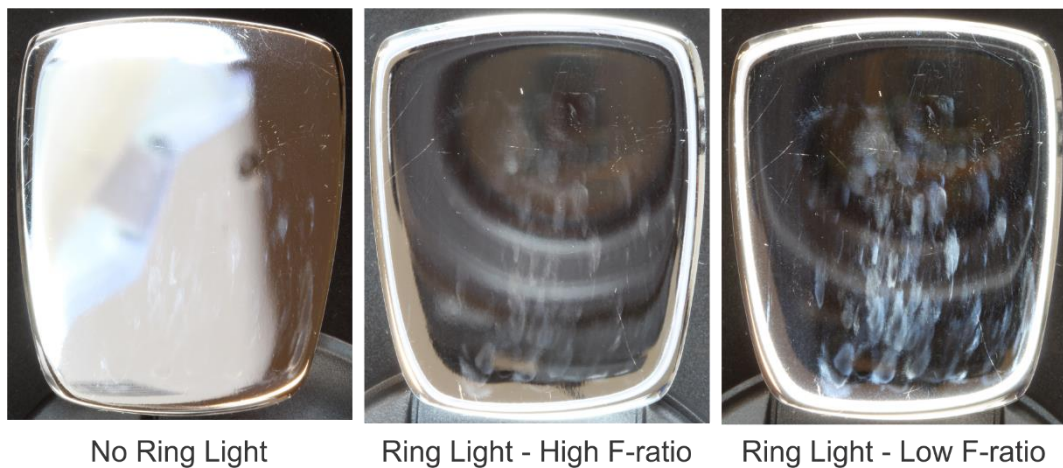
Figure 6.3. Examples of camera settings and the image output. The ring light improved visualisation of the bearing surface scratching. Low F-stop values reduced the depth of field, minimised reflections in the bearing surface and highlighted the scratching. Image post-processing reduced artefacts further.

c) Bearing Insert Surfaces

UHMWPE is challenging to photograph because it is monochromic, meaning its features cannot be distinguished by colour, unlike metallic surfaces. Also, changes in surface roughness between damage modes was not precisely detectable without the use of microscopy. This meant the photogrammetry protocol could not be used for the bearing insert surfaces. Individual damage modes on the bearing surface were photographed using an Olympus C-5050 digital camera attached to an Olympus SZ-ET Stereomicroscope (Olympus, Japan) with a Highlight 3001 ring light (Olympus, Japan). Photographs produced using this protocol were post-processed using the same processes as those produced using the photogrammetry protocol (see section 6.3.3).

d) Talar Component Surfaces

The curvature of the talar component fixation and bearing surfaces limited the analysis of the talar component to visual damage mode analysis. The greatest depth of field setting possible using the standardised photogrammetry protocol was not high enough to capture the entire surface in focus. Also, the excessive curvature also meant distance measures would not be accurately scaled due being at different heights relative to each other. The same photography/microscopy equipment used for the bearing insert was used for the talar component.

6.3.4 Image Post-processing

Photographs were processed using the open source image processing software ImageJ (Schindelin et al., 2012). For the tibial component, the outside edge was clearly identifiable, visually. All extraneous features captured in the background of each image were cropped until only the component remained. The damage features on the bearing surface, most notably scratching, could be visualised better in the images after converting the image to 16-bit grayscale and equalising the image brightness. Converting the image to grayscale reduced the file-size allowing for quicker processing and allowed the damage modes to be binarised later in the study, as the software used grayscale values to calculate binary values. The brightness values were spread evenly (equalised) across the brightness histogram. As long as the brightest and darkest pixels were comparable between components, the images would represent similar relative brightness values. For each component, the brightest values originated from the ring light and the darkest values originated from the dark background of the jig, which were kept consistent. The entire component area (i.e. sum of pixels within the constraints of the component edges) was calculated for each component and used as the total area value for relative (%) measurements of damage mode areas.

For the bearing insert and talar component, each image was converted to 16-bit grayscale and the brightness histogram equalised, as described above.

Damage modes specific to each component surface were identified using different protocols, analysed and discussed independently. Each of the following sections detail an analysis and discussion for each component surface.

6.4 Tibial Component Fixation Surface

The tibial component fixation surface was of specific interest for this chapter because of the speculation about wear at this surface in the published literature (Koivu et al., 2009, Besse, 2015, Cottrino et al., 2016).

6.4.1 Methods

As suggested in British Standard ISO 12891-2 (2014), a visual analysis of several fixation surface components was undertaken to identify the range of damage modes present on the target surface. Three important damage modes were identified and subsequently measured on the tibial component fixation surface: coating abrasion, coating delamination and substrate abrasion. The definitions of each damage mode were as follows:

a) Coating Abrasion

For devices with a dual-coating of hydroxyapatite and titanium, abrasion of the titanium formed a polished reflective surface classified as coating abrasion. For devices with a single layer of coating (e.g. titanium nitride, titanium alloy), areas of abraded coating resulting in polishing of the coating, but not substrate, were identified visually as coating abrasion. The first iteration of the AES TAR design featured a single layer of hydroxyapatite which was difficult to identify because it was absent in almost all cases, therefore this device type was excluded from the quantitative analysis.

b) Coating Delamination

The entire fixation surface captured by the camera was assumed to have once been coated with the material stipulated in the TAR design. Coating delamination was identified by the absence of coating revealing the substrate. Fixation coatings were generally >100 µm thick, therefore after delamination, a visible height change between the coating and the substrate was evident. The substrate material surface was also identifiable visually by its different colour and texture.

c) Substrate Abrasion

If coating delamination occurred, the exposed substrate may have undergone abrasion resulting in a scratched area within the bounds of the delamination area. In photographs, this damage mode appeared similar to coating abrasion but occurred exclusively where coating was absent. This area was measured independently from coating abrasion and delamination.

Two methods were used to extract abrasion (coating and substrate) and delamination damage modes. Coating delamination was selected manually using the hand-selection tools within the ImageJ software (Figure 6.4). After selecting the perimeter of the delamination, the total area of pixels within that area was measured.
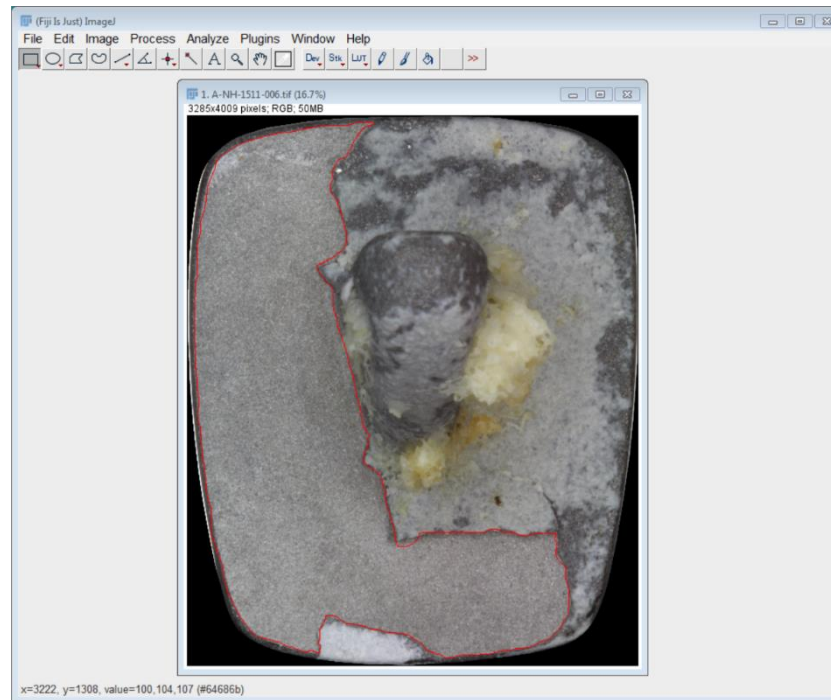
Figure 6.4. Manual selection of tibial component fixation surface coating delamination.

The manual selection of this damage mode may have been influenced by the operator, therefore a reliability analysis was undertaken (see section 6.4.1.1).

Unlike delamination, abrasion occurred in smaller patches of irregular shape which made it difficult to select manually. Using the relative brightness as a marker of abrasion, which was a consistent feature between photographs, allowed for this damage mode to be selected using an automated function. The auto-threshold function in ImageJ was used to select the brightest areas and operated using Equation 6.1.

Equation 6.1.
$$T = \frac{(B_a + R_a)}{2}$$

Where, T is the threshold, B_a is the average background grayscale value and R_a is the average region of interest grayscale value. The region of interest in this case was abrasion, but this applies to any foreground feature high in grayscale value and was used to identify bearing surface scratches (see section 6.5.1). Auto-threshold is an iterative algorithm that increases the threshold until the composite average between bisected histogram zones (i.e. region of interest and background) is greater than the threshold. In this analysis, the bright features (i.e. abrasion) were auto-selected against a back-drop of the relatively dark/rough manufactured substrate and fixation coating.

6.4.1.1 Reliability Analysis: Coating Delamination

The subjective selection of coating delamination area was tested for reliability.

Methods

Ten tibial components with evidence of fixation surface delamination were randomly selected using the method described in section 6.3.2. Images of the components' fixation surface were opened in ImageJ (Schindelin et al., 2012) and the area of delamination was manually selected by three observers. The three observers were familiar with orthopaedic devices but had not undertaken an analysis like this prior to this study. For the intra-rater analysis, one observer (the author) repeated the analysis three times on three different days.

Statistics

The mean area for delamination was compared between observers and between the results for the same observer who completed three trials. The maximum difference between observers for each image was calculated. Intraclass correlation coefficient (ICC) estimates and their 95% confidence intervals (CI) were determined using SPSS statistical package version 22 (IBM, Chicago, US). For inter-rater analyses, the ICC estimates were based on a mean-rating (k = 3), consistency, two-way random effects model. For intra-rater analyses, the ICC estimates were based on a mean-rating (k = 3), absolute, two-way mixed effects model. ICC estimates less than 0.5 indicated poor reliability, estimates between 0.5 and 0.75 indicated moderate reliability, estimates between 0.75 and 0.9 indicated good reliability and values above 0.9 were considered indicative of excellent reliability (Koo and Li, 2016). Systematic differences in intra- and inter-rater reliability were assessed using repeated measures ANOVAs. If the assumption of sphericity was violated, as indicated by Maulchy's test, then the Greenhouse-Geisser adjustment was used. The alpha value was 0.05 for all statistical comparisons.

Results

The ICC reliability between observers was: 0.999 (95% CI 0.999 to 0.999) for delamination area, which indicated excellent reliability (Figure 6.5). Tibial component fixation surface delamination areas were not significantly different between three observers (p = 0.105).

The ICC reliability for three tests by the same observer was: 0.999 (95% CI 0.999 to 0.999) for delamination area, which indicated excellent reliability. No significant differences were identified after three measurements from the same observer (p = 0.378).
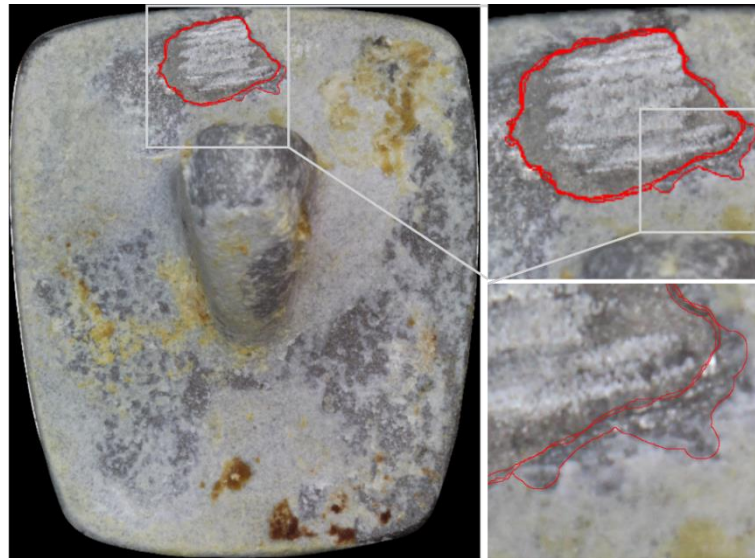
Figure 6.5. Fixation surface delamination measured by three observers. An example of area selection variation (red lines) is shown in the magnified regions; one line extends beyond the other lines.

Discussion

The manual selection of fixation surface delamination on the tibial fixation surface was highly reliable. Once delaminated, the relatively thick coating created a well-defined edge between the removed material and the material remaining which was simple to identify by the naked eye. The substrate surface (cobalt chromium alloy) below the fixation coating was a different colour and texture to the coating (titanium and hydroxyapatite), therefore identification of the substrate surface also aided determining delamination area. The high ICC estimates may also indicate the sample size was low or that the samples were heterogeneous. Despite this, the results of this reliability analysis suggest that for this cohort, manual measurement of the delamination surface was a repeatable method.

6.4.2 Statistics

The relative size (mean, standard deviation) and location of abrasion for the fixation surfaces of the tibial component were measured. Relative values were reported due to a range of tibial component sizes included in the analysis.

6.4.3 Results

Damage Type and Frequency

Only two of the retrieved TAR brands featured a dual titanium and hydroxyapatite coating, the AES (2nd Gen) and the Hintegra. Initial inspection of these devices indicated three important damage types present on the dual-coated fixation surfaces: 1) coating abrasion, 2) coating delamination and; 3) substrate abrasion (Figure 6.6).
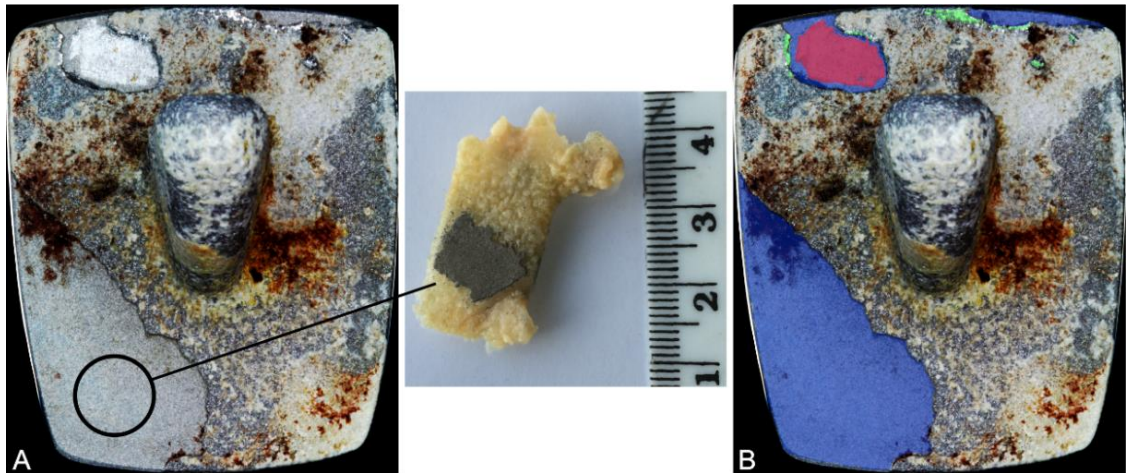
Figure 6.6. Tibial component fixation surface damage mode selection. A, Original post-processed photograph. B, Selected damage modes overlaid on the original image. Green denotes coating abrasion, blue denotes delamination and red denotes substrate abrasion. Retrieved bone sample with delaminated fixation surface attached (middle).

Of the 27 AES (2nd Gen) devices, 78% featured coating abrasion, 93% featured coating delamination and 89% featured substrate abrasion. Two AES (2nd Gen) devices showed no visible tibial component fixation surface damage. Of the three Hintegra devices, two featured all three of the damage modes and one featured coating delamination exclusively.

The Rebalance, Mobility, AES (1st Gen) and BP TARs all featured fixation surfaces that were difficult to analyse visually. Therefore, damage to these surfaces was not quantified using photogrammetry as the damage modes still required visual identification. The AES (1st Gen) TARs were coated with a single layer of hydroxyapatite which has a white appearance and had been removed or substantially diminished in all six devices. Abrasion of the fixation surface, which presented as areas of polished metallic worn areas, were evident for all of the Mobility, BP, AES (1st Gen) and Rebalance TARs except for one Rebalance TAR. In total, 39 of the 42 tibial components featured at least one of the defined fixation surface damage modes (Figure 6.7).
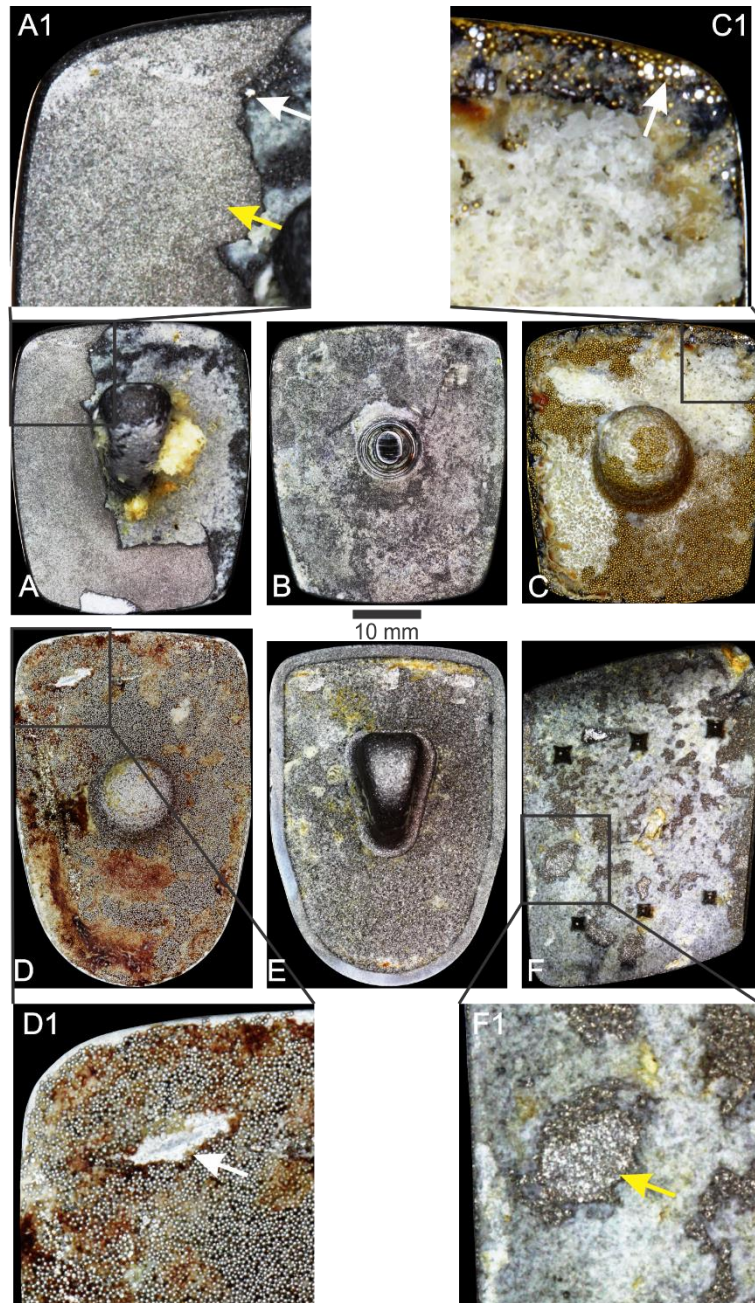
Figure 6.7. Examples of tibial component fixation surface damage from each brand. A, AES (2nd Gen). B, AES (1st Gen). C, BP. D, Mobility. E, Rebalance. F, Hintegra. Delamination (yellow arrows) and coating abrasion (white arrows) is shown.

Damage Extent

The AES (2nd Gen; n=27) tibial components showed 0.3% (± 0.4% SD) coating abrasion, 8.9% (± 11.3% SD) coating delamination and 1.7% (± 2.2% SD) substrate abrasion (Table 6.2). Coating delamination affected the greatest fixation surface area with a range between 0.2% and 43.9%. Seven AES (2nd Gen) tibial components presented with more than 10% of the total fixation surface coating delaminated. Substrate abrasion was the next most prevalent damage mode and affected less than 10% of the total fixation surface (range: 0.2% to 9.1%). Coating abrasion accounted for between 0.03% and 1.54% of the total fixation surface.

Table 6.2. Damage type and area for the AES (2nd Gen) and Hintegra TARs.

	AES (2nd gen) (n = 27)		Hintegra (n = 3)	
Damage Type	n	% Area	n	% Area
Coating Abrasion	21	0.27% (± 0.35%)	2	0.05% (± 0.05%)
Coating Delamination	25	8.87% (± 11.32%)	3	2.56% (± 0.55%)
Substrate Abrasion	24	1.71% (± 2.15%)	2	1.04% (± 0.94%)

Notes: Parentheses denote standard deviation. AES, Ankle Evolutive System.

The Hintegra devices (n = 3) all featured tibial fixation surface damage with 0.1% (± 0.1% SD) coating abrasion, 2.6% (± 0.6% SD) coating delamination and 1.0% (± 0.9% SD) substrate abrasion (Table 6.2). In total, the damage extent was less for the Hintegra devices than for the AES (2nd Gen). Delamination was the most extensive damage mode for the Hintegra devices with a range between 2.1% and 3.2% of the total fixation surface.

Damage Location

The three damage modes presented predominantly at the anterior of the AES (2nd Gen) tibial components (Figure 6.8). Of the AES (2nd Gen) tibial components with coating abrasion or delamination, the antero-medial corner was consistently affected. For all of the damage modes, the anterior was affected in more than 20 devices whereas the centre and posterior regions were affected in less than seven devices.

Coating delamination occurred on the medial side more frequently than the lateral side. The same trend was shown for substrate abrasion, whereas coating abrasion was almost symmetrical between sides. There were no observable patterns in damage location for the other TAR brands given their respective low sample sizes.
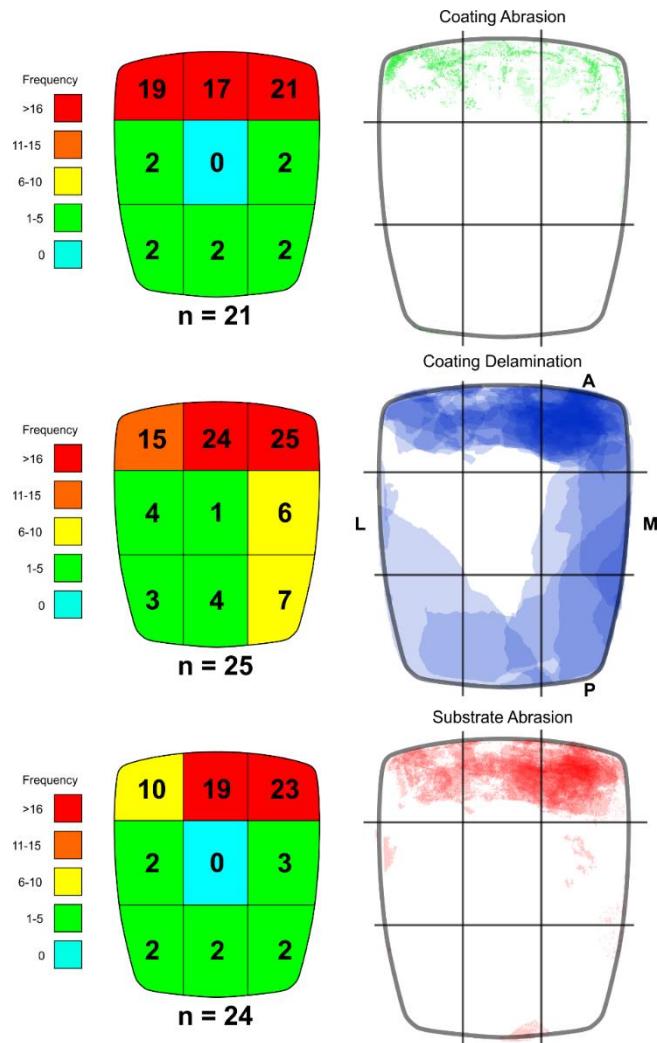
Figure 6.8. Frequency and location of damage to tibial component fixation surfaces. The dual-layered coating of the Ankle Evolutive System total ankle replacement underwent: 1) Superficial abrasion of the hydroxyapatite and titanium coating (coating abrasion); 2) Coating delamination which resulted in the loss of the titanium coating, and; 3) Substrate abrasion which was abrasion of the cobalt chromium substrate. A, Anterior; P, Posterior; M, Medial; L, Lateral. n, Number of explants.

6.4.4 Discussion

Damage to the tibial component fixation surface was evident for 93% of the retrieved TARs. Two of the retrieved TAR brands featured a dual-coating of titanium and hydroxyapatite, the AES (n = 27) and Hintegra (n = 3). Three important damage modes were common for these devices: 1) Coating abrasion, 2) Coating delamination, and; 3) Substrate abrasion. For the substrate to wear, both of the dual-coating layers were assumed to have also worn. Therefore, substrate abrasion was considered the most severe and occurred in 89% of TARs. Coating delamination was the most frequent damage mode and featured the largest area with up to 44% or 560 mm^2 of the coating surface removed. This equates to 56 mm^3 of potential wear debris entering the joint space if the coating thickness was assumed to be 0.1 mm thick. Using the same

calculation, the mean delamination area value represents an average potential wear volume of 11 mm^3, which is likely to be an important contribution to the total wear particle burden within the joint space. While these values are only estimates, they are likely to be underestimated as the additional volume of the substrate wear was not included in the calculation. Wear debris associated with the fixation surfaces of TAR (Ti, CoCr and HA) have previously been identified embedded in the bearing insert (Affatato et al., 2009, Vaupel et al., 2009, Cottrino et al., 2016) and/or within periprosthetic tissue samples (van Wijngaarden et al., 2015). Specific concerns for the integrity of the AES TAR fixation surface were raised in 2009 (Besse et al., 2009, Koivu et al., 2009) and the AES TAR was withdrawn from market in 2012 due to the early development of osteolysis. Excessive shear stresses at the bone-implant interface was suspected to cause the degradation of the fixation surface for the AES TAR (Koivu et al., 2009, Dalat et al., 2013, Besse, 2015). Cottrino et al. (2016) produced the first retrieval analysis of the AES TAR and identified titanium and CoCr particles embedded within the six AES bearing inserts analysed. However despite analysing each explant surface, wear of the fixation surface was not described specifically. To the author's knowledge, the current study is the first direct evidence of wear and delamination of the tibial fixation surface.

The possible causes for the three damage modes include: micromotion at the bone-implant interface, iatrogenic damage caused during implantation or removal of the component and insufficient adhesive properties between the coating and substrate. Micromotion at the bone-implant interface can only occur in locations where bone interfaces with the fixation surface. According to the medical imaging (see section 5.5.2.2), the under-hang of the tibia was typically located at antero-lateral and postero-lateral locations on the tibial component. The damage modes appeared to coincide with the antero-lateral under-hang of the tibial cortex but not the postero-lateral location. If the damage modes are related to tibial cortex under-hang, it seems under-hang, in and of itself, is not sufficient to cause fixation surface damage. The anterior approach used for stemmed device designs requires a cortical window to be cut into the tibia for the tibial component to be positioned. Intrinsic to BP-style stemmed design is the wedging of bone back into the cortical window to create a 'press fit' fixation (Buechel and Pappas, 2003, Asencio and Leonardi, 2005). However, this approach may not only create the risk of damaging the fixation surface when replacing the bone block. But also, if the bone block is not congruent with the tibial surface (i.e. proud or recessed), a situation arises where the edges of the bone may damage the fixation surface. This mode of failure is discussed in more detail in Chapter 10 (see section 10.3.3). The BP and Mobility TARs presented with areas of coating abrasion in a similar location. Upon retrieving the component, damage towards the anterior of the device could be created by the osteotome or surgical tool used to remove it. However, if true, this is a substantial amount of damage caused

by removing the devices, especially considering the fact the massive size of the osteolysis surrounding these devices would likely make removing them relatively simple. Finally, Cottrino et al. (2016) suggested manufacturing inconsistencies, in combination with the conditions of the ankle, may cause the fixation surface to delaminate. This damage mode analysis cannot infer the quality or repeatability of TAR component manufacture.

6.4.4.1   Limitations

Pixel brightness was the only variable able to be distinguished using an automated threshold function. Abrasion created areas reflective to light and could be visually identified, therefore the use of the auto threshold function was restricted to identifying abrasion. It is plausible that other damage modes were included within these measurements but were not distinguished visually. Damage modes identified using colour, rather than pixel brightness, such as delamination, were required to be selected manually using software draw tools. The reliability of manual measurements was tested using inter- and intra-rater analyses and found to be acceptable. Neither the bearing insert nor talar component could be processed using photogrammetry because these components feature small radii curvatures. These curvatures create surfaces with depths of field too great to capture with a standard camera. Also, UHMWPE is particularly difficult to photograph as the material properties create a near-featureless image. Changing the lighting conditions is a good way of identifying damage modes on UHMWPE, but this undermines the standardised protocol required for photogrammetry.

6.5   Tibial Component Bearing Surface

The wear and delamination of the tibial fixation surface likely resulted in the substantial production of third-body wear debris. The flat tibial component bearing surface was observed for damage using a similar photogrammetry protocol to that used to analyse the tibial component fixation surface.

6.5.1   Methods

Tibial component bearing surfaces were visually inspected and the damage modes identified, as suggested according to British Standard ISO 12891-2 (2014). Where scratching was evident, it appeared as multi-directional grooved lines that had a bright appearance on photographs. The region of the bearing surface absent of scratching appeared dark in the photographs. Three areas of interest associated with scratching were identified and measured on the tibial bearing surface (Figure 6.9):
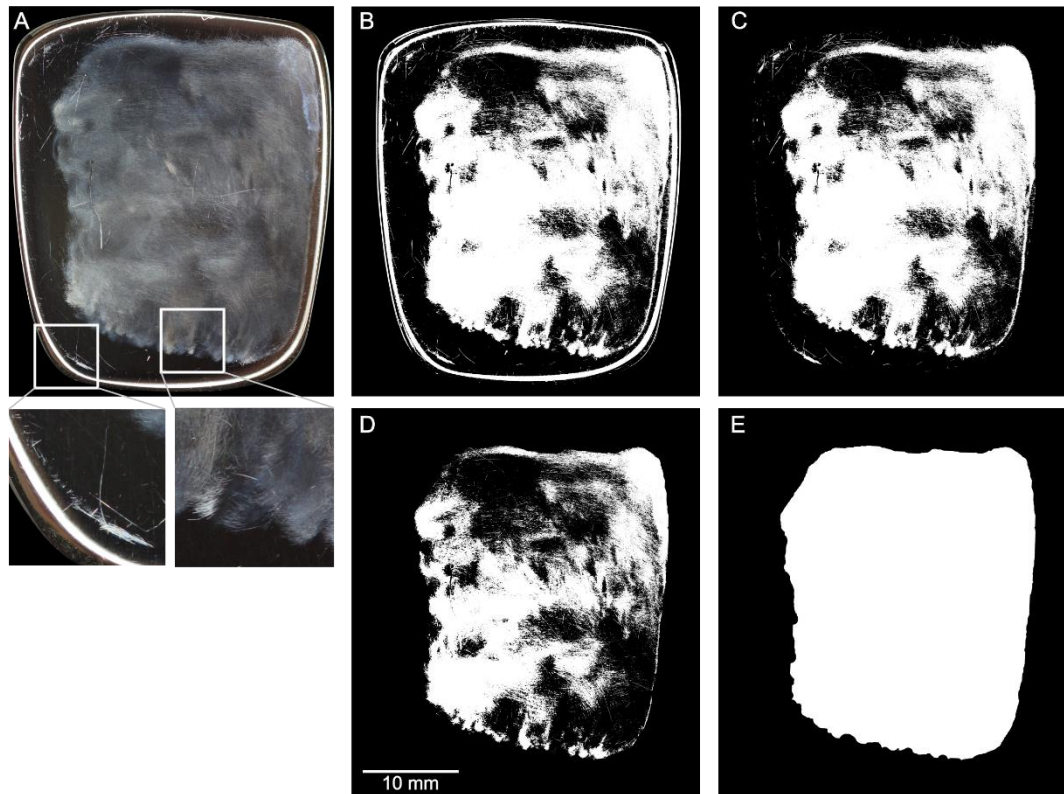
Figure 6.9. Binarisation of tibial component bearing surface scratching. A, Example of tibial component bearing surface image and scratching. B, Binarised original image with light artefact. C, Total scratch area which was the binarised original image without light artefact (7% crop). D, Marked scratch area was scratches within the 'discolouration area'. E, Discolouration area.

a) Total Scratch Area

The total scratch area was the sum of all pixels identified visually as scratching. Scratching appeared bright relative to a dark un-scratched surface. The auto threshold function on ImageJ (see section 6.4.1) was used to capture the areas of scratching. However, the geometry and reflectiveness of the tibial bearing surface created image artefacts at the periphery of the component in the form of a 'halo' of light. This artefact was a reflection of the ring light and was consistent between components. To remove this artefact, the image was eroded/cropped by 7% from the edge of the component towards the centre (Figure 6.10). The 7% value was determined by performing a parametric analysis using a range of cropping values (1% to 20%). The optimum amount of artefact excluded was determined visually and quantitatively (Figure 6.10). For example, '1%' represented the outside perimeter of the bearing surface downsized proportionally by 1%. The area of the bearing surface outside of the downsized perimeter was cropped. Downsizing the perimeter by 7% was shown to effectively eliminate extraneous light artefact at the edge of the components for the majority of photographs (Figure 6.10). The total scratch area minus the artefact was measured for each component.
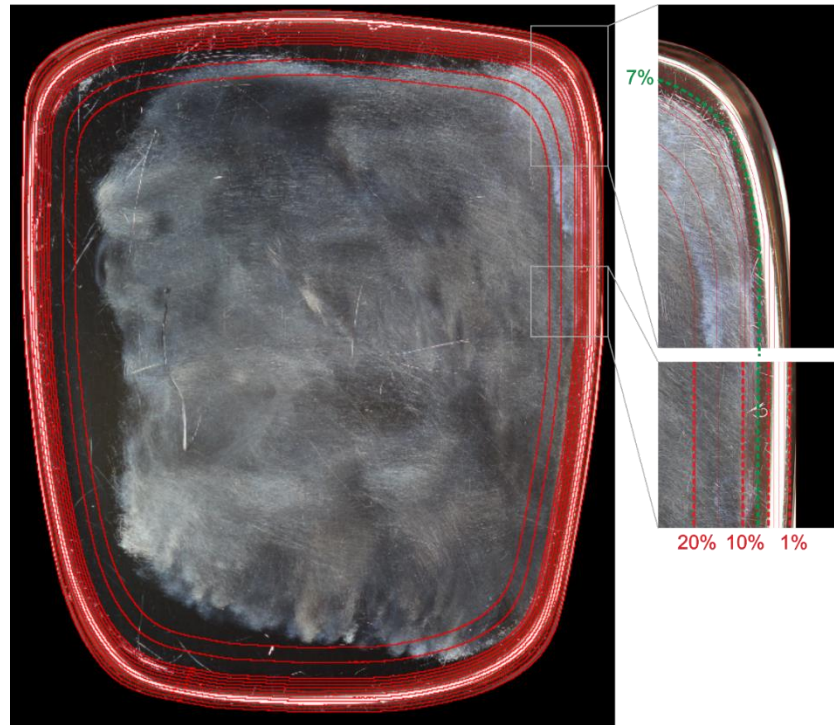
Figure 6.10. Parametric analysis to remove light artefact from the tibial component bearing surface. Each red line represents a scaled down perimeter of the total surface area.

b) Discolouration Area

The initial visual inspection identified densely packed scratching often within a well demarcated area on each tibial component bearing surface. This area could be distinguished visually for most components and was defined as the wear patch or discolouration area. This zone included areas of scratching and regions absent of scratching however, the boundary of this zone was able to be determined visually by a change colour, often created by scratching. This area was selected manually using the hand-selection tools provided by the ImageJ software and measured.

The manual selection of this zone may have been influenced by the operator, therefore a reliability analysis was undertaken (see section 6.5.1.1).

c) Marked Scratch Area.

After applying the auto-threshold function to the total surface, scratching within the 'discolouration area' was isolated by cropping everything outside of that area from the image. The isolated scratching within the discolouration area was identified as the marked scratch area, the pixels within which were summated to calculate the scratch area.

The area of each damage mode/region of interest was converted into relative (%) areas of the total component surface area.

6.5.1.1   Reliability Analysis: Discolouration Area

The subjective selection of the discolouration area was tested for reliability and repeatability.

Methods

The same explants, experimental approach, observers and statistics were used for identifying the discolouration area as the selection of coating delamination (see section 6.4.1.1). The area of discolouration was selected as defined in section 6.5.1.

Statistics

The statistical tests used to analyse the inter- and intra-rater reliability of segmentation were the same as those detailed in section 6.4.1.1. In brief, intraclass correlation coefficient (ICC) estimates and their 95% confidence intervals were determined. For inter-rater analyses, the ICC estimates were based on a mean-rating (k = 3), consistency, two-way random effects model. For intra-rater analyses, the ICC estimates were based on a mean-rating (k = 3), absolute, two-way mixed effects model. Systematic differences between observers or between the three tests of the same observer were calculated using repeated measures ANOVAs. The alpha value was 0.05 for all statistical comparisons.

Results

The ICC reliability between observers was: 0.998 (95% CI 0.995 to 0.999) for discolouration area, which indicated excellent reliability (Figure 6.11A). Tibial component bearing insert contact areas were not significantly different between three observers (p = 0.053). While not statistically different on average, the scratch areas for several devices were less clearly demarcated than other devices which led to a high variance of selection area for these devices (Figure 6.11B).

The ICC reliability for three tests by the same observer was: 0.999 (95% CI 0.998 to 0.999) for discolouration area, which indicated excellent reliability. No significant differences were measured after three measurements from the same observer (p = 0.223).
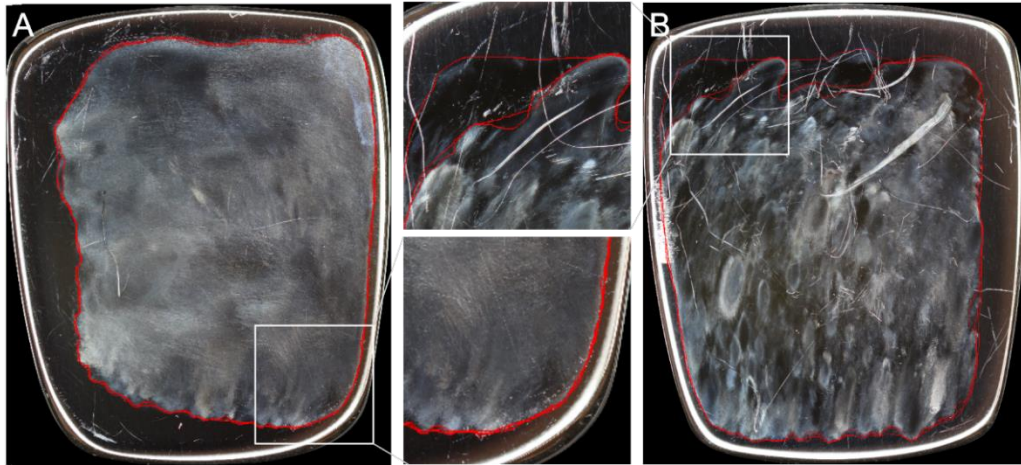
Figure 6.11. Examples of discolouration area being manually selected. Example A shows good agreement between all three observers whereas example B featured areas that were inconsistently selected between the observers.

Discussion

Similarly to the manual selection of fixation surface delamination, manually identifying the discolouration area on the tibial component bearing surface was highly reliable. The presence of dense micro-scratching in the majority of bearing surfaces created a well demarcated region which was repeatably outlined by the observers.

The high ICC estimates may indicate, similarly to fixation surface delamination, that the samples were heterogeneous and that using the numerical total area as a measure of agreement may not indicate how similarly the observer traces were spatially. However, overlaying the traces from each observer and each trial for the same observer showed a high repeatability (Figure 6.11), which was reflected in the results of this reliability study.

6.5.2 Statistics

Bearing surface abrasion was measured relative to the total area of the bearing surface. The size of the 'bearing insert movement area' was measured relative to the total area of the bearing surface. The location of bearing insert movement area was determined in absolute terms (millimetres) relative to the centre of the tibial component bearing surface in both antero-posterior and medio-lateral planes. Pearson's correlation coefficient (r) was used to test the association between the locations of the bearing inserts from the segmented CT scans from Chapter 5 and the locations of the bearing inserts determined from the bearing surface abrasion analysis. Bearing insert scratch areas were stratified into two groups, '>2 mm' and '≤ 2 mm' from the centre of the tibial component in both antero-posterior and medio-lateral planes. An independent t-test was used to compare the two scratching area location groups for size of scratch area. An alpha value of 0.05 was used for all statistical analyses in this chapter.

6.5.3 Results

Damage Type and Frequency

Wear of the bearing surface was evident for all 42 tibial components. Four damage modes were identified on the tibial bearing surface:

I.   **Discolouration.**

Forty-one devices showed a defined region of discolouration on the tibial bearing surface. The region of discolouration was formed by a combination of the following three damage modes (deep gouges, micro-scratching, gross material loss) and/or a texture change indicative of adhesive UHMWPE wear. This phenomena created a well demarcated region of discolouration on the bearing surface, often with a similar geometry to the bearing insert (Figure 6.12).
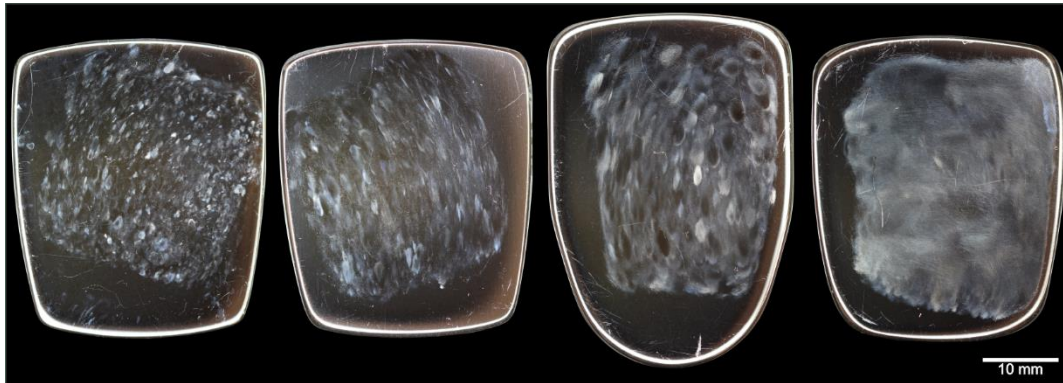
Figure 6.12. Examples of tibial component bearing surface damage.

The two AES (2nd Gen) devices featured discolouration and an irregular pattern consistent with a change in surface texture, possibly caused by adhesive UHMWPE wear (Figure 6.13). The titanium nitride coated BP TAR featured a dulled region in the surface coating which was consistent with wear. Defined discoloured regions with or without scratching were defined as the 'Discolouration area'.
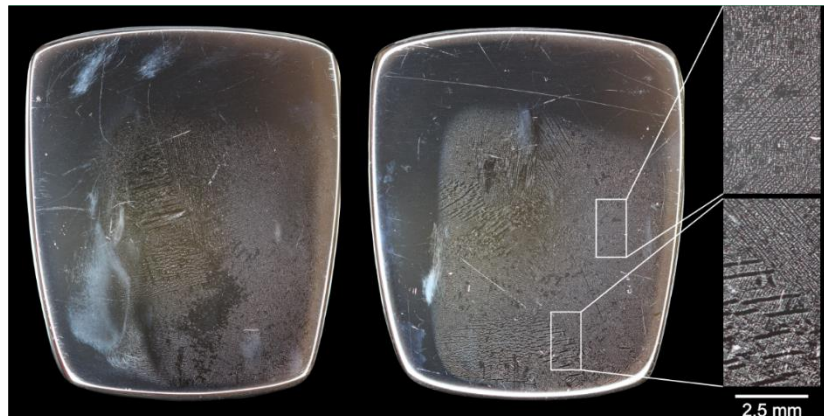
Figure 6.13. Examples of discolouration without marked scratches.

One device showed no observable discolouration area (i.e. no discolouration). This TAR was a Hintegra which had been in-vivo for 36 months and revised because of pain (Figure 6.14).

Figure 6.14. Two tibial components from Hintegra TARs, one with a demarcated scratch area (left) and one without (right).

II.   Micro-scratches.

Thirty-nine tibial component bearing surfaces featured dense areas of micro-scratches, often grouped within a specific region on the bearing surface (Figure 6.15). The discolouration area exclusively featured the dense areas of micro-scratches. The micro-scratches were often extensive enough to cover the entire discolouration area and formed a similar shape to the geometry of the bearing insert. However, micro-scratches also presented as small circular areas, only a couple of millimetres in diameter. Three devices were absent of micro-scratches, one Hintegra (Figure 6.14), one AES (2nd Gen) and one BP TAR.
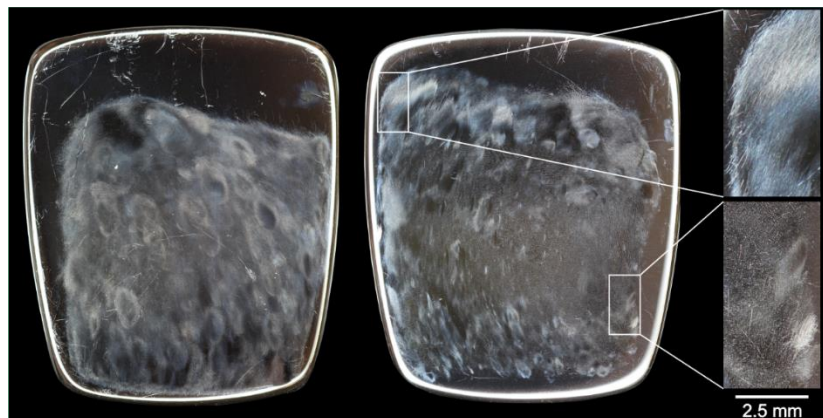
Figure 6.15. Examples of tibial components with areas of well-demarcated scratches.

III.   Deep gouges.

All of the tibial components featured deep gouges in the bearing surface. These scratches appeared to be randomly distributed across the surface and ranged in size

between a couple of millimetres in length and the full length of the component (approx. 3.5 cm) (Figure 6.16).
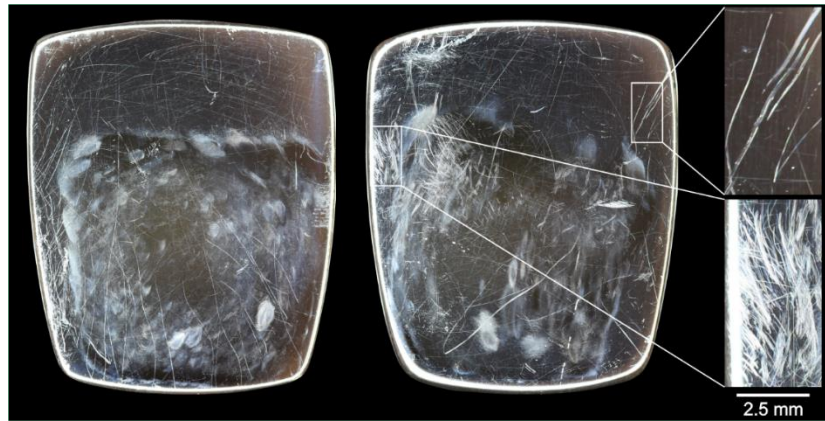
Figure 6.16. Examples of deep gouging on the tibial component bearing surface.

Eight tibial components (19%) featured distinct uni-directional medio-lateral scratches which were consistently located at the medial or lateral edge of the component (Figure 6.17). The scratch pattern was regular which may indicate iatrogenic damage.
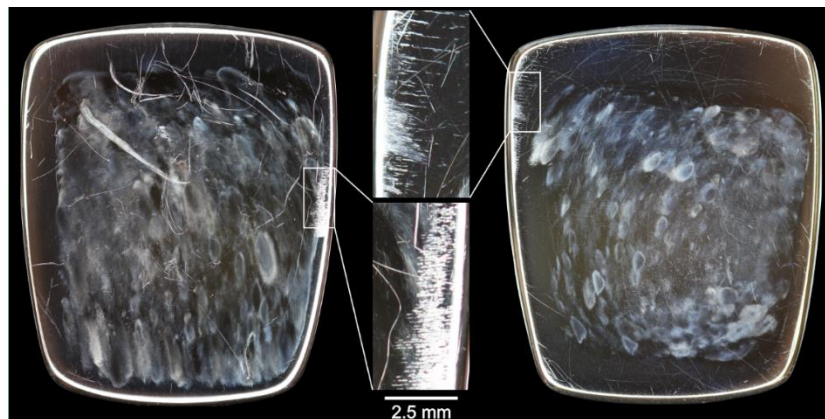
Figure 6.17. Examples of distinct uni-directional scratches in the medio-lateral direction, the origin of which may be iatrogenic.

IV.   Substantial localised material loss

Three devices (Two BP TARs and one AES 2nd Gen) showed substantial localised material loss to the bearing surface which was consistent with metal-on-metal wear and matched with damage (i.e. material loss, cracks) on the edge of the metallic talar component (see section 6.7.3).
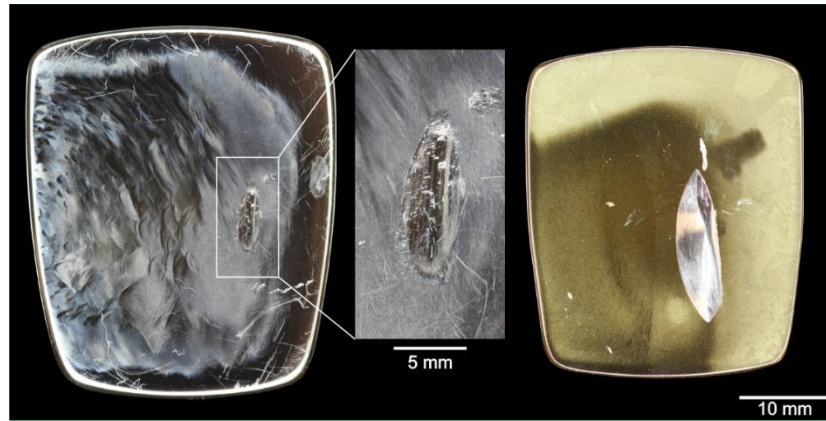
Figure 6.18. Examples of substantial bearing insert wear possibly caused by contact between the metallic tibial and talar components.

Damage Extent

The mean discolouration area was 59.7% (± 11.9% SD; range: 0 to 77.6%). Total scratch area was the total area of micro-scratching and deep gouging, combined (Figure 6.19). The mean total scratch area was 35.3% (± 9.8% SD; range: 0 to 51.2%). Micro-scratching occurred within the discolouration area and composed the majority of bearing surface scratches (27.8 ± 8.5% SD; range: 0% to 47.8%). Whereas, 7.5% (± 4.0% SD; range: 0 to 15.4%) of the total scratch area was outside of the discolouration area and was representative of the quantity of deep gouging.
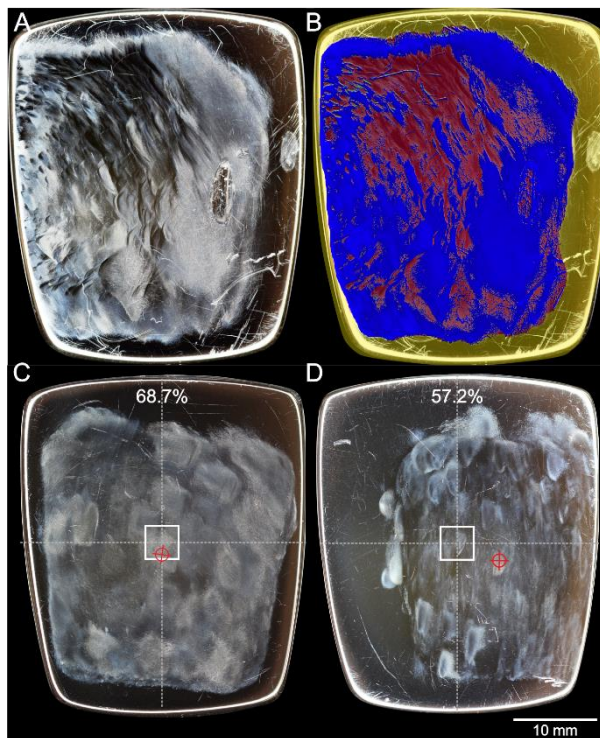
Figure 6.19. Examples of bearing different bearing scratch areas and offsets. A, original image. B, Thresholded regions indicate different damage modes including micro-scratching (blue) and discolouration area (red and blue). C, Example of centred discolouration area (± 2 mm). D, Example of offset discolouration area (>2 mm). Percentage values identify the discolouration area relative to the total area (yellow).

Damage Location

The centre of the discolouration area was offset posteriorly by -0.7 mm (± 2.7 mm SD; range: -5.5 to 3.7 mm; negative is posterior) in the AP plane and laterally by -0.1 mm (± 2.1 mm SD; range: -6.0 to 4.3 mm; negative is lateral) (Figure 6.19).

Fifteen components featured a discolouration area centred within 2 mm from the centre of the tibial component. Whereas, 26 components (63.4%) showed a Discolouration area outside of 2 mm from the centre of the tibial component. For the components with discolouration areas centred within 2 mm from tibial component centre, the total zonal area was significantly greater (67.2 ± 5.7% SD) than components with Discolouration areas more than 2 mm from the tibial component centre (57.7 ± 5.9% SD; $p < 0.05$) (Figure 6.20).
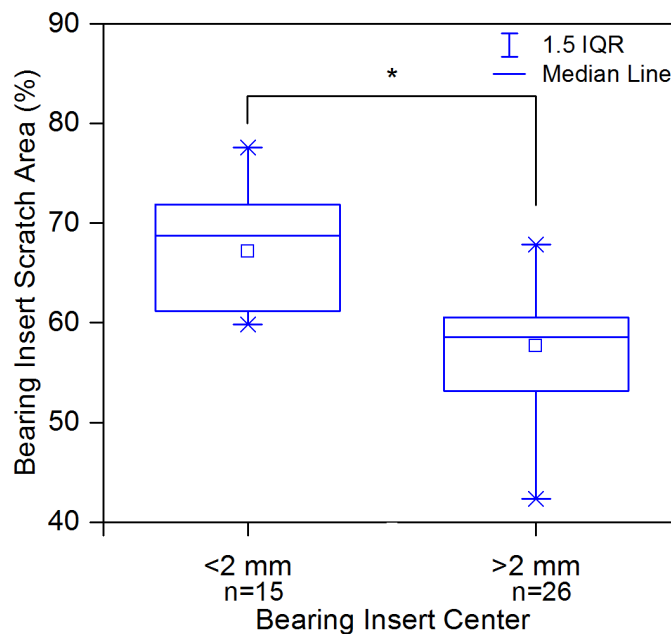
Figure 6.20. Percentage scratch area between two groups of different tibial component scratch patterns. Scratch areas with the centre of the scratches within 2 mm of the centre of the tibial component were compared with scratch patterns with a centre more than 2 mm from the centre of the tibial component. * Independent t-test ($p < 0.05$).

The location of bearing inserts relative to the tibial component was determined for 21 components using computed tomography imaging (see section 5.5.2.2). The centre of the discolouration area was moderately correlated with the bearing insert location the medio-lateral plane (r = 0.59) and antero-posterior plane (r = 0.36) (Figure 6.21).
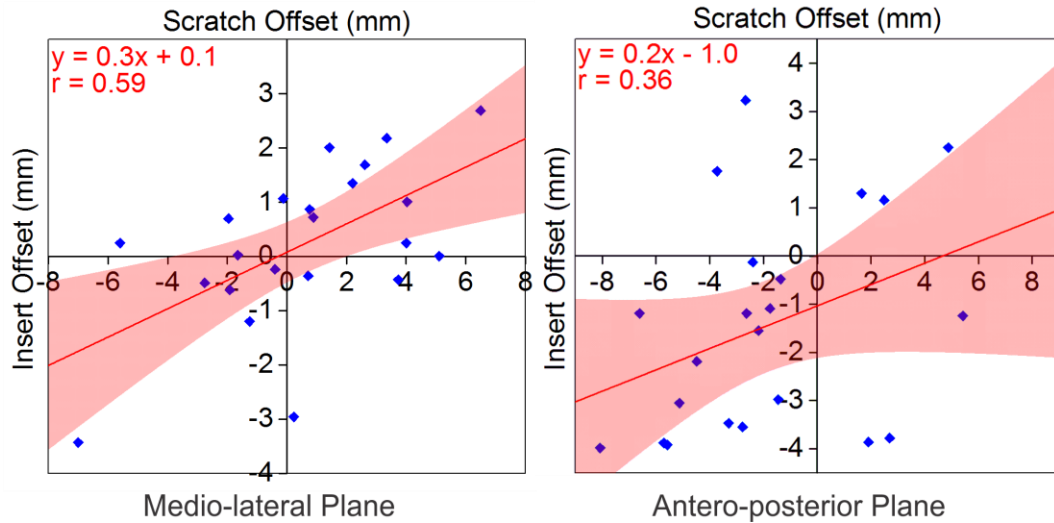
Figure 6.21. Association between bearing insert location identified using segmented CT scans and the centre of the bearing insert contact area. The bearing insert contact area was defined as a well demarcated area of scratching indicative of bearing insert articulation. Left, Medio-lateral plane (negative denotes lateral). Right, Antero-posterior plane (negative denotes posterior). r, Pearson's correlation coefficient.

6.5.4 Discussion

Discolouration of the bearing surface was evident across the cohort which was primarily composed of micro-scratches and to a lesser extent, deep gouges. For 41 of the 42 tibial components, the area of discolouration: covered up to 77.6% of the tibial bearing surface, was well-demarcated, and; formed in a similar geometry to that of the bearing insert. The mean total scratch area, which was all of the micro-scratching and deep gouging combined was 35.3% or 4.5 cm^2 of the total surface. If the scratch depth was assumed to be 2 µm deep, on average (Fisher et al., 1995), and wear was assumed to have been released evenly, approximately 0.9 mm^3 of cobalt chromium alloy may have been released. This is equivalent to more three times the steady state annual wear rate of well-aligned metal-on-metal THRs (Angadji et al., 2009). This additional wear volume will contribute to the total wear particle burden within the ankle joint.

Micro-scratching likely originated from third-body wear debris, given the articulating UHMWPE bearing insert does not have the hardness to scratch the metallic bearing surface by itself. Cottrino et al. (2016) described "significant signs of wear" and a change in tibial bearing surface flatness due to friction yet no photographs, profilometry or description of wear was provided. Third-body debris originating at the fixation surface likely contributed to the bearing surface abrasion, particularly as the fixation surface in this cohort was heavily worn (see section 6.4.3). Abrasion at the bone-implant interface was previously attributed to third-body wear at the tibial bearing surface (Cottrino et al., 2016). Alternatively, high contact stresses could have caused substrate fatigue and the release of carbides or impurities from the tibial bearing surface (Cottrino et al., 2016).

Roughening of the tibial bearing surface may also have increased the production of UHMWPE wear debris in this cohort, as seen in other total joint replacements (Fisher et al., 1995).

The centre of the area of discolouration was >2 mm from the centre of the tibial component for 26 TARs. For these devices, the area of discolouration was significantly smaller than those with an area of discolouration ≤ 2 mm from the centre of the tibial component. Assuming the area of discolouration represents the area of articulation between the tibial component and the bearing insert, less articulation may have occurred between the bearing insert and tibial component for devices with discolouration >2 mm from the centre of the tibial component.

The centre of the area of discolouration was moderately correlated with the bearing insert location identified in the medical imaging (see section 5.5.2.2) and was stronger in the medio-lateral direction (r = 0.59) than the antero-posterior direction (r = 0.36). The variance in correlation between the two planes of motion may be due to the variance of range of motion between the two planes. Translation of the bearing insert for mobile bearing TAR is thought to be between 1 mm and 6 mm, on average, in the antero-posterior direction (Watanabe et al., 2009, Lundeen et al., 2016). Whereas, in the medio-lateral direction, translation was measured in a cadaveric model under physiological loads to be less than 1.5 mm (Watanabe et al., 2009). Internal/external rotation for mobile bearing TAR is between 6° and 10.6°, on average (Watanabe et al., 2009, Lundeen et al., 2016). The tibial component surface is longer than it is wide, therefore if the component rotates in addition to translating, there is more space lengthways for damage to occur. Also, using weight bearing CT imaging rather than the non-weight bearing CT used may have increased the accuracy of determining insert location relative to the damage.

Deep gouges on the bearing surface were identified across the entire bearing surface in several cases and appeared not to form a specific pattern of wear, unlike the areas of micro-scratches. While third-body debris trapped between the articulating surfaces is likely to have caused the micro-scratches within the bounds of the discoloured region, this hypothesis is insufficient to describe the deep gouges that extended across the entire bearing surface. The medical imaging analysis in Chapter 5 identified hard tissue growth within the joint space, often proximate to the bearing insert. Contact between the bone and tibial bearing surface may have created these deep gouges, however the mapping of bone ingrowth at the point of revision surgery would be required to validate this observation. Iatrogenic damage during the removal of the tibial components may also have contributed to this type of damage. This cause is unlikely to explain deep gouges

towards the posterior of the device because for these TAR designs, an anterior approach was used for the revision procedure.

Gross localised material loss from the tibial bearing surface was identified for three TAR devices (Two BP and one AES). For these devices, the edge of the talar component had contacted the tibial bearing surface causing catastrophic wear. The bearing insert had either subluxed or dislocated and the talar component rotated in the coronal plane to a high varus or valgus angle. Gross material loss at the tibial bearing surface increased the risk of pathologies associated with high metal content within the joint space, such as metallosis, however to the author's knowledge, no such cases have been reported in the literature.

6.5.4.1   Limitations

The same limitations of photogrammetry affected bearing insert measurements as well as damage to the fixation surface. As with fixation surface measurements, selection bias was accounted for by undertaking inter- and intra-rater analyses, the results of which were considered acceptable. The ring light created an artefact which could not be excluded using the auto thresholding function. The lighting conditions were standardised allowing the artefact to be repeatably excluded using the data cropping method detailed within this section. The specific causes of the damage identified in this section were difficult to deduce because the research was conducted independent of the hospital site from where the devices were retrieved. Identifying the possible causes of the damage at the time of revision would be desirable in future studies.

6.6   Bearing Insert Surfaces

Superior (flat) Insert Surface

The high prevalence of edge-loading and impingement identified in the medical imaging (Chapters 4 and 5) suggested substantial geometrical changes were likely to have occurred to the superior bearing insert surface. A separate investigation into the deformation and damage identified on the superior bearing insert surface was undertaken in the following chapter (Chapter 7).

Inferior (curved) Insert Surface

Damage modes present on the inferior bearing insert surface were identified using established semi-quantitative methods (Wasielewski et al., 1994). The steep curvature of the inferior surface made using quantitative analyses (e.g. photogrammetry, non-contacting surface profilometry) a challenge. Also, investigating the full range of damage modes was desirable given the scarcity of published TAR retrieval analyses.

6.6.1 Method Development: Damage Mode Scoring

Structured semi-quantitative damage scoring methods have not previously been applied to TAR. The original scoring methods were designed around total knee replacement bearing inserts (Hood et al., 1983), however different measurement zones were applied between research groups and may affect the quality of comparison (Wasielewski et al., 1994, Brandt et al., 2012) (Figure 6.22). The total damage score is calculated by summating each measurement zone with equal weighting, despite large disparities in area between each measurement zone. To authors knowledge, this is the first study to score damage modes for TAR, therefore a development study was undertaken to determine a practical method of assessing damage scores for the inferior bearing insert surface.
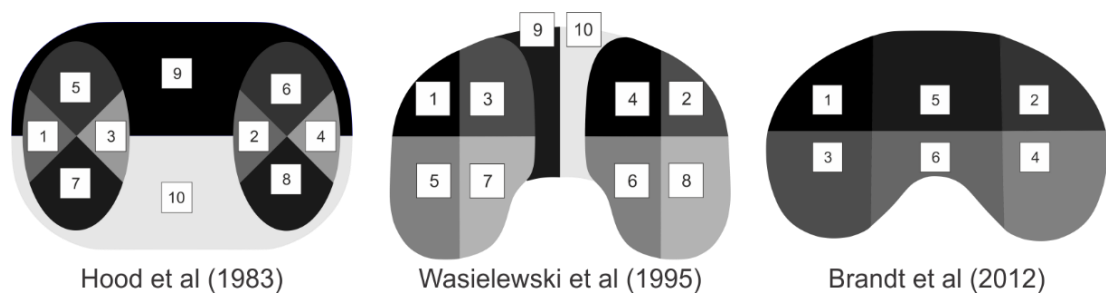
Figure 6.22. Previously published zonal methods for semi-quantitatively assessing damage modes of total knee replacements.

6.6.1.1 Method

Three different measurement areas were designed in CorelDraw X8 version 18 (Corel Corporation, CA) and the individual areas composing each design were measured using ImageJ (Figure 6.23). The area of each measurement zone was converted to a percentage of the total area. The practicality of using each of the damage mode zones was considered by attempting to score an implant using the different zones.
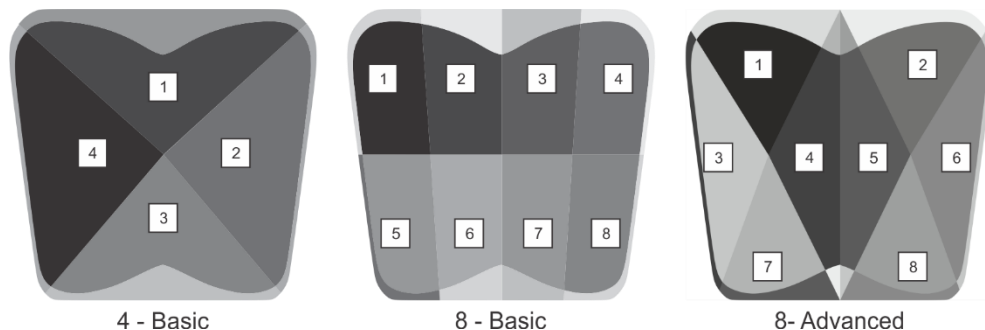
Figure 6.23. Different zonal templates for the semi-quantitative damage mode assessment of the inferior bearing insert surface. Left, 4-Basic. Centre, 8-Basic, Right, 8-Advanced.

6.6.1.2   Results and Discussion

From the established methods, Hood et al. (1983) featured the largest disparity of 23% between the largest and smallest measurement zone (Figure 6.24). Wasielewski et al. (1994) and Brandt et al. (2012) featured at least half of the disparity of Hood et al. (1983) both of which were 6% and 11%, respectively. This means for the same device, a damage mode of a given size would likely score differently between two zones between the different methods.

For the novel TAR measurement zones, 4-Basic featured the largest disparity of 7% whereas 8-Advanced and 8-Basic featured similarly small disparities of 2% and 3% respectively. Visualising the zonal boundaries through a microscope was challenging, particularly where the measurement boundary crosses the surface diagonally for the 8-Advanced design. The anterior (top) and posterior (bottom) zones were easier to track through a microscope and therefore the perpendicular lines of the 8-basic pattern made distinguishing the zonal boundaries easier. The 8-Basic design features the smallest zonal measurement area disparity and was the easiest design to implement practically, therefore this design was used for the main study.
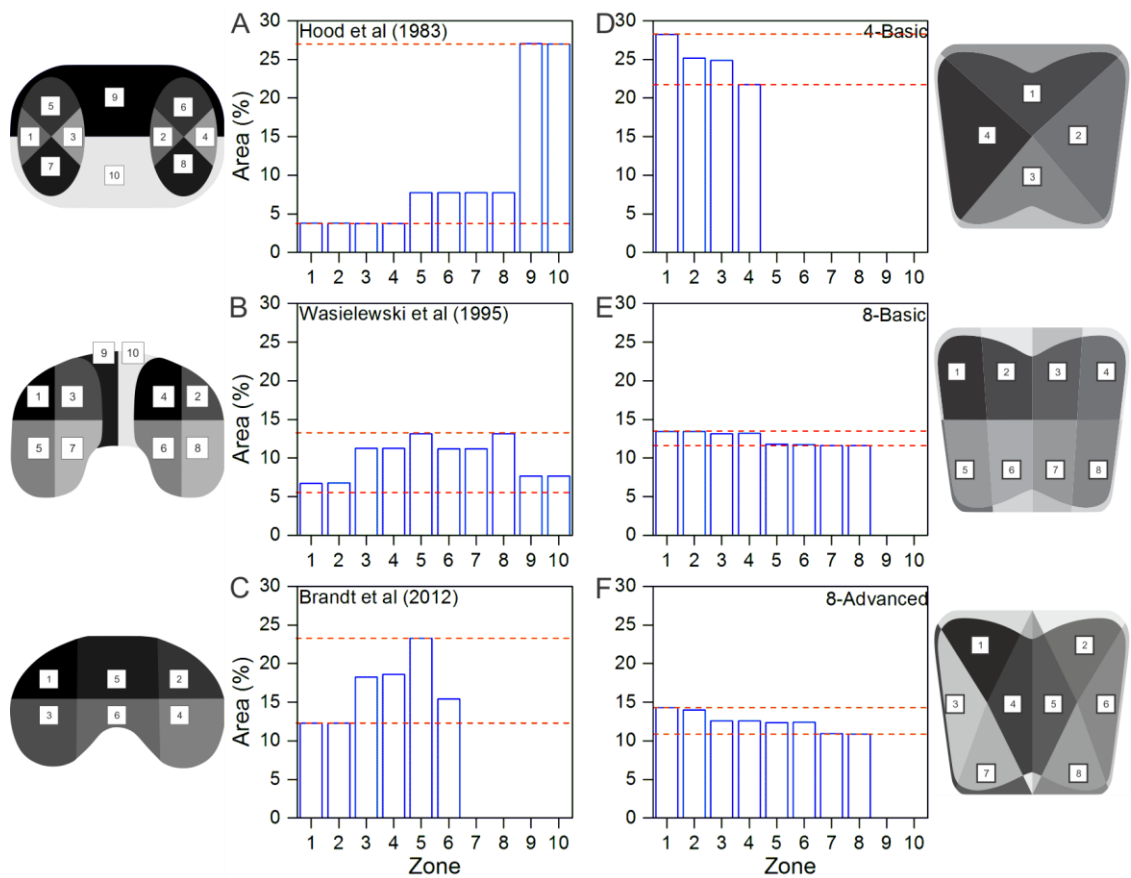
Figure 6.24. Differences in zonal areas for three published semi-quantitative damage mode methods for total knee replacement (A-C) and three developmental zones for damage mode assessment of total ankle replacement (D-F). Dashed red lines denote the greatest difference between zones for each method.

6.6.2 Methods

6.6.2.1 Semi-quantitative Damage Mode Scoring

An Olympus SZ-ET Stereomicroscope (Olympus, Japan) with a Highlight 3001 ring light (Olympus, Japan) was used to view the inferior surface of each bearing insert (Figure 6.25). Magnifications between four times and 110 times were used to characterise the damage modes visually.
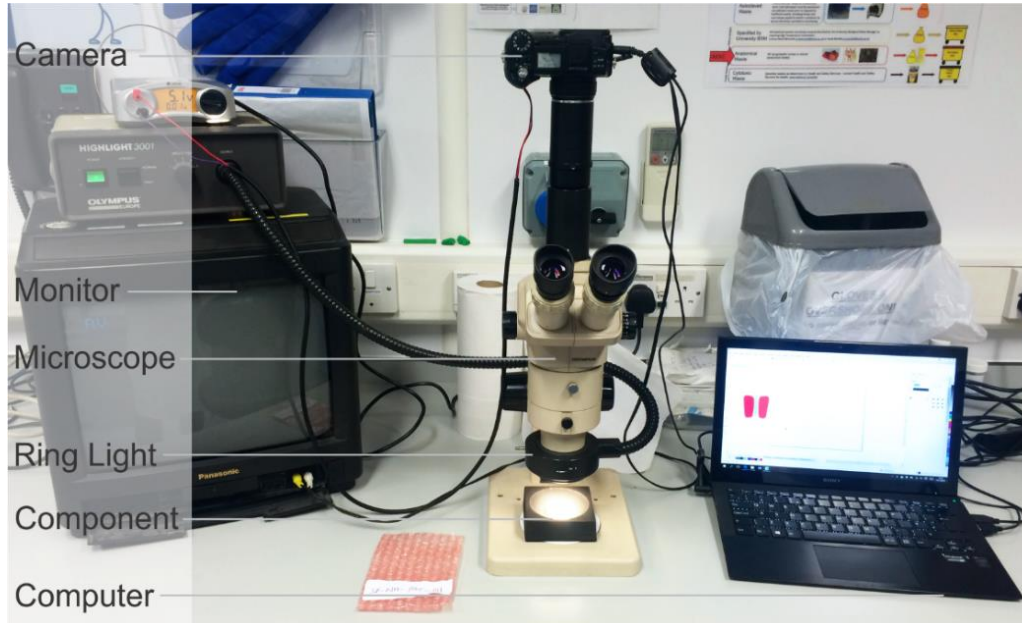
Figure 6.25. Semi-quantitative damage mode analysis setup. Stereomicroscope with ring light linked to an Olympus digital camera. Real-time images were viewed using a monitor. Computer used to sketch damage mode location on a generic inferior bearing insert template.

Several established semi-quantitative damage mode methods were described in section 2.5.2.1. The method developed by Hood et al. (1983) was simple but does not distinguish between perceived damage mode severity and extent. The method used by Brandt et al. (2012) featured separate severity and extent scores with 10 possible scores in each. This was laborious and impractical for large explant cohorts, such as the TAR cohort in this project. The method used by Wasielewski et al. (1994) was selected for this project because it balanced the value of having separate extent and severity scores but only featured four possible scores in each.

Each damage mode was described in section 2.5.2.1, however in relation to TAR, the damage modes were defined as:

Burnishing: Progressive erasure of machining marks resulting in a highly polished surface.

Scratching: Indented lines parallel with the direction of articulation, which for the inferior bearing insert surface of TAR is antero-posterior.

Pitting: Depressions visible to the eye typically indicative of deformation caused by the impression and release of embedded wear debris.

Abrasion: Tufts of material remaining suggestive of material avulsion from the substrate.

Destruction: The method by Wasielewski et al. (1994) originally featured delamination as a damage mode, as did the method by Hood et al. (1983). After initial inspection of the components, delamination was not obviously present across the cohort and may require methods such as Fourier-transform infrared spectroscopy to determine its presence. Delamination was substituted for destruction. Destruction was characterised as a gross loss of material but distinguished from delamination by the absence of visible sub-surface oxidation.

Deformation: Permanent distortion of the surface geometry, presumably due to cold flow/creep. Substantial areas of wear were included in this classification as it could not be distinguished from visually from deformation.

Embedded Debris: Particles of material other than UHMWPE embedded in the surface. Identified by a different colour and/or texture.

Each damage mode was scored between 0 and 3 for extent (% area) and the same scale for severity (e.g. mild/severe) (see section 2.5.2.1). The product of the extent and severity scores was the damage mode score for that specific measurement zone (Figure 6.26). All of the damage mode scores for each measurement zone were summed to create the total damage score per bearing insert (see Equation 2.1).
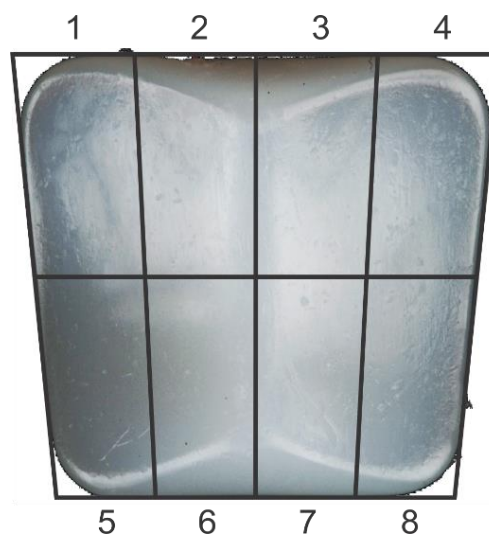
Figure 6.26. The zonal arrangement for the inferior bearing insert surface used in the current study.

Once scored, the location of each damage mode was mapped electronically using the manual-draw tools in the software CorelDraw X8 version 18 (Corel Corporation, CA).

Machining marks signified the absence of damage and were therefore also mapped but not scored. Machining marks were characterised as either congruent lines forming a regular pattern or as a consistent stippled-like effect, depending on how the surface had been manufactured. While the manufacturing methods were not known for the bearing inserts included in this project, the consistent patterns indicative of machining marks could be identified using a pictographic atlas for reference (Harman et al., 2011). The non-articulating surfaces of the bearing insert were checked visually to verify the type of machining marks present on the bearing surface.

6.6.2.2   Reliability Analysis: Semi-quantitative Damage Mode Scoring

Semi-quantitative damage mode scoring is known to have a broad variance between users but is generally accepted as a limitation of the method in the published literature (Harman et al., 2011, Brandt et al., 2012, Childs et al., 2016). The subjective analysis of damage modes for the inferior bearing surface was tested for repeatability and reliability.

Method

Ten bearing inserts were randomly selected using the method described in section 6.3.2. Using the same visual analysis techniques described in section 6.6.2.1, seven damage modes were identified by three observers using the Wasielewski et al. (1994) damage mode scoring method. For the intra-rater analysis, one observer (the author) repeated the analysis three times on three different days. The total damage mode scores for each bearing insert were compared between the observers and within the results for the one observer who completed three trials.

To compare damage mode scores between observers (inter-rater) and within the same observer (intra-rater), Spearman's rank correlation coefficient (ρ) was used to associate the relationship between the total and individual damage mode scores.

Results and Discussion

Damage mode scores were moderately correlated between observers, the average rank correlation coefficient was $\rho=0.60$. The individual associations between observers were $\rho = 0.82$ (1 vs 2), $\rho = 0.43$ (1 vs 3) and $\rho = 0.55$ (2 vs 3). Between observers, pitting, destruction and embedded debris showed a good to excellent reliability, indicating these were the most consistently identified damage modes (Table 6.3). The damage mode least consistently identified was deformation and was therefore the most challenging damage mode to identify between observers. The absent relationship between observers for scratching was likely an artefact of the ranked-statistical test. All of the

bearing inserts featured substantial areas of scratching and often reached maximum score. Therefore, when ranked, the order may not have been similar between observers but scratching overall was highly prevalent.

Table 6.3. Inter-rater reliability analysis for damage mode score.

	1 vs 2	1 vs 3	2 vs 3	Mean (ρ)	Reliability
Burnishing	0.73	0.72	0.39	0.61	Moderate
Scratches	-0.18	-0.18	0.31	-0.02	None
Deformation	0.16	0.33	0.27	0.25	Poor
Pitting	0.79	0.69	0.82	0.77	Good
Abrasion	0.89	0.44	0.29	0.54	Moderate
Destruction	0.92	0.94	0.86	0.91	Excellent
E. Debris	0.71	0.88	0.83	0.81	Good

Notes: E. Debris, Embedded debris. ρ, mean Spearman's rank correlation.

The intra-rater analysis included three damage mode scores measured by the same observer on different days. Damage mode scores were strongly correlated between observations, the average rank correlation coefficient was $\rho = 0.89$. The individual associations between observations were $\rho = 0.94$ (1 vs 2), $\rho = 0.88$ (1 vs 3) and $\rho = 0.85$ (2 vs 3). All of the damage modes except scratching showed a good to excellent reliability between observations which suggested an excellent reliability overall for the one observer (Table 6.4). For the same reasons identified for the intra-rater analysis, scratching may not have been ranked similarly but was extremely prevalent across the cohort.

Table 6.4. Intra-rater reliability analysis for damage mode score.

	1 vs 2	1 vs 3	2 vs 3	Mean (ρ)	Relationship
Burnishing	0.97	0.77	0.79	0.84	Good
Scratches	0.20	0.44	0.70	0.45	Poor
Deformation	0.92	0.95	0.94	0.94	Excellent
Pitting	0.85	0.95	0.88	0.89	Good
Abrasion	0.94	0.77	0.89	0.86	Good
Destruction	1.00	0.92	0.90	0.94	Excellent
E. Debris	0.94	0.71	0.69	0.78	Good

Notes: E. Debris, Embedded debris. ρ, mean Spearman's rank correlation.

6.6.2.3 Radiopaque Marker Extrusion

UHMWPE components cannot be identified in standard X-ray imaging without the presence of radiopaque markers. Radiopaque markers are pieces of high density material (e.g. stainless steel) implanted within UHMWPE components to highlight the location of the component on X-ray imaging. Radiopaque markers have been shown to become extruded from the bearing insert of TAR (Dahabreh et al., 2006). Two

radiopaque markers were shown to be completely extruded from bearing inserts after being identified from the medical imaging in Chapter 5.

Radiopaque marker extrusion was defined as the extrusion of the radiopaque marker from the bearing insert by at least 0.1 mm. The minimum distance of 0.1 mm was selected to allow for manufacturing tolerances, as the radiopaque marker may not have been congruent with the anterior or posterior component edges when manufactured. A CD-6" CP electronic digital calliper (Mitutoyo ltd., UK) was used to measure the length of radiopaque marker extrusion from the anterior and posterior edges of the bearing component. The frequency and location of radiopaque marker extrusion was counted and the mean of three length measurements was reported.

6.6.2.4 Scanning Electron Microscopy and Energy Dispersive X-ray Spectroscopy

Scanning electron microscopy was predominantly used to identify the elemental composition of the TAR device components and embedded debris. A Carl Zeiss Evo MA15 Tungsten Scanning Electron Microscope was used in variable pressure (10-30 pascals) mode at 20 kV with magnifications between 50 and 1000 times. Two different detectors were used, secondary electron and backscattered electron detectors, in addition to energy dispersive X-ray (EDX) analysis (X-Max EDX system, Oxford, UK) to determine material composition. The two different detectors (secondary electron and backscattered electron) produce images with different contrast characteristics depending on the material composition. The EDX analysis directly identifies the elemental composition of the material of interest. An unimplanted AES tibial component was analysed to confirm the elemental composition of this TAR design as described in the literature (Figure 6.27).

The inferior bearing surface of nine explanted AES inserts, representative of the cohort, were assessed for the presence of third-body debris using the SEM. The composition of the third body wear debris was identified using EDX analysis.
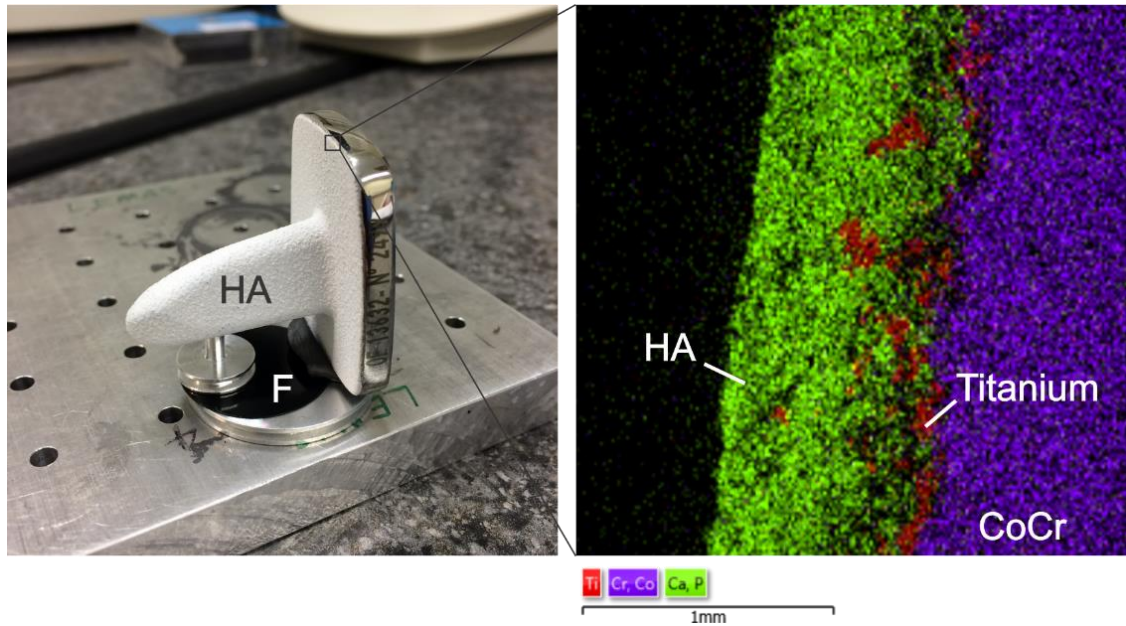
Figure 6.27. Energy dispersive X-ray analysis of the tibial component fixation surface. HA, Hydroxyapatite; CoCr, Cobalt Chromium; F, Fixture.

6.6.3 Statistics

Descriptive statistics were reported for the frequency of damage modes and the total damage mode scores (mean and standard deviation). An independent t-test was used to compare the total damage mode score between the 1st and the 2nd generation AES TARs. A difference in survivorship between these generations had previously been identified (Koivu et al., 2009) and this may be reflected by a difference in damage mode score. Pearson's correlation coefficient (r) was used to test the association between osteolysis volume, identified in section 5.5.2.2, and each individual damage mode. Many of the damage modes are associated with the production of wear debris, and this may be related statistically to the total volume of osteolysis.

6.6.4 Results

Damage Type and Frequency

Seven damage modes: burnishing, scratching, deformation, pitting, abrasion, destruction and embedded debris, were identified on the bearing insert inferior surfaces (Figure 6.28). Scratching was predominantly orientated in the antero-posterior direction which is consistent with the intended direction of articulation.
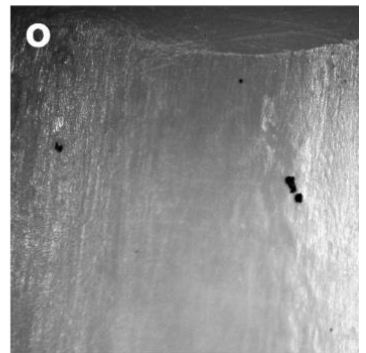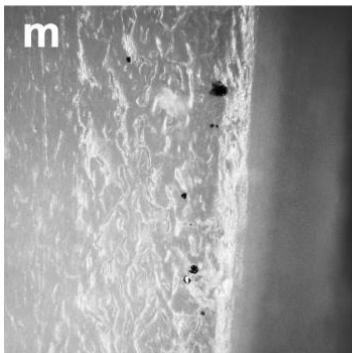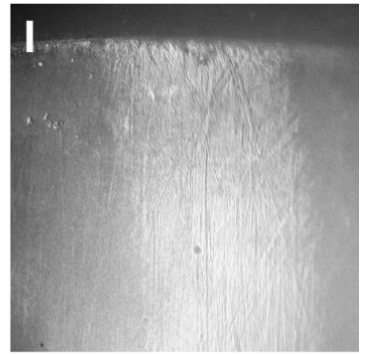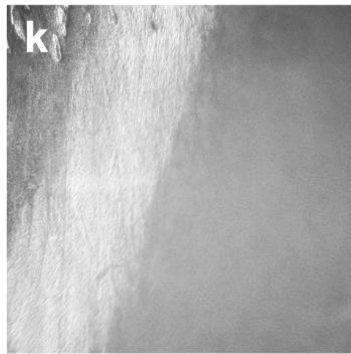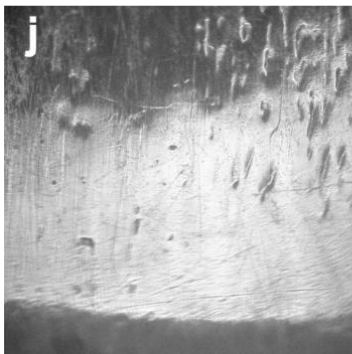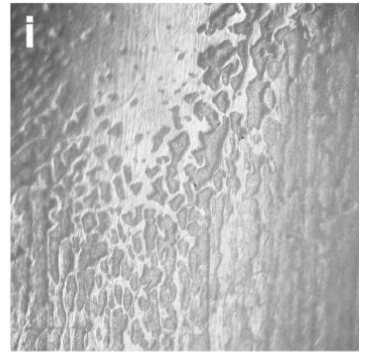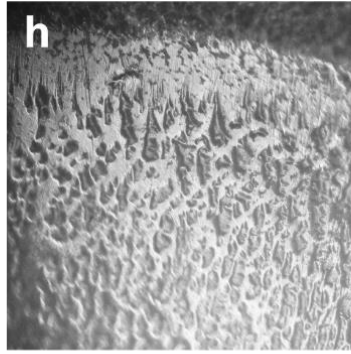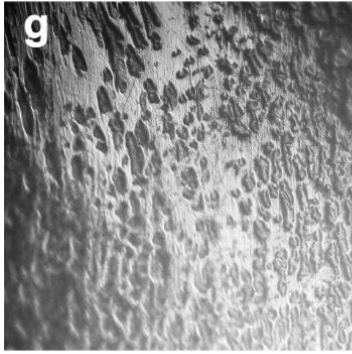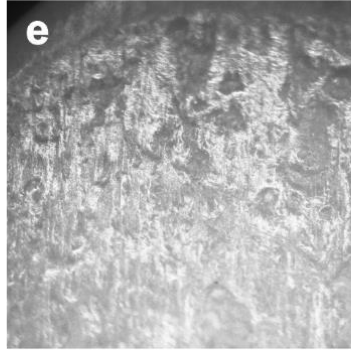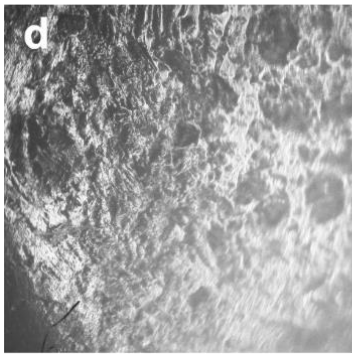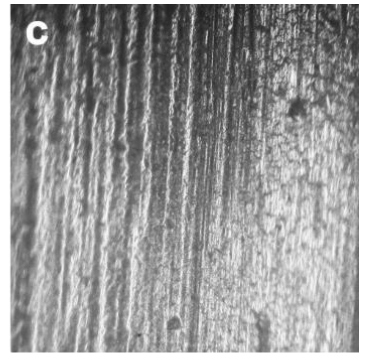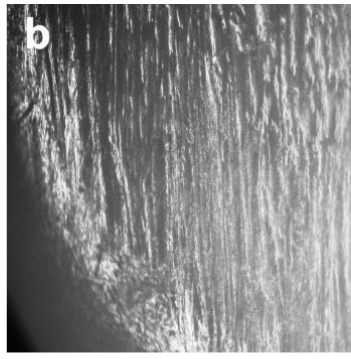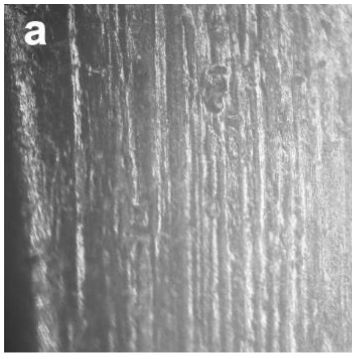
0.5 mm
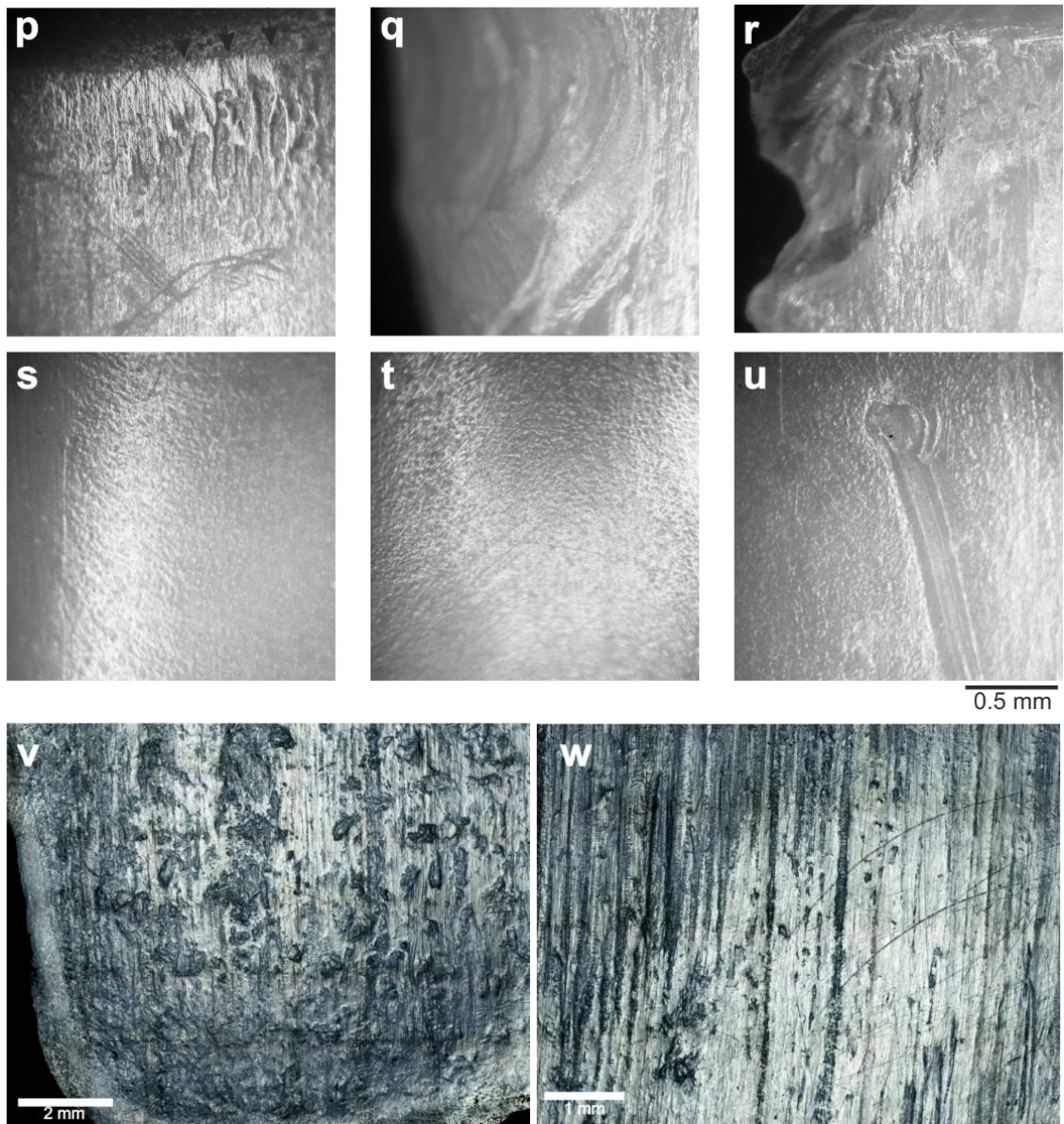
Figure 6.28. Damage modes on the inferior bearing insert surface of retrieved Ankle Evolutive System (AES) total ankle replacements. A-C, Scratching. D-F, Pitting. G-I, Abrasion. J-L, Burnishing. M-O, Embedded debris. P-R, Deformation (P) and Destruction (Q-R). S-T, Machining Marks. U, Deep scratch/gouge surrounded by machining marks. V-W, Multiple damage modes captured with the Alicona InfiniteFocus microscope.

Six bearing inserts featured all seven of the damage modes (4 AES (2ndGen); 1 AES (1st Gen); and 1 BP). Scratching was the most commonly identified damage mode and was present on all bearing inserts (n = 42) (Figure 6.29). Burnishing (83.3%), pitting (92.9%) and abrasion (88.1%) were highly prevalent, each present on more than 35 bearing inserts. Deformation and embedded debris affected 25 (59.5%) and 26 (61.9%) bearing inserts, respectively. Gross UHMWPE destruction was the least commonly identified damage mode (n = 16; 38.1%). Although minor material destruction was also identified. In total, material destruction (both gross and minor) was present for 57% (n = 25) of bearing inserts.
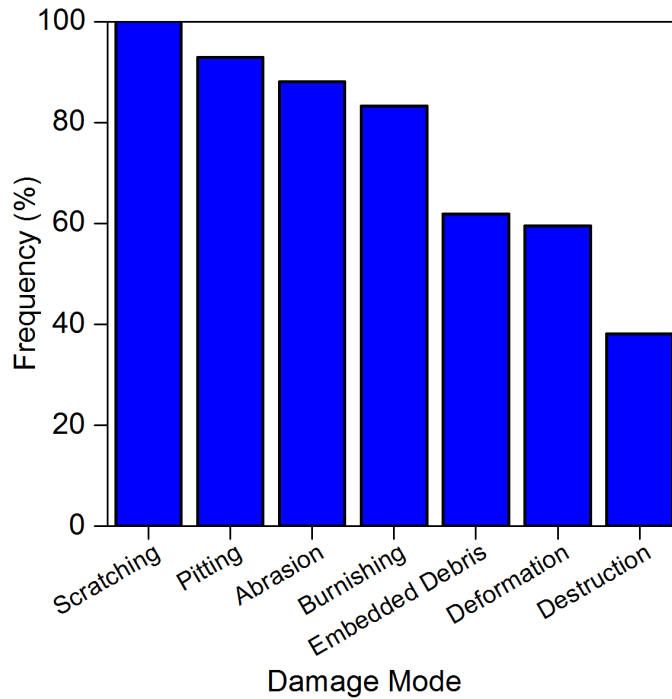
Figure 6.29. Damage mode frequency for the inferior bearing insert surface of total ankle replacement (n = 42).

The damage caused by minor material destruction was typically located inferior to the superior surface and was on the sides or inferior bearing surface of the bearing insert. This damage was often in the millimetre size range (Figure 6.30). An EDX analyses of the damage revealed the presence of calcium phosphate (Figure 6.30). All of the TAR brands except the Rebalance featured minor impingement for at least one bearing insert.
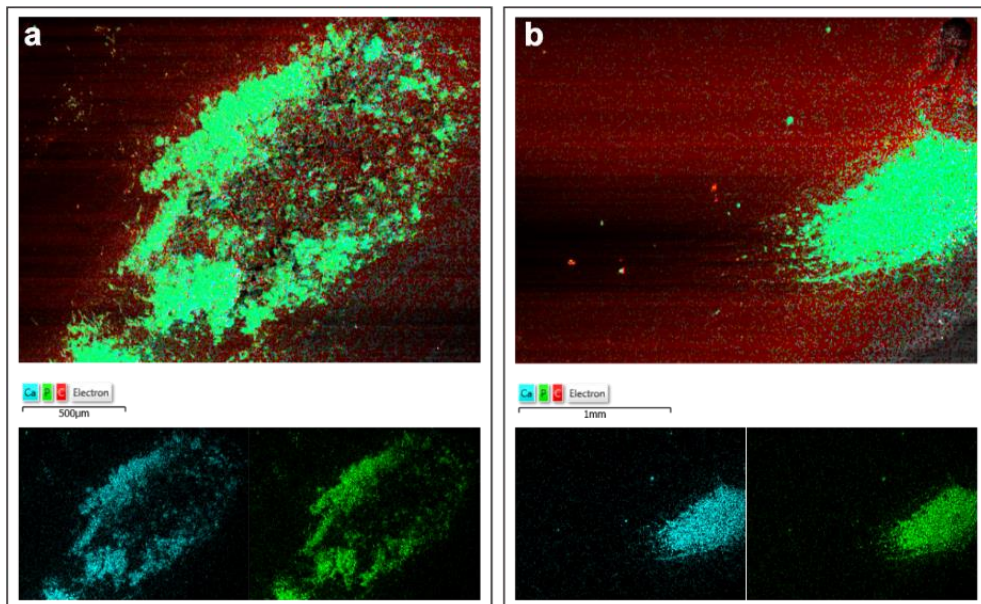
Figure 6.30. Energy dispersive X-ray analysis of bone contact on the UHMWPE bearing insert. Unlike impingement, where gross material loss was identified, small areas of bone contact and damage were visually located. The examples (a,b) are approximately 2.5 mm in length.

Embedded debris was commonly black in colour, often featuring a polished flat surface, suggestive of wear. Pale yellow/off-white wear particles were identified, often coating the trough of a deep scratch, yet these particles were challenging to see with the light microscope because their colour matched that of the bearing insert. Therefore, these type of wear particles are likely to be under-reported.

At approximately 1000 times magnification, mixed populations of embedded debris appeared visually similar, but could be distinguished using energy dispersive X-ray analysis (Figure 6.31 and Figure 6.32). The composition of embedded wear particles were titanium, calcium phosphate and cobalt chromium for the AES TAR. Both hydroxyapatite and bone are composed of calcium phosphate but neither the crystalline structure characteristic of hydroxyapatite nor the histoarchitecture of bone were visible at the magnifications used. These particles were typically between 50 µm to 100 µm in size.
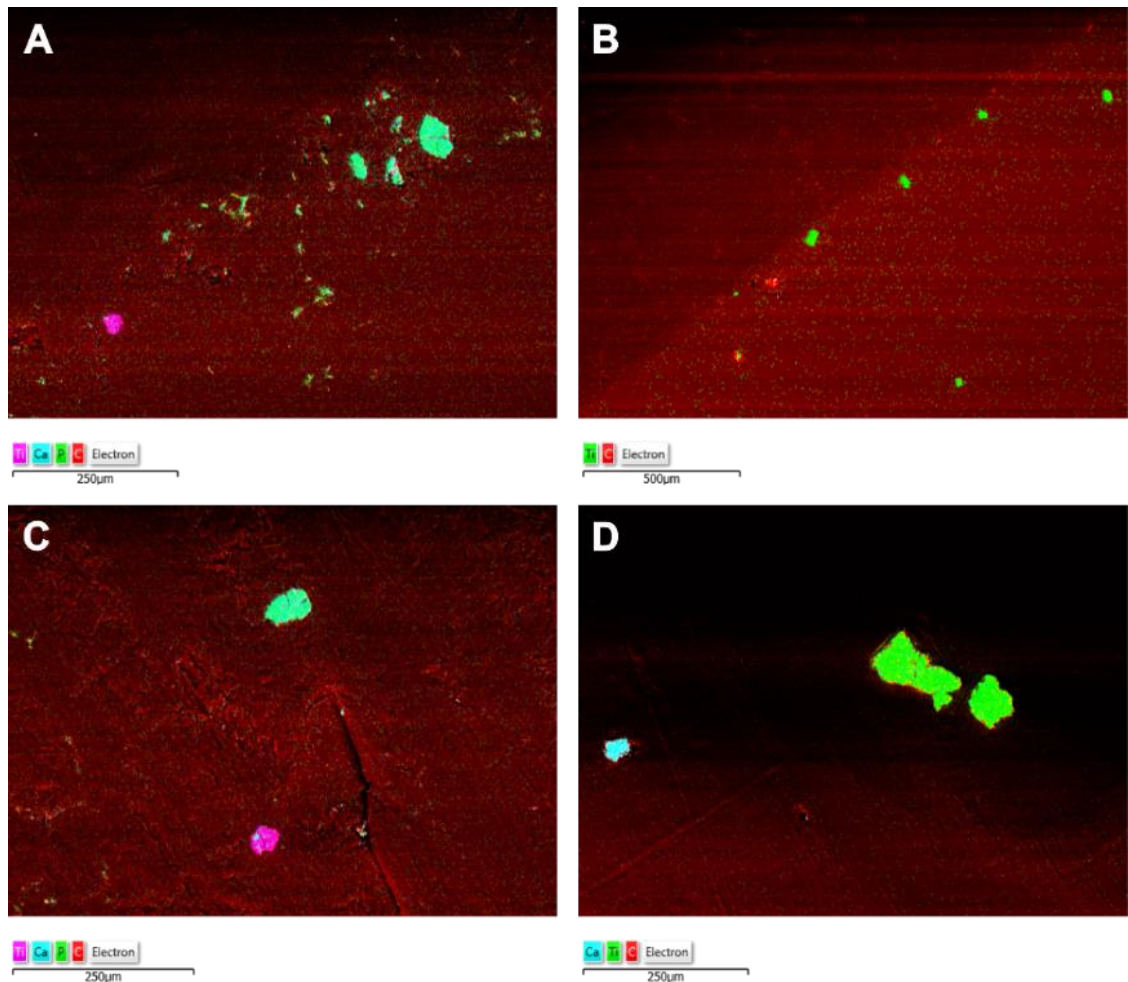
Figure 6.31. Examples of embedded debris in the inferior bearing insert surface of four Ankle Evolutive System (AES) total ankle replacements with energy dispersive X-ray analysis.
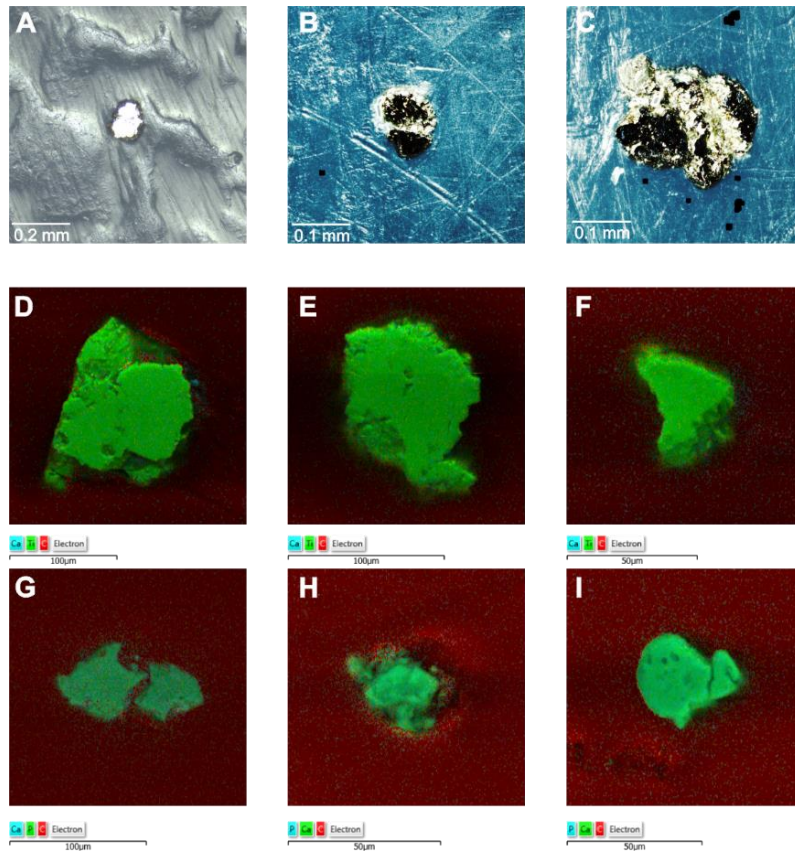
Figure 6.32. Examples of individual titanium (ti) and bone (CaP) embedded debris in the inferior bearing insert surface of Ankle Evolutive System (AES) total ankle replacements (A-C) with energy dispersive X-ray analysis (D-I). These examples were approximately 50 μm to 100 μm in size.

Radiopaque marker extrusion was identified for nine bearing inserts (21%) (Figure 6.33). Two bearing inserts (One AES and One BP) were missing the anterior radiopaque marker despite there being a posterior marker present and a manufactured hole on the anterior surface, suggesting the anterior marker had once been embedded. Three bearing inserts (All AES TARs) appeared not to have been manufactured with holes to embed radiopaque markers in and therefore radiopaque markers were not identified for these components.
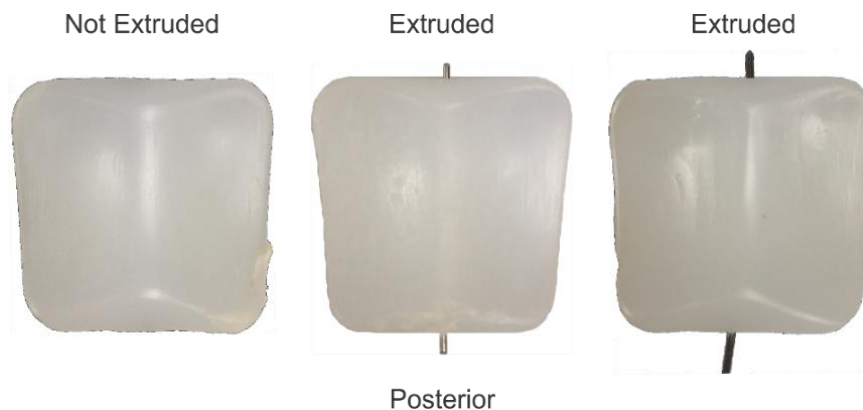
Figure 6.33. Examples of radiopaque marker extrusion. Show the different extents and also the fact some of the inserts had not been manufactured with tags.

Seven of the nine components with extruded radiopaque tags featured scratch areas on the tibial bearing surface that were more than 2 mm from the centre of the component in both medio-lateral and antero-posterior planes.

Damage Extent

The damage mode score (DMS) theoretical maxim was 504, although a score this high would be highly improbable because if gross UHMWPE destruction was prevalent across the surface, then no other damage mode would likely be observable. The mean damage score for the inferior insert bearing surface was 185.3 (± 71.0 SD; range: 19.0 to 314.0), which represented 36.8% of the theoretical maxim (Table 6.5). A BP TAR had the highest damage mode score of 314.0 which was 62.3% of the theoretical maxim. This device had evidence of bearing insert subluxation, impingement and metal-on-metal contact between the tibial and talar components. The lowest reported score was for a Rebalance TAR (DMS =19) and was 3.8% of the theoretical maxim. This device had retained the majority of its machining marks across the surface which may suggest the bearing insert had a short implantation time, however the demographic information for this device was not available.

The theoretical DMS maxim for an individual damage mode was 72. Scratching was also the highest scoring individual damage mode at 52.1 (± 20.6 SD; range: 15.0 to 72.0), which was 72.4% of the maxim. Abrasion, pitting and burnishing scored 60.5%, 52.0% and 43.3%, respectively. Gross UHMWPE destruction scored the lowest with 5.6% of the maxim, on average.

Table 6.5. Mean damage mode scores.

	All n = 42	AES[a] n = 27	AES[b] n = 6	Rebalance n = 2	BP n = 2	Hintegra n = 3	Mobility n = 2
Total	185.3 (71.0)	208.3 (45.6)	157.0 (50.2)	25.5 (9.2)	226.0 (124.5)	70.3 (14.2)	226.0 (124.5)
Scratch.	52.1 (20.6)	55.8 (18.0)	56.5 (17.2)	20.5 (4.9)	51.0 (29.7)	18.7 (29.7)	72.0 (0)
Pitting	37.4 (25.7)	40.9 (21.9)	36.8 (28.8)	1.0 (1.4)	42.0 (42.4)	5.3 (9.2)	72.0 (0)
Abras.	43.6 (25.2)	51.6 (20.3)	28.5 (20.3)	0 (0)	42.0 (42.4)	13.0 (17.6)	72.0 (0)
Burnish.	21.2 (23.6)	36.0 (23.1)	31.7 (29.7)	3.0 (1.4)	27.0 (4.2)	29.7 (10.7)	0 (0)
E.D.	9.6 (18.2)	11.9 (19.8)	1.0 (2.0)	1.0 (1.4)	5.5 (7.8)	1.7 (2.9)	28.5 (40.3)
Deform.	7.3 (11.4)	7.7 (10.0)	2.0 (3.1)	0 (0)	40.5 (6.4)	2.0 (3.5)	0 (0)
Dest.	4.0 (7.2)	4.4 (7.6)	0.5 (0.8)	0 (0)	18.0 (0)	0 (0)	6.5 (7.8)

Notes: Parentheses denote standard deviation. Scratch., Scratching. Abras., Abrasion. Burnish., Burnishing. E.D., Embedded Debris. Deform., Deformation. Dest., Destruction. [a] Ankle Evolutive System (2nd Generation). [B] Ankle Evolutive System (1st Generation).

The mean damage score for the AES (2nd Gen) TARs were similar to the two BP TARs (Table 6.5). Both BP TARs had evidence of bearing insert subluxation, impingement and metal-on-metal contact between the tibial and talar components.

The total damage score for AES (1st Gen) devices was significantly less than AES (2nd Gen) devices (p = 0.02) (Figure 6.34). Abrasion was the only individual damage score to be significantly less between these two device types (p = 0.015).
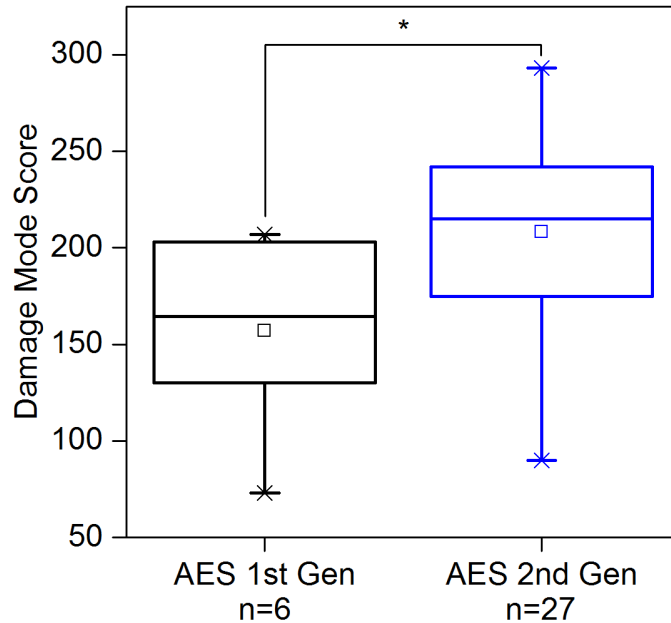
Figure 6.34. Total damage mode score for the 1st and 2nd generation (Gen) Ankle Evolutive System (AES) total ankle replacement. * Independent t-test (p=0.02).

The volume of osteolysis related to each of the 22 TARs with medical imaging was moderately correlated (ρ = 0.56) with the total damage mode score (Figure 6.35). Abrasion and embedded debris were the only statistically significant damage modes associated with osteolysis volume, with moderate correlations of ρ = 0.51 (p = 0.016) and ρ = 0.48 (p = 0.23), respectively.
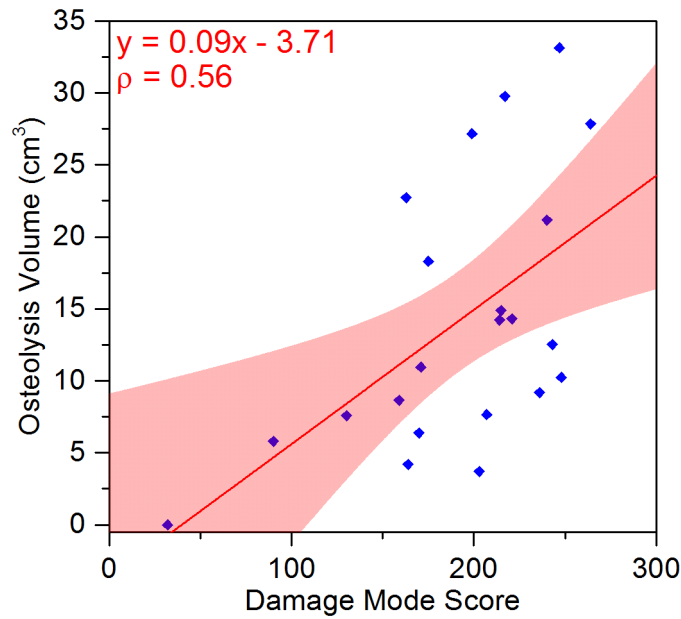
Figure 6.35. Association between osteolysis volume and total damage mode score. A moderate correlation ($\rho = 0.58$) was identified using Spearman's rank correlation coefficient (ρ).

The mean anterior radiopaque marker extrusion was 1.25 ± 1.15 mm (range: 0.1 to 3.71 mm). The mean posterior radiopaque marker extrusion was 1.47 ± 1.17 mm (range: 0.2 to 3.59 mm). Two radiopaque markers had been extruded to the extent they had been removed completely from the component.

Damage Location

Burnishing, pitting, scratching and abrasion occurred across the entire bearing surface for the AES (2nd Gen) TARs (Figure 6.36). Identifiable deformation/wear occurred predominantly towards lateral side of the concave surfaces. None of the bearing inserts featured visible deformation/wear zones on the medial side of the lateral concave surface. Machining marks typically featured in the areas absent of visible deformation/wear. The centre of the component commonly featured machining marks. Destruction of the inferior surface occurred on the medial and posterior edges. Embedded debris generally accumulated in the centre of the component and towards the anterior and posterior edges of the articulating surfaces.
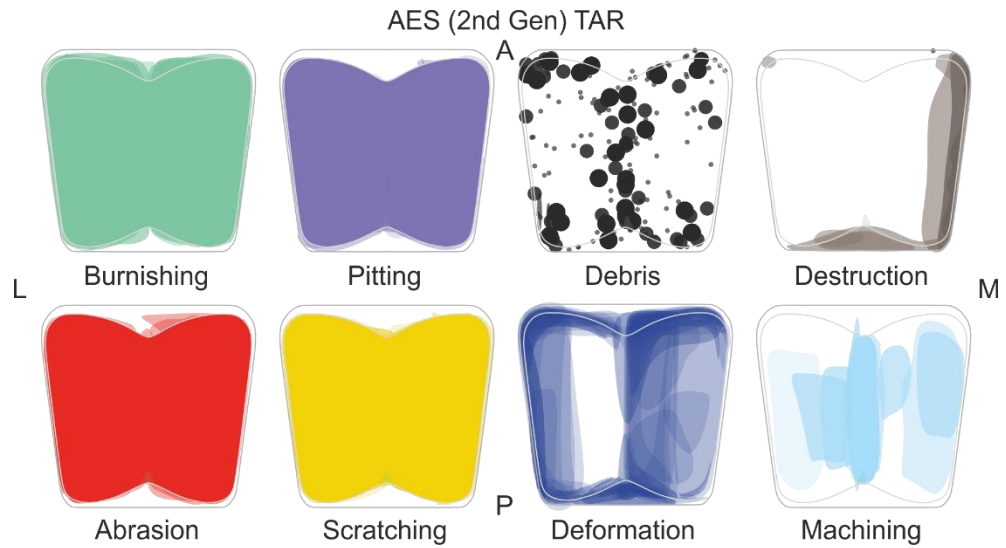
Figure 6.36. Damage mode location for AES (2nd Gen) TARs. A, anterior. P, posterior. L, lateral. M, medial.

Burnishing, pitting, scratching and abrasion occurred across the entire bearing surface for the AES (1st Gen) TARs (Figure 6.37). Identifiable deformation/wear occurred predominantly towards lateral side of the concave surfaces. One bearing insert featured a region of deformation/wear that was orientated diagonally across the lateral concave articulating surface. The majority of the wear/deformation was located on the lateral side of the articulating surfaces. Machining marks typically featured in the areas absent of visible deformation/wear. The centre of the component commonly featured machining marks. Material destruction and embedded debris were evident but no specific pattern was identified.

Figure 6.37. Damage mode location for AES (1st Gen) TARs. A, anterior. P, posterior. L, lateral. M, medial.

The sample size for the other TAR brands retrieved were too small to adequately identify patterns. The BP TARs (n=2) presented with a different pattern of damage to the AES (1st and 2nd Gen) TARs (Figure 6.38). Both BP TARs had material destruction (one medial, one lateral) and both TARs featured substantial deformation/wear in a hyperboloid shape at the centre of the component. This was different to the other BP-style devices with similar component geometries.
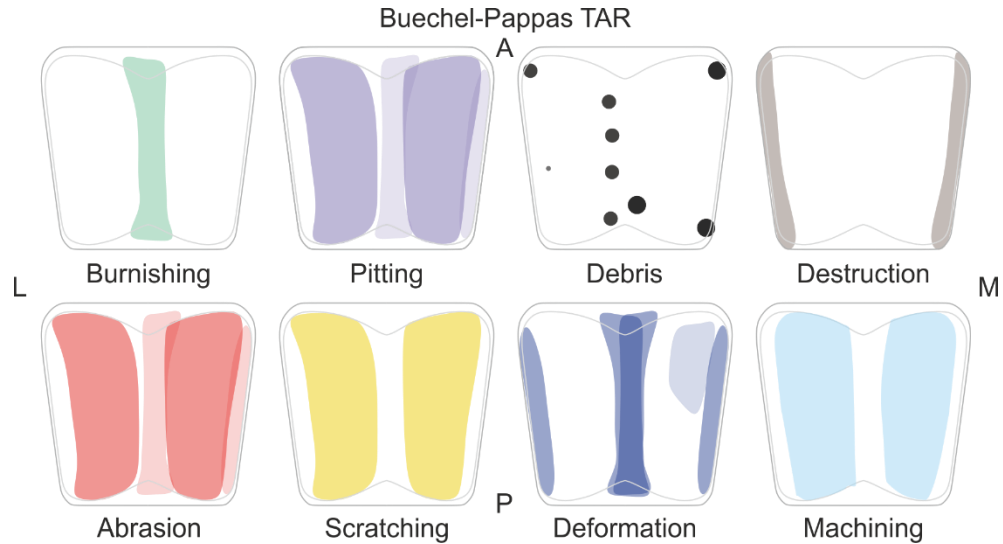
Figure 6.38. Damage mode location for BP TARs. A, anterior. P, posterior. L, lateral. M, medial.

The Hintegra bearing inserts (n=3) were shaped differently to the BP-style bearing inserts (Figure 6.39). Burnishing occurred in striped pattern perpendicular to the expected antero-posterior direction of articulation. The machining marks for the BP, Rebalance and Hintegra TARs were clearly identifiable due to their regular groove-like pattern and morphology. These marks covered a greater area of the articulating surfaces than the AES (1st and 2nd Gen) TARs.

Figure 6.39. Damage mode location for Hintegra TARs. A, anterior. P, posterior. L, lateral. M, medial.

Of the nine bearing inserts with extruded radiopaque markers, eight featured anterior marker extrusion whereas all nine featured posterior marker extrusion.

6.6.5 Discussion

Scratching (100%), Pitting (93%), Abrasion (88%) and Burnishing (83%) were prevalent damage modes across the cohort, all of which often covered the majority of the inferior bearing surface. Scratching, burnishing and abrasion were indicative of normal antero-posterior articulation with the talar component and had previously been identified in explanted mobile-bearing TARs (Small Bones Innovations Inc., 2007, Affatato et al., 2009) and fixed-bearing TARs (Vaupel et al., 2009). Pitting can be a product of third-body debris being imprinted into the bearing surface and subsequently released (Hood et al., 1983). Embedded debris was evident in 62% of bearing inserts which, after EDX analysis, were found to be composed of titanium and calcium phosphate, specifically for the AES (2nd Gen). Embedded debris of this composition was consistent with the wear identified on the tibial fixation surface (see section 6.4.3). Cottrino et al. (2016) found titanium and cobalt chromium alloy wear debris particle types embedded in the bearing insert surfaces for six AES TARs. Cobalt chromium alloy wear particles were not found to be embedded within the bearing surface of the cohort included in the current study, however the size of these particles may have been too small to be identified using an SEM at 1000 times magnification.

The mean total damage score for the AES (2nd Gen) TAR was 41.3% of the maximum theoretical damage score. This was similar to the BP TARs which had undergone catastrophic failure featuring insert subluxation, impingement and metal-on-metal contact between the tibial and talar components. The magnitude of damage associated with the AES (2nd Gen) TARs was due to high damage scores for embedded debris, abrasion and material destruction, which were also high for the BP TARs.

The total damage score for the AES (2nd Gen) TARs (41.3%) was significantly more than that for the AES (1st Gen) TARs (31.2%). Koivu et al. (2009) reported osteolysis rates for the AES (2nd Gen) TAR to be 3.1 times higher than the AES (1st Gen). High levels of titanium were measured in periprosthetic tissue surrounding the dual-coated AES (2nd Gen) TARs and wear of the fixation surface was speculated to have caused the disparity. In the current study, disparities between the embedded debris and abrasion scores explain the difference in damage mode scores and also support the hypothesis proposed by Koivu et al. (2009). A limitation of the visual damage mode analysis was that HA wear particles could not be adequately identified by the eye, given the white colour blends in with UHMWPE bearing insert. The AES (1st Gen) TARs featured a single layer coating of HA, therefore it is possible HA wear particles were not identified. Between the short term-follow-up (31 months) and the medium to long-term follow-up (96 months) of the

same cohort of AES TARs, Koivu et al. (2017) found the disparity in osteolysis rates had diminished. The dual-coated AES (2nd Gen) may lead to the early development of osteolysis but both TAR designs resulted in a 70% osteolysis incidence by 96 months (Koivu et al., 2017). The volume of osteolysis identified in the medical imaging (see section 5.5.2.2) was moderately associated with embedded debris (ρ = 0.48) and abrasion (ρ = 0.51) which may be an indicator of these two damage modes affecting osteolysis size. However, visually identifying particle types, other than metallic particles such as hydroxyapatite, was challenging due to their small size and pale colour. The statistical association between osteolysis volume and embedded debris could therefore be considered a relationship between osteolysis volume and the presence of titanium wear particles specifically, which had originated from the fixation surface in the current study.

The Rebalance TAR had the lowest damage mode score, which was 5.1% of the theoretical maximum damage score. Machining marks were visible across the surface for both TARs and this may have been related to a relatively short implantation time of 22 months (data missing for the 2nd Rebalance TAR).

Deformation occurred on the lateral side of each bi-concave surface more commonly than the medial side for the AES (1st and 2nd Gen) TARs. The BP-style TAR designs, such as the AES, allow for inversion and eversion motions at the inferior bearing surface (Buechel and Pappas, 2003). Inversion motions during walking may have caused the talar component to wear/deform this surface asymmetrically. The BP devices showed an abnormal deformation pattern which occurred central to the bearing insert, and may be related to the wear/deformation of the bearing insert after subluxation. Deformation/wear was a challenging damage mode to identify as it was often indicated by a subtle change in surface geometry. The coordinate measurement machine has been used to determine surface changes on this surface for the BOX TAR (Affatato et al., 2009), however for this thesis, computed tomography was used to obtain similar geometrical information (see Chapter 8).

Hard tissue contact resulting in material destruction featured in the majority (57%) of bearing inserts. This damage mode was identified visually but was validated using EDX analysis which revealed embedded calcium phosphate particles in the affected area. Minor impingement could be easily overlooked given the damage caused for several cases was < 2.5 mm in length and width. A more in depth discussion of gross and minor impingement is included in Chapter 7.

Radiopaque markers are an important aid for identifying the location and alignment of the bearing insert and whether it remains intact or is fractured (Dahabreh et al., 2006). Radiopaque marker extrusion was identified in 21% of the TARs, all of which were either

AES or BP devices. Dahabreh et al. (2006) published a case report of a patient with an AES TAR who had evidence of radiopaque extrusion. The posterior radiopaque marker had been completely removed from the bearing insert and was situated posterior of the talar component. The ankle was revised for a suspected bearing insert fracture and substantial talar component varus tilt. Varus malalignment was suspected to have created abnormal stresses within the bearing insert and facilitated the extrusion of the marker. Two bearing inserts included in the current study had their anterior radiopaque markers completely removed which was consistent with the case report. The medical imaging analysis could not accurately measure varus or valgus alignment of the ankle, therefore associating this metric with radiopaque marker extrusion could not be achieved. However, of the nine TARs with extruded radiopaque markers, seven showed discolouration areas (i.e. discolouration area on the tibial component bearing surface) >2 mm from the centre of the tibial component. This may suggest that these bearing inserts underwent abnormal loading, possibly including excessive version (Dahabreh et al., 2006). Unilateral deformation identified in the damage mode analysis also contributes evidence to suggest asymmetrical loading was prevalent in this cohort.

Three devices were absent of radiopaque marker holes which suggests the markers were not embedded within the bearing insert at the point of manufacture. Brooke et al. (2012) included an image within a publication which showed an AES TAR without evidence of radiopaque markers and no mention of radiopaque marker extrusion. Manufacturing inconsistencies related to the quality of the fixation surface have been suggested about the AES TAR (Besse et al., 2009, Cottrino et al., 2016), however to the author's knowledge, this is the first incidence of inconsistencies relating to the inclusion of radiopaque markers.

6.6.5.1   Limitations

Many of the damage modes were superimposed making them challenging to identify precisely. Quantitative analysis methods are currently not capable of distinguishing between all seven damage modes automatically, therefore semi-quantitative analyses were required. The semi-quantitative identification of damage modes relies on the observer's expertise and is subject to selection bias. This is a well-known limitation of damage mode analyses and reliability analyses were undertaken to help interpret the results. The variability between observers was considered acceptable, as was the variability between results for the same observer.

6.7   Talar Component Surfaces

The talar component surfaces were the most challenging to identify and quantify damage modes from. The metallic curved surfaces unique to the talar component of a TAR created reflections which limited the capturing of high fidelity images of the entire component surface. A qualitative analysis of damage modes was undertaken but further method development is required for a more comprehensive analysis of these surfaces.

6.7.1   Methods

After visual inspection, selected damage modes (e.g. scratching, fixation surface coating abrasion) were photographed on both the fixation and bearing surfaces but a systematic photogrammetric method was not achieved and would require further development.

6.7.2   Statistics

Damage modes were qualitatively described for the talar component bearing and fixation surface.

6.7.3   Results

Talar Bearing Surface Damage Modes

Unidirectional scratching in the antero-posterior direction was prevalent across the cohort of talar components (Figure 6.40AB). Scratching, perpendicular to the direction of primary articulation, was also identified (Figure 6.40C). Localised scratches on the anterior edge of the bearing surface were evident, particularly for the BP-style devices (Figure 6.40D).
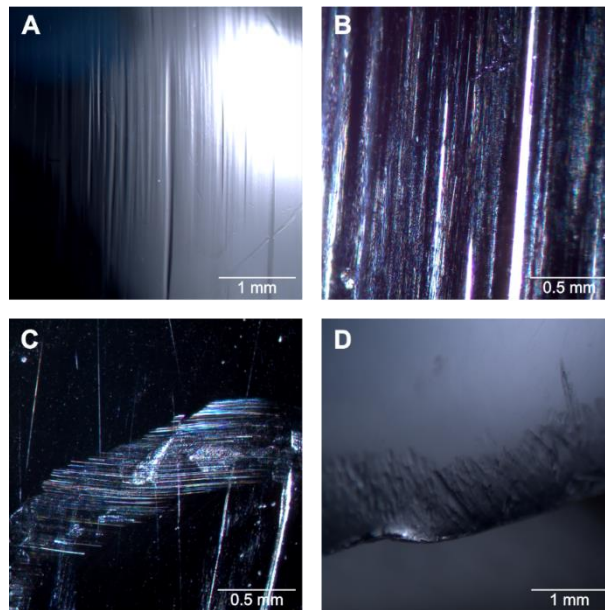
Figure 6.40. Damage modes on the talar component bearing surface. A-B, Deep longitudinal scratching in the direction of expected articulation (anteroposterior). C, Light scratching perpendicular to the expected direction of articulation. D, Wear at the anterior edge, presumably caused by micromotion between the talar component and the talus.

Three devices (Two BP TARs and one AES 2nd Gen) featured massive material loss on both the tibial bearing surface and the edge of the talar component. This damage was consistent with a dislocated/subluxed bearing insert (Figure 6.41). Cracks in the metallic substrate were identified in the area of metal-on-metal contact.
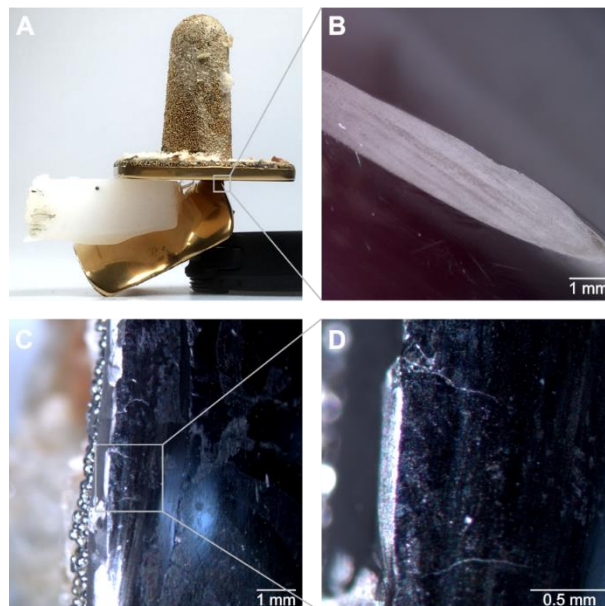
Figure 6.41. Substantial material wear and visible cracks caused by metal-on-metal contact between the tibial and talar components after bearing insert dislocation.

Talar Fixation Surface Damage Modes

Coating delamination, similar to that identified on several of the AES (2nd Gen) and Hintegra tibial components, was present for the talar component fixation surfaces (Figure 6.42). Several of the AES (2nd Gen) devices featured large areas of what appeared to be hydroxyapatite coating remaining intact. The coating was uniform across the surface, discoloured and was visually absent of bone ongrowth. The single-layer hydroxyapatite coating on the talar components of the AES (1st Gen) had been either completely removed or diminished substantially (Figure 6.42D-F).
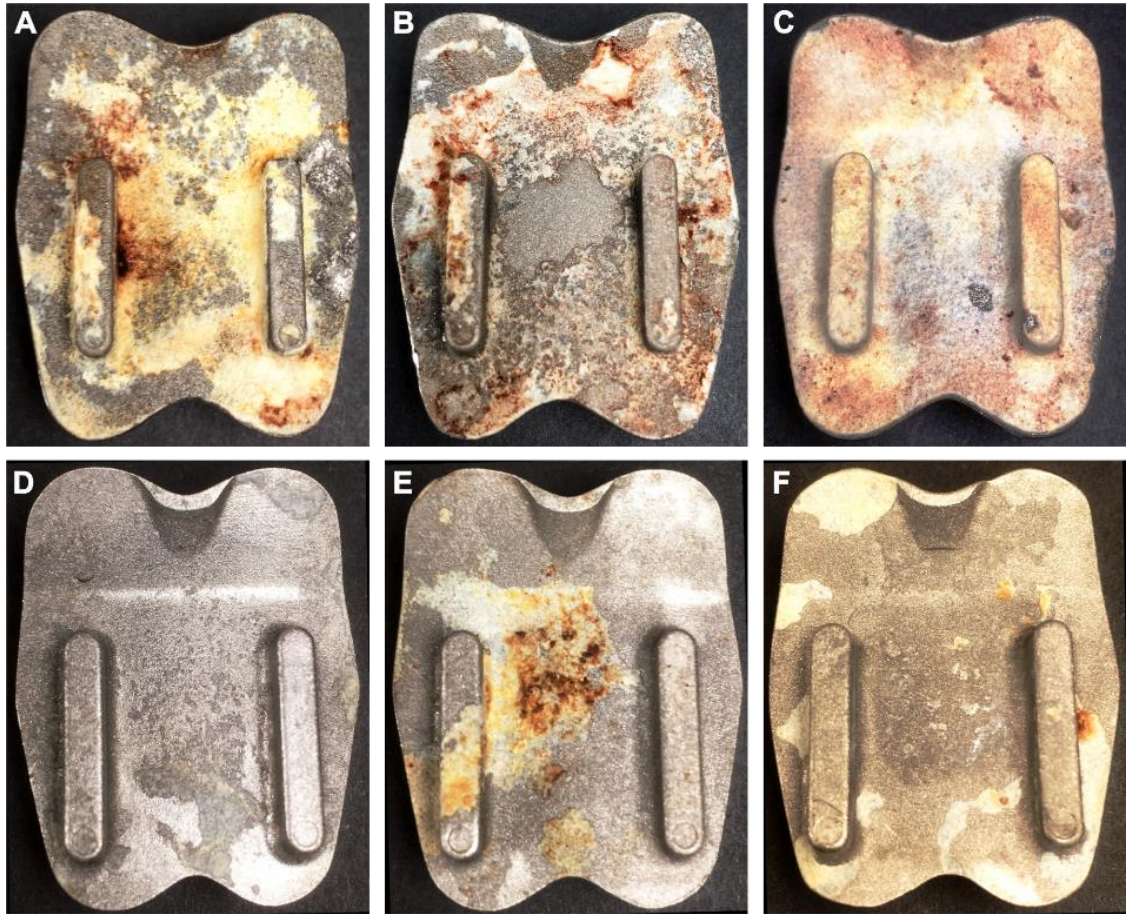
Figure 6.42. Examples of talar component fixation surfaces for the AES (2nd Gen) TAR (A-C) and the AES (1st Gen) TAR (D-F).

The talar component fixation surfaces for the Hintegra and BP TARs, bone ongrowth was evident with minimal damage to the surface coating. The Rebalance and Mobility TARs, were generally absent of bone ongrowth but also, equally absent of coating damage (Figure 6.43).
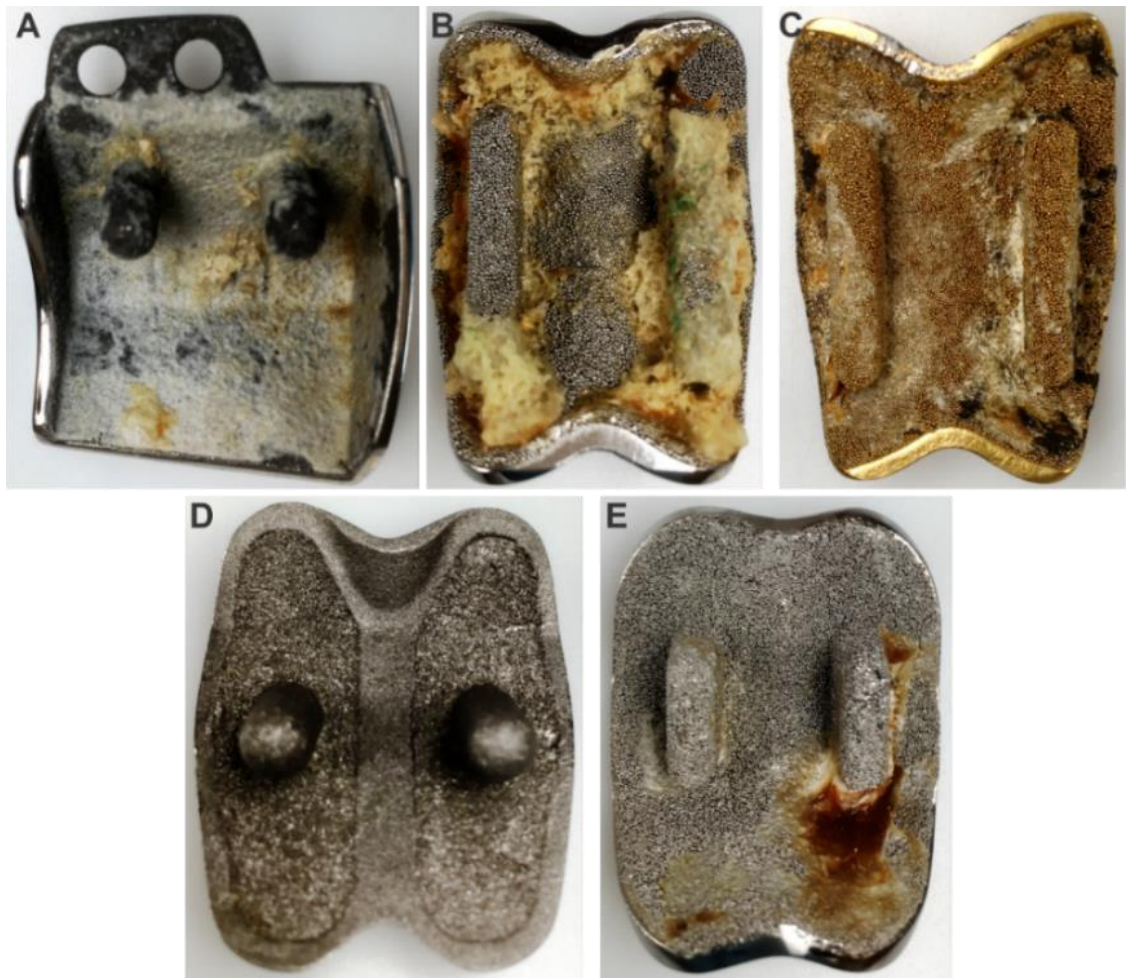
Figure 6.43. Examples of talar component fixation surfaces for the Hintegra (A), BP (B,C), Rebalance (D) and Mobility (E) TARs.

.

6.7.4 Discussion

Deep scratching along the talar component bearing surface in the antero-posterior direction was prevalent across the cohort. Cottrino et al. (2016) reported similar deep scratches in the direction of the sliding plane. The talar component articulates with the inferior bearing insert surface which, after visual inspection (see section 6.6.4), featured embedded debris across the surface and likely caused the majority of talar component scratches. Abrasion at the anterior edge of the bearing surface suggested an interaction of this bearing surface with the talus or ossifications extending to this location on the device. The talar component had subsided into the talus for several ankles in this cohort (see section 4.3.1.2) and wear between bone and the bearing surface may have been facilitated in this way. For the three components featuring metal-on-metal contact between the talar component and the tibial bearing surface, a chamfered edge had formed at the point of contact between the two components. Massive metallic material loss occurred after this metal-on-metal contact.

On the fixation surface, similar damage modes to the tibial component were identified which included delamination and coating abrasion. Substrate abrasion was not identified for the talar components which differed to the tibial components for which substrate abrasion was common. For the AES 1st Gen TARs the single layer of HA had seemingly been removed completely which was similar to the tibial components of the same devices. Wear on the surfaces of the talar component contribute to the total wear particle burden within the joint, however further method development is required before this can be quantified.

6.8 Summary

The aim of this chapter was to identify the type, extent and possible causes of damage/wear modes present on the components of failed TARs.

Tibial component fixation surface wear was prevalent across all TAR designs. For AES (2nd Gen) TARs, 89% featured substrate abrasion in addition to degradation of the fixation coating. More than 10% of the coating had delaminated in seven TARs. On average, approximately 11 mm^3 of delaminated fixation coating (titanium/hydroxyapatite) could be released into the joint space of TAR. Micromotion at the bone-implant interface and iatrogenic damage are possible causes for fixation wear.

Discolouration of the tibial bearing surface (i.e. wear patch) was identified for 98% of the TARs. This area was representative of bearing insert contact and was significantly smaller for the TARs (63.4%) with wear patches >2 mm from the centre of the tibial component. Micro-scratching and deep gouges were prevalent and likely caused by third-body wear and/or bone contact with the surface. On average, the total scratch area was 35.3% of the tibial bearing surface which suggests approximately 0.9 mm^3 of cobalt chromium alloy wear could be liberated. In three TARs, the bearing insert had dislocated and the talar component had contacted the tibial bearing surface producing substantial quantities of metallic wear debris.

On the inferior bearing insert surface, all seven damage modes were identified on the bearing inserts but burnishing, scratching, pitting and abrasion were the most prevalent (>80%). Embedded debris was also commonly identified (>60%). Impingement between the bearing insert and bone caused material destruction in 57% of TARs. Radiopaque marker extrusion was identified more frequently than in the medical imaging (21%). Asymmetrical changes to bearing insert geometry were identified visually and predominantly evident on the lateral edges of the articulating surface. The mean damage score for the AES (2nd Gen) TAR was equivalent to the two BP TARs which had both undergone bearing insert dislocation and metal-on-metal contact. Additionally, the AES

(2nd Gen) TARs featured damage mode scores significantly higher than the AES (1st Gen). Total damage mode score was moderately correlated ($r = 0.56$) with osteolysis volume. Damage mode scores for abrasion and embedded debris were the statistical contributors to the disparity between AES (1st Gen) and AES (2nd Gen) TARs and the correlation with osteolysis volume. However, methodological limitations of visual analysis such as selection bias may confound the veracity of these results.

The talar component featured similar damage modes to the tibial component on both the bearing and fixation surfaces. However, method development is required for a comprehensive quantitative damage mode analysis of the highly curved surfaces associated with this component.

In the next chapter, the effect of edge-loading, impingement and normal articulation is characterised from the superior surface of the bearing insert.

Chapter 7
Surface Characterisation of Edge-loading

7.1   Introduction

Modern mobile-bearing TARs feature a separate bearing insert which is semi-constrained between the metallic tibial and talar components. Constraint is provided by the curvature of the talar component which is highly conforming with the inferior surface of the bearing insert. In Chapter 5, rotation of the bearing insert was shown to be highly correlated with the rotation of the talar component (r = 0.98). The superior bearing insert surface is manufactured flat for the majority of BP-type TARs, the rationale for which is to allow unconstrained multidirectional motion. However, not all TARs feature a flat superior bearing surface, for example the BOX TAR, which has a curved superior surface (Giannini et al., 2011).

The stability of mobile-bearing TARs was of concern in the 1980s which led to devices using this design principle being classified as higher risk compared to fixed-bearing alternatives in the US (Food and Drugs Administration, 1982). The excessive offset of the bearing insert resulting in overlap with the edge of the tibial component is called 'edge-loading'. This phenomenon can have catastrophic clinical consequences, for example, Morgan et al. (2010) identified 10 edge-loaded AES TARs, of which nine were revised within the first year after implantation.

In Chapters 4 and 5, edge-loading was shown to be highly prevalent (77%) for the TARs with retrieved medical imaging. However, the clinical definition of edge-loading is variable between authors. Rippstein et al. (2011) defined edge-loading as a coronal plane mismatch between the tibial and talar components of ≥2 mm. Koivu et al. (2009) reported a similar definition for edge-loading but used ≥3 mm rather than ≥2 mm. Edge-loading cannot be accurately identified using standard X-ray imaging. Only the radiopaque marker is visible using this imaging modality and not the geometry of the component. Computed tomography (CT) can be used to visualise the entire bearing insert. The re-orientated CT scans used in Chapter 5, showed translation and rotation of the bearing insert to be clinically relevant and to cause edge-loading. Also, only half of the bearing inserts were within 2 mm from the centre of the tibial component in the coronal plane.

Changes to surface geometry of explanted bearing inserts have been measured for the BOX TAR, but only for three components with short implantation times of 24, 24 and 9 months (Affatato et al., 2009). Consequentially, the change in surface geometry

measured was small, up to 0.091 mm when compared to a computer aided design (CAD) model. None of the components analysed were reported to have undergone edge-loading.

The use of quantitative surface characterisation for the analysis of the full cohort of explants retrieved for the research in this thesis (n = 44) may offer a greater insight into the prevalence and effects of edge-loading in TAR.

The aim of this chapter was to:

- Identify the prevalence of edge-loading for a cohort of retrieved TAR explants and characterise the surface changes associated with the damage.

The objectives were:

- Develop a method using non-contacting 3D surface profilometry to measure the surface heights of the superior surface of the bearing insert.
- Identify the surface features characteristic of edge-loading, and other wear/deformation phenomena, and report the prevalence of the associated damage modes.
- Characterise the surface height distributions for the identified damage modes using established quantitative parameters.

7.2   Explant Details

The entire cohort of 44 bearing inserts were analysed for this study (Table 3.1). Individual explant details are reported in section 3.4.1.

7.3   Method Development

Surface characterisation can be achieved using different methods (see section 2.5.2.4). The precision of the equipment and the practicality of the method should be considered prior to implementation. Affatato et al. (2009) used a coordinate measurement machine (CMM) to determine the surface deviation of the bearing insert surfaces of the BOX TAR. The CMM relies on physical contact (contacting profilometry) with the target surface, whereas non-contacting methods, such as the InfiniteFocus microscope (Alicona Imaging GmbH, HR), use the visible light spectrum as a measurement source and does not require contact. Affatato et al. (2009) measured 4000 data points across each TAR surface at a resolution of 0.4 mm. Non-contacting methods can measure at resolutions in the submicron range which is beneficial for the accuracy of the surface height data

produced. Additionally, non-contacting methods acquire data quicker, which aids processing large cohorts more efficiently, such as in this project.

The InfiniteFocus microscope can capture surface height information from slopes of up to ~ 20°. This was deemed sufficient for characterising the superior surface of the bearing insert, which is planar. However, the technology cannot be used to measure the inferior bearing insert surface as the curves are too steep for non-contacting profilometry to capture.

The visible light spectrum is used by the InfiniteFocus microscope to capture data, similar to a camera. The two key user-defined parameters which affect how the camera perceives a surface are exposure time (µs) and contrast. Exposure time determines how long the sensor captures light for per acquisition and the contrast is a digital function within the software that changes the relative brightness across the image. The aim of this preliminary analysis was to identify by how much changing the two parameters affected quantitative outputs from the microscope.

Method

A range of values for each parameter was tested on two different UHMWPE TAR explant surfaces, one visually smooth surface and one visually rough surface. The quantitative measure used for comparison was surface roughness (Sa) which is a commonly used measure of surface texture (see section 2.5.2.4).

Results and Discussion

Neither contrast nor exposure varied the results for surface roughness of smooth UHMWPE (Figure 7.1). However, surface roughness results for the rough UHMWPE varied substantially when exposure changed at the extremes. A relatively stable value for surface roughness occurred in the mid-range of exposure between 150 and 190 µs. Contrast remained stable throughout the parametric range for the rough surface.

Rough UHMWPE

Smooth UHMWPE
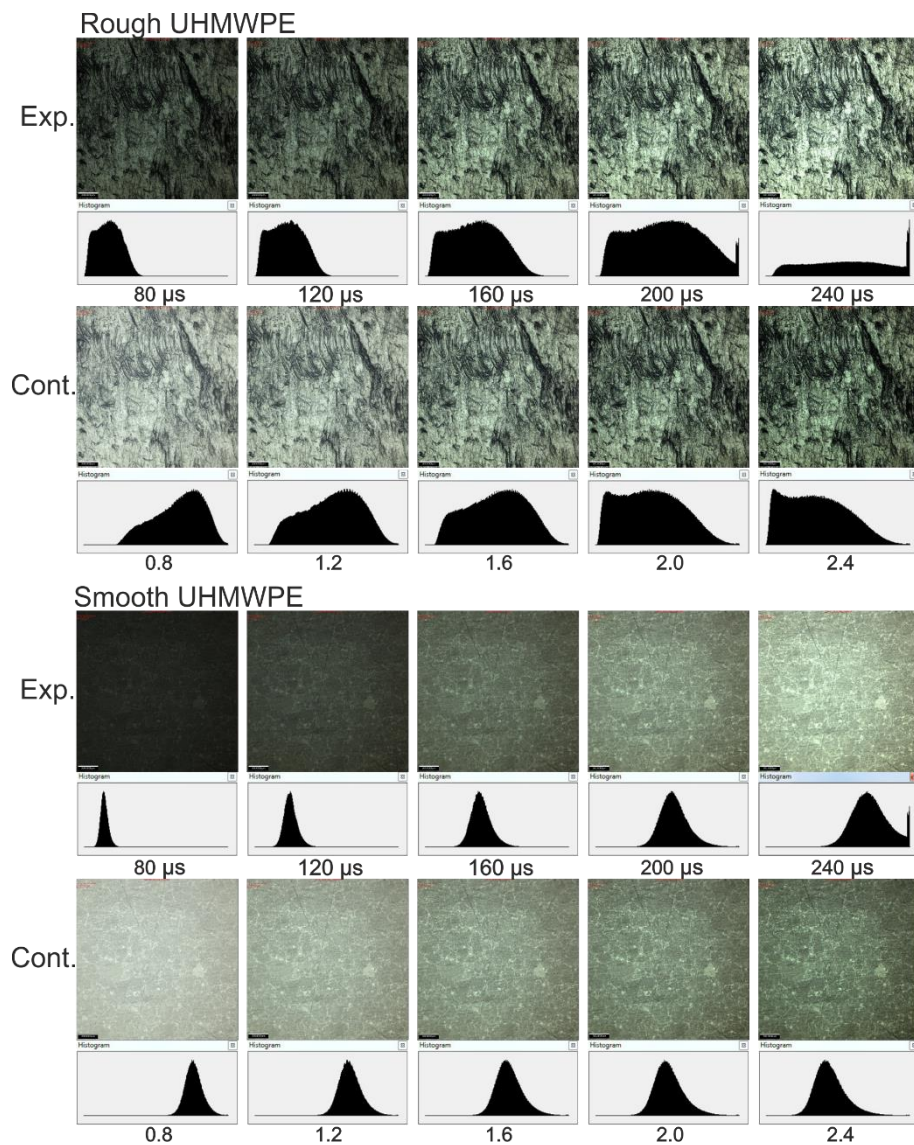
Figure 7.1. Parametric analysis to identify the effect of exposure (exp.) and contrast (cont.) on a quantitative measure (roughness). Two sample areas on the superior bearing insert surface were measured, one visually rough (A) and one visually smooth (B), using a range of different exposure and contrast values. Histograms quantify the light sensor input. Overexposure was undesirable and shown by the values peaking at the far right of the respective histogram (e.g. Rough UHMWPE at exposure 240 μs).

Exposure appeared to affect quantitative data when measuring a rough surface (Figure 7.2). This was because at low exposures, the sensor struggled to capture sufficient light from the dales on the surface. With the data missing from the deepest dales, the surface roughness values were lower, suggesting the surface was smoother than it was. The inverse was apparent for when the exposure was high, the entire surface was captured and included in the surface roughness measurement. However, once the sensor became overexposed, the sensor produced peaks of spurious data which were subsequently included in the surface roughness data, increasing the roughness as a result. Spurious data was identifiable because it often took the form of a discrete peak extending far

beyond the surface data that could be checked against the physical bearing insert visually.
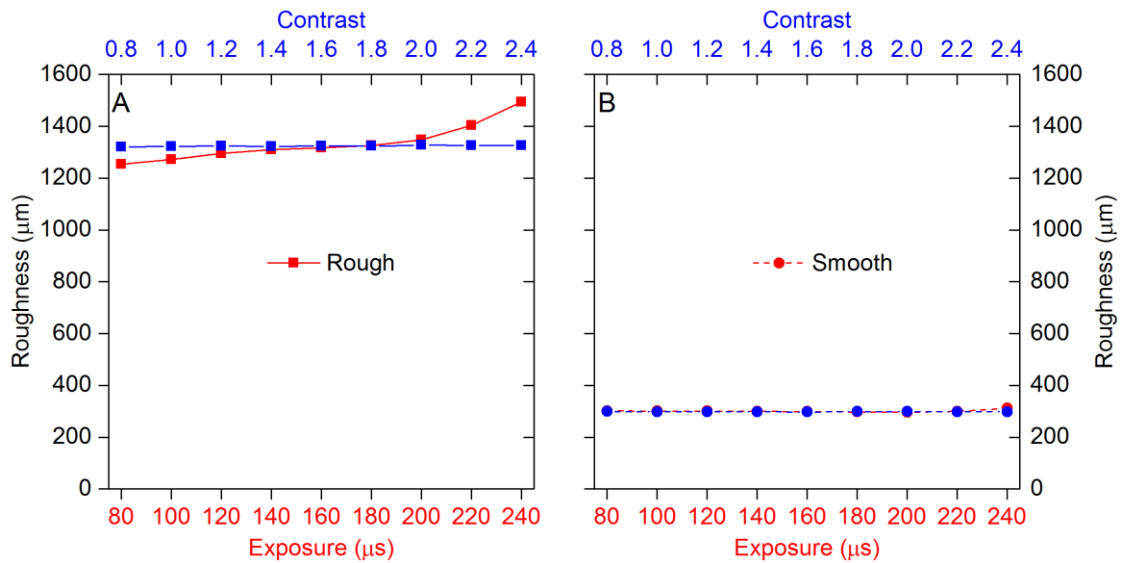
Figure 7.2. (A-B) Roughness values for the parametric analysis of rough (A) and smooth (B) UHMWPE bearing insert surfaces. Exposure had the greatest effect on roughness values for the rough UHMWPE surface. Changes in contrast did not affect surface height measurement.

A mid-range value for exposure (163 µs) and contrast (1.5) were selected using the acquisition histogram as a guide. The same parameter values were used throughout the following study for consistency.

7.4   Methods

7.4.1   Surface Height Acquisition

Using the bearing insert component holder (see section 6.3.1), the bearing inserts were fixed with the superior bearing surface facing perpendicular to the microscope lens (Figure 7.3). The microscope lens (10x Magnification) was configured to a standardised resolution (1.8 µm), contrast (1.5) and exposure (163 µs). These values had been selected as a product of the preliminary study (see section 7.3). The InfiniteFocus microscope captures surface height data by scanning a 3D point space defined by the user. The larger the surface in the XYZ axes, the longer the duration of the scan and more data is collected. Each scan took between 40 and 100 minutes.
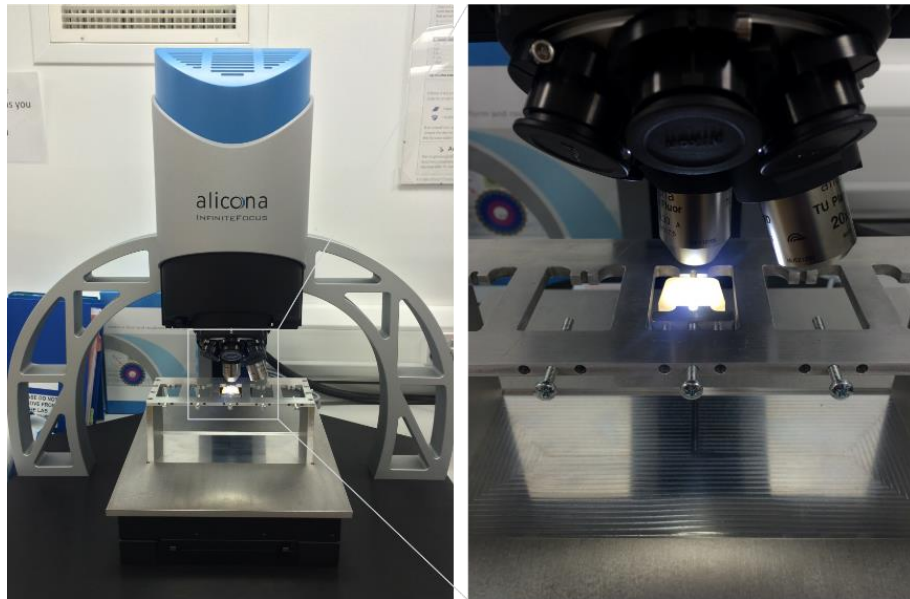
Figure 7.3. Alicona InfiniteFocus microscope (Alicona Imaging GmbH, HR) superior bearing insert surface measurement setup.

Once the scan had finished, the final image/data was stitched automatically together by the Alicona Software IF-MeasureSuite Version 5.1 (Alicona Imaging GmbH, HR) from the individual stacks of images taken at the specified resolution. The files were exported as .SUR surface files and opened for post-processing in Talymap Gold Version 5.1 (Taylor Hobson Ltd, UK).

7.4.2 Data Processing

Non-contacting profilometry may produce spurious data, which was identified in the method development (see section 7.3). Post-processing was used to remove extraneous features measured outside of the target surface (e.g. jig) and to ensure the surface heights measured were representative of the physical target surface. Raw data was processed with three different functions: levelling, cropping and noise reduction filtering (Figure 7.4).
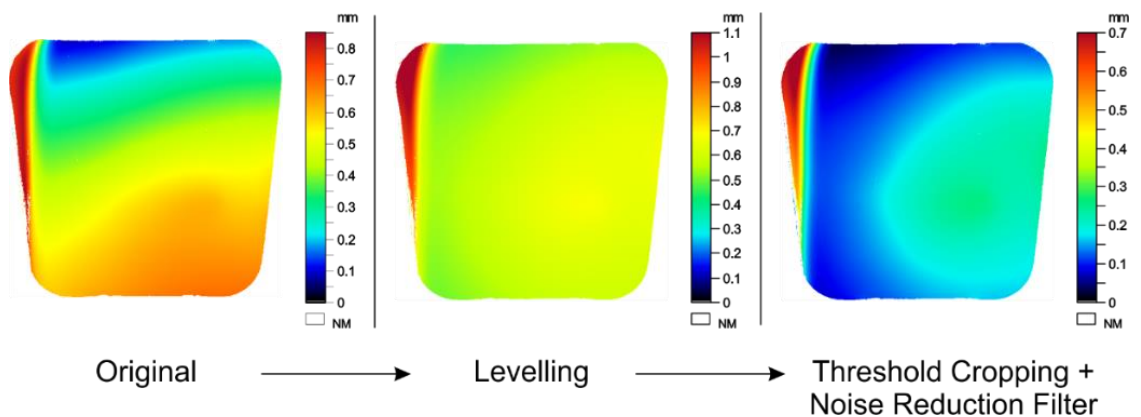
Figure 7.4. Schematic of surface height data post-processing.

I. Levelling Filter

A planar surface levelling filter was applied to the entire data set. This filter type calculates whether a consistent gradient exists across the nominal form of the dataset and, if so, it is removed. Levelling adjustments are typically small because significant effort was made to ensure the component was flat when constrained by the jig.

II. Threshold Cropping

Extraneous data from the jig may have been captured at the periphery of the bearing insert, the data for which may skew the overall surface height distribution. Therefore, a threshold cropping function was used to exclude the data associated with the jig. Care was taken not to exclude bearing surface data by visually comparing the actual bearing insert to the three-dimensional representation of the data.

III. Noise Reduction Filter

The discrete peaks of spurious data identified in the method development (see section 7.3) were able to be reduced by using a noise reduction filter. It was important to eliminate as much spurious data as possible because individual peaks in the data that extend beyond the actual surface will affect the surface height parameters, specifically maximum height. A 9x9 pixel noise reduction surface filter was applied to eliminate individual spurious data points. The 9x9 pixel size was sufficient to reduce spurious data when the data was inspected visually. The total size of the dataset was approximately 16,500 by 15,500 data points, therefore a 9x9 point filter did not change the overall trend of the data except for removing features less than approximately 9 pixels in size, such as discrete individual peaks of erroneous data.

7.4.3 Damage Mode Stratification

Following an initial visual inspection of the bearing inserts, the components were stratified into three groups based on the damage modes present to the superior bearing surface. The three groups were named and defined as:

I. Edge-loading

Deformed material at any edge of the surface suggestive of an offset between the tibial component and bearing insert.

II. Impingement

Gross material loss of the superior bearing surface consistent with contact on hard tissue such as bone.

III. Normal

No evidence of edge loading or impingement.

Two and three dimensional images of the surface data were observed, in addition to the explant itself, to determine how to classify each insert. Two observers analysed the components independently and any conflicts were discussed.

7.4.4 Surface Height Parameters

Selected British Standard ISO 25178-2 (2012) stratified surface height parameters were calculated for the entire surface of all bearing inserts. The analysis focussed on four height parameters: Maximum height (Sz), core height (Sk), peak height (Spk) and dale height (Svk). Each of these parameters were calculated by Talymap Gold Version 5.1 (Taylor Hobson Ltd, UK) using the following definitions.

7.4.4.1 Maximum Height (Sz)

The maximum height (Sz) is calculated by the peak height (Sp) minus the peak dale or the lowest point (Sv) (Equation 7.1). Peak height is always a positive value and peak dale is always negative considering these points are relative to the mean surface height plane.

Equation 7.1. $$Sz = Sp + |Sv| = Sp - Sv$$

Maximum height is sensitive to isolated peak and pit values which may be artefacts. Therefore, the filtering protocols discussed in section 7.4.2 were important to ensure spurious data was removed.

7.4.4.2 Stratified Surface Parameters (Sk, Spk and Svk)

Stratified surface parameters (Sk, Spk and Svk) were used to quantify differences between surfaces exposed to different damage modes. These parameters are calculated from the surface height cumulative distribution curve (Abbott-Firestone curve) and are defined in British Standard ISO 25178-2 (2012) (Figure 7.5). Briefly, to determine core height (Sk), peak height (Spk) and void height (Svk), the 'equivalent straight line' is calculated. The 'equivalent straight line' is the secant line of the Abbott-Firestone curve which has the smallest gradient but still comprises at least 40% of the curve. The secant line is extended between 0% and 100% of the cumulative heights which represents both the 'equivalent straight line' and the core height (Sk).The area above and below the equivalent straight line represent the void height (Svk) and the peak height (Spk), respectively.
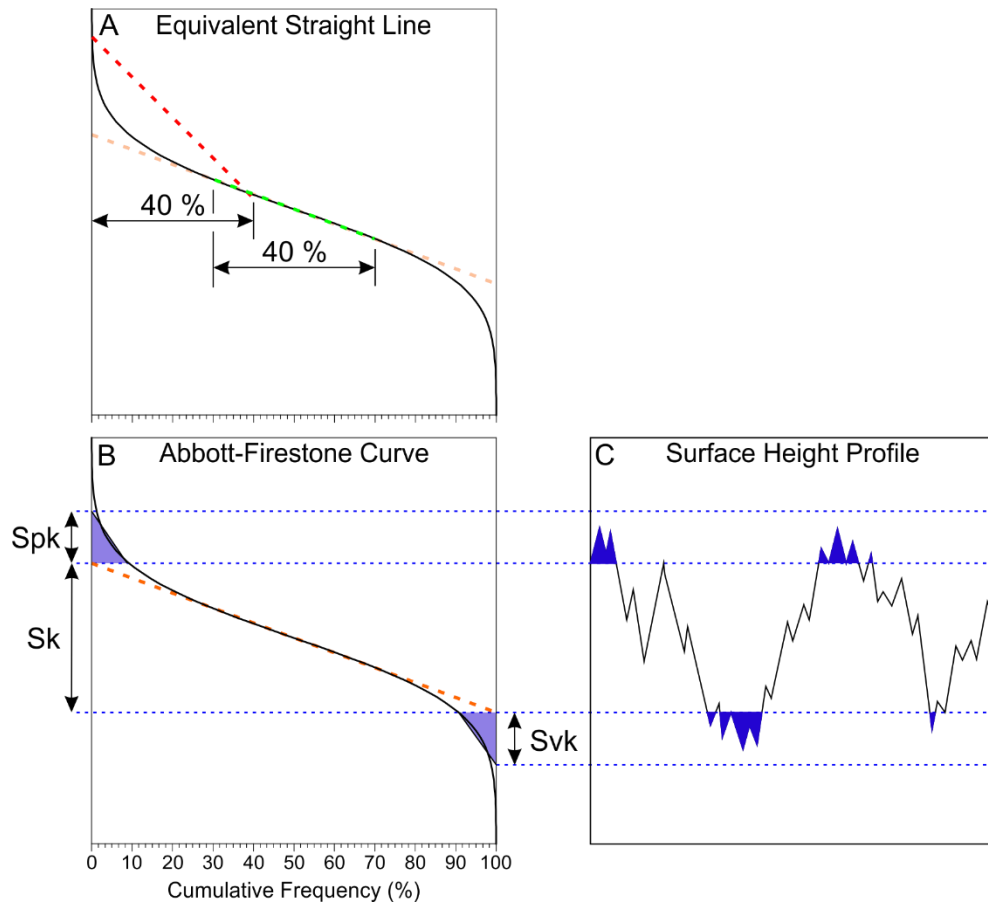
Figure 7.5. Calculation of the stratified surface parameters. A, the 'equivalent straight line' is the secant of the cumulative frequency surface height distribution curve (Abbott-Firestone curve) which has the smallest gradient but features at least 40% of the curve (orange dashed line). B, Core height (Sk) is the region of surface heights within the bounds of the equivalent straight line. Peak height (Spk) and void height (Svk) are the regions of surface heights beyond the core height in either the hill (left) or dale (right) region of the Abbott-Firestone curve. C, raw surface profile with the peaks and voids shaded in blue. Adapted from British Standard ISO 25178-2 (2012)

The stratified surface parameters were used because different wear modes (e.g. edge-loading, impingement) may be represented differently using these parameters by the differences in surface height distribution skewness. For example, a bearing insert with a localised region of raised peaks, such as in edge-loading, would theoretically have a positive skew towards the 'hill' region of the surface height distribution curve (Figure 7.6). Whereas, the inverse would be hypothesised for a surface with a substantial number of dales or voids, such as after material wear. The core surface height (Sk) may remain the same, but the proportion and magnitude of peaks and dales between the two hypothetical surfaces would differ (Figure 7.6). A surface with an equivalent magnitude of surface heights about the mean (i.e. normally distributed) may be expected for an unworn surface or a surface with symmetrical surface height changes
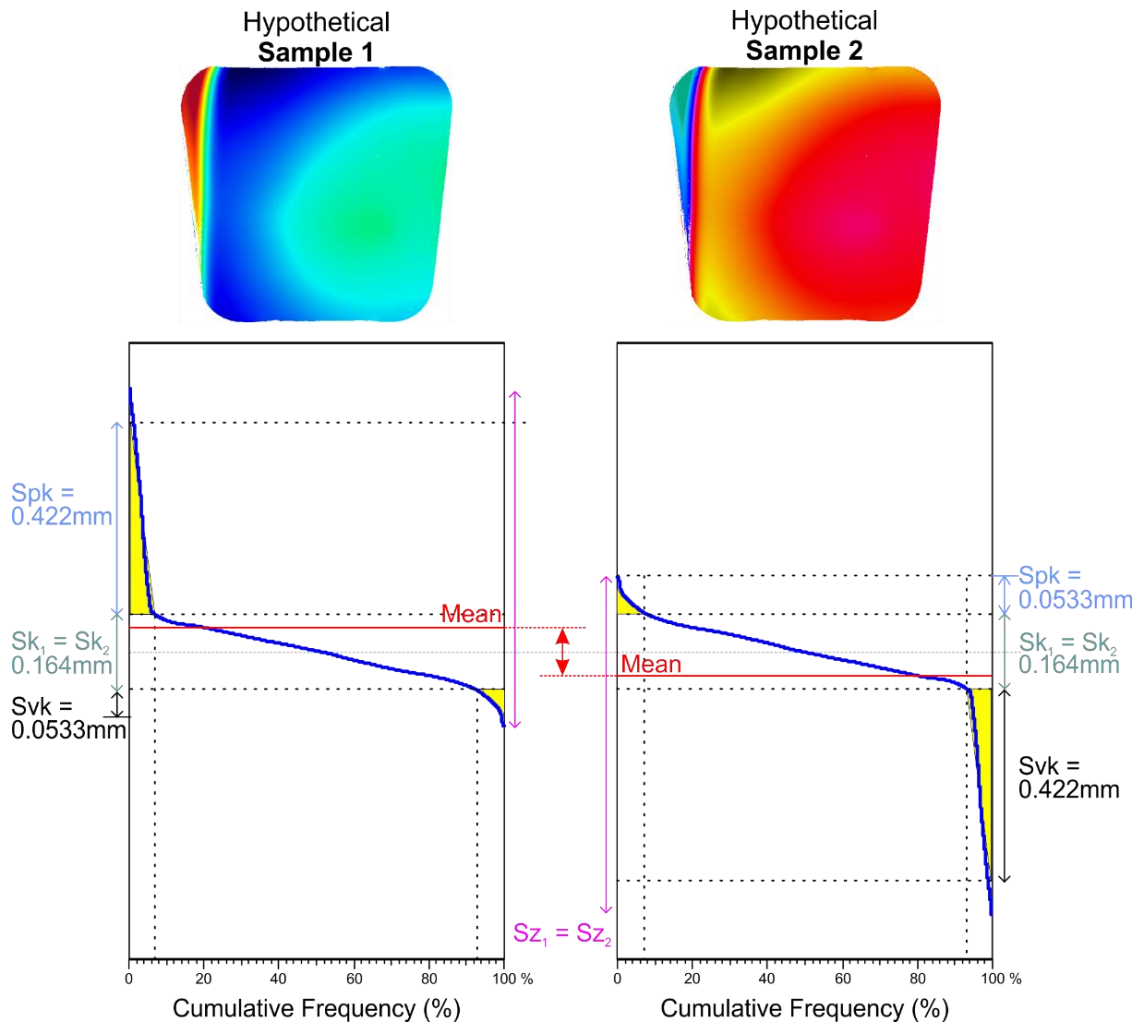
Figure 7.6. Example of two identical surfaces but with inverse surface heights. Sample 1 features a small region of peaks which is reflected by the large peak height (Spk) value. Sample 2 features an equally small region of dales which is reflected in the high void height (Svk) value. Mean surface height changes proportionally to the magnitude of the hils and dales. Maximum height (Sz) and core height (Sk) are equivalent between each sample.

7.4.5 Statistics

The frequency and location of edge-loading and impingement. Bone contact frequency and location on any bearing insert surface was also recorded. Four surface height parameters (Sz, Sk, Spk, Svk) were compared for each of the stratified groups; normal, edge-loaded and impinged. For this comparison, an ANOVA was used ($p = 0.05$). An independent t-test was used to compare the location of any edge-loading on the bearing insert to the medio-lateral offset ratio (MOR) determined from segmented CT scans in section 5.5.2.2.

7.5   Results

Damage Type and Frequency

Of the 44 bearing inserts, nine (20.5%) were considered normal, 25 (56.8%) were edge-loaded and 10 (22.7%) were impinged (Table 7.1).

Table 7.1. Frequency of 'normal', edge-loading and impingement conditions identified on the superior bearing insert surface.

Device Type	Insert Condition Normal	Edge-loading	Impingement	Total
AES (2nd Gen)	4 (14%)	19 (66%)	6 (21%)	29
AES (1st Gen)	3 (50%)	3 (50%)	0 (0%)	6
Rebalance	2 (100%)	0 (0%)	0 (0%)	2
BP	0 (0%)	0 (0%)	2 (100%)	2
Hintegra	0 (0%)	3 (100%)	0 (0%)	3
Mobility	0 (0%)	0 (0%)	2 (100%)	2
Total	**9 (20%)**	**25 (57%)**	**10 (23%)**	**44**

Notes: Only the primary damage mode is indicated. Several impinged devices were also considered edge-loaded. AES, Ankle Evolutive System. Gen, generation. BP, Buechel Pappas.

Normal bearing inserts were absent of edge-loading and impingement (Figure 7.7). Edge-loaded inserts presented with an inflection of material at least one edge of the component. Impinged inserts featured gross material wear at least one edge.
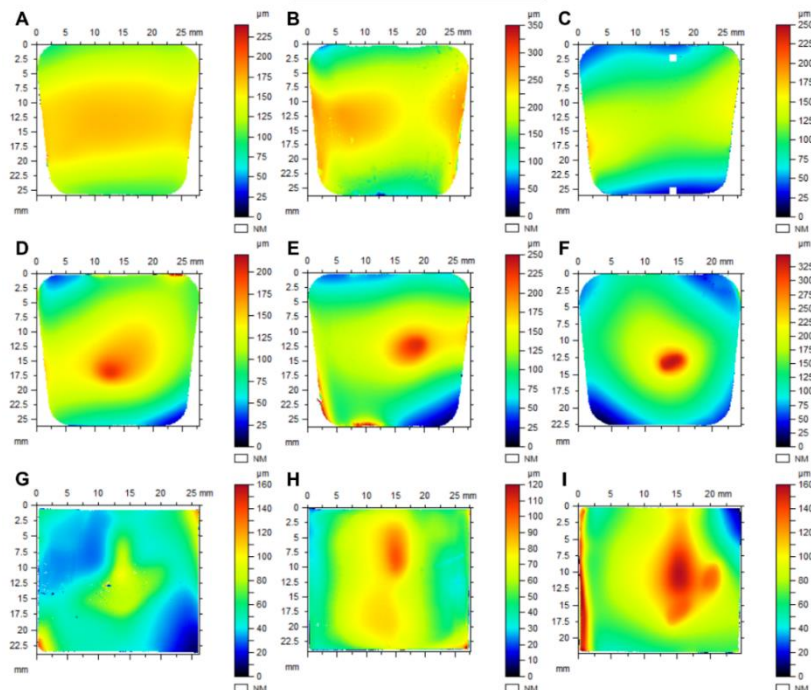
Figure 7.7. 'Normal' bearing inserts. Normal components lacked evidence of edge-loading or impingement (A-C). D-I, Components that presented with a raised area, often absent of scratches, in the centre of the component which may indicate the components' centre of rotation. E, Edge-loading present at the bottom-left of the component. G-I are Hintegra TARs showing similar damage patterns to the AES TAR (A-F).

The nine normal TARs typically featured less surface deviation from flat, visually, relatively to edge-loaded and impinged bearing inserts. However, a circular raised feature had developed in 19 devices (43%) (Figure 7.7). This feature occurred on the surfaces of the AES (2nd Gen), AES (1st Gen) and Hintegra TARs, although the feature was elongated for the Hintegra TARs.

Of the AES (2nd Gen) TARs, 86% were either edge-loaded (66%) (Figure 7.8) or impinged (21%) (Figure 7.9), resulting in four (14%) devices being considered normal. All of the BP and Mobility TARs were impinged. All of the Hintegra devices were edge-loaded. The AES (1st Gen) devices were 50% normal and 50% edge loaded. Both of the Rebalance TARs were considered normal.
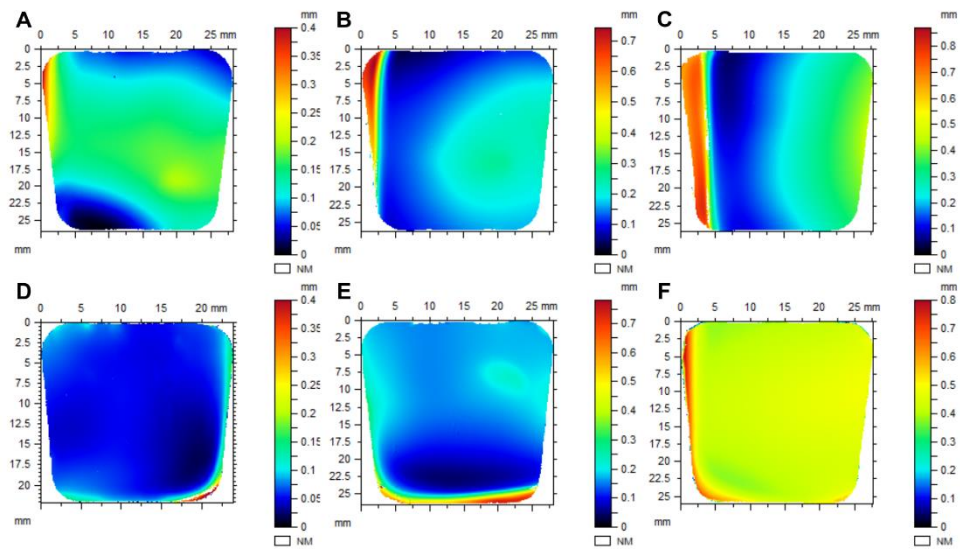
Figure 7.8. 'Edge-loaded' bearing inserts. Edge-loading presented as an inflection of deformed material near the edge of the component. A-C, Components with edge-loading at the medio-lateral edges. B-F, Components with edge-loading at the posterior edge.

Edge-loading and impingement were not mutually exclusive. Six of the 10 impinged inserts were also edge-loaded, therefore, in total, 70.5% of the inserts were edge-loaded including those with impingement. One BP TAR was impinged and edge-loaded, and featured machining marks at the peak of the edge-loaded inflection of material despite having been implanted for more than 10 years (139 months) (Figure 7.9F).
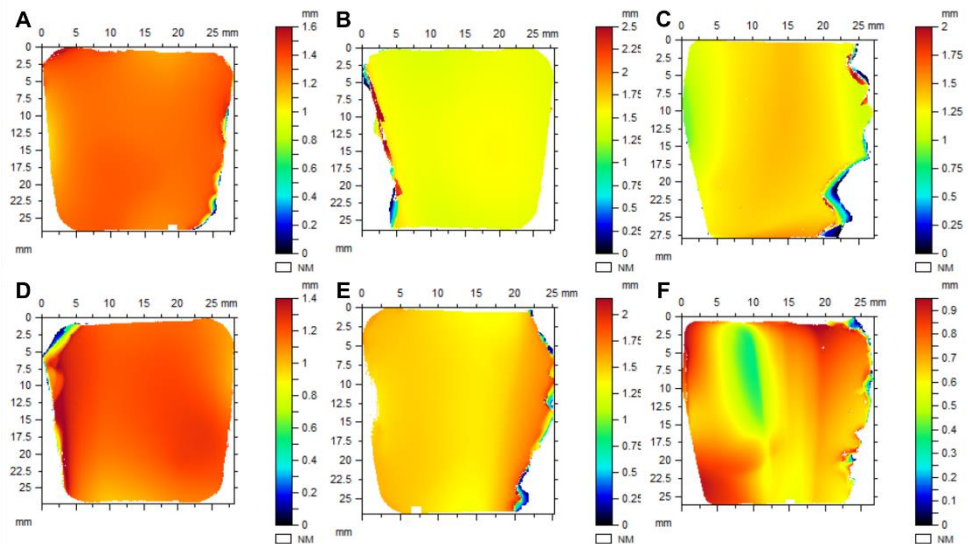
Figure 7.9. 'Impinged' bearing inserts. Impingement resulted in gross loss of material presumably on hard tissue (e.g. bone). A-C, Impinged bearing inserts without evidence of edge-loading. D-F, Impinged bearing inserts with evidence of edge-loading.

Independent of the 'minor' impingement identified on the bearing surface inferior surface in section 6.6.4, nine TARs were considered normal. However if minor impingement is included in the analysis, three devices remain with no evidence of edge-loading, impingement or minor bone contact.

Damage Extent

Normal inserts had the lowest mean maximum height (Sz) at 183.01 µm (± 111.32 µm SD) followed by edge-loading at 251.65 µm (± 175.99 µm SD). Impinged inserts had a significantly larger mean maximum height at 861.54 µm (± 560.56 µm SD) (p<0.05). Large variances were evident within groups and represented the differences in wear and deformation between individual components.

Edge-loaded components featured an inflection of material which was essentially a raised area relative to the majority of the rest of the surface. Impingement represented the inverse of this, areas of gross material loss resulting in deep gouges in the surface relative to the majority of the surface.

Differences in the distribution of surface heights between edge-loaded, normal and impinged bearing inserts could be distinguished using Abbott-Firestone curves (Figure 7.10). For the bearing insert surfaces considered normal, the distribution of surface heights were symmetrical about the mean. The mean surface height for normal bearing inserts occurred at 50.1% of the cumulative distribution curve.

The mean surface height for edge-loaded bearing inserts occurred at 27.0% of the cumulative distribution curve, whereas for impinged components, the mean surface height occurred at 86%. These percentages represent the proportion of the maximum

height above the mean height for each condition. Edge-loaded components featured a minority (27.0%) of relatively high peaks compared to the remainder of the distribution curve. Whereas, impinged devices featured a minority (14.0%) of relatively low dales compared to the remainder of the distribution curve.
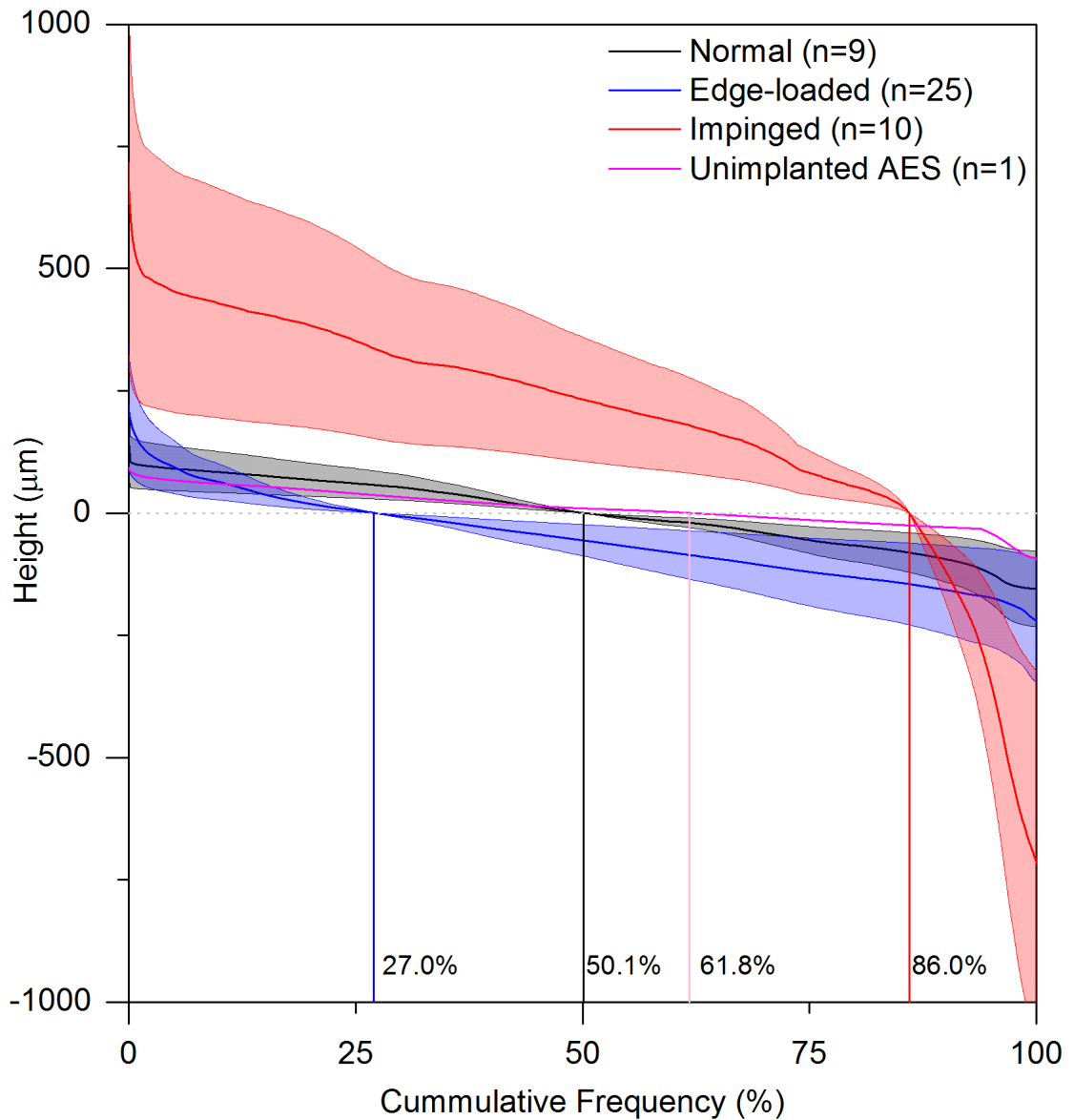
Figure 7.10. Mean Abbott-Firestone curves for the stratified bearing insert conditions (normal, edge-loaded and impinged). The magenta line represents an unimplanted and unworn Ankle Evolutive System (AES) bearing insert.

The differences in surface height symmetry about the mean between groups was reflected in the stratified surface height parameters (see section 7.4.4.2). The parameters Sk (p = 0.11) and Spk (p = 0.12) were not significantly different between all three insert conditions (Figure 7.11). Impinged bearing inserts featured a significantly greater peak dale height (Svk) relative to both edge-loaded and normal inserts.
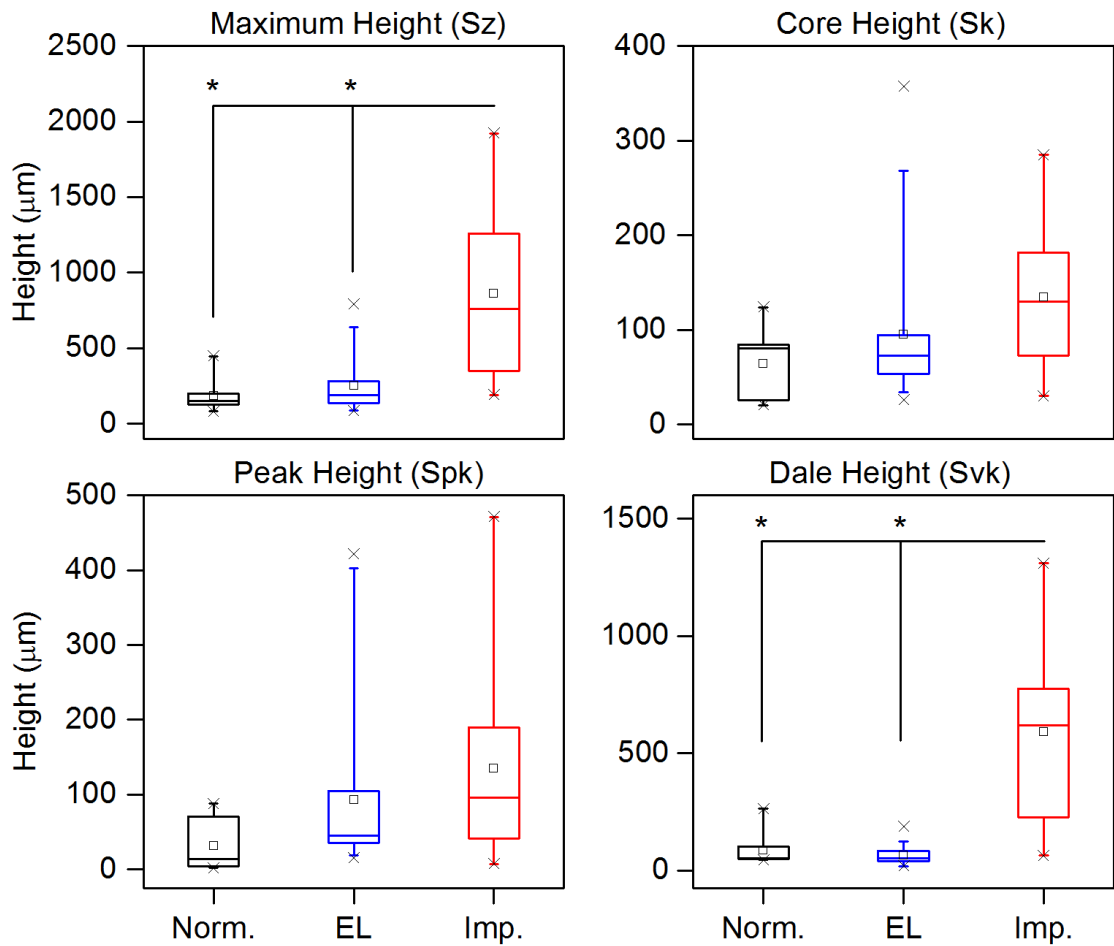
Figure 7.11. Surface height parameter results compared for all included bearing inserts (n = 44) stratified to normal (Norm.), edge-loaded (EL) and impingement (Imp.) groups. * ANOVA (p < 0.05).

Damage Location

The location of edge-loading occurred equally between the lateral (n = 16) and medial (n = 16) edges (Figure 7.12). Six devices had edge-loading on more than one surface, often either the medial or lateral edge in combination with the posterior edge. No inserts were solely edge-loaded on the anterior edge.

Impingement (including minor and gross wear) occurred primarily on the medial (n = 8) and posterior edge (n = 8). Impingement was absent from at the antero-lateral edge for all inserts.
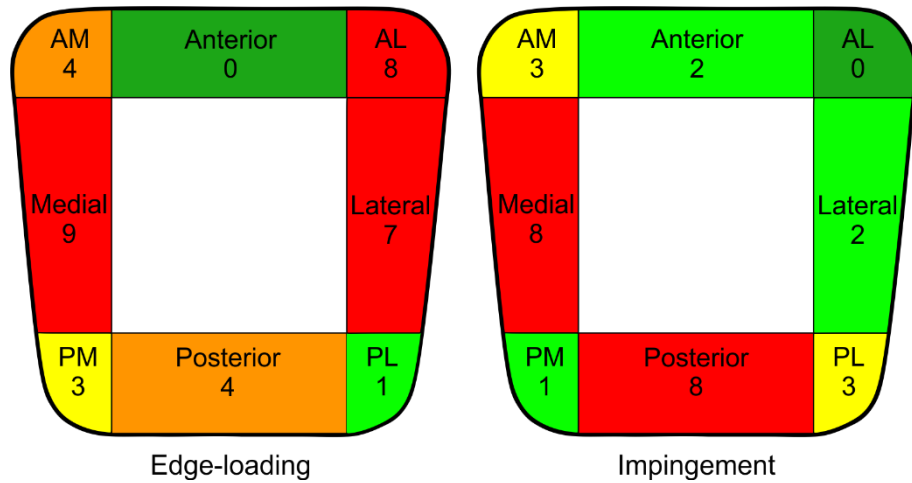
Figure 7.12. Location of edge-loading (A) and any bone contact (including impingement) (B). AM, Antero-medial. AL, Antero-lateral. PM, Postero-medial. PL, Postero-lateral.

In Chapter 5, the medio-lateral offset of 22 bearing inserts relative to the tibial axis was determined. For the same devices, medial and lateral edge-loading location were compared for medio-lateral offset ratio (MOR) and a significant difference was identified between medial (MOR: medial 7.2 ± 1.4) and lateral (MOR: lateral -9.0 ± 13.0) edge-loading locations (p = 0.02) (Figure 7.13). The MOR values are a distance measurement relative to the width of the tibial component. Therefore, bearing inserts edge-loaded on their lateral edge are 9% of the width of the tibial component from the tibial axis, whereas inserts edge-loaded on their medial edge are 7.2%. This equates to 3.1 mm and 2.5 mm for lateral and medial groups, respectively.
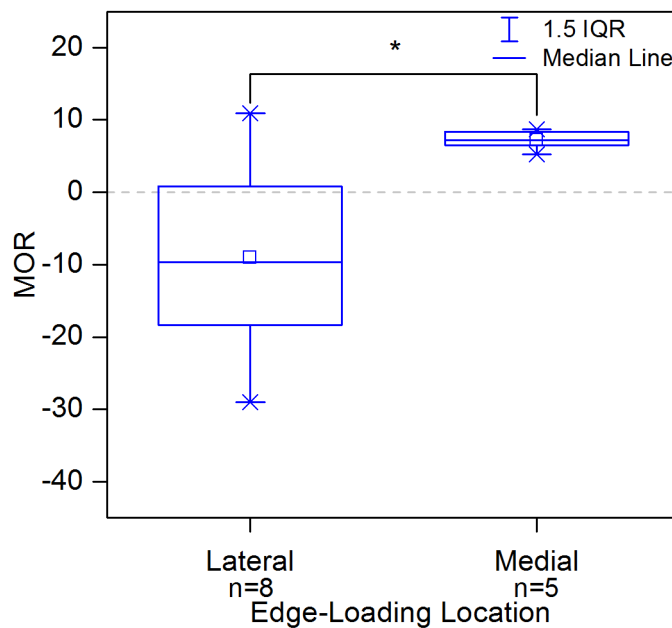
Figure 7.13. Comparison of medio-lateral offset ratio (MOR) for bearing inserts with medial and lateral side edge loading.Bearing inserts with only posterior edge loading were excluded from the analysis due to the low frequency. * Independent t-test (p < 0.05).

7.6   Discussion

After implantation, the superior surface of each bearing insert underwent geometrical changes that deviated from 'flat'. The retrieved bearing inserts were considered primarily edge-loaded (57%), impinged (23%) or 'normal' (20%). Edge-loading was identified by an inflection of material, characteristic of deformation caused by the offset between the bearing insert and tibial component. On average, the inflection of material was 252 ± 176 μm in height. For several devices, the manufacturing marks remained present at the peak of the deformed material suggesting the edge-loading occurred early after implantation. Morgan et al. (2010) identified ten patients with edge-loading of the AES TAR who required corrective surgery within the first post-operative year. Contrary to these early failures, one BP TAR from the current study featured machining marks on the deformed edge after being in-vivo for 139 months. This example shows an implant can survive 10 years in vivo after undergoing edge-loading early in its lifetime. Despite this, edge-loading identified using X-ray imaging is sufficient to warrant revision surgery (Morgan et al., 2010). CT imaging is more effective than X-ray imaging for its detection (Chapter 5) and retrieval analysis methods such as those implemented in this chapter are more accurate than CT for identifying the prevalence of edge-loading.

The medio-lateral offset ratio (MOR), as defined in section 5.5.1.2, was significantly different between components edge-loaded medially and laterally. On average, medially edge-loaded bearing inserts were offset from the tibial axis by 2.5 mm and laterally edge-loaded components were offset by 3.1 mm. This suggests independent of tibial component location, a 2.5 mm bearing insert medio-lateral offset is sufficient to create conditions by which edge-loading is likely. Rippstein et al. (2011) defined edge-loading as a mismatch of translational alignment in the coronal plane between the tibial and talar component by at least 2 mm. While the value reported by Rippstein et al. (2011) corroborates with the results from the current study, this metric does not separate rotation from translation, which are equally important for the risk of edge-loading. From the medical imaging analysis (see section 5.5.2.2), the bearing insert with the least translation also featured the greatest axial rotation. This bearing insert was considered edge-loaded from the medical imaging which corroborated with an inspection of the component. Multiple factors contribute to the cause of edge loading, the current study shows component translation and rotation are important and clinically relevant.

Impingement of the bearing insert was defined by gross material loss at the edge of the bearing insert. This was reflected in the quantitative characteristics which showed high peaks, characteristic of fractured and highly deformed material, and low dales representative of material wear. Impingement was likely caused by an interaction with

surrounding bone/hard tissue, which is supported by the results from the CT medical imaging (see section 5.5.2.2). Stereomicroscopic examination of the bearing inserts for 35 mobile-bearing STAR devices was undertaken for a US Food and Drugs Administration (FDA) pre-market approval application (Small Bones Innovations Inc., 2007). Nine STAR devices (26%) presented with gross material loss at the bearing insert edges which was speculated to be caused by impingement on bone. This result was similar to the rates of gross material loss reported in the current study (23%). Koivu et al. (2012) identified masses of necrotic bone particles in the periprosthetic tissue surrounding failed AES TARs. It was speculated that the necrotic bone particles originated from the bone-implant interface or due to ischemic damage of the talar component bone. However, impingement damage between the bearing insert and the surrounding anatomy was not reported or suggested as a possible cause. This may have been because Koivu et al. (2012) investigated histology slides independent of the context of the explant or CT imaging. Impingement occurred predominantly on the medial and posterior sides of the bearing insert. The TAR device is typically positioned as close to the junction of the medial malleolus and the tibial plateau as possible, therefore the proximity of the bearing insert to this bony anatomy makes impingement more likely, in the absence of heterotopic ossifications.

Edge-loading and impingement were not mutually exclusive which was evident from both this retrieval analysis and the associated medical imaging (see chapter 5.5.2.2). For several cases of impingement, evidence of material deformation consistent with edge-loading was present. This may suggest that for these cases, the bearing insert was offset sufficiently to be edge-loaded and sufficiently proximate to bone for impingement. Whereas several bearing inserts featured impingement independently of edge-loading. Analysis of the medical imaging showed hard tissue growth (i.e. heterotopic ossifications) within the joint space for several TARs which may have been the cause of damage to the bearing insert in these cases.

When all three damage modes: edge-loading, gross impingement, and minor impingement (as identified in Chapter 6) were accounted for, the retrieved bearing inserts were either considered edge-loaded (70.5%), impinged (57%) or normal (7%).

'Normal' bearing inserts lacked edge-loading and impingement. On average, the surface height of the normal devices was 183 ± 111 µm. Affatato et al. (2009) used a coordinate measuring machine (CMM) to identify surface changes for three explanted mobile-bearing BOX TAR bearing insert. The surface height change was between 25 and 91 µm which was at least half the surface height measured for the normal devices in the current study. The implantation time for the three BOX TARs was 24, 24 and 9 months which was substantially less than the average 88 months implantation time for the current

study and may have affected the extent of surface change. Also, Affatato et al. (2009) reported the surface change relative to a computational model because the surface geometry is curved for the BOX TAR design, whereas the surface height reported in the current study was the surface height without a comparator. The superior surface of the TAR designs included in the current study were designed flat, therefore, these two studies cannot be compared directly. Affatato et al. (2009) measured surface height change from an ideal model and the current study identified the objective surface height relative to itself without a comparator.

The surface heights representing normal bearing inserts were symmetrical about the mean and represented a normal distribution curve. Edge-loaded components featured a negatively skewed distribution suggesting the majority of surface heights were below the mean. Whereas, impinged bearing inserts showed a positively skewed surface height distribution. Simply put, normal bearing insert surfaces had not worn flat but had equal amounts of peaks and dales. Edge-loaded components featured a higher percentage of peaks relative to the rest of the surface (i.e. deformed material) and impinged devices featured more dales relative to the rest of the surface (i.e. missing material). Despite the difference between the height distribution curves, there were no statistical differences in the surface characteristics between normal and edge-loaded bearing inserts. Raised surface features indicative of wear, deformation and the change in conformity between the two articulating surfaces created the high variance of surface heights within groups, particularly for the devices considered normal. The raised features were generally circular for the AES TARs but elongated for the Hintegra TARs. The different pattern for the Hintegra TARs may be due to the fact that the Hintegra design restricts inversion and eversion motion at the talar component, and may lead to a different wear pattern (Hintermann et al., 2004). However, only a small sample of three Hintegra TARs were retrieved and analysed.

The origin of the damage modes in this section is likely caused by component position variance (rotation and translation) and bone contact (possibly ossifications).

7.6.1 Limitations

The non-contacting quantitative method used in the current study could only be applied to the superior bearing insert surface as curvatures greater than ~ 20°, such as those on the inferior bearing insert surface, cannot be measured. Therefore the effect of edge-loading on the other surfaces could not be determined using this method. Manufacturing tolerances could not be accounted for in this analysis. The superior bearing insert surface for all TAR brands included in this analysis were presumed to be manufactured 'flat'. Although, only the variance of surface geometry was compared between conditions, no comparison to 'flat' was made throughout the analysis. Post-processing of the raw data

was required to remove observer error caused by minor differences in the component set up between scans. For example, a planar levelling filter was used to ensure consistent angular misplacements of the component were removed after data acquisition. However, care was taken to ensure the post-processed datasets were not manipulated to an extent that changed the results. Identifying damage modes from the surface height data by itself was not possible. Substantial geometrical changes resulting in a large distribution of surface heights was evident for normal, edge-loading and impinged bearing inserts. Also, surface height parameters were not statistically different between normal and edge-loading conditions. Therefore, the damage modes were required to be identified subjectively by an observer. Two observers viewed each TAR independently to improve the reliability of the damage mode stratification. Finally, only geometrical changes, not wear volume loss, could not be determined using this type of analysis. A volumetric wear analysis such as that undertaken in the following chapter (Chapter 8) is required to determine volumetric wear loss.

7.7 Summary

Edge-loading affected 70.5% of the cohort either independent of- or combined with impingement. Gross impingement affected Ten TARs (22.7%). Only three bearing inserts were absent of edge-loading, impingement and 'minor' impingement which was identified in Chapter 6.

The magnitude of surface geometry change for bearing inserts considered 'normal' was substantial relative to an unimplanted TAR, although the distribution of surface heights was symmetrical about the mean. Edge-loaded TARs featured a 252 µm inflection of material, on average. Material deformation of this magnitude may be sufficient to constrain the bearing insert to the affected side of the tibial component.

Edge-loading occurred evenly on both medial (n=16) and lateral (n=16) edges of the bearing inserts. The average medio-lateral offset from the tibial axis was 3.1 mm and 2.5 mm for laterally and medially edge-loaded components. Therefore, >2 mm offsets should be considered clinically relevant for identifying edge-loading. Impingement (including minor and gross wear) occurred primarily on the medial (n=8) and posterior edge (n=8). This was likely related to anatomical constraints created by the surrounding bone, the medial malleolus in particular.

The next chapter investigates the total volume loss affecting retrieved TAR bearing inserts.

Chapter 8
Volumetric Wear Analysis of the Bearing Insert

8.1 Introduction

Wear particle induced osteolysis is a limiting factor for total joint replacement longevity and commonly causes loosening of the device and failure (Ingham and Fisher, 2000). Wear volume, in addition to wear particle size, morphology and composition, is critical to the development of osteolysis (Tipper et al., 2000, Hallab and Jacobs, 2009). While osteolysis is prevalent in TAR, excessive primary bearing wear is not commonly identified as an indication for TAR failure (National Joint Registry, 2017). The early onset of osteolysis has led some authors to favour other hypotheses for TAR failure such as insufficient component fixation (Koivu et al., 2009, Besse, 2015) and stress shielding (Waizy et al., 2017) rather than the rapid accrual of biological reactive UHMWPE wear particles.

The indication for failure for 98% of TARs retrieved for the research in this thesis was osteolysis and/or pain and only seven TARs (16%) were implanted for more than 10 years (see Chapter 3). Several indicators of primary bearing wear were identified in Chapter 6, these include:

- Roughened tibial component bearing surfaces suggesting third body abrasion.
- Embedded debris in the bearing insert also suggesting third body abrasion.
- Scratching, burnishing and abrasion on the bearing insert bearing surfaces indicative of wear.
- Asymmetrical wear/deformation patterns on the inferior bearing insert surface.
- Impingement damage resulting in gross material loss.

In addition to the damage modes listed, substantial geometrical changes were measured at the superior bearing insert surface in Chapter 7. Identifying the quantity of wear produced by these damage modes will further inform hypotheses of TAR failure.

Currently, the wear rates of TAR have only been established from in vitro simulation studies (Affatato et al., 2007, Bell and Fisher, 2007, Bischoff et al., 2015, Reinders et al., 2015, Smyth et al., 2017). The wear rates reported for a range of different TARs were between 2.1 and 25.8 mm^3 per million cycles which was considered comparable to the wear of total knee replacements (TKR) (Affatato et al., 2007, Bell and Fisher, 2007, Bischoff et al., 2015, Smyth et al., 2017). The validation of wear simulators often takes

the form of a damage mode comparison between the wear tested samples and explants (Affatato et al., 2009, Smyth et al., 2017). However clinically relevant wear rates have yet to be determined for TAR using wear volume analyses.

Gravimetric analysis is the gold standard method for calculating component volume in orthopaedic applications, particularly for determining wear loss for in vitro simulations (Affatato et al., 2007, Bell and Fisher, 2007, Bischoff et al., 2015, Reinders et al., 2015, Smyth et al., 2017). The measurements are simple to acquire and the equipment is low cost and commonly found in engineering laboratories. The limitations of gravimetric analysis include the fact measurement accuracy can be affected by adsorbed liquids and the requirement for the component material density to be known. Sometimes the material density is not known, such as the vitamin E infused UHMWPE used in the Rebalance TAR. The Rebalance TAR is currently being implanted but technically remains in development under controlled release (Harris et al., 2014). A consequence of which is that material properties have not been published by the manufacturers. In the case that a retrieval laboratory receives a device with a material of unknown density (e.g. a new composite), pycnometry or computed tomography may be a viable alternative to gravimetric analyses for calculating volumetric loss.

Pycnometry is yet to be used for determining orthopaedic component volume however its strengths compared to gravimetric analysis includes that it does not rely on the assumption of material density and fluid absorption does not affect volume measurements (Muratoglu et al., 2003).

Computed tomography (CT) is an imaging modality that uses X-ray technology to create three-dimensional images of the target material's radiodensity. Unlike gravimetric analysis or pycnometry, CT analysis provides spatial information of wear volumetric loss which is valuable because this can be related to component alignment or previously identified damage modes. Methodologies using CT have been developed to identify wear loss in TKR (Teeter et al., 2011a, Teeter et al., 2011b, Teeter et al., 2014), glenoid components (Day et al., 2012), uni-compartmental knee replacement (Teeter et al., 2017) and acetabular liners (Bowden et al., 2005, Teeter et al., 2010), however it has not been used to identify wear volumetric loss in TAR. Cottrino et al. (2016) used CT to identify embedded debris in the bearing insert of an AES TAR, however volumetric loss was not determined and details of the method used to capture the bearing insert was not reported. Computed tomography is a highly complex method of determining volumetric loss, often requiring an expert user. Yet, this modality has the capacity to create spatial maps and location specific quantitative comparisons of wear.

The aim of this chapter was to:

- Quantify and locate the volumetric wear loss for retrieved TAR bearing inserts.

The objectives were to:

- Identify the total volumetric loss of retrieved bearing inserts using established gravimetric analyses and estimated material properties.
- Validate the measures of total volumetric loss determined using gravimetric analyses with pycnometry.
- Develop and apply a novel method for identifying the spatial distribution and volume change using computed tomography.

8.2 Explant Details

Eight bearing inserts were analysed, all of which were 5 mm AES (2nd Gen) bearing inserts (Table 8.1). An unimplanted comparator was used to determine volumetric loss which was also a 5 mm AES (2nd Gen) bearing insert.

Table 8.1. Summary of demographic and device details for TARs included for wear volume analysis.

Factor		n	Factor	Mean (range)
Total		8	Time In vivo (Mo) Missing[a] (n)	88.7 (70-109) 2
Device Type	AES (2nd generation)	8	Age (years) Missing[a] (n)	66 (55-71) 2
Side	Right Left	2 6		
Sex	Male Female	8 0		
Diagnosis	OA PTOA Missing[a]	4 3 1		
Indicator for Revision	Osteolysis	8		

Notes: AES, Ankle Evolutive System (Transysteme, Fr); [a] Data not available; Age was true at the time of primary surgery; OA, osteoarthritis; PTOA, post-traumatic osteoarthritis; n, frequency; Mo, Months. All of the bearing inserts were 5 mm.

8.3   Methods

8.3.1   Gravimetric Analysis

All of the included explants had been retrieved and dried for a minimum of one month prior to gravimetric analysis. Each of the components were cleaned thoroughly using a soft brush, distilled water and 70% (v/v) isopropanol to ensure all contaminants were removed. The bearing inserts were air dried for at least 72 hours in a controlled environment prior to analysis.

The bearing inserts were weighed using a Mettler XP205 balance (Mettler Toledo, UK) with a resolution of 0.01 mg. Five measurements were captured per bearing insert and the mean was accepted as the final weight. The weight was converted to volume (mm^3) using Equation 2.2 (see section 2.5.2.5).

8.3.2   Pycnometry

Pycnometry is a measurement method that uses pressurised gas to calculate a volume of a material previously unknown (see section 2.5.2.5). The assumptions of the pycnometer can be controlled and measured (e.g. temperature, gas constants) rather than assumed, like material density for gravimetric analysis. Since the withdrawal of the AES TAR in 2012, information about the device design can only be found in the published literature. Documents from the manufacturer about the materials and methods used to fabricate the device are not available. The AES TAR featured non-crosslinked UHMWPE as the material for the bearing insert however, the exact material properties have not been reported. The density of non-crosslinked UHMWPE is typically 0.93 g/cm^3 and was presumed to be the density of the bearing inserts tested in this study.

A Pycnomatic (Meritics, UK) pycnometer was used with helium gas and the temperature controlled to 21°C by internal thermoregulators. Five measurements of volume were captured automatically by the pycnometer and the average calculated.

8.3.3   Computed Tomography

Several factors needed to be considered throughout the process of CT scanning TAR bearing inserts, such as: scan orientation, artefact reduction, image acquisition parameters, image post-processing and measurement. The following sections detail these factors.

8.3.3.1   Bearing Insert Orientation

Radiopaque markers attenuate X-rays and create artefacts. In previous studies, radiopaque markers on the components CT scanned were external to the bulk material

and easily removed prior to scanning. The TAR Bearing inserts in this project were composed of a UHMWPE bulk with metallic radiopaque tags embedded centrally. Destructive methods would have been required to extract them which was not possible for this cohort as the donors had not consented to destructive testing. To reduce the effect of metal artefact, the orientation of the component within the scanner was optimised.

An initial study of bearing insert orientation was conducted to minimise computational expense and metal artefact. Two bearing insert orientations were explored (Figure 8.1). CT scanner slice orientation was axial and fixed relative to the polymeric sample container. One possible orientation was the bearing insert resting on the posterior edge (Figure 8.1B). However, the further the sample extended in the axial plane, the more slices were required to capture the entire component. Also, metal artefact occurred in the slice plane (i.e. axial plane, in this case), therefore to avoid disruption to the bearing surfaces, the bearing insert orientation was changed so that neither bearing surface transected the axial plane.
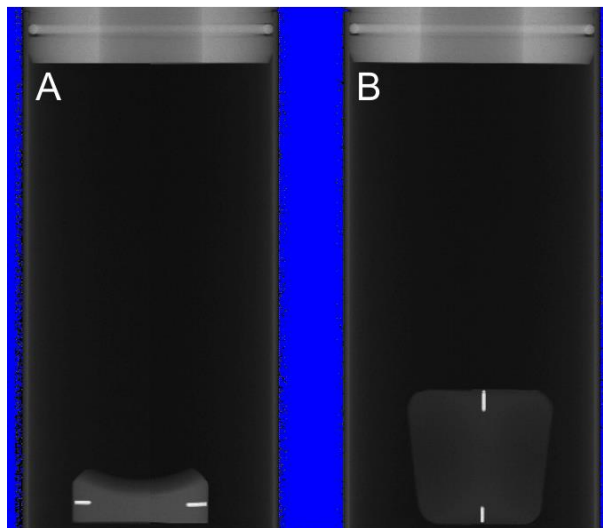
Figure 8.1. Two bearing insert orientations for computed tomography scanning. Orientation A was used for two reasons: 1) Scan height was proportional to scan file size and therefore computation cost. The low profile insert orientation reduced scan height; 2) The axial slice direction created metal artefacts which interfered with the bearing surface for orientation B and not for orientation A.

The bearing insert was placed with the superior surface facing towards the bottom of the sample container. This reduced the number of slices required to image the entire component and the metal artefact avoided the bearing surfaces.

With the component in its optimised position, metal artefact created a channel-like feature within the bearing insert which appeared like a manufactured feature (Figure 8.2). A cross-sectional scan was taken of the same component in a different orientation and the channel-like feature was determined to be an artefact (Figure 8.2D).
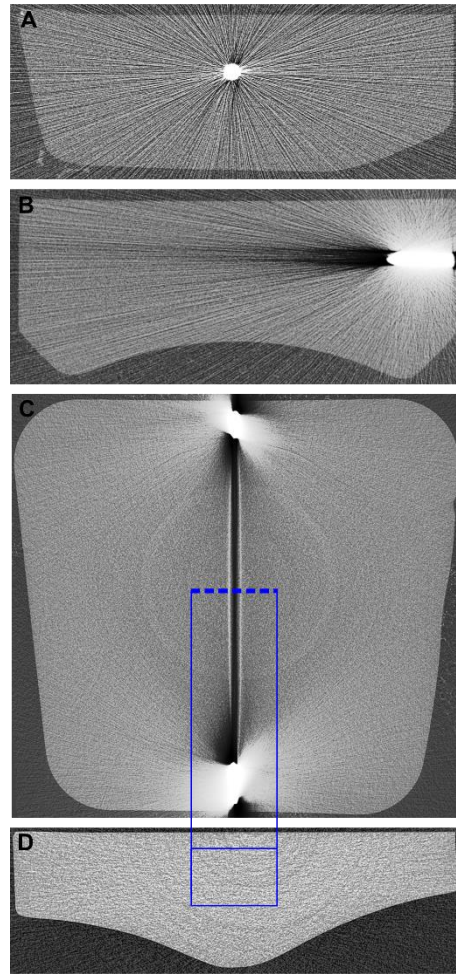
Figure 8.2. Computed tomography scan protocol development. A-C, Different scan orientations and the associated metal artefact. C, Axial scan orientation with a channel-like feature throughout the component. D, Cross-sectional scan captured to determine whether the channel-like feature was manufactured or a result of the artefact.

8.3.3.2 CT Acquisition Protocol

A µCT 100 (Scanco, Medical, CH) cabinet cone-beam microCT was used to scan each of the selected bearing inserts. Bearing inserts are composed of UHMWPE (low density) and metal radiopaque tags (high density). The parameters used were optimised to minimise metal artefact and effectively show the entirety of the UHMWPE aspect (Table 8.2).

Table 8.2. CT scan acquisition parameters.

Parameter	Value
Voltage	55 V
Current	72 A
Integration Time	200 µs
Number of Slices	~ 1150
Voxel Size (resolution)[a]	10 µm^3

Note: [a] Scan resolution was down-sampled to 30 µm^3 in post-processing.

UHMWPE formed the majority material of the bearing insert therefore the acquisition protocol reflected this (i.e. Low beam power and high resolution). Voltage and current dictate the X-ray beam intensity which was set as low because UHMWPE does not attenuate photons to a great extent.

A 0.5 mm aluminium mechanical filter was used to homogenise the beam intensity across the beam's width. Mechanical filters can reduce artefacts caused by stray low energy photons which create noise in the final image. The beam settings applied for this cohort of bearing inserts were focussed on the UHMWPE material, not metal. However, for one scan, maximum beam power and a 0.5 mm copper mechanical filter, typically used for high density materials, was implemented in an attempt to reduce metal artefact but metal artefact worsened. The amount of metal artefact was determined visually and easily identifiable as it appears very bright (Figure 8.2A).

Integration time is the amount of time the X-ray detector collects data. This parameter is balanced to ensure the resultant image is not overexposed and that the acquisition time is as short as practicable.

Resolution is also a parameter used to improve quality of image. CT scans are effectively a stack of 2D X-ray images compiled at a specified distance apart, known as the slice thickness (or z-axis resolution). Generally, image quality and resolution are proportional, therefore higher resolution is typically best. The higher the resolution, the greater the data file size and computational expense. The resolution for this cohort was 10 x 10 x 10 μm which was higher than the values reported in the previous literature (Bowden et al., 2005, Teeter et al., 2011a). Once each component had been scanned, the image files were exported as .Tiff files.

8.3.3.3   CT Post-processing

Once exported, each CT scan was processed in ScanIP (Simpleware, UK). Bearing insert orientation was optimised to minimise metal artefact disruption but post-processing was still required to remove residual artefact in order to acquire total volume.

Processing scans at an isotropic 10 μm resolution was too computationally expensive resulting in prolonged processing times and inoperable software, therefore each scan was resampled to 30 x 30 x 30 μm resolution.

Bearing inserts were positioned in the scanner manually and therefore slightly misaligned when compared with each other. The anterior surface of the bearing insert was used as the reference surface because this was the largest surface, manufactured flat and was generally absent of damage. The scans were aligned in two planes to ensure the anterior edge was in-line with the slice orientation. Each scan was cropped in all three planes to reduce the overall image file size.

Otsu thresholding was used to create the bulk mask of the bearing insert (Otsu, 1979). This thresholding method clusters grayscale values into a user defined number of bins which for the bearing inserts was three. These bins represented the: radiopaque marker/metal artefact (bright pixels), UHMWPE (mid-range pixel grayscale), and the background colour (dark pixels). This method effectively segmented the majority of bearing insert from the surrounding noise and background data.

Large holes created in the mask by the metal artefact were smoothed using the 'cavity fill' function and manual selection tools. The 'cavity fill' function filled enclosed voids within the bearing insert mask.

Extraneous noise outside of the mask introduced by metal artefact and the container to hold the bearing inserts in the scanner was eliminated using the 'flood fill' feature. By selecting the bearing insert mask using this function, all other masked regions in the image were deselected which included noise that wasn't in contact with the bearing insert mask.

Finally, the 'close' function was used to smooth noise in contact with the bearing insert. The 'close' function dilates and erodes the mask by three pixels creating a smoothed surface. These processing steps may have reduced the size of deep scratching or large pits, however this was balanced visually against the removal of metal artefact.

Finally, the masks were binarised and exported as metafiles, a file type compatible with ImageJ.

8.3.3.4   Volume Measurement Using CT

Using ImageJ, the area representing the bearing insert in each slice was measured using the 'Analyse Particles' feature. Total volume was calculated by summing all of the pixels in a bearing insert mask (Figure 8.3). Pixels were converted to mm^3. The measurement of area per slice was performed in both the anteroposterior and mediolateral planes so to isolate directional differences in wear. Area per slice data was interpolated to 1000 points to analyse the wear pattern across the bearing insert surfaces normalised to percentage of total length (or width, dependent on direction).
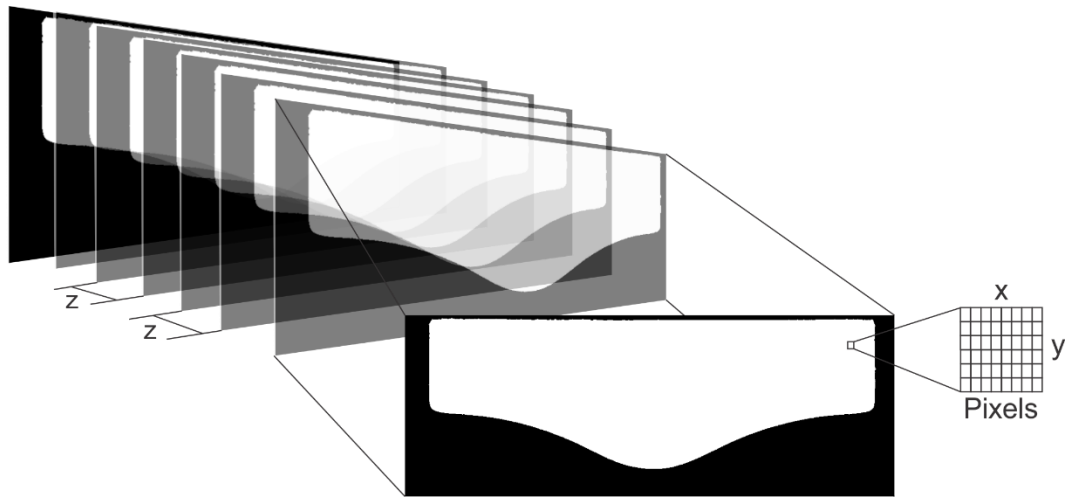
Figure 8.3. Bearing insert volume was calculated by the sum of calibrated voxels. Voxels were comprised of the sum of size of each XY pixel multiplied by the slice thickness (Z).

8.3.4 Statistics

Pearson's correlation coefficient (r) was used to test the association between gravimetric analysis, pycnometry, and computed tomography. All three methods for measuring bearing insert volume were compared using a repeated measures ANOVA. Volumetric loss of material from the explants relative to the unworn bearing insert was reported. The location of volumetric loss was assessed using CT slice-by-slice reductions in volume in both antero-posterior and medio-lateral planes and reported graphically. Colour maps were produced to show relative thickness of material in the axial plane.

8.4 Results

8.4.1 Gravimetric Analysis

The weight of the unimplanted 5 mm bearing insert was 4.59 g (± 1.7E^{-6} SD) which equated to a volume of 4930 mm^3. The mean weight loss for the explants was 0.34 g (± 0.23 SD) and the representative volumetric loss was 370 mm^3 (± 250 SD). The mean percentage of weight loss was 7.38% (± 4.92 SD).

One of the bearing inserts featured gross material loss consistent with impingement. The weight loss for this explant was 0.87 g (18.9%) which was more than double the material loss than the next highest wearing insert (8.0%); this insert was considered an outlier. The mean weight loss excluding the outlier was 0.26 g (± 0.08 SD) and the representative volumetric loss was 280 mm^3 (± 90 SD). The mean percentage of weight loss, excluding the outlier, was 5.74% (± 1.76 SD).

Six bearing inserts, excluding the outlier, had implantation time data available. A moderate correlation between volumetric loss and implantation time was identified (r = 0.63). Volumetric loss was 65 mm^3 per year (Figure 8.4).
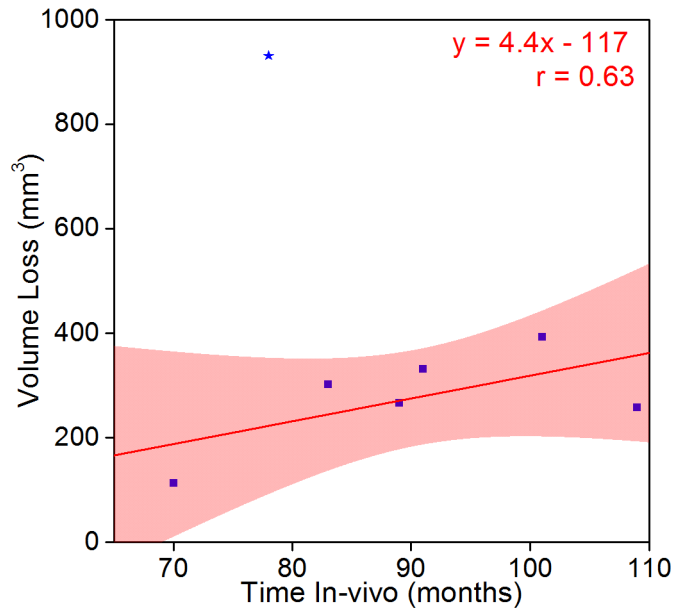
Figure 8.4. Volumetric loss over implantation duration for seven retrieved Ankle Evolutive System (AES) total ankle replacement bearing inserts. Pearson's correlation coefficient (r). Shaded red denotes 95% confidence interval. Star denotes outlier which was a grossly impinged component.

8.4.2 Pycnometric Analysis

The unimplanted 5 mm bearing insert had a volume of 4920 mm^3 (± 0.02 SD). The mean volumetric loss was 360 mm^3 (± 240 SD). The bearing insert featuring gross material loss (the outlier) had a volumetric loss of 930 mm^3. Mean volumetric loss (excluding the outlier), identified using pycnometry, was 280 mm^3 (± 90 SD; range: 120 to 400 mm^3). Volume measurements determined using pycnometry were highly correlated (r = 0.99) with the measurements from the gravimetric analysis (Figure 8.5).
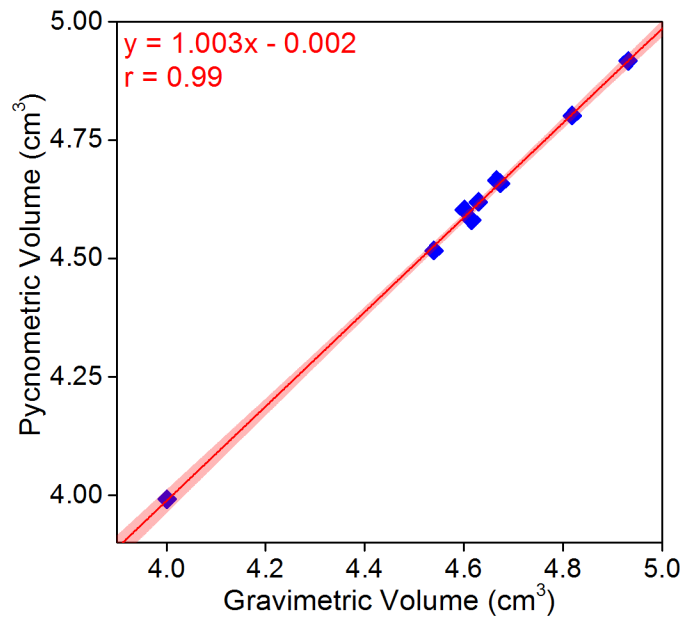
Figure 8.5. Volumetric loss measured by two methods, gravimetric analysis and pycnometry. Pearson's correlation coefficient (r). Shaded red denotes 95% confidence interval.

8.4.3 Computed Tomography

The unimplanted 5 mm bearing insert had a volume of 5470 mm^3, which was 540 mm^3 and 560 mm^3 more than the volume calculated by gravimetric analysis and pycnometry, respectively.

Bearing insert volume was strongly correlated with volume determined gravimetrically (r = 0.99) (Figure 8.6). However, a comparison of volume between the three measurement methods showed a significant difference for the CT measurement (p = 0.001) of a mean difference of 520 mm^3 (± 32 mm^3 SD).The variance associated with the mean difference was low, suggesting the magnitude of difference in volume was consistent for most of the bearing inserts. Despite the systematic difference, the mean percentage of volumetric loss, excluding the outlier, was 5.70% (± 1.64 SD), which was comparable to the outcome of the gravimetric analysis (5.74% (± 1.76 SD)).
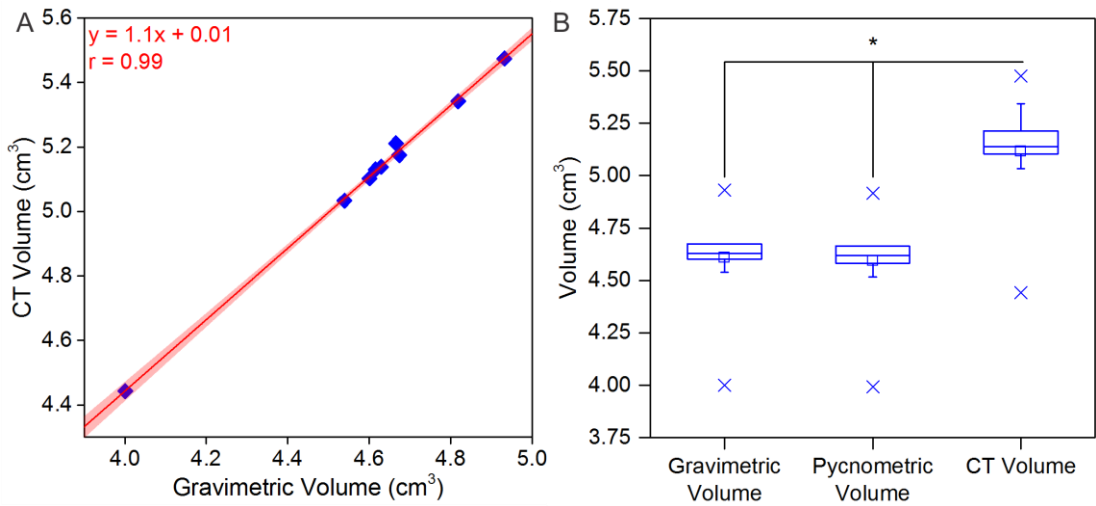
Figure 8.6. Comparison and association between volume measurement methods. A, Strong association between computed tomography (CT) and gravimetric analysis for measuring component volume (r = 0.99). However, CT volume was approximately 10% greater for all components measured (B). * ANOVA (p<0.05). Shaded red denotes 95% confidence interval.

Computed tomography can be used to produce 3D renderings and calculate location specific volumetric changes, unlike gravimetric analysis and pycnometry (Figure 8.7).

25 mm
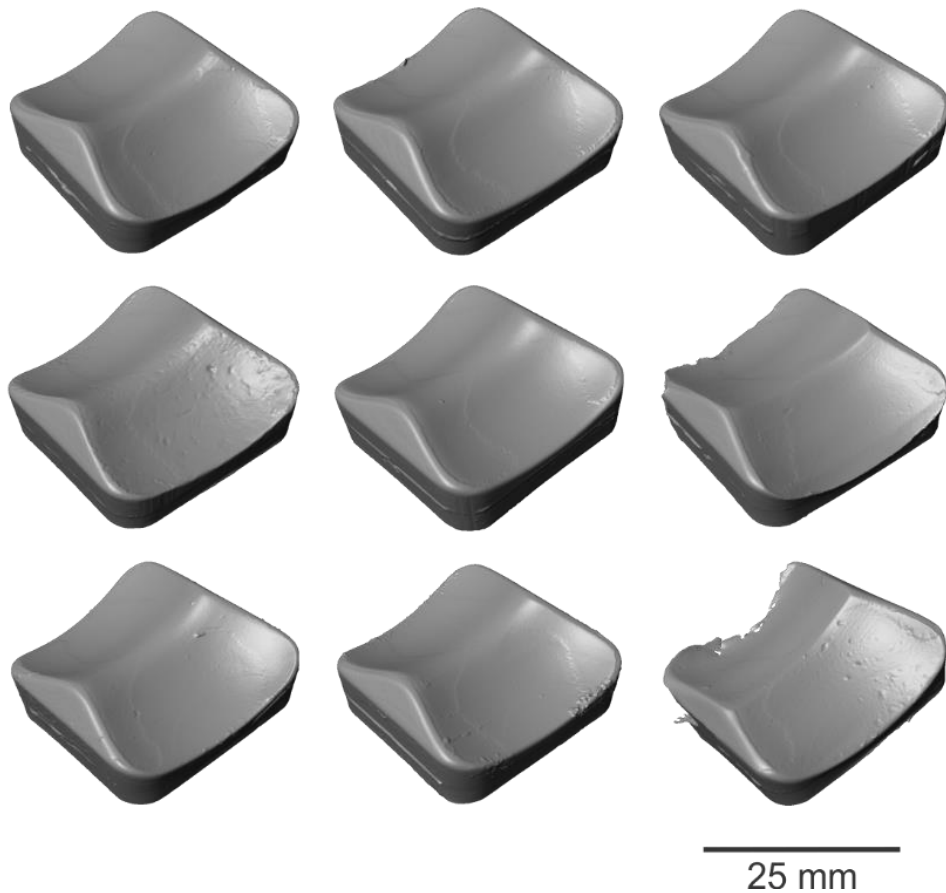
Figure 8.7. Three dimensional rendering of each bearing insert scanned using computed tomography.The inferior bearing insert surface is shown. Centre, Unimplanted bearing insert. All components were 5 mm Ankle Evolutive System (AES) total ankle replacements.

The unimplanted bearing insert was considered symmetrical in volume, given the difference in material volume between the medial and lateral sides was 0.2%. On average, the wear volume between the medial and lateral sides of the explant cohort was equivalent with a mean difference of 0.04%. Four bearing inserts featured more volume on the lateral side (4.9% ± 1.3 SD) and four featured more volume on the medial side (4.9% ± 2.8 SD). The largest asymmetry in volume was 8.8%, with more material on the medial side. This component was not the impinged bearing insert featuring gross material loss (outlier), which had 6.1% more volume on the medial side (Figure 8.8).
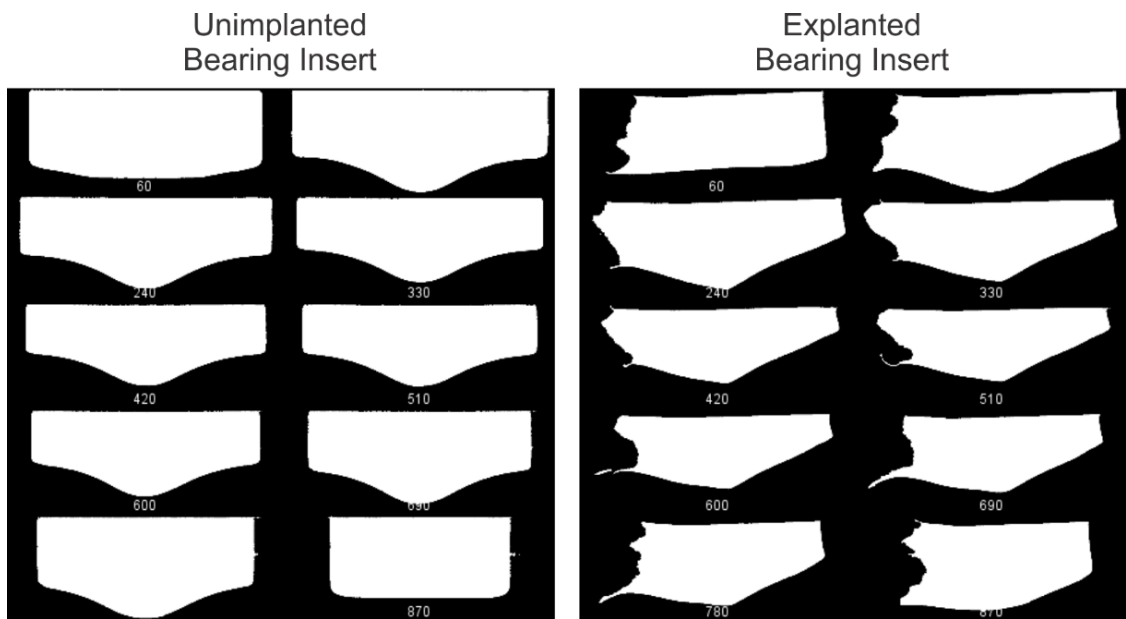
Figure 8.8. Matched CT slices between two bearing inserts. Left, unimplanted bearing insert. Right, impinged bearing insert. Note the asymmetry of wear throughout the explanted bearing insert.

When the bearing insert volume was orientated split between anterior and posterior sides, a 10.4% asymmetry in material volume towards the anterior of the device was evident. This was considered normal because the geometry of the bearing insert in this orientation was asymmetrical. On average, the explant cohort featured a 10.6% asymmetry which was 0.1% more than the unimplanted bearing insert and therefore, the wear was considered symmetrical, on average (Figure 8.9). Four bearing inserts featured more volume on the anterior side (2.5% ± 1.1 SD) and four featured more volume on the posterior side (2.9% ± 2.9 SD). The largest asymmetry in volume was the impinged bearing insert (outlier) with 7.9% more material at the posterior side.
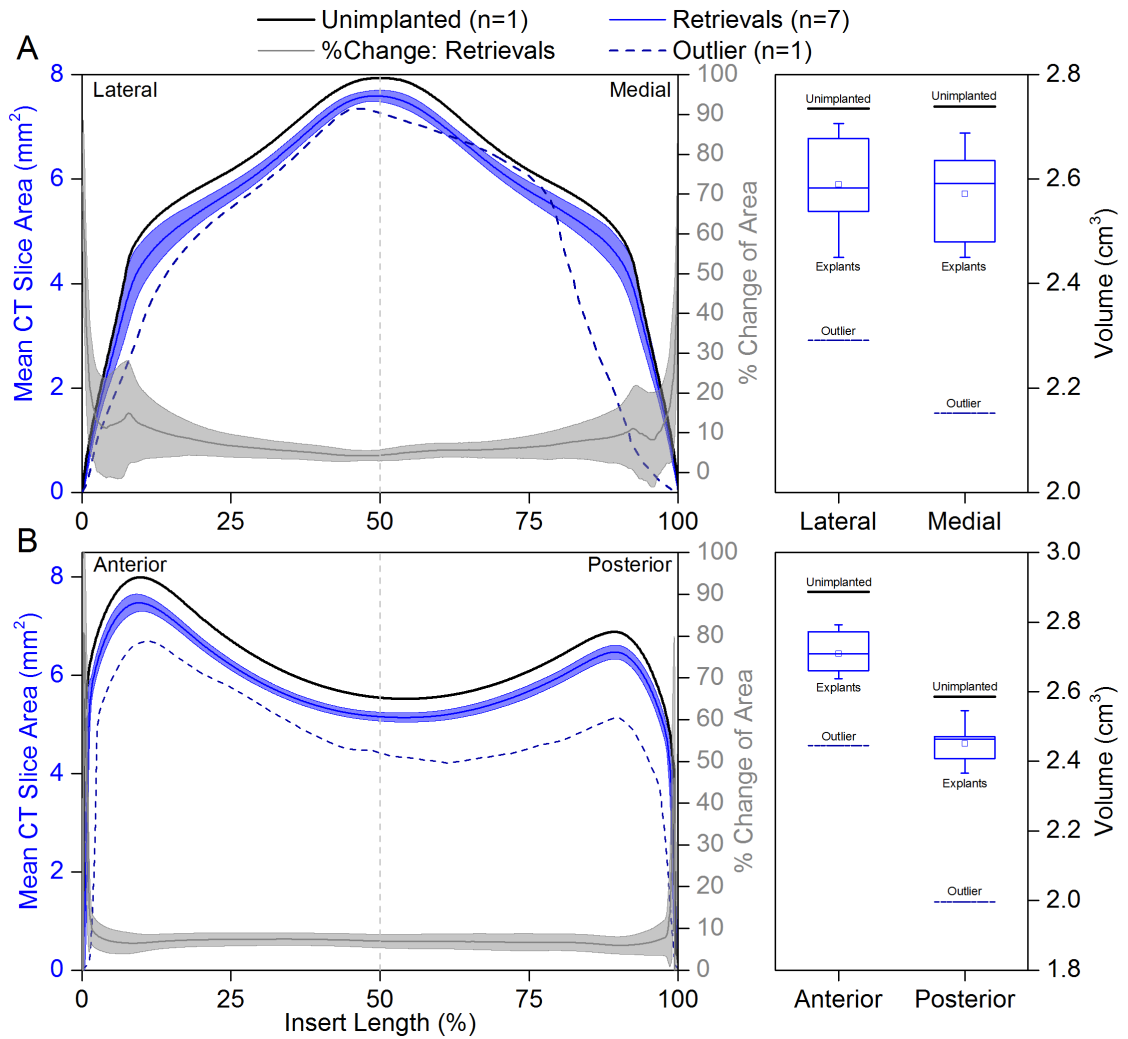
Figure 8.9. Mean change in CT slice area between retrieved 5mm Ankle Evolutive System (AES) bearing inserts compared to an unplanted bearing insert of the same brand and size. A, Medio-lateral view. B, Antero-posterior view. One of the inserts was impinged featuring gross material loss and was excluded as an outlier. Shaded blue area denotes one standard deviation. Medio-lateral and antero-posterior asymmetries are presented (right).

Colour maps showing the location of wear were produced (Figure 8.10 and Figure 8.11). Each of the images represent the relative thickness of the explant compared to the unimplanted bearing insert. The unimplanted bearing insert was symmetrical between the medial and lateral sides. The brighter shades of yellow represent regions of greater material thickness. The inferior 66% of each insert showed a concentration of wear towards the centre of component and along one edge of the component, usually on the opposing side (Figure 8.10).
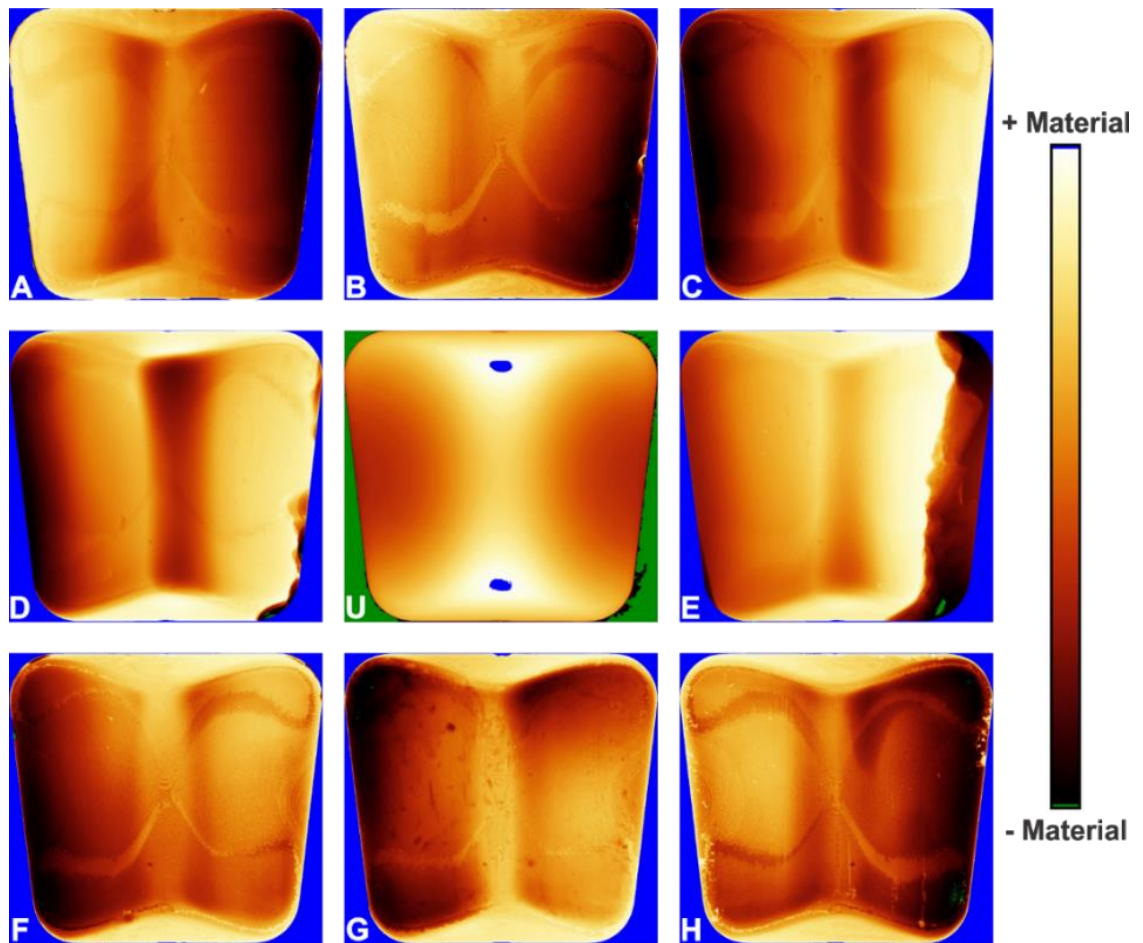
Figure 8.10. Thickness colour maps for the inferior surface of each bearing insert scanned by computed tomography (CT). The inferior 66% of the CT scan were compiled and subtracted from the unimplanted bearing insert (U). The thickness is represented relatively by colour; bright yellow is thicker than dark orange. Black is thinner than orange whereas green is zero thickness. Blue is the maximum thickness and is shown in the unimplanted bearing insert.

The superior 33% of each insert showed varied patterns of wear but a raised central region was common between devices (Figure 8.11). Edge loading was evident and presented as a bright yellow region representing a region of high material thickness. For the same edge-loaded components, the material thickness was low for the opposing side, as seen in the images of the inferior 66% of the corresponding explants. Impingement was also identified and represented a gross loss of material (Figure 8.11E).
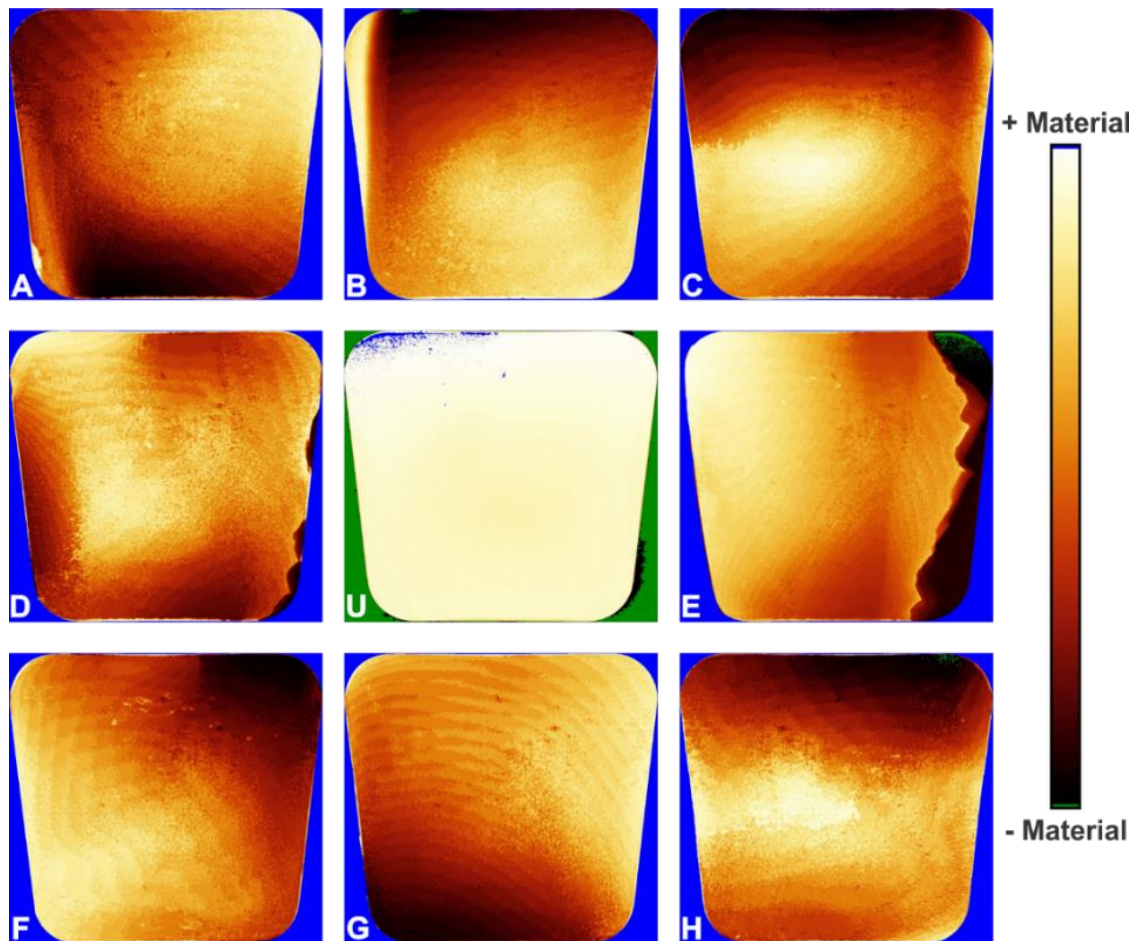
Figure 8.11. Thickness colour maps for the inferior surface of each bearing insert scanned by computed tomography (CT). The superior 33% of the CT scan was compiled and subtracted from the unimplanted bearing insert (U). The thickness is represented relatively by colour; bright yellow is thicker than dark orange. Black is thinner than orange whereas green is zero thickness. Blue is the maximum thickness and is shown in the unimplanted bearing insert.

8.5   Discussion

The gold standard method for determining volumetric loss in orthopaedic devices is gravimetric analysis (Affatato et al., 2007, Bell and Fisher, 2007, Bischoff et al., 2015, Reinders et al., 2015, Smyth et al., 2017). The retrieved bearing inserts in the current study featured a mean percentage weight loss of 7.4% (± 4.9 SD). However, one component underwent gross material loss caused by impingement and had lost 18.9% (0.87 g) of its mass. Therefore, excluding this component, the volumetric loss per year in vivo for the cohort was approximately 65 mm^3. Wear simulation studies for TAR are the only available wear loss TAR comparator, all of which report wear volumetric loss per million gait cycles (Affatato et al., 2007, Bell and Fisher, 2007, Bischoff et al., 2015, Reinders et al., 2015, Smyth et al., 2017). Three BP-style TAR devices have been simulator tested in vitro. Bell and Fisher (2007) tested BP and Mobility TARs and

reported wear rates of 16.4 ± 17.4 mm^3/Mc and 10.4 ± 14.7 mm^3/Mc, respectively. Smyth et al. (2017) tested the Zenith TAR using a range of kinematics based on the gait conditions defined by Bell and Fisher (2007). The maximum wear rate reported was 25.8 ± 3.1 mm^3/Mc, although the wear rate decreased following this due to polishing of the bearing insert. Affatato et al. (2007) wear tested the BOX TAR using water rather than proteinaceous lubricant, and was therefore susceptible to tribological artefact and not considered clinically relevant. The wear rate calculated from explants in the current study was at least 2.5 times greater than the highest recorded wear rate by Smyth et al. (2017). An important difference between in vitro tested samples and explants is the presence of third-body debris. Third-body debris can exacerbate wear substantially and has been demonstrated previously using in vitro simulation (Schroeder et al., 2013). Schroeder et al. (2013) tested conventional UHMWPE uni-compartmental knee replacements doped with either bone particles or cement particles in an in vitro knee simulator. The wear rate remained unchanged after bone particles were introduced, but increased 5.7 times after being doped by bone cement particles. While TAR devices in Europe do not used bone cement, the relative increase in wear due to 3rd body wear is relevant but shows the importance of how the material properties of the debris may affect the outcome. Titanium, cobalt chromium alloy and HA have all been identified as third body wear particles in TAR (Koivu et al., 2009, Koivu et al., 2012, Dalat et al., 2013, van Wijngaarden et al., 2015, Schipper et al., 2017), yet no such wear tests featuring third-body wear have been published for TAR. The measurements captured in the current study are the first to report explant-derived wear rates for TAR devices. The limitations include a small sample size (six bearing inserts had implantation time recorded for the wear rate calculation) and the explants were failed devices, possibly caused in part, by high wear rates. Therefore, the reported wear rate cannot be assumed to be equivalent to well-functioning TARs.

Gravimetric analysis requires material density to be assumed. If the material density is unobtainable however, an estimate is required. With the development of modern biomaterials, it is possible a retrieval laboratory may encounter devices with unconventional materials with properties that may be unknown. Novel variations of UHMWPE, such as the vitamin E infused UHMWPE used for the Rebalance TAR, may have material properties different to that of the known characteristics of conventional UHMWPE. Therefore alternative methods for calculating component volume may be desired, if not, required. Pycnometry uses pressure change to determine unknown volumes and CT imaging recreates the component in 3D space for measurement, neither of which require material density to be assumed. Also, neither method is affected by fluid absorption, unlike gravimetric analysis (Muratoglu et al., 2003). Both pycnometry and CT imaging were shown to be very strongly correlated with gravimetric analysis (r = 0.99). However, CT imaging featured a systematic increase in measured volume of 52 mm^3.

This error was approximately 10% of the total volume measured and was likely a product of the post-processing filtering used to reduce the metal artefact caused by the radiopaque markers. Another source of error may have been insufficient calibration of the voxel size prior to image acquisition, given the repeatability of the error. Teeter et al. (2011a) compared gravimetric and CT measures of volume for TKR inserts, without radiopaque markers, and found a difference of 0.04% in volume. Bowden et al. (2005) completed a similar analysis with retrieved acetabular liners and identified differences of 0.6%. Therefore the error associated with CT imaging was substantial relative to the accuracy previously reported for other total joint replacements. Pycnometry was not significantly different to gravimetric analysis for measures of volume and is a valuable alternative.

Computed tomography allows spatial measures of volume change. Material thickness maps and a method of determining asymmetrical wear were developed. On average, the material volume was symmetrical between medial and lateral sides of the bearing insert. However, there was an equal number of bearing inserts with a medial asymmetry (n = 4; 4.9% ± 2.8 SD) as lateral asymmetry (n = 4; 4.9% ± 1.3 SD). In the analysis of the superior bearing insert surface (Chapter 7), edge-loading was found to occur equivalently on both medial and lateral sides. In this current study however, not all of the components tested were edge-loaded which suggests asymmetrical wear is not solely an outcome of edge-loading. Espinosa et al. (2010) used a finite element model to determine stress concentrations within the Mobility TAR under static load in a range of component malalignment scenarios. The talar component was orientated in version by 2°, 5° and 10°. Contact stresses shifted markedly to the edge of the component for all three version angles. It was also noted, the same pattern was observed when the tibial component was in version instead of the talar component. The patterns described by Espinosa et al. (2010) were simulacra to the wear patterns observed in the current study. It is plausible, offsets in version angle between the tibial and talar components led to the asymmetric wear of the bearing insert. Version angle could not be accurately measured using the retrieved clinical X-ray imaging and therefore, future work is required to further support this hypothesis.

The greatest asymmetry in volume was for an edge-loaded component, not the impinged outlier. The side of the component featuring material deformation indicative of edge-loading had more volume than the opposing edge. The impinged outlier was also substantially asymmetric, however the material loss on the impinged edge reduced the material volume on that affected side, resulting in reduced asymmetry.

8.5.1 Limitations

Metal artefacts due to the presence of radiopaque markers created erroneous data points within the CT imaging which were challenging to remove entirely. Ideally, the radiopaque markers would have been removed prior to the CT scanning protocol, however this would risk causing damage the bearing insert. Component orientation was changed to minimise the effect of metal artefact on the bearing surfaces however, the total volume was systematically and significantly increased. Metal artefacts were manually removed from the image space surrounding the bearing insert. A reliability analysis comparing different observers may have identified if the origin of erroneous data points was caused by the researcher. However, because these points were external to the bearing insert, these were relatively simple to remove and unlikely to be a significant contributor to the overall error. Erroneous volume inflation may have been caused by offset CT scanner calibration, although this was unlikely as an expert technician serviced and prepared the equipment. The source of the error is likely to be predominantly caused by the presence of metal artefact.

The retrievals were compared to an unimplanted bearing insert of the same size. Manufacturing tolerances between devices could not be accounted for using this method. Idealised geometries such as spheres have been used to compare wear losses for glenoid components when the original device was not pre-measured (Day et al., 2012). The same limitation exists for idealised shapes. Teeter et al. (2011b) averaged the geometries of six unworn total knee replacement inserts and determined the mean manufacturing variability, which was 15 ± 59 μm for the bearing surface. Yet, obtaining six unworn TAR bearing inserts of the same size relevant to a cohort of retrievals would be challenging.

Only eight bearing inserts were measured for volume loss of which six were used for the determination of annual wear loss. While a small sample size is typical of in vitro simulation tests, explants may be expected to show more variation between ankles. This would be due to different kinetics and kinematics between participants. The statistical analyses were interpreted with this limitation in mind.

8.6 Summary

The aim of this chapter was to quantify and locate the volumetric wear loss for retrieved TAR bearing inserts.

The mean volumetric loss for all bearing inserts was 7.4% or 370 mm^3. One bearing insert was grossly impinged and having lost 19% of its volume was considered an outlier.

The adjusted volumetric loss excluding the outlier was 5.74% which after accounting for implantation time represented an annual wear loss of 65 mm^3. This wear rate was 2.5 times greater than the highest wear rate reported for in vitro simulation of TAR.

Gravimetric and pycnometric measures of volume were not significantly different and highly correlated (r = 0.99). Pycnometry can be considered a useful alternative for determining wear volume for devices with unknown material properties.

Volumetric measures determined using computed tomography were systematically and significantly greater than gravimetric measures. This was likely caused by the ineffective erasure of metal artefact during data post-processing and originated from embedded radiopaque markers. However, CT measures were highly correlated with gravimetric measures (r = 0.99), meaning relative spatial assessments of wear could be captured accurately.

Asymmetrical wear patterns were evident and evenly distributed between the medial (n = 4) and lateral (n = 4) sides of the bearing insert. On average, the disparity in volume was 4.9% between sides. For bearing inserts featuring edge-loading or impingement, more volume was identified at the side with the damage mode. Under adverse conditions such as edge-loading, the talar component may pull towards the centre of the tibial component during motion subsequently generating an asymmetrical wear pattern.

In the next chapter, periprosthetic tissue samples are processed using a novel wear particle isolation method to determine the composition, size and morphology of wear debris produced by TAR.

Chapter 9
Wear Debris Isolation and Characterisation

9.1   Introduction

The biological theory for aseptic loosening identifies wear debris as the most important contributor to osteolysis (Willert and Semlitsch, 1977), a phenomenon that has declined with the advent of advanced biomaterials (e.g. highly crosslinked, anti-oxidant polymers) (Veruva et al., 2015). The accumulation of wear particles usually develops as a function of implantation time and frustrate the cellular equilibrium between osteogenesis and osteoclastogenesis, resulting in osteolysis. Because of this, wear-particle induced osteolysis is predominantly a late complication (i.e. >10 years in-vivo) for total hip and knee replacement (THR, TKR) (Ulrich et al., 2008, Gallo et al., 2013). However, osteolysis remains an early to mid-term problem for TAR (Lucas y Hernandez et al., 2014).

The biological response to wear debris is also primarily reliant on wear particle: volume, composition, size, and; morphology (Ingham and Fisher, 2000, Sieving et al., 2003, Hallab and Jacobs, 2009). The UHMWPE wear particles produced by TARs have been shown to be similar in size to those produced by TKRs (Kobayashi et al., 2004). Fifteen synovial fluid aspirates were obtained after 23.0 ± 6.5 months from patients with non-failed TARs; four of the devices were the fixed-bearing Agility TAR and 11 were mobile-bearing STAR devices. The mean aspect ratio and roundness values were significantly less than the TKR controls, a discrepancy attributed to differences in the biomechanical environment between joint types (Kobayashi et al., 2004). The synovial fluid retrieved for their study was from non-failing TARs considered to be well-functioning. Therefore the particle characteristic reported may not be characteristic of failing devices. Histological studies have also identified UHMWPE wear particles from tissue samples surrounding TAR, but at a much lower imaging resolution (Valderrabano et al., 2004, Johl et al., 2006, Harris et al., 2009, Koivu et al., 2009, Kokkonen et al., 2011, Koivu et al., 2012, Dalat et al., 2013, Yoon et al., 2014, van Wijngaarden et al., 2015, Gross et al., 2016, Schipper et al., 2017). Dalat et al. (2013) measured UHMWPE particles between 2 and 25 µm and metallic particles between 0.3 and 1.5 µm in size. Dalat et al. (2013) identified UHMWPE particles sized between 3 and 83 µm. Histological analyses are often limited to the resolution of light microscopy (~0.2µm) (Shanbhag et al., 1994) and are therefore not sensitive enough to measure nanoscale wear particles (Richards et al., 2008). This

explains the larger particle size ranges reported in histological studies compared to Kobayashi et al. (2004).

Metallic and organic (e.g. bone) wear particles have also been identified surrounding TAR (Koivu et al., 2009, Koivu et al., 2012, Dalat et al., 2013). Small sharp particles of unknown composition were identified within histiocytes surrounding the AES TAR (Koivu et al., 2009). In a follow-up study, high volumes of necrotic bone fragments were subsequently identified from a similar cohort (Koivu et al., 2012). Other authors have observed unidentifiable wear particles surrounding TAR, Dalat et al. (2013) identified pale particles in the cell cytoplasm which featured a flaky morphology and were non-birefringent under polarised light. All of these studies agreed that the disintegration of the fixation surface was likely to produce such particles but further analysis of composition was required. Hydroxyapatite coatings from 4 different TAR devices (STAR, Hintegra, Salto and Taric) were suggested to contribute to osteolysis after elemental analysis indicated substantial calcium deposits with no bony architecture within the tissue samples (Singh et al., 2016). High concentrations of calcium (>0.5 g/g), which were suggested to have originated from the hydroxyapatite coating, were associated with a 297-fold increased risk of ballooning osteolysis (Singh et al., 2016). However, a mechanistic link was not described, only that high concentrations were statistically associated with osteolysis.

In the preceding chapters, estimations of volumetric wear loss were reported to be ~ 65 mm^3 per year for the UHMWPE bearing insert (Chapter 8). The tibial component was estimated to have worn by ~ 11 mm^3 at the fixation surface and ~ 1 mm^3 at the bearing surface (Chapter 6). High rates of bearing insert impingement were also identified (Chapters 5, 6 and 7) which suggested an unquantifiable volume of bone debris may have been produced in-vivo. The evidence for UHMWPE and high density material wear identified in the research in this thesis corroborates with the results from previous histological analyses. Isolating and characterising the wear particle types present in the periprosthetic tissue will further elucidate the potential of such wear debris to cause osteolysis.

Particle isolation protocols combined with high resolution imaging modalities are required to precisely identify biologically reactive particles, especially in the nano- to submicron size range (British Standard ISO 17853, 2011). These techniques have been developed since the early 1990's (Campbell et al., 1994) and aim to remove all adherent molecules from the desired particles. Ultra-high molecular weight polyethylene wear particles have been isolated from synovial fluid surrounding TAR (Kobayashi et al., 2004), however high density wear particle types are yet to be isolated. Wear particle isolation methods are currently used specifically to isolate either UHMWPE or high density materials (e.g

metals, ceramics), independently (Campbell et al., 1994, Margevicius et al., 1994, Maloney et al., 1995, Scott et al., 2001, Richards et al., 2008, Billi et al., 2012a, Lal et al., 2016). Several of the first wear particle isolation methods were capable of isolating multiple material types simultaneously (Campbell et al., 1994, Margevicius et al., 1994, Maloney et al., 1995), however more sensitive methods able to isolate wear particles in the nanometre size-range have since been developed (Richards et al., 2008, Billi et al., 2012a, Lal et al., 2016). These more modern approaches are specific to isolating either UHMWPE (Richards et al., 2008, Billi et al., 2012a) or high density materials (Billi et al., 2012b, Lal et al., 2016). Adapting two modern wear particle isolation methods to extract wear particles of different composition (i.e. UHMWPE and metallic) was required to determine the total wear particle content of periprosthetic tissue samples surrounding failed TAR.

The aim of this chapter was to:

- Isolate wear particles from periprosthetic tissue surrounding failed TAR and characterise their composition, size and morphology.

In order to achieve this aim, the following objectives were explored:

- Develop and validate a wear particle isolation method capable of isolating UHMWPE and metal/ceramic wear particles from periprosthetic tissue.
- Characterise the composition, size and morphology of wear particles isolated from periprosthetic tissue surrounding TAR.

9.2 Method Development

Wear particle isolation methods typically follow four principles, which include: tissue digestion, particle isolation, particle cleansing, and; imaging and characterisation (Nine et al., 2014). To isolate and characterise UHMWPE and high density wear particles using the same method, each of these steps needed to be considered with the material properties of the target particles kept in mind. For example, acid and base methods are effective at digesting tissue samples for the isolation of UHMWPE wear particles (Campbell et al., 1994, Niedzwiecki et al., 2001), however they may also change the composition and morphology of metallic wear debris (Catelas et al., 2001).

Campbell et al. (1994) successfully isolated both UHMWPE and metallic wear debris from THR tissue samples. The method used included delipidisation of the tissue samples using chloroform:methanol prior to digestion with sodium hydroxide (NaOH). Following this, a sucrose density gradient was used to separate UHMWPE wear particles, high density wear particles and proteins, simultaneously. Further cleansing steps were taken

prior to the imaging and characterisation of each particle type. The method used by Campbell et al. (1994) was later used extensively to isolate UHMWPE wear debris only (Campbell et al., 1995, Kobayashi et al., 1997, Minoda et al., 2003, Kobayashi et al., 2004). Using chloroform:methanol on tissue with metallic and organic (e.g. bone) particles embedded within may alter the composition and shape of such particles. Also, the method was not optimised to isolate nanoscale wear particles, unlike the more recently published approaches (Richards et al., 2008, Billi et al., 2012a, Lal et al., 2016). Therefore, specific elements from two wear particle isolation methods published more recently (Richards et al., 2008, Lal et al., 2016) were adopted to create a modified method capable of isolating multiple particle types.

The Institute of Medical and Biological Engineering at the University of Leeds has extensive academic experience developing and applying wear particle isolation methods (Ingham and Fisher, 2000, Tipper et al., 2000, Richards et al., 2008, Lal et al., 2016). The two methods chosen to be combined to create the novel modified method were developed at the University of Leeds and have been both shown to be sensitive enough to isolate nanoscale wear debris (Tipper et al., 2000, Richards et al., 2008, Lal et al., 2016). The two methods referred to throughout the current study are outlined briefly below and the relevant methodological sections are detailed more extensively in the final method (see section 9.3.2).

UHMWPE Wear Particle Isolation Method (Richards et al., 2008)

Developed to isolate nanometre-sized UHMWPE wear particles from human periprosthetic tissue, Richards et al. (2008) used a strong base solution (12 M potassium hydroxide (KOH) to digest tissue samples without damaging polymer wear particles. Exploiting the relatively low density of UHMWPE ($\rho = 0.93$), the particles were isolated by density using two chloroform:methanol (2:1) ($\rho = \sim 1.2$) mix steps. These step are particularly effective at precipitating lipids and were adopted from a commonly used lipid extraction technique developed by Folch et al. (1957). Following these steps, floating UHMWPE wear particles were subsequently cleansed of remaining proteins and contaminants using ethanol and water washes (Figure 9.1).
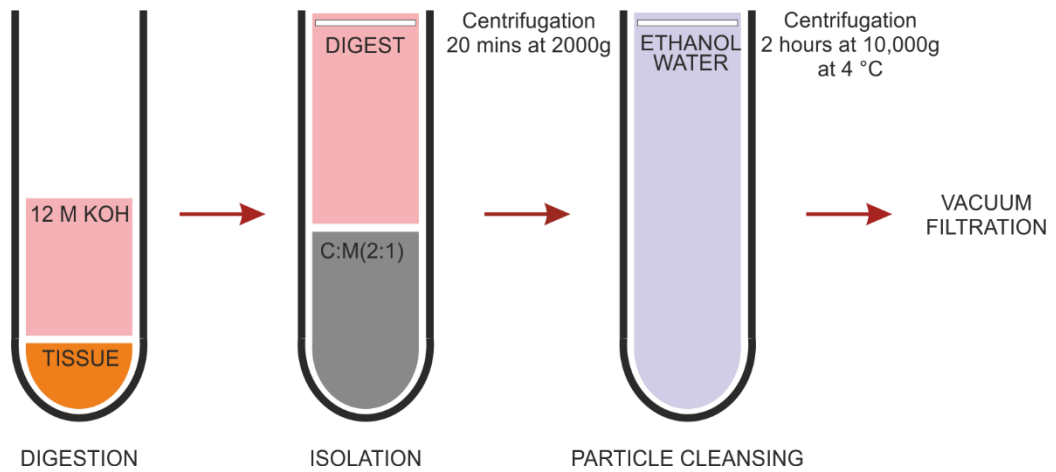
Figure 9.1. Ultra-high molecular weight polyethylene wear particle isolation method developed by Richards et al. (2008). KOH, potassium hydroxide. C:M, chloroform:methanol.

Metal and Ceramic Wear Particle Isolation Method (Lal et al., 2016)

The method developed by Lal et al. (2016) was created to effectively isolate nanometre-sized metal or ceramic wear particles from joint replacement wear simulator lubricant (e.g. 25% (v/v) bovine serum) (Figure 9.2). The development of this method focussed on silicon nitride wear particles which dissolve in solution over time. Therefore, the method was developed to be as minimally destructive to these particle types as possible. The digestion method was enzymatic, using proteinase K and buffers to cleave proteins without damaging the wear particles (Lal et al., 2016). Using a density gradient composed of sodium polytungstate (SPT) and ultracentrifugation forces greater than 200,000 g, high density wear particles were pelleted and proteins separated. Several wash steps in water using ultracentrifugation followed the density gradient isolation to ensure the particles were cleansed adequately for image analysis.
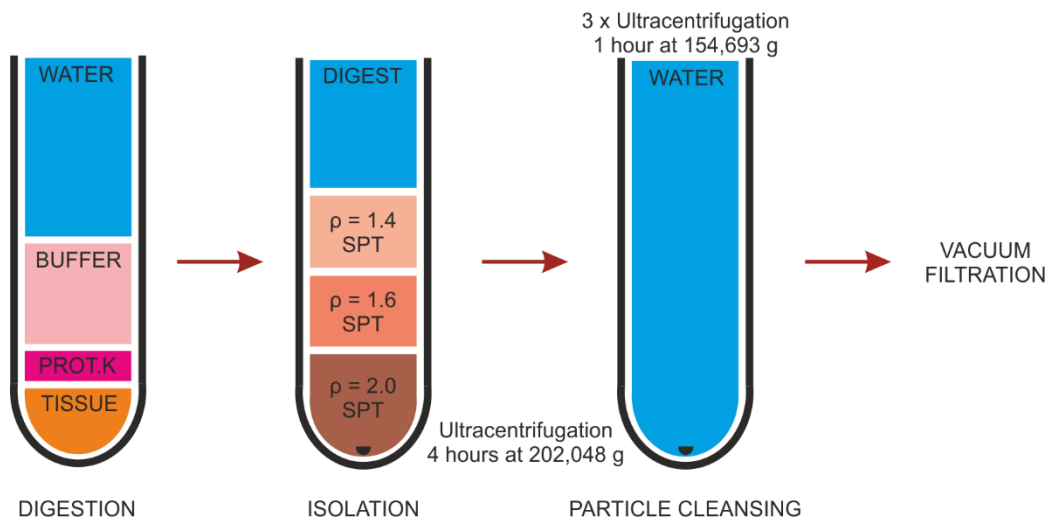
Figure 9.2. High density wear particle isolation method developed by Lal et al. (2016). Prot. K, Proteinase K. SPT, sodium polytungstate at different densities.

Combining the two particle isolation methods required several alterations to the protocols. The development process included three important aspects:

Study 1: Initial particle isolation attempt

Study 2: Separation step development

Study 3: Density analysis of UHMWPE particle recovery

This method development is detailed in the following sections.

9.2.1 Study 1: Initial Particle Isolation Attempt

The first attempt to isolate UHMWPE and high density wear particles used the complete method by Lal et al. (2016). In theory, this method is capable of isolating both high density materials (ρ = >2 g/cm^3) and UHMWPE (ρ = 0.93 g/cm^3) because the density gradient range is between 1.2 and 2.0 g/cm^3. The simplest alteration to the method by Lal et al. (2016) was to extract the top level of the density gradient. This was hypothesised to contain floating UHMWPE wear particles, similar to the method developed by Campbell et al. (1995). High density materials such as metals/ceramics would sediment at the bottom of the tube. The following study was conducted to test whether or not UHMWPE wear particles could be isolated using the method developed by Lal et al. (2016) without substantial methodological alterations.

9.2.1.1 Method

Three samples of porcine joint capsule (1 gram) were chopped into small pieces (Figure 9.3). The tissue was added to an ultracentrifuge tube (Beckman Coulter, USA) coated with siliconizing fluid (Surfasil, Sigma, UK). Titanium alloy wear particles produced on a pin-on-plate rig for a previous project (not conducted by the author) were donated for use in this current study and used as model particles to visualise high density wear particles progressing through the method. Titanium alloy particles at a concentration high enough to visualise with the naked eye were added to water and 1 ml of this suspension was added to the centrifuge tube. The equivalent of 1 mm^3 of model UHMWPE 'Ceridust 3615' (Hoechst, Germany) particles were also added to each tube.

An enhanced digestion protocol was selected from the previous literature (Nine et al., 2014) which used the enzyme papain in addition to the proteinase K. Lal et al. (2016) used proteinase K by itself as that was deemed sufficient to digest simulator serum proteins. Tissue samples are challenging to digest completely (Campbell et al., 1994), therefore an enhanced digestion method was decided to be used from the conception of the development of this modified method. Each sample was digested over two days using 1mg/ml papain and 0.1 M MOPS Buffer (pH 7.8) with 20 mM L-Cysteine (pH 6.5) at 60°C for 24 hours; then 1 mg/ml proteinase K in a mix with 0.5% (w/v) sodium dodecyl

sulphate (SDS), HEPES Buffer (working concentration 0.1 M) (pH 7.8), 3 mM $CaCl_2$ and ultrapure water for another 24 hours at 37°C.
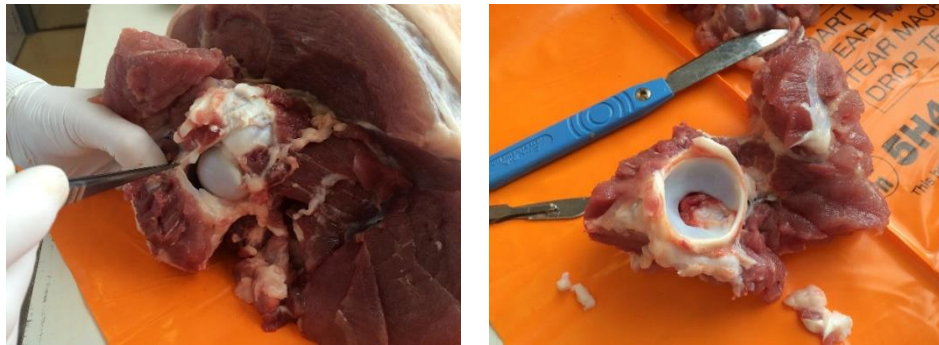
Figure 9.3. Porcine hip tissue dissection.

A density gradient was compiled in a 12.5 ml ultracentrifuge tube with 2 ml of 60% (v/v), 2 ml of 40% (v/v) and 2 ml of 20% (v/v) concentrations of sodium polytungstate, each carefully layered on top of each other. Samples were centrifuged for 4 hours at 202,048 g at 25°C.

In the original method, Lal et al. (2016) discarded the density gradient leaving just the pellet of high density wear particles, after centrifugation. Instead of discarding the supernatant, the aim of this development study was to extract the top layer of the SPT density gradient.

A thick layer of congealed lipids covered the top layer of the centrifuge tube. The model UHMWPE particles were not visible. Unable to extract the supernatant with a pipette, the experiment ceased at this point (Figure 9.4).
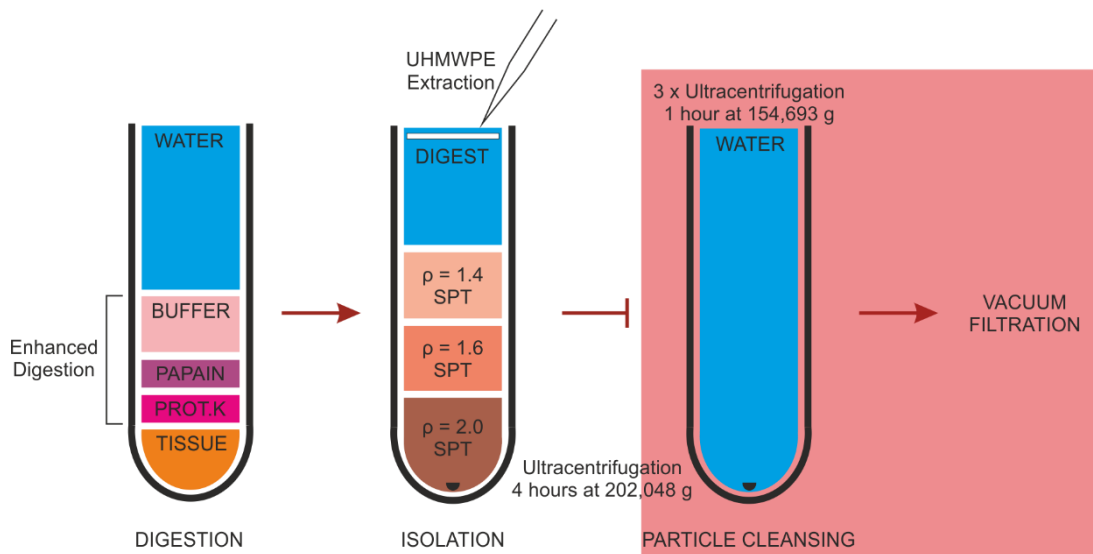
Figure 9.4. Schematic of the initial tissue digestion and wear particle isolation study using the method developed by Lal et al. (2016). A thick layer of lipids prevented the extraction of UHMWPE wear particles from the top of the density gradient in the isolation step. Shaded red denotes the processes not completed. Prot. K, Proteinase K. SPT, sodium polytungstate at different densities.

9.2.1.2 Results and Discussion

The histoarchitecture of the tissue samples had diminished visibly which indicated the enhanced digestion protocol had been effective. However, before the removal of proteinaceous material from the particles could be confirmed, a more comprehensive analysis of the isolated wear particles was required.

Lipids within the tissue samples coated and obscured the UHMWPE particles following the use of the method by Lal et al. (2016) (Figure 9.5). Lipids float in water due to their relatively low density resulting in both the UHMWPE wear particles and the lipids being accumulated at the same level as each other after ultracentrifugation. The lipids were viscous, adhesive and unable to be extracted using a pipette. The model UHMWPE particles were not observed on or within the lipid layer and may have resided below it. The lipid content of the tissue samples needed to be reduced for the UHMWPE to be extracted.
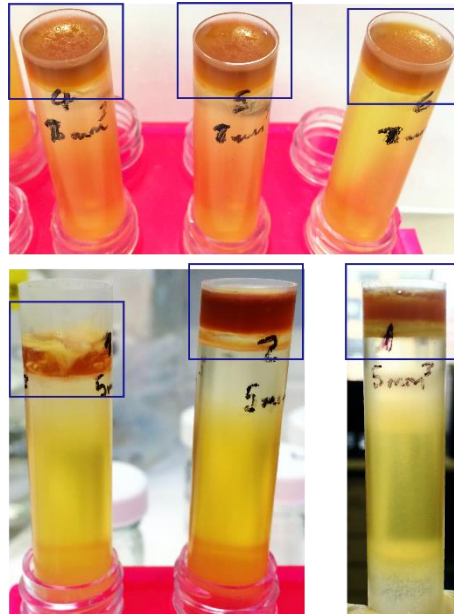
Figure 9.5. Viscous lipid layer floating after the density gradient step (blue squares). An additional separation step would be required to isolate low density wear particles from lipids.

A larger ultracentrifuge tube may have dispersed lipids more effectively, making them possible to extract. The integrity of the density gradient levels was not maintained in a larger ultracentrifuge tube, resulting in the dilution of the density gradient structure. Campbell et al. (1995) immersed tissue samples in a chloroform:methanol (2:1 v/v) mix prior to digestion to delipidise the samples. However, metal wear particles are sensitive to compositional changes and dissolution after exposure to harsh reagents (Catelas et al., 2001), therefore avoiding the contact between metallic particles and chloroform was considered desirable. Chloroform:methanol was used by Richards et al. (2008) after digestion to precipitate lipids from tissue samples. This approach was deemed possible

if a separation step was introduced to create two specific pathways for the high and low density materials following digestion. The following development study investigated the feasibility of a separation step.

9.2.2   Study 2: Separation Step Development

In order to precipitate and separate lipids from wear particles without damage, another protocol step was introduced called the 'separation step'. This step aimed to combine the effective lipid extraction technique used by Richards et al. (2008) with the method by Lal et al. (2016) after high density wear particles had been separated from UHMWPE wear particles.

Richards et al. (2008) used the principles of the Folch method (Folch et al., 1957), a method used to extract lipids from solutions, to isolate UHMWPE wear particles. The Folch method was developed to extract lipids for analysis rather than to be discarded, but the same principles apply to both applications. Briefly, a chloroform:methanol (2:1) mix is added to diced tissue samples and agitated using an orbital shaker. After slow speed centrifugation, two phases appear within the sample, the top phase containing predominantly methanol, and the bottom phase, containing chloroform and lipids. In the original method by Folch et al. (1957), the top phase would be discarded and the bottom phase analysed. However, in the method developed by Richards et al. (2008), the UHMWPE wear particles accrue in the top phase which is extracted for further cleansing steps. Chloroform:methanol mixes have been used to reduce the lipid content in other wear particle isolation methods (Campbell et al., 1995). Campbell et al. (1995) treated the tissue samples with chloroform:methanol prior to digestion, however the effectiveness of the Folch method is heavily reliant on the quality of tissue disruption (Ametaj et al., 2003). Tipper et al. (2000) recommended adding chloroform:methanol after the tissue digestion step in order to effectively reduce lipid content. Therefore, in the current study the wear particle isolation method developed by Richards et al. (2008), which included the Folch method, was integrated into the method by Lal et al. (2016).

To combine the methods developed by Lal et al. (2016) and Richards et al. (2008), an ultracentrifugation step was added after sample digestion. The aim of this step was to pellet as much of the high density material in the sample (i.e. metallic/ceramic wear particles and proteins) as possible, and to float the UHMWPE particles and lipids in the supernatant. It was hypothesised, the pellet could then be processed through the method by Lal et al. (2016) to isolate high density wear particles from proteins, and the supernatant processed through the method by Richards et al. (2008) to cleanse UHMWPE wear particles of lipids.

9.2.2.1 Method

For this study, two 1 gram periprosthetic tissue samples were randomly selected from one AES (2nd Gen) TAR and diced into small pieces. The metallic components of this TAR design were composed of cobalt chromium alloy, commercially pure titanium and hydroxyapatite. The bearing insert was made of conventional UHMWPE. Observable metallic wear debris were visible within the tissue samples. Metallic wear particles were grey in appearance and sufficient in volume to discolour the tissue. These samples were selected to minimise the chance of a false negative result (Figure 9.6).
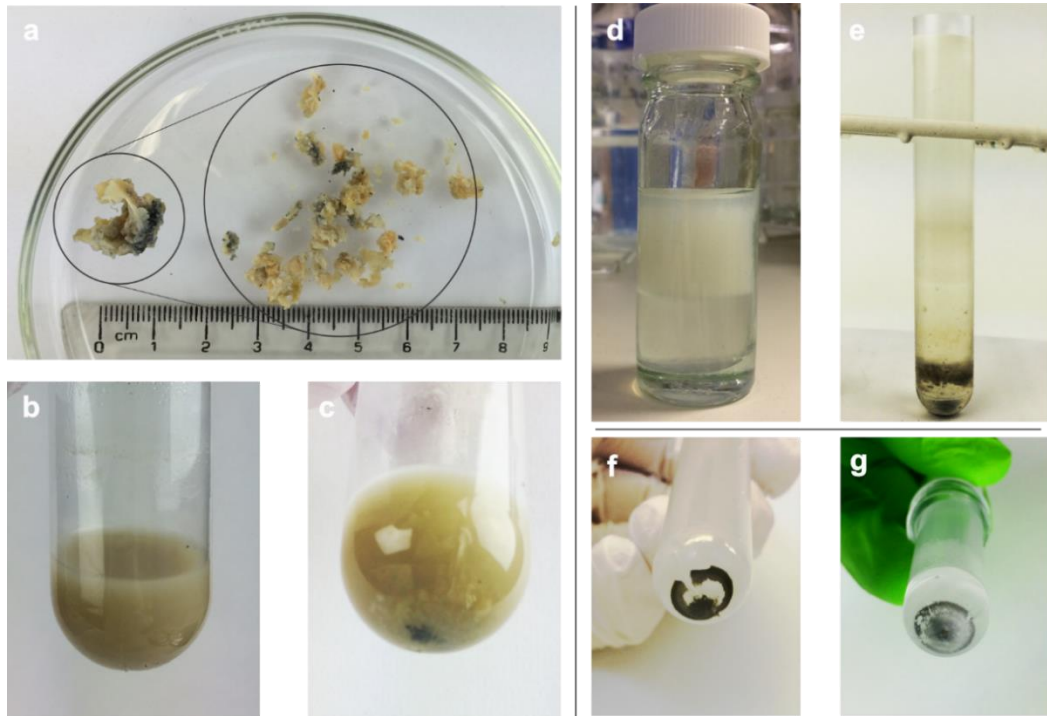
Figure 9.6. Development of an isolation method able to isolate high and low density wear particles. A, tissue before and after dicing. B, tissue during digestion. C, metallic particles liberated from tissue. D, Chloroform:methanol separation of lipids. E, density gradient step. F, pre-washing step high density wear particle pellet. G, isolated and cleansed high density wear particles ready for filtration.

One sample was processed using the modified protocol with the separation step (Sample 1) whereas the other sample (Sample 2) was processed using the original method developed by Richards et al. (2008), to act as a comparator.

'Sample 1' (Modified Method) (Figure 9.7) was digested in an ultracentrifugation tube (38.5 ml) using the same papain and proteinase K protocol detailed in section 9.2.1.1. After digestion, the tube was filled with ultra-pure water in preparation for ultracentrifugation.

Ultracentrifugation can be used to extract particles in a solution by pelleting them, the efficacy of which is determined by a balance between the buoyancy of the particles,

friction within the solution and the opposing centrifugal field forces. Sedimenting wear particles is reliant on several factors explained by Stoke's law (Equation 9.1):

Equation 9.1.
$$g = \frac{18\mu V_t}{d^2(P_p - P_m)}$$

Where, g is the acceleration due to gravity, V_t is terminal velocity, d is particle diameter, P_p is density of particle, P_m is density of medium and μ is viscosity of medium. Equation 9.1 was used to determine the force that the ultracentrifuge needs to generate in order to achieve sedimentation of any given particle type and size, in any given solution. The medium at the time of centrifugation was assumed to be sufficiently dilute to be considered similar to water. For a total volume of water of 38.5 ml, approximately 1 gram of tissue and less than 5 ml of enzymatic solutions were added. The material with the lowest density to be sedimented was partially hydrolysed human protein. The density of which was assumed to be approximately 1.6 g/cm^3. The smallest particle diameter was assumed to be 50 nm, which was a value deemed low enough to capture the vast majority of protein. Terminal velocity was calculated from a centrifuge duration of 3 hours and a maximum displacement of 92.1 mm (i.e. the centrifuge tube length).
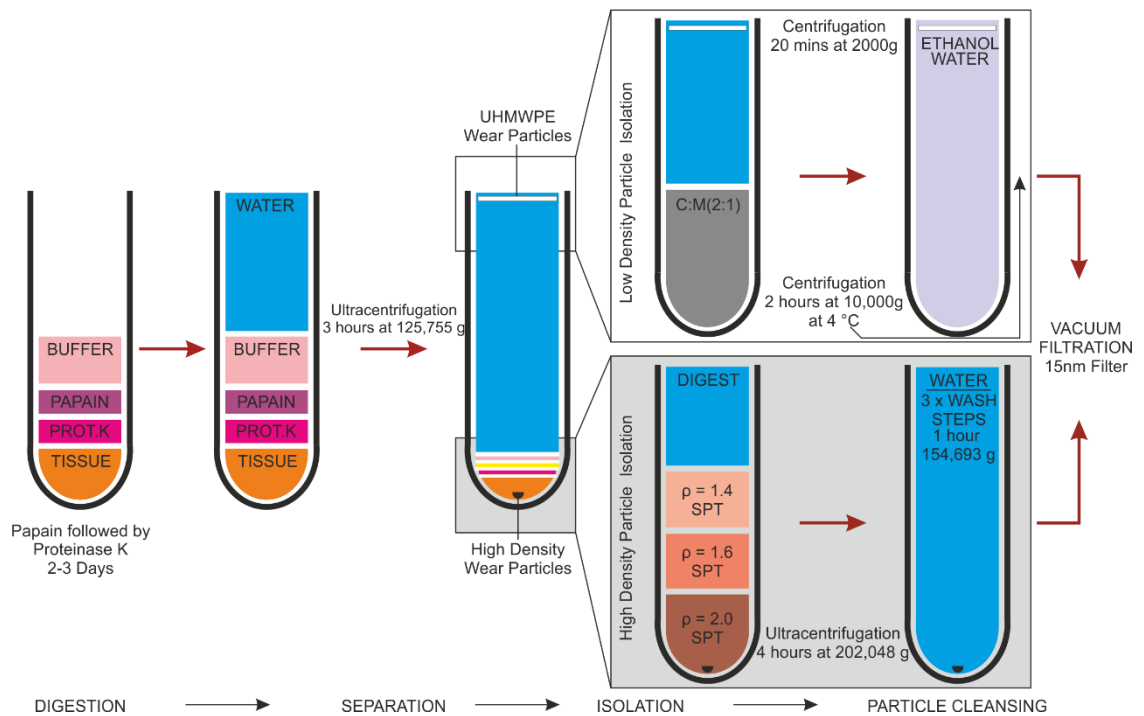
Figure 9.7. Modified wear particle isolation method. This method was developed to isolate high and low density wear particles from periprosthetic tissue. Prot. K, proteinase K. C:M, chloroform:methanol. SPT, sodium polytungstate.

Sample 1 was centrifuged at 125,755 g at 20°C for 3 hours (Optima L80 ultracentrifuge, Beckman Coulter, USA). The supernatant (i.e. solution above the pellet) was decanted into three universal tubes (10 ml in each) in preparation for the chloroform:methanol

steps. The pellet at the bottom of the centrifuge tube was sonicated in 2 ml of ultra-pure water and carefully pipetted into the top of pre-prepared sodium polytungstate density gradients, as described in section 9.2.1.1.

'Sample 2' (Richards et al., 2008) was digested in a glass universal tube with 10 ml of 12 M KOH. The sample was agitated at 240 rpm on an orbital shaker while being incubated at 60°C for three days. After digestion, this sample (sample 2) and the supernatant of Sample 1 were processed using the method by Richards et al. (2008). Briefly, ten millilitres of chloroform:methanol (2:1 v/v) mix was added to each glass universal, shaken at 240 rpm for two minutes on an orbital shaker and incubated at room temperature for at least 24 hours. The chloroform:methanol mix separated creating two phases; lipids within the supernatant precipitated and sank to the bottom phase. The top phase was clear in appearance and contained the UHMWPE particles. The glass universals were centrifuged at 2000 g for 20 mins at room temperature. The top phase was removed with a glass pipette and added to another 10 ml of chloroform:methanol. The samples were shaken again using the same method and incubated at room temperature for at least 24 hours. The supernatant was removed with a glass pipette and accumulated into a 250 ml high speed centrifugation tube. The sample was diluted with ultrapure water and ethanol (99.6% v/v) (3:1) at 4°C and centrifuged for 2 hours at 10,000 g at 4°C, after which, the supernatant was extracted and retained for filtration.

The pellet of Sample 1 was processed through the SPT density gradient and wash steps developed by Lal et al. (2016). The density gradient was compiled in a 12.5 ml ultracentrifuge tube with 2 ml of 60% (v/v), 2 ml of 40% (v/v) and 2 ml of 20% (v/v) concentrations of sodium polytungstate, each carefully layered on top of each other. The sample was centrifuged for 4 hours at 202,048 g at 25°C to pellet high density wear particles. Importantly, the supernatant layers of the density gradient were absent of the thick layer of lipids identified in the previous development study. This enabled the simple extraction of these layers leaving just the pellet at the bottom of the centrifugation tube. The pellet was sonicated in 2 ml of ultrapure water and extracted with a pipette. The wear particle aspirate was washed in ultrapure water using sonication and ultracentrifugation at 154,693 g for 1 hour. This was repeated three times with the supernatant being discarded after each centrifugation. The sample was ready for filtration and imaging.

Both the high density wear particles and the UHMWPE wear particles from Sample 1, and the UHMWPE particles from Sample 2 were filtered onto separate 0.015 µm filter membranes (GE Whatman, UK) and coated with 5 nm of carbon (Figure 9.8). The filter membranes were imaged using a Hitachi SU8230 high resolution cold-field emission scanning electron microscope (CFE-SEM) between 50 and 200,000 times magnification

(Figure 9.9). Particle composition was identified using energy-dispersive X-ray spectroscopy.
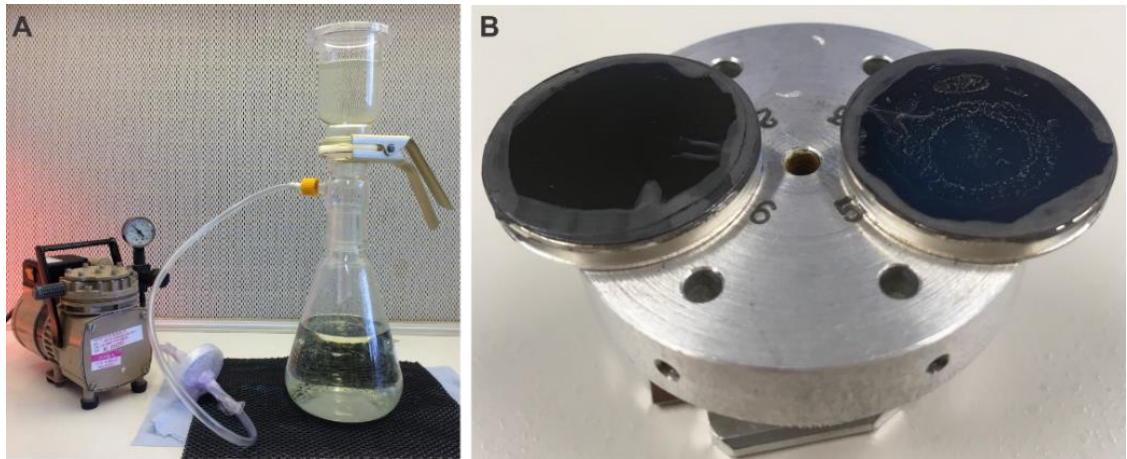
Figure 9.8. Filtration equipment (A) and scanning electron microscope stubs (B).
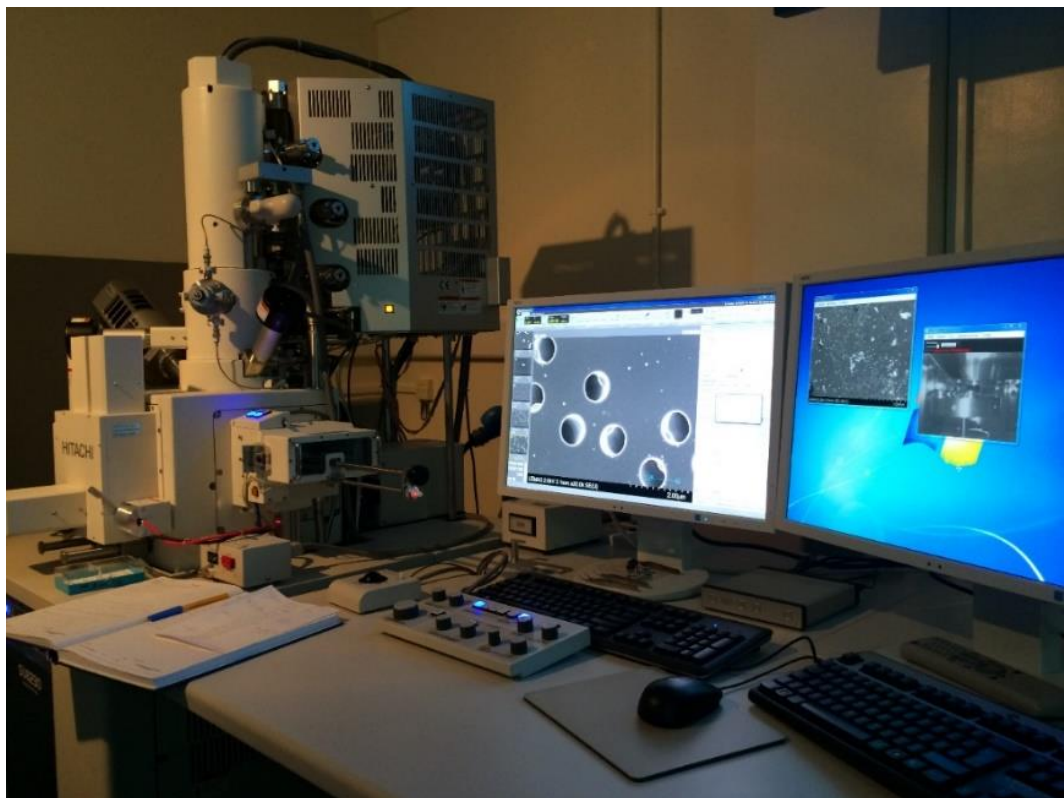
Figure 9.9. Scanning electron microscope used for wear particle characterisation.

9.2.2.2   Results and Discussion

UHMWPE wear particles in the micron and submicron size range were isolated from both samples (Figure 9.10). The particles were predominantly identified by their morphology which was similar to UHMWPE wear particles identified in the published literature (Campbell et al., 1995, Tipper et al., 2000, Richards et al., 2008). Flakes, fibrils and

granular type wear particles were identified. In combination with the morphology, the composition of the particles were carbon and hydrogen which formed a similar composition to UHMWPE but was indistinguishable from the filter membrane. The presence of UHMWPE wear particles indicated that the separation step was successful for Sample 1.
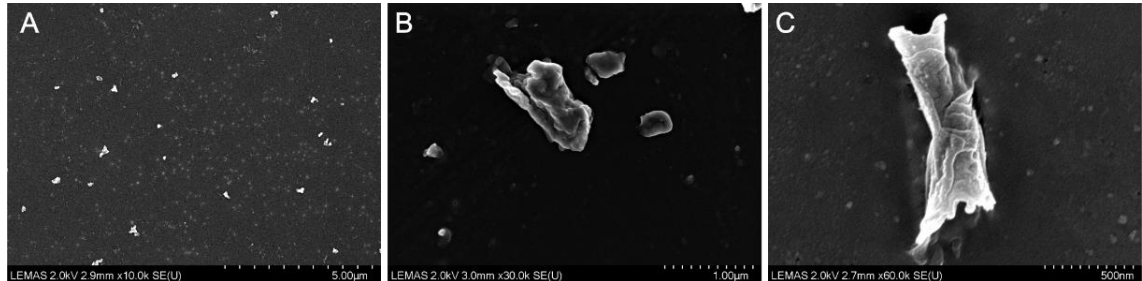
Figure 9.10. Examples of UHMWPE wear particles isolated from periprosthetic tissue using the modified isolation method. A, granules. B, mixed particles types. C, flake.

Following the separation step, the supernatant of Sample 1 (modified method) appeared visually clearer than Sample 2 during the chloroform:methanol steps. The separation step may have reduced the content of lipids in the supernatant by pelleting a proportion of the denser lipids. This reduction of lipids may have increased the efficiency of the chloroform:methanol step by decreasing the lipid to chloroform:methanol ratio. Another possibility was a heterogeneity of composition between the two tissue samples. One sample may have contained more lipids than the other. The following development study investigated the effect of tissue heterogeneity on the isolation process (see section 9.2.3).

After the separation step, the pelleted material from Sample 1 was also processed through an SPT density gradient. Viscous lipids were absent from the top of the density gradient and the supernatant was capable of being discarded carefully. A visible metallic pellet was evident at the bottom of the density gradient and throughout the wash steps.

Interestingly, the majority of the high density wear particles were calcium phosphate in composition. These wear particles appeared either in their bulk urchin-like crystalline form (Figure 9.11), or as individual shards (Figure 9.12A). The urchin-like wear particles were large (>10 µm) and coated the filter membrane. Individual shards were in the micron to submicron size range. Commercially pure titanium and cobalt chromium wear particles were also present in the sample.
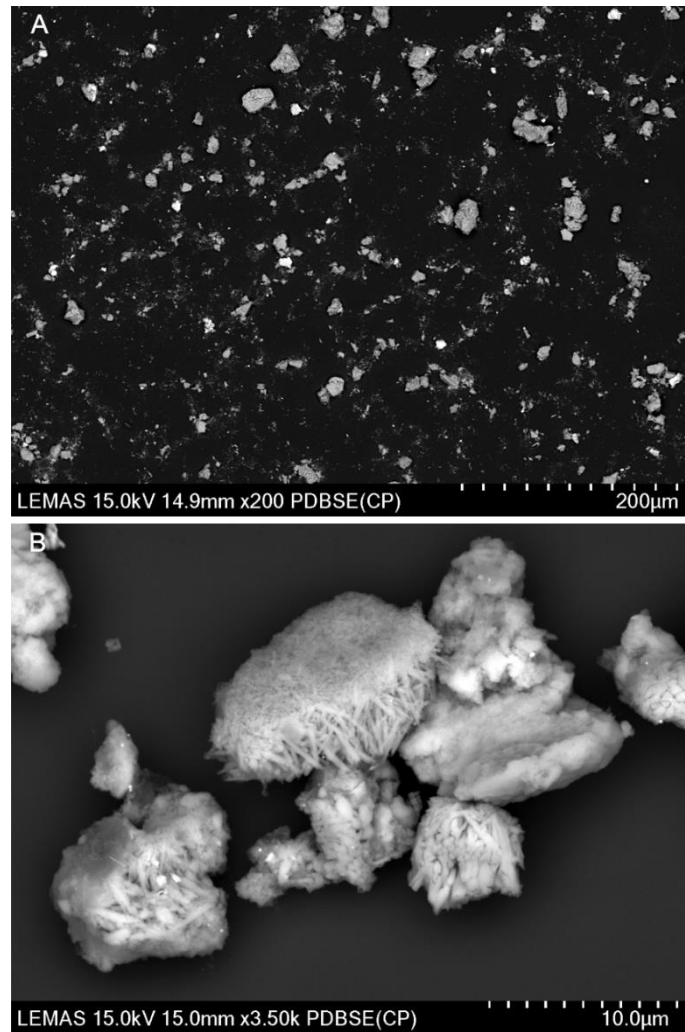
Figure 9.11. Examples of calcium phosphate wear particles. Note the crystalline urchin morphology indicative of hydroxyapatite fixation surface coating.

The calcium phosphate wear particles were likely to originate from the hydroxyapatite fixation surface coating because the crystalline appearance and absence of bony histoarchitecture. Calcium phosphate wear particles were not expected to be on the filter membrane as they may have been dissolved throughout the isolation process. This corroborated the decision not to use chloroform:methanol prior to tissue digestion as particles susceptible to dissolution may be affected by harsh chemicals such as chloroform.
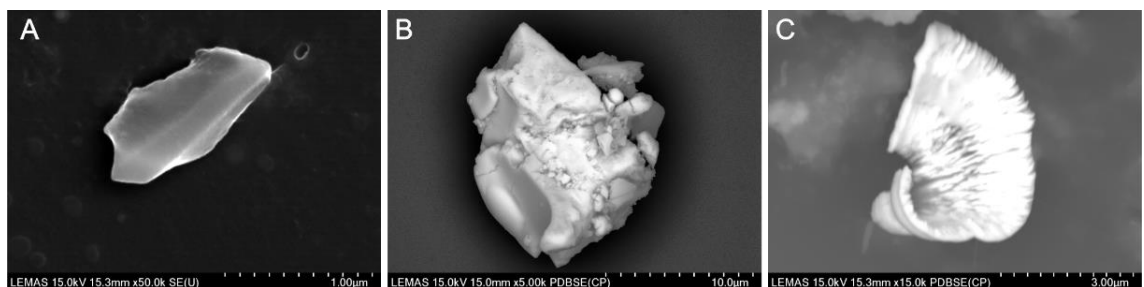
Figure 9.12. Examples of shard-like hydroxyapatite (A), commercially pure titanium (B) and cobalt chromium alloy (C) wear particles.

The presence of calcium phosphate wear particles suggested the centrifugation speeds used for both the separation step and density gradients had to be considered. Despite the fact this development study showed calcium phosphate wear particles were able to be isolated using the current centrifugation parameters. The material density of calcium phosphate is approximately 3.1 g/cm^3 which is similar to the density of silicon nitride (3.4 g/cm^3), the material Lal et al. (2016) originally developed and validated the method using. The current method was deemed appropriate to achieve its aims, therefore no changes were made to the centrifugation speeds.

The modified method was effective at isolating UHMWPE and high density wear particles from human periprosthetic tissue samples. During this development study, the chloroform:methanol step could have been affected by the heterogeneity of lipid content between samples. This posed the corollary question of whether the absence of 12 M potassium hydroxide digestion from the modified method affected UHMWPE recovery during the chloroform:methanol steps adopted from Richards et al. (2008).

9.2.3 Study 3: Density Analysis of UHMWPE Particle Recovery

The modified isolation method developed in this current study used an enzymatic digestion similar to that developed by Lal et al. (2016). Acid and base digestion methods change the composition and morphology of metallic wear debris (Catelas et al., 2001), therefore these techniques were avoided. The original method by Richards et al. (2008) used 12 M potassium hydroxide (KOH) to digest tissue. In solution, the density of 12 M KOH was approximately 1.3 g/ml which is denser than water (1 g/ml) and UHMWPE (0.93 g/ml). The high density of 12 M KOH enhanced the efficacy of the original method by creating a density difference between UHMWPE and the KOH-containing solution, resulting in UHMWPE wear particles floating throughout the protocol. Using enzymatic digestion the density of the solutions throughout the chloroform:methanol steps relative to the UHMWPE wear particles was unknown and may have affected the recovery of UHMWPE wear particles.

In the separation step development study (see section 9.2.2), the top phase was a visually clearer after the chloroform:methanol steps for the modified method compared to the control sample, which was processed using the original method by Richards et al. (2008). While this could have been caused solely by the absence of KOH, the separation step may have removed a proportion of the lipids, or alternatively, heterogeneity between tissue samples for lipid content may also have contributed. Regardless of the cause, the density of the top phase was required to be sufficiently high enough to ensure UHMWPE wear particles remained within it (i.e. >0.93 g/cm^3), and not in the bottom phase which was to be discarded. Maintaining a density difference between solutions used throughout the modified isolation method was crucial to maximise wear particle recovery.

A study was undertaken to test the density of the top phase of the two chloroform:method (2:1) steps adopted from Richards et al. (2008). Two variables were investigated:

I. Digestion method (i.e. enzymatic vs 12 M KOH)
II. Tissue lipid quantity (i.e. pure fat, pure muscle and mixed fat/muscle)

The aim of the study was to determine whether the top phase density of the chloroform:methanol steps were greater than the density of UHMWPE wear particles (>0.93 g/cm^3), for differing digestion methods and tissue lipid quantities.

9.2.3.1 Method

Varied tissue compositions were emulated by mixing porcine tissue dissected from different anatomical locations from surrounding a porcine hip joint. The following conditions were tested:

Digestion Method Variables

A. 12 M KOH Digestion: Fat Tissue Only
B. Enzymatic Digestion: Mixed Tissue - Muscle + Fatty Tissue (1:1)

Tissue Lipid Quantity Variables

C. Enzymatic Digestion: Muscle Tissue – Low Lipid Condition
D. Enzymatic Digestion: Fatty Tissue – High Lipid Condition

Control Variables

E. 12 M KOH Digestion: No Tissue
F. Enzymatic Digestion: No Tissue
G. Water Only (10 ml)

The method developed by Richards et al. (2008) is well established, therefore only the presumed worst case scenario for lipid content was tested for 12 M KOH digestion, which was fat only tissue. Adding more low density material to the sample was hypothesised to reduce the solution density. All three tissue lipid quantity conditions were tested for the enzymatic digestion method, given this was the untested experimental approach. Statistical analysis between variables was not necessary for this study because each variable was compared for density against the density of UHMWPE (0.93 g/cm^3).

Each experimental variable was repeated three times. Twelve 1 gram porcine tissue samples were created from tissue samples dissected from a porcine hip joint. Muscle only and fat only conditions were solely composed of their respective tissue types. Muscle and fat tissue was mixed in a 1:1 ratio to create the mixed tissue condition (Figure 9.13). These variables were devised to mimic the range of possible tissue types retrieved from human tissue donors.
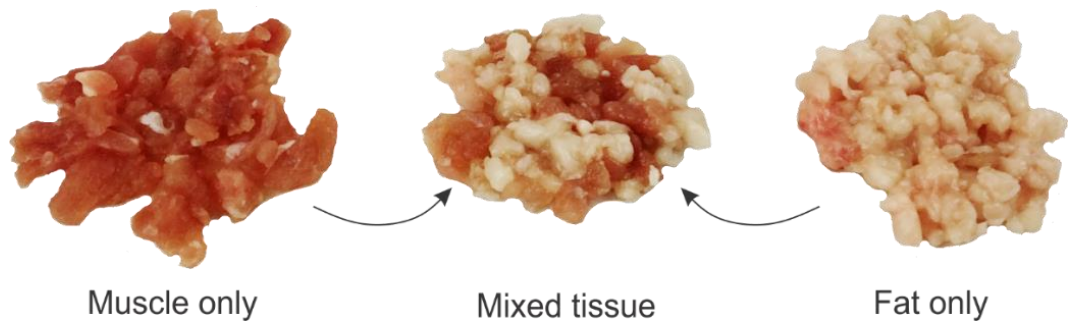
Figure 9.13. Porcine tissue types used as a model for the density analysis. Mixed tissue was formed by mixed equal amounts of muscle and fat tissue.

For the conditions that underwent enzymatic digestion, the same protocol was used as 'Sample 1' in the separation development study until the end of the second chloroform:methanol step (see section 9.2.2.1). For conditions that underwent 12 M KOH digestion, the same protocol was used as 'Sample 2' in the separation development study until the end of the second chloroform:methanol step (see section 9.2.2.1). The control variables were processed using the same protocol as their tissue counterparts. The water only control underwent the same protocol as the 12 M KOH samples but without the addition of any solutions or tissue except chloroform:methanol for the two lipid reduction steps.

Measurements were taken at two time points for all conditions: 1) after the first chloroform:methanol step, and; 2) after the second chloroform:methanol step. A 1 ml sample was captured from the centre of the top phase, which was approximately 10 ml in total volume. The sample was deposited into a pre-weighed 1.5 ml bijou and weighed using an ABJ-220-4NM Analytical balance (Kern, HR). The density was calculated as the mass (or weight) divided by volume. One millilitre of pure water weighs 1 g. Therefore, 1 ml of solution that weights 0.95 g has a density of 0.95 g/cm^3. The 1 ml sample was returned to the main sample once the measurement had been acquired.

Where the solution density reached 0.93 g/ml or less, that condition was considered high risk for particle loss.

9.2.3.2   Results and Discussion

None of the conditions tested resulted in a top phase density of less than or equal to the density of UHMWPE (0.93 g/cm^3) (Figure 9.14).
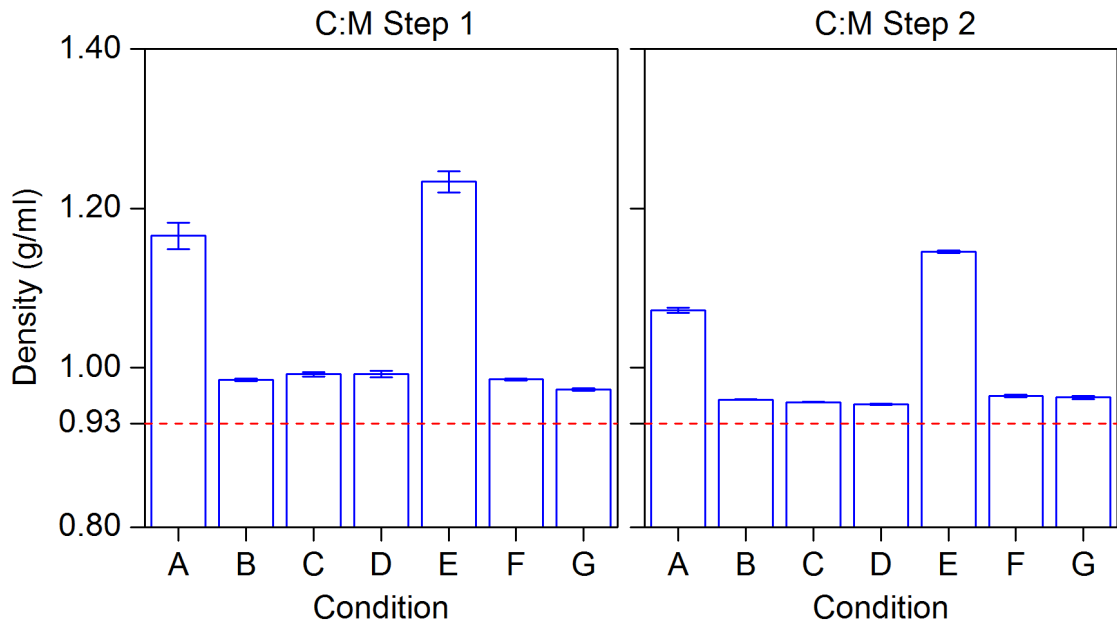
Figure 9.14. Solution density after the first and second chloroform:methanol steps in the particle isolation process. Post-Conc, post-concentration. C:M, Chloroform:methanol. Red dashed line represents the density of ultra-high molecular weight polyethylene (0.93 g/ml). A, 12 M KOH Digestion: Fat Tissue Only; B, Enzymatic Digestion: Mixed Tissue; C, Enzymatic Digestion: Muscle Tissue; D, Enzymatic Digestion: Fatty Tissue; E, 12 M KOH Digestion: No Tissue; F, Enzymatic Digestion: No Tissue; G, Water Only.

After the first chloroform:methanol step, the 12 M KOH digestion conditions featured the highest densities of 1.23 ± 0.01 g/cm^3 with no tissue and 1.17 ± 0.02 g/cm^3 with fat tissue only. A 5.5% difference was measured between these conditions which was attributable to the effect of the presence of fat tissue on density. All of the enzymatic digestion conditions yielded similar results to the water only control (0.97 ± 0.002 g/cm^3). The effect of fatty tissue for the enzymatic digestion conditions was negligible. There was a 0.05% difference between the enzymatic condition with fat tissue compared to the without tissue control. It was possible a substantial quantity of fatty tissue was not digested and subsequently pelleted during the separation step.

After the second chloroform:methanol step, all of the conditions had reduced in density. The greatest percentage change of density was for the 12 M KOH fat tissue only condition which featured a reduction of 8.0%. The water only control reduced in density by 1.0% and the enzymatic digestion conditions reduced by 3.9%, 3.5% and 2.5% for muscle only, fat only, mixed tissue conditions, respectively. The reduced density of the top phase between chloroform:methanol steps was likely caused by the precipitation and loss of protein and lipids, combined with an increased quantity of methanol. Protein has density of approximately 1.6 g/cm^3 whereas methanol has a density of 0.79 g/cm^3. The lowest density measured following the second chloroform:methanol step was the enzymatic digestion with muscle only condition (0.95 ± 0.001 g/cm^3). While the density

value for this condition was greater than the density of UHMWPE, more than two chloroform:menthanol steps risk reducing the top phase density too low for an effective particle recovery.

9.3   Modified Particle Isolation Method Validation

Building on the results from the development studies, a final wear particle isolation method was applied to total hip and knee replacement (THR, TKR) tissue samples for validation. The wear particle types produced by THR and TKR are well known and include wear particles composed of UHMWPE, cobalt chromium alloy, titanium alloy and particles associated with bone cement (Topolovec et al., 2013, Topolovec et al., 2014). The aim of this study was to isolate and characterise high and low density wear particles from periprosthetic tissue surrounding THR and TKRs.

9.3.1   Periprosthetic Tissue Samples from THR and TKR

Periprosthetic tissue samples from 10 THRs and eight TKRs had been retrieved through the same process detailed in section 3.3. The THR samples were from at least four metal-on-polyethylene (MoP) and three ceramic-on-polyethylene (CoP) bearing combinations (Table 9.1). All of the TKRs were MoP bearing combinations. The complete explant was not available for the majority of tissue samples therefore the biomaterial composition, particularly the fixation surfaces and whether the devices were cemented or uncemented, was largely unknown for the THRs and TKRs. The mean participant age at revision surgery was 64.4 years (range: 48 to 79) for THR and 71.0 years (range: 62 to 84) for TKRs. The mean time in-vivo for the samples was 161.3 months (range: 52 to 288) for THR and 167.6 months (range: 86 to 224) for TKRs.

Table 9.1. Participant demographics for periprosthetic tissue samples retrieved from total hip and knee replacements.

	Bearing Couple	Sex	Side	Age (yrs)	Time In-vivo (mo)	Initial Diagnosis	Reason for Revision
Hips							
1	MoP	F	R	79	-	OA	Wear, nickel allergy, dislocation
2	-	F	R	48	108*	OA	Tight joint
3		M	R	49	288	AVN	Pain, reduced mobility, crunching noise
4	CoP	M	R	72	71	-	Dislocated liner from a cup
5	MoP	M	R	73	250	OA	Activity related pain in hip and thigh
6	CoP	F	R	58	168*	-	Pain, aseptic loosening of cup
7	MoP	F	R	78	192*	OA	Recurrent dislocation (x 7)
8	MoP	-	-	-	-	-	-
9	CoP	M	L	53	52	-	Septic loosening
10	-	M	R	70	9	OA	Loose stem
Knees							
1	MoP	F	L	62	182*	RA	Loose tibial component
2	MoP	F	R	70	101*	OA	Displacement of tibial component
3	MoP	M	L	73	86*	OA	Loosening
4	MoP	M	R	84	181	OA	Loose tibial component
5	MoP	F	R	62	224*	RA	Instability, worn tibial base plate and insert
6	MoP	F	R	73	-	-	-
7	MoP	F	R	63	219*	RA	Wear
8	MoP	F	L	81	180*	RA	Loose femoral component

Notes: *Approximate time; M, Male; F, Female; L, Left; R, Right; OA, Osteoarthritis; PT, Post-traumatic; AVN, Avascular necrosis; RA, Rheumatoid arthritis; MoP, metal-on-polyethylene; CoP, ceramic-on-polyethylene.

9.3.2   Modified Wear Particle Isolation Method

To separate materials by density, the modified method featured two processes that diverge after the digestion and separation step. The separation step uses ultracentrifugation to float particles with a material density less than ~1.0 g/cm^3 (Process 1, low density; e.g. UHMWPE; Density = 0.93 g/cm^3) and to sediment particles with a material density greater than ~2.0 g/cm^3 (Process 2, high density; e.g. calcium phosphate; density = ~3.1 g/cm^3). Processes 1 and 2 reflect two previously published methods (Richards et al., 2008, Lal et al., 2016) and were combined to form a method to isolate high and low density materials from the same tissue sample (Figure 9.7).

9.3.2.1   Sample Preparation and Digestion

All reagents were filtered through a 20 nm Whatman® Anodisc membrane filters (GE Whatman, UK) to remove external contaminants prior to use. Approximately 1 gram of

tissue was randomly dissected from each donor sample and chopped into ~1 mm^3 pieces. In order to preserve calcium phosphate and metallic particles, acid and base digestion methods were avoided. The tissue was added to a 38.5 ml ultracentrifuge tube (Beckman Coulter, USA) coated with siliconizing fluid (Surfasil,, Sigma UK) and digested over two days using 1 mg/ml papain and 0.1 M MOPS Buffer with 20 mM L-Cysteine (pH 6.5) at 60°C for 24 hours; then 1 mg/ml proteinase K in a mix with 0.5% (w/v) sodium dodecyl sulphate (SDS), HEPES Buffer (working concentration 0.1 M) (pH 7.8), 3 mM CaCl$_2$ and ultrapure water for another 24 hours at 37°C. The samples were shaken at 240 rpm throughout digestion.

9.3.2.2 Particle Separation Step

Ultra-pure water was added to fill each ultracentrifugation tube and the tubes were centrifuged at 125,755 g at 20°C for 3 hours (Optima L80 ultracentrifuge, Beckman Coulter, USA). All materials with a density greater than water (~1.0 g/cm^3) which included: proteins, metal, calcium phosphate, bone cement, extracellular matrix and high density lipids, were pelleted. The supernatant contained materials with a density less than water such as UHMWPE wear particles and lipids. The supernatant for each sample was decanted 5 ml at a time into clean glass universals ready for process 1. The pellet of particles remaining in the ultracentrifuge tube was continued to process 2.

9.3.2.3 Process 1: Isolation of particles with a density < 1.0 g/cm^3

Ten millilitres of chloroform:methanol (2:1 v/v) mix was added to each glass universal, shaken at 240 rpm for two minutes and incubated for at least 24 hours. The chloroform:methanol mix separates creating two phases; lipids within the supernatant precipitate and sink to the bottom. The glass universals were centrifuged at 2000 g for 20 mins at room temperature. The supernatant was removed with a glass pipette and added to another 10 ml of chloroform:methanol. The samples were shaken and incubated for at least 24 hours. The supernatant was removed with a glass pipette and accumulated into a 250 ml high speed centrifugation tube. Twenty millilitres of filtered ethanol was added, followed by 60 ml of Ultrapure water. Finally, the sample was centrifuged for 2 hours at 10,000 g at 4°C, after which, the sample was ready for filtration.

9.3.2.4 Process 2: Isolation of particles with a density >2.0 g/cm^3

A density gradient was compiled in a 12.5 ml ultracentrifuge tube with 2 ml of 60% (v/v) (ρ = 2.0 g/cm^3), 2 ml of 40% (v/v) (ρ = 1.6 g/cm^3) and 2 ml of 20% (v/v) (ρ = 1.2 g/cm^3) concentrations of sodium polytungstate, each carefully layered on top of each other. The pelleted sample from the separation step was sonicated with ultrapure water and carefully pipetted on top of the density gradient. Samples were centrifuged for 4 hours at

202,048 g at 25°C. After centrifugation, the top 3-5 ml of the sample was added to Process 1 to recover as many low density particles as possible. The sodium polytungstate was discarded and the pellet was sonicated with 2 ml of ultrapure water. The sample was transferred to a clean 12.5 ml ultracentrifuge tube and washed in ultrapure water three times followed by centrifugation at 154,693 g at 20°C for 1 hour. In between each centrifugation wash, the ultrapure water was exchanged. Finally, the pellet contained cleansed particles was ready for filtration.

9.3.2.5   Particle Characterisation

Both high and low density particles were filtered onto separate 0.015 µm filter membranes (GE Whatman, UK) and coated with 5 nm of carbon. The filter membranes were imaged using a Hitachi SU8230 high resolution cold-field emission scanning electron microscope (CFE-SEM) between 50 and 200,000 times magnification. The backscatter detector on the SEM was used to highlight high-density materials (Topolovec et al., 2013). Particle composition was identified using energy-dispersive X-ray spectroscopy.

Particle size and morphology was characterised manually using ImageJ (Schindelin et al., 2012). Kobayashi et al. (2004) reported equivalent circle diameter (ECD) to describe particle size however ImageJ, the software available and used in this project, could not calculate this parameter because it cannot calculate minimum width and length, both of which are needed to calculate ECD. Therefore, Feret's diameter was used as an alternative which is also commonly used in wear particle isolation studies (Billi et al., 2012a, Billi et al., 2012b). Kobayashi et al. (2004) used aspect ratio and roundness to describe particle morphology. ImageJ does not report roundness for the same reason as ECD but uses the parameter circularity as an analogous measure. Aspect ratio and circularity were reported in this study which were comparable to the metrics used by Kobayashi et al. (2004).

9.3.2.6   Statistical Analysis

Statistical analysis was performed using SPSS Statistics Version 22 (IBM Corp, USA). Non-parametric descriptive statistics (e.g. median and interquartile range) were reported for wear particle size. Parametric descriptive statistics (e.g. mean and standard distribution) were reported for morphological characteristics. The proportion of wear particles in the submicron (< 1 µm), 1 to 10 µm and >10 µm size ranges were also reported.

9.3.3 Results

9.3.3.1 Particle Composition

Ultra-high molecular weight polyethylene particles were isolated from all tissue samples, the mean number of particles characterised for the THR and TKR tissue samples were 228 (range: 120 to 431) and 211 (range: 78 to 303), respectively. Flakes, fibrils and granules of UHMWPE were identified in both joint replacement types (Figure 9.15).
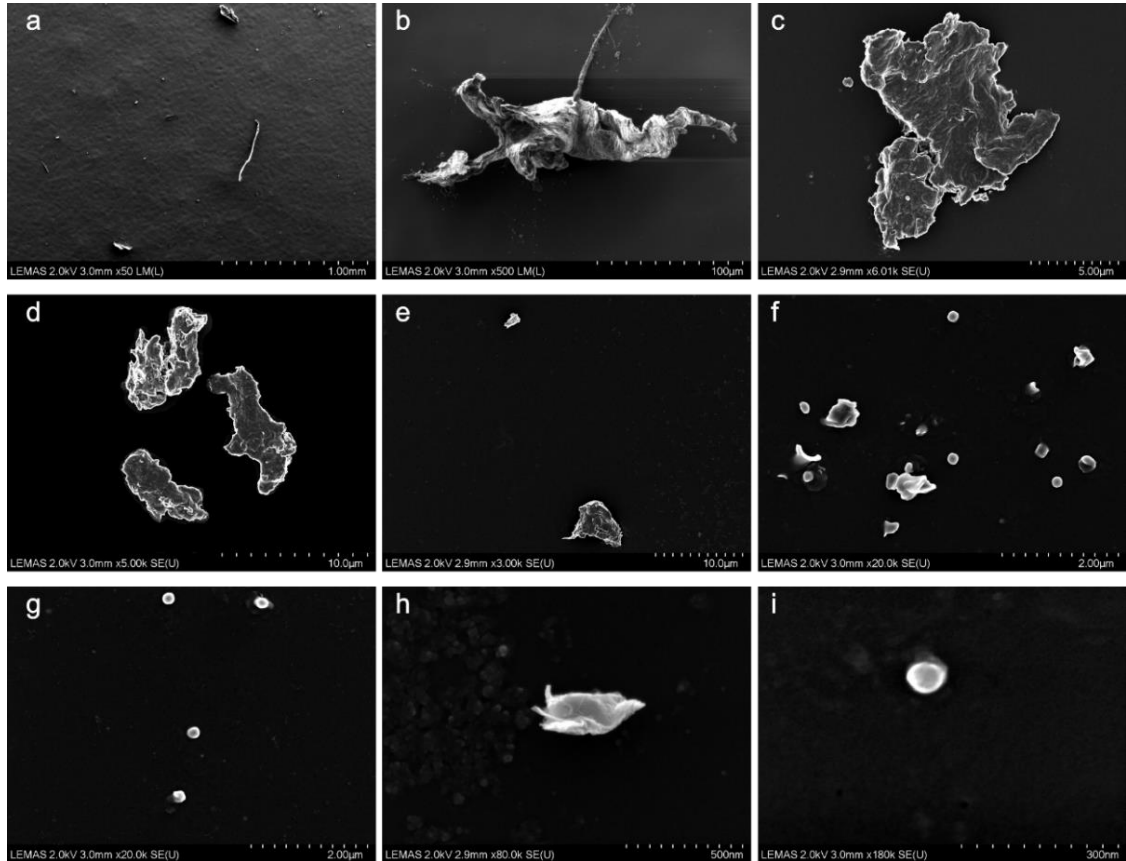
Figure 9.15. Ultra-high molecular weight polyethylene wear particle types isolated from periprosthetic tissue surrounding total hip and knee replacements. A, fibril. B, fibril-flake. C, flake. D-E, irregular shaped particles. F-I, granules.

Both THR and TKR tissue samples contained: zirconia (THR 63.6%, TKR 53.8%), titanium alloy (THR 20.5%, TKR 38.9%), stainless steel (THR 5.8%, TKR 3.0%), barium sulphate (THR 7.4%, TKR 2.2%), polymethylmethacrylate (PMMA; THR 2.5%, TKR 1.5%) and cobalt chromium alloy (THR 0.2%, TKR 0.6%) (Figure 9.16).

Granules of zirconia, a radiopacifier in bone cement, were the most prevalent particle type for THR (n = 4 of 10) and TKR (n = 7 of 8). Zirconia also took the form of larger mulberry-like particles composed of hundreds of tessellating zirconium granules (Figure 9.16A-C). Barium sulphate, an alternative radiopacifier commonly used in bone cement, was present in tissue from one THR and one TKR (Figure 9.17).
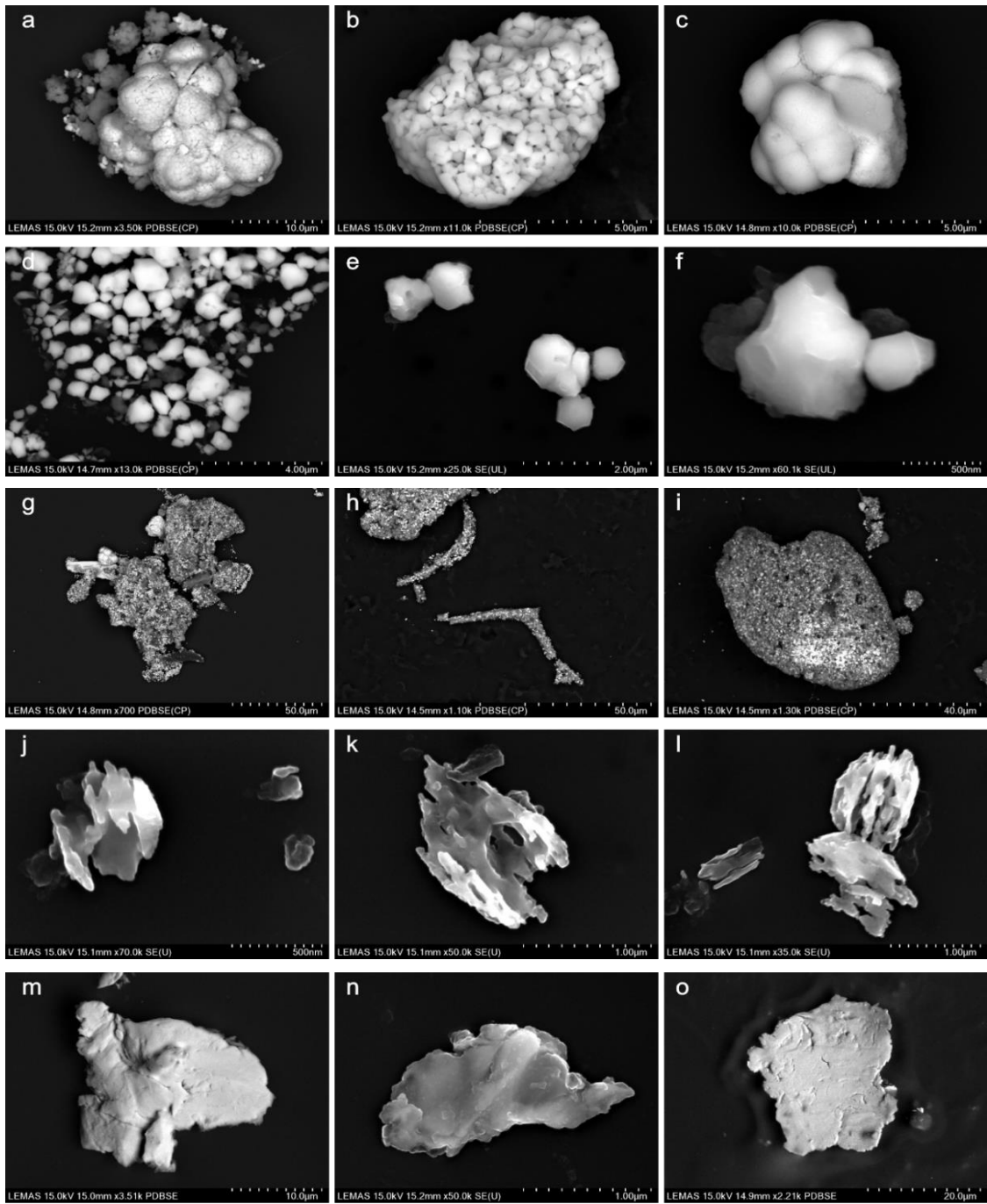
Figure 9.16. High density wear particles isolated from periprosthetic tissue surrounding total hip and knee replacements. A-C, Mulberry-like zirconia. D-F, Zirconia granules. G-I, Bulk bone cement. J-L, barium sulphate. M-O, stainless steel.
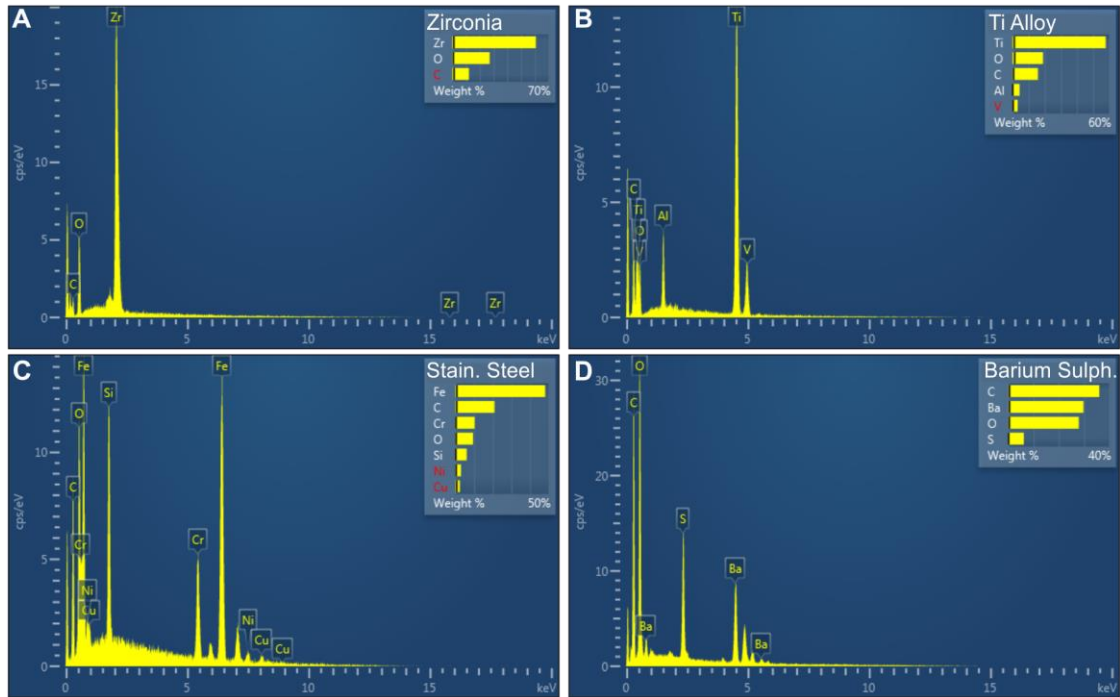
Figure 9.17. Examples of energy dispersive X-ray analysis traces for zirconia (A), titanium alloy (B), stainless steel (C) and barium sulphate (D).

9.3.3.2 Particle Characterisation

The wear particle characteristics were similar for all material types for both THR and TKR (Figure 9.18). The median maximum diameter for UHMWPE and high-density wear particles for THR samples was 0.09 µm (IQR = 0.05 – 0.90) and 0.56 µm (IQR = 0.23 – 1.15), respectively. For TKR, UHMWPE and high density wear particles were 0.08 µm (IQR = 0.05 – 0.64) and 0.86 µm (IQR = 0.30 – 2.17), respectively.

The median maximum diameter of all wear particles combined for THR and TKR was 0.25 µm (IQR = 0.07 – 1.09) and 0.34 µm (IQR = 0.07 – 1.39), respectively. UHMWPE wear debris was the smallest wear particle population for both joints, with 73.1% being in the submicron size range. The largest wear particle isolated was comprised of UHMWPE and was 464.56 µm in diameter from tissue surrounding a THR.

The smallest high density wear particle populations were the individual grains of zirconia (THR, 0.29 µm IQR = 0.16 – 0.55; TKR, 0.23 µm IQR = 0.11 – 0.64). The largest high density wear particle population was PMMA in its bulk form from TKR, which had a median particle size of 17.19 µm (IQR = 8.86 – 30.11).
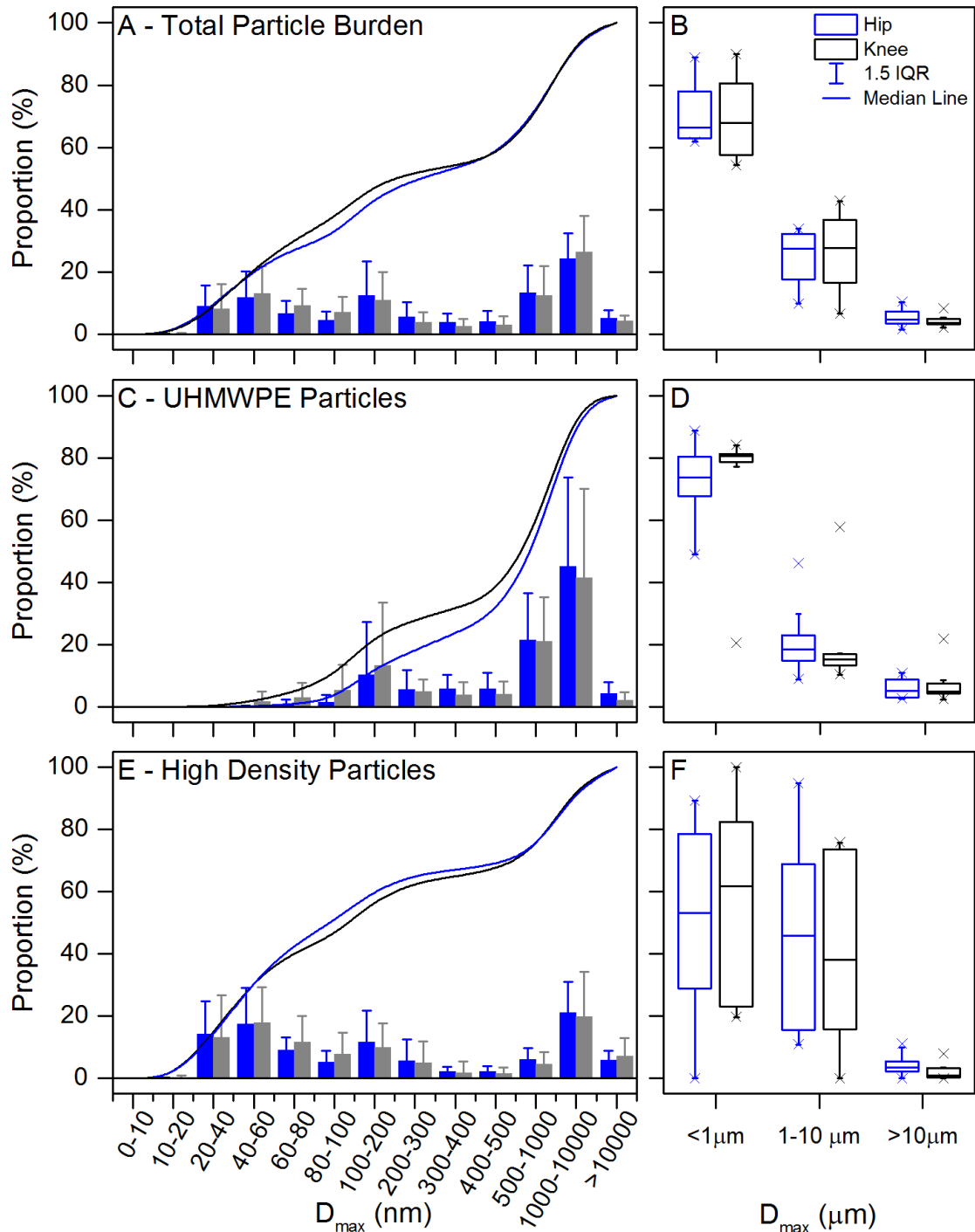
Figure 9.18. (A-F) Size distribution of wear particles isolated from periprosthetic tissue surrounding for total hip and knee replacement. A,C,E, size distribution graphs with cumulative frequency. B,D,F, Binned size distribution data. A, total particle burden was ultra-high molecular weight polyethylene (UHMWPE; C) and high density (E) wear particle sizes combined. D_{max}, maximum diameter.

Titanium alloy wear particles had the greatest aspect ratio (THR, 2.14 ± 1.24; TKR, 2.91 ± 1.70). Individual grains of zirconia had the lowest aspect ratio (THR, 1.35 ± 0.24; TKR, 1.37 ± 0.26) and the highest circularity (THR, 0.80 ± 0.10; TKR, 0.84 ± 0.06). Zirconia in its bulk particle form featured similar morphological characteristics to its granular form but was substantially larger (Figure 9.19).
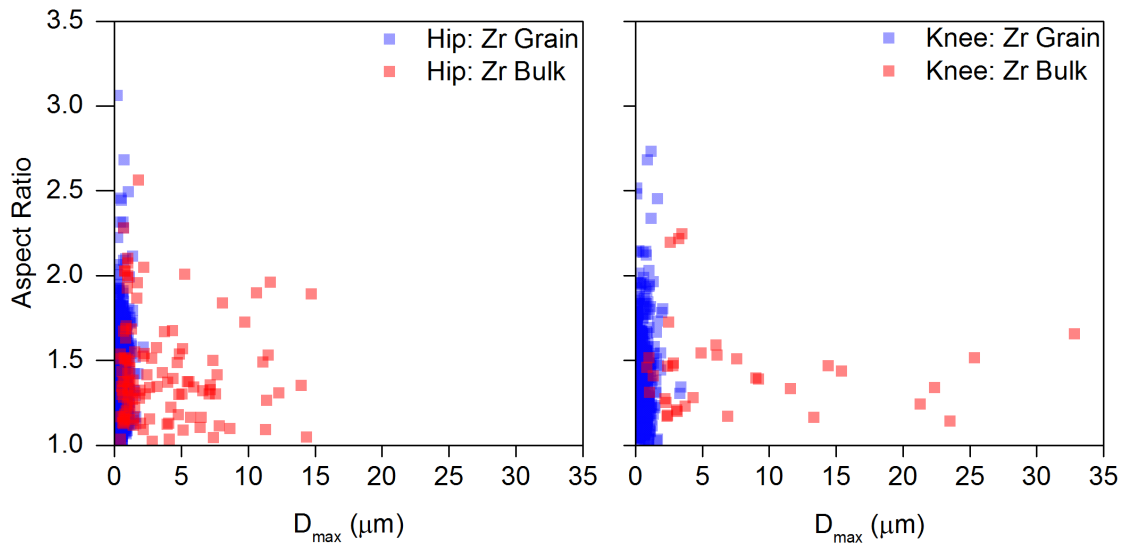
Figure 9.19. Aspect ratio of zirconia wear particles isolated from periprosthetic tissue surrounding total hip and knee replacements. Individual grains and agglomerated bulk particles were stratified for both joint types. D_{max}, maximum diameter.

9.3.4 Discussion

A modified wear particle isolation method was developed to isolate UHMWPE and high density wear particles from the same tissue sample. An enhanced enzymatic digestion protocol was introduced to ensure tissue proteins were effectively cleaved from wear particles. The density gradient and modified-Folch method were adopted from the methods developed by Lal et al. (2016) and Richards et al. (2008), respectively, to further cleanse the UHMWPE and high density wear particle populations of proteins and lipids. Finally, filtration using a 0.015 µm filter membrane ensured nanometre-sized wear particle populations were captured for all wear particle types. This method was shown to be effective at isolating both UHMWPE and high density wear particles from periprosthetic tissue samples.

Complete digestion occurred for most of the samples in this study. Organic material did occasionally precipitate onto the filter membrane but not in enough quantity to obscure characterisation. Modern imaging techniques such as scanning electron microscopy with a back-scattered detector aided the visualisation of high density wear particles (Topolovec et al., 2013). Despite this, other approaches to enhance the effectiveness of digestion could have been taken. For example, Maloney et al. (1995) balanced the weight of the tissue sample against the amount of enzyme used. Alternatively, the quantity of tissue could be reduced to achieve the same end point. A defective enzyme source or incorrect storage of the digestants may also have reduced the efficacy of the papain or proteinase K. The knowledge acquired from this validation study can be applied to the following study using the same method to isolate wear particles from periprosthetic tissue samples surrounding TAR.

Several particle isolation methods have isolated both high and low density materials from the same periprosthetic tissue sample (Lee et al., 1992, Campbell et al., 1994, Margevicius et al., 1994, Shanbhag et al., 1994, Maloney et al., 1995). However, since the development of such methods, several key principles have been identified for isolating specific material types. Acid or base digestion is contraindicated for the isolation of nanoscale metallic particles, PMMA and calcium phosphate particles (Margevicius et al., 1994, Shanbhag et al., 1994, Catelas et al., 2001, Zolotarevova et al., 2010), although these digestion methods provide a more complete digestion of proteins (Campbell et al., 1994, Baxter et al., 2009). Maloney et al. (1995) developed the first dual material isolation method to use an enzymatic digestion protocol to process soft tissue membranes from 35 THR. Using a papain suspension, tissue samples were digested resulting in liberated metallic particles sinking to the bottom of the vessel and UHMWPE wear particles floating to the top. The digested tissue was spread thinly on a microscope slide and imaged using light microscopy and scanning electron microscopy. An automated particle sizer was also used to calculate wear particle size. The mean size of isolated UHMWPE and titanium wear particles was 0.5 ± 0.3 µm and 0.7 ± 0.3 µm, respectively. Which has since been found to be generally representative of the wear particle sizes identified for both THR and TKR (Margevicius et al., 1994, Shanbhag et al., 1994, Tipper et al., 2000, Mochida et al., 2002).

Ultra-high molecular weight polyethylene wear particles were identified in all THR and TKR tissue samples for the current study. The median wear debris size was 0.09 µm (IQR = 0.05 – 0.90) for THR and 0.08 µm (IQR = 0.05 – 0.64) for TKR. These particle distributions were smaller than the values reported in the literature (Margevicius et al., 1994, Shanbhag et al., 1994, Mochida et al., 2002). Retrieval studies have reported THR UHMPWE wear particle mean size to be 0.53 ± 0.3 µm (Shanbhag et al., 1994), and between 0.58 and 0.79 µm (Margevicius et al., 1994). However, the maximum resolution of the automated analysis methods were reported to be 0.4 µm (Maloney et al., 1995, Mochida et al., 2001) and 0.58 (Margevicius et al., 1994), which are insufficient to characterise nanoscale particles produced by metal-on-polyethylene articulations (Tipper et al., 2000, Richards et al., 2008, Topolovec et al., 2013, Liu et al., 2015). These commonly used automated analysis methods had a minimum resolution approximately 20 times larger than the smallest particle identified in the current study. A more recent retrieval study measured a mean UHMWPE wear particle size of 0.21 ± 0.44 µm from tissues surrounding failed THR (Topolovec et al., 2013). Topolovec et al. (2013) noted 51% of their particles were smaller than 0.1 µm and that only 7% of particles were larger than 0.5 µm. Wear particle distributions are not parametric (Billi et al., 2009), therefore the median wear particle size is likely to be lower than the mean for that study.

Magnification is the factor found to have the greatest effect on reported wear particle distributions (Schroder et al., 2013). The earliest wear particle isolation studies were unable to confidently analyse nanometre wear particles due to the resolution of their analysis methods (Margevicius et al., 1994, Maloney et al., 1995). Additionally, the filtration equipment pore size was often 0.1 µm or larger (Sieving et al., 2003), allowing particles in the nanometre size range to flow through and be omitted from analysis. Nanometre wear particles have been identified but often require manual characterisation which may introduce observer selection bias (Richards et al., 2008). Manual characterisation allows for individual particles to be analysed rather than agglomerates, a distinction automated analysis cannot distinguish. Yet, manual characterisation is laborious and fewer particles can be analysed as a proportion of the total wear particle population (Richards et al., 2008). Automated characterisation can analyse millions of wear particles rapidly. The method developed for the current study used manual characterisation to ensure each particle type was adequately identified, imaged and characterised. This was particularly important given high density wear particle types surrounding TAR devices have only been imaged in histological tissue slices using relatively low resolution methods (i.e. light microscopy). The modified method used in this current study used a filter size of 0.015 µm which was used to minimise wear particle losses in the nanometre size range. Also, an ultra-high resolution scanning electron microscope was used to create clear images up to a resolution of approximately 1 nm. Tipper et al. (2006) observed nanometre wear particles using magnifications up to 65,000 times. Magnifications up to 200,000 times were used for wear particle characterisation in the current study. This may have reduced the median size of UHMWPE wear particles identified in this study relative to previously published studies. These results are in-line with the prediction that improvements in technology result in a smaller wear particle size distribution (Schroder et al., 2013).

High density wear particles are commonly found within periprosthetic tissue surrounding THR and TKR (Topolovec et al., 2013, Topolovec et al., 2014). The composition, size and shape of high density wear particles surrounding total joint replacements depends on the location and mechanism of wear. For example, trunnion wear against the inside of a ceramic THR head produces 0.02 to 0.05 µm sized titanium alloy wear debris (Milošev et al., 2000), whereas titanium alloy wear debris produced at the stem of ceramic-on-ceramic THRs was substantially larger at 0.61 ± 0.31 µm (Lerouge et al., 1996). The most common high density wear particle type identified in this validation study was zirconia ceramic. Zirconia particles were present in both mulberry-type agglomerate particle form and individual grains for both THR and TKR samples. These particles had a median size of 0.29 µm (IQR = 0.16 – 0.55) and 0.23 µm (IQR = 0.11 – 0.64) for THR and TKR, respectively. Zirconia, a radiopacifier used in bone cement, has been identified

previously (Keen et al., 1992, Savio et al., 1994, Bos and Johannisson, 2004). Bos and Johannisson (2004) using histology with SEM and identified zirconia oxide particles in lymph nodes from 17 patients with THR. Zirconia particle size was between 0.02 µm and 0.75 µm and large mulberry-like and small granular particles were characterised. PMMA particles were sized between 0.5 and 20 µm. Lerouge et al. (1996) is the only study to isolate zirconia particles from tissue samples and found the average size to be 0.28 ± 0.08 µm and no mulberry-type particles were reported. The median zirconia grain size identified in the current study was 0.28 µm (IQR = 0.16 – 0.55) which was the same value reported by Lerouge et al. (1996). Zirconia particles in this study were both mulberry-like and granular, both of which have been acknowledged in a study of retrieved bone cement (Schunck et al., 2016). Zirconia granules were predominantly submicron sized and had a low aspect ratio. Zirconia ceramic particles likely originated from the bone cement in this study, however information on device fixation for the retrieved tissues was missing for this cohort. All of the TKR devices were likely to be cemented devices given uncemented TKRs are relatively uncommon (National Joint Registry, 2017).

Both UHMWPE and high density wear particles were isolated from the same THR and TKR tissue samples. The modified wear particle isolation method was considered successful and suitable to be applied to periprosthetic tissue samples from TAR.

9.3.4.1 Limitations

The tissue samples processed for the method validation were from unknown failed THR and TKR devices. Implicitly, the type of UHMWPE used for these devices was also unknown. Different variants of UHMWPE produce wear particles with different characteristics, therefore the broad wear particle size variation across the cohort may have been a result of different material types being characterised. Also, the anatomical location of where the sample was extracted from was unknown and may affect wear particle size distribution (Maloney et al., 1995). This validation study was used to test the reliability of the isolation method and was deemed acceptable because UHMWPE and high density wear particles were isolated from all 18 tissue samples.

Carbon coated filter membranes prepared for SEM analysis featured a similar carbon-oxygen elemental make-up as UHMWPE. Elemental analysis was not sufficient to determine the presence of UHMWPE wear particles. In-house research expertise, personal experience and EDX analysis were combined to visually identify particles with morphology similar to those previously identified. Also, contaminants such as atmospheric silicon particles, for example, could be excluded based on their elemental composition. This was a strength of manual particle characterisation, however a different wear particle size distribution would be expected from manual analyses. The full breadth of the available magnification provided by the SEM was utilised to identify and

characterise individual particles. More particles at the extremes of the size range would be expected and was reflected in the results. This differs from automated particle sizers which have a fixed size range and cannot discriminate between target particles and contaminants. Observer bias was also a substantial limitation of manual characterisation. Only approximately 100 to 400 UHMWPE wear particles were characterised per sample, the distribution of which may not be representative of the billions of wear particles produced by a joint replacement (Richards et al., 2008).

9.4   Wear Particle Isolation and Characterisation of Periprosthetic Tissue Surrounding TAR.

A modified method capable of isolating UHMWPE and high density wear particles from periprosthetic tissue was developed and validated (see sections 9.2 and 9.3). The novel method was used to process periprosthetic tissue from surrounding failed TAR. The aim was to determine wear particle composition, size and morphology for both UHMWPE and high density materials within TAR tissue samples.

9.4.1   Periprosthetic Tissue Samples from TAR

Periprosthetic tissue samples from 15 TARs (20 samples) were retrieved through the process detailed in section 3.3. All of the TARs were mobile-bearing uncemented metal-on-polyethylene bearing combinations, except the BP TAR which featured a ceramic titanium nitride coating the bearing and fixation surfaces. Two AES (2nd Gen) TARs had two samples from the same ankle and one had three samples. One Rebalance TAR had two samples retrieved from the same ankle. The total number of samples processed was 20.

The demographic details are summarised in Table 9.2. Individual explant details are reported in section 3.4.1.

Table 9.2. Participant demographics for periprosthetic tissue samples retrieved from total ankle replacements.

Factor		n	Factor	Mean (range)
Total		15	Time In-vivo (Mo)	99.2 (4-168)
			Missing[c] (n)	3
Device Type	AES (2nd generation)[a,a,b]	12		
	AES (1st generation)	1	Age (years)	63 (49-71)
	Rebalance[a]	1	Missing[c] (n)	4
	BP	1		
Side	Right	6		
	Left	9		
Sex	Male	15		
	Female	0		
Diagnosis	OA	9		
	PTOA	3		
	Missing[c]	3		
Indicator for Revision	Osteolysis	13		
	Missing[c]	2		

Notes: [a], two samples; [b], three samples; Each [a] or [b] denotes number of TARs; AES, Ankle Evolutive System (Transysteme, Fr); Rebalance (Zimmer Biomet, UK); BP, Buechel Pappas (Endotec, US); [c] Data not available; Age was true at the time of primary surgery; OA, osteoarthritis; PTOA, post-traumatic osteoarthritis; n, frequency; Mo, Months.

9.4.2   Wear Particle Isolation Method

The complete modified method was used for all TAR samples (see section 9.3.2). Only one alteration was made for this study. The quantity of tissue processed was changed from 1 g to 0.8 g to increase the potential effectiveness of the enzymatic digestion. Also, more care was taken to mince the tissue prior to digestion. No further alterations were deemed necessary. The same particle characteristics such as Feret's diameter, aspect ratio and circularity were used as in section 9.3.2.5.

9.4.2.1   Statistical Analysis

Statistical analysis was performed using SPSS Statistics Version 22 (IBM Corp, USA). Non-parametric descriptive statistics were reported for wear particle size. Parametric morphological characteristics were also reported. The proportion of wear particles in the submicron (< 1 µm), 1 to 10 µm and >10 µm size ranges were also reported.

9.4.3   Results

Periprosthetic tissue samples from TAR were mostly beige in colour but speckled with metallic debris. In several cases, large areas of metal were attached to the tissue samples, presumably from the fixation surface (Figure 9.20). Several tissue samples were brittle to the touch and disintegrated into smaller pieces without requiring dicing with scissors.

20 mm
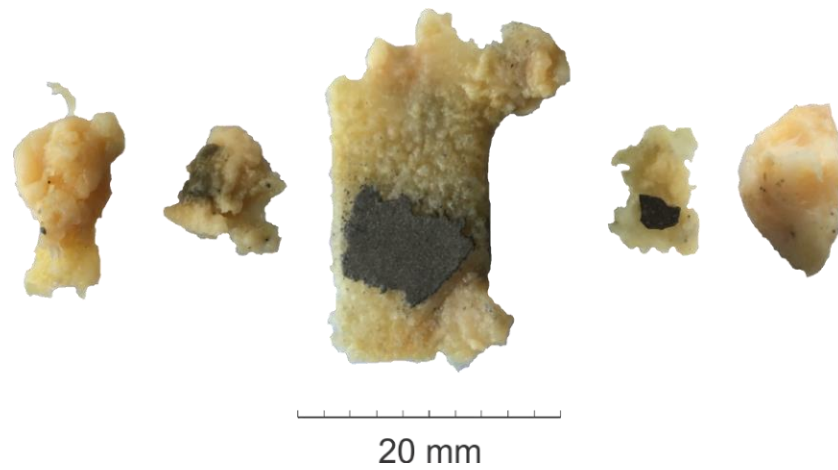
Figure 9.20. Examples of tissue samples with large metal particles attached. The central tissue sample was composed of bone and not processed for wear particle isolation, however a large area of delaminated fixation surface was attached. Speckles of metallic wear particles could be identified visually in several tissue samples.

After the final three centrifugal wash steps, masses of wear particle populations were commonly visible at the bottom of the centrifuge tube. Typically, the wear particle populations appeared pale in colour (e.g. cream/off-white), black or a combination of the two (Figure 9.21).

5 mm
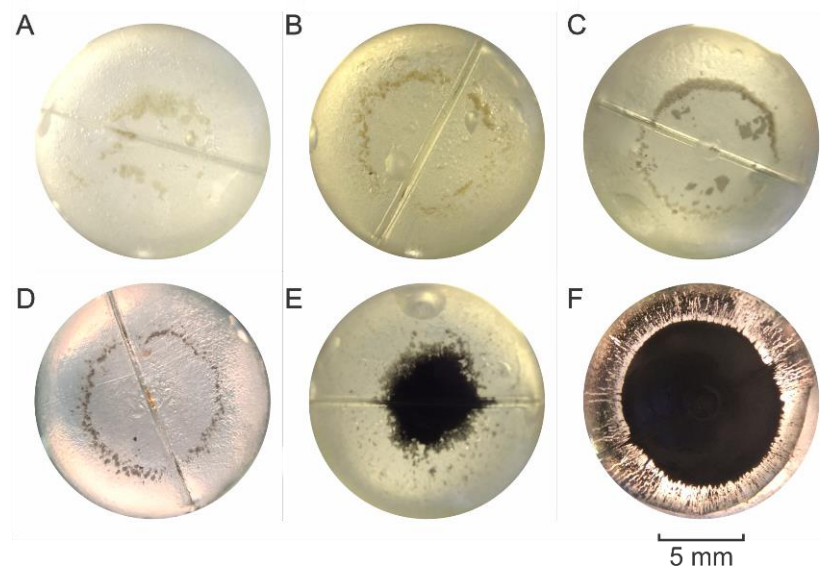
Figure 9.21. Examples of visible wear particle populations pelleted after the final washing step of the wear particle isolation method. A-C, visually light calcium phosphate particles. D-F, visually dark metallic particles.

A large volume of metallic wear debris were isolated from one tissue sample originating from an ankle implanted with the BP TAR. The metallic wear debris was visible throughout the isolation process, from the original tissue sample through to the last wash steps (Figure 9.22). The BP TAR had undergone metal-on-metal contact between the tibial and talar bearing surfaces caused by bearing insert subluxation.
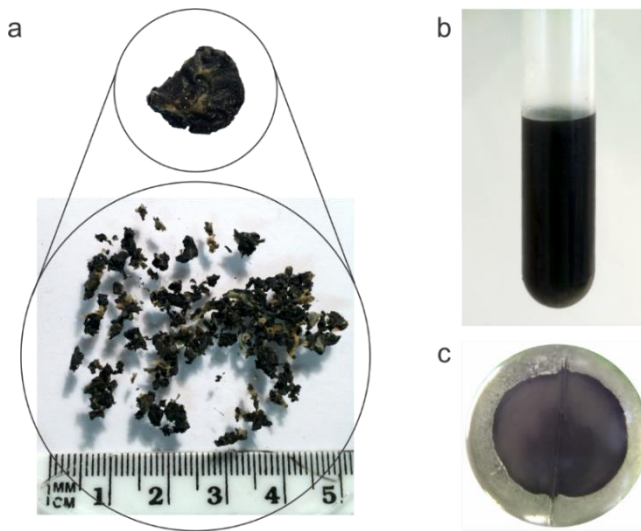
Figure 9.22. Periprosthetic tissue sample from a BP TAR which had undergone metal-on-metal contact in-vivo. The majority of wear particles in this example were titanium alloy, the substrate material of the TAR. A, tissue sample before and after dicing. B, cleansed wear particles in suspension. C, Cleansed and pelleted wear particles.

9.4.3.1 Particle Composition

Ultra-high molecular weight polyethylene particles were isolated from all tissue samples, the mean number of particles characterised per sample was 176 (range: 56 to 403). Flakes, fibrils and granules of UHMWPE were identified (Figure 9.23).
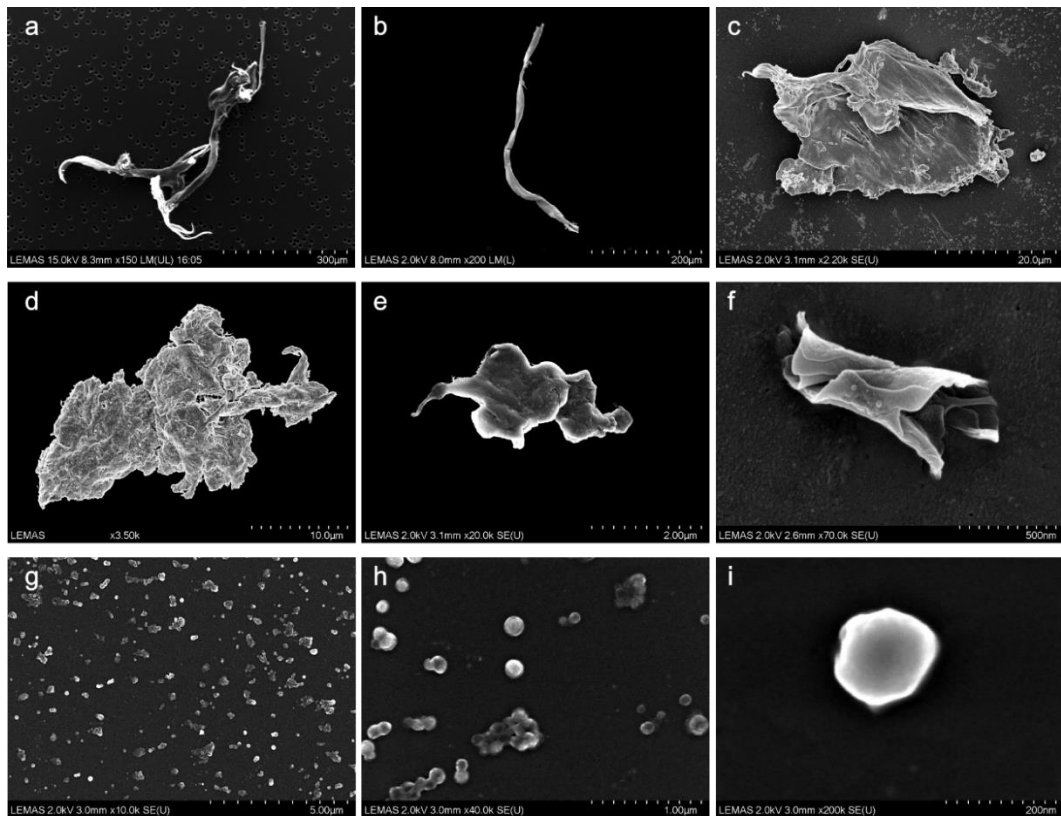
Figure 9.23. Ultra-high molecular weight polyethylene wear particle types isolated from periprosthetic tissue surrounding total ankle replacements. A-B, fibrils. C-F, flakes. G-I, granules.

The high-density particle materials identified in TAR samples included: calcium phosphate (63.3%), cobalt chromium alloy (15.3%), titanium alloy (14.2%), commercially pure titanium (6.9%), and stainless steel (0.3%; percentages denote proportion of high-density particles characterised) (Figure 9.24 and Figure 9.25). Calcium phosphate particles in the form of urchin-like (Figure 9.24A-C) and shard-like (Figure 9.24D-F) morphologies were isolated from all HA coated TARs (n = 13). Cobalt chromium alloy particles were the second most prevalent particle type for TAR devices and had a flake-like morphology. Titanium alloy was the substrate material for the BP TAR and the fixation surface material for the Rebalance TAR. The BP TAR had failed due to bearing dislocation, therefore high volumes of titanium alloy particles had been produced by the consequential metal-on-metal articulation between the tibial and talar components. Spheroidal titanium nitride coated beads originating from the BP TAR fixation surface were identified but not in sufficient numbers for characterisation. The Rebalance TAR featured both titanium alloy and cobalt chromium alloy particles which represented the composition of the substrate and fixation surfaces. Although, the 'Bone Master' HA coating was not isolated in particulate form. Nine individual stainless steel particles were identified across the cohort and were considered to be contaminants.
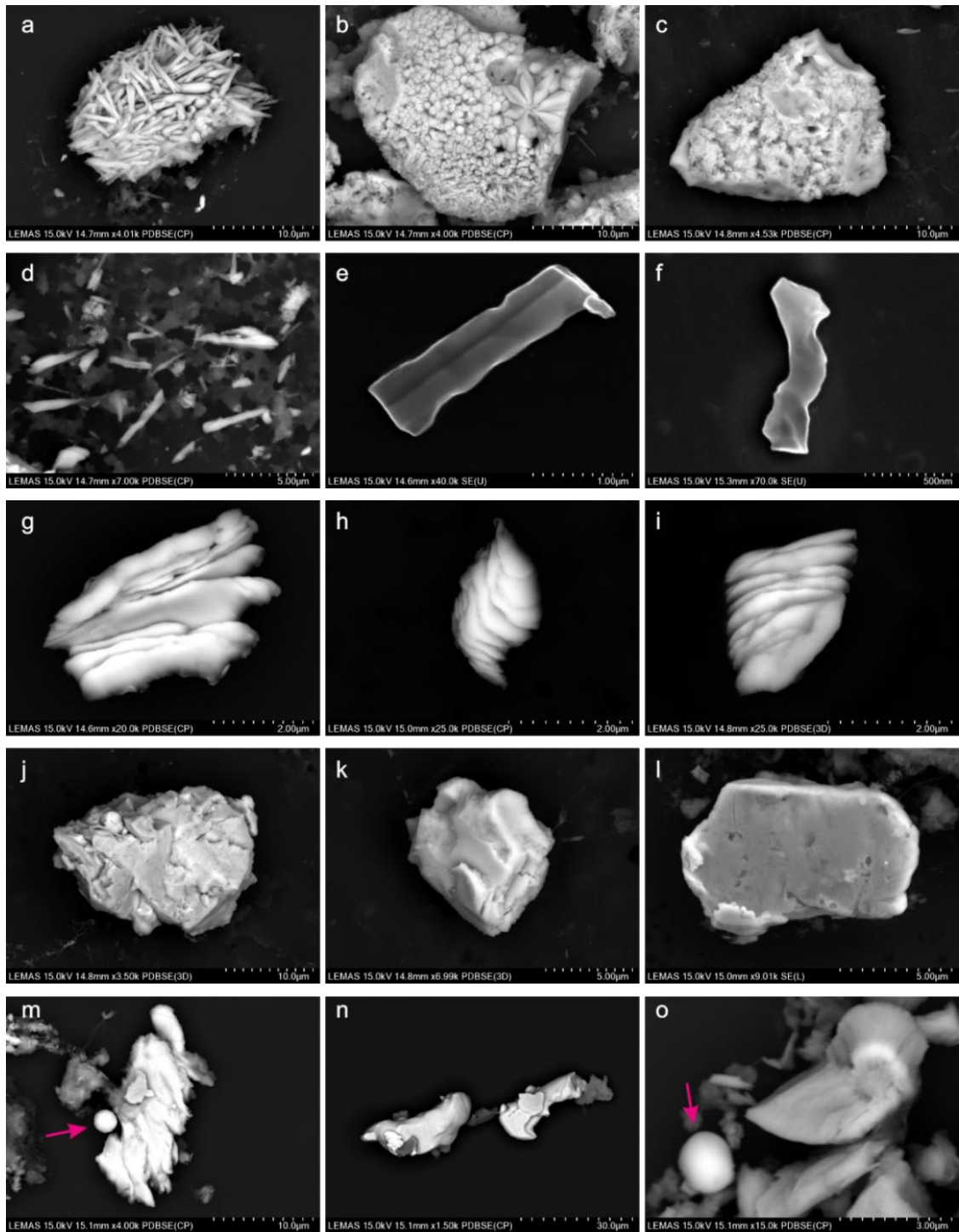
Figure 9.24. (A-O) High density wear particles isolated from periprosthetic tissue surrounding total ankle replacements. A-C, Urchin-like hydroxyapatite. D-F, Shard-like hydroxyapatite. G-I, Flake-like cobalt chromium alloy. J-L, Commercially pure titanium. M-O, Titanium alloy. Pink arrow, titanium nitride coated fixation beads from the Buechel Pappas TAR.
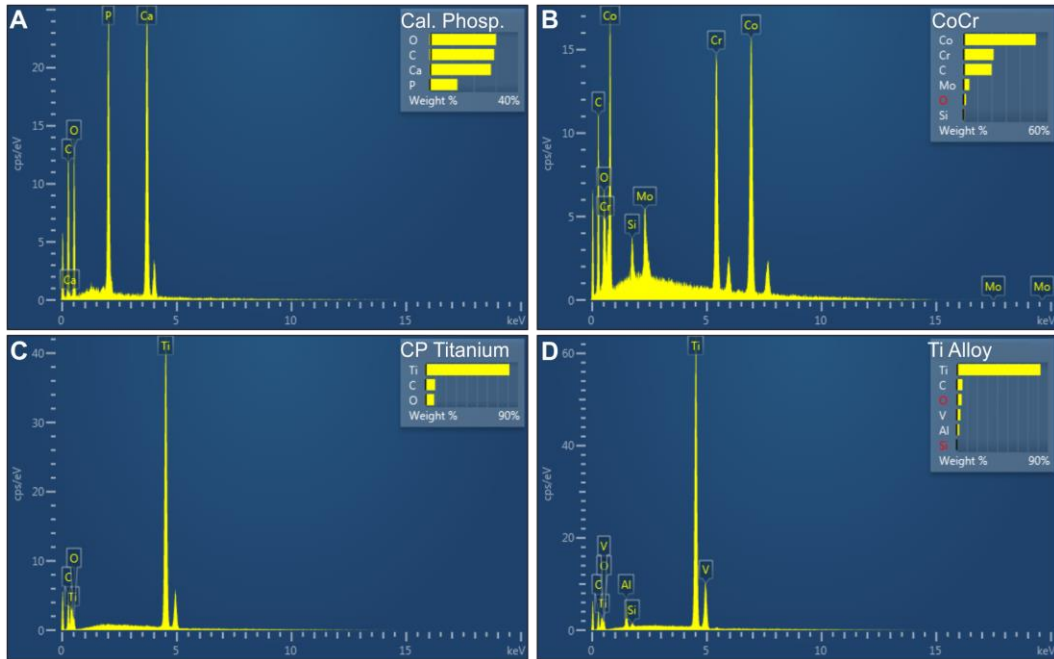
Figure 9.25. Examples of energy dispersive X-ray analysis traces for calcium phosphate (A), cobalt chromium alloy (B), commercially pure titanium (C) and titanium alloy (D).

The different wear debris populations were often seen attached to each other or clustered together on the filter membrane (Figure 9.26). Each particle type exhibited distinct morphological properties making it possible to distinguish particle types.
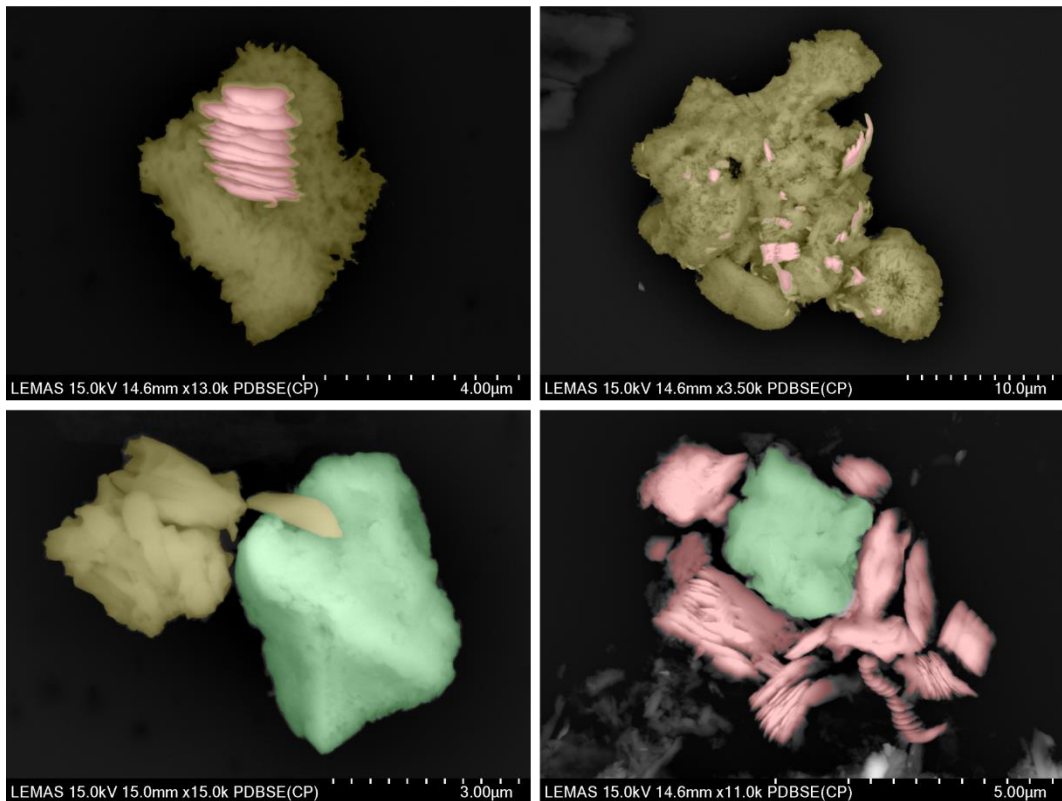
Figure 9.26. Examples of high density wear particles (mixed populations) isolated from total ankle replacements. Yellow, calcium phosphate. Red, cobalt chromium. Green, commercially pure titanium.

9.4.3.2 Particle Characterisation

The median maximum diameter for all UHMWPE wear particles and all high-density wear particles was 0.15 μm (IQR = 0.06 – 0.70), and 1.67 μm (IQR = 0.91 – 3.44), respectively. The median maximum diameter of all wear particles combined was 0.85 μm (IQR = 0.15 – 2.46). UHMWPE wear debris was the smallest wear particle population, with 71.9 ± 20.3% being in the submicron size range. However, the largest wear particle isolated was also comprised of UHMWPE and was 630.20 μm in diameter.

The majority of high density wear particles were in the 1 to 10 μm range (60.7 ± 19.5%). The smallest high density wear particle populations were the shards of calcium phosphate (1.21 μm IQR = 0.70 – 2.02) and cobalt chromium alloy particles (1.29 μm IQR = 0.85 – 2.04). The largest high density wear particle population was calcium phosphate in its bulk form, which had a median particle size of 11.58 μm (IQR = 5.11 – 21.41). Commercially pure titanium and titanium alloy were similar in size (Table 9.3) although, commercially pure titanium featured the largest wear particle out of all high density wear particles at 102.89 μm.

The AES (1st Gen) TAR featured a single layer fixation surface coating of HA, deposited directly onto the cobalt chromium alloy substrate. For this sample, calcium phosphate and cobalt chromium alloy particles were identified. The median size for each particle type was 1.09 μm (IQR = 0.58 – 1.98), 10.90 μm (IQR = 3.55 – 18.41) and 1.23 μm (IQR = 1.17 – 2.04) for shard-like HA, urchin-like HA and cobalt chromium alloy, respectively.

The Rebalance TAR had a fixation surface composed of a dual layered titanium alloy coating with a 'Bone master' HA top layer. The substrate was cobalt chromium alloy. For both samples, only titanium alloy and cobalt chromium alloy wear particles were identified for this device. The median size for each particle type was 4.37 μm (IQR = 2.47 – 7.20) and 2.48 μm (IQR = 1.58 – 6.39) for titanium alloy and cobalt chromium alloy, respectively. No calcium phosphate wear particles were identified in the tissue for this TAR.

The BP TAR tissue sample was black in colour and featured large volumes of titanium alloy wear particles. The median size for titanium alloy wear particles from this TAR was 2.27 μm (IQR = 1.45 – 7.20).

Both UHMWPE and high density wear particles featured a similar percentage of wear particles in the >10 μm size range, which were 9.9 ± 11.5% and 6.8 ± 9.3%, respectively (Figure 9.27).

Table 9.3. Particle characteristics for particles isolated from TAR.

	Particle Count	Diameter (µm)	Circularity (SD)	Aspect Ratio (SD)
All Particles	6920	0.85	0.64	2.23
Max		630.20	0.21	1.5
Min		0.02		
UHMWPE	3522	0.15	0.72	1.61
Max		630.20	0.22	0.75
Min		0.02		
All High Density	3407	1.67	0.56	2.87
Max		102.89	0.18	1.78
Min		0.09		
All CaP	2155	1.50	0.53	3.28
Max		81.33	0.17	1.91
Min		0.09		
CaP Shards	1738	1.21	0.51	3.7
Max		16.19	0.16	1.89
Min		0.09		
CaP Urchins	417	11.58	0.65	1.56
Max		81.33	0.16	0.42
Min		0.44		
CoCr	520	1.29	0.54	2.34
Max		18.72	0.17	1.15
Min		0.26		
CP. Titanium	236	2.57	0.68	1.58
Max		102.89	0.12	0.39
Min		0.36		
Titanium Alloy	487	3.04	0.6	2.25
Max		48.14	0.19	1.49
Min		0.29		

Notes: UHMWPE, Ultra-high molecular weight polyethylene; CaP, Calcium Phosphate; CoCr, Cobalt Chromium; CP, Commercially pure; ECD, Equivalent circle diameter.
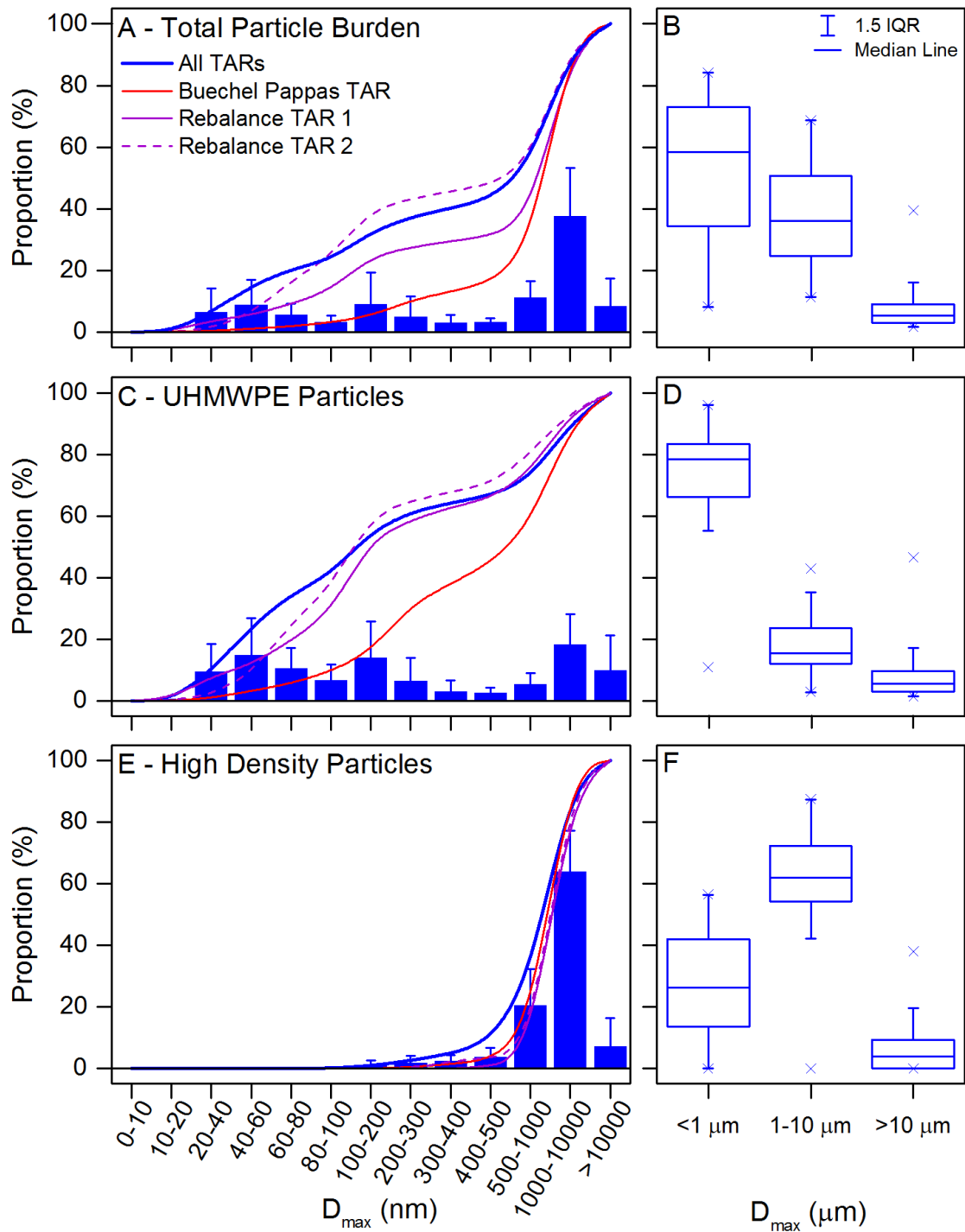
Figure 9.27. Size distribution of wear particles isolated from periprosthetic tissue surrounding for total ankle replacement (TAR). A,C,E, size distribution graphs with cumulative frequency. B,D,F, Binned size distribution data. A, total particle burden was ultra-high molecular weight polyethylene (UHMWPE; C) and high density (E) wear particle sizes combined. D_{max}, maximum diameter. Of the 15 devices, one was a Buechel Pappas (BP) TAR (red line) and two were Rebalance TARs (purple lines).

Aspect ratio and circularity were reported for each particle type (Table 9.3). For both measures, a value of 1 indicates a perfect circle. Shard-like calcium phosphate particles had the greatest aspect ratio (3.70 ± 1.89) and the lowest circularity (0.50 ± 0.16). Whereas calcium phosphate in its bulk form had the lowest aspect ratio at 1.56 ± 0.41

(Figure 9.28) and UHMWPE wear particles had the highest circularity at 0.71 ± 0.22. Both cobalt chromium alloy and titanium alloy wear particles featured relatively high aspect ratios of 2.34 ± 1.15 and 2.25 ± 1.49, respectively.
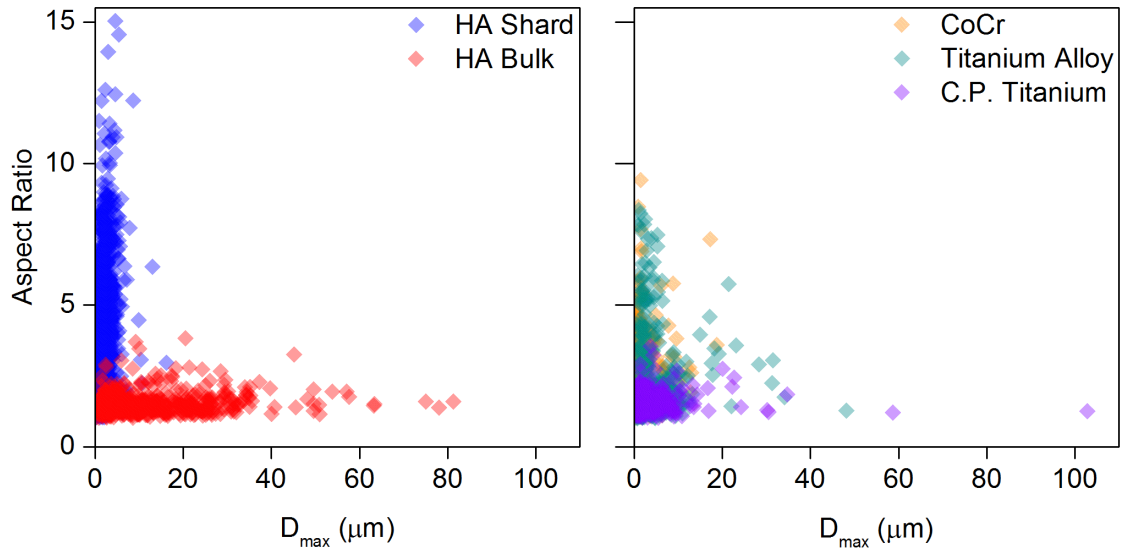
Figure 9.28. Aspect ratio of different high density wear particles isolated from periprosthetic tissue surrounding total ankle replacement. Individual shards and bulk particles of calcium phosphate (or hydroxyapatite, HA) were stratified (left). CoCr, cobalt chromium. C.P. Titanium, commercially pure titanium. D_{max}, maximum diameter.

9.4.3.3   Total Wear Particle Population

The three different joint types included in the current study were not statistically comparable due to featuring different fixation materials, properties and small sample sizes. However, a descriptive comparison between the three joint types showed a slightly different total wear particle burden for TAR compared to THR and TKR (Figure 9.29). The primary difference between the joints was the size of the high density wear particles for TAR. Only 27.5 ± 17.1% of high density wear particles in TAR were in the submicron range, compared to 50.7 ± 31.1% and 56.7 ± 32.2% in THR and TKR, respectively. The percentage of UHMWPE wear particles in the submicron range were similar between TAR (71.9 ± 20.3%), THR (73.1 ± 11.1%) and TKR (73.1 ± 21.3%).

For all high density wear particles combined, the aspect ratio for wear particles surrounding TAR was greater (2.9 ± 1.8) than those surrounding THR (1.5 ± 0.7) and TKR (2.1 ± 1.4). The aspect ratio for all UHMWPE wear particles were similar between joints; TAR (1.6 ± 0.8), THR (1.5 ± 0.6) and TKR (1.5 ± 0.6).
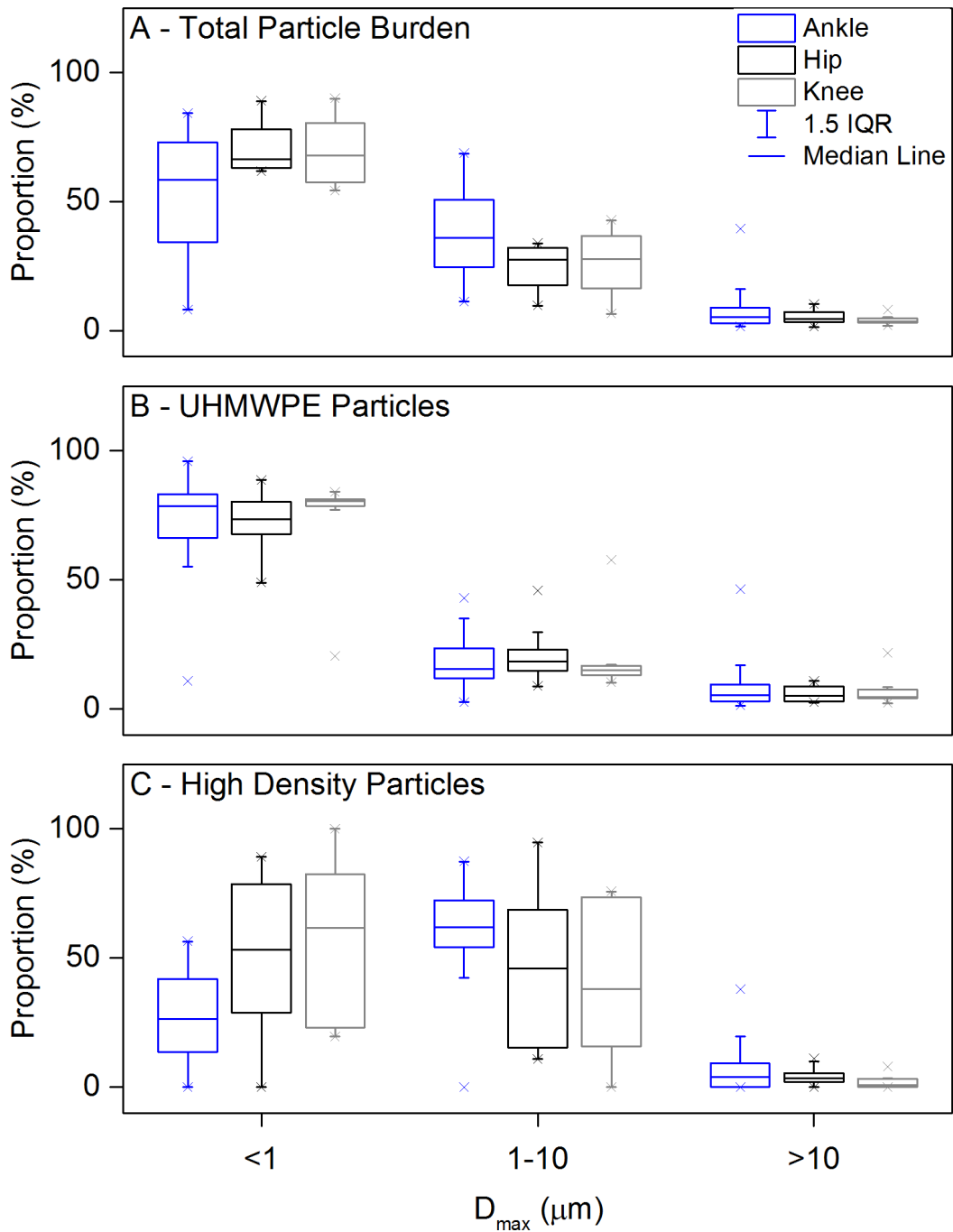
Figure 9.29. Total hip, knee and ankle replacement wear particle populations. D_{max}, maximum diameter.

9.4.4 Discussion

The total wear particle burden in periprosthetic tissue is a contributor to imbalances in homeostasis and inducers of inflammation (Ingham and Fisher, 2000). Particle isolation studies have isolated both UHMWPE and high density particles (e.g. metal, ceramic) for THR (Margevicius et al., 1994, Shanbhag et al., 1994, Maloney et al., 1995) and TKR (Margevicius et al., 1994) but to date, not for TAR. This study aimed to identify the

composition, size and morphology of UHMWPE and high density wear particles isolated from periprosthetic tissue samples surrounding failed TAR.

UHMWPE wear particles from periprosthetic tissue surrounding *failed* TAR have not be previously fully isolated and characterised. In THRs and TKRs, Conventional UHMWPE wear particles have been shown to be sized from 15 nm granules (Scott et al., 2001, Richards et al., 2008) to millimetre fibrils (Tipper et al., 2000). The UHMWPE wear particles isolated from periprosthetic tissue surrounding failed TAR ranged 15 nm to 630 µm in size and the median maximum diameter was 0.15 µm (IQR = 0.06 – 0.70). One study isolated UHMWPE wear particles from joint aspirates of two types of TAR, the fixed-bearing Agility TAR (n=4) and the mobile-bearing STAR (n=11), all of which were asymptomatic and functioning well (Kobayashi et al., 2004). The mean ECD was reported to be 0.82 ± 0.11 µm for the mobile-bearing STAR TAR, which was larger than the median maximum diameter presented in the current study. Kobayashi et al. (2004) used the methods developed by Margevicius et al. (1994) which included filtration using a 0.1 µm filter membrane and an automated particle sizer for analysis. As discussed in the method development, a 0.015 µm filter was used for the current study to minimise nanometre-sized particle losses and, manual characterisation was used to characterise individual particles as opposed to agglomerates. This difference in methods likely caused the substantial disparity in particle size. Analysis magnification has been shown to be the greatest factor affecting particle size distributions between studies (Schroder et al., 2013). Histological studies investigating wear particle populations in TAR identified UHMWPE particles to be between 2 and 83 µm (Dalat et al., 2013, van Wijngaarden et al., 2015). The larger size range likely reflects the difficulty imaging submicron and nanometre scale particles in tissue using relatively low resolution light microscopy.

Aspect ratio is an indicator of shape and was similar between the UHMWPE wear particles isolated by Kobayashi et al. (2004) for mobile-bearing TARs (1.57 ± 0.05) and the TARs investigated in this current study (1.61 ± 0.75). As a rule of thumb, an aspect ratio of 1.0 to 2.39 suggest the particles are globular/spherical, whereas particles with an aspect ratio of between 2.4 and 5 are considered to have elongated/fibrillar morphologies (Sieving et al., 2003, Day et al., 2012). The UHMWPE wear particles isolated from TAR were typically more spheroidal than fibrillar. Another morphological parameter, roundness, was reported by Kobayashi et al. (2004). UHMWPE wear particles were shown to be more circular than the particles isolated from the TKR control samples. The open source software used for the current study calculated the parameter 'circularity' as an analogous measure to roundness. Both parameters classify the value 1 as a perfect circle. The difference between the parameters is that for circularity, values decrease from 1 for more irregular shapes, whereas for roundness, values increase from 1 to represent irregular shapes. The circularity value for UHMWPE particles isolated in this current

study was 0.72 ± 0.22, which was similar to the UHMWPE wear particles isolated from the THR (0.70 ± 0.22) and TKR (0.74 ± 0.23) samples in the validation study (see section 9.3.3.2). Notably, the variance in values was much broader for the parameters calculated in the current study compared to Kobayashi et al. (2004). Each individual particle was manually characterised for the current study, therefore agglomerates were excluded and particles up to 630 µm were included. Larger wear particles tended to be in the flake/irregular form, whereas nanometre sized particles are typically spheroidal. Characterising the full breadth of particle types likely created a broader variance for morphological parameters.

The most common type of high density wear particle isolated from TAR tissue was calcium phosphate. Calcium phosphate particles have been identified histologically in studies investigating TAR devices (Koivu et al., 2009, Koivu et al., 2012, Dalat et al., 2013, van Wijngaarden et al., 2015, Singh et al., 2016) and have been suggested to originate either from the hydroxyapatite coating (Dalat et al., 2013, Singh et al., 2016) or from surrounding hard tissue such as bone (Koivu et al., 2012, van Wijngaarden et al., 2015). Given the similarity in elemental composition between hydroxyapatite coatings and bone, it is difficult to differentiate the origin of such wear debris solely using elemental analysis. Urchin-like particles have been suggested to originate from hydroxyapatite coatings due to their crystalline features (Willie et al., 2000). The absence of a bone-like architecture has also been used to identify particles of hydroxyapatite coating (Singh et al., 2016). The crystallised nature of the calcium phosphate particles isolated in this current study suggested they originated from the HA fixation coating. Calcium phosphate particles were not identified in non-HA-coated TAR devices, nor in in the validation study using THR and TKR periprosthetic tissue samples.

Cobalt chromium alloy and commercially pure titanium wear particles were commonly identified in the AES (2nd Gen) TAR tissue samples and have been identified previously in histological studies for several TAR designs (Koivu et al., 2009, Koivu et al., 2012, Dalat et al., 2013, van Wijngaarden et al., 2015, Singh et al., 2016, Schipper et al., 2017). Koivu et al. (2009) reported more titanium wear particles to be present in AES TAR tissue samples compared to cobalt chromium particles at 31.3 months follow-up, whereas Singh et al. (2016) measured more cobalt chromium than titanium particles in tissue samples using Inductively Coupled Plasma Mass Spectrometry (ICPMS) at 74 ±33 months follow-up for the STAR, Hintegra, Salto and Taric TARs. Proportionally more cobalt chromium alloy particles were identified in this current study than titanium particles, with a similar follow-up time to Singh et al. (2016). Cobalt chromium alloy wear particles in TAR tissue may have originated from the bearing surfaces after fatigue failure and/or 3rd body wear, in which case the number of particles produced may be expected to increase as a function of time. Alternatively, cobalt chromium alloy particles may also

have been produced at the fixation surface after extensive abrasive wear and/or fixation surface delamination (see section 6.4.3). In the latter scenario, the relatively thin coating of titanium fixation coating may have worn away allowing repeated and sustained wear of the cobalt chromium alloy substrate.

Submicrometre-sized cobalt chromium alloy and titanium wear particles have been suggested to contribute to the development of aseptic loosening (Shanbhag et al., 1995, Catelas et al., 2011, Yao et al., 2017). Cobalt chromium alloy particles produced by metal-on-metal THR articulation tend to be in the nanometre size range (Brown et al., 2007a), whereas, particles produced at the fixation surface tend to be larger in size (Maloney et al., 1995). The difference in particle size is attributed different mechanisms of wear, for example, fretting versus abrasive wear (Brown et al., 2007b). Particles with a higher aspect ratio are also considered more biologically reactive (Hallab and Jacobs, 2009). In this current study, cobalt chromium alloy particles were flake-like particles which were smaller and had a greater aspect ratio than titanium particles. Both wear particle populations were typically in the micron-size range (Table 9.3). Shard-like calcium phosphate particles were similar in size to cobalt chromium wear particles but featured the greatest aspect ratio (3.7 ± 1.9) of all the characterised wear particle populations in this study. Enhancements in fixation materials and design are yet to completely diminish wear particle release (Endrizzi et al., 2016) and appear to be a problem for the TAR designs included in the current study.

One AES (1st Gen) TAR, one Rebalance TAR (two samples) and one BP TAR were analysed in addition to the 12 AES (2nd Gen) TARs. Each TAR design featured wear particles characteristic of both the fixation surface and substrate materials. Although, the 'Bone Master' HA coating was not detected for the Rebalance TAR, in neither of the two tissue samples. The titanium alloy wear particles produced by the Rebalance TAR were twice as large as the same particle material produced by the BP TAR. A difference in the wear mechanisms for both TARs is likely the cause for the difference in wear particle size. The Rebalance TAR featured titanium alloy on the fixation surface which was likely abraded by micromotion at the implant-bone interface. Whereas, titanium alloy wear particles produced by the BP TAR were likely to be caused by metal-on-metal contact between the tibial bearing surface and the edge of the talar component, the evidence for which was shown in Chapter 6.

The total wear particle population for TAR was found to be different than the comparable characteristics of wear particles isolated from THR and TKR in the validation study. The primary difference was the percentage of high density wear particles in the submicron size range. The wear debris produced at the fixation surfaces and substrate materials was generally larger than the high density wear particles isolated from THR and TKR.

Zirconia wear particles were submicron in size in granular form and originated from bone cement for THR and TKR. Bone cement is a commonly used method for achieving primary fixation for these joint types (National Joint Registry, 2017). Whereas, cemented fixation was largely disbanded in Europe for TAR in the 1980's following poor clinical results (Gougoulias and Maffulli, 2013). The fixation surface materials identified in the TAR samples were generally in the micron-size range and were likely produced by abrasion at the bone-implant interface. Zirconia mulberry-like bulk particles were likely broken down into granules at the bone implant interface or within the joint space and later phagocytosed. For all high density wear particles combined, the TAR particles had the greatest aspect ratio, followed by TKR particles and then THR particles. According to the definitions of particle shape reported by Sieving et al. (2003), the high density wear particles produced by TAR were generally elongated or fibrillar (aspect ratio >2.39), whereas the aspect ratio values for THR and TKR particles reflected globular/spherical wear particle types (aspect ratio < 2.39). Kobayashi et al. (2004) showed TAR UHMWPE particles to be similar in size to TKR particles but different in shape. The UHMWPE wear particles from TAR had a significantly lower aspect ratio and roundness compared to TKRs. The present study showed aspect ratio and circularity to be similar between all three joint types. The particle characteristics all had a high variance in this study, which may be associated with the low sample size, using a combination of different THR and TKR designs with different types of UHMWPE, most of which were unknown, and/or tissue samples with a broad spectrum of implantation times were included. With all particle types considered, the total wear particle population for TAR was larger (but in the submicron size range) and more elongated than THR and TKR. Submicron wear particle sizes and elongated morphologies are considered the most high risk wear particle characteristics to cause an adverse biological response (Ingham and Fisher, 2000, Tipper et al., 2000, Sieving et al., 2003, Hallab and Jacobs, 2009).

9.4.4.1 Limitations

The limitations of the isolation method in general were discussed in section 9.3.4.1. These included the limitations of manual characterisation and the challenges of identifying UHMWPE wear particles. Specific to the TAR tissue samples, it was challenging to distinguish between hydroxyapatite and bone wear particles. Both particle types register as calcium phosphate using EDX analysis therefore identifying each particle types was based on morphology alone. No particles with a bone-like morphology were identified, but this does not exclude the possibility of bone particles being present within the sample. The sample size was relatively low (20 samples from 15 ankles) given the high variance associated with the manual characterisation method. This represents a limitation of the retrieval approach as opposed to the isolation method.

9.5 Summary

The aim of this chapter was to isolate wear particles from periprosthetic tissue surrounding failed TAR and characterise their composition, size and morphology. A novel wear particle isolation method was developed and validated to isolate UHMWPE and high density wear particles from the same human tissue sample.

Flakes, fibrils and granules of UHMWPE wear particles were characterised from all tissue samples (n = 20). The majority (72%) of UHMWPE wear particles were in the submicron size range and the largest particle was 630 μm. This population of wear particles were considered similar to other TJRs.

High density wear particle populations were generally larger than UHMWPE wear particles with the majority (61%) of particles being sized between 1 and 10 μm. Calcium phosphate, cobalt chromium alloy and commercially pure titanium wear particles were isolated from tissue surrounding the AES TAR. Calcium phosphate appeared crystalline and was characterised in two morphologies; shards and urchins. The shard-like calcium phosphate particles featured the highest aspect ratio (AR = 3.7). Commercially pure titanium was large in size with a low aspect ratio and had likely originated with the calcium phosphate (i.e. hydroxyapatite) from the fixation surface. Cobalt chromium wear particles were flake-like with a high aspect ratio (AR = 2.3) which was consistent with micro-scratching of the bearing surfaces. Wear particles of composition consistent with the substrate and fixation materials used for the Rebalance and BP TARs were also isolated.

The total wear particle population for TAR was generally larger (but still in the submicron size range) and more elongated than the wear particle characteristics identified for THR and TKR in the validation study.

Chapter 10
Discussion

10.1 Introduction

The aim of the research in this thesis was to identify the wear modes and failure mechanisms of total ankle replacement (TAR) (see Chapter 1). A non-destructive retrieval analysis approach was used to understand the types and location of damage/wear on failed TAR devices. To achieve this aim, several novel methods were developed, validated for reliability, and applied to three different retrieved resources: (1) medical imaging, (2) the explant, and (3) periprosthetic tissue. Combining the results from a comprehensive and quantitative medical imaging analysis with a rigorous damage/wear mode analysis has given a unique insight into how TARs function, wear and fail.

In Chapter 2 (Literature Review), ankle osteoarthritis (OA) was identified as the primary indication for TAR. Approximately 3,000 patients require surgical treatment for ankle OA in the UK each year, however only ~ 600 patients undergo TAR. Poor implant survivorship and conflicting opinions on which design principles are most efficacious has resulted in low implantation rates. The early development of osteolysis is commonly identified for TAR and can result in device failure but the causes of this are yet to be elucidated. Many hypotheses for the mechanisms of TAR failure have been suggested, such as insufficient primary fixation and the excessive production of wear debris, yet only four retrieval studies investigating the condition of retrieved TARs have been published over its 40 year development. A retrieval analysis was undertaken over the period of three years and this thesis describes the process and outcomes, which are highlighted in the following paragraphs.

In Chapter 3 (Retrieval Processes), the demographic profile and device types of the participants who consented for this study were detailed. The resources retrieved included: 44 explants, 28 weight bearing X-rays, 22 CT scans and 20 periprosthetic tissue samples (from 15 ankles). The cohort featured five TAR brands, the majority of which were mobile bearing, semi-constrained BP-type TARs. The cohort represented a higher percentage of young male participants relative to the implantation statistics of TAR for the UK. Osteolysis and/or pain was the predominant indication for failure.

In Chapter 4 (X-ray Imaging), weight-bearing X-ray images were analysed for features indicative of device dysfunction. Edge-loading, collapse of the talus, varus/valgus

malalignment, radiopaque maker extrusion, and massive osteolysis were recurring features. Despite the presence of these features, quantitative measures of device alignment were within the variances considered acceptable in the published literature.

In Chapter 5 (CT Imaging), re-orientated CT scans highlighted the prevalence of edge-loading (77%) and impingement (55%) in this cohort. Half of the bearing inserts (50%) were considered aligned (≤ 2 mm) with the tibial component in the coronal plane. Bearing insert translation and rotation, independent of each other, and combined, were clinically relevant risk factors for edge-loading. The measurement of medio-lateral offset ratio (MOR) was measured for the first time using CT scans and may be a useful metric to better understand medio-lateral edge-loading. Varus/valgus talar component tilt was prevalent (64%) but challenging to quantify. Osteolysis identified in the cohort was massive and prevalent, the size of which was similar to other published TAR studies but larger than osteolytic lesions reported for total hip replacement (THR). Clinical areal measurements of osteolysis were considered an acceptable representation of osteolysis volume.

In Chapter 6 (Damage Mode Analysis), retrieved TAR explants were analysed for established damage modes. Tibial component fixation surface wear was prevalent across all TAR designs. For AES (2nd Gen) TARs, 89% featured substrate abrasion in addition to degradation of the fixation coating. Micro-scratching and deep gouges were prevalent on the tibial component bearing surface and likely caused by third-body wear and/or bone contact with the surface. On average, the total scratch area was 35.3% of the tibial bearing surface and the scratch area was indicative of bearing insert location. Bearing insert dislocation caused the talar component to articulate with the tibial bearing surface in three TARs, producing substantial quantities of metallic wear debris as a result. On the inferior bearing insert surface, all seven damage modes were identified. Burnishing, scratching, pitting and abrasion were the most prevalent (>80%). Impingement between the bearing insert and bone caused material destruction for 57% of the TARs. Radiopaque marker extrusion was identified more frequently than in the medical imaging (21%). Total damage mode score was moderately correlated (r = 0.56) with osteolysis volume. However, methodological limitations of visual analysis such as selection bias may affect the precision of these results.

In Chapter 7 (Characterisation of Edge-Loading), edge-loading affected 70.5% of the cohort independent of- or combined with impingement. Only three bearing inserts were absent of edge-loading and all forms of impingement or bone contact. Edge-loaded TARs featured a 252 μm inflection of material, on average which may be sufficient to constrain the bearing insert to the affected side of the tibial component. Edge-loading occurred evenly on both medial (n=16) and lateral (n=16) sides. Bearing insert offsets of >2 mm

from the tibial axis should be considered clinically relevant for identifying edge-loading. Impingement (including minor and gross wear) occurred primarily on the medial (n=8) and posterior edge (n=8) and anatomical constraints created by the surrounding bone increase the probability for impingement, particularly the medial malleolus.

In Chapter 8 (Volumetric Wear Analysis), a sample of eight bearing inserts were analysed for volumetric wear loss. The volumetric loss excluding the outlier was 5.74% which after accounting for implantation time represented an annual wear loss of 65 mm^3. This wear rate was 2.5 times greater than the highest wear rate reported for in vitro simulation of TAR. Pycnometry was identified as a useful method of calculating wear loss, particularly for devices with unknown material properties. Volumetric measures determined using computed tomography were systematically and significantly greater than gravimetric measures. This was likely caused by the ineffective erasure of metal artefact during data post-processing. However, CT measures were highly correlated with gravimetric measures (r = 0.99), meaning relative spatial assessments of wear could be captured accurately. Asymmetrical wear patterns were evident and evenly distributed between the medial (n = 4) and lateral (n = 4) sides of the bearing insert.

In Chapter 9 (Wear Debris Analysis), a novel wear particle isolation method was developed and validated to isolate UHMWPE and high density wear particles from the same human tissue sample. Flakes, fibrils and granules of UHMWPE were characterised from all tissue samples (n = 20), the majority of which were in the submicron size range. Hydroxyapatite (HA), cobalt chromium alloy (CoCr) and commercial pure titanium (CPTi) wear particles were isolated from tissue surrounding the AES TAR. Shard-like HA particles had the highest aspect ratio (AR = 3.7). Cobalt chromium wear particles were flake-like and also featured a high aspect ratio (AR = 2.3). Wear particles of composition consistent with the substrate and fixation materials used for the Rebalance and BP TARs were also isolated. The total wear particle population for TAR was generally larger (but submicron on average) and more elongated than the wear particle characteristics identified for total hip and knee replacement.

Several novel methods were developed, validated and applied to TAR for the research in this thesis, for example:

- CT scan re-orientation and segmentation had not been applied to TAR previously. This method was validated against weight-bearing X-ray imaging and showed excellent reliability between observers. This method could be used to plan revision procedures and obtain more accurate alignment metrics of the individual TAR components.
- Photogrammetry used in conjunction with automated threshold analysis produced quantitative metrics of component damage which had not been

achieved previously for TAR. This method is useful for comparing the severity of component damage between device brands and reduces observer bias between research centres.

- Pycnometry was used for the first time for orthopaedic components to determine volumetric wear loss. This method was found to be excellently correlated and non-significantly different to gravimetric analysis which is the current gold standard for measuring wear.

- The modified wear particle isolation method developed to process tissue samples surrounding TAR was the first time nanometre UHMWPE and metallic/ceramic wear debris were extracted from the same periprosthetic tissue sample and characterised. Methods such as this are required to understand the total wear particle burden produced by orthopaedic devices and indicate the propensity of the particles to aggravate an adverse tissue reaction.

The novel methods used in this thesis, some of which are outlined in the section above, represent the broad range of non-destructive techniques available to researchers for the advanced characterisation of TAR explants.

In the following sections, the wear modes and possible failure mechanisms identified from the results in this thesis are discussed.

10.2 Wear Modes of Total Ankle Replacement

The damage and wear caused to an orthopaedic device following implantation are a blueprint of how the device functioned in vivo. Patterns of wear may indicate biomechanical function which is valuable to validate how the device actually functioned against the expected function. However, perhaps more importantly, once defined, modes of wear can be minimised or eradicated by manufacturers and orthopaedic surgeons.

McKellop (2007) identified four distinct wear modes by which total joint replacements function (Table 10.1). Mode 1 describes wear for a device functioning as intended. This wear mode is inevitable and should be minimised by design and biomaterial selection. Modes 2, 3 and 4 indicate device dysfunction should be eliminated where possible.

The wear modes of TAR have not been specifically defined previously, therefore the following sections identify the wear modes of TAR evidenced in this thesis (Figure 10.1).

Table 10.1. Joint replacement wear modes defined by McKellop (2007).

Mode	Description	Surfaces in contact	Mathematical Analog
1	Two bearing surfaces are contacting each other and are articulating together as intended	Primary vs. primary	1 x 1 = 1
2	A bearing surface wears against a non-bearing surface	Primary vs. secondary	1 x 2 = 2
3	Abrasive third-body debris introduced between the primary bearing surfaces	Primary vs. primary vs. third bodies	1 x 1 x 3 = 3
4	Two non-bearing surfaces articulate with each other under load	Secondary vs. Secondary	2 x 2 = 4
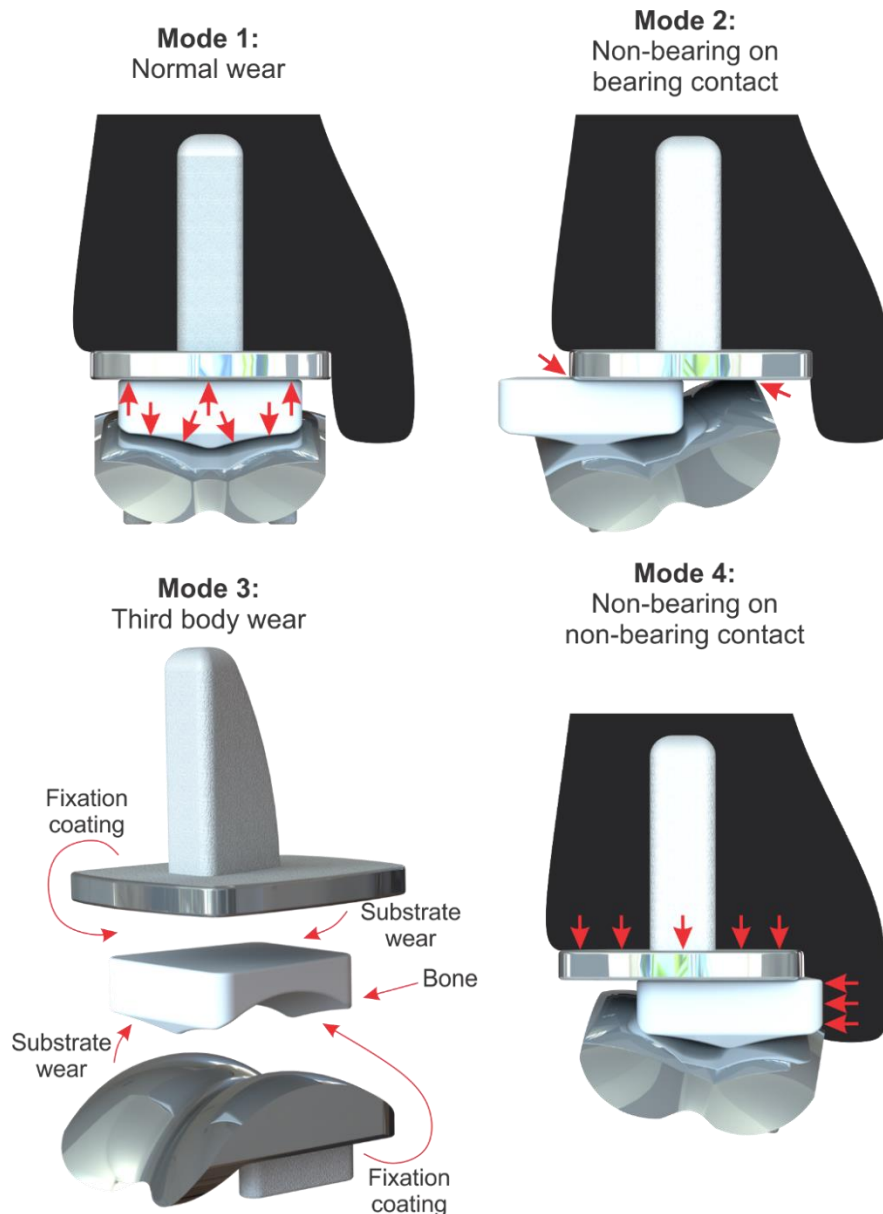
Figure 10.1. Wear modes of total ankle replacement. Mode 1 wear is primary bearing surface wear intended by the manufacturer. Mode 2 wear involves non-bearing on bearing contact, such as edge-loading and metal-on-metal contact between the tibial and talar components. Mode 3 wear is abrasion of the bearing surfaces by third-body wear particles. Mode 4 wear includes the interaction between two non-bearing surfaces such as the fixation surface and bone at the implant-bone interface or impingement between the bearing insert and the surrounding anatomy.

10.2.1 Mode 1: Normal bearing wear

Volumetric wear loss was calculated for eight bearing inserts in Chapter 8. For the six devices with implantation time data available (and excluding an outlier) the annual wear rate was estimated to be 65 mm^3. Defining this wear rate as mode 1 wear may not be accurate because of the prevalence of wear modes 2, 3 and 4 (detailed in the following sections). For example, wear rate is likely to be highly sensitive to third body debris (mode 3), evidence for which was shown by heavily scratched bearing surfaces.

In vitro wear simulation studies have attempted to replicate ankle kinematics to determine mode 1 wear of TAR (Affatato et al., 2007, Bell and Fisher, 2007, Reinders et al., 2015, Smyth et al., 2017). The maximum wear rate reported for a BP-style TAR, the Zenith TAR, was 25.8 mm^3 per million cycles (Smyth et al., 2017) and 18.2 mm^3 per million cycles for the non-BP type Hintegra TAR (Reinders et al., 2015). The wear rate for explanted AES (2nd Gen) TARs reported in Chapter 8 was approximately 2.5 times that of the highest reported mode 1 wear study (Smyth et al., 2017). Wear modes other than mode 1 wear were likely the cause of this discrepancy for this cohort, but the kinematic profile used for in vitro testing may also have differed to the retrieved TAR cohort and affected the wear rate. The results should be interpreted cautiously as the small sample size may limit statistical generalisability.

10.2.2 Mode 2: Non-bearing on bearing contact

Edge-loading

Edge-loading was frequently identified in both the medical imaging (Chapter 5) and the explant analysis (Chapter 7). Edge-loading may occur due to excessive motion in the given plane (including adverse device loading such as a sprain), component subsidence, or malpositioning at the primary surgery. A product of edge loading is the inflection of deformed material on the superior bearing insert surface which may restrict the 'unconstrained' motion of the mobile-bearing design (Figure 10.2). Reduced articulation for edge-loaded devices was suspected after a smaller scratching area, on average, was measured on the tibial component bearing surface for these devices (Chapter 6). Edge-loaded devices occasionally featured machining marks on the peak of the deformed material which suggested that that aspect of the bearing insert surface had not been articulating and remained unworn. With the device under compression, it seems unlikely that the bearing insert would be able to articulate naturally after edge-loading. The mobile-bearing nature of BP-type devices was credited with allowing coupled translational and rotational motions to occur simultaneously (Pappas, 2004). In a well-functioning TAR, this would reduce torsional shear stresses within the device to the low values represented by friction between the flat unconstrained surfaces (Pappas, 2004).

In the case of edge-loading however, torsional forces would likely be maximised within the device, creating shear stresses at the bone-implant interface and asymmetric wear patterns on the bearing insert.
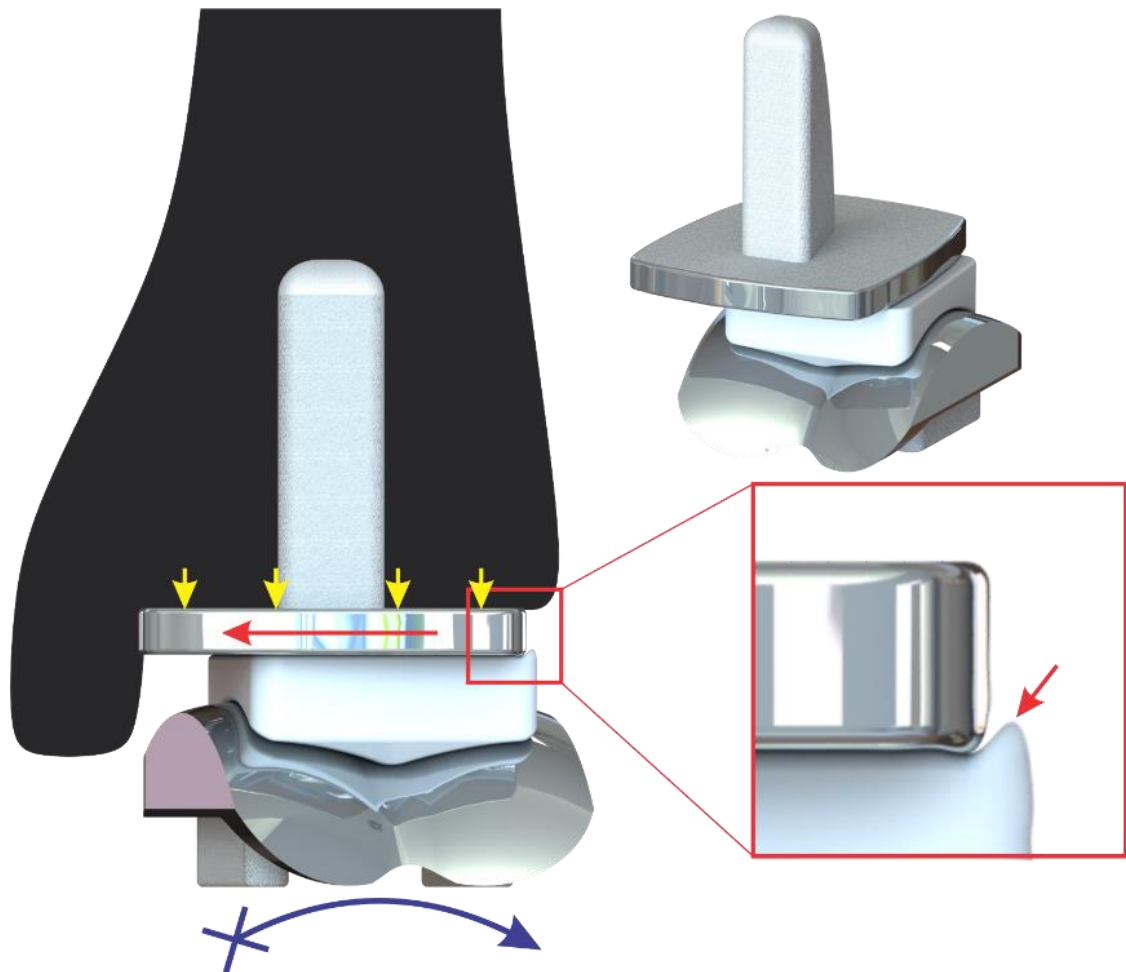
Figure 10.2. Device constraint caused by edge-loading. The inflection of deformed material created after edge-loading (red lines) may prevent axial plane translation in the opposing direction to the damage (blue arrow). Shear stresses may be redistributed to the bone-implant interface (yellow arrows).

It remains unknown what effect edge-loading may have on wear but the reduction of contact area and therefore sliding distance may result in a reduction of wear. The decreased contact area may subsequently increase the risk of bearing insert fracture, given contact stresses measured for several TAR designs are already close to the yield strength of UHMWPE (Espinosa et al., 2010).

Bearing Insert Subluxation and Metal-on-Metal Contact

Contact between the edge of the talar component and bearing surface of the tibial component occurred for three TARs (Figure 10.3). This was caused by excessive talar component varus/valgus rotation, resulting from or resulting in, bearing insert subluxation and dislocation. This phenomenon resulted in substantial wear of the metallic surfaces and represented a substantial risk of metallosis to the patients.
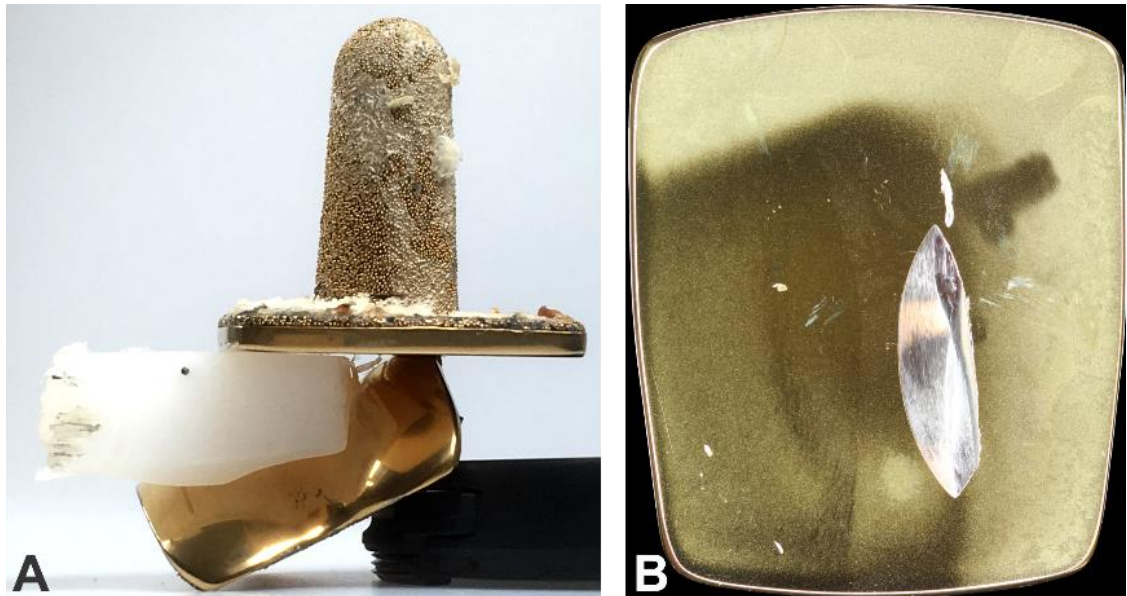
Figure 10.3. Buechel Pappas (BP) total ankle replacement with evidence of bearing insert subluxation. A, retrieved device arranged to mimic the possible in vivo position. B, massive material loss of the tibial component bearing surface due to talar component contact.

10.2.3 Mode 3: Third Body Wear

The highly polished bearing surfaces of the metallic components were deeply scratched across the cohort of failed TARs. All tibial components, except one, featured discolouration indicative of a wear patch. Within this area of discolouration, scratching was prevalent and affected 59.7% of the bearing surface, on average. The talar component bearing surfaces were deeply scratched in the direction of articulation which was highly prevalent across the cohort. For 61.9% of bearing inserts, embedded debris was observable with a microscope. Each of these was evidence of third body wear (mode 3) within the primary bearing articulations.

Similar damage has been described previously (Cottrino et al., 2016), yet, not quantified. In the Chapter 6, wear at the tibial bearing surface was estimated to produce approximately 1 mm^3 of metallic wear debris in addition to the wear debris that caused the scratching originally. The wear rate of the UHMWPE bearing insert was estimated to be at least 2.5 times the wear rate reported by in vitro simulations of TAR. This may reflect the detrimental effect of mode 3 wear on TAR. Mode 4 wear was likely the predominant cause of third body wear debris in this cohort which is described in the following section.

10.2.4 Mode 4: Non-bearing on non-bearing contact

Fixation surface wear

The tibial component fixation coating had worn through to the substrate in 89% of the AES (2nd Gen) TARs (Chapter 6). On average, 9% of the area of dual titanium and hydroxyapatite coating been removed. If this wear occurred during the time in vivo, rather than at the point of extraction (i.e. iatrogenic damage), then the area of coating delamination would reflect an additional estimated 11 mm^3 of wear within the ankle. Micromotion at the bone-implant interface was reported to cause wear of the fixation surface for several different TARs (Koivu et al., 2009, Vaupel et al., 2009, Besse, 2015, Cottrino et al., 2016). However, this thesis features the first quantitative analysis of wear at this surface. There are several possible causes for fixation surface wear which includes iatrogenic damage at implantation or removal and micromotion at the bone-implant interface caused by high shear stresses.

Impingement

Impingement of the bearing insert on the surrounding bone appeared to be a consequence of excessive edge-loading, for the majority of cases. The medio-lateral offset ratio (MOR) was significantly different between the devices considered to be edge-loaded medially and those edge-loaded laterally. Bearing inserts underwent less offset, on average, to impinge medially due to the proximity of the medial malleolus compared to bearing inserts which were offset laterally. However, for 9% of TARs, the anatomy surrounding the TAR entered the joint space. Impingement was not mutually inclusive with edge-loading. Therefore heterotopic ossification should be investigated prior to the assumption of excessive bearing insert translation or rotational offset.

Impingement can have a catastrophic effect on bearing insert wear. In one case, 18.9% of the component volume was lost due to impingement (Chapter 8). However, in several cases, minor impingement had created damage to the bearing insert which was only a couple of millimetres in diameter (Chapter 6). The volumetric loss of bone as a result of impingement was unquantifiable, however it was likely to be substantial, given the extent of damage caused by impingement to the 23% of bearing inserts featuring superior surface destruction (Chapter 7). In a histological analysis of TAR failure, large quantities of necrotic bone was identified (Koivu et al., 2012). Koivu et al. (2012) suggested implant-bone wear to be the likely cause of bone particle production, although without an explant analysis, impingement cannot be ruled out as a potential contributor to degradation of the surrounding bone in their study.

10.2.5 Summary

Edge-loading, bearing insert subluxation and impingement contributed to wear modes 2, 3 and 4. These wear modes may be caused by mobile-bearing designs; namely the lack of constraint during ankle version, varus/valgus alignment and/or after asymmetric wear. Fixation surface wear is mode 4 and contributed substantially to the total wear particle burden within the ankle joint. Unlike the UHMWPE wear particles produced by the bearing insert, the materials used for the fixation surface are highly abrasive when degraded which resulted in mode 3 wear. Surgical approach and fixation method may have facilitated wear at these surfaces. Identifying the specific origins of failure may help focus future efforts when attempting to eradicate wear modes 2, 3, and 4, by design. The following sections identify possible hypotheses of TAR failure based on the results of this thesis.

10.3 Origins of Total Ankle Replacement Failure

The five TAR design principles highlighted in the literature review (Chapter 1), were: mobile or fixed bearing design, 'anatomical' or non-anatomical device geometry, surgical approach, fixation method, and; biomaterial selection. The following sections detail the possible origins of TAR failure in the context of these design principles and the results of this thesis.

10.3.1 Mobile-Bearing Design

In the UK, all TAR devices are classified in the second highest risk category, class IIb. In the US however, fixed-bearing designs are designated as class II, whereas mobile-devices devices are classified as the more risky class III. In 1982, the US Food and Drugs Administration (FDA) ruled the higher risk classification was, in part, due to the lack of constraint (Food and Drugs Administration, 1982). Relating how the wear patterns identified in the research in this thesis are associated with TAR constraint may inform the future interpretation of damage observed on TAR.

Ankle Version

Pappas (2004), on behalf the manufacturer of the BP TAR, made a bid to reclassify their TAR from class III to class II (Pappas, 2004). Pappas (2004) claimed the semi-constrained bicondylar design of the talar component created normal inversion-eversion motions, which was unachievable using fixed-bearing designs (Figure 10.4). Also, that congruence between the three components was maintained throughout these motions (Buechel and Pappas, 2003). Theoretically, the high congruence of the bearing insert

with the tibial and talar components during inversion-eversion movements would reduce the contact stresses on the UHMWPE bearing insert.
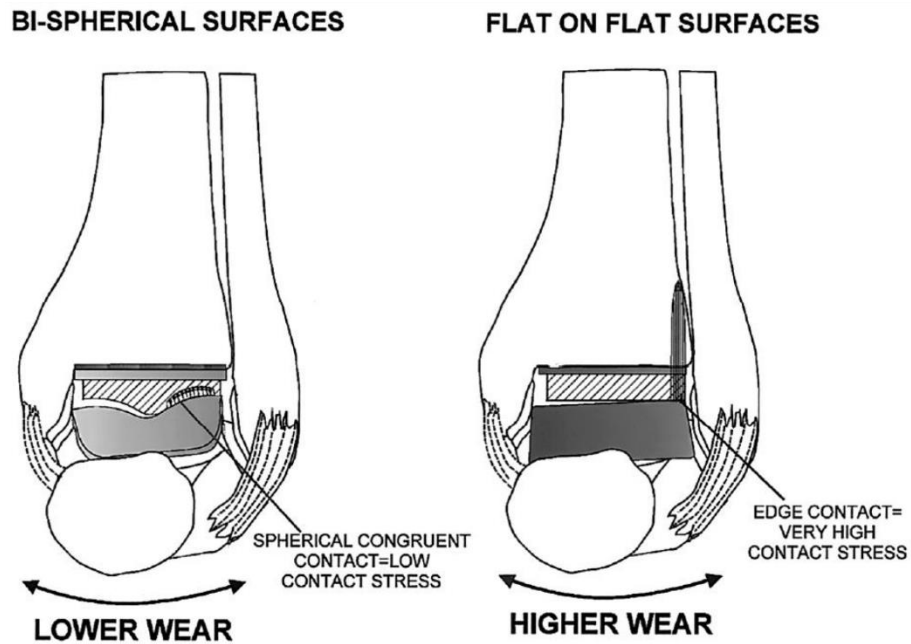
Figure 10.4. Original design rationale for the bi-spherical surfaces typical of the Buechel-Pappas (BP) type total ankle replacement. During inversion-eversion, greater conformity was anticipated from bi-spherical surfaces (left) compared to flat on flat device designs (right). Adopted from Buechel and Pappas (2003).

However, the prediction by Buechel and Pappas (2003) may not be accurately replicated in vivo. Espinosa et al. (2010) undertook a finite element analysis model of contact stress distributions across a mobile-bearing TAR design in varying extents of 'version' (Figure 10.5). The static model showed stress concentrations to rise considerably at the central sulcus and edge of the bearing insert for all version conditions (from 2° to 10° version).
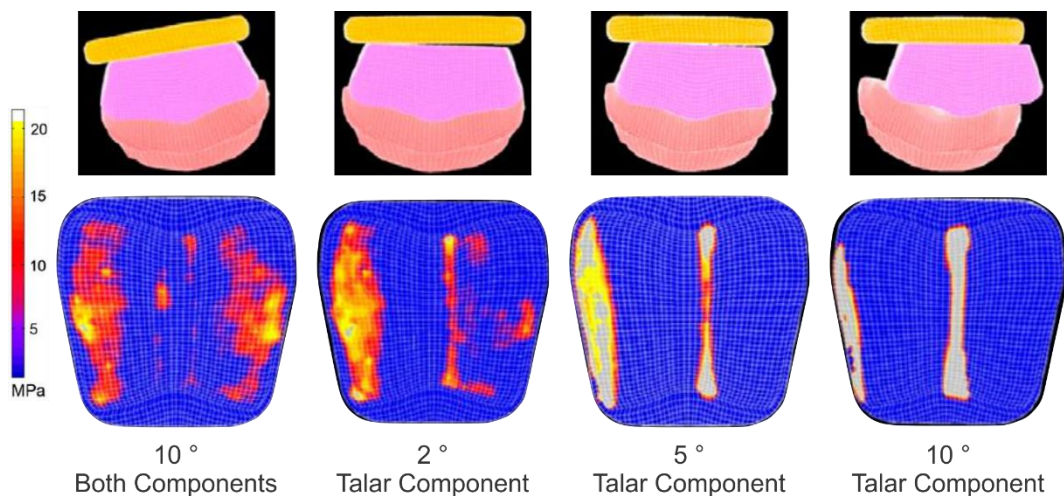
Figure 10.5. Pressure distributions for the Mobility total ankle replacement in different coronal plane alignment determined by finite element simulation. Adapted from Espinosa et al. (2010).

The wear patterns identified from the bearing insert damage mode analysis (Chapter 6) and the volume analysis (Chapter 8) appear similar to the areas of increased stress identified by Espinosa et al. (2010). Areas of deformation/wear could be identified visually on the inferior bearing insert surface which corroborated with the wear patterns identified using spatial maps from computed tomography (CT) scans (Figure 10.6). These wear patterns were indicative of either an imbalance between the amount of eversion and inversion motions during the time in vivo, or alternatively, the tibial or talar component were not positioned parallel relative to each other. Talar component migration was identified in at least 41% of TARs and therefore malalignment could have occurred at primary surgery or throughout the lifetime of the device.
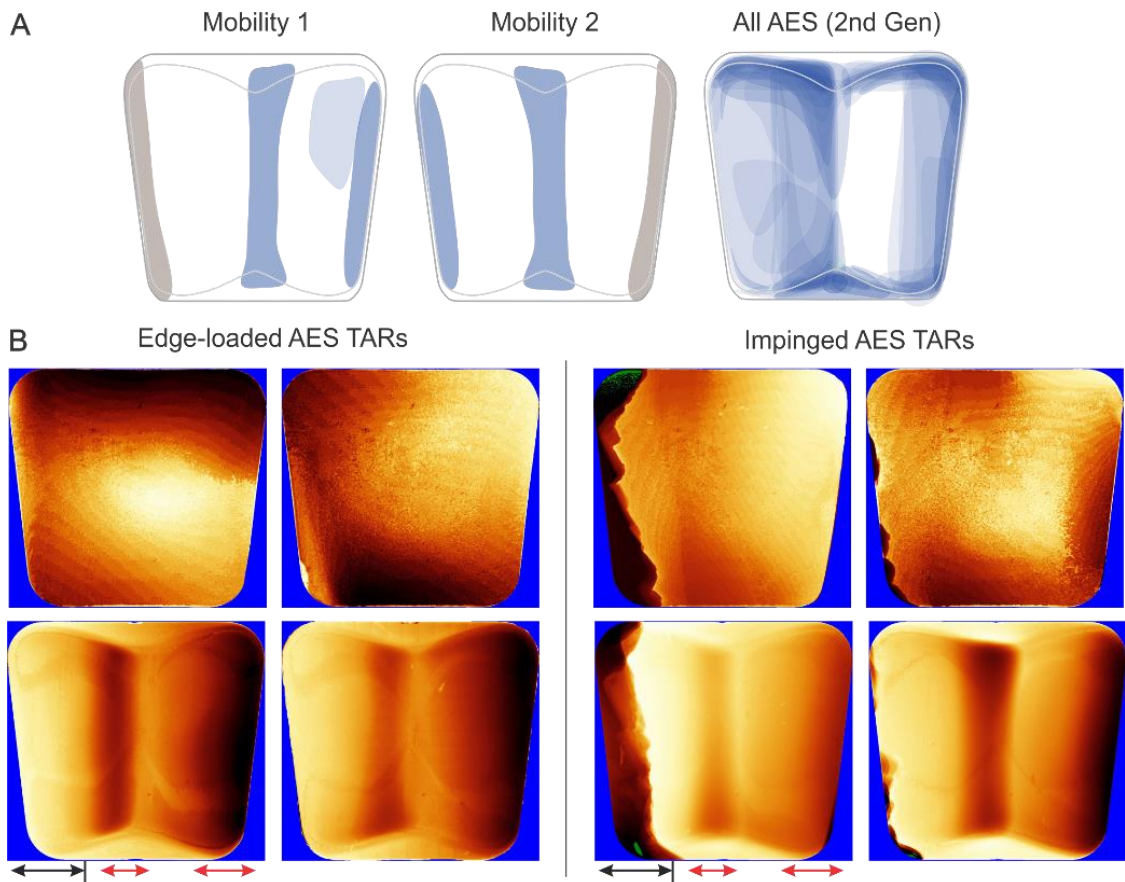
Figure 10.6. Bearing insert wear/deformation patterns identified: visually with a microscope in Chapter 6(A), and; using computed tomography generated renderings in Chapter 8 (B). Dark regions represent surface changes consistent with wear and deformation. Red arrows denote regions of asymmetrical volume change. Black arrow identifies the side affected by edge-loading or impingement.

In a healthy natural ankle, range of motion (ROM) for inversion and eversion is between 23 degrees and 12 degrees, respectively (Stauffer et al., 1977). These are maximum values and they decrease substantially during day to day activities. How inversion-eversion motions change after TAR is not well understood. Several in vivo fluoroscopic imaging studies have been undertaken to better understand the in vivo biomechanical function of TAR (Komistek et al., 2000, Leszko et al., 2008, Yamaguchi et al., 2011,

Cenni et al., 2012, List et al., 2012, Yamaguchi et al., 2012, Cenni et al., 2013, Iwamoto et al., 2014). List et al. (2012) measured dynamic inversion-eversion ROM for the Mobility TAR using in vivo video fluoroscopy. The mean ROM was 2.6 ± 0.6° during the stance phase of gait. In a similar study, Iwamoto et al. (2014) used video fluoroscopy to measure the motions of the mobile-bearing FINE TAR (Nakashima Medical, Japan). The mean inversion-eversion range of motion during stance was 2.7 ± 1.0° and four (of 27 ankles) showed more than 3° inversion-eversion. The FINE TAR was thought to be constrained to inversion-eversion motions, so the motion was attributed to coronal plane incongruency. Inversion-eversion ROM for the fixed-bearing TNK TAR was shown to be less (0.8 ± 0.4°) than the mobile-bearing alternatives presented in the other studies (Yamaguchi et al., 2012). Fixed-bearing designs are often designed to be constrained for inversion-eversion motions. Yamaguchi et al. (2012) reported medio-lateral component lift-off for four of 18 participants during stance. Three of these cases could not be determined using static medical imaging. 'Normal' inversion-eversion motions are unlikely to be recovered by TAR, regardless of design, but more than 2° may be expected from mobile-bearing TARs.

A possible consequence of large version angles is edge-loading and impingement. During version motions, the bearing insert likely translates in the same direction as the rotation of the talar component (Figure 10.7). If the bearing insert translates beyond the edge of the tibial component, particularly during the stance phase of gait, edge-loading or impingement may ensue. Bearing insert translation is likely to be underestimated by in vivo fluoroscopy studies because for these studies the metallic components are tracked, not the bearing insert (List et al., 2012, Yamaguchi et al., 2012). Edge-loading can be caused by excessive translational or rotational malalignment of the talar component relative to the tibial component in the axial plane (Chapter 5). Also, ankle version and varus/valgus alignment may affect the incidence of edge loading. Translation and/or rotation of the bearing insert in either the axial or coronal planes can cause edge-loading independently or simultaneously.
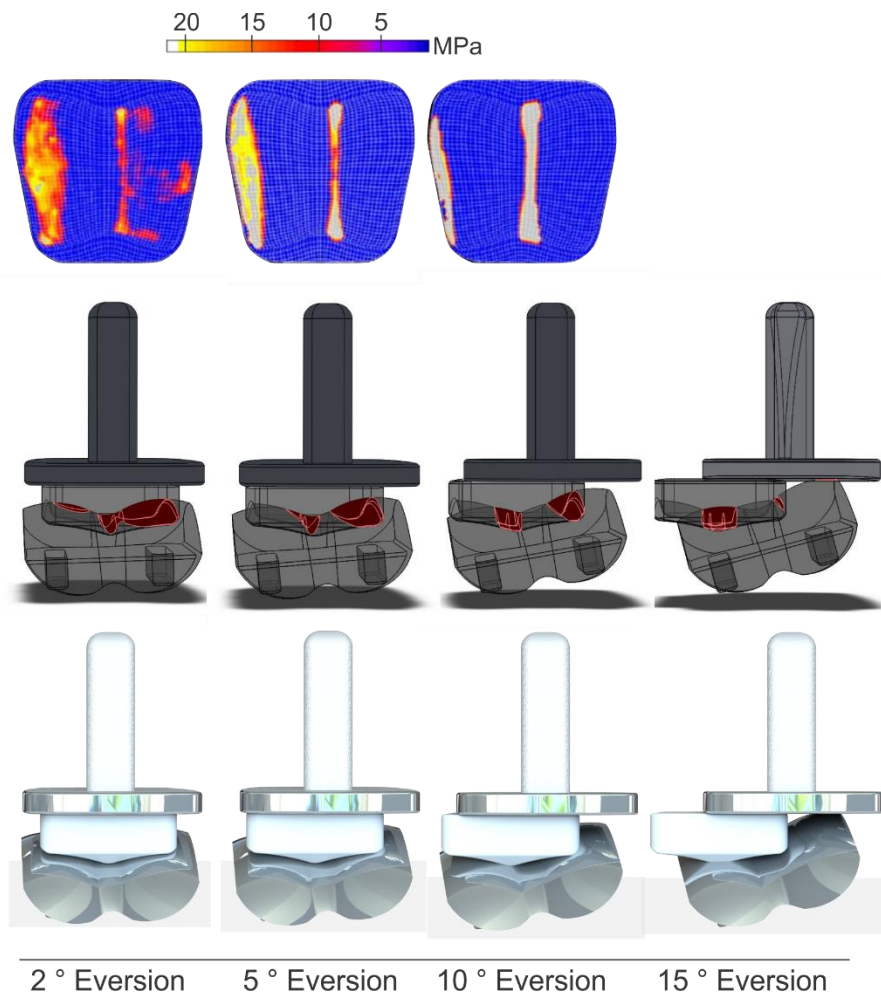
Figure 10.7. Graphical representation of bearing insert position for a BP-type total ankle replacement in different coronal plane alignments. Espinosa et al. (2010) determined pressure distributions on the bearing insert using finite element simulation (top row). Bearing insert translation may increase with inversion-eversion angle. Contact between the talar component and the bearing insert may not conform at high angles (middle row). The risk of edge-loading, impingement and bearing insert subluxation may increase as a result of inversion-eversion angle (bottom row).

Varus/Valgus TAR Alignment

Ankle version describes the rotation of the talar component in motion, whereas varus/valgus malalignment may occur in either metallic component and relates specifically to the fixed coronal plane alignment. Similar to ankle version, once the tibial or talar components are rotated relative to each other in the coronal plane, translation of the bearing insert is likely to occur and may be proportional to the magnitude of rotation. Over time, this may result in the redistribution of stresses within the bearing insert, altered wear patterns, and ultimately, edge-loading and/or impingement.

Radiopaque marker extrusion has been linked with excessive varus/valgus alignment (Dahabreh et al., 2006). Dahabreh et al. (2006) reported radiopaque marker extrusion in a case study of an AES TAR. Extrusion of the posterior radiopaque marker was attributed to excessive varus malalignment of the talar component, which was 9° relative to the

tibial component in this case study. The redistribution of contact stresses within the bearing insert was speculated to be important and Espinosa et al. (2010) later demonstrated the theory in their finite element analysis. Radiopaque marker extrusion was identified for 21% of the AES TARs analysed in Chapter 6. The radiopaque markers were extruded by 1.25 mm, on average, and for three devices, the radiopaque markers had been completely removed from the bearing insert. A photograph of the inferior bearing insert was published for the case study of marker extrusion reported by Dahabreh et al. (2006) (Figure 10.8). The pattern of wear is visible and corroborates with the damage and wear patterns identified in Chapter 6 (Figure 10.8).

Extruded radiopaque marker

Possible bone contact

Substantial wear

Missing radiopaque marker

Dahabreh et al., 2006
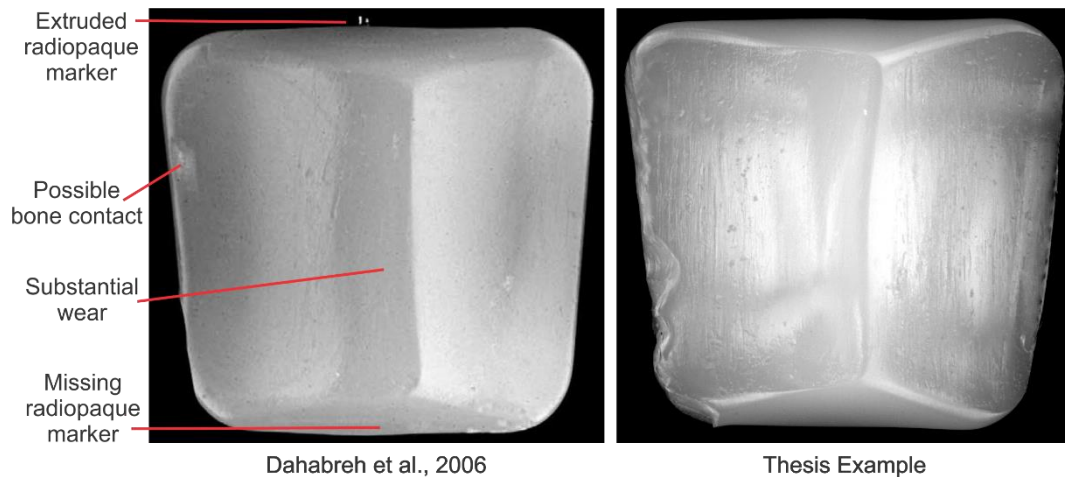
Thesis Example

Figure 10.8. Wear patterns on a bearing insert considered to be caused by varus/valgus malalignment reported by Dahabreh et al. (2006) (left). An example of a bearing insert retrieved for the research in this thesis with similar damage mode patterns.

Edge-loading caused by varus/valgus malalignment may not be recognised using X-ray imaging because the published definitions of edge-loading describe a translational offset between the tibial and talar components in the coronal plane of at least 2 mm (Koivu et al., 2009, Rippstein et al., 2011). However, rotation of the talar component, without substantial translation, in the coronal plane may sublux the bearing insert. The edges of the bearing insert cannot be identified using X-ray images which may contribute to edge-loading being underreported. Furthermore, axial rotation and translation were identified as risk factors for edge-loading (Chapter 5), which may all occur concurrently with varus/valgus malalignment, creating a complex mechanical environment, particularly when considering the high risk of instability for mobile-bearing TAR.

Direct measurement of varus/valgus alignment was not captured in this study because without a standardised imaging protocol, the metallic components were rotated in more than one plane making the edges of the components difficult to identify. However, even with repeatable medical imaging, it would be challenging to identify which component is

rotated abnormally, given both the tibial and talar components could be rotated simultaneously.

Vicious Cycle of Asymmetric Wear

Wear patterns caused by ankle version and/or varus/valgus alignment are likely to be asymmetric and worsen over time. All eight of the bearing inserts measured for wear using CT (Chapter 8) showed asymmetrical medio-lateral wear patterns with a ~ 5% difference in volume between sides. The asymmetries were evenly distributed between medial (50%) and lateral (50%) sides. The translation of the bearing insert relative to rotated tibial or talar components allows for the redistribution of stresses within the bearing insert and possibly a change in wear patterns (Espinosa et al., 2010).

Asymmetrical wear/deformation may commence at the first instance of weight-bearing movement following the primary surgery. Haskell and Mann (2004a) reported initial post-operative tibial component alignment compared to post-operative talar component alignment (Figure 10.9). The statistical agreement between the measures was strong (r = 0.91), but only 39% of the TARs featured parallel components in the coronal plane and 31% were malaligned by ≥2°. According to the results reported by Espinosa et al. (2010), malalignments of ≥2° may indicate important stress redistributions within the device (Figure 10.5). Although, the TAR modelled by Espinosa et al. (2010) was different to that used by Haskell and Mann (2004a) and may not be directly comparable.
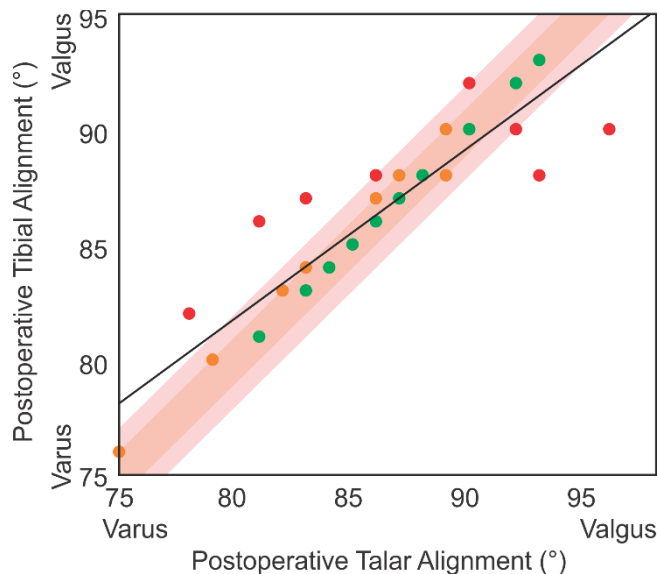
Figure 10.9. Initial post-operative coronal plane alignment for the Scandinavian total ankle replacement reported by Haskell and Mann (2004a). Black line denotes a correlation of r = 0.91. Data point colours represent the following magnitudes of malalignment between the tibial and talar components: 0° (green), 1° (orange) and ≥2° (red).

Once an asymmetrical wear pattern has emerged, wear of the bearing insert surfaces are likely to penetrate in that pattern further, subsequently increasing the varus/valgus

angle with time. There is a potential for small asymmetries in wear/deformation to develop into edge-loading and/or impingement by the gradual increase of varus/valgus angle and subsequent translation of the bearing insert as a consequence.

This hypothesis highlights a limitation of calculating varus/valgus malalignment by measuring the angle between the tibial and talar components. The addition of anatomical markers to the measurement may be required to avoid conflating component malalignment with bearing insert wear.

10.3.2 'Anatomical' vs Non-anatomical Device Geometry

Whether a TAR is anatomical or not, generally refers to the geometry of the talar component. Anatomical talar components are designed to mimic the geometry of the talus as closely as possible with the intent to emulate natural biomechanics. Non-anatomical devices tend to have a symmetrical talar component geometry in the coronal plane and a constant radii in the sagittal plane.

The BP-type TARs retrieved for the research in this thesis were non-anatomical devices (AES, BP, Mobility and Rebalance). The asymmetric wear patterns identified in Chapters 6 and 8 suggest the TAR designs retrieved for the research in this thesis may not be optimised by design to replicate normal ankle function. Pappas (2004) stated that the radii of the talar component of the BP TAR was equal to that of the lateral radii of the natural talar dome. However, since 2014, the geometry and biomechanics of the talus were redefined (Siegler et al., 2014). The radius of the medial aspect of the talus was found to be ~ 4 mm larger than the radius of the lateral aspect. This was the inverse of how talar geometry was once thought to be (Close and Inman, 1952, Close, 1956, Inman, 1976). No TAR device currently on the commercial market has attempted to accurately emulate natural talar geometry, as determined by Siegler et al. (2014). Both the Hintegra TAR (released before 2014) (Barg et al., 2012) and the Cadence TAR (released after 2014) feature a larger lateral talar component radii relative to the medial radii. Both of these devices are marketed as anatomical devices; in terms of talar component geometry, this claim is not accurate.

The high incidence of edge loading and asymmetrical wear patterns identified in the research for this thesis may indicate that natural biomechanics are not being adequately replicated by the BP-type TARs as intended. Whether 'anatomical' TARs better facilitate natural kinematics is yet to be identified. However, to date, no TAR available commercially, mimics the natural anatomy of the talus, even if it is marketed as 'anatomical'.

10.3.3 'Cortical Window' Surgical Approach and Fixation Method

Wear of the tibial fixation surface has been of particular concern for TAR and is not exclusive to one device design (Koivu et al., 2009, Besse, 2015, Singh et al., 2016). Fixation surface wear has been either inferred from the wear particle types identified using histology (Koivu et al., 2009, Dalat et al., 2013, Singh et al., 2016) or by embedded debris identified in retrieval analyses (Vaupel et al., 2009, Cottrino et al., 2016). Part of the research in Chapter 6 identified and quantified damage to the tibial fixation surface. All of the tibial components, except one, featured damage to the fixation surface (Chapter 6). The damage location was predominantly towards the anterior of the tibial component and often resulted in substrate wear once the fixation coating had been worn through or delaminated. There are several possible causes for fixation coating damage in this location on the fixation surface. These include: iatrogenic damage, micromotion between the bone and implant, and; failure of the coating due to manufacturing inconsistencies.

All of the TARs retrieved for the research in this thesis were implanted using an anterior approach. Of the 44 TARs, 41 devices were BP-type designs and featured stemmed tibial components which required a 'cortical window' to be cut during implantation. The 'cortical window' describes a surgical cut which aims to remove a bone block large enough to slot the tibial stem into the tibia. The bone block is then replaced to enclose the tibial stem and create a press fit attachment for the component (Figure 10.10). Surgical guidelines for the AES TAR recommended the cortical window to be blocked with the extracted bone block and "bits of bone graft" (Asencio and Leonardi, 2005). For the BP TAR, the cortical window graft was "impacted into the distal tibia" (Buechel and Pappas, 2003). The guidelines for the Mobility TAR suggested trimming the extracted cortical bone block for it to be subsequently replaced and secured with slivers of bone from the previous bone cuts (DePuy International Ltd, 2010). Similar guidelines remain in use for the Zenith TAR. The manufacturers suggest replacing the "bone wedge" and grafting it in place with small pieces of cancellous bone (Corin, 2010).
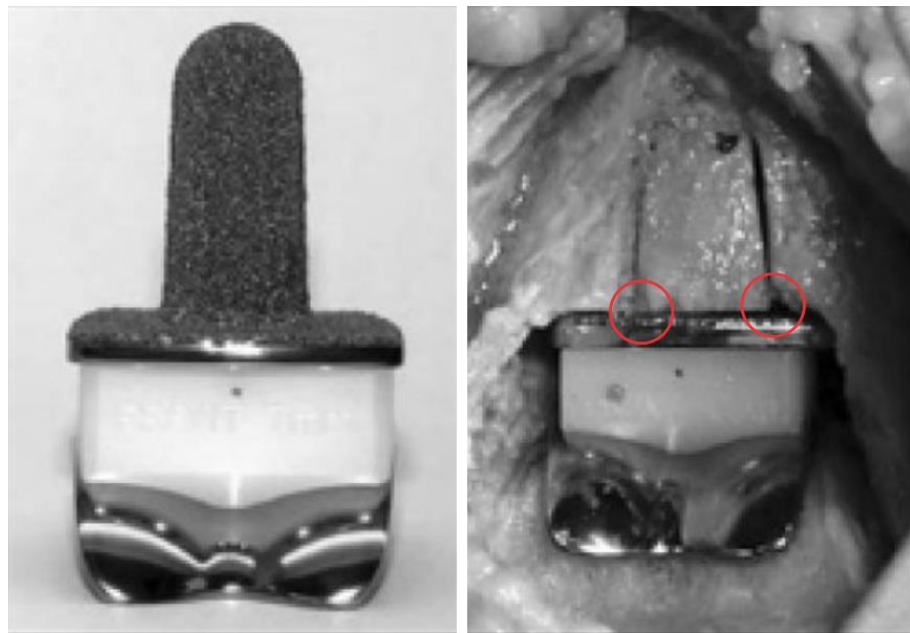
Figure 10.10. Anterior cortical window approach used for Buechel-Pappas (BP) type total ankle replacements. The BP TAR (left) and its placement in the ankle joint space (right). The cortical window cut to implant the device is filled with bone. The bone block may or may not be congruent with the tibial component fixation surface (red circles). Adapted from Buechel (2008).

Micromotion and shear stresses transmitted between the implant-bone interface have been suggested to cause fixation surface wear previously (Besse et al., 2009, Koivu et al., 2009, Dalat et al., 2013, Besse, 2015), however exacerbation of this effect, caused by the cortical window surgical approach, has not previously been suggested. If the cortical window is replaced proud, recessed or uneven, then substantial wear on the fixation surface is possible (Figure 10.11). During impaction, bone may scrape along the fixation surface producing wear particles. Hydroxyapatite is brittle under shear stresses (Ben-Nissan, 2014) and is therefore particularly susceptible to wear in these conditions. In 89% of AES (2nd Gen) TARs, wear at this surface penetrated the substrate material following the abrasion of the fixation coating.
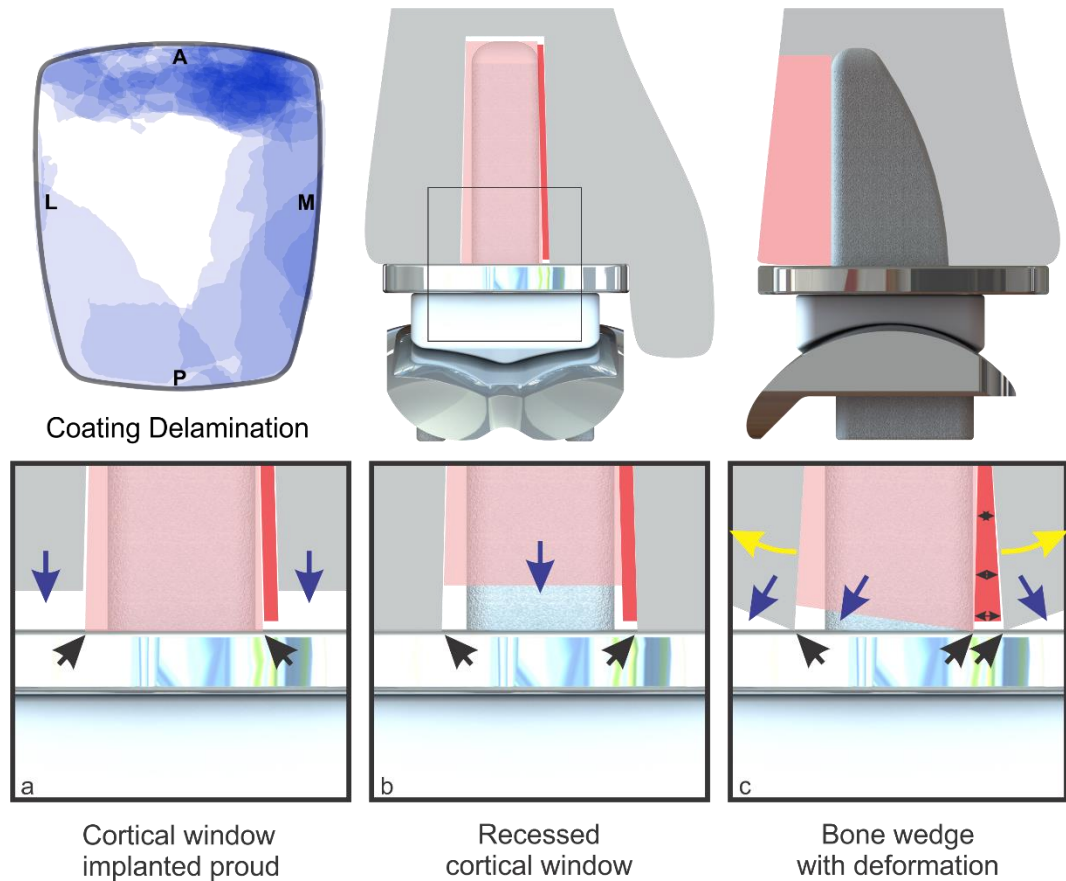
Figure 10.11. Anterior cortical window surgical approach with possible scenarios leading to fixation surface damage. When the bone block (pink) is replaced and fixed with additional bone slivers (dark pink), it should be fixed congruent with the tibial plateau and fixation surface. Fixation surface damage or bone degradation may occur if the cortical window Is implanted proud (a) or recessed (b) relative to the anatomical plateau. Blue arrows indicate prominent gaps absent of bone or implant. Black arrows show possible locations for wear. The additional bone sliver may wedge or deform the tibia outwards (c), subsequently undermining the press-fit. Coating delamination identified in Chapter 6 occurred predominantly towards the anterior of the tibial component (top left). A, anterior. P, posterior. M, medial. L, lateral.

The replacement and wedging of the cortical window with bone graft may undermine the press-fit between the bone and the implant. Wedging the cortical window using a sliver of bone too thick may cause the distal tibia to deform from the centre in the medial and lateral direction (Figure 10.11C). Impacting the cortical window is one of the last steps in the surgical procedure, therefore the quality of the press-fit following impaction may remain unchecked. The result may be an uneven tibial plateau caused by the deformed bone which would be susceptible to wear, or a looser fit around the tibial stem creating an unstable environment.

This hypothesis only applies to surgical approaches using the cortical window or the replacement of cortical bone graft. The STAR and BOX TAR require holes to be cut in the tibial plateau to attach the fixation barrels. Bone is not replaced for either of these designs (Small Bone Innovations Inc., 2009, MatOrtho Ltd, 2011). The Hintegra TAR

required no interference with the tibial plateau other than the initial cut to place the tibial component (Integra Life Sciences Services, 2011). Despite this, damage to the fixation surface was still evident on the Hintegra TARs retrieved for this study. Micromotion and consequential damage at the bone-implant interface can occur regardless of design but the cortical window may exacerbate damage to the fixation coating.

10.3.4 Biomaterial Selection and Wear

Osteolysis develops earlier for TAR than total hip and knee replacement, despite the selected biomaterials being similar between the joint types and are generally considered safe. Many failure modes for TAR have been suggested (see section 2.4) for example stress shielding (Waizy et al., 2017), device alignment (Datir et al., 2013) and edge-loading (Morgan et al., 2010), yet wear particle induced osteolysis is not a commonly cited indication for failure (National Joint Registry, 2017). This is due, in part, to the early development of osteolysis and the perception that wear particle concentrations do not accrue in sufficient quantities within the relatively shorter implantation times of TAR. However, two hypotheses have been identified from the results of the research in this thesis: (1) early accrual of wear particles, and; (2) the biological response to hydroxyapatite wear particles. Both hypotheses are detailed in the following sections.

Total Wear Particle Burden

The accrual of a wear particles in periprosthetic tissue contributes to imbalances in homeostasis and may induce inflammation (Hallab and Jacobs, 2009). Over time, wear particles can be redistributed from the joint through the lymphatic system (Urban et al., 2000). However, if the accumulation of wear debris is too rapid and the joint overwhelmed, osteolysis may develop (Koivu et al., 2012).

In this thesis, substantial metallic wear was quantified on the tibial fixation and bearing surfaces. Approximately 11 mm^3 of titanium and ~ 1 mm^3 of cobalt chromium alloy was estimated to have liberated into the joint space for the AES (2nd Gen) TAR. This was in addition to the estimated ~ 65 mm^3 per annum of UHMWPE wear debris also accumulating within the joint space. The estimates of metallic wear required the depth of the surface scratches to be assumed, therefore actual values of wear may be highly variable between TARs. Additional volumes of wear debris is likely to originate from bone following impingement, which occurred in 57% of the retrieved TARs. Also, wear liberated from the talar component also needs to be considered. The visual damage mode score for embedded debris was moderately correlated with osteolysis volume ($\rho =$ 0.56) in Chapter 6. It is possible the quantity of wear estimated in this thesis may be inflammatory to the biological environment surrounding the TAR, particularly if the wear accumulated within a short period of time.

The titanium wear particles isolated from the AES (2nd Gen) TARs, were larger in size relative to the cobalt chromium alloy, calcium phosphate and UHMWPE wear particles. Therefore, much of the volume produced at the fixation surface may exist in relatively large particles (>10 μm) and are not typically considered particularly bioreactive (Ingham and Fisher, 2000). However, of more concern was the submicron to micron-sized flake-like cobalt chromium alloy particles and shard-like calcium phosphate particles. Both of these particle types were frequently identified and met all three of the generally accepted particle characteristics associated with adverse biological reactions: (1) phagocytosable particle size and high volume; (2) high aspect ratio particle morphology, and; (3) chemically reactive composition (Hallab and Jacobs, 2009). Cobalt chromium alloy has an extensive history of toxicity when in particulate form (Brown et al., 2007a, Bradberry et al., 2014). However, metallosis is yet to be reported for TAR, even for TARs with the most volumetric metal wear, the ankles with metal-on-metal mode 2 wear.

The substantial total volume of wear combined with its possible early genesis may be consistent with the early development of osteolysis, particularly given the theoretically reactive nature of some of the wear particle populations. It was not possible to determine the biological reactivity of the isolated wear particles using the studies included in this thesis, further research is required to ensure metallic ion levels are suitably low.

The wear particle characteristics of hydroxyapatite identified in this thesis were of particular concern for their potential to cause an inflammatory reaction. The possible biological response to hydroxyapatite wear particles is detailed in the following section.

Potential Biological Response of Hydroxyapatite Wear Particles

The first isolation and characterisation of HA wear particles from periprosthetic tissue surrounding retrieved total joint replacements was achieved in this thesis. Hydroxyapatite wear particles were large (>10 μm) and urchin-like in their bulk form, and; phagocytosable (~ 1 μm) with a high aspect ratio (AR >3) in its shard-like form. To the authors knowledge, Bloebaum et al. (1994) is the only study to characterise HA particles from surrounding TJRs. The biological response to such wear particles is currently unknown.

The wear of hydroxyapatite coating has been linked to osteolysis in TAR. Singh et al. (2016) used elemental analyses to quantify calcium content in the periprosthetic tissue from 71 patients with HA-coated total ankle replacements. The odds of having ballooning osteolysis were 297-fold greater if the calcium content within the tissue was >0.5 mg/g. Singh et al. (2016) reported the concentration of calcium but not wear particle size or morphology. Also, the origin of the calcium was not clearly identified but suspected to be the fixation coating due to its lack of bony histoarchitecture when viewed using histological techniques. A limitation of both this thesis and the study by Singh et al. (2016)

was that the biological reactivity of the HA wear particles could not be determined from the methods used, nor could its contribution to causing osteolysis, if at all.

While the liberation of HA wear particles is thoroughly documented for total joint replacement technologies (Bauer et al., 1991, Bloebaum and Dupont, 1993, Bauer et al., 1994, Bloebaum et al., 1994, Hardy et al., 1994, Lintner et al., 1994, Nilsson et al., 1994, Buma and Gardeniers, 1995, Morscher et al., 1998, Tonino et al., 1999, Coathup et al., 2001, Tonino et al., 2001, Rokkum et al., 2003, Tonino et al., 2003, Nehme et al., 2005, Koivu et al., 2009, Dalat et al., 2013, Martinez-Carranza et al., 2014), only a minority of case studies reported early device failure due to HA coating dissociation (Bloebaum and Dupont, 1993, Nilsson et al., 1994, Buma and Gardeniers, 1995, Morscher et al., 1998) and excessive HA crystal release (Nilsson et al., 1994, Nehme et al., 2005, D'Angelo et al., 2008) resulting in massive osteolysis (Bloebaum and Dupont, 1993, Morscher et al., 1998, Nehme et al., 2005). Many of the THR cases that reported HA particle release also reported good component fixation and function (Bauer et al., 1991, Bauer et al., 1994, Bloebaum et al., 1994, Hardy et al., 1994, Lintner et al., 1994, Tonino et al., 1999, Coathup et al., 2001, Tonino et al., 2001, Rokkum et al., 2003, Tonino et al., 2003). The variation of outcome due to HA coating wear is likely due to differences in the concentration, size and morphology of the wear particles produced (Hallab and Jacobs, 2009).

Conflicting results exist within the literature regarding the effect of HA particle size on biological response. Markers of inflammation and reduced cell viability have been reported (Nagase et al., 1988, Evans, 1991, Harada et al., 1996, Nordsletten et al., 1996, Sun et al., 1999, Anderson et al., 2001, Eid et al., 2001, Ninomiya et al., 2001, Laquerriere et al., 2003, Matesanz et al., 2014) but conversely, in several studies bone apposition was promoted and normal cell function was observed (Santavirta et al., 1991, Goodman et al., 1993, Wang et al., 1994, Cheung et al., 1997, Gauthier et al., 1999, Malard et al., 1999, Sun et al., 1999). Manufactured (or synthesised) HA particles between 0.1 μm and 50 μm in diameter were used for the majority of studies which cannot be considered clinically relevant. Differences in particle morphology, crystallinity and concentration may explain the mixed results (Laquerriere et al., 2001, Laquerriere et al., 2003). Needle-shaped HA particles produced the most TNF-a, IL-6 and IL-10 by monocytes in a study using a variety of HA particle characteristics (Laquerriere et al., 2003). The smallest particles (1 μm to 30 μm) also provoked a similar expression of inflammatory cytokine types, but to a lesser extent. Particles too big to be phagocytosed (>10 μm) had no effect on inflammatory markers. Despite this breadth of research, biological studies analysing clinically relevant HA wear particles from total joint replacements are yet to be undertaken. This is because the characteristics of HA particles produced at the fixation surface of TJRs has previously been undetermined.

Hydroxyapatite wear particle size and morphology have been quantified for failed TAR in this thesis, the values of which can be used to inform clinically relevant biological response studies in the future.

10.3.5 Summary

The origins of failure were formed from the results of this thesis and the previously published literature. Four hypotheses were outlined as potential origins of TAR failure:

(1) Talar component translation, axial plane rotation and coronal plane TAR alignment are risk factors for edge-loading, when combined, and independent of each other.

(2) Non-anatomical TAR designs may wear asymmetrically due to the complex and relatively unknown biomechanical conditions within the foot.

(3) The cortical window surgical approach for TAR designs reliant on stemmed fixation may result in excessive wear at the bone-implant interface.

(4) The early accrual of high concentrations of wear particles with characteristics indicative of being biologically reactive.

A consequence of each hypothesis is the creation of wear modes other than that of normal bearing wear (mode 1). The identification of possible causes of TAR failure may provide the orthopaedic engineering and clinical communities focus on which features of TAR may require further improvement.

10.4 Limitations

Retrieval analyses capture the end-point condition of devices' that have functioned over a prolonged time period. Assigning a timeline to each wear and damage mode cannot be achieved precisely, yet specific indicators of time, such as the presence of machining marks on the deformed lip of an edge-loaded bearing insert, may suggest that wear mode occurred early in a TAR's lifetime. Other clinical factors such as pre-operative alignment, ligament tension, nerve manipulation damage and blood vessel disruption may have contributed to the failure of these devices, but could not be identified using a retrieval analysis approach and was beyond the scope of this research.

The clinical 'weight' of each wear mode identified as dysfunctional (modes 2, 3 and 4) on the outcome of each participant was also unknown. Edge-loading may have been present throughout the entire lifetime of the TAR, therefore whether this caused solely a stiff joint or was critical to failure remains unknown. Many of the damage modes identified within this thesis were proximate causes of joint dysfunction. For example, edge-loading may have caused a stiff joint and perhaps excessive micromotion at the bone-implant

interface resulting in osteolysis, this is the proximate cause of failure. However, the ultimate cause of failure may have been poor bone quality in the talus resulting in talar component varus/valgus subsidence and consequentially, edge-loading. The ultimate causes of TAR failure, as opposed to the proximate causes, were hypothesised in this chapter, yet the level of evidence provided by retrieval analysis is typically limited to just the direct effects of the more important failure mechanisms.

The majority of the retrieved TARs included in this thesis had been withdrawn from market at the time of writing. Also, all of the TARs were mobile-bearing devices. Many of the conclusions and implications affect solely this class of device. However, several important wear modes such as the degradation of the fixation surface would not be specific to mobile-bearing or BP-style TARs (Vaupel et al., 2009), therefore the results are relevant between design types. Additionally, the hypotheses relating to the anterior cortical window surgical approach may also affect fixed-bearing devices with this design feature. The results of this thesis offer an important insight into the similar wear modes and failure mechanisms between different TARs.

How each retrieved TAR was implanted and retrieved was unknown. Iatrogenic damage to the components may have contributed to the results of this study but was unidentifiable as such. Tibial component fixation wear may have been caused, in part, by the actions of the surgeon during revision surgery. However, not only has fixation surface failure has been implied by several authors (Besse, 2015, Cottrino et al., 2016, Singh et al., 2016), but even if this damage was cause at component removal, efforts should be made to reduce the production of wear at this time point too. In Chapter 9, the delaminated fixation surface was shown to remain attached to the surrounding bone within the joint in several cases (Figure 9.20). These large metal fragments may be left within the joint after revision surgery and possibly cause further problems.

10.5 Further Work

The fixed-bearing Infinity TAR is currently being implanted at the highest rate of all TARs available in the UK (National Joint Registry, 2017). This suggests the dominance of mobile-bearing TAR designs in the UK could soon be changing to fixed-bearing devices. Currently, the clinical and functional outcomes between fixed and mobile-bearing TAR designs are not statistically different (Gaudot et al., 2013), however, several wear modes identified in this thesis, such as bearing insert subluxation and edge-loading, could not have occurred in the same way for fixed-bearing TARs. Failure mechanisms between fixed and mobile-bearing TARs may be different and therefore an equivalent retrieval analysis for fixed-bearing TARs is necessary. The same is true for a greater diversity of

TAR brands. Comparisons between 'anatomical' and non-anatomical TARs may also yield important differences in wear patterns.

Standardised medical imaging protocols should be developed to make it easier to identify coronal plane TAR alignment. Specifically, the differences in orientation between the tibial and talar components and their position relative to repeatable anatomical landmarks.

An improved understanding of ankle biomechanics after TAR is desirable, particularly focussing on the limits of inversion-eversion allowed between TAR types. Recent fundamental developments in the understanding of talar geometry (Siegler et al., 2014) suggest more can learned about how this bone interacts with other bones within the foot during motion. Static imaging studies cannot acquire this information, therefore advancements in in vivo fluoroscopy methods may be required.

Below the ankle joint, a stable plantigrade foot is also required for desirable ankle replacement function (Coetzee, 2010). The hindfoot is fundamental in producing version motions within the ankle, therefore a well-aligned TAR placed on a malaligned hindfoot may result in abnormal function and failure (Greisberg et al., 2004). Similarly, a TAR with hindfoot arthrodesis may produce different wear patterns to those without arthrodesis. Different biomechanical scenarios of TAR function also need to be considered for pre-clinical testing.

In vivo identification of 'normal' mode 1 wear in the absence of third body wear (mode 3) is required to validate pre-clinical in vitro simulator studies. Volumetric wear loss was obtained in this thesis but from TARs considered 'failed' and may not be representative of the majority of TARs implanted. This may be achieved by retrieving bearing inserts from the cadavers of people who died from unrelated causes or from bearing insert exchanges of revision cases with unrelated causes of failure.

The size and morphology of cobalt chromium alloy and calcium phosphate wear particles were detailed in this thesis and appear potentially unique to the ankle joint. Clinically relevant biological response cell studies can be achieved by replicating the wear particle characteristics reported in this thesis. This would further elucidate the possibility of wear particle induced osteolysis in TAR.

The liberation of HA wear particles was hypothesised to cause heterotopic ossifications by Morscher (1991) however there was no clinical evidence for this at the time. Heterotopic ossification is a common feature to TAR (Lee et al., 2011, Schuberth et al., 2016). In Chapter 5, calcified tissue had grown within the joint space for at least 9% of the retrieved TARs with CT scans (n = 22). Also, HA coating wear was prevalent. A study could be undertaken to compare the incidence of heterotopic ossification for matched

cohorts of ankles with HA coated and non-HA coated TARs. Explaining the origin of complications such as heterotopic ossification and engineering solutions to prevent them is part of the continual design process from which TAR performance will improve.

10.6 Conclusion

Despite 40 years of development, a reliable set of design principles for TAR are yet to be combined to result in a device for ankle replacement with a better than 90% survivorship at 10 years. Consequently, survivorship for TAR lags far behind equivalent figures for THR and TKR. The translation of knowledge from THR and TKR has not yielded acceptable results for TAR and as such, tailored analysis methods for TAR are required to further understand why ankle replacements underperform relative to other weight bearing joints.

In this thesis, several novel methods were developed, validated and applied to retrieved TARs, the result of which was the formulation of a series of new hypotheses about the various origins of TAR failure. Edge-loading, impingement, bearing insert subluxation, fixation coating wear and bearing surface wear were all identified as being relevant in TAR. Importantly, all of these are indicative of device dysfunction (wear modes 2, 3 and 4) and are therefore potentially preventable in future designs. The volume of wear and specifically, the wear particle characteristics were of concern and may explain the early onset of osteolysis for some devices. Further investigation of the identified hypotheses would likely contribute to the iterative eradication of non-normal wear modes, which is perhaps the greatest opportunity for rapid improvements in TAR longevity. Retrieval analysis comprises the direct measurement of such wear modes and is therefore an essential yet underused process in the development of TAR.

The stakeholders associated with ankle replacement as a therapy such as: industry, retrieval centres, the clinical community and regulators each have some responsibility to balance the risks to patient safety with the benefits of innovation. Safeguards for patients include: extensive pre-clinical testing, intensive surgeon training and effective post-marketing surveillance strategies. The research in this thesis also highlights the lack of validated methods suitable for assessing TAR failure and the scarcity of knowledge relating to in vivo TAR function as it might be applied to in vitro preclinical testing processes.

More directly linking our understanding of in vivo function to more comprehensive in vitro and pre-clinical testing would improve patient safety and reduce the risks associated with innovation for all stakeholders. The following recommendations have arisen from the work presented in this thesis and are proposed here as potential improvements to the

pre-clinical and post-marketing clinical testing pipelines, which will in future enable us to better understand and minimise risks associated with existing failure mechanisms:

- The current understanding of ankle bone geometry and biomechanics in the published literature is insufficient to create a TAR able to replicate the natural joint and its motions. Given that this underpinning knowledge is fundamental to the concept of TAR, further research into the structure and function of the ankle and healthy and diseased states is necessary and a strong case can be made for prioritised funding from either within the implant industry or from health related funders such as NIHR.

- Acceptable alignment limits for each component should be detailed by manufacturers in their instructions for use, and repeatable medical imaging protocols with improved analysis methods, such as those developed in this thesis, should be adopted by the clinical community. Existing, low cost technologies such as plain X-ray could be more rigorously applied and the potential gains arising from the enhanced capabilities associated with novel technologies such as metal-suppression MRI and CT should be explored and potentially included in post-marketing surveillance protocols

- All failed TARs should be retrieved by the operating surgeon following consent of the patient and analysed by the manufacturer or an independent retrieval centre. The methods and range of wear modes identified in this thesis should be used as basis for this analysis. Each of these failures and the results of the analysis should be included in reports to the manufacturer, the regulatory body (e.g. MHRA) and the National Joint Registry for performance review.

Retrieval analysis is an essential process within an effective post-market surveillance strategy, it closes the feedback loop between the results of pre-clinical testing and in vivo device performance. A comprehensive approach to the retrieval analysis of TAR is detailed in this thesis which should be emulated by industry and improved on by researchers in retrieval centres and the clinical community.

In summary, in this body of work I set out to identify the wear modes and possible origins of failure for a cohort of failed TARs using a retrieval analysis approach. Forty-four participants donated their explanted TARs, medical imaging and tissue samples for this research. These resources were processed using a range of novel experimental methods specifically developed and validated for ankle replacements. The main findings were that an entire class of mobile-bearing TARs may be susceptible to dysfunction and instability caused by a range of factors including asymmetric wear, component malpositioning and non-anatomical component geometries. Also, that specific aspects of the cortical window anterior surgical approach may contribute to the rapid

accumulation of wear debris within the joint space potentially resulting in poor survivorship. Finally, that enhanced medical imaging acquisition and analysis protocols may be used effectively for the early identification of the failure modes described in this thesis. For future innovation in TAR to thrive and more importantly, in the interest of patient safety, a collaborative effort between the stakeholders of TAR should be made to further understand the failure of TAR. One of the first steps should be to ensure all TARs are retrieved as part of routine clinical practice, analysed and reported on, in a timely manner, by the device manufacturer or by researchers at an independent retrieval centre.

References

AFFATATO, S., LEARDINI, A., LEARDINI, W., GIANNINI, S. & VICECONTI, M. 2007. Meniscal wear at a three-component total ankle prosthesis by a knee joint simulator. *J Biomech,* 40**,** 1871-6.

AFFATATO, S., TADDEI, P., LEARDINI, A., GIANNINI, S., SPINELLI, M. & VICECONTI, M. 2009. Wear behaviour in total ankle replacement: a comparison between an in vitro simulation and retrieved prostheses. *Clin Biomech (Bristol, Avon),* 24**,** 661-9.

AJIS, A., HENRIQUEZ, H. & MYERSON, M. 2013. Postoperative range of motion trends following total ankle arthroplasty. *Foot and Ankle International,* 34**,** 645-656.

ALI, M., HIGGINS, G. A. & MOHAMED, M. 2007. Intermediate results of Buechel Pappas unconstrained uncemented total ankle replacement for osteoarthritis. *The Journal of foot and ankle surgery,* 46**,** 16-20.

ALIDOUSTI, H., TAYLOR, M. & BRESSLOFF, N. W. 2014. Periprosthetic wear particle migration and distribution modelling and the implication for osteolysis in cementless total hip replacement. *Journal of the mechanical behavior of biomedical materials,* 32**,** 225-244.

ALVINE, F. G. 2002. The Agility ankle replacement: the good and the bad. *Foot and ankle clinics,* 7**,** 737-753.

AMETAJ, B. N., BOBE, G., LU, Y., YOUNG, J. W. & BEITZ, D. C. 2003. Effect of sample preparation, length of time, and sample size on quantification of total lipids from bovine liver. *Journal of agricultural and food chemistry,* 51**,** 2105-2110.

ANDERSON, D. D., CHUBINSKAYA, S., GUILAK, F., MARTIN, J. A., OEGEMA, T. R., OLSON, S. A. & BUCKWALTER, J. A. 2011. Post-traumatic osteoarthritis: Improved understanding and opportunities for early intervention. *Journal of Orthopaedic Research,* 29**,** 802-809.

ANDERSON, G. I., MACQUARRIE, R., OSINGA, C., CHEN, Y. F., LANGMAN, M. & GILBERT, R. 2001. Inhibition of leukotriene function can modulate particulate-induced changes in bone cell differentiation and activity. *Journal of Biomedical Materials Research,* 58**,** 406-414.

ANDERSON, T., MONTGOMERY, F. & CARLSSON, Å. 2004. Uncemented STAR total ankle prostheses. *The Journal of Bone & Joint Surgery Essential Surgical Techniques,* 86**,** 103-111.

ANGADJI, A., ROYLE, M., COLLINS, S. N. & SHELTON, J. C. 2009. Influence of cup orientation on the wear performance of metal-on-metal hip replacements. *Proceedings of the Institution of Mechanical Engineers, Part H: Journal of Engineering in Medicine,* 223**,** 449-457.

ASENCIO, J.-G. & LEONARDI, C. 2005. Ankle evolutive system prosthesis: a simple, accurate, and reliable specific concept for primary and revision ankle surgery. *Techniques in Foot & Ankle Surgery,* 4**,** 119-124.

ASSAL, M., AL-SHAIKH, R., REIBER, B. H. & HANSEN, S. T. 2003. Fracture of the polyethylene component in an ankle arthroplasty: a case report. *Foot & Ankle International,* 24**,** 901-903.

ASTM STANDARD F561 2013. Standard Practice for Retrieval and Analysis of Medical Devices, and Associated Tissues and Fluids. *F561-13.* West Conshohocken, PA.: ASTM International.

AUSTEN, S., PUNT, I. M., CLEUTJENS, J. P., WILLEMS, P. C., KURTZ, S. M., MACDONALD, D. W., VAN RHIJN, L. W. & VAN OOIJ, A. 2012. Clinical, radiological, histological and retrieval findings of Activ-L and Mobidisc total disc replacements: a study of two patients. *European Spine Journal,* 21**,** 513-520.

BAI, L.-B., LEE, K.-B., SONG, E. K., YOON, T. R. & SEON, J. K. 2010. Total ankle arthroplasty outcome comparison for post-traumatic and primary osteoarthritis. *Foot & Ankle International,* 31**,** 1048-1056.

BARG, A., ELSNER, A., ANDERSON, A. E. & HINTERMANN, B. 2011a. The effect of three-component total ankle replacement malalignment on clinical outcome: pain relief and functional outcome in 317 consecutive patients. *J Bone Joint Surg Am,* 93**,** 1969-78.

BARG, A., ELSNER, A., CHUCKPAIWONG, B. & HINTERMANN, B. 2010a. Insert position in three-component total ankle replacement. *Foot Ankle Int,* 31**,** 754-9.

BARG, A., ELSNER, A., HEFTI, D. & HINTERMANN, B. 2010b. Haemophilic arthropathy of the ankle treated by total ankle replacement: a case series. *Haemophilia,* 16**,** 647-55.

BARG, A., HENNINGER, H. & HINTERMANN, B. 2011b. Risk factors for symptomatic deep-vein thrombosis in patients after total ankle replacement who received routine chemical thromboprophylaxis. *Journal of Bone & Joint Surgery, British Volume,* 93**,** 921-927.

BARG, A. & HINTERMANN, B. 2010. Takedown of painful ankle fusion and total ankle replacement using a 3-component ankle prosthesis. *Techniques in Foot & Ankle Surgery,* 9**,** 190-198.

BARG, A., KNUPP, M., HENNINGER, H. B., ZWICKY, L. & HINTERMANN, B. 2012. Total ankle replacement using HINTEGRA, an unconstrained, three-component system: surgical technique and pitfalls. *Foot and ankle clinics,* 17**,** 607-635.

BARG, A., KNUPP, M. & HINTERMANN, B. 2010c. Simultaneous bilateral versus unilateral total ankle replacement:A patient-based comparison of pain relief, quality of life and functional outcome. *Journal of Bone & Joint Surgery, British Volume,* 92**,** 1659-1663.

BARG, A., PAGENSTERT, G. I., HORISBERGER, M., PAUL, J., GLOYER, M., HENNINGER, H. B. & VALDERRABANO, V. 2013a. Supramalleolar osteotomies for degenerative joint disease of the ankle joint: Indication, technique and results. *International Orthopaedics,* 37**,** 1683-1695.

BARG, A. & SALTZMAN, C. L. 2014. Single-stage supramalleolar osteotomy for coronal plane deformity. *Current Reviews in Musculoskeletal Medicine,* 7**,** 277-291.

BARG, A., ZWICKY, L., KNUPP, M., HENNINGER, H. B. & HINTERMANN, B. 2013b. HINTEGRA total ankle replacement: Survivorship analysis in 684 patients. *Journal of Bone and Joint Surgery - Series A,* 95**,** 1175-1183.

BARNETT, C. & NAPIER, J. 1952. The axis of rotation at the ankle joint in man. Its influence upon the form of the talus and the mobility of the fibula. *Journal of anatomy,* 86**,** 1.

BARTEL, D., RAWLINSON, J., BURSTEIN, A., RANAWAT, C. & FLYNN JR, W. 1995. Stresses in polyethylene components of contemporary total knee replacements. *Clinical orthopaedics and related research,* 317**,** 76-82.

BAUER, T. W., GEESINK, R. C. T., ZIMMERMAN, R. & MCMAHON, J. T. 1991. Hydroxyapatite-coated femoral stems. Histological analysis of components retrieved at autopsy. *Journal of Bone and Joint Surgery - Series A,* 73**,** 1439-1452.

BAUER, T. W., TAYLOR, S. K., JIANG, M. & MEDENDORP, S. V. 1994. An indirect comparison of third-body wear in retrieved hydroxyapatite-coated, porous, and cemented femoral components. *Clinical orthopaedics and related research,* 298**,** 11-18.

BAXTER, R. M., STEINBECK, M. J., TIPPER, J. L., PARVIZI, J., MARCOLONGO, M. & KURTZ, S. M. 2009. Comparison of periprosthetic tissue digestion methods for ultra-high molecular weight polyethylene wear debris extraction. *J Biomed Mater Res B Appl Biomater,* 91**,** 409-18.

BEHREND, H., GIESINGER, K., GIESINGER, J. M. & KUSTER, M. S. 2012. The "forgotten joint" as the ultimate goal in joint arthroplasty: validation of a new patient-reported outcome measure. *The Journal of arthroplasty,* 27**,** 430-436. e1.

BELL, C. J. & FISHER, J. 2007. Simulation of polyethylene wear in ankle joint prostheses. *J Biomed Mater Res B Appl Biomater,* 81**,** 162-7.

BEN-NISSAN, B. 2014. *Advances in calcium phosphate biomaterials*, Springer Science & Business.

BERLET, G. C., PENNER, M. J., LANCIANESE, S., STEMNISKI, P. M. & OBERT, R. M. 2014. Total ankle arthroplasty accuracy and reproducibility using preoperative CT scan-derived, patient-specific guides. *Foot and Ankle International,* 35**,** 665-676.

BESSE, J.-L., BEVERNAGE, B. D. & LEEMRIJSE, T. 2011. Revision of total ankle replacements. *Techniques in Foot & Ankle Surgery,* 10**,** 176-188.

BESSE, J. L. 2015. Osteolytic cysts with total ankle replacement: Frequency and causes? *Foot and Ankle Surgery,* 21**,** 75-76.

BESSE, J. L., BRITO, N. & LIENHART, C. 2009. Clinical evaluation and radiographic assessment of bone lysis of the AES total ankle replacement. *Foot Ankle Int,* 30**,** 964-75.

BESSE, J. L., COLOMBIER, J. A., ASENCIO, J., BONNIN, M., GAUDOT, F., JARDE, O., JUDET, T., MAESTRO, M., LEMRIJSE, T., LEONARDI, C., TOULLEC, E. & L'AFCP 2010. Total ankle arthroplasty in France. *Orthop Traumatol Surg Res,* 96**,** 291-303.

BESTIC, J. M., PETERSON, J. J., DEORIO, J. K., BANCROFT, L. W., BERQUIST, T. H. & KRANSDORF, M. J. 2008. Postoperative evaluation of the total ankle arthroplasty. *AJR Am J Roentgenol,* 190**,** 1112-23.

BIANCHI, A., MARTINELLI, N., SARTORELLI, E. & MALERBA, F. 2012. The Bologna–Oxford total ankle replacement A mid-term follow-up study. *Journal of Bone & Joint Surgery, British Volume,* 94**,** 793-798.

BIBBO, C. 2013. Temporary cementation in total ankle arthroplasty. *J Foot Ankle Surg,* 52**,** 650-4.

BILLI, F., BENYA, P., EBRAMZADEH, E., CAMPBELL, P., CHAN, F. & MCKELLOP, H. A. 2009. Metal wear particles: What we know, what we do not know, and why. *SAS Journal,* 3**,** 133-142.

BILLI, F., BENYA, P., KAVANAUGH, A., ADAMS, J., EBRAMZADEH, E. & MCKELLOP, H. 2012a. The John Charnley Award: an accurate and sensitive method to separate, display, and characterize wear debris: part 1: polyethylene particles. *Clin Orthop Relat Res,* 470**,** 329-38.

BILLI, F., BENYA, P., KAVANAUGH, A., ADAMS, J., MCKELLOP, H. & EBRAMZADEH, E. 2012b. The John Charnley Award: An Accurate and Extremely Sensitive Method to Separate, Display, and Characterize Wear Debris Part 2: Metal and Ceramic Particles. *Clinical Orthopaedics and Related Research®,* 470**,** 339-350.

BISCHOFF, J. E., FRYMAN, J. C., PARCELL, J. & OROZCO VILLASENOR, D. A. 2015. Influence of crosslinking on the wear performance of polyethylene within total ankle arthroplasty. *Foot and Ankle International,* 36**,** 369-376.

BISCHOFF, J. E., SCHON, L. & SALTZMAN, C. 2017. Influence of Geometry and Depth of Resections on Bone Support for Total Ankle Replacement. *Foot & Ankle International,* 38**,** 1026-1034.

BLATEYRON, F. 2013. The areal field parameters. *Characterisation of Areal Surface Texture.* Springer.

BLEAZEY, S. T., BRIGIDO, S. A. & PROTZMAN, N. M. 2013. Perioperative complications of a modular stem fixed-bearing total ankle replacement with intramedullary guidance. *J Foot Ankle Surg,* 52**,** 36-41.

BLOCH, B., SRINIVASAN, S. & MANGWANI, J. 2015. Current Concepts in the Management of Ankle Osteoarthritis: A Systematic Review. *Journal of Foot and Ankle Surgery,* 54**,** 932-939.

BLOEBAUM, R. D., BEEKS, D., DORR, L. D., SAVORY, C. G., DUPONT, J. A. & HOFMANN, A. A. 1994. Complications With Hydroxyapatite Participate Separation in Total Hip Arthroplasty. *Clinical orthopaedics and related research,* 298**,** 19-26.

BLOEBAUM, R. D. & DUPONT, J. A. 1993. Osteolysis from a press-fit hydroxyapatite-coated implant: a case study. *The Journal of arthroplasty,* 8**,** 195-202.

BONASIA, D. E., DETTONI, F., FEMINO, J. E., PHISITKUL, P., GERMANO, M. & AMENDOLA, A. 2010. Total ankle replacement: why, when and how? *The Iowa orthopaedic journal,* 30**,** 119.

BONNIN, M., GAUDOT, F., LAURENT, J. R., ELLIS, S., COLOMBIER, J. A. & JUDET, T. 2011. The Salto total ankle arthroplasty: survivorship and analysis of failures at 7 to 11 years. *Clin Orthop Relat Res,* 469**,** 225-36.

BOS, I. & JOHANNISSON, R. 2004. Foreign body reactions in lymph nodes of oncology patients with joint prostheses—light-, electron microscopic and immunohistological investigations. *Pathology-Research and Practice,* 200**,** 189-196.

BOWDEN, A., KURTZ, S. & EDIDIN, A. 2005. Validation of a micro-CT technique for measuring volumetric wear in retrieved acetabular liners. *Journal of Biomedical Materials Research Part B: Applied Biomaterials,* 75**,** 205-209.

BRADBERRY, S., WILKINSON, J. & FERNER, R. 2014. Systemic toxicity related to metal hip prostheses. *Clinical toxicology,* 52**,** 837-847.

BRAITO, M., DAMMERER, D., REINTHALER, A., KAUFMANN, G., HUBER, D. & BIEDERMANN, R. 2015a. Effect of Coronal and Sagittal Alignment on Outcome after Mobile-Bearing Total Ankle Replacement. *Foot and Ankle International,* 36**,** 1029-1037.

BRAITO, M., LIEBENSTEINER, M., DAMMERER, D., KRISMER, M., PFURNER, M. & BIEDERMANN, R. 2015b. Poor accuracy of plain radiographic measurements of prosthetic migration and alignment in total ankle replacement. *Journal of Orthopaedic Surgery,* 10**,** 71.

BRANDT, J.-M., HAYDON, C., HARVEY, E., MCCALDEN, R. & MEDLEY, J. 2012. Semi-quantitative assessment methods for backside polyethylene damage in modular total knee replacements. *Tribology International,* 49**,** 96-102.

BRIGIDO, S. A., GALLI, M. M., BLEAZEY, S. T. & PROTZMAN, N. M. 2014. Modular stem fixed-bearing total ankle replacement: prospective results of 23 consecutive cases with 3-year follow-up. *J Foot Ankle Surg,* 53**,** 692-9.

BRITISH STANDARD ISO 12891-2 2014. Retrieval and analysis of surgical implants Part 2: Analysis of retrieved surgical implants. *BS ISO 12891-2:2014.* London, UK: British Standards Institute.

BRITISH STANDARD ISO 17853 2011. Wear of implant materials — Polymer and metal wear particles — Isolation and characterization. *BS ISO 17853:2011.* London, UK: British Standards Institute.

BRITISH STANDARD ISO 25178-2 2012. Geometrical product specifications (GPS) — Surface texture: Areal Part 2: Terms, definitions and surface texture parameters (ISO 25178-2:2012). *BS EN ISO 25178-2:2012.* London, UK: BSI Standards Limited 2012.

BRODSKY, J. W., POLO, F. E., COLEMAN, S. C. & BRUCK, N. 2011. Changes in gait following the Scandinavian Total Ankle Replacement. *J Bone Joint Surg Am,* 93**,** 1890-6.

BROOKE, B. T., HARRIS, N. J. & MORGAN, S. 2012. Fibula lengthening osteotomy to correct valgus mal-alignment following total ankle arthroplasty. *Foot Ankle Surg,* 18**,** 144-7.

BROOMFIELD, J. A., MALAK, T. T., THOMAS, G. E., PALMER, A. J., TAYLOR, A. & GLYN-JONES, S. 2017. The Relationship Between Polyethylene Wear and Periprosthetic Osteolysis in Total Hip Arthroplasty at 12 Years in a Randomized Controlled Trial Cohort. *J Arthroplasty,* 32**,** 1186-1191.

BROWN, C., WILLIAMS, S., TIPPER, J. L., FISHER, J. & INGHAM, E. 2007a. Characterisation of wear particles produced by metal on metal and ceramic on metal hip prostheses under standard and microseparation simulation. *J Mater Sci Mater Med,* 18**,** 819-27.

BROWN, L., ZHANG, H., BLUNT, L. & BARRANS, S. 2007b. Reproduction of fretting wear at the stem—cement interface in total hip replacement. *Proceedings of the Institution of Mechanical Engineers, Part H: Journal of Engineering in Medicine,* 221**,** 963-971.

BUCKWALTER, J. A., SALTZMAN, C. & BROWN, T. 2004. The impact of osteoarthritis: implications for research. *Clinical orthopaedics and related research,* 427**,** S6-S15.

BUECHEL, F. F., BUECHEL, F. F. & PAPPAS, M. J. 2004. Twenty-Year Evaluation of Cementless Mobile-Bearing Total Ankle Replacements. *Clinical Orthopaedics and Related Research,* 424**,** 19-26.

BUECHEL, F. F. & PAPPAS, M. J. 2003. Ten-year evaluation of cementless Buechel-Pappas meniscal bearing total ankle replacement. *Foot & Ankle International,* 24**,** 462-472.

BUECHEL, F. F., PAPPAS, M. J. & IORIO, L. J. 1988. New Jersey low contact stress total ankle replacement: biomechanical rationale and review of 23 cementless cases. *Foot & Ankle International,* 8**,** 279-290.

BUECHEL, F. F., SR. 2008. Evolution of the Buechel-Pappas mobile-bearing total ankle replacement. *Foot Ankle Spec,* 1**,** 363-7.

BUMA, P. & GARDENIERS, J. W. 1995. Tissue reactions around a hydroxyapatite-coated hip prosthesis: case report of a retrieved specimen. *The Journal of arthroplasty,* 10**,** 389-395.

BURNELL, C. D., BRANDT, J. M., PETRAK, M. J. & BOURNE, R. B. 2011. Posterior condyle surface damage on retrieved femoral knee components. *J Arthroplasty,* 26**,** 1460-7.

BUTTERFIELD, R., HARKNESS, R. & ANDREWS, K. 1970. A stero-photogrammetric method for measuring displacement fields. *Geotechnique,* 20**,** 308-314.

CADAMBI, A., ENGH, G. A., DWYER, K. A. & VINH, T. N. 1994. Osteolysis of the distal femur after total knee arthroplasty. *The Journal of arthroplasty,* 9**,** 579-594.

CALDERALE, P., GARRO, A., BARBIERO, R., FASOLIO, G. & PIPINO, F. 1983. Biomechanical design of the total ankle prosthesis. *Engineering in medicine,* 12**,** 69-80.

CAMPBELL, P., MA, S., SCHMALZRIED, T. & AMSTUTZ, H. C. 1994. Tissue digestion for wear debris particle isolation. *Journal of biomedical materials research,* 28**,** 523-526.

CAMPBELL, P., MA, S., YEOM, B., MCKELLOP, H., SCHMALZRIED, T. & AMSTUTZ, H. 1995. Isolation of predominantly submicron-sized UHMWPE wear particles from periprosthetic tissues. *Journal of Biomedical Materials Research Part A,* 29**,** 127-131.

CARLSSON, Å., MARKUSSON, P. & SUNDBERG, M. 2005. Radiostereometric analysis of the double-coated STAR total ankle prosthesis: a 3–5-year follow-up of 5 cases with rheumatoid arthritis and 5 cases with osteoarthrosis. *Acta orthopaedica,* 76**,** 573-579.

CATELAS, I., BOBYN, J. D., MEDLEY, J. B., KRYGIER, J. J., ZUKOR, D. J., PETIT, A. & HUK, O. L. 2001. Effects of digestion protocols on the isolation and characterization of metal–metal wear particles. I. Analysis of particle size and shape. *Journal of biomedical materials research,* 55**,** 320-329.

CATELAS, I., WIMMER, M. A. & UTZSCHNEIDER, S. Polyethylene and metal wear particles: characteristics and biological effects. Seminars in immunopathology, 2011. Springer, 257-271.

CENNI, F., LEARDINI, A., CHELI, A., CATANI, F., BELVEDERE, C., ROMAGNOLI, M. & GIANNINI, S. 2012. Position of the prosthesis components in total ankle

replacement and the effect on motion at the replaced joint. *Int Orthop,* 36**,** 571-8.

CENNI, F., LEARDINI, A., PIERI, M., BERTI, L., BELVEDERE, C., ROMAGNOLI, M. & GIANNINI, S. 2013. Functional performance of a total ankle replacement: thorough assessment by combining gait and fluoroscopic analyses. *Clin Biomech (Bristol, Avon),* 28**,** 79-87.

CHALAYON, O., WANG, B., BLANKENHORN, B., JACKSON, J. B., BEALS, T., NICKISCH, F. & SALTZMAN, C. L. 2015. Factors affecting the outcomes of uncomplicated primary open ankle arthrodesis. *Foot and Ankle International,* 36**,** 1170-1179.

CHANG, K.-V., HSIAO, M.-Y., CHEN, W.-S., WANG, T.-G. & CHIEN, K.-L. 2013. Effectiveness of intra-articular hyaluronic acid for ankle osteoarthritis treatment: a systematic review and meta-analysis. *Archives of physical medicine and rehabilitation,* 94**,** 951-960.

CHARNLEY, J. 1951. Compression arthrodesis of the ankle and shoulder. *J Bone Joint Surg Br,* 33**,** 180-91.

CHEUNG, H. S., DEVINE, T. R. & HUBBARD, W. 1997. Calcium phosphate particle induction of metalloproteinase and mitogenesis: Effect of particle sizes. *Osteoarthritis and Cartilage,* 5**,** 145-151.

CHILDS, K., CROSBY, L. & GOSWAMI, T. 2016. Quantitative Analysis of Retrieved Glenoid Liners. *Lubricants,* 4**,** 3.

CHOI, G., KIM, H., YEO, E. & SONG, S. 2013. Comparison of the HINTEGRA and Mobility total ankle replacements Short-to intermediate-term outcomes. *Bone & Joint Journal,* 95**,** 1075-1082.

CHRISTENSEN, J. C., SCHUBERTH, J. M. & STECK, J. K. 2016. Flawed Technique for Measuring Total Ankle Component Migration. *The Journal of Foot and Ankle Surgery,* 55**,** 434-435.

CLAES, L. & HEIGELE, C. 1999. Magnitudes of local stress and strain along bony surfaces predict the course and type of fracture healing. *Journal of biomechanics,* 32**,** 255-266.

CLARIDGE, R. J. & SAGHERIAN, B. H. 2009. Intermediate term outcome of the Agility™ total ankle arthroplasty. *Foot & Ankle International,* 30**,** 824-835.

CLAUS, A. M., ENGH, C. A., SYCHTERZ, C. J., XENOS, J. S., ORISHIMO, K. F. & ENGH, C. A. 2003. Radiographic definition of pelvic osteolysis following total hip arthroplasty. *The Journal of Bone & Joint Surgery,* 85**,** 1519-1526.

CLEMENT, R. C., KRYNETSKIY, E. & PAREKH, S. G. 2013. The total ankle arthroplasty learning curve with third-generation implants: a single surgeon's experience. *Foot Ankle Spec,* 6**,** 263-70.

CLOSE, J. & INMAN, V. 1952. The action of the ankle joint. Prosthetic devices research project, Institute of engineering research. *University of California, Berkeley, Ser,* 11.

CLOSE, J. R. 1956. Some applications of the functional anatomy of the ankle joint. *JBJS,* 38**,** 761-781.

COATHUP, M., BLUNN, G., FLYNN, N., WILLIAMS, C. & THOMAS, N. 2001. A comparison of bone remodelling around hydroxyapatite-coated, porous-coated and grit-blasted hip replacements retrieved at post-mortem. *Journal of Bone & Joint Surgery, British Volume,* 83**,** 118-123.

COETZEE, J. C. 2010. Surgical strategies: lateral ligament reconstruction as part of the management of varus ankle deformity with ankle replacement. *Foot Ankle Int,* 31**,** 267-74.

CONTI, S. F., DAZEN, D., STEWART, G., GREEN, A., MARTIN, R., KUXHAUS, L. & MILLER, M. C. 2008. Proprioception after total ankle arthroplasty. *Foot & Ankle International,* 29**,** 1069-1073.

CORIN 2010. Zenith Total Ankle Replacement: Surgical Technique. Cirencester, UK: Corin.

CORNWALL, G. B., BRYANT, J. T., HANSSON, C. M., RUDAN, J., KENNEDY, L. A. & COOKE, T. D. V. 1995. A quantitative technique for reporting surface degradation patterns of UHMWPE components of retrieved total knee replacements. *Journal of Applied Biomaterials,* 6**,** 9-18.

COTTINO, U., COLLO, G., MORINO, L., COSENTINO, A., GALLINA, V., DEREGIBUS, M. & TELLINI, A. 2012. Arthroscopic ankle arthrodesis: a review. *Current reviews in musculoskeletal medicine,* 5**,** 151-155.

COTTRELL, J. M., TOWNSEND, E., LIPMAN, J., SCULCO, T. P. & WRIGHT, T. M. 2007. Bearing surface design changes affect contact patterns in total knee arthroplasty. *Clinical orthopaedics and related research,* 464**,** 127-131.

COTTRINO, S., FABREGUE, D., COWIE, A. P., BESSE, J. L., TADIER, S., GREMILLARD, L. & HARTMANN, D. J. 2016. Wear study of Total Ankle Replacement explants by microstructural analysis. *Journal of the Mechanical Behavior of Biomedical Materials,* 61**,** 1-11.

CRISWELL, B. J., DOUGLAS, K., NAIK, R. & THOMSON, A. B. 2012. High Revision and Reoperation Rates Using the AgilityTM Total Ankle System. *Clinical Orthopaedics and Related Research®,* 470**,** 1980-1986.

D'ANGELO, F., MOLINA, M., RIVA, G., ZATTI, G. & CHERUBINO, P. 2008. Failure of dual radius hydroxyapatite-coated acetabular cups. *Journal of orthopaedic surgery and research,* 3**,** 1.

DAHABREH, Z., GONSALVES, S., MONKHOUSE, R. & HARRIS, N. J. 2006. Extrusion of metal radiological marker from a total ankle replacement insert: a case report. *J Foot Ankle Surg,* 45**,** 185-9.

DALAT, F., BARNOUD, R., FESSY, M. H. & BESSE, J. L. 2013. Histologic study of periprosthetic osteolytic lesions after AES total ankle replacement. A 22 case series. *Orthopaedics and Traumatology: Surgery and Research,* 99**,** S285-S295.

DANIELS, T. R., CADDEN, A. R. & LIM, K.-K. 2008. Correction of Varus Talar Deformities in Ankle Joint Replacement. *Operative Techniques in Orthopaedics,* 18**,** 282-286.

DATIR, A., XING, M., KAKARALA, A., TERK, M. R. & LABIB, S. A. 2013. Radiographic evaluation of INBONE total ankle arthroplasty: a retrospective analysis of 30 cases. *Skeletal Radiol,* 42**,** 1693-701.

DAY, J. S., MACDONALD, D. W., OLSEN, M., GETZ, C., WILLIAMS, G. R. & KURTZ, S. M. 2012. Polyethylene wear in retrieved reverse total shoulder components. *J Shoulder Elbow Surg,* 21**,** 667-74.

DEMETRACOPOULOS, C. A., HALLORAN, J. P., MALOOF, P., ADAMS JR, S. B. & PAREKH, S. G. 2013. Total ankle arthroplasty in end-stage ankle arthritis. *Current Reviews in Musculoskeletal Medicine,* 6**,** 279-284.

DEPUY INTERNATIONAL LTD 2010. Mobility Total Ankle System: Design Rationale & Surgical Technique. Leeds, UK: DePuy International Ltd, .

DHAWAN, R., TURNER, J., SHARMA, V. & NAYAK, R. K. 2012. Tri-component, mobile bearing, total ankle replacement: mid-term functional outcome and survival. *J Foot Ankle Surg,* 51**,** 566-9.

DOETS, H. C. 2009. *Mobile-bearing total ankle arthroplasty: a fundamental assessment of the clinical, radiographic and functional outcomes*, Faculty of Medicine/Leiden University Medical Center (LUMC), Leiden University.

DOETS, H. C., BRAND, R. & NELISSEN, R. G. 2006. Total ankle arthroplasty in inflammatory joint disease with use of two mobile-bearing designs. *The Journal of Bone & Joint Surgery,* 88**,** 1272-1284.

DOETS, H. C., VAN DER PLAAT, L. W. & KLEIN, J.-P. 2008. Medial malleolar osteotomy for the correction of varus deformity during total ankle arthroplasty: results in 15 ankles. *Foot & Ankle International,* 29**,** 171-177.

DOLAN, R., HAYDEN, B. & HEYWOOD, J. 1978. A new photogrammetric method for determining shoreline erosion. *Coastal Engineering,* 2**,** 21-39.

DOORN, P. F., CAMPBELL, P. A., WORRALL, J., BENYA, P. D., MCKELLOP, H. A. & AMSTUTZ, H. C. 1998. Metal wear particle characterization from metal on

metal total hip replacements: transmission electron microscopy study of periprosthetic tissues and isolated particles. *Journal of biomedical materials research,* 42**,** 103-111.

DÖRENBERG, K. 1983. [Contact surfaces and anatomical joint surfaces of the upper ankle joint--methods for the determination of facet size and case representation]. *Morphologia medica,* 3**,** 97-108.

EGLOFF, C., HÜGLE, T. & VALDERRABANO, V. 2012. Biomechanics and pathomechanisms of osteoarthritis. *Swiss Med Wkly,* 142.

EID, K., ZELICOF, S., PERONA, B. P., SLEDGE, C. B. & GLOWACKI, J. 2001. Tissue reactions to particles of bone-substitute materials in intraosseous and heterotopic sites in rats: Discrimination of osteoinduction, osteocompatibility, and inflammation. *Journal of Orthopaedic Research,* 19**,** 962-969.

ELLIOTT, B. & GOSWAMI, T. 2012. Implant material properties and their role in micromotion and failure in total hip arthroplasty. *International Journal of Mechanics and Materials in Design,* 8**,** 1-7.

ELLIS, S. & DEORIO, J. K. 2010. The INBONE Total Ankle Replacement. *Operative Techniques in Orthopaedics,* 20**,** 201-210.

ELLISON, P., HALLAN, G., HØL, P. J., GJERDET, N. R. & HAVELIN, L. I. 2012. Coordinating retrieval and register studies improves postmarket surveillance. *Clinical Orthopaedics and Related Research®,* 470**,** 2995-3002.

ENDO, M., TIPPER, J., BARTON, D., STONE, M., INGHAM, E. & FISHER, J. 2002. Comparison of wear, wear debris and functional biological activity of moderately crosslinked and non-crosslinked polyethylenes in hip prostheses. *Proceedings of the Institution of Mechanical Engineers, Part H: Journal of Engineering in Medicine,* 216**,** 111-122.

ENDRIZZI, D. P., MACKENZIE, J. A. & HENRY, P. D. 2016. Early Debris Formation with a Porous Tantalum Glenoid Component. *J Bone Joint Surg Am,* 98**,** 1023-1029.

ENGH, G. A., PARKS, N. L. & AMMEEN, D. J. 1994. Tibial Osteolysis in Cementless Total Knee Arthroplasty: A Review of 25 Cases Treated With and Without Tibial Component Revision. *Clinical orthopaedics and related research,* 309**,** 33-43.

ESPINOSA, N., WALTI, M., FAVRE, P. & SNEDEKER, J. G. 2010. Misalignment of total ankle components can induce high joint contact pressures. *J Bone Joint Surg Am,* 92**,** 1179-87.

EVANS, E. J. 1991. Toxicity of hydroxyapatite in vitro: the effect of particle size. *Biomaterials,* 12**,** 574-576.

FEVANG, B. T., LIE, S. A., HAVELIN, L. I., BRUN, J. G., SKREDDERSTUEN, A. & FURNES, O. 2007. 257 ankle arthroplasties performed in Norway between 1994 and 2005. *Acta Orthop,* 78**,** 575-83.

FISHER, J., FIRKINS, P., REEVES, E., HAILEY, J. & ISAAC, G. 1995. The influence of scratches to metallic counterfaces on the wear of ultra-high molecular weight polyethylene. *Proceedings of the Institution of Mechanical Engineers, Part H: Journal of Engineering in Medicine,* 209**,** 263-264.

FLAVIN, R., COLEMAN, S. C., TENENBAUM, S. & BRODSKY, J. W. 2013. Comparison of gait after total ankle arthroplasty and ankle arthrodesis. *Foot Ankle Int,* 34**,** 1340-8.

FOLCH, J., LEES, M. & SLOANE STANLEY, G. 1957. A simple method for the isolation and purification of total lipids from animal tissues. *J biol Chem,* 226**,** 497-509.

FOOD AND DRUGS ADMINISTRATION 1982. Federal Register Section 888.3110: Docket No 78N-3061: Ankle joint metal/polymer non-constrained prosthesis. USA: National Archives and Records Administration (NARA).

FUKUDA, T., HADDAD, S. L., REN, Y. & ZHANG, L. Q. 2010. Impact of talar component rotation on contact pressure after total ankle arthroplasty: a cadaveric study. *Foot Ankle Int,* 31**,** 404-11.

GADD, R. J., BARWICK, T. W., PALING, E., DAVIES, M. B. & BLUNDELL, C. M. 2014. Assessment of a three-grade classification of complications in total ankle replacement. *Foot Ankle Int,* 35**,** 434-7.

GALLO, J., GOODMAN, S. B., KONTTINEN, Y. T. & RASKA, M. 2013. Particle disease: biologic mechanisms of periprosthetic osteolysis in total hip arthroplasty. *Innate immunity,* 19**,** 213-224.

GALVIN, A., TIPPER, J., JENNINGS, L., STONE, M., JIN, Z., INGHAM, E. & FISHER, J. 2007. Wear and biological activity of highly crosslinked polyethylene in the hip under low serum protein concentrations. *Proceedings of the Institution of Mechanical Engineers, Part H: Journal of Engineering in Medicine,* 221**,** 1-10.

GAUDOT, F., COLOMBIER, J.-A., BONNIN, M. & JUDET, T. 2013. A controlled, comparative study of a fixed-bearing versus mobile-bearing ankle arthroplasty. *Foot & ankle international***,** 1071100713517094.

GAUTHIER, O., BOULER, J.-M., WEISS, P., BOSCO, J., AGUADO, E. & DACULSI, G. 1999. Short-term effects of mineral particle sizes on cellular degradation activity after implantation of injectable calcium phosphate biomaterials and the consequences for bone substitution. *Bone,* 25**,** 71S-74S.

GIANNINI, S., ROMAGNOLI, M., O'CONNOR, J. J., CATANI, F., NOGARIN, L., MAGNAN, B., MALERBA, F., MASSARI, L., GUELFI, M. & MILANO, L. 2011. Early clinical results of the BOX ankle replacement are satisfactory: a multicenter feasibility study of 158 ankles. *The Journal of Foot and Ankle Surgery,* 50**,** 641-647.

GLAZEBROOK, M., DANIELS, T., YOUNGER, A., FOOTE, C. J., PENNER, M., WING, K., LAU, J., LEIGHTON, R. & DUNBAR, M. 2008. Comparison of health-related quality of life between patients with end-stage ankle and hip arthrosis. *J Bone Joint Surg Am,* 90**,** 499-505.

GLAZEBROOK, M. A., ARSENAULT, K. & DUNBAR, M. 2009. Evidence-based classification of complications in total ankle arthroplasty. *Foot Ankle Int,* 30**,** 945-9.

GOETZ, J. E., RUNGPRAI, C., TENNANT, J. N., HUBER, E., URIBE, B., FEMINO, J., PHISITKUL, P. & AMENDOLA, A. 2016. Variable Volumes of Resected Bone Resulting from Different Total Ankle Arthroplasty Systems. *Foot and Ankle International,* 37**,** 898-904.

GOLDBERG, A. J., MACGREGOR, A., DAWSON, J., SINGH, D., CULLEN, N., SHARP, R. J. & COOKE, P. H. 2012. The demand incidence of symptomatic ankle osteoarthritis presenting to foot & ankle surgeons in the United Kingdom. *The Foot,* 22**,** 163-166.

GOLDBERG, A. J., SHARP, B. & COOKE, P. 2009a. Early failure in total ankle replacements due to component malposition: a report of two cases. *Foot & ankle international,* 30**,** 783-787.

GOLDBERG, A. J., SHARP, R. J. & COOKE, P. 2009b. Ankle replacement: current practice of foot & ankle surgeons in the United kingdom. *Foot Ankle Int,* 30**,** 950-4.

GOLDBERG, A. J., ZAIDI, R., THOMSON, C., DORE, C. J., SKENE, S. S., CRO, S., ROUND, J., MOLLOY, A., DAVIES, M., KARSKI, M., KIM, L. & COOKE, P. 2016. Total ankle replacement versus arthrodesis (TARVA): protocol for a multicentre randomised controlled trial. *BMJ Open,* 6 (9) (no pagination).

GOLDVASSER, D., MARCHIE, A., BRAGDON, L. K., BRAGDON, C. R., WEIDENHIELM, L. & MALCHAU, H. 2013. Incidence of osteolysis in total knee arthroplasty: comparison between radiographic and retrieval analysis. *The Journal of arthroplasty,* 28**,** 201-206.

GOODMAN, S. B., DAVIDSON, J. A. & FORNASIER, V. L. 1993. Histological reaction to titanium alloy and hydroxyapatite particles in the rabbit tibia. *Biomaterials,* 14**,** 723-728.

GOUGOULIAS, N., KHANNA, A. & MAFFULLI, N. 2010. How successful are current ankle replacements?: a systematic review of the literature. *Clin Orthop Relat Res,* 468**,** 199-208.

GOUGOULIAS, N. & MAFFULLI, N. 2013. History of total ankle replacement. *Clin Podiatr Med Surg,* 30**,** 1-20.

GREISBERG, J., HANSEN JR, S. T. & DIGIOVANNI, C. 2004. Alignment and technique in total ankle arthroplasty. *Operative Techniques in Orthopaedics,* 14**,** 21-30.

GROCHOWSKY, J., ALAWAYS, L., SISKEY, R., MOST, E. & KURTZ, S. 2006. Digital photogrammetry for quantitative wear analysis of retrieved TKA components. *Journal of Biomedical Materials Research Part B: Applied Biomaterials,* 79**,** 263-267.

GROSS, C. E., HUH, J., GREEN, C., SHAH, S., DEORIO, J. K., EASLEY, M. & NUNLEY, J. A. 2016. Outcomes of bone grafting of bone cysts after total ankle arthroplasty. *Foot and Ankle International,* 37**,** 157-164.

HALLAB, N. J. & JACOBS, J. J. 2009. Biologic effects of implant debris. *Bulletin of the NYU hospital for joint diseases,* 67**,** 182.

HANNA, R. S., HADDAD, S. L. & LAZARUS, M. L. 2007. Evaluation of periprosthetic lucency after total ankle arthroplasty: helical CT versus conventional radiography. *Foot Ankle Int,* 28**,** 921-6.

HARADA, Y., WANG, J. T., DOPPALAPUDI, V. A., WILLIS, A. A., JASTY, M., HARRIS, W. H., NAGASE, M. & GOLDRING, S. R. 1996. Differential effects of different forms of hydroxyapatite and hydroxyapatite/tricalcium phosphate particulates on human monocyte/macrophages in vitro. *Journal of biomedical materials research,* 31**,** 19-26.

HARDY, D. R., FRAYSSINET, P., BONEL, G., AUTHOM, T., NAELOU, S. A. L. & DELINCÉ, P. E. 1994. Two-year outcome of hydroxyapatite-coated prostheses: two femoral prostheses retrieved at autopsy. *Acta Orthopaedica Scandinavica,* 65**,** 253-257.

HARMAN, M., CRISTOFOLINI, L., ERANI, P., STEA, S. & VICECONTI, M. 2011. A pictographic atlas for classifying damage modes on polyethylene bearings. *Journal of Materials Science: Materials in Medicine,* 22**,** 1137-1146.

HARMAN, M. K., BANKS, S. A. & HODGE, W. A. 2007. Backside damage corresponding to articular damage in retrieved tibial polyethylene inserts. *Clinical orthopaedics and related research,* 458**,** 137-144.

HARRIS, N., HENDRICSON, A., RYDHOLM, U., KNUTSON, K. & POPELKA, S. 2014. The early multicentre results of the rebalance total ankle replacement. *Bone & Joint Journal Orthopaedic Proceedings Supplement,* 96-B**,** 2-2.

HARRIS, N. J., BROOKE, B. T. & STURDEE, S. 2009. A wear debris cyst following STAR Total Ankle Replacement—surgical management. *Foot and Ankle Surgery,* 15**,** 43-45.

HASKELL, A. & MANN, R. A. 2004a. Ankle Arthroplasty with Preoperative Coronal Plane Deformity. *Clinical Orthopaedics and Related Research,* 424**,** 98-103.

HASKELL, A. & MANN, R. A. 2004b. Perioperative Complication Rate of Total Ankle Replacement is Reduced by Surgeon Experience. *Foot & Ankle International,* 25**,** 283-289.

HENRICSON, A. & ÅGREN, P.-H. 2007. Secondary surgery after total ankle replacement. *Foot and Ankle Surgery,* 13**,** 41-44.

HENRICSON, A. & CARLSSON, A. 2015. Survival analysis of the single- and double-coated STAR ankle up to 20 years: Long-term follow-up of 324 cases from the Swedish ankle registry. *Foot and Ankle International,* 36**,** 1156-1160.

HENRICSON, A., CARLSSON, A. & RYDHOLM, U. 2011a. What is a revision of total ankle replacement? *Foot Ankle Surg,* 17**,** 99-102.

HENRICSON, A., KNUTSON, K., LINDAHL, J. & RYDHOLM, U. 2010. The AES total ankle replacement: A mid-term analysis of 93 cases. *Foot Ankle Surg,* 16**,** 61-4.

HENRICSON, A., NILSSON, J. A. & CARLSSON, A. 2011b. 10-year survival of total ankle arthroplasties: a report on 780 cases from the Swedish Ankle Register. *Acta Orthop,* 82**,** 655-9.

HENRICSON, A., SKOOG, A. & CARLSSON, A. 2007. The Swedish Ankle Arthroplasty Register: An analysis of 531 arthroplasties between 1993 and 2005. *Acta Orthop,* 78**,** 569-74.

HICKS, J. 1953. The mechanics of the foot: I. The joints. *Journal of Anatomy,* 87**,** 345.

HINTERMANN, B., KNUPP, M., ZWICKY, L. & BARG, A. 2012. Total ankle replacement for treatment of end-stage osteoarthritis in elderly patients. *J Aging Res,* 2012**,** 345237.

HINTERMANN, B., RUIZ, R. & BARG, A. 2017. Dealing with the Stiff Ankle: Preoperative and Late Occurrence. *Foot & Ankle Clinics,* 22**,** 425-453.

HINTERMANN, B., VALDERRABANO, V., DEREYMAEKER, G. & DICK, W. 2004. The HINTEGRA Ankle: Rationale and Short-Term Results of 122 Consecutive Ankles. *Clinical Orthopaedics and Related Research,* 424**,** 57-68.

HOBSON, S., KARANTANA, X. & DHAR, S. 2009. Total ankle replacement in patients with significant pre-operative deformity of the hindfoot. *Bone & Joint Journal,* 91**,** 481-486.

HOOD, R. W., WRIGHT, T. M. & BURSTEIN, A. H. 1983. Retrieval analysis of total knee prostheses: a method and its application to 48 total condylar prostheses. *Journal of biomedical materials research,* 17**,** 829-842.

HOSMAN, A. H., MASON, R. B., HOBBS, T. & ROTHWELL, A. G. 2007. A New Zealand national joint registry review of 202 total ankle replacements followed for up to 6 years. *Acta Orthop,* 78**,** 584-91.

HUROWITZ, E. J., GOULD, J. S., FLEISIG, G. S. & FOWLER, R. 2007. Outcome analysis of agility total ankle replacement with prior adjunctive procedures: two to six year followup. *Foot Ankle Int,* 28**,** 308-12.

INGHAM, E. & FISHER, J. 2000. Biological reactions to wear debris in total joint replacement. *Proceedings of the Institution of Mechanical Engineers, Part H: Journal of Engineering in Medicine,* 214**,** 21-37.

INGROSSO, S., BENEDETTI, M., LEARDINI, A., CASANELLI, S., SFORZA, T. & GIANNINI, S. 2009. Gait analysis in patients operated with a novel total ankle prosthesis. *Gait & posture,* 30**,** 132-137.

INMAN, V. T. 1976. *The joints of the ankle*, Williams & Wilkins.

INTEGRA LIFE SCIENCES SERVICES 2011. Hintegra Total Ankle Prosthesis: Surgical Technique. Saint Priest, FR: Integra LifeSciences Services (France) SAS,.

ISO STANDARD 2011. Wear of implant materials, polymer and metal wear particles. Isolation, characterisation and quantification. *17853:2011.*

IWAMOTO, K., SHI, K., TOMITA, T., HASHIMOTO, J., YAMAZAKI, T., YOSHIKAWA, H. & SUGAMOTO, K. 2014. In vivo kinematics of three-component mobile-bearing total ankle replacement in rheumatoid ankle with talocalcaneal arthrodesis and spontaneous talocalcaneal fusion. *Mod Rheumatol,* 24**,** 897-903.

JAMAL, B., HALAI, M. & PILLAI, A. 2014. The Evolution of Total Ankle Arthroplasty. *Orthop Muscul Syst,* 3**,** 2161-0533.1000145.

JASTY, M., GOETZ, D. D., BRAGDON, C. R., LEE, K. R., HANSON, A. E., ELDER, J. R. & HARRIS, W. H. 1997. Wear of polyethylene acetabular components in total hip arthroplasty. An analysis of one hundred and twenty-eight components retrieved at autopsy or revision operations. *JBJS,* 79**,** 349-58.

JEFFCOATE, W. 2004. Vascular calcification and osteolysis in diabetic neuropathy—is RANK-L the missing link? *Diabetologia,* 47**,** 1488-1492.

JEHAN, S. & HILL, S. O. 2012. Operative Technique of Two Parallel Compression Screws and Autologous Bone Graft for Ankle Arthrodesis after Failed Total Ankle Replacement. *Foot & Ankle International,* 33**,** 767-771.

JENSEN, J., FROKJAER, J., GERKE, O., LUDVIGSEN, L. & TORFING, T. 2014. Evaluation of periprosthetic bone cysts in patients with a scandinavian total ankle replacement: Weight-bearing conventional digital radiographs versus weight-bearing multiplanar reconstructed fluoroscopic imaging. *American Journal of Roentgenology,* 203**,** 863-868.

JOHL, C., KIRCHER, J., POHLMANNN, K. & JANSSON, V. 2006. Management of failed total ankle replacement with a retrograde short femoral nail: a case report. *Journal of orthopaedic trauma,* 20**,** 60-65.

JUNG, H.-G., JEON, S.-H., KIM, T.-H. & PARK, J.-T. 2013. Total Ankle Arthroplasty With Combined Calcaneal and Metatarsal Osteotomies for Treatment of Ankle Osteoarthritis With Accompanying Cavovarus Deformities Early Results. *Foot & Ankle International,* 34**,** 140-147.

JUNG, H. G., LEE, S. H., SHIN, M. H., LEE, D. O., EOM, J. S. & LEE, J. S. 2016. Anterior Heterotopic Ossification at the Talar Neck after Total Ankle Arthroplasty. *Foot and Ankle International,* 37**,** 703-708.

KANDALA, N.-B., CONNOCK, M., PULIKOTTIL-JACOB, R., SUTCLIFFE, P., CROWTHER, M. J., GROVE, A., MISTRY, H. & CLARKE, A. 2015. Setting benchmark revision rates for total hip replacement: analysis of registry evidence. *Bmj,* 350**,** h756.

KARACHALIOS, T., KOMNOS, G. & KOLONIA, K. 2014. Current Evidence in Designs and Fixation Surfaces in Total Hip Arthroplasty. *Bone-Implant Interface in Orthopedic Surgery.* Springer.

KEEN, C., PHILIP, G., BRADY, K., SPENCER, J. & LEVISON, D. 1992. Histopathological and microanalytical study of zirconium dioxide and barium sulphate in bone cement. *Journal of clinical pathology,* 45**,** 984-989.

KEPLER, C. K., NHO, S. J., BANSAL, M., ALA, O. L., CRAIG, E. V., WRIGHT, T. M. & WARREN, R. F. 2010. Radiographic and histopathologic analysis of osteolysis after total shoulder arthroplasty. *Journal of Shoulder and Elbow Surgery,* 19**,** 588-595.

KERKHOFF, Y. R. A., KOSSE, N. M. & LOUWERENS, J. W. K. 2016a. Short term results of the Mobility Total Ankle System: Clinical and radiographic outcome. *Foot and Ankle Surgery,* 22**,** 152-157.

KERKHOFF, Y. R. A., KOSSE, N. M., METSAARS, W. P. & LOUWERENS, J. W. K. 2016b. Long-term clinical and radiographic outcome of the scan dinavian total ankle replacement (STAR). *Foot and Ankle Surgery,* 1)**,** 95.

KERKHOFF, Y. R. A., KOSSE, N. M., METSAARS, W. P. & LOUWERENS, J. W. K. 2016c. Long-term Functional and Radiographic Outcome of a Mobile Bearing Ankle Prosthesis. *Foot and Ankle International,* 37**,** 1292-1302.

KIM, D. R., CHOI, Y. S., POTTER, H. G., LI, A. E., CHUN, K. Y., JUNG, Y. Y., KIM, J. S. & YOUNG, K. W. 2016. Total ankle arthroplasty: An imaging overview. *Korean Journal of Radiology,* 17**,** 413-423.

KING, C. M., SCHUBERTH, J. M., CHRISTENSEN, J. C. & SWANSTROM, K. M. 2013. Relationship of Alignment and Tibial Cortical Coverage to Hypertrophic Bone Formation in Salto Talaris Total Ankle Arthroplasty. *Journal of Foot and Ankle Surgery,* 52**,** 355-359.

KITAOKA, H. B., PATZER, G. L., ILSTRUP, D. M. & WALLRICHS, S. L. 1994. Survivorship analysis of the Mayo total ankle arthroplasty. *Journal of Bone and Joint Surgery-A-American Volumes,* 76**,** 974-979.

KNECHT, S. I., ESTIN, M., CALLAGHAN, J. J., ZIMMERMAN, M. B., ALLIMAN, K. J., ALVINE, F. G. & SALTZMAN, C. L. 2004. The agility total ankle arthroplastySeven to sixteen-year follow-up. *The Journal of Bone & Joint Surgery,* 86**,** 1161-1171.

KOBAYASHI, A., BONFIELD, W., KADOYA, Y., YAMAC, T., FREEMAN, M., SCOTT, G. & REVELL, P. 1997. The size and shape of particulate polyethylene wear debris in total joint replacements. *Proceedings of the Institution of Mechanical Engineers, Part H: Journal of Engineering in Medicine,* 211**,** 11-15.

KOBAYASHI, A., MINODA, Y., KADOYA, Y., OHASHI, H., TAKAOKA, K. & SALTZMAN, C. L. 2004. Ankle Arthroplasties Generate Wear Particles Similar to Knee Arthroplasties. *Clinical Orthopaedics and Related Research,* 424**,** 69-72.

KOFOED, H. & DANBORG, L. 1995. Biological fixation of ankle arthroplasty: A sequential consecutive prospective clinico-radiographic series of 20 ankles with arthrosis followed for 1–4 years. *The Foot,* 5**,** 27-31.

KOFOED, H. & LUNDBERG-JENSEN, A. 1999. Ankle arthroplasty in patients younger and older than 50 years: a prospective series with long-term follow-up. *Foot & ankle international,* 20**,** 501-506.

KOHONEN, I., KOIVU, H., PUDAS, T., TIUSANEN, H., VAHLBERG, T. & MATTILA, K. 2013. Does computed tomography add information on radiographic analysis in detecting periprosthetic osteolysis after total ankle arthroplasty? *Foot Ankle Int,* 34**,** 180-8.

KOIVU, H., KOHONEN, I., MATTILA, K., LOYTTYNIEMI, E. & TIUSANEN, H. 2017. Medium to long-term results of 130 Ankle Evolutive System total ankle replacements—Inferior survival due to peri-implant osteolysis. *Foot and Ankle Surgery.*

KOIVU, H., KOHONEN, I., SIPOLA, E., ALANEN, K., VAHLBERG, T. & TIUSANEN, H. 2009. Severe periprosthetic osteolytic lesions after the Ankle Evolutive System total ankle replacement. *Journal of Bone & Joint Surgery, British Volume,* 91**,** 907-914.

KOIVU, H., MACKIEWICZ, Z., TAKAKUBO, Y., TROKOVIC, N., PAJARINEN, J. & KONTTINEN, Y. T. 2012. RANKL in the osteolysis of AES total ankle replacement implants. *Bone,* 51**,** 546-52.

KOKKONEN, A., IKAVALKO, M., TIIHONEN, R., KAUTIAINEN, H. & BELT, E. A. 2011. High rate of osteolytic lesions in medium-term followup after the AES total ankle replacement. *Foot Ankle Int,* 32**,** 168-75.

KOMISTEK, R. D., STIEHL, J. B., BUECHEL, F. F., NORTHCUT, E. J. & HAJNER, M. E. 2000. A Determination of Ankle Kinematics Using Fluoroscopy. *Foot & Ankle International,* 21**,** 343-350.

KONTTINEN, Y. T., ZHAO, D., BEKLEN, A., MA, G., TAKAGI, M., KIVELÄ-RAJAMÄKI, M., ASHAMMAKHI, N. & SANTAVIRTA, S. 2005. The microenvironment around total hip replacement prostheses. *Clinical orthopaedics and related research,* 430**,** 28-38.

KOO, T. K. & LI, M. Y. 2016. A guideline of selecting and reporting intraclass correlation coefficients for reliability research. *Journal of chiropractic medicine,* 15**,** 155-163.

KOPP, F. J., PATEL, M. M., DELAND, J. T. & O'MALLEY, M. J. 2006. Total Ankle Arthroplasty With the Agility Prosthesis: Clinical and Radiographic Evaluation. *Foot & Ankle International,* 27**,** 97-103.

LACROIX, D. & PRENDERGAST, P. 2002. A mechano-regulation model for tissue differentiation during fracture healing: analysis of gap size and loading. *Journal of biomechanics,* 35**,** 1163-1171.

LAGAAY, P. M. & SCHUBERTH, J. M. 2010. Analysis of ankle range of motion and functional outcome following total ankle arthoplasty. *J Foot Ankle Surg,* 49**,** 147-51.

LAL, S., HALL, R. & TIPPER, J. 2016. A Novel Method for Isolation and Recovery of Ceramic Nanoparticles and Metal Wear Debris from Serum Lubricants at Ultra-low Wear Rates. *Acta Biomaterialia.*

LAQUERRIERE, P., GRANDJEAN-LAQUERRIERE, A., JALLOT, E., BALOSSIER, G., FRAYSSINET, P. & GUENOUNOU, M. 2003. Importance of hydroxyapatite particles characteristics on cytokines production by human monocytes in vitro. *Biomaterials,* 24**,** 2739-2747.

LAQUERRIERE, P., KILIAN, L., BOUCHOT, A., JALLOT, E., GRANDJEAN, A., GUENOUNOU, M., BALOSSIER, G., FRAYSSINET, P. & BONHOMME, P.

2001. Effect of hydroxyapatite sintering temperature on intracellular ionic concentrations of monocytes: A TEM-cryo-x-ray microanalysis study. *Journal of biomedical materials research,* 58**,** 238-246.

LEARDINI, A., O'CONNOR, J., CATANI, F., ROMAGNOLI, M. & GIANNINI, S. 2008. Preliminary results of a biomechanics driven design of a total ankle prosthesis. *Journal of Foot and Ankle Research,* 1**,** O8.

LEE, J.-M., SALVATI, E., BETTS, F., DICARLO, E., DOTY, S. & BULLOUGH, P. 1992. Size of metallic and polyethylene debris particles in failed cemented total hip replacements. *Journal of Bone & Joint Surgery, British Volume,* 74**,** 380-384.

LEE, K. B., CHO, S. G. & SEON, J. K. 2008. Cementless total ankle arthroplasty in diabetic neuropathic arthropathy. *Diabet Med,* 25**,** 1358-60.

LEE, K. B., CHO, Y. J., PARK, J. K., SONG, E. K., YOON, T. R. & SEON, J. K. 2011. Heterotopic ossification after primary total ankle arthroplasty. *J Bone Joint Surg Am,* 93**,** 751-8.

LEE, K. T., LEE, Y. K., YOUNG, K. W., KIM, H. J., PARK, S. Y., KIM, J. S. & KIM, K. C. 2010. Perioperative complications of the MOBILITY total ankle system: comparison with the HINTEGRA total ankle system. *J Orthop Sci,* 15**,** 317-22.

LEE, K. T., LEE, Y. K., YOUNG, K. W., KIM, J. B. & SEO, Y. S. 2013. Perioperative complications and learning curve of the Mobility Total Ankle System. *Foot Ankle Int,* 34**,** 210-4.

LEROUGE, S., HUK, O., YAHIA, L. H. & SEDEL, L. 1996. Characterization of in vivo wear debris from ceramic—ceramic total hip arthroplasties. *Journal of biomedical materials research,* 32**,** 627-633.

LESZKO, F., KOMISTEK, R. D., MAHFOUZ, M. R., RATRON, Y. A., JUDET, T., BONNIN, M., COLOMBIER, J. A. & LIN, S. S. 2008. In vivo kinematics of the salto total ankle prosthesis. *Foot Ankle Int,* 29**,** 1117-25.

LEUNG, S. B., EGAWA, H., STEPNIEWSKI, A., BEYKIRCH, S., ENGH, C. A. & ENGH, C. A. 2007. Incidence and volume of pelvic osteolysis at early follow-up with highly cross-linked and noncross-linked polyethylene. *The Journal of arthroplasty,* 22**,** 134-139.

LEWIS, J. S., ADAMS JR, S. B., QUEEN, R. M., DEORIO, J. K., NUNLEY, J. A. & EASLEY, M. E. 2014. Outcomes after total ankle replacement in association with ipsilateral hindfoot arthrodesis. *Foot and Ankle International,* 35**,** 535-542.

LEWIS, J. S., GREEN, C. L., ADAMS, S. B., EASLEY, M. E., DEORIO, J. K. & NUNLEY, J. A. 2015. Comparison of First- and Second-Generation Fixed-Bearing Total Ankle Arthroplasty Using a Modular Intramedullary Tibial Component. *Foot and Ankle International,* 36**,** 881-890.

LINDER, L. 1994. Implant stability, histology, RSA and wear-more critical questions are needed: A view point. *Acta Orthopaedica,* 65**,** 654-658.

LINTNER, F., BOHM, G., HUBER, M. & SCHOLZ, R. 1994. Histology of tissue adjacent to an HAC-coated femoral prosthesis. A case report. *Journal of Bone & Joint Surgery, British Volume,* 76**,** 824-830.

LIST, R., FORESTI, M., GERBER, H., GOLDHAHN, J., RIPPSTEIN, P. & STÜSSI, E. 2012. Three-Dimensional Kinematics of an Unconstrained Ankle Arthroplasty: A PreliminaryIn VivoVideofluoroscopic Feasibility Study. *Foot & Ankle International,* 33**,** 883-892.

LIU, A., RICHARDS, L., BLADEN, C. L., INGHAM, E., FISHER, J. & TIPPER, J. L. 2015. The biological response to nanometre-sized polymer particles. *Acta biomaterialia,* 23**,** 38-51.

LIZA, S., HASEEB, A., ABBAS, A. & MASJUKI, H. 2011. Failure analysis of retrieved UHMWPE tibial insert in total knee replacement. *Engineering Failure Analysis,* 18**,** 1415-1423.

LORD, G. & MAROTTE, J. 1979. [Total ankle replacement (author's transl)]. *Revue de chirurgie orthopedique et reparatrice de l'appareil moteur,* 66**,** 527-530.

LUCAS Y HERNANDEZ, J., LAFFENÊTRE, O., TOULLEC, E., DARCEL, V. & CHAUVEAUX, D. 2014. AKILE™ total ankle arthroplasty: Clinical and CT scan

analysis of periprosthetic cysts. *Orthopaedics & Traumatology: Surgery & Research,* 100**,** 907-915.

LUNDBERG, A., SVENSSON, O., NEMETH, G. & SELVIK, G. 1989. The axis of rotation of the ankle joint. *Bone & Joint Journal,* 71**,** 94-99.

LUNDEEN, G. A., CLANTON, T. O., DUNAWAY, L. J. & LU, M. 2016. Motion at the Tibial and Polyethylene Component Interface in a Mobile-Bearing Total Ankle Replacement. *Foot and Ankle International,* 37**,** 848-854.

MALARD, O., BOULER, J. M., GUICHEUX, J., HEYMANN, D., PILET, P., COQUARD, C. & DACULSI, G. 1999. Influence of biphasic calcium phosphate granulometry on bone ingrowth, ceramic resorption, and inflammatory reactions: preliminary in vitro and in vivo study. *Journal of biomedical materials research,* 46**,** 103-111.

MALONEY, W. J., SMITH, R. L., SCHMALZRIED, T. P., CHIBA, J., HUENE, D. & RUBASH, H. 1995. Isolation and characterization of wear particles generated in patients who have had failure of a hip arthroplasty without cement. *The Journal of Bone & Joint Surgery,* 77**,** 1301-1310.

MANN, J. A., MANN, R. A. & HORTON, E. 2011. STAR ankle: long-term results. *Foot Ankle Int,* 32**,** S473-84.

MARGEVICIUS, K. J., BAUER, T. W., MCMAHON, J. T., BROWN, S. A. & MERRITT, K. 1994. Isolation and characterization of debris in membranes around total joint prostheses. *The Journal of Bone & Joint Surgery,* 76**,** 1664-1675.

MARTIN, R. L., STEWART, G. W. & CONTI, S. F. 2007. Posttraumatic ankle arthritis: an update on conservative and surgical management. *J Orthop Sports Phys Ther,* 37**,** 253-9.

MARTINEZ-CARRANZA, N., BERG, H. E., LAGERSTEDT, A. S., NURMI-SANDH, H., SCHUPBACH, P. & RYD, L. 2014. Fixation of a double-coated titanium-hydroxyapatite focal knee resurfacing implant: A 12-month study in sheep. *Osteoarthritis and Cartilage,* 22**,** 836-844.

MATESANZ, M. C., FEITO, M. J., OÑADERRA, M., RAMÍREZ-SANTILLÁN, C., DA CASA, C., ARCOS, D., VALLET-REGÍ, M., ROJO, J. M. & PORTOLÉS, M. T. 2014. Early in vitro response of macrophages and T lymphocytes to nanocrystalline hydroxyapatites. *Journal of colloid and interface science,* 416**,** 59-66.

MATORTHO LTD 2011. BOX Total Ankle Replacement: Operative Technique. Surrey, UK: MatOrtho Ltd,.

MCEWEN, H. M. J., BARNETT, P. I., BELL, C. J., FARRAR, R., AUGER, D. D., STONE, M. H. & FISHER, J. 2005. The influence of design, materials and kinematics on the in vitro wear of total knee replacements. *Journal of Biomechanics,* 38**,** 357-365.

MCIFF, T. E., ALVINE, F. G., SALTZMAN, C. L., KLAREN, J. C. & BROWN, T. D. 2004. Intraoperative Measurement of Distraction for Ligament Tensioning in Total Ankle Arthroplasty. *Clinical Orthopaedics and Related Research,* 424**,** 111-117.

MCINNES, K. A., YOUNGER, A. S. E. & OXLAND, T. R. 2014. Initial instability in total ankle replacement: A cadaveric biomechanical investigation of the star and agility prostheses. *Journal of Bone and Joint Surgery - American Volume,* 96**,** e147.1-e147.8.

MCKELLOP, H. A. 2007. The lexicon of polyethylene wear in artificial joints. *Biomaterials,* 28**,** 5049-5057.

MCKINLEY, T. O., RUDERT, M. J., KOOS, D. C., PEDERSEN, D. R., BAER, T. E., TOCHIGI, Y. & BROWN, T. D. 2006. Contact stress transients during functional loading of ankle stepoff incongruities. *Journal of biomechanics,* 39**,** 617-626.

MERCER, J., PENNER, M., WING, K. & YOUNGER, A. S. 2016. Inconsistency in the Reporting of Adverse Events in Total Ankle Arthroplasty: A Systematic Review of the Literature. *Foot & Ankle International,* 37**,** 127-36.

MERIAN, M., GLISSON, R. R. & NUNLEY, J. A. 2011. Ligament Balancing for Total Ankle Arthroplasty: An in vitro Evaluation of the Elongation of the Hind-and Midfoot Ligaments. *Foot & Ankle International,* 32**,** 457-472.

MICHELSON, J. D., SCHMIDT, G. R. & MIZEL, M. S. 2000. Kinematics of a Total Arthroplasty of the Ankle: Comparison to Normal Ankle Motion. *Foot & Ankle International,* 21**,** 278-284.

MIGLIORE, A., GIOVANNANGELI, F., BIZZI, E., MASSAFRA, U., ALIMONTI, A., LAGANÀ, B., PICCHIANTI, A. D., GERMANO, V., GRANATA, M. & PISCITELLI, P. 2011. Viscosupplementation in the management of ankle osteoarthritis: a review. *Archives of orthopaedic and trauma surgery,* 131**,** 139-147.

MILOŠEV, L., ANTOLIČ, V., MINOVIČ, A., CÖR, A., HERMAN, S., PAVLOVČIČ, V. & CAMPBELL, P. 2000. Extensive metallosis and necrosis in failed prostheses with cemented titanium-alloy stems and ceramic heads. *Bone & Joint Journal,* 82**,** 352-357.

MINODA, Y., KOBAYASHI, A., IWAKI, H., MIYAGUCHI, M., KADOYA, Y., OHASHI, H., YAMANO, Y. & TAKAOKA, K. 2003. Polyethylene wear particles in synovial fluid after total knee arthroplasty. *Clin Orthop Relat Res,* 165-72.

MOCHIDA, Y., BAUER, T. W., KOSHINO, T., HIRAKAWA, K. & SAITO, T. 2002. Histologic and quantitative wear particle analyses of tissue around cementless ceramic total knee prostheses. *The Journal of arthroplasty,* 17**,** 121-128.

MOCHIDA, Y., BOEHLER, M., SALZER, M. & BAUER, T. W. 2001. Debris from failed ceramic-on-ceramic and ceramic-on-polyethylene hip prostheses. *Clinical orthopaedics and related research,* 389**,** 113-125.

MORGAN, S., BROOKE, B. & HARRIS, N. 2010. Total ankle replacement by the Ankle Evolution System: Medium-term outcome. *Journal of Bone & Joint Surgery, British Volume,* 92**,** 61-65.

MORGAN, S. S., BROOK, B. & HARRIS, N. 2012. Is there a role for total ankle replacement in polio patients?: A case report and review of the literature. *Foot and Ankle Surgery,* 18**,** 74-76.

MORSCHER, E. 1991. Hydroxyapatite coating of prostheses. *Bone & Joint Journal,* 73**,** 705-706.

MORSCHER, E., HEFTI, A. & AEBI, U. 1998. Severe osteolysis after third-body wear due to hydroxyapatite particles from acetabular cup coating. *Journal of Bone & Joint Surgery, British Volume,* 80**,** 267-272.

MROCZEK, K. 2003. Perioperative complications of total ankle arthroplasty. *Foot & Ankle International,* 24**,** 17-21.

MUIR, D., AOINA, J., HONG, T. & MASON, R. 2013. The outcome of the Mobility total ankle replacement at a mean of four years Can poor outcomes be predicted from pre-and post-operative analysis? *Bone & Joint Journal,* 95**,** 1366-1371.

MULCAHY, H. & CHEW, F. S. 2015. Current concepts in total ankle replacement for radiologists: Complications. *American Journal of Roentgenology,* 205**,** 1244-1250.

MURATOGLU, O. K., PERINCHIEF, R. S., BRAGDON, C. R., O'CONNOR, D. O., KONRAD, R. & HARRIS, W. H. 2003. Metrology to quantify wear and creep of polyethylene tibial knee inserts. *Clinical orthopaedics and related research,* 410**,** 155-164.

MURNAGHAN, J., WARNOCK, D. & HENDERSON, S. 2005. Total ankle replacement. Early experiences with STAR prosthesis. *The Ulster medical journal,* 74**,** 9.

NAGASE, M., BAKER, D. G. & SCHUMACHER JR, H. R. 1988. Prolonged inflammatory reactions induced by artificial ceramics in the rat air pouch model. *Journal of Rheumatology,* 15**,** 1334-1338.

NAGASHIMA, M., TAKAHASHI, H., KAKUMOTO, S., MIYAMOTO, Y. & YOSHINO, S. 2004. Total ankle arthroplasty for deformity of the foot in patients with rheumatoid arthritis using the TNK ankle system: clinical results of 21 cases. *Mod Rheumatol,* 14**,** 48-53.

NAM, D., BOSTROM, M. P. & FAHLGREN, A. 2013. Emerging Ideas: Instability-induced Periprosthetic Osteolysis Is Not Dependent on the Fibrous Tissue Interface. *Clinical Orthopaedics and Related Research®,* 471**,** 1758-1762.

NATIONAL JOINT REGISTRY. 2017. *National Joint Registry 14th Annual Report 2017 for England, Wales and Northern Ireland* [Online]. Hertfordshire, UK: National Joint Registry. Available: www.njrreports.org.uk [Accessed 26th December 2017 2017].

NEHME, A., OAKES, D. A., MARCHEIX, B., GOMEZ-BROUCHET, A. & PUGET, J. 2005. Compressive intrapelvic synovial cysts: an early complication of an HA-coated cup. *Clinical orthopaedics and related research,* 430**,** 232-236.

NIEDZWIECKI, S., KLAPPERICH, C., SHORT, J., JANI, S., RIES, M. & PRUITT, L. 2001. Comparison of three joint simulator wear debris isolation techniques: acid digestion, base digestion, and enzyme cleavage. *Journal of biomedical materials research,* 56**,** 245-249.

NIEUWE WEME, R. A., VAN SOLINGE, G., J, N. D., SIEREVELT, I., HAVERKAMP, D. & DOETS, H. C. 2015. Total ankle replacement for posttraumatic arthritis. Similar outcome in postfracture and instability arthritis: a comparison of 90 ankles. *Acta Orthopaedica,* 86**,** 401-6.

NILSSON, K. G., CAJANDER, S. & KARRHOLM, J. 1994. Early failure of hydroxyapatite-coating in total knee arthroplasty. A case report. *Acta Orthopaedica Scandinavica,* 65**,** 212-214.

NINE, M., CHOUDHURY, D., HEE, A., MOOTANAH, R. & OSMAN, N. 2014. Wear Debris Characterization and Corresponding Biological Response: Artificial Hip and Knee Joints. *Materials,* 7**,** 980-1016.

NINOMIYA, J. T., STRUVE, J. A., STELLOH, C. T., TOTH, J. M. & CROSBY, K. E. 2001. Effects of hydroxyapatite participate debris on the production of cytokines and proteases in human fibroblasts. *Journal of Orthopaedic Research,* 19**,** 621-628.

NOELLE, S., EGIDY, C. C., CROSS, M. B., GEBAUER, M. & KLAUSER, W. 2013. Complication rates after total ankle arthroplasty in one hundred consecutive prostheses. *Int Orthop,* 37**,** 1789-94.

NORDSLETTEN, L., HOGASEN, A. K. M., KONTTINEN, Y. T., SANTAVIRTA, S., ASPENBERG, P. & AASEN, A. O. 1996. Human monocytes stimulation by particles of hydroxyapatite, silicon carbide and diamond: In vitro studies of new prosthesis coatings. *Biomaterials,* 17**,** 1521-1527.

OPPERMANN, J., FRANZEN, J., SPIES, C., FAYMONVILLE, C., KNIFKA, J., STEIN, G. & BREDOW, J. 2013. The microvascular anatomy of the talus: a plastination study on the influence of total ankle replacement. *Surgical and Radiologic Anatomy***,** 1-8.

OTSU, N. 1979. A threshold selection method from gray-level histograms. *IEEE transactions on systems, man, and cybernetics,* 9**,** 62-66.

PAGENSTERT, G. I., HINTERMANN, B., BARG, A., LEUMANN, A. & VALDERRABANO, V. 2007. Realignment surgery as alternative treatment of varus and valgus ankle osteoarthritis. *Clin Orthop Relat Res,* 462**,** 156-68.

PAPPAS, M. 2004. *Reclassification Petition - Amendment: Ankle Joint Metal/Polymer/Metal Anatomically Semi-constrained, Congruent, Mobile Bearing, Porous-coated, Uncemented Prosthesis* [Online]. USA,: Food and Drugs Admistration (FDA). Available: https://www.fda.gov/ohrms/dockets/dailys/04/oct04/.../04p-0457-sup0001-01-vol3.pd [Accessed 08/01/2018 2018].

PAPPAS, M., BUECHEL JR, F. & DEPALMA, A. 1976. Cylindrical total ankle joint replacement: surgical and biomechanical rationale. *Clinical orthopaedics and related research,* 118**,** 82-92.

PEGG, E. C., MELLON, S. J. & GILL, H. S. 2014. Early and Late Mechanical Stability of the Cementless Bone-Implant Interface in Total Joint Arthroplasty. *Bone-Implant Interface in Orthopedic Surgery.* Springer.

PHILIPPE, P., PAUL, C., MARK, M., JEAN-NOEL, C., DELPHINE, P. & THIERRY, J. 2008. Ankle replacement versus arthrodesis: a comparative gait analysis study. *Foot & Ankle International,* 29**,** 3-9.

PINAR, N., VERNET, E., BIZOT, P. & BRILHAULT, J. 2012. Total ankle arthroplasty - total ankle arthroplasty in Western France: influence of volume on complications and clinical outcome. *Orthop Traumatol Surg Res,* 98**,** S26-30.

PREYSSAS, P., TOULLEC, E., HENRY, M., NERON, J.-B., MABIT, C. & BRILHAULT, J. 2012. Total ankle arthroplasty–Three-component total ankle arthroplasty in western France: A radiographic study. *Orthopaedics & Traumatology: Surgery & Research,* 98**,** S31-S40.

PRISSEL, M. A. & ROUKIS, T. S. 2014. Management of Extensive Tibial Osteolysis with the AgilityTM Total Ankle Replacement Systems Using Geometric Metal-Reinforced Polymethylmethacrylate Cement Augmentation. *Journal of Foot and Ankle Surgery,* 53**,** 101-107.

PRISSEL, M. A. & ROUKIS, T. S. 2016. Total ankle replacement based on worldwide registry data trends. *Primary and Revision Total Ankle Replacement.* Springer.

PUGELY, A. J., LU, X., AMENDOLA, A., CALLAGHAN, J. J., MARTIN, C. T. & CRAM, P. 2013. Trends in the Use of Total Ankle Replacement and Ankle Arthrodesis in the United States Medicare Population. *Foot & Ankle International***,** 1071100713511606.

PYEVICH, M. T., SALTZMAN, C. L., CALLAGHAN, J. J. & ALVINE, F. G. 1998. Total Ankle Arthroplasty: a Unique Design. Two to Twelve-Year Follow-up*. *The Journal of Bone & Joint Surgery,* 80**,** 1410-20.

RAIKIN, S. M., RASOULI, M. R., ESPANDAR, R. & MALTENFORT, M. G. 2013. Trends in treatment of advanced ankle arthropathy by total ankle replacement or ankle fusion. *Foot & Ankle International***,** 1071100713517101.

RANAWAT, C., WRIGHT, T. & SCHWARTZ, R. 1986. Retrieval analysis of porous-coated components for total knee arthroplasty: a report of two cases. *Clinical orthopaedics and related research,* 209**,** 244-248.

REGINSTER, J. Y. 2002. The prevalence and burden of arthritis. *Rheumatology,* 41**,** 3-6.

REINDERS, J., VON STILLFRIED, F., ALTAN, E., SONNTAG, R., HEITZMANN, D. W. W. & KRETZER, J. P. 2015. Force-controlled dynamic wear testing of total ankle replacements. *Acta Biomaterialia,* 12**,** 332-340.

RENTFROW, E., JAMES, S., BEAUREGARD, G., LEE, K. & MCLAUGHLIN, J. 1996. Comparison of the in vivo wear rates of 43 surgically retrieved direct compression molded and ram extruded ultra high molecular weight polyethylene acetabular components. *Biomedical sciences instrumentation,* 32**,** 135.

RICHARDS, L., BROWN, C., STONE, M., FISHER, J., INGHAM, E. & TIPPER, J. 2008. Identification of nanometre-sized ultra-high molecular weight polyethylene wear particles in samples retrieved in vivo. *Journal of Bone & Joint Surgery, British Volume,* 90**,** 1106-1113.

RICHARDSON, A. B., DEORIO, J. K. & PAREKH, S. G. 2012. Arthroscopic debridement: effective treatment for impingement after total ankle arthroplasty. *Curr Rev Musculoskelet Med,* 5**,** 171-5.

RIPPSTEIN, P. F., HUBER, M., COETZEE, J. C. & NAAL, F. D. 2011. Total ankle replacement with use of a new three-component implant. *J Bone Joint Surg Am,* 93**,** 1426-35.

ROBERTSSON, O., WINGSTRAND, H., KESTERIS, U., JONSSON, K. & ÖNNERFÄLT, R. 1997. Intracapsular pressure and loosening of hip prostheses Preoperative measurements in 18 hips. *Acta Orthopaedica,* 68**,** 231-234.

RODRIGUES-PINTO, R., MURAS, J., MARTIN OLIVA, X. & AMADO, P. 2013. Functional results and complication analysis after total ankle replacement: early to medium-term results from a Portuguese and Spanish prospective multicentric study. *Foot Ankle Surg,* 19**,** 222-8.

RODRIGUES, D. S. D. O. S. 2013. Biomechanics of the Total Ankle Arthroplasty: Stress Analysis and Bone Remodeling. *STAR,* 1**,** 24.

RODRIGUEZ, D., BEVERNAGE, B. D., MALDAGUE, P., DELEU, P. A., TRIBAK, K. & LEEMRIJSE, T. 2010. Medium term follow-up of the AES ankle prosthesis: High rate of asymptomatic osteolysis. *Foot Ankle Surg,* 16**,** 54-60.

ROKKUM, M., REIGSTAD, A., JOHANSSON, C. B. & ALBREKTSSON, T. 2003. Tissue reactions adjacent to well-fixed hydroxyapatite-coated acetabular cups. Histopathology of ten specimens retrieved at reoperation after 0.3 to 5.8 years. *Journal of Bone and Joint Surgery - Series B,* 85**,** 440-447.

ROSTOKER, W., CHAO, E. & GALANTE, J. 1978. The appearances of wear on polyethylene—a comparison of in vivo and in vitro wear surfaces. *Journal of biomedical materials research,* 12**,** 317-335.

ROUKIS, T. S. & BARTEL, A. F. 2016. Survivorship of First-, Second-, and Third-Generation Total Ankle Replacement Systems. *Primary and Revision Total Ankle Replacement.* Springer.

ROUKIS, T. S. & PRISSEL, M. A. 2013. Registry data trends of total ankle replacement use. *J Foot Ankle Surg,* 52**,** 728-35.

ROUKIS, T. S. & PRISSEL, M. A. 2014. Management of Extensive Talar Osteolysis with AgilityTM Total Ankle Replacement Systems Using Geometric Metal-reinforced Polymethylmethacrylate Cement Augmentation. *Journal of Foot and Ankle Surgery,* 53**,** 108-113.

SALTZMAN, C., TOCHIGI, Y., RUDERT, M., MCIFF, T. & BROWN, T. 2004. The effect of agility ankle prosthesis misalignment on the peri-ankle ligaments. *Clinical orthopaedics and related research,* 424**,** 137-142.

SALTZMAN, C. L., AMENDOLA, A., ANDERSON, R., COETZEE, J. C., GALL, R. J., HADDAD, S. L., HERBST, S., LIAN, G., SANDERS, R. W. & SCIOLI, M. 2003. Surgeon training and complications in total ankle arthroplasty. *Foot & Ankle International,* 24**,** 514-518.

SALTZMAN, C. L., MANN, R. A., AHRENS, J. E., AMENDOLA, A., ANDERSON, R. B., BERLET, G. C., BRODSKY, J. W., CHOU, L. B., CLANTON, T. O., DELAND, J. T., DEORIO, J. K., HORTON, G. A., LEE, T. H., MANN, J. A., NUNLEY, J. A., THORDARSON, D. B., WALLING, A. K., WAPNER, K. L. & COUGHLIN, M. J. 2009. Prospective controlled trial of STAR total ankle replacement versus ankle fusion: initial results. *Foot Ankle Int,* 30**,** 579-96.

SALTZMAN, C. L., SALAMON, M. L., BLANCHARD, G. M., HUFF, T., HAYES, A., BUCKWALTER, J. A. & AMENDOLA, A. 2005. Epidemiology of ankle arthritis: report of a consecutive series of 639 patients from a tertiary orthopaedic center. *The Iowa orthopaedic journal,* 25**,** 44.

SAMMARCO, J. 1977. Biomechanics of the ankle:I. Surface velocity and instant center of rotation in the sagittal plane. *The American Journal of Sports Medicine,* 5**,** 231-234.

SAN GIOVANNI, T. P., KEBLISH, D. J., THOMAS, W. H. & WILSON, M. G. 2006. Eight-year results of a minimally constrained total ankle arthroplasty. *Foot & Ankle International,* 27**,** 418-426.

SANTAVIRTA, S., NORDSTROM, D., YLINEN, P., KONTTINEN, Y. T. & SILVENNOINEN ROKKANEN, T. P. 1991. Biocompatibility of hydroxyapatite-coated hip prostheses. *Archives of Orthopaedic and Trauma Surgery,* 110**,** 288-292.

SAVIO, J., OVERCAMP, L. & BLACK, J. 1994. Size and shape of biomaterial wear debris. *Clinical Materials,* 15**,** 101-147.

SCHENK, K., LIESKE, S., JOHN, M., FRANKE, K., MOULY, S., LIZEE, E. & NEUMANN, W. 2011. Prospective study of a cementless, mobile-bearing, third generation total ankle prosthesis. *Foot & ankle international,* 32**,** 755-763.

SCHIMMEL, J. J., WALSCHOT, L. H. & LOUWERENS, J. W. K. 2014. Comparison of the Short-Term Results of the First and Last 50 Scandinavian Total Ankle

Replacements Assessment of the Learning Curve in a Consecutive Series. *Foot & Ankle International,* 35**,** 326-333.

SCHINDELIN, J., ARGANDA-CARRERAS, I., FRISE, E., KAYNIG, V., LONGAIR, M., PIETZSCH, T., PREIBISCH, S., RUEDEN, C., SAALFELD, S. & SCHMID, B. 2012. Fiji: an open-source platform for biological-image analysis. *Nature methods,* 9**,** 676-682.

SCHIPPER, O. N., HADDAD, S. L., PYTEL, P. & ZHOU, Y. 2017. Histological Analysis of Early Osteolysis in Total Ankle Arthroplasty. *Foot Ankle Int,* 38**,** 351-359.

SCHMALZRIED, T. P., AKIZUKI, K. H., FEDENKO, A. N. & MIRRA, J. 1997. The Role of Access of Joint Fluid to Bone in Periarticular Osteolysis: A Report of Four Cases*. *The Journal of Bone & Joint Surgery Case Connector,* 79**,** 447-52.

SCHMALZRIED, T. P. & CALLAGHAN, J. J. 1999. Current Concepts Review-Wear in Total Hip and Knee Replacements*. *The Journal of Bone & Joint Surgery,* 81**,** 115-136.

SCHMIEDBERG, S. K., CHANG, D. H., FRONDOZA, C. G., VALDEVIT, A. D. & KOSTUIK, J. P. 1994. Isolation and characterization of metallic wear debris from a dynamic intervertebral disc prosthesis. *Journal of biomedical materials research,* 28**,** 1277-1288.

SCHRODER, C., REINDERS, J., ZIETZ, C., UTZSCHNEIDER, S., BADER, R. & KRETZER, J. P. 2013. Characterization of polyethylene wear particle: The impact of methodology. *Acta Biomater,* 9**,** 9485-91.

SCHROEDER, C., GRUPP, T. M., FRITZ, B., SCHILLING, C., CHEVALIER, Y., UTZSCHNEIDER, S. & JANSSON, V. 2013. The influence of third-body particles on wear rate in unicondylar knee arthroplasty: a wear simulator study with bone and cement debris. *Journal of Materials Science: Materials in Medicine,* 24**,** 1319-1325.

SCHUBERTH, J. M., WOOD, D. A. & CHRISTENSEN, J. C. 2016. Gutter Impingement in Total Ankle Arthroplasty. *Foot & Ankle Specialist,* 9**,** 145-58.

SCHUNCK, A., KRONZ, A., FISCHER, C. & BUCHHORN, G. H. 2016. Release of zirconia nanoparticles at the metal stem–bone cement interface in implant loosening of total hip replacements. *Acta biomaterialia,* 31**,** 412-424.

SCOTT, M., WIDDING, K. & JANI, S. 2001. Do current wear particle isolation procedures underestimate the number of particles generated by prosthetic bearing components? *Wear,* 251**,** 1213-1217.

SHANBHAG, A. S., JACOBS, J. J., BLACK, J., GALANTE, J. O. & GLANT, T. T. 1995. Human monocyte response to particulate biomaterials generated in vivo and in vitro. *Journal of orthopaedic research,* 13**,** 792-801.

SHANBHAG, A. S., JACOBS, J. J., GLANT, T. T., GILBERT, J. L., BLACK, J. & GALANTE, J. O. 1994. Composition and morphology of wear debris in failed uncemented total hip replacement. *Journal of Bone & Joint Surgery, British Volume,* 76**,** 60-67.

SHON, W. Y., GUPTA, S., BISWAL, S., HAN, S. H., HONG, S. J. & MOON, J. G. 2009. Pelvic osteolysis relationship to radiographs and polyethylene wear. *The Journal of arthroplasty,* 24**,** 743-750.

SIEGLER, S., CHEN, J. & SCHNECK, C. 1988. The three-dimensional kinematics and flexibility characteristics of the human ankle and subtalar joints—Part I: Kinematics. *Journal of biomechanical engineering,* 110**,** 364-373.

SIEGLER, S., TOY, J., SEALE, D. & PEDOWITZ, D. 2014. The Clinical Biomechanics Award 2013 -- presented by the International Society of Biomechanics: new observations on the morphology of the talar dome and its relationship to ankle kinematics. *Clin Biomech (Bristol, Avon),* 29**,** 1-6.

SIEVING, A., WU, B., MAYTON, L., NASSER, S. & WOOLEY, P. H. 2003. Morphological characteristics of total joint arthroplasty-derived ultra-high molecular weight polyethylene (UHMWPE) wear debris that provoke

inflammation in a murine model of inflammation. *Journal of biomedical materials research Part A,* 64**,** 457-464.

SINGER, S., KLEJMAN, S., PINSKER, E., HOUCK, J. & DANIELS, T. 2013. Ankle arthroplasty and ankle arthrodesis: gait analysis compared with normal controls. *J Bone Joint Surg Am,* 95**,** e191(1-10).

SINGH, G., REICHARD, T., HAMEISTER, R., AWISZUS, F., SCHENK, K., FEUERSTEIN, B., ROESSNER, A. & LOHMANN, C. 2016. Ballooning osteolysis in 71 failed total ankle arthroplasties: Is hydroxyapatite a risk factor? *Acta Orthopaedica,* 87**,** 401-405.

SKYTTA, E. T., KOIVU, H., ESKELINEN, A., IKAVALKO, M., PAAVOLAINEN, P. & REMES, V. 2010. Total ankle replacement: a population-based study of 515 cases from the Finnish Arthroplasty Register. *Acta Orthop,* 81**,** 114-8.

ŠLOUF, M., ŠLOUFOVÁ, I., HORAK, Z., ŠTÉPÁNEK, P., ENTLICHER, G., KREJČÍK, M., RADONSKÝ, T., POKORNÝ, D. & SOSNA, A. 2004. New fast method for determination of number of UHMWPE wear particles. *Journal of Materials Science: Materials in Medicine,* 15**,** 1267-1278.

SMALL BONE INNOVATIONS INC. 2009. STAR: Surgical Technique. Morrisville, PA, USA: Small Bone Innovations Inc, .

SMALL BONES INNOVATIONS INC. 2007. *Summary of Safety and Effectiveness (SSED): Scandinavian Total Ankle Replacement System (STAR Ankle)* [Online]. USA,: Food and Drugs Admistration (FDA). Available: https://www.accessdata.fda.gov/cdrh_docs/pdf5/P050050b.pdf [Accessed 08/01/2018 2018].

SMITH, R. & WOOD, P. 2007. Arthrodesis of the ankle in the presence of a large deformity in the coronal plane. *Journal of Bone & Joint Surgery, British Volume,* 89**,** 615-619.

SMYTH, A., FISHER, J., SUNER, S. & BROCKETT, C. 2017. Influence of kinematics on the wear of a total ankle replacement. *J Biomech.*

SOPHER, R. S., AMIS, A. A., CALDER, J. D. & JEFFERS, J. R. T. 2017. Total ankle replacement design and positioning affect implant-bone micromotion and bone strains. *Medical Engineering and Physics,* 42**,** 80-90.

SPIRT, A. A., ASSAL, M. & HANSENJR, S. T. 2004. Complications and failure after total ankle arthroplasty. *The Journal of Bone & Joint Surgery,* 86**,** 1172-1178.

SPROULE, J., CHIN, T., AMIN, A., DANIELS, T., YOUNGER, A., BOYD, G. & GLAZEBROOK, M. 2013. Clinical and Radiographic Outcomes of the Mobility Total Ankle Arthroplasty System Early Results From a Prospective Multicenter Study. *Foot & Ankle International,* 34**,** 491-497.

STAUFFER, R., CHAO, E. & BREWSTER, R. 1977. Force and motion analysis of the normal, diseased, and prosthetic ankle joint. *Clinical orthopaedics and related research,* 127**,** 189-196.

STENGEL, D., BAUWENS, K., EKKERNKAMP, A. & CRAMER, J. 2005. Efficacy of total ankle replacement with meniscal-bearing devices: a systematic review and meta-analysis. *Arch Orthop Trauma Surg,* 125**,** 109-19.

SUMMERS, J. C. & BEDI, H. S. 2013. Reoperation and patient satisfaction after the Mobility total ankle arthroplasty. *ANZ J Surg,* 83**,** 371-5.

SUN, J. S., LIN, F. H., HUNG, T. Y., TSUANG, Y. H., CHANG, W. H. S. & LIU, H. C. 1999. The influence of hydroxyapatite particles on osteoclast cell activities. *Journal of biomedical materials research,* 45**,** 311-321.

SUNG, K.-S., AHN, J., LEE, K.-H. & CHUN, T.-H. 2014. Short-term Results of Total Ankle Arthroplasty for End-stage Ankle Arthritis With Severe Varus Deformity. *Foot & Ankle International,* 35**,** 225-231.

TARR, R. R., RESNICK, C. T., WAGNER, K. S. & SARMIENTO, A. 1985. Changes in tibiotalar joint contact areas following experimentally induced tibial angular deformities. *Clinical orthopaedics and related research,* 199**,** 72-80.

TEETER, M. G., HOWARD, J. L., MCCALDEN, R. W. & NAUDIE, D. D. 2017. Comparison of articular and backside polyethylene wear in mobile bearing unicompartmental knee replacement. *Knee,* 24**,** 429-433.

TEETER, M. G., MILNER, J. S., NAUDIE, D. D. & MACDONALD, S. J. 2014. Surface extraction can provide a reference for micro-CT analysis of retrieved total knee implants. *Knee,* 21**,** 801-5.

TEETER, M. G., NAUDIE, D. D., CHARRON, K. D. & HOLDSWORTH, D. W. 2010. Three-dimensional surface deviation maps for analysis of retrieved polyethylene acetabular liners using micro-computed tomography. *J Arthroplasty,* 25**,** 330-2.

TEETER, M. G., NAUDIE, D. D., MCERLAIN, D. D., BRANDT, J. M., YUAN, X., MACDONALD, S. J. & HOLDSWORTH, D. W. 2011a. In vitro quantification of wear in tibial inserts using microcomputed tomography. *Clin Orthop Relat Res,* 469**,** 107-12.

TEETER, M. G., NAUDIE, D. D., MILNER, J. S. & HOLDSWORTH, D. W. 2011b. Determination of reference geometry for polyethylene tibial insert wear analysis. *J Arthroplasty,* 26**,** 497-503.

TENNANT, J. N., RUNGPRAI, C., PIZZIMENTI, M. A., GOETZ, J., PHISITKUL, P., FEMINO, J. & AMENDOLA, A. 2014. Risks to the blood supply of the talus with four methods of total ankle arthroplasty: A cadaveric injection study. *Journal of Bone and Joint Surgery - Series A,* 96**,** 395-402.

TIPPER, J., INGHAM, E., HAILEY, J., BESONG, A., FISHER, J., WROBLEWSKI, B. & STONE, M. 2000. Quantitative analysis of polyethylene wear debris, wear rate and head damage in retrieved Charnley hip prostheses. *Journal of Materials Science: Materials in Medicine,* 11**,** 117-124.

TIPPER, J. L., GALVIN, A. L., WILLIAMS, S., MCEWEN, H. M., STONE, M. H., INGHAM, E. & FISHER, J. 2006. Isolation and characterization of UHMWPE wear particles down to ten nanometers in size from in vitro hip and knee joint simulators. *J Biomed Mater Res A,* 78**,** 473-80.

TOCHIGI, Y., RUDERT, M., BROWN, T., MCIFF, T. & SALTZMAN, C. 2005. The effect of accuracy of implantation on range of movement of the Scandinavian Total Ankle Replacement. *Journal of Bone & Joint Surgery, British Volume,* 87**,** 736-740.

TONINO, A., OOSTERBOS, C., RAHMY, A., THERIN, M. & DOYLE, C. 2001. Hydroxyapatite-coated acetabular components. Histological and histomorphometric analysis of six cups retrieved at autopsy between three and seven years after successful implantation. *Journal of Bone and Joint Surgery - Series A,* 83**,** 817-825.

TONINO, A. J., ROKKUM, M., REIGSTAD, A. & JOHANSSON, C. 2003. HA particles can be released from well-fixed HA-coated stems. *Acta Orthopaedica Scandinavica,* 74**,** 365-368.

TONINO, A. J., THERIN, M. & DOYLE, C. 1999. Hydroxyapatite-coated femoral stems. Histology and histomorphometry around five components retrieved at post mortem. *Journal of Bone & Joint Surgery - British Volume,* 81**,** 148-54.

TOPOLOVEC, M., COR, A. & MILOSEV, I. 2014. Metal-on-metal vs. metal-on-polyethylene total hip arthroplasty tribological evaluation of retrieved components and periprosthetic tissue. *J Mech Behav Biomed Mater,* 34**,** 243-52.

TOPOLOVEC, M., MILOŠEV, I., CÖR, A. & BLOEBAUM, R. D. 2013. Wear debris from hip prostheses characterized by electron imaging. *Central European Journal of Medicine,* 8**,** 476-484.

ULRICH, S. D., SEYLER, T. M., BENNETT, D., DELANOIS, R. E., SALEH, K. J., THONGTRANGAN, I., KUSKOWSKI, M., CHENG, E. Y., SHARKEY, P. F. & PARVIZI, J. 2008. Total hip arthroplasties: what are the reasons for revision? *International orthopaedics,* 32**,** 597-604.

URBAN, R. M., JACOBS, J. J., TOMLINSON, M. J., GAVRILOVIC, J., BLACK, J. & PEOC'H, M. 2000. Dissemination of wear particles to the liver, spleen, and abdominal lymph nodes of patients with hip or knee replacement. *JBJS,* 82**,** 457.

USUELLI, F. G., MACCARIO, C., INDINO, C., MANZI, L. & GROSS, C. E. 2016a. Tibial slope in total ankle arthroplasty: Anterior or lateral approach. *Foot and Ankle Surgery.,* 07.

USUELLI, F. G., MANZI, L. & MACCARIO, C. 2016b. Posterior talar shifting in mobile-bearing and fix-bearing total ankle replacement. *Foot and Ankle Surgery,* 1)**,** 50.

VALDERRABANO, V., HINTERMANN, B. & DICK, W. 2004. Scandinavian total ankle replacement: a 3.7-year average followup of 65 patients. *Clinical orthopaedics and related research,* 424**,** 47-56.

VALDERRABANO, V., NIGG, B. M., VON TSCHARNER, V., FRANK, C. B. & HINTERMANN, B. 2007a. J. Leonard Goldner Award 2006. Total ankle replacement in ankle osteoarthritis: an analysis of muscle rehabilitation. *Foot Ankle Int,* 28**,** 281-91.

VALDERRABANO, V., NIGG, B. M., VON TSCHARNER, V., STEFANYSHYN, D. J., GOEPFERT, B. & HINTERMANN, B. 2007b. Gait analysis in ankle osteoarthritis and total ankle replacement. *Clin Biomech (Bristol, Avon),* 22**,** 894-904.

VAN DER HEIDE, H. J., SCHUTTE, B., LOUWERENS, J. W. K., VAN DEN HOOGEN, F. H. & DE WAAL MALEFIJT, M. C. 2009. Total ankle prostheses in rheumatoid arthropathy: outcome in 52 patients followed for 1–9 years. *Acta orthopaedica,* 80**,** 440-444.

VAN WIJNGAARDEN, R., VAN DER PLAAT, L., NIEUWE WEME, R. A., DOETS, H. C., WESTERGA, J. & HAVERKAMP, D. 2015. Etiopathogenesis of osteolytic cysts associated with total ankle arthroplasty, A histological study. *Foot and Ankle Surgery,* 21**,** 132-136.

VAUPEL, Z., BAKER, E. A., BAKER, K. C., KURDZIEL, M. D. & FORTIN, P. T. 2009. Analysis of retrieved agility total ankle arthroplasty systems. *Foot Ankle Int,* 30**,** 815-23.

VERUVA, S. Y., LANMAN, T. H., ISAZA, J. E., MACDONALD, D. W., KURTZ, S. M. & STEINBECK, M. J. 2015. UHMWPE wear debris and tissue reactions are reduced for contemporary designs of lumbar total disc replacements. *Clinical Orthopaedics and Related Research®,* 473**,** 987-998.

VISTE, A., N, A. L. Z., BRITO, N., LIENHART, C., FESSY, M. H. & BESSE, J. L. 2015. Periprosthetic osteolysis after AES total ankle replacement: Conventional radiography versus CT-scan. *Foot and Ankle Surgery,* 21**,** 164-170.

WAIZY, H., BEHRENS, B.-A., RADTKE, K., ALMOHALLAMI, A., STUKENBORG-COLSMAN, C. & BOUGUECHA, A. 2017. Bone cyst formation after ankle arthroplasty may be caused by stress shielding. A numerical simulation of the strain adaptive bone remodelling. *The Foot,* 33**,** 14-19.

WALDE, T. A., WEILAND, D. E., LEUNG, S. B., KITAMURA, N., SYCHTERZ, C. J., ENGH JR, C. A., CLAUS, A. M., POTTER, H. G. & ENGH SR, C. A. 2005. Comparison of CT, MRI, and radiographs in assessing pelvic osteolysis: a cadaveric study. *Clinical orthopaedics and related research,* 437**,** 138-144.

WANG, J. S., GOODMAN, S. & ASPENBERG, P. 1994. Bone formation in the presence of phagocytosable hydroxyapatite particles. *Clinical Orthopaedics and Related Research***,** 272-279.

WASIELEWSKI, R. C., GALANTE, J. O., LEIGHTY, R. M., NATARAJAN, R. N. & ROSENBERG, A. G. 1994. Wear patterns on retrieved polyethylene tibial inserts and their relationship to technical considerations during total knee arthroplasty. *Clinical orthopaedics and related research,* 299**,** 31-43.

WATANABE, K., CREVOISIER, X. M., KITAOKA, H. B., ZHAO, K. D., BERGLUND, L. J., KAUFMAN, K. R. & AN, K. N. 2009. Analysis of joint laxity after total ankle arthroplasty: cadaver study. *Clin Biomech (Bristol, Avon),* 24**,** 655-60.

WEBER, M., BONNIN, M., COLUMBIER, J. & JUDET, T. 2004. Erste Ergebnisse der SALTO-Sprunggelenkendoprothese: Eine französische Multizenterstudie mit 115 Implantaten. *Fuß & Sprunggelenk,* 2**,** 29-37.

WILLERT, H., LUDWIG, J. & SEMLITSCH, M. 1974. Reaction of bone to methacrylate after hip arthroplasty: a long-term gross, light microscopic, and scanning electron microscopic study. *The Journal of bone and joint surgery. American volume,* 56**,** 1368.

WILLERT, H. G. & SEMLITSCH, M. 1977. Reactions of the articular capsule to wear products of artificial joint prostheses. *Journal of biomedical materials research,* 11**,** 157-164.

WILLIE, B., SHEA, J., BLOEBAUM, R. & HOFMANN, A. 2000. Elemental and morphological identification of third-body particulate and calcium stearate inclusions in polyethylene components. *Journal of biomedical materials research,* 53**,** 137-142.

WOLFF, J., MAQUET, P. & FURLONG, R. 1986. *The law of bone remodelling,* Springer-Verlag Berlin.

WOOD, P. & DEAKIN, S. 2003. Total ankle replacement The results in 200 ankles. *Journal of Bone & Joint Surgery, British Volume,* 85**,** 334-341.

WOOD, P., PREM, H. & SUTTON, C. 2008. Total ankle replacement MEDIUM-TERM RESULTS IN 200 SCANDINAVIAN TOTAL ANKLE REPLACEMENTS. *Journal of Bone & Joint Surgery, British Volume,* 90**,** 605-609.

WOOD, P., SUTTON, C., MISHRA, V. & SUNEJA, R. 2009. A randomised, controlled trial of two mobile-bearing total ankle replacements. *Bone & Joint Journal,* 91**,** 69-74.

WOOD, P. L., CLOUGH, T. M. & JARI, S. 2000. Clinical comparison of two total ankle replacements. *Foot & Ankle International,* 21**,** 546-550.

WRIGHT, T. M., RIMNAC, C. M., STULBERG, S. D., MINTZ, L., TSAO, A. K., KLEIN, R. W. & MCCRAE, C. 1992. Wear of polyethylene in total joint replacements: Observations from retrieved PCA knee implants. *Clinical orthopaedics and related research,* 276**,** 126-134.

YAMAGUCHI, S., TANAKA, Y., BANKS, S., KOSUGI, S., SASHO, T., TAKAHASHI, K. & TAKAKURA, Y. 2012. In vivo kinematics and articular surface congruency of total ankle arthroplasty during gait. *J Biomech,* 45**,** 2103-8.

YAMAGUCHI, S., TANAKA, Y., KOSUGI, S., TAKAKURA, Y., SASHO, T. & BANKS, S. A. 2011. In vivo kinematics of two-component total ankle arthroplasty during non-weightbearing and weightbearing dorsiflexion/plantarflexion. *J Biomech,* 44**,** 995-1000.

YAMAMOTO, K., IMAKIIRE, A., MASAOKA, T., SHISHIDO, T., MIZOUE, T., CLARKE, I. C., SHOJI, H., KAWANABE, K. & TAMURA, J. 2003. Wear mode and wear mechanism of retrieved acetabular cups. *International orthopaedics,* 27**,** 286-290.

YAN, Y., NEVILLE, A., DOWSON, D., WILLIAMS, S. & FISHER, J. 2010. Tribofilm formation in biotribocorrosion–does it regulate ion release in metal-on-metal artificial hip joints? *Proceedings of the Institution of Mechanical Engineers, Part J: Journal of Engineering Tribology,* 224**,** 997-1006.

YAO, J. J., LEWALLEN, E. A., TROUSDALE, W. H., XU, W., THALER, R., SALIB, C. G., REINA, N., ABDEL, M. P., LEWALLEN, D. G. & VAN WIJNEN, A. J. 2017. Local Cellular Responses to Titanium Dioxide from Orthopedic Implants. *BioResearch open access,* 6**,** 94-103.

YOON, H. S., LEE, J., CHOI, W. J. & LEE, J. W. 2014. Periprosthetic osteolysis after total ankle arthroplasty. *Foot Ankle Int,* 35**,** 14-21.

ZAIDI, R., CRO, S., GURUSAMY, K., SIVA, N., MACGREGOR, A., HENRICSON, A. & GOLDBERG, A. 2013. The outcome of total ankle replacement: A systematic review and meta-analysis. *Bone and Joint Journal,* 95 B**,** 1500-1507.

ZHAO, H., YANG, Y., YU, G. & ZHOU, J. 2011. A systematic review of outcome and failure rate of uncemented Scandinavian total ankle replacement. *Int Orthop,* 35**,** 1751-8.

ZOLOTAREVOVA, E., ENTLICHER, G., PAVLOVA, E., SLOUF, M., POKORNY, D., VESELY, F., GALLO, J. & SOSNA, A. 2010. Distribution of polyethylene wear

particles and bone fragments in periprosthetic tissue around total hip joint replacements. *Acta biomaterialia,* 6**,** 3595-3600.

ZWEYMULLER, K. A., LINTNER, F. K. & SEMLITSCH, M. F. 1988. Biologic fixation of a press-fit titanium hip joint endoprosthesis. *Clinical orthopaedics and related research,* 235**,** 195-206.

Appendix A: Design Drawings

This appendix includes the design drawings for the component holders used to constrain the individual TAR components for Chapter 6. The component holder for the tibial component and the bearing insert used an interchangeable top plate which was specific to the respective component. The talar component holder was a separate device.

A.1   Tibial Component and Bearing Insert Holder
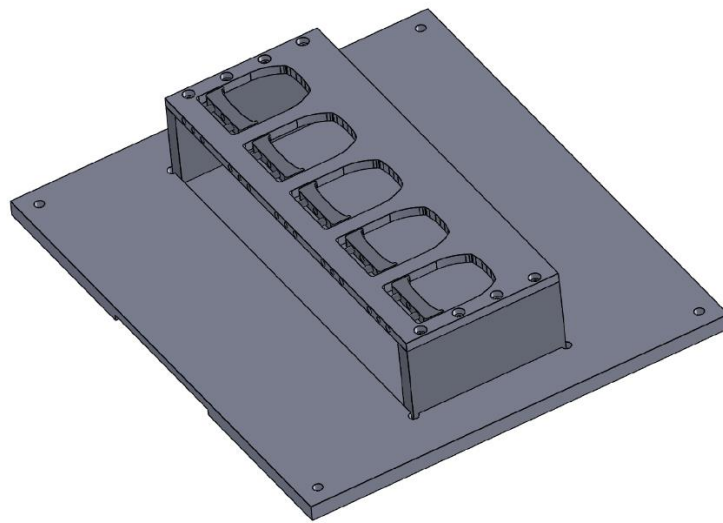
Assembly
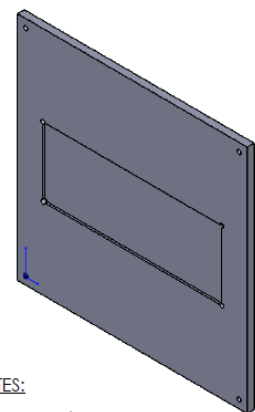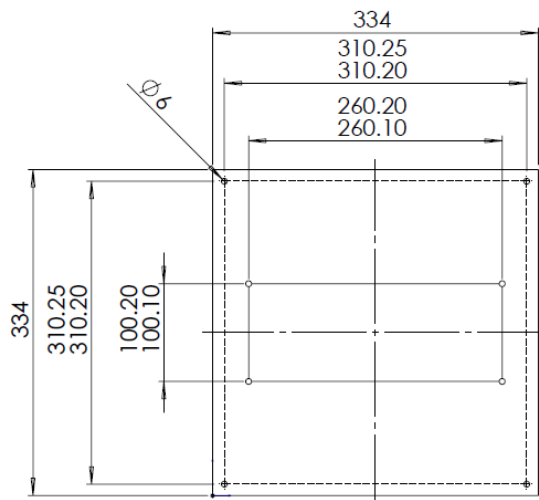
NOTES:

ALL HOLES ⌀6mm

TOP 260x100 RECESS = 3mm DEEP

BOTTOM 300X250 RECESS = 4mm DEEP

PLEASE BREAK ALL EDGES AND CORNERS WITH A SMALL CHAMFER

Component Holder Base Plate

Top Plate Legs

100.00
99.90

12.50   25   25   25   12.50

16
14

50.00
49.90

M4   M4   M4   M4

10.00
9.90

Clamp Pins

20

⌀ 4.00
3.98

Bearing Insert Clamp

R0.50   R0.50

12

5

R2   R2

30

10   10

6

⌀ 4.02
4.00   ⌀ 4.15   ⌀ 4.02
4.00

R1   R1

12

5

R2   R2

38

10   10

6

∅4.02
4.00

∅4.15

∅4.02
4.00

Tibial Component Clamp

NOTES:

PLEASE BREAK ALL EDGES AND CORNERS WITH A SMALL CHAMFER

260.00
259.90

12.50

25

25

25

100.00
99.90

40

57

R2   R2

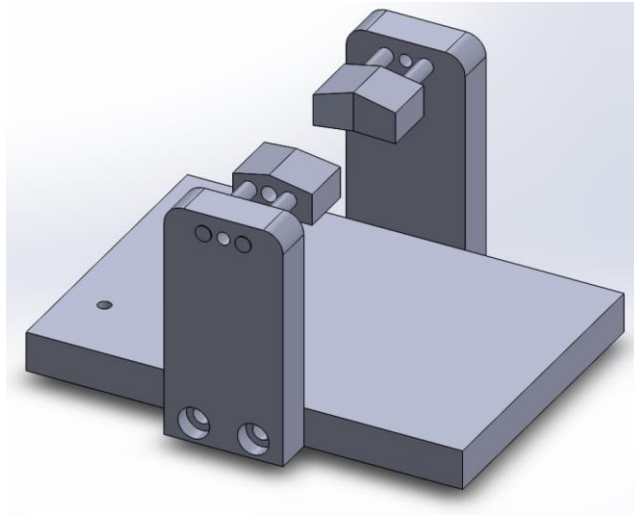14

12.50

5

50   50   50   50

6

∅7.20

4

∅4.15

10

10

∅4.15

M4
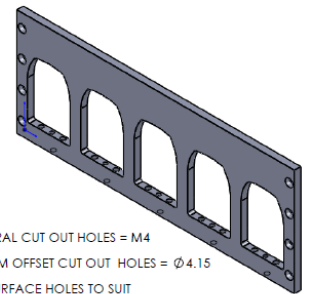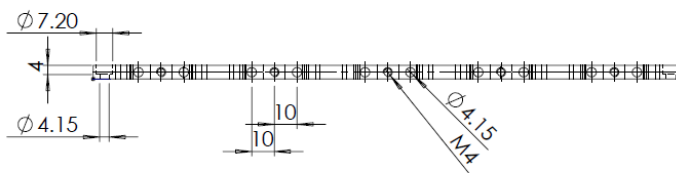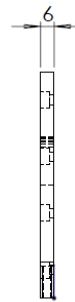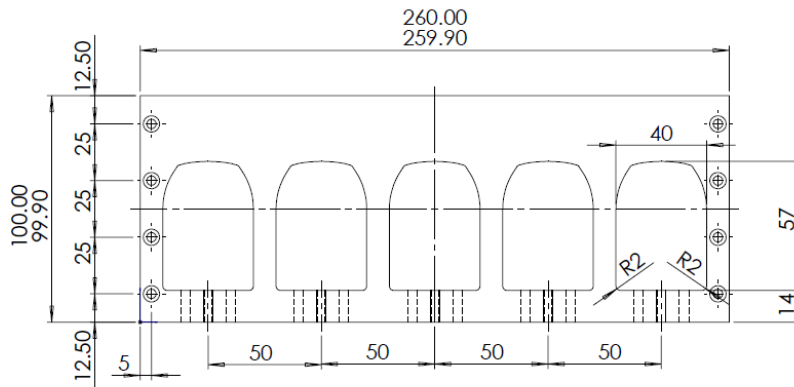
NOTES:

ALL (5x) CENTRAL CUT OUT HOLES = M4

ALL (10X) 10MM OFFSET CUT OUT HOLES = ∅4.15

ALL (8x) TOPSURFACE HOLES TO SUIT
M4 SOCKETHEAD CAPHEAD WITH CLEARANCE

1MM ROUNDED FILLET ON INSIDE EDGES OF EACH SIDE
OF EVERY CUT OUT

PLEASE BREAK ALL OTHER EDGES AND CORNERS
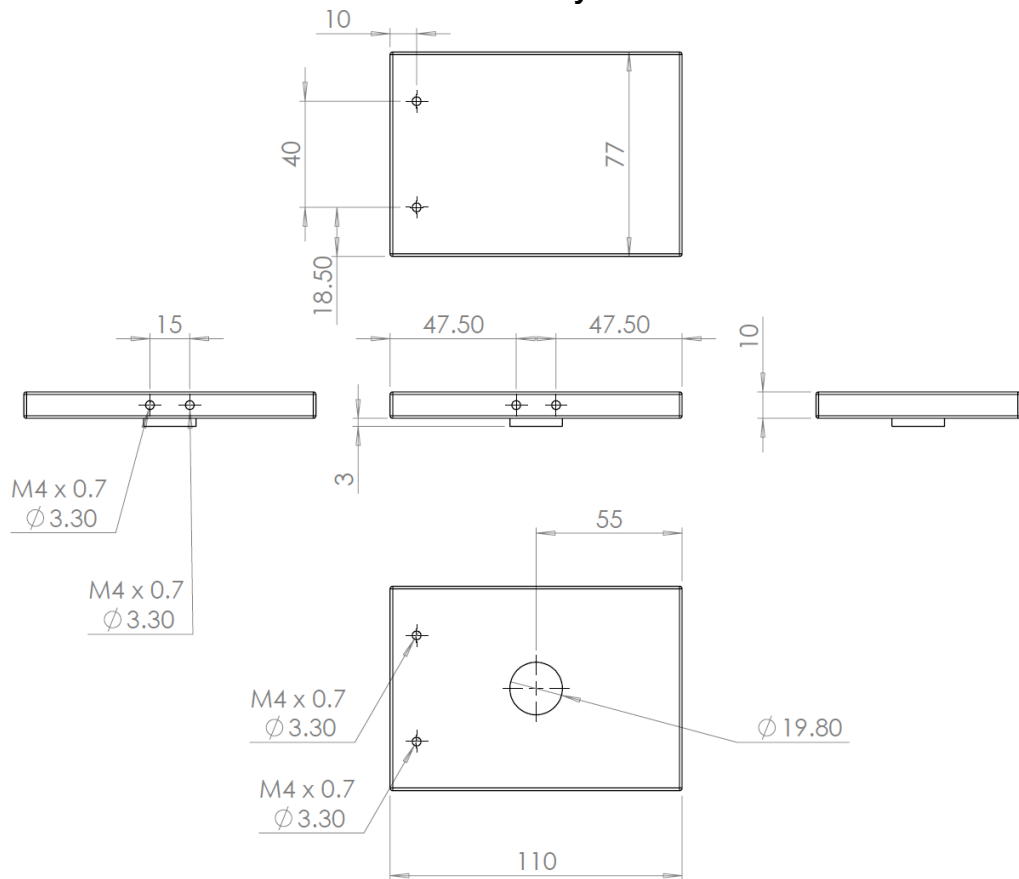WITH A SMALL CHAMFER
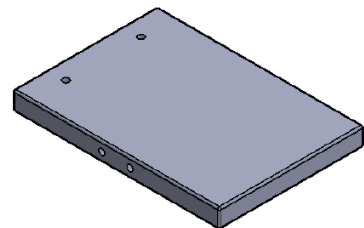
Tibial Component Top Plate

260.00
259.90

12.50

100.00
99.90

25

25

25

25

12.50

32

40.84

R2 R2

22.16

5 50 50 50 50 5

Ø7.20

4

Ø4.15

10

10

M4

Ø4.15

NOTES:

ALL (5x) CENTRAL CUT OUT HOLES = M4

ALL (10X) 10MM OFFSET CUT OUT HOLES = Ø4.15

ALL (8x) TOPSURFACE HOLES TO SUIT
M4 SOCKETHEAD CAPHEAD WITH CLEARANCE

1MM ROUNDED FILLET ON INSIDE EDGES OF EACH SIDE
OF EVERY CUT OUT

PLEASE BREAK ALL OTHER EDGES AND CORNERS
WITH A SMALL CHAMFER

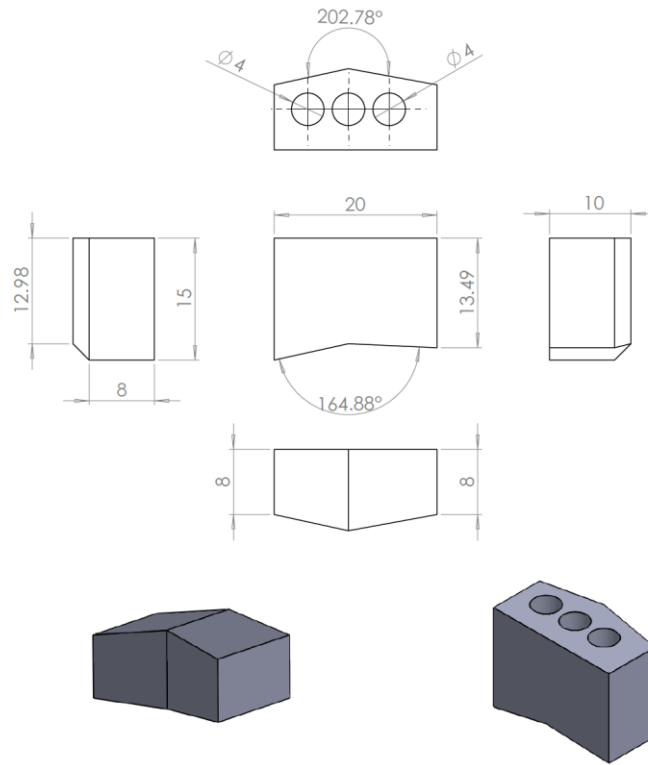**Bearing Insert Top Plate**

A.2 Talar Component Holder

Assembly

10

40

77

18.50

15

47.50

47.50

10

M4 x 0.7
⌀ 3.30

3

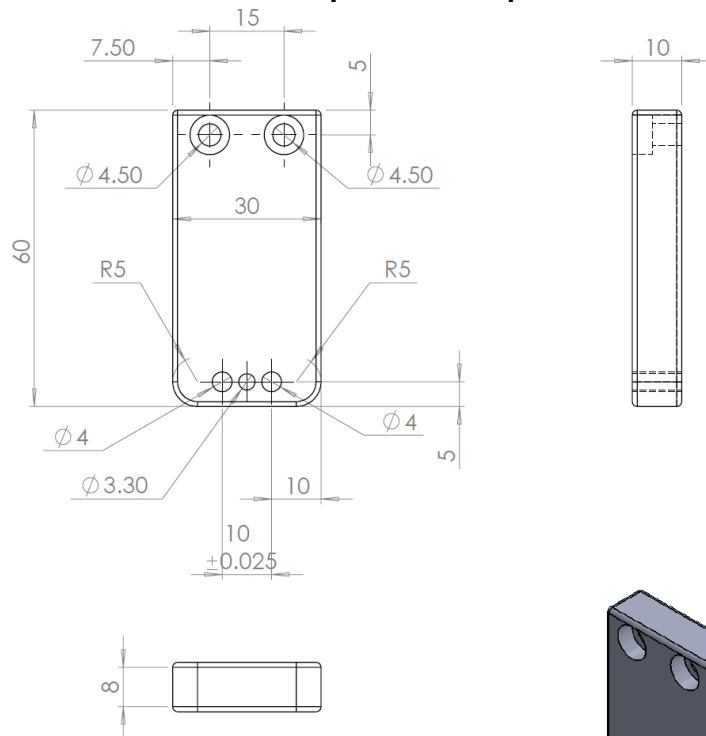M4 x 0.7
⌀ 3.30

55

M4 x 0.7
⌀ 3.30

⌀ 19.80

M4 x 0.7
⌀ 3.30

110

Notes:
Please break all edges with a 1mm
45 deg chamfer

Finish:
3.2um Ra Max
Tolerance on machined
dimensions as follows:
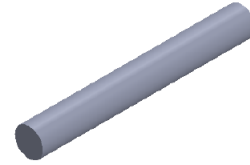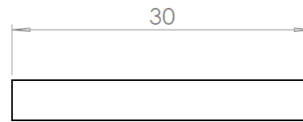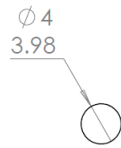0-500±0.1 500-1000±0.2

Talar Component Holder Base Plate

202.78°

Ø4   Ø4

20   10

12.98   15   13.49

8   164.88°

8   8

Talar Component Clamp

15   10

7.50   5

Ø4.50   Ø4.50

30

60

R5   R5

Ø4   Ø4

Ø3.30   10

5

10
±0.025

8

Notes:
Please break all edges with a 1mm
45 deg chamfer

Finish:
3.2um Ra Max
Tolerance on machined
dimensions as follows:
0-500±0.1 500-1000±0.2

Component Holder Support Arm

⌀ 4
3.98

30

Notes:
Please break all edges with a small chamfer
Finish:
3.2um Ra Max
Tolerance on machined dimensions as follows:
0-500±0.1 500-1000±0.2

Support Arm Pin